Adsorption Science & Technology

# Adsorption Properties of Advanced Functional Materials for Environmental Applications

Lead Guest Editor: Hesham Hamad
Guest Editors: Mona M. Abd El-Latif and Randa Khalifa

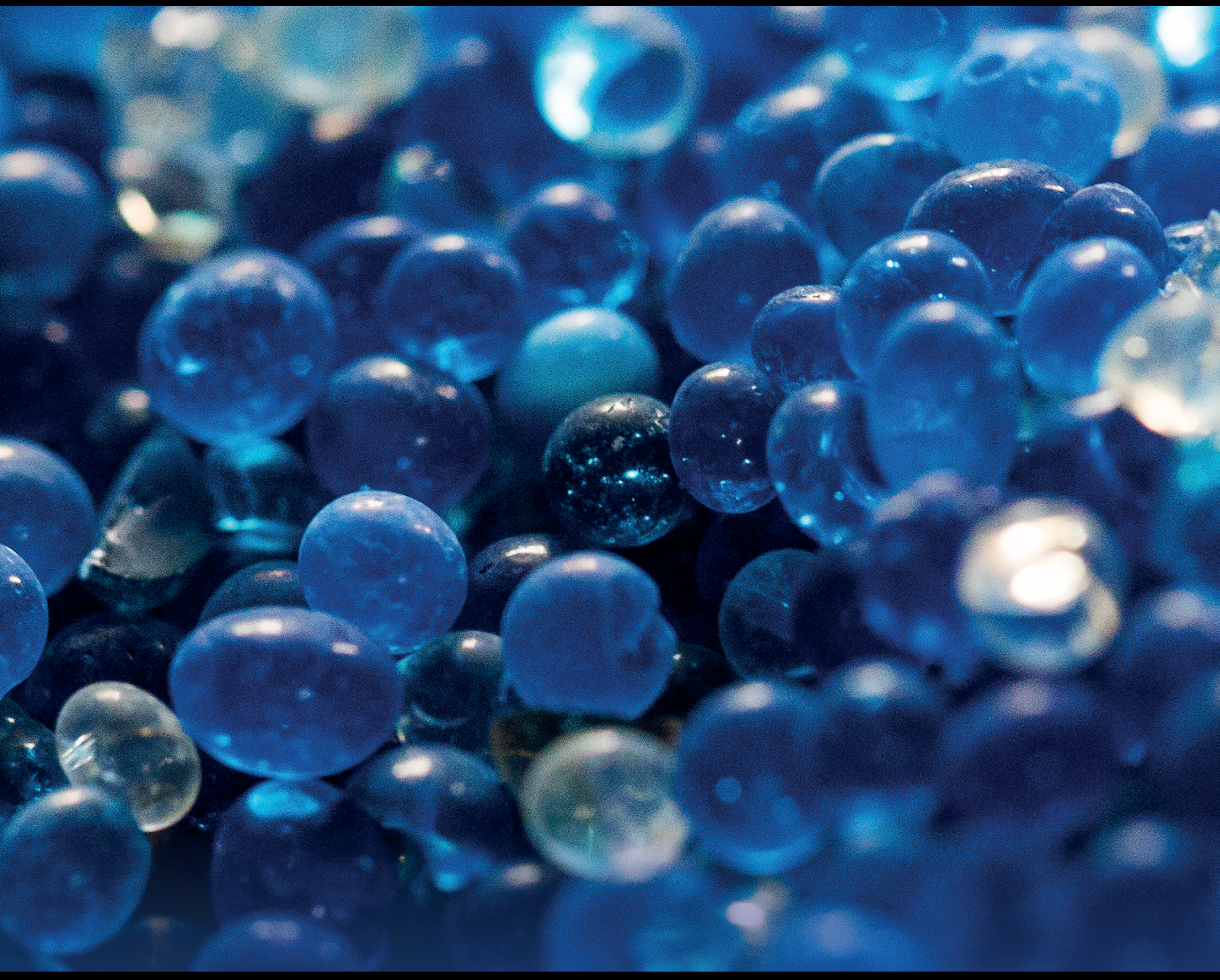

# Adsorption Properties of Advanced Functional Materials for Environmental Applications

Adsorption Science & Technology

# Adsorption Properties of Advanced Functional Materials for Environmental Applications

Lead Guest Editor: Hesham Hamad
Guest Editors: Mona M. Abd El-Latif and Randa Khalifa

# Contents

# Contents

Hindawi
Adsorption Science & Technology
Volume 2023, Article ID 1475278, 12 pages
https://doi.org/10.1155/2023/1475278

*Research Article*

# Green Synthesis of Calcium/Iron-Layered Double Hydroxides-Sodium Alginate Nanoadsorbent as Reactive Barrier for Antibiotic Amoxicillin Removal from Groundwater

**Marwa F. Abed and Ayad A. H. Faisal**

*Department of Environmental Engineering, College of Engineering, University of Baghdad, Baghdad, Iraq*

Correspondence should be addressed to Marwa F. Abed; marwaspider@gmail.com

Received 24 July 2022; Revised 4 January 2023; Accepted 28 March 2023; Published 17 April 2023

Academic Editor: Muhammad Raziq Rahimi Kooh



This work uses a new nanoadsorbent after chemically synthesis from chicken eggshell wastes for removing amoxicillin (AMX) from aqueous solution. This removal was examined as a time function, initial concentration of AMX, pH, agitation speed, and adsorbent dosage. The study achieved the optimum time for equilibration in (90) min, at pH = 7 with an adsorbent dosage of 1.2 g. We applied many kinetic models to the sorption kinetic data where the pseudo-second-order model ($R^2 = 0.9924$) was used to interpret the gained data at a rate constant $K_2$ of (0.0077) g/(mg. min) at 200 rpm. Moreover, the adsorption calculated amount reached the experimentally required value and isotherm data best fitted the Langmuir model with $R^2$ (≥0.9486) than the Freundlich model. The intraparticle diffusion model revealed a diffusion dependent process. The different functional sets on the calcium/iron-surface as a layered double hydroxide (Ca/Fe)-LDH were important in sorpting the selected antibiotic. Forming (Ca/Fe)-LDH nanoparticles in the manufactured beads interacted with polluted water confirming that the nanoparticles own the prospective for acting as a latent sorbent to remove contaminants from aquatic media.

## 1. Introduction

A very significant natural resource is groundwater to both terrestrial and aquatic ecosystems. One third of the world's population drinks groundwater as their primary potable source and uses it for domestic, production of food, industry [1], and irrigation of 40% of the food worldwide [2], despite its limited ecological resources consisting of a small portion of the total water distribution [3, 4]. While the standards and needs of living on our natural environment are expanding, rising populations, ongoing urbanization, and industry increase the risk of groundwater contamination [5]. In addition, numerous reports showed dangerous groundwater contamination caused by accidental spills, unsafe disposing industrial chemicals, agricultural practices, mining, etc. Contaminants are dangerous to human health. They also make natural ecosystems vulnerable, and the same is true with the long-term socioeconomic [6] including toxic metals and hydrocarbons. In addition, the organic trace pollutants, pharmaceutical polluting elements, and pesticides face the same, and if managed improperly, groundwater reservation can result in the release of these pollutants into the environment [7, 8]. Antibiotics are one of the most commonly used classes of pharmaceutical compounds, and they are perhaps the most effective class of drugs ever created for enhancing human health. They also prevent and treat animal and plant infections and raise productivity in the livestock industry [9]. Its use is expected to be on the order of 100 000 to 200 000 tons per year throughout the world [10]. Yet, the World Health Organization [11] claimed that only some nations possess national statistics of the antibiotic usage, quantities, and patterns. As a result, the quantity of antibiotics consumed is not clear. Its main sources are human and animal incompletely metabolized antibiotics in the environment. Since humans excrete a large portion of their antibiotics in the form of feces or urine, as well as through disposing

leftover hospital antibiotics and wastes, antibiotics are ubiquitous in nature, and their residues have frequently been found in various environmental matrices [12, 13]. AMX was first made available for human use in the early 1970s in the United Kingdom. Since then, it has been discovered in a variety of water bodies due to its widespread use to resist many gram-positive and -negative microorganisms and its status as a first-line antibiotic in numerous nations [14]. Beside the human medicine use, amoxicillin treats and prevents animal infections for increasing growth in a variety of domestic and food animals for broiler chickens, dogs, cats, horses, pigeons, pigs, sheep, goats, preruminating calves, cattle, and fish [15]. Usually, amoxicillin environmental degradation by a number of processes, such as (1) sorption, (2) transformation in biotics, and (3) transformation in abiotics, can influence the destiny and transit of organic compounds in the environment [16]. Over the years, the developments of treatment technologies and approaches for contaminated groundwater have become available allowing flexibility in how clean-up goals can be achieved. Permeable reactive barriers (PRBs) as treatments, depending on sorption process since it removes groundwater contaminants, have been widely examined [17]. It has to be reactive. In addition, it has permeability bigger or equal to the ambient aquifer; thus, the right material choice for the barriers is important [18]. The previous research focused on using wastes, recycled, and by-product materials in PRB technology to enhance their activity in using sustainable (green) concepts, such as activated neem leaves [19], coir pith [20], recycled concrete [21], municipal composts, leaf composts, wood chips, limestone, silica sand [22], and peat and sawdust [23] in treating water contaminated with pollutants. Eggs represent as one of the most ingredient used in variety of products resulting in several daily tons of eggshell which is ranked as the 15th major food industry pollution problem by the EPA, and most of these quantities are accumulated on site or disposed annually as waste in landfills without any pretreatment and become as an organic environmental pollution source [24]. Furthermore, with increasing urgent recently to converting worthwhile waste into useful commodities for sustainable development by recycle, reuse for manufacturing high-value products, managing agricultural wastes is vital and a crucial strategy [25]. Eggshells are one such agrowaste that can be used as a useful source of material in a variety of applications, including the manufacturing of fertilizer and feed as well as other environmentally friendly catalysts in biological, environmental, and agricultural engineering applications [26]. The structural aspect of eggshell comprises of calcium carbonate as the main component with (94-95%) [27], so utilizing eggshells can provide biocompatible calcium (it is environmentally friendly and nontoxic) which lowers not only the impact of pollution but also the associated financial costs and serves as a commercial replacement for calcium carbonate, calcium hydroxide, and calcium oxide [28], and it is also utilized for fertilization, soil conditioning, or animal feed ingredients [29] and manufacturing food products including calcium additives [30]. Layered double hydroxides (LDHs) are unique in structure which is a two-dimensional structure in which the cations are in the centers of edge-sharing octahedral, with vertexes containing OH ions connecting and constituting infinite 2D sheets as [31], with high positive charge densities of layers and high contents of interlayer anionic species which result in strong electrostatic interactions that made the layers hold together in LDHs beside the hydrogen bond [32]. LDHs are active adsorbents, so most scholars have synthesized many LDHs to remove antibiotics from wastewater [33], additionally, and it is prepared relatively simply and economically through a coprecipitation method under laboratory setting in big quantities [34]. The previous studies concentrated on the using of LDHs for antibiotics removal such as in [35] adsorption of AMX that was studied were performed on *Cladophora* and Spirulina algae biomass immobilized in alginate beads in batch mode with algal biomass doses of 1.25 g/100 ml and 0.5 g/100 ml in respect, achieving 98% of removal, and maximal adsorption capacity was 7.89, 17.4 mg/g for AMX, while Yang et al. [36] studied synthesis as novel adsorbents Mg-Al LDH/cellulose nanocomposite beads (LDH@CB) by coprecipitation procedure utilized as a new adsorbent to remove AMX from the aqueous solution in kinetically and isothermally batch adsorption experiment and fitted with the Freundlich isotherm and pseudo-second-order model, respectively, and AMX LDH@CB qm adsorption capacity equals 138.3 mg $g^{-1}$. Elhaci et al. [37] also investigated the LDH material synthesis by $Mg^{2+}/Al^{3+}$ molar rate of 2 by coprecipitation at pH 9 to remove AMX from aqueous media by pseudo-second-order kinetics with highest adsorption monolayer capacity recorded at pH = 6, with 30.42 mg/g at $C_o$ = 240 mg/L. This work is aimed at using the eggshell wastes usefully for sustainable development by extracting calcium ions from eggshell wastes to synthesis (Ca/Fe)-LDH nanoabsorbent and entrapped in sodium alginate beads to forming (Ca/Fe)-LDH-sodium alginate beads or (Ca/Fe)-LDH-SA beads for AMX removal with finding the optimal operation parameters and implement this aim through diverse isothermal and kinetic models for the estimation of the chosen antibiotic on absorbent adsorption parameters.

## 2. Methodology and Materials

*2.1. Reagents and Chemicals.* Calcium chloride dihydrate ($CaCl_2.2H_2O$) was bought to be available and of an analytical grade from AVONCHEM, UK; ferric nitrate ($Fe(NO_2)_3,9H_2O$) from Scharlau, Spain; and sodium alginate powder (food grade, China) with a $2.5 \times 10^5$ g/mol molecular. Also, sodium hydroxide (NaOH) from Alpha Chemika, India, and hydrochloric acid (HCl, 35-38% pure) were also bought from CDH, India, and were used in this work. We used amoxicillin powder ($C_{16}H_{19}N_3O_5S$) with purity: 97.5% from the general drug company in Samarra, Iraq, specifically, the antibiotic chosen in this work in order to simulate contamination within the studied groundwater and used in experiments without any further purification. During batch experiments, we prepared one litter of aqueous solution with a 1000 mg contamination and kept at room temperature, and the dilution of stock solution was conducted

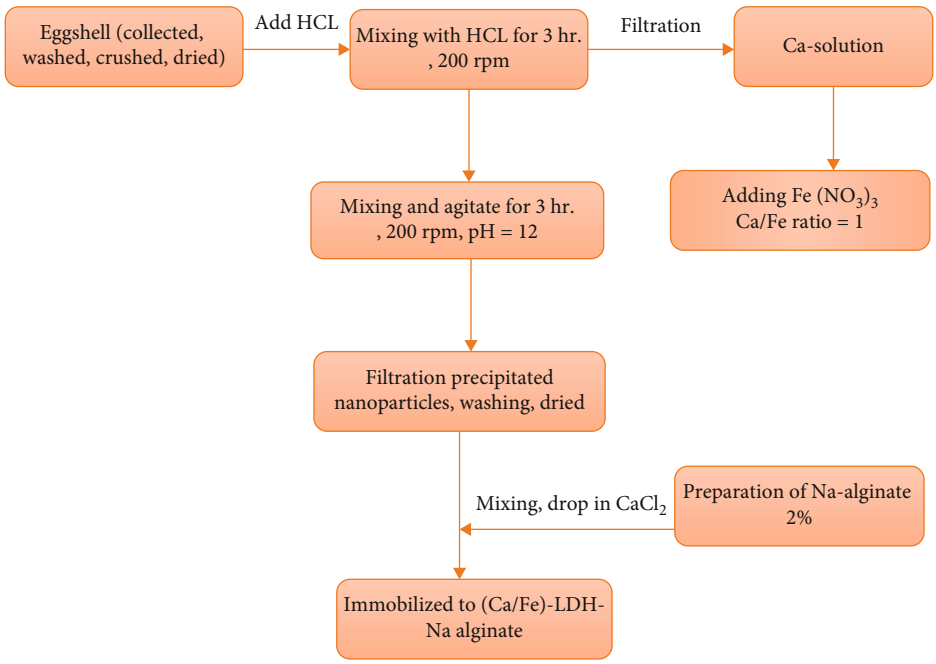


Figure 1: Flowchart of preparing (Ca/Fe)-LDH-SA beads.

with distilled deionized water for obtaining the required target contaminant solution concentration.

*2.2. Synthesizing (Ca/Fe)-LDH-SA Beads.* The main concept used in synthesizing (Ca/Fe)-LDH adsorbent as in Figure 1 involves five steps illustrated below:

(1) From chicken eggshells, calcium ions are extracted, which gathering from household wastes, requiring mixing 20 gram of crushed and dried shells (after collecting from the source, rinsing with water several times, air-drying, crushing, drying at 105°C, passing on sieving for gaining (0.6 mm) are shown in Figure 2, then adding 100 mL of solution made of distilled water and 10 mL from 35–38% hydrochloric acid to prepare mixture stirred vigorously at room temperature for 3 h at 200 rpm. To obtain a clear calcium solution, the residual solid shell particles can be separated using filter paper from the calcium ion-rich aqueous solution

(2) Preparing aqueous solution reached with $Fe^{+3}$ by dissolved specific mass of Fe $(NO_2)_3$. This dissolving process happened in distilled water (DW), then mixing this iron solution with the calcium ion-rich aqueous solution obtained from first step to obtain solution of (Ca/Fe) with molar ratio = 1

(3) In flask, changing the alkalinity of the mixture by adding 1 M NaOH to reach a value of around 12 ensured forming (Ca/Fe)-LDH nanoparticles with continuous agitation over 3 hours and 200 rpm, and then, the slurry that formed should be filter on filter paper, collect it and wash it with distilled water, and dry and grind to obtain the nanoparticles as a powder as shown in Figure 3.

(4) Sodium alginate is made through the same procedure of previous studies [38]. This procedure involves dissolving 2 g Na-alginate in 100 mL of DW and comprehensively agitated through magnetic stirring at room ambient over twenty-four hours.

5.Adding the mass of (Ca/Fe) nanoparticles equal 5 g/100 mL (as optimum value obtained from [39]) that formed in the previous step for the sodium alginate introduced by 10 mL syringe into 0.1 M of $CaCl_2$ (dissolving 1 g of $CaCl_2$ in 100 mL DW) so that polymerization and beads are formed at 4 mm. They should cure in this solution for one hour and followed by washing it two times by DW and keeping it in 5 mM of $CaCl_2$ (0.278 g of $CaCl_2$ is dissolved in 500 mL DW) at 4°C for additional uses (Figure 4).

*2.3. Batch Methodology.* It is recommended that batch adsorption experiments be analysed using phenomenological models in order to obtain the appropriate values of operating conditions needed for removing the large percentage of adopted contaminant concentrations that are applicable to other systems and for reducing the number of experiments to fully describe the kinetics of adsorption, which is typically characterized on the basis of empirical models [40]. Some flasks of 250 mL were made, and simulated contaminated water (100 mL) is put in each flask with certain values of concentrations. We repeated experiments by changing variables to obtain important information about the behaviors of antibiotics sorption onto (Ca/Fe)-LDH-immobilized beads and the best parameters to remove it (primary pH, contact time, the amount of beads, and the speed of agitation or the initial concentration of the solution), for getting the

(a) (b)

Figure 2: Eggshell (a) before and (b) after dried, crushed, and sieved.

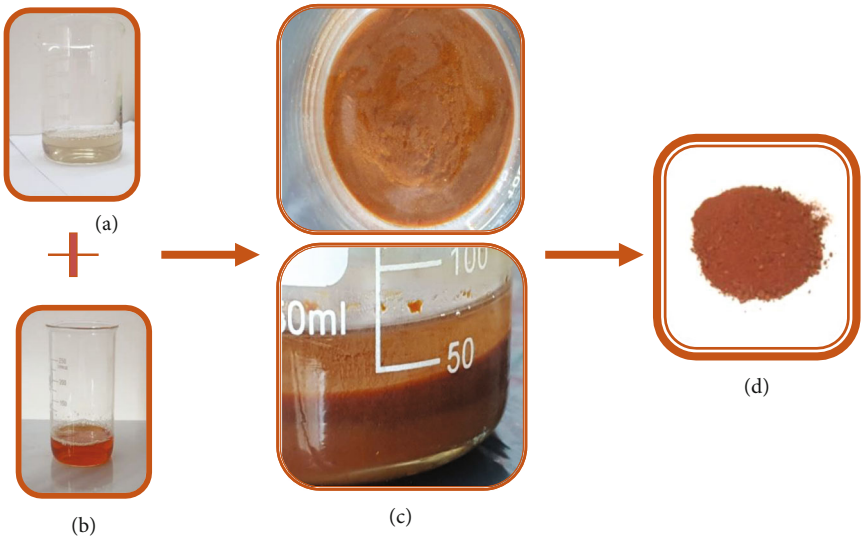


Figure 3: (a) Solution of extracted calcium; (b) iron solution; (c) after coprecipitation (Ca/Fe)-LDH; (d) (Ca/Fe)-LDH nanoparticles after filtration and drying.

isotherms and kinetics of adsorption at the end. Diverse concentration solutions of AMX were obtained from 1000 mg. $L^{-1}$ stock solution through dilution methods in different intervals of time for three hours. For adsorption kinetics, different initial concentrations of AMX, i.e., from 100 mg.$L^{-1}$ to 250 mg.$L^{-1}$ in 100 mL volume, are connected to 0.5 g of adsorbent beads. We examined pH on AMX adsorption in range 2-12 where we adjusted pH of solutions by the NaOH and HCl solution, while the agitation speed did not exceed 250 rpm. While studying the isotherm, we added various masses of (Ca/Fe)-LDH-SA beads of 0.10-1.2 g to some flasks with 100 mL solution for everyone. We interpreted the adsorption isotherm data for various isotherm models. We used filter paper to separate the alginate beads from

Figure 4: Beads of (Ca/Fe)-LDH-SA.

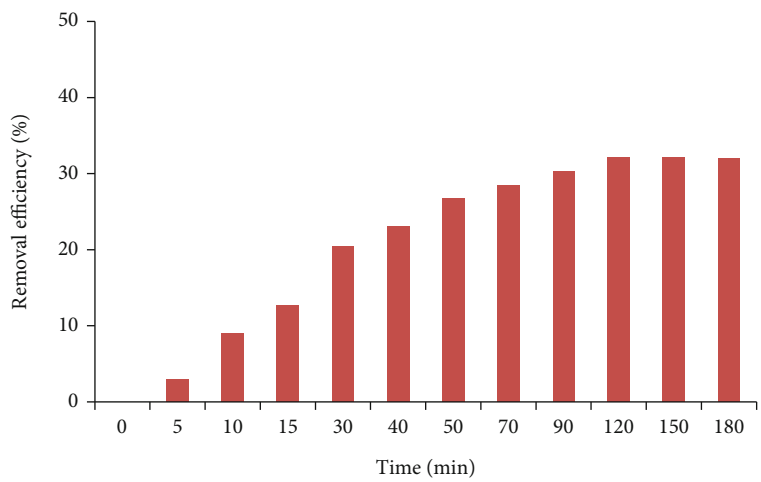


Figure 5: Contact time influence on the adsorbent bead behavior utilized to remove AMX from contaminated water.

the water and measured AMX antibiotic concentrations by ultraviolet-visible (UV) spectrophotometer (Model Varian Cary 100 conc., England) at wavelengths of 270 nm. Also, the mean for three readings of the sorption can be gained from each point.

*2.4. Data Analysis.* At the equilibrium ($q_e$) according to the variance between initial concentration ($C_o$) and final concentration ($C_e$), Equation (1) is applied for the calculation of the quantity of antibiotics of the alginate beads at [41].

$$q_e = (C_o - C_e)\frac{V}{m}. \quad (1)$$

Here, $m$ is the mass adsorbent beads in grams and $V$ is the litter (L) volume of AMX solution, and we measured the antibiotics ($R$) percentage that is removed from solution onto adsorbent by Equation (2) as in [42].

$$R = \frac{(C_o - C_e)}{C_o} \times 100. \quad (2)$$

## 3. Results and Discussion

*3.1. Time Influence in Batch Testing.* We identified the adsorption equilibrium time through the antibiotic concentrations change with the time. Figure 5 is the change in the AMX uptake efficiencies from contaminated water onto the made adsorbent to contact time not more than three hours at operational settings of initial concentration $(C_o) = 100$ mg/L, pH $= 7$, mass of beads $= 0.5$ g/100 mL, and speed of agitation $=$ 200 rpm. We removed the antibiotic rapidly for initial times until balance is achieved, or complete absorption for reducing 30.3% AMX at one hours and a half when $C_o$ 100 mg/L is decreased after that time because of reducing binding sites

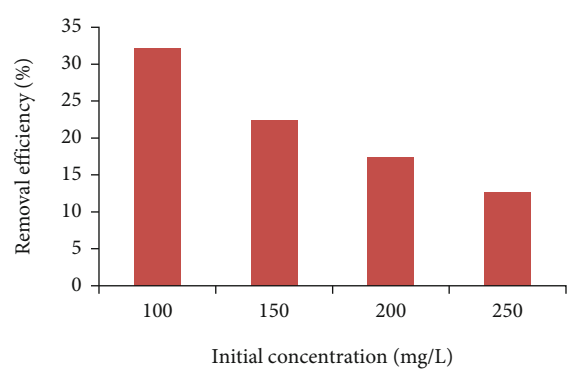


Figure 6: Effects of initial concentration on the adsorbent bead behavior used to remove AMX from contaminated water.

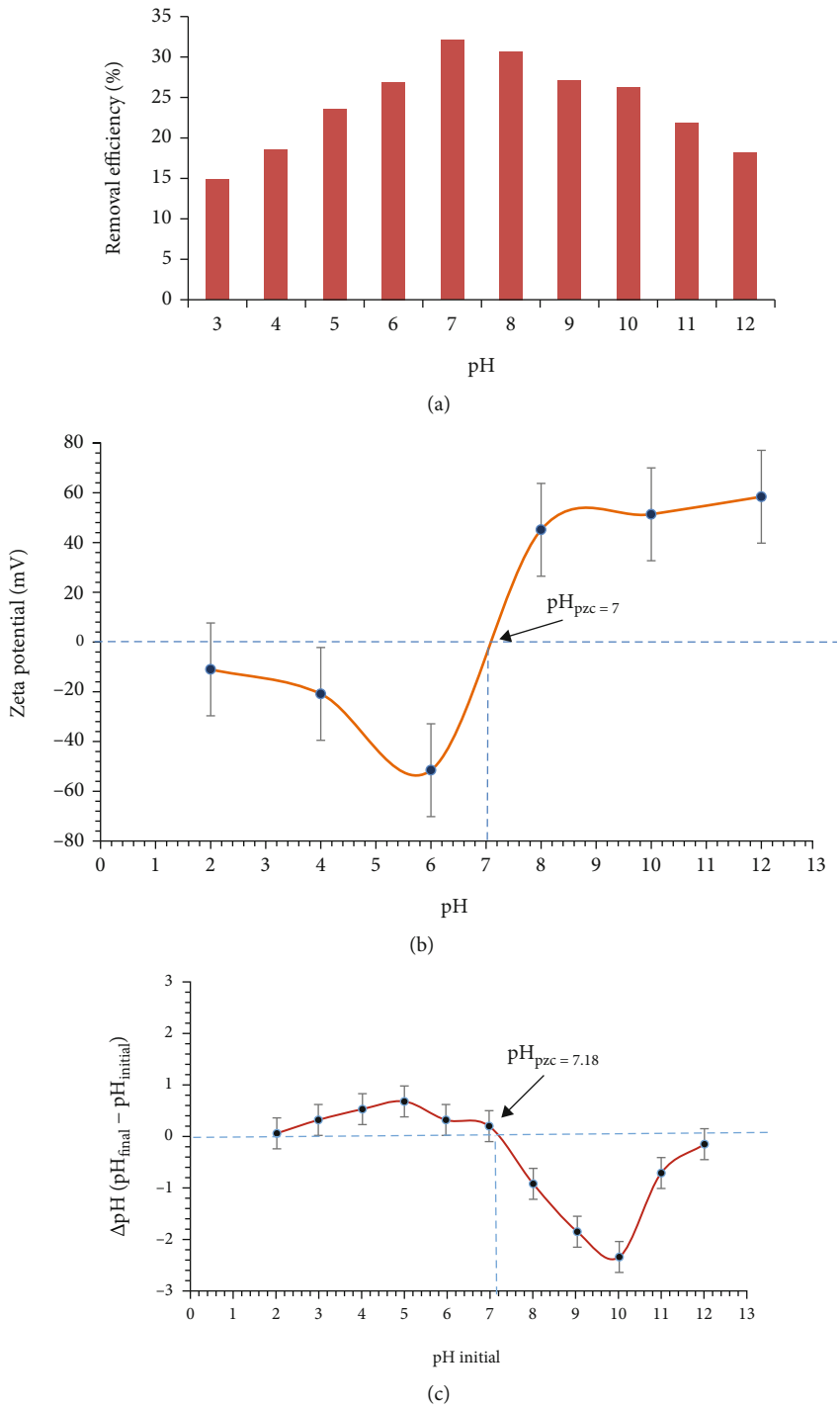


Figure 7: (a) Initial pH effect with removal of AMX from contaminated water, (b) pH $_{PZC}$ for Ca/Fe LDH, and (c) pH $_{PZC}$ of beads.

for AMX molecule sorption [43]. The increase in the adsorption time does not make the adsorption rate obviously change since the removal percentages had been slowly tended to be stable till 180 min because the quantity of free sites drops, and the binding of adsorbate from the aqueous solution is harder, and the sorption processes, thus, decreases [44].

*3.2. AMX Initial Concentration Influence.* According to Figure 6, the AMX antibiotic removing efficiencies onto synthesized adsorbent beads decreased intensely from 32.1% for $C_o$ 100 mg/L to 12.72% for $C_o$ 250 mg/L at 90 min, pH 7, mass of beads 0.5 g/100 mL, and speed of agitation 200 rpm. With the existing binding sites, all contaminant molecules interacted at lesser concentrations causing a remarkable rise in the sorption efficiency. So, these contaminants sorbed per unit mass of adsorbent reduced with the rise in initial concentration based on the sites of the process which was less favorable sites with the decrease in the concentration [45]. Although

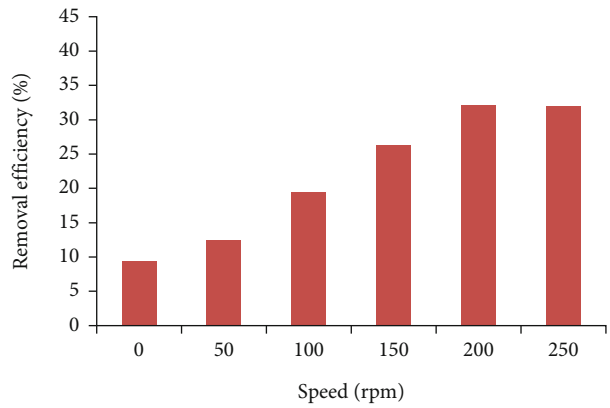


Figure 8: Effects of agitation speed on the behavior of adsorbent beads to remove AMX from contaminated water.

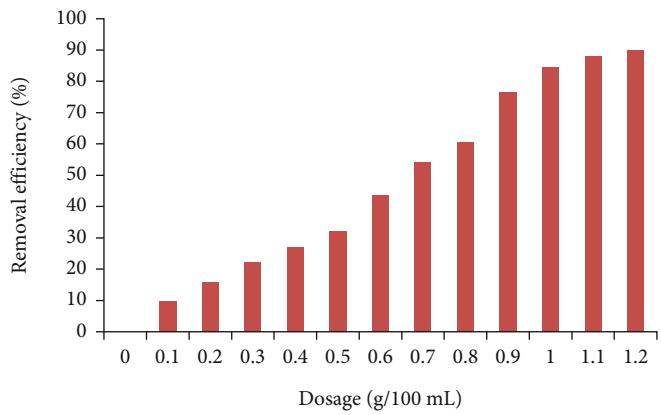


Figure 9: Relation between sorbent dosage and removals of AMX.

adsorbent removed all antibiotics at one and half hours under the same conditions, possibly, the antibiotic showed higher removal if the concentration was lower than the detecting limit as in environmental concentrations.

*3.3. Impacts of pH on Removal Efficiency of AMX.* The contaminated aqueous pH that contact with the synthesized adsorbent beads is important in eliminating antibiotic as this variable may influence the exterior charges of beads, the AMX ionization degree, and the dissociation of the functional groups [46]. Figure 7(a) is the plots of removing efficiencies of AMX versus various initial pH different from 3 to 12. The process of removing was low (≤14.9% at pH 3.0) because antibiotic competes $H^+$ ions. The rise of the pH towards the neutral condition is followed by a rise in the sorption effectiveness higher than 32.1% for the used antibiotics at pH 7. The antibiotic ionization and hydration decrease at neutral conditions, enhancing removal by the hydrogen bonds and $\pi-\pi$ stacking influence. The figure also reveals a decrease in the removing efficiency because solution changed towards the basic form, and the AMX competences are bigger than 18.2%. This efficiency reduction with higher pH could be due to generating $OH^-$ attenuating the hydrogen bonding. Figure 7(b) shows the pHpzc of Ca/Fe-LDH at 7 and for beads calculated as around 7.18, and Figure 7(c) reveals a positive charge of the $pH < pH_{pzc,}$ the

Table 1: Kinetic models for sorption of AMX antibiotic onto the synthesized nanoadsorbent.

| Model | Parameter | Value |
|---|---|---|
| Pseudo-first-order | $q_e$ (mg/g) | 3.2828 |
| | $k_1$ ($min^{-1}$) | 0.0298 |
| | $R^2$ | 0.9899 |
| | SSE | 0.1554 |
| Pseudo-second-order | $q_e$ (mg/g) | 4.0288 |
| | $k_2$ (g/mg min) | 0.0077 |
| | $R^2$ | 0.9924 |
| | SSE | 0.1287 |
| Intraparticle diffusion | Portion 1 | |
| | $k_{int}$ (mg/g $min^{0.5}$) | 0.3958 |
| | $R^2$ | 0.9519 |
| | Portion 2 | |
| | $k_{int}$ (mg/g $min^{0.5}$) | 0.1431 |
| | $R^2$ | 0.9615 |
| | Portion 3 | |
| | $k_{int}$ (mg/g $min^{0.5}$) | 0.0182 |
| | $R^2$ | 0.6334 |

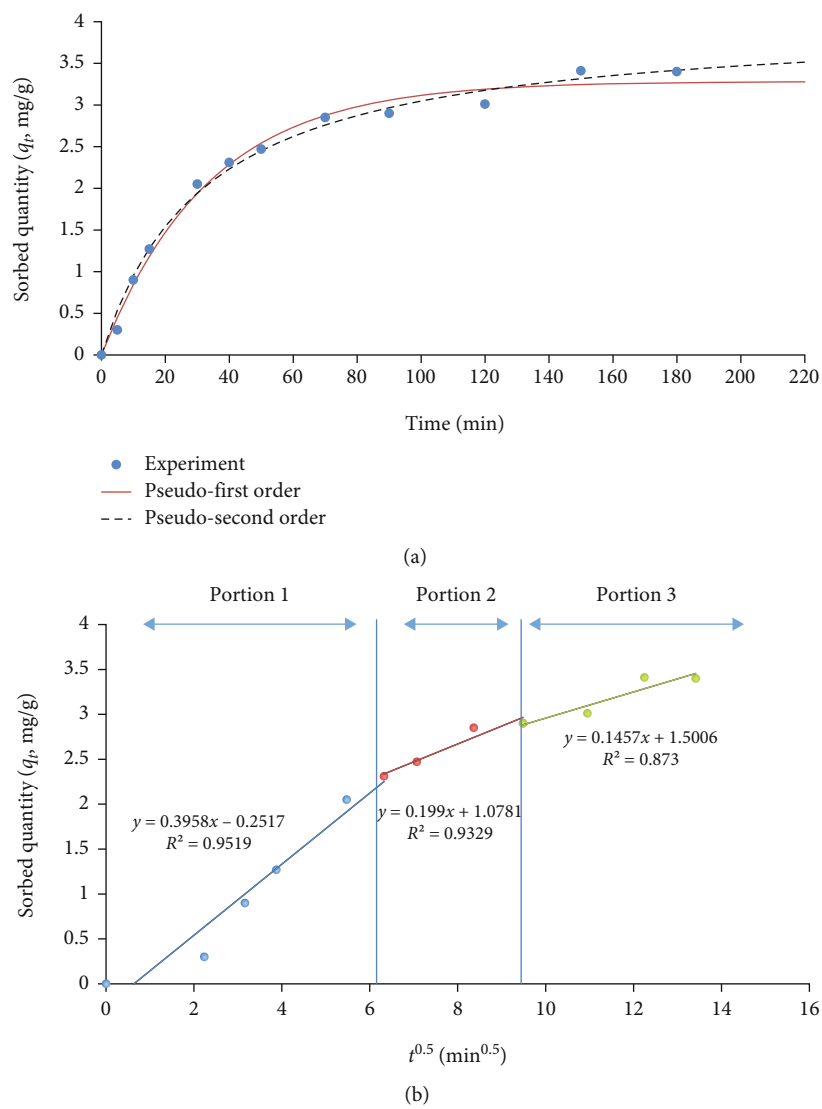


Figure 10: (a) Kinetic (b) and intraparticle diffusion models for interaction of sodium alginate beads with water-contained AMX.

adsorbent surface ,and the negative one at pH > $pH_{pzc}$. As the initial pH rose, zeta potential significantly rose from range 2-6 with the AMX adsorption of onto Ca/Fe-LDH-Na-alginate beads. So, the adsorption of the AMX on bead at pH range 2-6 seemed to be low because electrostatic attraction AMX electrostatically attracts bead surface which confirm well the results above. So, at higher pH (6 < pH < 8), AMX on the adsorbent did not leak our acting as the adsorption sites for AMX. So, the reduction in the AMX and bead reaction caused a higher adsorption of AMX. While the pH rose more, the adsorption capacity reduced, so we conducted other AMX adsorption experiments at pH 7.

*3.4. Influence of Agitation Speed.* The agitation percentage influenced highly that of adsorption which rises when the speed of agitation rises. According to Figure 8, the increase in agitation speed is essential to enhance AMX removal from polluted water because of diffusion rate of AMX molecules that rise towards the adsorbent bead surface under operational parameters of time = 90 min, pH = 7, 0.5 g/100 mL beads mass, and primary adsorbate = 100 mg/L concentration. Removing AMX efficiencies was not bigger than 9.4%

Table 2: Isotherm model parameters in the AMX sorption onto adsorbent beads.

| Model | Parameter | Value |
|---|---|---|
| Langmuir | $q_{max}$ (mg/g) | 6.7362 |
| | $b$ (L/mg) | 0.2077 |
| | $R^2$ | 0.9467 |
| | SSE | 1.35814 |
| Freundlich | $K_f$ (mg/g)(L/mg)$^{1/n}$ | 3.32892 |
| | $n$ | 7.96808 |
| | $R^2$ | 0.622078 |
| | SSE | 9.30767 |

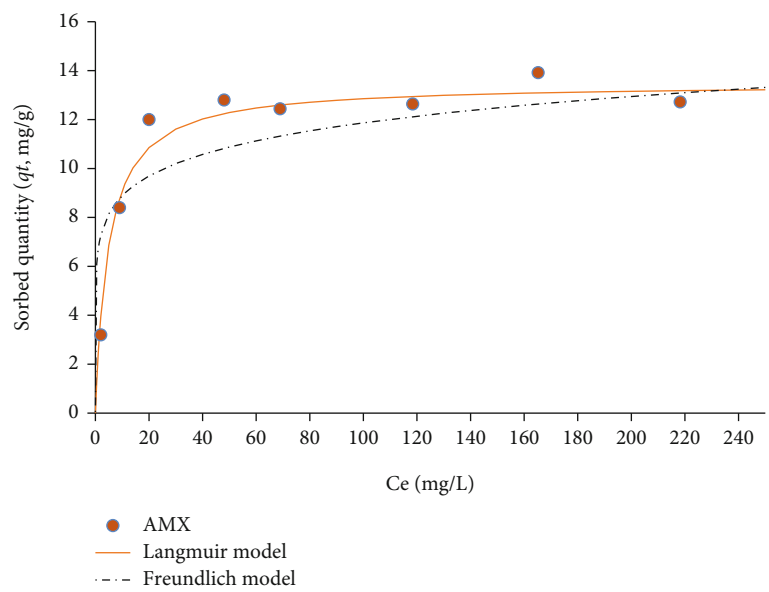


Figure 11: Sorption isotherms for interaction of designed sorbent—AMX water contaminated.

for static aqueous solutions, although dramatically rose at 32.1% at 200 rpm. Yet, the figure also explains that the adsorption rises when agitation speeds rise only up to a specific limit, so speed to 250 rpm increase does not make any changes in the removal efficiencies because beyond, there is no rise in the adsorption capacity [47].

*3.5. Adsorbent Alginate Bead Mass Impacts.* Figure 9 shows the adsorbent alginate beads mass effect on removing AMX efficiencies. Thus, when the dosage changes from 0.1 to 1.2 g, the removing efficiencies increase from the least (9.8%) to more than 90% for the used antibiotic. The bead quantity rise indicates a growth in the empty sites ready to interact with contaminant molecules leading to increase the removing efficiencies of these molecules [48].

*3.6. Kinetics of Antibiotic Sorption.* Adsorption kinetics from batch study is one of the most important features of such processes that control the sorbent's capacity for adsorption and rate of adsorption at the interface of solid-liquid phases due to the equilibrium state in batch mode, and the kinetics helps researchers who conducted laboratory scale research to estimate an adsorbent's performance before applying it on a larger scale [49]. This work measures the kinetic data in the experiment by kinetic models; pseudo-first-order and pseudo-second-order models are shown in Equations (3) and (4), respectively, and intraparticle diffusion model is shown in Equation (5) [50–52]:

$$q_t = q_e\left(1 - e^{-k_1 t}\right), \tag{3}$$

$$q_t = \frac{k_2 q_e^2 t}{(1 + k_2 q_e t)}, \tag{4}$$

$$q_t = k_{\text{int}} t^{0.5} + C. \tag{5}$$

Here, $q_e$ is the solid matrix at equilibrium and $q_t$ is the time which the quantities of pollutant were adsorbed in mg/g, $k_1$ refers to the pseudo first order model rate constant (1/min), $k_2$ stands for the sorption (g/mg min) rate constant, and $k_{\text{int}}$ is the sorption rate constant of for this model (mg/g min 0.5); $C$ is the intercept. We used kinetic models for formulating the sorption of the antibiotic AMX over time by alginate beads for various initial pollutant concentration. We also used Excel 2016's "Solver" nonlinear regression feature for completing the formulation process. Table 1 is the parameters for kinetic models determined by fitting, confirming the second model AMX interaction represented by alginate because of the determination coefficient ($R^2$) which is bigger than 0.9924, and squared error sum (SSE) is lower than 0.1287. Also, from Figure 10(a), the calculated AMX sorbed quantity onto the alginate beads at 4.0288 mg/g, nearly approaching the calculated quantity as a sign for the second order model applicability. So, the AMX sorption onto alginate beads happened through the chemisorption (i.e., chemical reaction). The study used the intraparticle diffusion (Equation (5)) model and the equation of constants between $q_t$ and $t^{0.5}$ in measuring nonlinear regression fitting (Table 1). Figure 10(b) shows this relationship for the investigated antibiotic represented through the straight lines with intercept not equal to zero. Thus, intraparticle diffusion needs the AMX sorption with no depiction of the rate-controlling step [53]. This is a multilinearity plot, meaning it is two or more simultaneous methods in the AMX sorption. So, the line slope in "portion 1" is sharp; so, removing contaminant rates could increase in the primary sorption because of the external surface adsorption caused by the existing vacant site. The line slope in the "portion 2" changed gradually to the intraparticle diffusion possibly rate-controlled. At the end, the "portion 3" is the equilibrium stage connected to the diffusion reducing the speed because of low remaining contaminant concentration in the liquid [54–56].

*3.7. Isotherms for Equilibrium Sorption Readings.* Adsorption is, in general, conducted by equilibrium isotherm relationship correlating between the solute-sorbed quantity on the solid materials ($q_e$, mg/g) and its concentration (Ce, mg/L) staying in the aqueous solution at certain temperatures. So, there could be an increase in the solute which removed solid particle per unit mass because of the rise in the concentration yet not directly [57]. An isotherm is possibly recognized "favorable" if the convex is upward due to the high loading that could occur the solid particles if the concentrations are low in the water phases [58]. The relationships described that the sorption isotherms are divided into Freundlich and Langmuir models.

For heterogeneous sites, Freundlich model can be applied with sorption in a multilayer scheme [59].

$$q_e = K_F C_e^{1/n}. \tag{6}$$

Langmuir model suits single-layer adsorption [60]:

$$q_e = \frac{q_{\max} b C_e}{1 + b C_e}, \tag{7}$$

where $K_F$ is linked to the maximum adsorption capacity, $1/n$ refers to the sorption intensity, $b$ is the solute affinity with solid phases (L/mg), and $q_{\max}$ is the highest sorption (mg/g). We calculated any constants in the used isotherm models as Table 2 shows by nonlinear regression by applying "solver" option in Excel software 2016. According to the $R^2$ and SSE, Langmuir model stated that the AMX sorption depiction is made on adsorbent beads. The experimental measurement matching with the sorption isotherms is observed from Figure 11; yet, this is recognized from highest $R^2$ (≥6.7362) and lowest SSE (≤1.35814). The AMX sorption maximum ability is 6.7362 mg/g, meaning that the alginate beads showed capability in the AMX removal. Freundlich constant ($K_f$) reached 3.32892 (mg/g) $(\text{L/mg})^{1/n}$ for AMX onto Na-alginate while $(n) > 1$; so, the isotherm curves could be "favorable."

## 4. Conclusions

In this study, egg shell waste was used as crucial source of calcium ions to synthesize a nanobiosorbent from calcium and iron and immobilized into alginate to formed (Ca/Fe)-LDH-SA beads and studied the relevance of using it as a reactive material in permeable barrier utilized for removing AMX from aqueous solution. This works confirmed the AMX antibiotic efficiency in removal from solution through the sorbent. The AMX sorption was explored the time function and primary concentration of AMX, pH of AMX, and sorbent dosage. The equilibrium time for the removal of AMX on adsorbent beads was achieved over one and a half hours and maximum removed at pH = (7). Based on the results, the appropriate operational settings need for assuring the efficacy of removing AMX ≥ 95% were 1.2 g/100 mL dosage for $C_o$ 100 mg/L at 200 rpm. Langmuir adsorption isotherm explained the adsorption isotherm data. Also, chemical forces (i.e., chemisorption) governed this process because of applying the pseudo-second-order model, so the adsorbent was effective in removing chosen pollutant, and its utilization could be expanded to other antibiotics too. So, the manufactured (Ca/Fe)-LDH-SA beads could be competent in the permeable technology adsorption barrier and suitable in the fixed bed columns in removing AMX from water.

## Data Availability

All the available data are incorporated in the MS.

## Conflicts of Interest

No known personal relationships and competing financial interests are influencing this paper.

## References


[1] P. Li, D. Karunanidhi, T. Subramani, and K. Srinivasamoorthy, "Sources and consequences of groundwater contamination," *Archives of Environmental Contamination and Toxicology*, vol. 80, no. 1, pp. 1–10, 2021.

[2] R. Thiruvenkatachari, S. Vigneswaran, and R. Naidu, "Permeable reactive barrier for groundwater remediation," *Journal of Industrial and Engineering Chemistry*, vol. 14, no. 2, pp. 145–156, 2008.

[3] UK Environmental Agency, 2005, http://www.environment-agency.gov.uk/.

[4] S. S. D. Foster, *Groundwater-Past Achievements and Future Challenges*, O. Sililo, Ed., Balkema, Rotterdam, The Netherlands, 2000.

[5] P. Bayer and M. Finkel, "Life cycle assessment of active and passive groundwater remediation technologies," *Journal of Contaminant Hydrology*, vol. 83, no. 3-4, pp. 171–199, 2006.

[6] USEPA, *Evaluation of Groundwater Extraction Remedies: Phase II, vol. 1, Summary Report, Publication 9355.4-05*, EPA Office of Emergency and Remedial Responses, Washington, DC, 1992.

[7] P. Li and J. Wu, "Sustainable living with risks: meeting the challenges," *Human and Ecological Risk Assessment: An International Journal*, vol. 25, no. 1-2, pp. 1–10, 2019.

[8] M. Lu, Y. Y. Chen, M. Chiou, M. Y. Chen, and H. Fan, "Occurrence and treatment efficiency of pharmaceuticals in landfill leachates," *Waste Management*, vol. 55, pp. 257–264, 2016.

[9] R. S. Singer, R. Finch, H. C. Wegener, R. Bywater, J. Walters, and M. Lipsitch, "Antibiotic resistance–the interplay between antibiotic use in animals and human beings," *The Lancet Infectious Diseases*, vol. 3, no. 1, pp. 47–51, 2003.

[10] K. Kümmerer, "Significance of antibiotics in the environment," *Journal of Antimi-crobial Chemotheraphy*, vol. 52, pp. 5–7, 2003.

[11] WHO, *Overcoming antibiotic resistance, World Health Organization Report in Infectious Diseases*, WHO, Geneva, 2002.

[12] A. K. Sarmah, M. T. Meyer, and A. Boxall, "A global perspective on the use, sales, exposure pathways, occurrence, fate and effects of veterinary antibiotics (VAs) in the environment," *Chemosphere*, vol. 65, no. 5, pp. 725–759, 2006.

[13] K. D. Brown, J. Kulis, B. Thomson, T. H. Chapman, and D. B. Mawhinney, "Occurrence of antibiotics in hospital, residential,

and dairy effluent, municipal wastewater, and the Rio Grande in New Mexico," *Science of the Total Environment*, vol. 366, no. 2–3, pp. 772–783, 2006.

[14] C. Suarez and F. Gudiol, "Beta-lactam antibiotics," *Enfermedades Infecciosas Y Microbiología Clínica*, vol. 27, no. 2, pp. 116–129, 2009.

[15] M. Larramendy and S. Soloneski, Eds., *Environmental Health Risk: Hazardous Factors to Living Species*, BoD-Books on Demand, 2016.

[16] R. Andreozzi, V. Caprio, C. Ciniglia et al., "Antibiotics in the environment: occurrence in Italian STPs, fate, and preliminary assessment on algal toxicity of amoxicillin," *Environmental Science & Technology*, vol. 38, no. 24, pp. 6832–6838, 2004.

[17] M. A. Carey, B. A. Fretwell, N. G. Mosley, and J. W. N. Smith, "Guidance on the use of permeable reactive barriers for remediating contaminated groundwater," in *National Groundwater and Contaminated Land Centre Report NC/01/51*, Bristol, UK Environment Agency, 2002.

[18] Y. Chen, J. Li, C. Lei, and H. Shim, "Interactions between BTEX, TPH, and TCE during their bio-removal from the artificially contaminated water," in *Bionature 2011: The Second International Conference on Bioenvironment*, pp. 33–37, Biodiversity and Renewable Energies, Venice, Italy, 2011.

[19] B. V. Babu and S. Gupta, "Adsorption of Cr(VI) using activated neem leaves: kinetic studies," *Adsorption*, vol. 14, no. 1, pp. 85–92, 2008.

[20] H. Parab, S. Joshi, N. Shenoy, A. Lali, U. S. Sarma, and M. Sudersanan, "Determination of kinetic and equilibrium parameters of the batch adsorption of Co(II), Cr(III) and Ni(II) onto coir pith," *Process Biochemistry*, vol. 41, no. 3, pp. 609–615, 2006.

[21] G. Regmi, B. Indraratna, L. D. Nghiem, A. N. Golab, and B. G. Prasad, "Treatment of acidic groundwater in acid sulfate soil terrain using recycled concrete: column experiments," *Journal of Environmental Engineering, ASCE*, vol. 137, no. 6, pp. 433–443, 2011.

[22] S. G. Benner, D. W. Blowes, C. J. Ptacek, and K. U. Mayer, "Rates of sulfate reduction and metal sulfide precipitation in a permeable reactive barrier," *Applied Geochemistry*, vol. 17, no. 3, pp. 301–320, 2002.

[23] P. K. Mondal, G. Lima, D. Zhang et al., "Evaluation of peat and sawdust as permeable reactive barrier materials for stimulating in situ biodegradation of trichloroethene," *Journal of Hazardous Materials*, vol. 313, pp. 37–48, 2016.

[24] S. K. Mahmood, G. A. Sultan, S. K. Ebrahim, and A. G. M. Alhaaik, "Recycling of chicken egg shells into nanopowder: synthesis, and its properties," *Baghdad Science Journal*, vol. 19, pp. 0759–0759, 2022.

[25] H. Faridi and A. Arabhosseini, "Application of eggshell wastes as valuable and utilizable products: a review," *Research in Agricultural Engineering*, vol. 64, no. 2, pp. 104–114, 2018.

[26] A. Laca, A. Laca, and M. Díaz, "Eggshell waste as catalyst: a review," *Journal of Environmental Management*, vol. 197, pp. 351–359, 2017.

[27] D. A. Oliveira, P. Benelli, and E. R. Amante, "A literature review on adding value to solid residues: egg shells," *Journal of Cleaner Production*, vol. 46, pp. 42–47, 2013.

[28] H. B. Lakshmi, B. J. Madhu, and M. Veerabhadraswamy, "Synthesis and characterization of nano-crystaline CaFe2O4 via solution combustion method from solid waste egg shells as source of calcium," *International Journal of Engineering Research And Advanced Technology*, vol. 3, pp. 21–30, 2017.

[29] J. Carvalho, J. Araujo, and F. Castro, "Alternative low-cost adsorbent for water and wastewater decontamination derived from eggshell waste: an overview," *Waste and Biomass Valorization*, vol. 2, no. 2, pp. 157–167, 2011.

[30] A. Q. Muryoush, D. Hussain, and A. H. Ali, "Antibacterial activity with eggshell nano-particles activated by microwave plasma," *Journal of Optoelectronic and Biomedical Materials*, vol. 13, no. 4, pp. 177–182, 2021.

[31] S. N. Ishak and N. A. N. N. Malek, "Functionalized layered double hydroxide with compound to remove cationic and anionic pollutants: a review," *Environmental and Toxicology Management*, vol. 1, no. 1, pp. 26–29, 2021.

[32] X. Wang, H. Zhao, L. Chang et al., "First-principles study on interlayer spacing and structure stability of NiAl-layered double hydroxides," *ACS Omega*, vol. 7, no. 43, pp. 39169–39180, 2022.

[33] M. N. Sepehr, T. J. Al-Musawi, E. Ghahramani, H. Kazemian, and M. Zarrabi, "Adsorption performance of magnesium/aluminum layered double hydroxide nanoparticles for metronidazole from aqueous solution," *Arabian Journal of Chemistry*, vol. 10, no. 5, pp. 611–623, 2017.

[34] Y. Kuang, L. Zhao, S. Zhang, F. Zhang, M. Dong, and S. Xu, "Morphologies, preparations and applications of layered double hydroxide micro-/nanostructures," *Materials*, vol. 3, no. 12, pp. 5220–5235, 2010.

[35] I. N. Abd and M. J. Mohammed-Ridha, "Simultaneous adsorption of tetracycline and amoxicillin by cladophora and spirulina algae biomass," *Iraqi Journal of Agricultural Sciences*, vol. 52, no. 5, pp. 1290–1303, 2021.

[36] C. Yang, L. Wang, Y. Yu et al., "Highly efficient removal of amoxicillin from water by Mg-Al layered double hydroxide/cellulose nanocomposite beads synthesized through in-situ coprecipitation method," *International Journal of Biological Macromolecules*, vol. 149, pp. 93–100, 2020.

[37] A. Elhaci, F. Labed, A. Khenifi, Z. Bouberka, M. Kameche, and K. Benabbou, "MgAl-layered double hydroxide for amoxicillin removal from aqueous media," *International Journal of Environmental Analytical Chemistry*, vol. 101, no. 15, pp. 2876–2898, 2021.

[38] M. Y. Arıca, Y. Kacar, and Ö. Genç, "Entrapment of white-rot fungus _Trametes versicolor_ in Ca-alginate beads: preparation and biosorption kinetic analysis for cadmium removal from an aqueous solution," *Bioresource Technology*, vol. 80, no. 2, pp. 121–129, 2001.

[39] M. F. Abed and A. A. Faisal, "Calcium/iron-layered double hydroxides-sodium alginate for removal of tetracycline antibiotic from aqueous solution," *Alexandria Engineering Journal*, vol. 63, pp. 127–142, 2023.

[40] V. P. Mulgundmath, R. A. Jones, F. H. Tezel, and J. Thibault, "Fixed bed adsorption for the removal of carbon dioxide from nitrogen: breakthrough behaviour and modelling for heat and mass transfer," *Separation and Purification Technology*, vol. 85, pp. 17–27, 2012.

[41] Y. Wang, S. Gong, Y. Li, Z. Li, and J. Fu, "Adsorptive removal of tetracycline by sustainable ceramsite substrate from bentonite/red mud/pine sawdust," *Scientific Reports*, vol. 10, no. 1, pp. 1–18, 2020.

[42] P. Das, P. Debnath, and A. Debnath, "Enhanced sono-assisted adsorptive uptake of malachite green dye onto magnesium ferrite nanoparticles: kinetic, isotherm and cost analysis," *Environmental Nanotechnology, Monitoring & Management*, vol. 16, article 100506, 2021.

[43] A. A. H. Faisal and L. A. Naji, "Simulation of ammonia nitrogen removal from simulated wastewater by sorption onto waste foundry sand using artificial neural network," *Association of Arab Universities Journal of Engineering Sciences*, vol. 26, pp. 28–34, 2019.

[44] A. R. Lucaci, D. Bulgariu, and L. Bulgariu, "In situ functionalization of iron oxide particles with alginate: a promising biosorbent for retention of metal ions," *Polymers*, vol. 13, no. 20, p. 3554, 2021.

[45] Z. T. Abd Ali, M. A. Ibrahim, and H. M. Madhloom, "Eggshell powder as an adsorbent for removal of Cu (II) and Cd (II) from aqueous solution: equilibrium, kinetic and thermodynamic studies," *Al-Nahrain Journal for Engineering Sciences*, vol. 19, no. 2, pp. 186–193, 2016.

[46] M. Wawrzkiewicz and Z. Hubicki, "Removal of tartrazine from aqueous solutions by strongly basic polystyrene anion exchange resins," *Journal of Hazardous Materials*, vol. 164, no. 2-3, pp. 502–509, 2009.

[47] H. A. Ihsanullah Asmaly, T. A. Saleh, T. Laoui, V. Kumar Gupta, and M. A. Atieh, "Enhanced adsorption of phenols from liquids by aluminum oxide/carbon nanotubes: comprehensive study from synthesis to surface properties," *Journal of Molecular Liquids*, vol. 206, pp. 176–182, 2015.

[48] L. Wei, F. Zietzschmann, L. C. Rietveld, and D. Van Halem, "Fluoride removal by Ca-Al-CO3 layered double hydroxides at environmentally-relevant concentrations," *Chemosphere*, vol. 243, article 125307, 2020.

[49] B. Debnath, M. Majumdar, M. Bhowmik, K. L. Bhowmik, A. Debnath, and D. N. Roy, "The effective adsorption of tetracycline onto zirconia nanoparticles synthesized by novel microbial green technology," *Journal of Environmental Management*, vol. 261, article 110235, 2020.

[50] S. Lagergren, "About the theory of so-called adsorption of soluble substances, K. seventeen," *The Hand*, vol. 24, pp. 1–39, 1989.

[51] Y. S. Ho and G. McKay, "Pseudo-second order model for sorption processes," *Process Biochemistry*, vol. 34, no. 5, pp. 451–465, 1999.

[52] S. Srivastava, R. Tyagi, and N. Pant, "Adsorption of heavy metal ions on carbonaceous material developed from the waste slurry generated in local fertilizer plants," *Water Research*, vol. 23, no. 9, pp. 1161–1165, 1989.

[53] F.-C. Wu, R.-L. Tseng, and R.-S. Juang, "Comparisons of porous and adsorption properties of carbons activated by steam and KOH," *Journal of Colloid and Interface Science*, vol. 283, no. 1, pp. 49–56, 2005.

[54] A. Özer, G. Gürbüz, A. Çalimli, and B. K. Körbahti, "Biosorption of copper(II) ions on *Enteromorpha prolifera* : application of response surface methodology (RSM)," *Chemical Engineering Journal*, vol. 146, no. 3, pp. 377–387, 2009.

[55] L. Wang, J. Zhang, R. Zhao, Y. Li, C. Li, and C. Zhang, "Adsorption of Pb(II) on activated carbon prepared from *Polygonum orientale* Linn.: kinetics, isotherms, pH, and ionic strength studies," *Bioresource Technology*, vol. 101, no. 15, pp. 5808–5814, 2010.

[56] W. H. Cheung, Y. S. Szeto, and G. McKay, "Intraparticle diffusion processes during acid dye adsorption onto chitosan," *Bioresource Technology*, vol. 98, no. 15, pp. 2897–2904, 2007.

[57] R. H. Perry and C. H. Chilton, *Chemical Engineers' Handbook*, pp. 10–46, McGraw-Hill Book Company, 1984.

[58] L. Warren and P. Harriott, *Unit Operation of Chemical Engineering*, McGraw-Hill Publ. Co, 1995.

[59] Y. S. Ho, J. F. Porter, and G. McKay, "Equilibrium isotherm studies for the sorption of divalent metal ions onto peat: copper, nickel and lead single component systems," *Water, Air, and Soil Pollution*, vol. 141, pp. 1–33, 2002.

[60] K. Y. Foo and B. H. Hameed, "Insights into the modeling of adsorption isotherm systems," *Chemical Engineering Journal*, vol. 156, no. 1, pp. 2–10, 2010.

Hindawi
Adsorption Science & Technology
Volume 2023, Article ID 6473526, 9 pages
https://doi.org/10.1155/2023/6473526

*Research Article*

# Recovery of Palladium from Acidic Solution Using Polyethylenimine-Crosslinked Calcium Silicate Hydrate Derived from Oyster Shell Waste: Adsorption and Mechanisms

**Su Bin Kang**,[1] **Zhuo Wang**,[1] **and Sung Wook Won**[1,2]

[1]*Department of Ocean System Engineering, Gyeongsang National University, 2 Tongyeonghaean-ro, Tongyeong, Gyeongnam 53064, Republic of Korea*
[2]*Department of Marine Environmental Engineering, Gyeongsang National University, 2 Tongyeonghaean-ro, Tongyeong, Gyeongnam 53064, Republic of Korea*

Correspondence should be addressed to Sung Wook Won; sungukw@gmail.com

Received 26 May 2022; Revised 6 August 2022; Accepted 13 October 2022; Published 15 April 2023

Academic Editor: Hesham Hamad



In this work, a new adsorbent with effective Pd(II) adsorption ability was synthesized using an oyster shell and fumed silica as the matrix materials and polyethyleneimine as the functional ligand. The adsorption performance of the developed adsorbent was evaluated for the recovery of palladium chloride ions (Pd(II)) from strong acid solutions. To understand the characteristics of the materials used in the study, samples were characterized by Fourier transform infrared spectroscopy (FT-IR), transmission electron microscopy (TEM), X-ray diffraction (XRD), and zeta potential analysis. Zeta potential analysis revealed that the isoelectric point of polyethylenimine-crosslinked calcium silicate hydrate (PEI-CSH) was 9.85. Isotherm experiments revealed that the maximum Pd(II) uptake estimated by the Langmuir model was 156.03 mg/g, which was 22.4 and 35.6 times higher than that of the oyster shell powder (OSP) and calcium silicate hydrate (CSH), respectively. The Pd(II) adsorption equilibrium was established in 180 minutes, according to kinetic experiments. These results suggested the possibility of Pd(II) recovery from oyster shell-based adsorbent. Through five adsorption and desorption cycles, the reusability of PEI-CSH was confirmed. PEI-CSH can therefore be considered a potential adsorbent for Pd(II) recovery.

## 1. Introduction

Palladium (Pd) has been widely used in automotive catalytic converters, jewellery, bimetallic catalysts, multilayer ceramic capacitors, fuel cell catalysis, and medical industries due to its unique properties [1–6]. With the rapid development of modern society, the demand for Pd is continuously increasing. But because of steady and constrained production, palladium is in greater demand than it is available [7, 8]. The ore only contains 2–6 g/t of Pd, but commonly phased out products like printed circuit boards and car catalytic converters have 100–10,000 g/t of Pd on average [9]. Therefore, the recovery of Pd from final items is therefore extremely important.

Leaching is commonly used to extract palladium from solid wastes, where large amounts of palladium-containing wastewater are generated. Recovery of Pd from wastewater is not only economically beneficial but also important in terms of public health, as excess Pd in water can have negative effects on human health. Consuming too much Pd can cause asthma, cancer, renal failure, and other illnesses [10–12]. Some methods such as ion exchange [13], hydrometallurgy [14], and solvent extraction [15] have been used to recover and reduce the Pd concentration in wastewater; nonetheless, there are several drawbacks to these techniques, including high running costs and poor efficiency. Pd is thus transmitted from improperly treated industrial effluent that contains Pd to water bodies like rivers and lakes, having a

negative impact on human and animal health. Therefore, it is vital to investigate low-cost and efficient Pd recovery techniques. Adsorption was therefore presented as a possible alternative for the recovery of palladium from wastewater since it overcomes the aforementioned drawbacks.

Natural materials often have complex hierarchical structures and thus can be used as adsorbent materials [16, 17]. A number of researchers have paid attention to the development of functional materials for environmental applications using agriculture [18], biological [19], and fermented [20] wastes. Oyster shell (OS) is an abundant biowaste that has attracted much attention [21]. It has been applied to remove heavy metals such as Ni(II) [22], Hg(II) [23], and Cd(II) [24] from wastewater. However, OS has low adsorption capacity and weak acid resistance, so there are limitations in treating acidic wastewater directly with OS. Aqua regia is commonly used to leach Pd from obsolete products, and the leachate is strongly acidic with large amounts of chloride ions. In order to use OS as an adsorbent for Pd recovery from acid solutions, the problem of low acid resistance must first be solved. Since OS (whose main component is $CaCO_3$) and fumed silica can be converted to acid-insoluble calcium silicate hydrate (CSH) by calcination, the conversion of OS to CSH can be an effective way to compensate for the disadvantages of OS when it is used as an adsorbent [25]. In previous studies, the preparation of CSH involves the utilization of expensive and toxic chemical reagents [26–28]. Here, OS, an abundant biowaste, was used to replace commercial calcium chloride and no toxic solvent was used in the preparation of CSH. Pd(II) exists mainly in the form of $PdCl_4^{2-}$ among several Pd-chloride complexes in strong acid solutions containing lots of chloride ions [29]. On the other hand, CHS synthesized from OS does not have a functional group capable of binding to $PdCl_4^{2-}$. Therefore, it is necessary to apply appropriate surface modification methods to greatly improve the adsorption capacity of CSH towards Pd(II). An amine-rich polymer known as polyethylenimine has been extensively employed to alter adsorbents for the recovery of precious metals including P(II), Pt(IV), and Au(III) [9, 30, 31].

In this study, a polyethylenimine-crosslinked CSH (PEI-CSH) adsorbent for Pd(II) recovery was successfully prepared by crosslinking polyethylenimine (PEI) on the surface of CSH synthesized from OS. Characteristic properties of PEI-CSH were identified through FT-IR, XRD, zeta potential analysis, and TEM. The basic interaction between PEI-CSH and Pd(II) was confirmed by batch experiments. Adsorption isotherm experiments and kinetic experiments were also performed to investigate the adsorption ability of Pd(II) on PEI-CSH.

## 2. Materials and Methods

*2.1. Materials.* Palladium(II) chloride (purity: 99.0%) was purchased from Kojima Chemicals Co., Ltd. (Saitama, Japan). OS waste was collected from a local market in Tongyeong, South Korea. Branched PEI ($M_w$: 70,000, content: 50%) was supplied by Habjung Moolsan Co., Ltd. (Seoul, Korea). 3-Aminopropyltriethoxysilane (APTES, 99%) was provided by Daejung Chemical & Metals Co., Ltd. (Siheung, Korea). Fumed silica was purchased from Sigma-Aldrich Korea Ltd. (Yongin, Korea). Glutaraldehyde (GA, 25% solution, extra pure) was supplied by Junsei Chemical Co., Ltd. (Tokyo, Japan). Other reagents such as ethanol, NaOH, and HCl used in this study were of analytical grade.

*2.2. Preparation of PEI-CSH.* To eliminate contaminants and silt, OS trash was first thoroughly cleaned with distilled water, followed by a day of drying in an air-drying oven. The washed OS was soaked in 5% sodium hypochlorite (NaClO) solution for 24 h to get rid of organic matters attached on the surface, then washed with distilled water, followed by a thorough drying. The dried OS was crushed by a ball mill (DW BM915, Dongwon Scientific System Co., Korea) with alumina balls at 500 rpm to produce oyster shell powder (OSP). The OSP (particle size < 90 $\mu$m) was collected through sieving. In order to manufacture CSH, a 1 : 1.2 weight ratio of OSP and fumed silica was combined. This mixture was then calcined at 800°C for 6 h. [25].

PEI-CSH was prepared based on previously reported methods with slight modification [32, 33]. Briefly, CSH (3 g) and APTES (3 mL) were added to 300 mL of 30% ethanol 300 mL and stirred at 25°C for 24 h. Then, the APTES-treated CSH was collected by filtration, washed with ethanol several times, and dried overnight at 100°C. Finally, PEI-CSH was produced by mixing 1% PEI solution with APTES-CSH at 40°C for 24 h, during which 1 mL of 25% GA was added dropwise. The produced PEI-CSH was repeatedly washed in deionized water, dried for 24 hours in an oven at 40°C, and then kept in a desiccator for further use.

*2.3. Analytical Methods.* The IR spectra of OSP, CSH, and PEI-CSH were investigated using a FT-IR spectrometer in the range of 4000–400 $cm^{-1}$ (Nicolet IS50, Thermo Fisher, USA). The compositions of OSP, CSH, and PEI-CSH were analyzed using XRD (D8 Advance A25, Bruker, USA) with Cu K$\alpha$ radiation ($\lambda = 1.54$ Å) and $2\theta$ range from 10° to 70°. A zeta potential analyzer was used to examine the zeta potential of CSH and PEI-CSH at various pH levels (ELSZ-2000, Otsuka, Japan). The surface morphologies of OSP, CSH, and PEI-CSH were observed by 300 kV TEM (Tecnai TF30, FEI, USA) at ×195,000 magnification.

*2.4. Batch Adsorption and Desorption Experiments.* The Pd(II) stock solution (1000 mg/L) was made by dissolving a particular amount of Pd(II) in 0.01 M HCl, and the Pd(II) concentrations used in this study were made by diluting the Pd(II) stock solution. Adsorption isotherm tests were conducted in the range of starting Pd(II) concentrations from 30 to 700 mg/L in order to determine the maximum adsorption capacity of the adsorbent for Pd(II). A shaking incubator was used to stir a 50 mL conical tube containing 0.06 g of adsorbent and 30 mL of Pd(II) solution for 24 hours at room temperature (25°C) and 160 rpm. Samples from the supernatant were taken after equilibrium to determine the final Pd content (II). At predetermined intervals during the

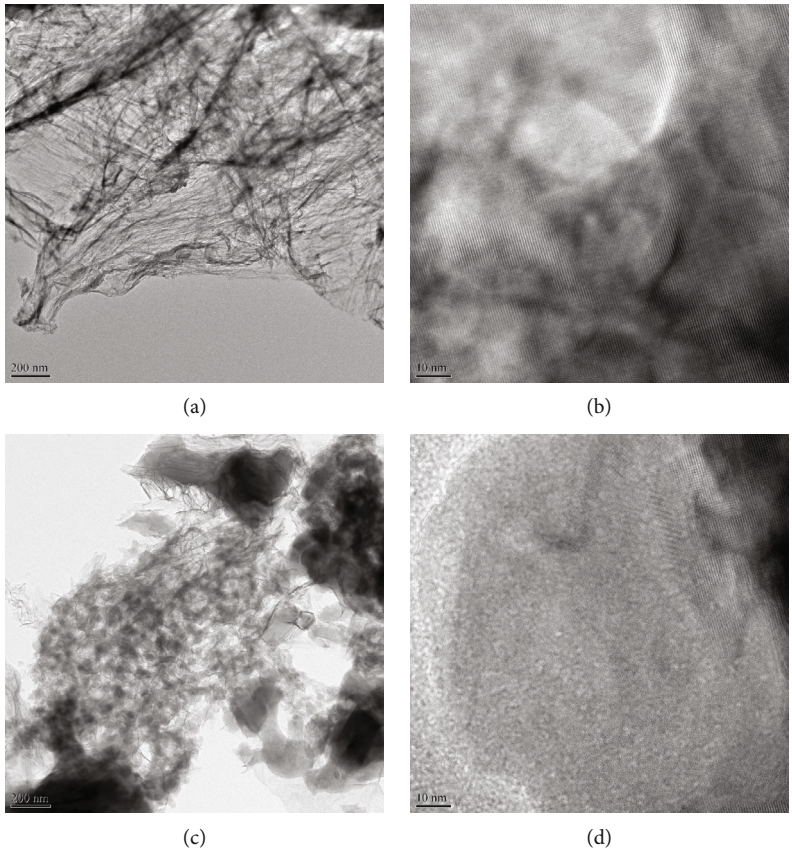


(a) (b) (c) (d)

Figure 1: TEM images of (a, b) CSH and (c, d) PEI-CSH at 12,000x (a, c) and 195,000x (b, d) magnification.

kinetic studies, samples from the supernatant were taken for concentration measurement at an initial Pd(II) concentration of 200 mg/L. All the samples were taken in triplicate. The obtained samples were diluted accordingly with tertiary distilled water after being centrifuged for 10 min at 10,000 rpm. ICP-OES (Avio200, PerkinElmer, USA) was used to detect the residual Pd(II) concentration, and Equation (1) was used to determine the Pd(II) adsorption quantity $q$ (mg/g).

$$q = \frac{(C_i - C_f)V}{m}, \tag{1}$$

where the initial and final Pd(II) concentrations, the working volume, and the weight of the adsorbent are expressed by $C_i$ and $C_f$ (mg/L), $V$ (L), and $m$ (g), respectively.

Prior to the desorption experiment, Pd(II)-loaded PEI-CSH was made by mixing 0.06 g of PEI-CSH with 30 mL of 200 ppm Pd(II) solution in a 50 mL conical tube. This adsorbent was promptly rinsed with deionized water and then resuspended in the eluent, which was a mixed solution of 0.01 M HCl and 0.01 M thiourea. A total of five repetitions were done for the adsorption and desorption cycles mentioned above. Following the proper dilution of the samples obtained from adsorption and desorption studies, the Pd(II) content of the samples was determined using an ICP-OES. The desorption efficiency was determined using the subsequent equation.

$$\text{Efficiency of desorption (\%)} = \frac{\text{Released Pd(II) weight (mg)}}{\text{Initially adsorbed Pd(II) weight (mg)}} \times 100. \tag{2}$$

## 3. Results and Discussion

### 3.1. Characterization

*3.1.1. TEM Image.* To explore the shape and crystal structure of the CSH-based adsorbent, TEM examination of CSH and PEI-CSH was performed. CSH composites with a hierarchical structure can be obtained by hydrothermal reaction of the OS and fumed silica (Figure 1(a)). Moreover, a close-up image of the CSH lattice is presented in Figure 1(b), which exhibits a small grid shape, suggesting that the precursors are formed along calcium and oxygen sheets surrounded by tetrahedral silica chains. Moreover, CSH demonstrate that channels are arranged orderly and uniformly [34]. After crosslinking with PEI, the hierarchical structure disappeared as shown in Figure 1(c). In the magnified image (Figure 1(d).), the surface of PEI-CSH is covered with polymer, and only a partial lattice pattern is observed. It indicates that during the preparation process,

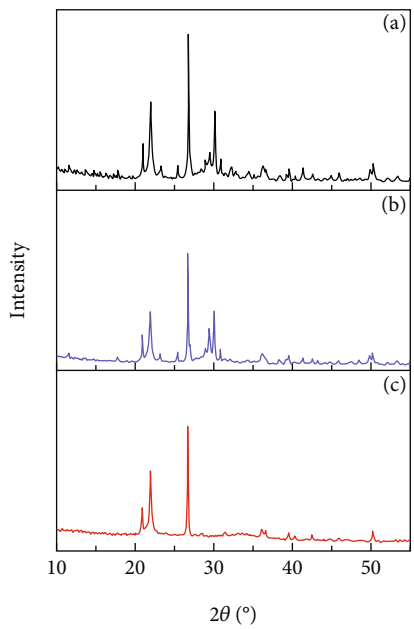


Figure 2: X-ray diffraction patterns of (a) CSH, (b) PEI-CSH, and (c) Pd-loaded PEI-CSH.

the intrinsic properties of CSH were not destroyed, as well as the PEI functional ligands were successfully bound to the CSH surface.

*3.1.2. XRD Analysis.* In Figure 2, the entire XRD pattern peaks are strong, indicating that the substance is highly crystallized. The characteristic peaks of CSH occur at 20°–30° and 50.8° [35, 36]. The grafting of PEI to the CSH surface may be the cause of the observed drop in the main peak diffraction intensity for PEI-CSH. After adsorption process, one of the main peaks disappeared. The missing peak was located at 29.8°, which is considered to be the effect of Pd(II)-induced destructive interference [37].

*3.1.3. FT-IR Analysis.* The FT-IR is a crucial tool for analyzing changes in chemical bonds in materials as well as potential interactions between metal ions and the surface functional groups of adsorbents. The FT-IR spectra of CSH, PEI-CSH, and Pd-loaded PEI-CSH are presented in Figure 3. As shown in Figure 3(a), the peaks in the range of 1200–400 $cm^{-1}$ represent the chemical bonds in the silica chains [38]. The peaks at 961, 641, and 443 $cm^{-1}$ were assigned to Si-O (asymmetric stretching vibration), Si-O-Si (out-of-plane bending vibration), and O-Si-O (in-plane bending vibration), respectively [39]. After PEI coating, the peaks at 961, 643, and 443 $cm^{-1}$ were shifted to 963, 643, and 451 $cm^{-1}$, respectively (Figure 3(b)). There were four new peaks found at 1073, 902, 796, and 697 $cm^{-1}$. The peak at 1073 $cm^{-1}$ was assigned to the C-N stretching vibration of aliphatic amines [40]. The band associated with amines was seen in the 910-665 $cm^{-1}$ range. Only primary and secondary amines were shown to have this robust, wide band, which was caused by N-H wagging [41]. Therefore, it can be explained that PEI was successfully crosslinked to the CSH surface. After the adsorption of Pd(II) (Figure 3(c)),

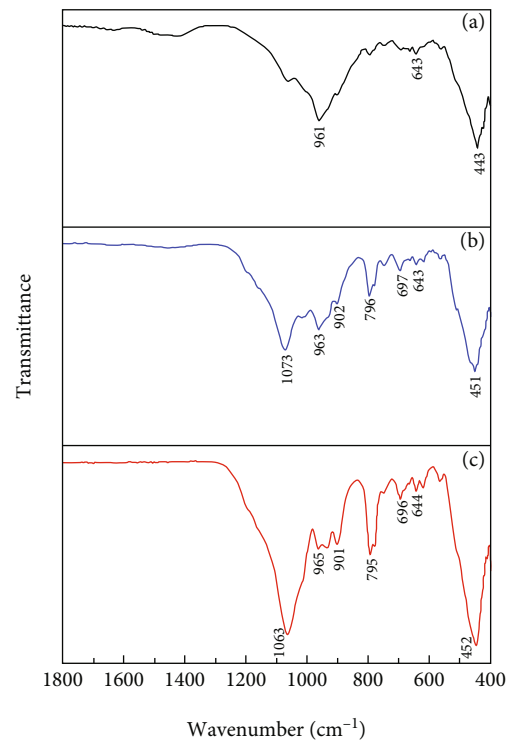


Figure 3: FT-IR spectra of (a) CSH, (b) PEI-CSH, and (c) Pd-loaded PEI-CSH.

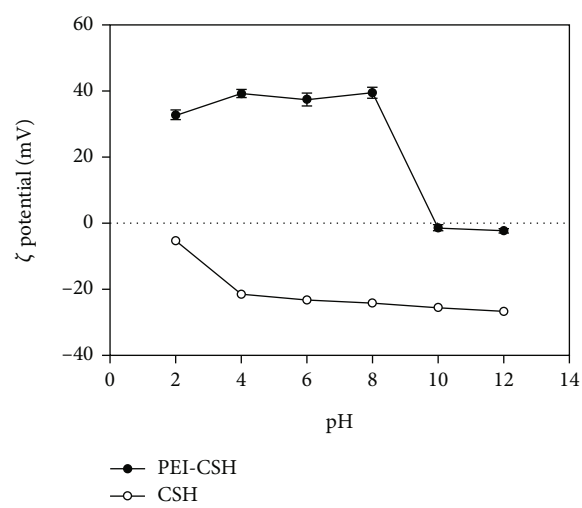


Figure 4: Surface zeta potential of CSH and PEI-CSH with different pH values.

the peaks at 1073, 902, 796, and 697 $cm^{-1}$ shifted slightly, and the intensity also changed. This change can be considered a result of the involvement of the amine group in the adsorption process [42].

*3.1.4. Zeta Potential.* According to Figure 4, the zeta potential of CSH decreased from -5.32 to -26.70 mV, with the pH value increasing from 2 to 12. On the other hand, PEI-CSH showed a high positive charge of +32.77 mV at below pH 8 and negative charge at -1.40 mV at above pH 10. In

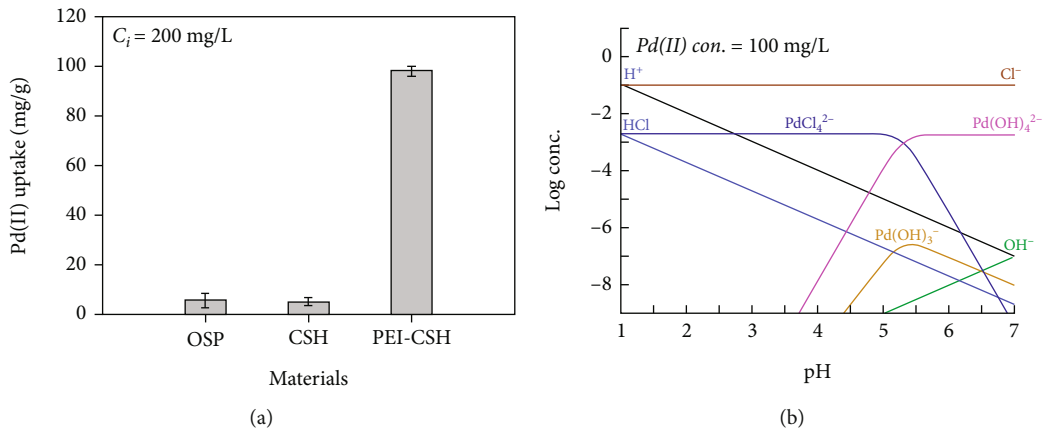


Figure 5: (a) Adsorption of Pd(II) onto different samples (OSP, CSH, and PEI-CSH) (experimental conditions: pH 2; volume of solution, 30 mL; mass of adsorbent, 60 mg; and initial Pd(II) concentration, 200 mg/L). (b) Pd(II)-pH equilibrium diagram for system hydrochloric acid (condition).

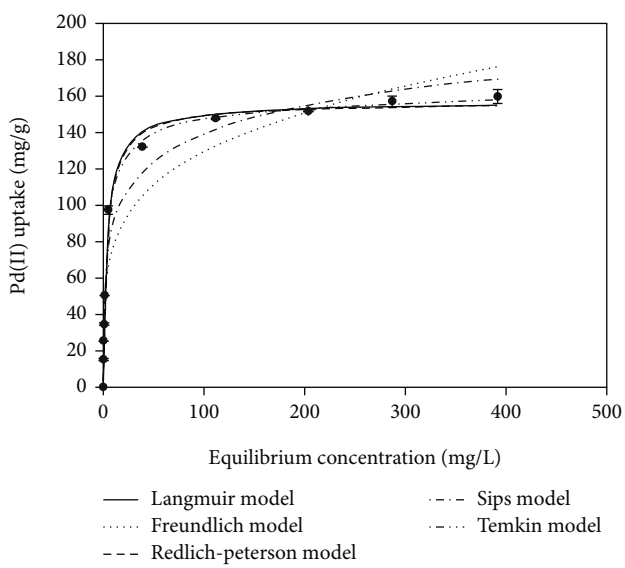


Figure 6: The isotherm models for Pd(II) adsorption onto PEI-CSH (experimental conditions: pH 2; volume of solution, 30 mL; mass of adsorbent, 60 mg; and initial Pd(II) concentration range, 30-700 mg/L).

Table 1: Isotherm parameters of Pd(II) adsorption onto PEI-CSH.

| Models | Parameter | Value |
|---|---|---|
| Langmuir | $q_{max}$ (mg/g) | 156.03 |
| | $b_L$ (L/mg) | 0.2344 |
| | $R^2$ | 0.994 |
| Freundlich | $K_F$ (L/g) | 46.34 |
| | $n$ | 4.47 |
| | $R^2$ | 0.913 |
| Sips | $q_{max}$ (mg/g) | 156.68 |
| | $K_S$ (L/mg) | 0.2374 |
| | $n$ | 1.0288 |
| | $R^2$ | 0.994 |
| Redlich-Peterson | $K_R$ (L/g) | 40.2145 |
| | $\alpha_R$ (L/mg) | 0.3005 |
| | $\beta$ | 0.9707 |
| | $R^2$ | 0.991 |
| Temkin | $K_T$ (L/mg) | 5.1132 |
| | $b_T$ (J/mol) | 110.8861 |
| | $R^2$ | 0.976 |

addition, the isoelectric point (PI) of PEI-CSH was 9.85, which was present at a higher pH than that of CSH. Consequently, the surface of PEI-CSH is positively charged at a pH lower than PI, which can be considered due to the amine groups such as $-NH^+$, $-NH_2^+$, and $NH_3^+$ in PEI coated on CSH.

*3.2. Adsorption Mechanism.* A large number of amine groups were produced on the surface of CSH as a result of PEI grafting onto CSH to generate PEI-CSH. The adsorption capacity of PEI-CSH for Pd(II) was significantly increased at pH 2 when amine groups were concentrated on the adsorbent surface (Figure 5(a)). The Pd(II) uptake of PEI-CSH was 99.54 mg/g, which is very high compared to that of OSP (6.97 mg/g) and CSH (4.38 mg/g). Interestingly, the difference in the amount of Pd(II) adsorption before and after the introduction of PEI into CSH is about 22.7-fold. As such, the presence/absence of PEI in the adsorbent largely affected the Pd(II) adsorption amount. To explain this result, it is necessary to check the form of Pd(II) at pH 2. As shown in Figure 5(b), Pd(II) exists as an anion in the form of $PdCl_4^{2-}$ in acidic conditions. Therefore, the anionic Pd(II) is likely to be bound with the positively charged amine groups in PEI-CSH through electrostatic attraction, which has been proved in our previous work [32].

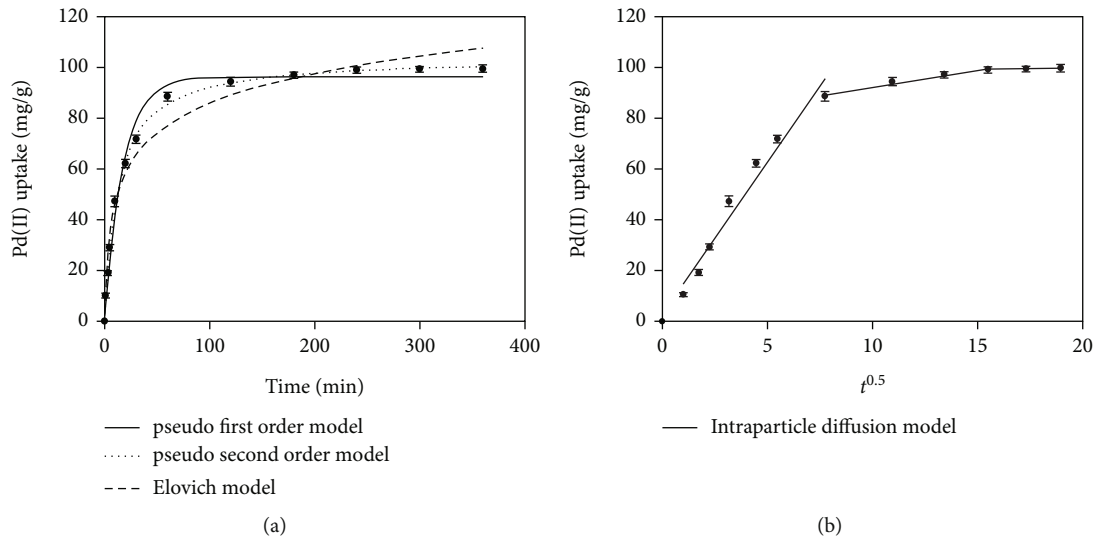


Figure 7: (a) The PFO, PSO, Elovich, and (b) intraparticle diffusion models for Pd(II) adsorption onto PEI-CSH (experimental conditions: pH 2; volume of solution, 60 mL; mass of adsorbent, 120 mg; and initial Pd(II) concentration, 200 mg/L).

*3.3. Adsorption Isotherms and Modeling.* To determine the maximal Pd adsorption capacity of PEI-CSH, isothermal adsorption studies were carried out at pH 2 (II). According to Figure 6, the PEI-Pd(II) CSH's uptakes increased as Pd(II) concentrations rose before reaching their maximum adsorption capacity. Adsorption isotherm models can offer crucial details on the adsorption process, surface characteristics, and interactions between the adsorbent and adsorbate. The experimental data were described by Langmuir, Freundlich, Sips, Redlich-Peterson, and Temkin isotherm models (see Supporting Information (available here)), and the corresponding parameters are listed in Table 1.

The Langmuir and Sips models had greater coefficient of determination ($R^2$) values than the other models, indicating that they were more suited to explain the adsorption of PEI-CSH for Pd(II) [6]. According to the Langmuir model, PEI-CSH was adsorbed on Pd(II) in a monolayer [43]. The $R_L$ values fell between 0 and 1, indicating that PEI-CSH adsorption for Pd(II) was favorable [44]. According to the Sips model, the PEI-Pd(II) CSH's adsorption process combines monolayer adsorption at high Pd(II) concentrations with diffusion at low Pd(II) concentrations [9]. Combining the Langmuir and Freundlich equations creates the Redlich-Peterson model. A value of 40.21 was determined for the Redlich-Peterson rate constant ($K_R$). The result was close to 1, indicating that the Pd(II) isotherms are compatible with the Langmuir and Redlich-Peterson models and that they are near to the Langmuir form [45]. According to the Temkin model, all molecules in the layer will experience a linear drop in the heat of adsorption as the layer's coverage increases due to the adsorbate-adsorbent interaction. As a result, the adsorption exhibits a consistent binding energy distribution up to a maximum level [46]. The exothermic nature of the adsorption process was suggested by the positive Temkin constant ($b_T$) value [9].

*3.4. Adsorption Kinetics and Modeling.* One of the key elements in determining the effectiveness of the overall adsorption process is adsorption kinetics, which also offers theoretical understanding of the reaction pathways and processes of adsorption [47]. To determine the time at which Pd(II) adsorption on PEI-CSH reaches equilibrium, the impact of contact time was assessed. The studies were conducted in an acidic environment (pH = 2) for 360 min at 25°C with an initial Pd(II) concentration of 200 mg/L. In the acidic setting, as shown in Figure 7, PEI-CSH adsorbed 95% of the Pd(II) during the first 120 min, reaching equilibrium at 180 min, demonstrating a very fast adsorption rate.

The pseudo-first-order (PFO), pseudo-second-order (PSO), Elovich, and intraparticle diffusion models (see Supporting Information) were used to explain kinetic data. Figure 7 and Table 2 show the fitting curves and accompanying parameters.

The parameters of kinetic models as well as $R^2$ values and $h$ are presented in Table 2. The experimental results confirmed that the PSO model, which had $R^2$ values near to unity, better suited the Pd(II) adsorption data when compared to the PFO and Elovich kinetic models. Additionally, the PSO model's projected value for the Pd(II) uptake at equilibrium, $q_2$, was quite similar to the experimental finding (99.67 mg/g). Since Pd(II) adsorption by PEI-CSH is a kinetic process, the PSO model proved effective in fitting the experimental data. It also suggests that chemisorption dominates physisorption during the adsorption process [48]. The chemisorption process is typically explained by the Elovich model [49]. The $R^2$ values of the Elovich model was 0.976, suggesting that chemisorption predominated in the adsorption process and that the model was acceptable for representing the kinetic adsorption process [49]. The three steps of the adsorption process are typically (1) film or external diffusion, (2) pore or intraparticle diffusion, and (3) adsorbate deposited on the adsorption site [50].

Table 2: Kinetic parameters of Pd(II) adsorption onto PEI-CSH.

| Models | Parameter | Value |
|---|---|---|
| PFO | $q_1$ (mg/g) | 96.43 |
| | $k_1$ (L/min) | 0.0564 |
| | $R^2$ | 0.966 |
| PSO | $q_2$ (mg/g) | 100.10 |
| | $k_2$ | 0.0008 |
| | $h$ | 8.65 |
| | $R^2$ | 0.998 |
| Elovich | $\alpha$ (mg/g•min) | 27.1856 |
| | $\beta$ (g/mg) | 0.0590 |
| | $R^2$ | 0.976 |
| Intraparticle diffusion | | |
| First stage | $k_{p1}$ (mg/g•min$^{0.5}$) | 12.0042 |
| | $C_1$ (mg/g) | 2.5736 |
| | $R^2$ | 0.964 |
| Second stage | $k_{p2}$ (mg/g•min$^{0.5}$) | 1.3402 |
| | $C_2$ (mg/g) | 78.8017 |
| | $R^2$ | 0.976 |
| Third stage | $k_{p3}$ (mg/g•min$^{0.5}$) | 0.1813 |
| | $C_3$ (mg/g) | 96.2293 |
| | $R^2$ | 0.999 |

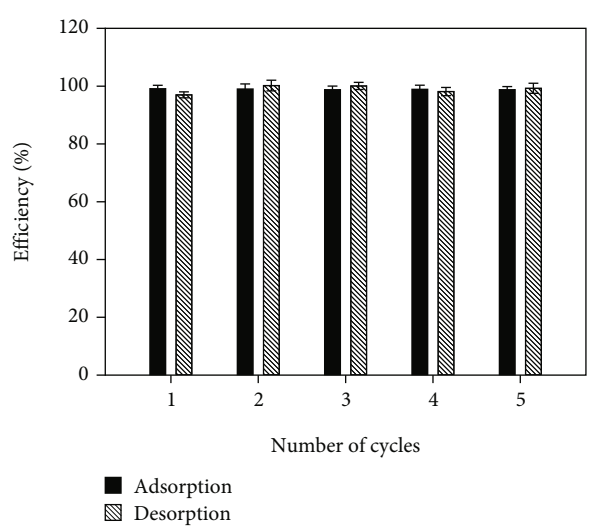


Figure 8: Repeated adsorption-desorption of Pd(II) on PEI-CSH in a batch process (adsorption conditions: pH 2; volume of solution, 30 mL; mass of adsorbent, 60 mg; initial Pd(II) concentration, 200 mg/L, desorption conditions: pH 2; volume of 0.01 M thiourea solution, 30 mL; and mass of Pd(II)-loaded adsorbent, 60 mg).

The rate-limiting phases of the adsorption process were identified using the intraparticle diffusion model. The results of $q_t$ vs. $t^{0.5}$ acquired from the Pd(II) adsorption experiment are displayed in Figure 7(b). Three separate stages were used to display the linear plot. Since the initial step did not go through the origin, it is likely that external diffusion and subsequently intraparticle diffusion were used preferentially to regulate the adsorption of Pd(II) on PEI-CSH until equilibrium was reached [51].

*3.5. Reusability of PEI-CSH.* For promising adsorbents, the capacity to be reused is a crucial characteristic. Adsorbent replacement cycles can be extended, and financial gain can be made if an exhausted adsorbent can be recycled. Each of the adsorption and desorption experiments was conducted up to five times. An acidified thiourea solution prepared by mixing 0.01 M HCl and 0.01 M thiourea was used as the eluent for desorbing Pd from the loaded adsorbent. The adsorption and desorption efficiencies were nearly constant at 100% across the five cycles, as illustrated in Figure 8. Desorption by thiourea is pH-dependent [52], and thiourea forms a coordination bond with metal ions at neutral pH but induces desorption by an anion-exchange mechanism with $PdCl_4^{2-}$ at acidic pH [32]. Since an acidified thiourea solution was used in this study, the desorption is considered to be due to anion exchange. It was also confirmed that the reusability of PEI-CSH was very excellent.

## 4. Conclusion

In summary, an oyster waste-based adsorbent, PEI-CSH, was developed, providing an alternative way for oyster shell waste recycling. According to the TEM image, the prepared CSH showed a hierarchical structure surface, and the PEI-CSH was covered with a polymer. As evidenced by XRD analysis, PEI-CSH was observed to have characteristic peaks of CSH, which was reduced in intensity by PEI. In addition, it was found through FT-IR analysis and one-point check adsorption experiments that the absorption performance of PEI-CSH was improved by amine groups. Modification of CSH with PEI also increased the point of zero charge to 9.85. These results revealed that the adsorbent was successfully prepared. The Langmuir model was more suitable for depicting adsorption of Pd(II) on PEI-CSH, and the maximum adsorption amount was 156.03 mg/g at pH 2. Kinetic experiment showed that the adsorption equilibrium for 200 mg/L of Pd(II) at pH 2 was reached within 180 min. According to the reusability research, PEI-CSH may be recycled at least five times without losing any of its adsorption capability. Overall, the PEI-CSH, fabricated from oyster shell waste, showed the possibility of eliminating anionic Pd(II) from a HCl solution.

## Data Availability

The raw data used to support the findings of this study are available from the corresponding author upon request.

## Conflicts of Interest

The authors declare that they have no conflicts of interest.

## Acknowledgments

This research was supported by Basic Science Research Program through the National Research Foundation of Korea (NRF) funded by the Ministry of Education (NRF-2020R1A6A3A13068967 and NRF-2020R1F1A1065937).

## Supplementary Materials

The following are the supplementary data to this article. *(Supplementary Materials)*

## References

[1] Y. Liu, L. Zhang, Q. Song, and Z. Xu, "Recovery of palladium as nanoparticles from waste multilayer ceramic capacitors by potential-controlled electrodeposition," *Journal of Cleaner Production*, vol. 257, article 120370, 2020.

[2] D. A. Jadhav, P. A. Deshpande, and M. M. Ghangrekar, "Enhancing the performance of single-chambered microbial fuel cell using manganese/palladium and zirconium/palladium composite cathode catalysts," *Bioresource Technology*, vol. 238, pp. 568–574, 2017.

[3] C. Icsel, V. T. Yilmaz, F. Ari, E. Ulukaya, and W. T. A. Harrison, "*trans* -Dichloridopalladium(II) and platinum(II) complexes with 2-(hydroxymethyl)pyridine and 2-(2-hydroxyethyl)pyridine: Synthesis, structural characterization, DNA binding and *in vitro* cytotoxicity studies," *European Journal of Medicinal Chemistry*, vol. 60, pp. 386–394, 2013.

[4] A. K. Mishra and N. K. Kaushik, "Synthesis, characterization, cytotoxicity, antibacterial and antifungal evaluation of some new platinum (IV) and palladium (II) complexes of thiodiamines," *European Journal of Medicinal Chemistry*, vol. 42, no. 10, pp. 1239–1246, 2007.

[5] K. Husain, M. Abid, and A. Azam, "Synthesis, characterization and antiamoebic activity of new indole-3-carboxaldehyde thiosemicarbazones and their Pd(II) complexes," *European Journal of Medicinal Chemistry*, vol. 42, no. 10, pp. 1300–1308, 2007.

[6] B. Veisi, B. Lorestani, S. Sobhan Ardakani, M. Cheraghi, and L. Tayebi, "Post synthetic modification of magnetite @MIL-53(Fe)-$NH_2$ core-shell nanocomposite for magnetic solid phase extraction of ultra-trace Pd(II) ions from real samples," *International Journal of Environmental Analytical Chemistry*, pp. 1–18, 2022.

[7] A. K. Mosai, R. H. Johnson, and H. Tutu, "Modelling of palladium(II) adsorption onto amine-functionalised zeolite using a generalised surface complexation approach," *Journal of Environmental Management*, vol. 277, article 111416, 2021.

[8] D. Bourgeois, V. Lacanau, R. Mastretta, C. Contino-Pépin, and D. Meyer, "A simple process for the recovery of palladium from wastes of printed circuit boards," *Hydrometallurgy*, vol. 191, article 105241, 2020.

[9] Z. Wang, S. B. Kang, and S. W. Won, "Selective adsorption of palladium(II) from aqueous solution using epichlorohydrin crosslinked polyethylenimine-chitin adsorbent: batch and column studies," *Journal of Environmental Chemical Engineering*, vol. 9, no. 2, article 105058, 2021.

[10] C. R. M. Rao and G. S. Reddi, "Platinum group metals (PGM); occurrence, use and recent trends in their determination," *TrAC Trends in Analytical Chemistry*, vol. 19, no. 9, pp. 565–586, 2000.

[11] G. Khayatian and K. Sharifi, "Development of a dispersive liquid–liquid microextraction method for determination of palladium in water samples using dicyclohexano-18- crown-6 as extracting agent," *Journal of Inclusion Phenomena and Macrocyclic Chemistry*, vol. 79, no. 1-2, pp. 185–191, 2014.

[12] M. R. Awual and T. Yaita, "Rapid sensing and recovery of palladium(II) using *N,N*-bis(salicylidene)1,2-bis(2-aminophenylthio)ethane modified sensor ensemble adsorbent," *Sensors and Actuators B: Chemical*, vol. 183, pp. 332–341, 2013.

[13] B. Swain, J. Jeong, S.-k. Kim, and J.-c. Lee, "Separation of platinum and palladium from chloride solution by solvent extraction using Alamine 300," *Hydrometallurgy*, vol. 104, no. 1, pp. 1–7, 2010.

[14] G. Kolliopoulos, E. Balomenos, I. Giannopoulou, I. Yakoumis, and D. Panias, "Behavior of platinum group during their pyrometallurgical recovery from spent automotive catalysts," *OALib*, vol. 1, no. 5, pp. 1–9, 2014.

[15] S. Zhang, S. Ning, H. Liu, X. Wang, Y. Wei, and X. Yin, "Preparation of ion-exchange resin via in-situ polymerization for highly selective separation and continuous removal of palladium from electroplating wastewater," *Separation and Purification Technology*, vol. 258, p. 117670, 2021.

[16] Y. Du, F. Lian, and L. Zhu, "Biosorption of divalent Pb, Cd and Zn on aragonite and calcite mollusk shells," *Environmental Pollution*, vol. 159, no. 7, pp. 1763–1768, 2011.

[17] D. Ding, Y. Zhao, S. Yang et al., "Adsorption of cesium from aqueous solution using agricultural residue–walnut shell: equilibrium, kinetic and thermodynamic modeling studies," *Water Research*, vol. 47, no. 7, pp. 2563–2571, 2013.

[18] A. Othmani, S. Magdouli, P. Senthil Kumar, A. Kapoor, P. V. Chellam, and Ö. Gökkuş, "Agricultural waste materials for adsorptive removal of phenols, chromium (VI) and cadmium (II) from wastewater: a review," *Environmental Research*, vol. 204, article 111916, Part A, 2022.

[19] J. Park, S. W. Won, J. Mao, I. S. Kwak, and Y. S. Yun, "Recovery of Pd(II) from hydrochloric solution using polyallylamine hydrochloride-modified *Escherichia coli* biomass," *Journal of Hazardous Materials*, vol. 181, no. 1-3, pp. 794–800, 2010.

[20] A. Jędrczak and M. Suchowska-Kisielewicz, "A comparison of waste stability indices for mechanical–biological waste treatment and composting plants," *International Journal of Environmental Research and Public Health*, vol. 15, no. 11, p. 2585, 2018.

[21] D. Alidoust, M. Kawahigashi, S. Yoshizawa, H. Sumida, and M. Watanabe, "Mechanism of cadmium biosorption from aqueous solutions using calcined oyster shells," *Journal of Environmental Management*, vol. 150, pp. 103–110, 2015.

[22] H. Y. Yen and J. Y. Li, "Process optimization for Ni(II) removal from wastewater by calcined oyster shell powders using Taguchi method," *Journal of Environmental Management*, vol. 161, pp. 344–349, 2015.

[23] C. He, J. Qu, Z. Yu et al., "Preparation of micro-nano material composed of oyster shell/$Fe_3O_4$ nanoparticles/humic acid and its application in selective removal of hg(II)," *Nanomaterials*, vol. 9, no. 7, p. 953, 2019.

[24] S. Wu, L. Liang, Q. Zhang et al., "The ion-imprinted oyster shell material for targeted removal of Cd(II) from aqueous solution," *Journal of Environmental Management*, vol. 302, article 114031, Part A, 2022.

[25] J. Chen, Y. Cai, M. Clark, and Y. Yu, "Equilibrium and kinetic studies of phosphate removal from solution onto a

hydrothermally modified oyster shell material," *PLoS One*, vol. 8, no. 4, article e60243, 2013.

[26] Z. Zhang, X. Wang, H. Wang, and J. Zhao, "Removal of Pb(II) from aqueous solution using hydroxyapatite/calcium silicate hydrate (HAP/C-S-H) composite adsorbent prepared by a phosphate recovery process," *Chemical Engineering Journal*, vol. 344, pp. 53–61, 2018.

[27] N. Shao, S. Li, F. Yan, Y. Su, F. Liu, and Z. Zhang, "An all-in-one strategy for the adsorption of heavy metal ions and photodegradation of organic pollutants using steel slag-derived calcium silicate hydrate," *Journal of Hazardous Materials*, vol. 382, article 121120, 2020.

[28] Z. Zhu, Z. Wang, L. Xu et al., "Synthesis and characterization of an intermediate for C-S-H structure tailoring," *Cement and Concrete Research*, vol. 160, article 106923, 2022.

[29] C.-W. Cho, S. B. Kang, S. Kim, Y.-S. Yun, and S. W. Won, "Reusable polyethylenimine-coated polysulfone/bacterial biomass composite fiber biosorbent for recovery of Pd(II) from acidic solutions," *Chemical Engineering Journal*, vol. 302, pp. 545–551, 2016.

[30] X. Lin, D. T. Tran, M.-H. Song, and Y.-S. Yun, "Development of polyethyleneimine-starch fibers stable over the broad pH range for selective adsorption of gold from actual leachate solutions of waste electrical and electronic equipment," *Journal of Cleaner Production*, vol. 328, article 129545, 2021.

[31] H. N. Park, H. A. Choi, and S. W. Won, "Fibrous polyethylenimine/polyvinyl chloride crosslinked adsorbent for the recovery of Pt(IV) from acidic solution: adsorption, desorption and reuse performances," *Journal of Cleaner Production*, vol. 176, pp. 360–369, 2018.

[32] S. B. Kang, Z. Wang, and S. W. Won, "Application of polyethylenimine multi-coated adsorbent for Pd(II) recovery from acidic aqueous solution: batch and fixed-bed column studies," *Korean Journal of Chemical Engineering*, vol. 38, no. 3, pp. 523–530, 2021.

[33] W. You, M. Hong, H. Zhang, Q. Wu, Z. Zhuang, and Y. Yu, "Functionalized calcium silicate nanofibers with hierarchical structure derived from oyster shells and their application in heavy metal ions removal," *Physical Chemistry Chemical Physics*, vol. 18, no. 23, pp. 15564–15573, 2016.

[34] M. Schönlein and J. Plank, "A TEM study on the very early crystallization of C-S-H in the presence of polycarboxylate superplasticizers: transformation from initial C-S-H globules to nanofoils," *Cement and Concrete Research*, vol. 106, pp. 33–39, 2018.

[35] Z. Zhu, Z. Wang, Y. Zhou, Y. Wei, and A. She, "Synthesis and structure of calcium silicate hydrate (C-S-H) modified by hydroxyl-terminated polydimethylsiloxane (PDMS)," *Construction and Building Materials*, vol. 267, article 120731, 2021.

[36] U. Zulfiqar, T. Subhani, and S. W. Husain, "Synthesis and characterization of silica nanoparticles from clay," *Journal of Asian Ceramic Societies*, vol. 4, no. 1, pp. 91–96, 2016.

[37] M. M. Tarekegn, R. M. Balakrishnan, A. M. Hiruy, and A. H. Dekebo, "Removal of methylene blue dye using nano zerovalent iron, nanoclay and iron impregnated nanoclay – a comparative study," *RSC Advances*, vol. 11, no. 48, pp. 30109–30131, 2021.

[38] L. Peng, H. Dai, Y. Wu, Z. Dai, X. Li, and X. Lu, "Performance and adsorption mechanism of a magnetic calcium silicate hydrate composite for phosphate removal and recovery," *Water Science and Technology*, vol. 2017, no. 2, pp. 578–591, 2018.

[39] Y. Li, H. Li, C. Jin et al., "Multi-scale investigation and mechanism analysis on Young's modulus of C-S-H modified by multi-walled carbon nanotubes," *Construction and Building Materials*, vol. 308, p. 125079, 2021.

[40] S. Murugesh and P. Vino, "Phytochemical constituents, antioxidant activity and FT-IR analysis of *Pisonia grandis* leaf extracts," *International Journal of Pharmacognosy and Phytochemical Research*, vol. 9, no. 7, 2018.

[41] H. Xu, L. Tan, H. Cui et al., "Characterization of Pd(II) biosorption in aqueous solution by *Shewanella oneidensis* MR-1," *Journal of Molecular Liquids*, vol. 255, pp. 333–340, 2018.

[42] B. N. Bhadra, P. W. Seo, and S. H. Jhung, "Adsorption of diclofenac sodium from water using oxidized activated carbon," *Chemical Engineering Journal*, vol. 301, pp. 27–34, 2016.

[43] Y. Liu, Y. Xiong, P. Xu, Y. Pang, and C. Du, "Enhancement of Pb (II) adsorption by boron doped ordered mesoporous carbon: isotherm and kinetics modeling," *Science of the Total Environment*, vol. 708, article 134918, 2020.

[44] S. N. Jain, S. R. Tamboli, D. S. Sutar et al., "Batch and continuous studies for adsorption of anionic dye onto waste tea residue: kinetic, equilibrium, breakthrough and reusability studies," *Journal of Cleaner Production*, vol. 252, article 119778, 2020.

[45] G. M. Kim, Z. Wang, S. B. Kang, and S. W. Won, "Polyethylenimine-crosslinked chitin flake as a biosorbent for removal of Acid Blue 25," *Korean Journal of Chemical Engineering*, vol. 36, no. 9, pp. 1455–1465, 2019.

[46] A. Maleki, U. Hamesadeghi, H. Daraei et al., "Amine functionalized multi-walled carbon nanotubes: single and binary systems for high capacity dye removal," *Chemical Engineering Journal*, vol. 313, pp. 826–835, 2017.

[47] N. Ayawei, A. N. Ebelegi, and D. Wankasi, "Modelling and interpretation of adsorption isotherms," *Journal of Chemistry*, vol. 2017, Article ID 3039817, 11 pages, 2017.

[48] L. Fan, Y. Lu, L. Y. Yang, F. Huang, and X. K. Ouyang, "Fabrication of polyethylenimine-functionalized sodium alginate/cellulose nanocrystal/polyvinyl alcohol core-shell microspheres ((PVA/SA/CNC)@PEI) for diclofenac sodium adsorption," *Journal of Colloid and Interface Science*, vol. 554, pp. 48–58, 2019.

[49] L. Sun, D. Chen, S. Wan, and Z. Yu, "Performance, kinetics, and equilibrium of methylene blue adsorption on biochar derived from eucalyptus saw dust modified with citric, tartaric, and acetic acids," *Bioresource Technology*, vol. 198, pp. 300–308, 2015.

[50] U. A. Qureshi, Z. Khatri, F. Ahmed, M. Khatri, and I.-S. Kim, "Electrospun zein nanofiber as a green and recyclable adsorbent for the removal of reactive black 5 from the aqueous phase," *ACS Sustainable Chemistry & Engineering*, vol. 5, no. 5, pp. 4340–4351, 2017.

[51] R. A. Fideles, G. M. D. Ferreira, F. S. Teodoro et al., "Trimellitated sugarcane bagasse: a versatile adsorbent for removal of cationic dyes from aqueous solution. Part I: batch adsorption in a monocomponent system," *Journal of Colloid and Interface Science*, vol. 515, pp. 172–188, 2018.

[52] S. Örgül and Ü. Atalay, "Reaction chemistry of gold leaching in thiourea solution for a Turkish gold ore," *Hydrometallurgy*, vol. 67, no. 1-3, pp. 71–77, 2002.

Hindawi
Adsorption Science & Technology
Volume 2023, Article ID 8217910, 15 pages
https://doi.org/10.1155/2023/8217910

*Research Article*

# $Na_4P_2O_7$-Modified Biochar Derived from Sewage Sludge: Effective Cu(II)-Adsorption Removal from Aqueous Solution

**Liangqian Fan,[1,2] Xianda Wang,[1,2] Jiaxin Miao,[1,2] Qin Liu,[1,2] Jie Cai,[3] Xiaochan An,[1,2] Fenghui Chen,[1,2] Lin Cheng,[1,2] Wei Chen,[1,2] Hongbing Luo,[1,2] Xiaoxiao Zhang,[1,2] Ke Zhang,[1,2] and Dandan Ma[1,2]**

[1]*College of Civil Engineering, Sichuan Agricultural University, Dujiangyan 611830, China*
[2]*Sichuan Higher Education Engineering Research Center for Disaster Prevention and Mitigation of Village Construction, Sichuan Agricultural University, Dujiangyan 611830, China*
[3]*Department of Physical and Chemical Analysis, Dujiangyan Center for Disease Control and Prevention, Dujiangyan 611830, China*

Correspondence should be addressed to Liangqian Fan; flqjacky@163.com

Received 9 August 2022; Revised 1 October 2022; Accepted 24 November 2022; Published 3 February 2023

Academic Editor: Hesham Hamad



With the rapid development of industrialization, the amount of copper-containing wastewater is increasing, thereby posing a threat to the aquatic ecological environment and human health. Sludge biochar has received extensive concern in recent years due to its advantages of low cost and sustainability for the treatment of heavy-metal-containing wastewater. However, the heavy-metal-adsorption capacity of sludge biochar is limited. This study prepared a sodium pyrophosphate- ($Na_4P_2O_7$-) modified municipal sludge-based biochar (SP-SBC) and evaluated its adsorption performance for Cu(II). Results showed that SP-SBC had higher yield, ash content, pH, Na and P content, and surface roughness than original sewage sludge biochar (SBC). The Cu(II)-adsorption capacity of SP-SBC was 4.55 times than that of SBC at room temperature. For Cu(II) adsorption by SP-SBC, the kinetics and isotherms conformed to the pseudo-second-order model and the Langmuir–Freundlich model, respectively. The maximum adsorption capacity of SP-SBC was 38.49 $mg \cdot g^{-1}$ at 35°C. Cu(II) adsorption by SP-SBC primarily involved ion exchange, electrostatic attraction, and precipitation. The desired adsorption performance for Cu(II) in the fixed-bed column experiment indicated that SP-SBC can be reused and had good application potential to treat copper-containing wastewater. Overall, this study provided a desirable sorbent (SP-SBC) for Cu(II) removal, as well as a new simple chemical-modification method for SBC to enhance Cu(II)-adsorption capacity.

## 1. Introduction

With the rapid development of industrialization, the heavy metals that enter the water environment through human activities inevitably increase [1–3]. Due to the persistence, bioaccumulation, pathogenicity, and carcinogenicity of heavy metals, the water-environment pollution they cause is attracting extensive attention [1, 4]. Copper, as an important heavy metal material, is widely used in the fields of electronics, energy, communications, and machinery production, resulting in a large amount of copper-containing wastewater. The concentration of copper in the wastewater varies from tens to thousands of milligrams per liter [5]. Once the wastewater is directly discharged into natural water bodies without proper treatment, it harms aquatic organisms and leads to a series of health problems to humans, such as nausea, diarrhea, liver, and kidney damage [1, 6]. Thus, the removal of copper from wastewater has become an important issue for heavy-metal pollution control. Several methods are presently used to deal with copper-containing wastewater, primarily including chemical precipitation, bioremediation, membrane separation, and adsorption [7]. Among these methods, adsorption has elicited extensive attention in view of its advantages of convenient operation, considerable efficiency, low cost, and strong anticontamination ability [8, 9]. For adsorption, sorbent development is an important research task [10–14].

Biochar is a porous and carbon-rich solid material obtained by pyrolyzing biomass under anoxic or anaerobic conditions [15, 16]. Due to the high porosity, large surface area, rich surface functional groups, and high pH value of biochar, it receives extensive attention in the field of heavy-metal-containing wastewater treatment [17]. In previous years, a large number of biochar materials such as discarded mushroom-stick biochar [18], corn straw biochar [19], date seed biochar [20], tobacco stem biochar [21], industrial alkali lignin biochar [22], and *Ascophyllum nodosum* seaweed biochar [23] have been successfully prepared to remove heavy metal from wastewater. These studies show that biochar is an environmentally friendly and cost-effective adsorption material for heavy-metal adsorption. With the deepening of research, some scholars have performed studies on biochar modification, particularly chemical modification, to improve the heavy-metal-adsorption capacity by raw biochar [24–31]. These studies have indicated that the heavy-metal-adsorption capacity of biochar can be significantly improved by an effective modifier. Such a modifier adds adsorption sites and enhances electrostatic attraction, surface complexation, or surface precipitation on biochar.

In China, the growing sewage sludge produced from sewage treatment has become a serious burden on ecology and society [32]. Accordingly, China has the urgent need for environment-friendly methods to realize the effective treatment of sewage sludge. However, the commonly used methods of incineration, sanitary landfilling, and land application [32] have some shortcomings that could lead to secondary pollution. For example, $NO_x$, $SO_2$, and volatile heavy metals produced from incineration can cause serious air pollution [33]. Sanitary landfilling can occupy land. Direct agricultural application may harm living organisms [34]. Many researchers have reported the related studies on converting sewage sludge to biochar for the treatment of heavy-metal-containing wastewater [35–41]. They found that preparing biochar from sewage sludge can realize the harmless and reductive treatments of sewage sludge and obtain a low-cost and sustainable sorbent for the treatment of heavy-metal-containing wastewater. However, the heavy-metal-adsorption capacity of sludge-based biochar is unsatisfactory, which limits its promotion and application to a certain extent [42, 43]. Some modifiers such as $Fe_3O_4$ [44], nanostructured $CaCO_3$ [45], trithiocyanuric acid trisodium salt [46], $\alpha$-$Fe_2O_3$ and $\alpha$-FeOOH [47], $K_2FeO_4$ [48], and hydroxyapatite [42] have been successfully applied to prepare modified sewage sludge biochar, and satisfactory heavy-metal-adsorption capacity has been achieved. At present, chemical modification is a noteworthy research direction for improving the adsorption capacity of heavy metals by sewage sludge biochar [45, 49]. In the present study, we used sodium pyrophosphate ($Na_4P_2O_7$), an additive widely used in the food industry, water industry, and daily chemical industry, as a modifier to prepare $Na_4P_2O_7$-modified sewage sludge-based biochar (SP-SBC). The desirable Cu(II)-adsorption capacity of SP-SBC was hoped to be achieved through the precipitation between pyrophosphate or phosphate and Cu(II). Although some similar reports exist on sewage sludge biochar modified with chemical modification for Cu(II) adsorption [42, 50, 51], to our knowledge, SP-SBC and its Cu(II)-adsorption performance are reported herein for the first time. Moreover, our one-pot preparation method of SP-SBC was simpler than those of biochars reported by Chen et al. [42], Phoungthong and Suwunwong [50], and Tang et al. [51]. This study could provide an alternative path for modifying sewage sludge biochar, which is beneficial to promote the practical application of sludge biochar.

The aims of this study were as follows: (i) to prepare SP-SBC and explore its properties, (ii) to investigate the adsorption behaviors of SP-SBC for Cu(II), and (iii) to understand the application potential of SP-SBC for Cu(II)-adsorption removal. Herein, SP-SBC was prepared. The properties of SP-SBC and original sewage sludge biochar (SBC) were characterized by the yield; ash content; pH, K, Ca, Na, Mg, and P contents; SEM; and FTIR. Then, the effects of sorbent dosage, initial pH, ionic strength, contact time, and temperature on the Cu(II) adsorption by SP-SBC were determined by batch-adsorption experiments. For Cu(II) adsorption by SP-SBC, the kinetics and isotherms were explored. Lastly, a fixed-bed column experiment was performed.

## 2. Materials and Methods

*2.1. Materials.* Sodium pyrophosphate ($Na_4P_2O_7$; AR, 99%), copper nitrate trihydrate ($Cu(NO_3)_2{\cdot}3H_2O$; AR, 99%), sodium nitrate ($NaNO_3$; AR, 99%), silica sand, nitric acid ($HNO_3$; AR, 65–68 wt%), and sodium hydroxide (NaOH, AR, 98%) were all supplied by Kelong Chemical Co., Ltd. (Chengdu, China) without further purification. Ultrapure water (18.25 MΩ) was used to prepare the used solutions. Sewage sludge was acquired from a local municipal wastewater-treatment plant in Chengdu city, China.

*2.2. Preparation of Biochar.* SP-SBC was prepared with a one-pot method (Figure 1). The specific procedures were as follows. Sewage sludge was ground and sieved to pass a 10-mesh sieve after natural drying. A part of sieved sludge was impregnated with $Na_4P_2O_7$ ($60\,g{\cdot}L^{-1}$) at a ratio of 1/20 (mass/volume) for 12 h in a constant-temperature shaker under the conditions of 25°C and 130 rpm. Afterwards, the impregnated sludge was dried at 60°C until the weight was stable. The dried impregnated sludge and the other part of the sieved sludge were loaded into different ceramic crucibles, sealed, and capped. Then, they were pyrolyzed for 2 h at 400°C in a muffle furnace. After grinding the pyrolyzed product of the original sludge and sieving (60 mesh), the acquired particles under the sieve were recorded as SBC. The pyrolyzed product of the impregnated sludge was washed several times with 55–65°C deionized water and dried at 60°C until the weight was stable. The dried product was passed through a sieve (60 mesh) after grinding. The obtained particles under the sieve were recorded as SP-SBC.

*2.3. Properties of Biochar.* The analysis methods for the properties of SBC or SP-SBC were as follows. Equation (1)

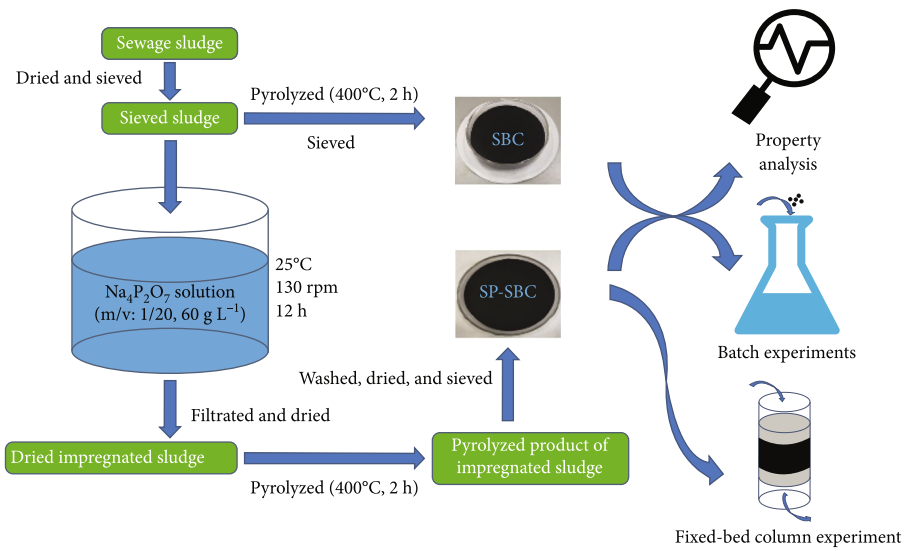


Figure 1: Flow chart of SP-SBC preparation.

Table 1: Specific conditions for each batch experiment.

| Batch experiment | Experimental conditions | | | | | |
|---|---|---|---|---|---|---|
| | Sorbent dosage (g) | Initial solution pH | Ionic strength ($NaNO_3$, M) | Contact time (h) | Temperature (°C) | Cu(II) concentration ($mg \cdot L^{-1}$) |
| Sorbent dosage | 0.025, 0.05, 0.075, 0.1, 0.2, 0.3, 0.5 | 5 | 0 | 12 | 25 | 50 |
| Initial solution pH | 0.1 | 3, 3.5, 4, 4.5, 5, 6 | 0 | 12 | 25 | 50 |
| Ionic strength | 0.1 | 5 | 0, 0.005, 0.01, 0.03, 0.05, 0.08, 0.10, 0.50 | 12 | 25 | 50 |
| Contact time | 0.1 | 5 | 0 | 0.5, 1, 2, 3, 4, 6, 8, 10, 12, 14 | 25 | 50 |
| Temperature | 0.1 | 5 | 0 | 12 | 15, 25, 35 | 50, 150, 200, 300, 400, 600 |

was used to calculate the yield ($Y$, %):

$$Y = \left(\frac{m_0}{m_t}\right) \times 100\%, \quad (1)$$

where $m_0$ and $m_t$ denote the weight of SBC (or SP-SBC) and sewage sludge (g), respectively. Ash content was detected by burning 1.00 g of samples in a muffle furnace at 700°C for 2 h and calculated by the following equation:

$$\text{Ash}(\%) = \left(\frac{M_0}{M_t}\right) \times 100\%, \quad (2)$$

where $M_0$ and $M_t$ represent the weight of SBC (or SP-SBC) after and before burning (g), respectively. The pH; contents of Na, K, Ca, Mg, and P; and the surface structural morphology (i.e., SEM images) were determined as in our previous methods [52]. The surface functional groups on SBC, SP-SBC, and SP-SBC after Cu(II) adsorption (SP-SBC+Cu) were recorded with a Nicolet iS50-type FTIR spectroscope (Thermo Fisher Scientific, Inc., Waltham, USA). At different solution pH values, the zeta potentials of SP-SBC were measured based on our previous methods to calculate the isoelectric point ($pH_{IEP}$) [52].

*2.4. Batch Experiments.* The influences of sorbent dosage, initial solution pH, ionic strength, contact time, and temperature on Cu(II) adsorption by SP-SBC were determined with batch experiments. For all batch experiments, the Cu(II) solution with a preset concentration was prepared by diluting 1000 $mg \cdot L^{-1}$ of Cu(II) stock solution, which was in turn prepared with $Cu(NO_3)_2 \cdot 3H_2O$ and ultrapure water (18.25 MΩ). In a typical procedure, a certain amount of SP-SBC was mixed with 50 mL of Cu(II) solution with a designed concentration, followed by adjusting the pH to a predesigned value. Then, the mixture was shaken for a certain time period at a preset temperature and at 130 rpm in a constant-temperature shaker. The specific conditions for each batch experiment are shown in Table 1. Furthermore,

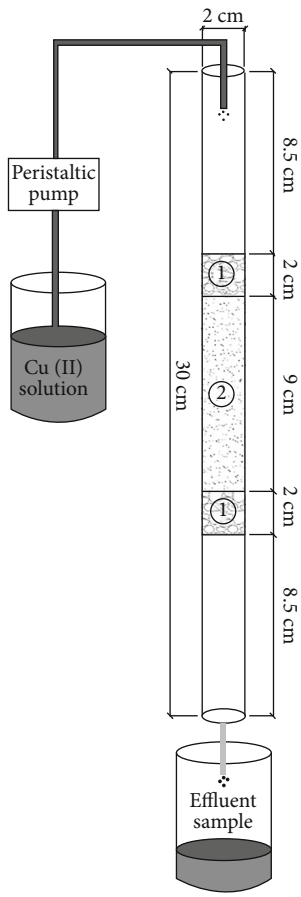


Figure 2: Sketch of fixed-bed column device (①: 2 cm thick quartz sand-packed layer; ②: 9 cm thick SP-SBC-packed layer).

Table 2: Some properties of SBC and SP-SBC.

| Items | SBC | SP-SBC |
|---|---|---|
| Yield (%) | 60.57 ± 0.17 | 68.34 ± 0.21 |
| Ash content (%) | 66.77 ± 0.39 | 75.23 ± 0.33 |
| pH value | 8.13 ± 0.03 | 10.54 ± 0.05 |
| Na ($mg{\cdot}g^{-1}$) | 1.76 ± 0.41 | 31.72 ± 1.97 |
| K ($mg{\cdot}g^{-1}$) | 6.81 ± 0.36 | 3.68 ± 0.28 |
| Ca ($mg{\cdot}g^{-1}$) | 27.48 ± 0.57 | 20.63 ± 2.57 |
| Mg ($mg{\cdot}g^{-1}$) | 7.87 ± 0.18 | 5.34 ± 0.38 |
| P ($mg{\cdot}g^{-1}$) | 24.94 ± 1.46 | 40.86 ± 3.32 |

SP-SBC was replaced by SBC and subjected to the same experiment processes in the batch experiment of the effect of contact time to compare the difference in adsorption capacity between SP-SBC and SBC.

Once a batch experiment was completed, the mixture was taken out and the suspension was passed through a 0.45 $\mu$m microfiltration membrane. In the filtrate, the Cu(II) concentration was tested with a PinAAcle900T-type flame atomic adsorption spectrophotometer (FAAS) (PerkinElmer Instrument Co., Ltd., Akron, USA). Then, Equation (3) was used to calculate the Cu(II)-adsorption capacity ($q_e$):

$$q_e = \frac{0.05(C_0 - C_e)}{W}, \tag{3}$$

where $C_0$ refers to the initial Cu(II) concentration ($mg{\cdot}L^{-1}$) at the beginning of experiment, $C_e$ refers to the detected Cu(II) concentration ($mg{\cdot}L^{-1}$) at the end of experiment, and $W$ is the amount of biochar (g).

*2.5. Adsorption Kinetics and Isotherms.* For Cu(II) adsorption by SP-SBC, the acquired data in the batch experiment of the effect of contact time were simulated with the pseudo-first-order (PFO) model, the pseudo-second-order (PSO) model, and the intraparticle diffusion (IPD) model (Equations (4)–(6)) to analyze the kinetic characteristics [12].

$$Q_t = Q_{\mathrm{et}}\left(1 - e^{-k_1 t}\right), \tag{4}$$

$$Q_t = \frac{t{Q_{\mathrm{et}}}^2 k_2}{1 + tQ_{\mathrm{et}}k_2}, \tag{5}$$

$$Q_t = k_i t^{1/2} + C, \tag{6}$$

where $Q_{\mathrm{et}}$ is the adsorption capacity ($mg{\cdot}g^{-1}$) at equilibrium and $Q_t$ is the adsorption capacity ($mg{\cdot}g^{-1}$) at time $t$. $k_1$, $k_2$, and $k_i$ denote the constants of the PFO model ($h^{-1}$), the PSO model ($g{\cdot}mg^{-1}{\cdot}h^{-1}$), and the rate constant of the IPD diffusion ($mg{\cdot}(g{\cdot}min^{0.5})^{-1}$), respectively. $C$ indicates the boundary-layer thickness ($mg{\cdot}g^{-1}$). The acquired data in the batch experiment of the effect of temperature was matched with the Langmuir (L) model, the Freundlich (F) model, the Langmuir–Freundlich (L-F) model, and the Dubinin–Radushkevich (D-R) model (Equations (7)–(12)) [16, 53–56] to explain the adsorption isotherms, respectively.

$$Q_e = \frac{Q_m K_L C_e}{1 + K_L C_e}, \tag{7}$$

$$Q_e = K_f {C_e}^{1/n}, \tag{8}$$

$$Q_e = \frac{Q_m (K_a C_e)^{n'}}{1 + (K_a C_e)^{n'}}, \tag{9}$$

$$\varepsilon = \mathrm{RT}\ln\left(1 + \frac{1}{C_{\mathrm{eD}}}\right), \tag{10}$$

$$Q_{\mathrm{eD}} = Q_{\mathrm{mD}} \exp\left(-\beta\varepsilon^2\right), \tag{11}$$

$$E = \frac{1}{\sqrt{2\beta}}, \tag{12}$$

where $K_L$ is the constant of the L model ($L{\cdot}mg^{-1}$). $K_f$ is the constant of the F model ($mg^{(1-n)}{\cdot}L^n{\cdot}g^{-1}$). $1/n$ is an empirical constant representing adsorption intensity. $K_a$ is the constant of the L-F model ($L{\cdot}mg^{-1}$), which can be used to reflect

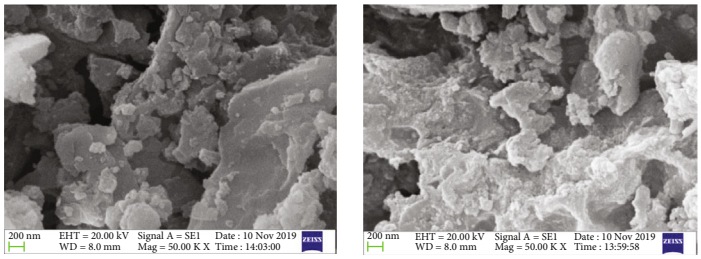


(a) (b)

Figure 3: SEM image of biochar: (a) SBC and (b) SP-SBC.

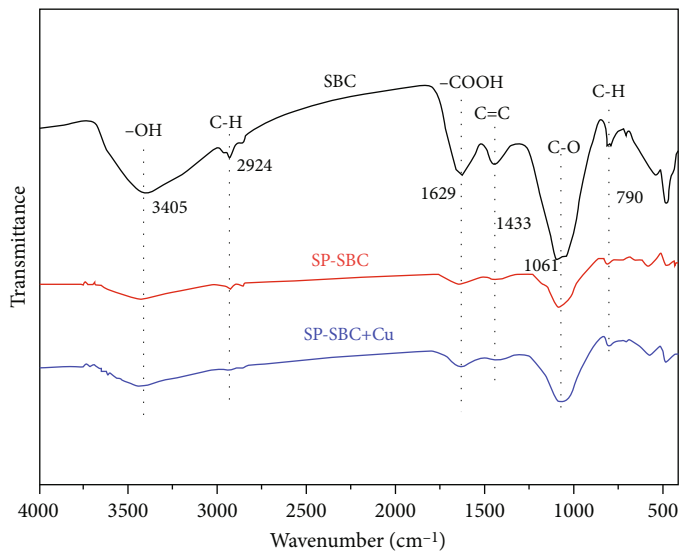


Figure 4: FTIR spectra of SBC, SP-SBC, and SP-SBC+Cu.

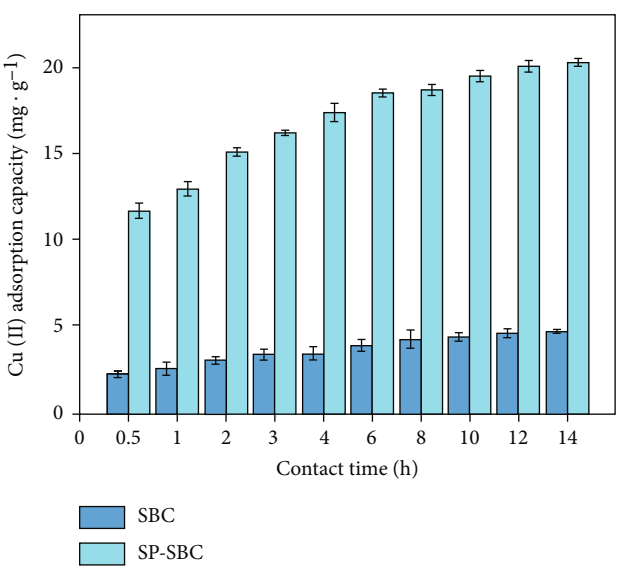


Figure 5: Adsorption capacities of SBC and SP-SBC for Cu(II) at different contact times.

the adsorption affinity. $n'$ is the heterogeneity factor. $Q_e$ is the equilibrium adsorption capacity at the end of the experiment (mg·g$^{-1}$). $Q_m$ is the maximum adsorption capacity (mg·g$^{-1}$). $\varepsilon$ is the Polanyi potential constant (J·mol$^{-1}$). $C_{ed}$ is the detected Cu(II) concentrations (mol·L$^{-1}$) at the equilibrium. $Q_{eD}$ and $Q_{mD}$ are the equilibrium adsorption capacity (mol·g$^{-1}$) and the maximum adsorption capacity (mol·g$^{-1}$), respectively. $R$ is the gas constant (8.314 J·(mol·K)$^{-1}$). $T$ is the absolute temperature (K).

*2.6. Fixed-Bed Column Experiment.* A fixed-bed column experiment was conducted to understand the application potential of SP-SBC for Cu(II) adsorption. The sketch map of the fixed-bed column device is shown in Figure 2. Four cycles were performed in the fixed-bed column experiment. Each cycle included two processes, i.e., adsorption process and desorption process. For the adsorption process, the Cu(II) solution ($C_{in} = 50\,\text{mg} \cdot \text{L}^{-1}$, pH 5) was pumped into the top of the column (flow rate $(Q) = 15\,\text{mL} \cdot \text{min}^{-1}$). The effluent samples were collected every 15 min, and the Cu(II) concentrations of samples ($C_{en}$, mg·L$^{-1}$) were measured by the FAAS to draw the breakthrough curve. Based on the acquired breakthrough curve, the total inputted Cu(II) amount ($M$, mg), total Cu(II)-adsorption amount ($M'$, mg), volume of treated Cu(II) solution ($V_{eff}$, mL), and equilibrium adsorption capacity of SP-SBC ($q_{ec}$, mg·g$^{-1}$) were calculated by Equations (13)–(16), respectively. For the desorption process, a certain volume of 0.5 M NaOH

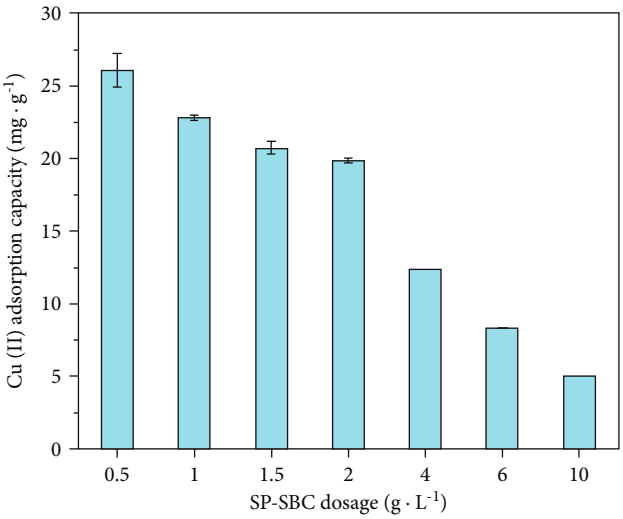


Figure 6: Effect of SP-SBC dosage on the adsorption capacity of SP-SBC for Cu(II).

solution was added to the fixed-bed column until the solution level was kept above the top quartz sand-packed layer. After soaking for 12 h, the fixed-bed column was rinsed with ultrapure water several times until the eluent pH was about neutral. Then, the regenerated fixed-bed column reactor was obtained. The regenerated fixed-bed column was reused for the next cycle.

$$M = \frac{Qt_e C_{\text{in}}}{1000}, \tag{13}$$

$$M' = \frac{Q}{1000}\int_0^{t_e}(C_{\text{in}} - C_{\text{en}})\text{dt}, \tag{14}$$

$$V_{\text{eff}} = Qt_e, \tag{15}$$

$$q_{\text{ec}} = \frac{M'}{m}, \tag{16}$$

where $t_e$ is the adsorption saturation time (min), which is the corresponding time when $C_t/C_0 = 0.9$ [57, 58]. $m$ is the SP-SBC mass packed in the experimental device (g).

*2.7. Statistical Analysis.* To ensure the reliability of experimental data, all experiments were repeated three times in this study. Origin 8.0 was used for plotting. SPSS Statistics 23.0 was used to analyze the experimental data.

## 3. Results and Discussion

*3.1. Properties of SBC and SP-SBC.* The property parameters of SBC and SP-SBC are shown in Table 2. The yields of SBC and SP-SBC were 60.57% and 68.34%, respectively, which were close to those of other sludge biochars prepared at the same pyrolysis temperature [59, 60]. Compared with those of SBC, the Na and P contents of SP-SBC significantly increased ($p < 0.05$), indicating that pyrophosphate was successfully introduced onto SP-SBC. However, the K, Ca, and Mg contents of SP-SBC decreased, which may be related to the dilution effect resulting from the increase in Na and P contents after modification. The ash content of SP-SBC was higher ($p < 0.05$) than that of SBC, which was due to the introduction of Na and P elements after modification. The alkalinity of SP-SBC was higher than that of SBC, which could be attributed to the increase in ash content and the alkalinity of the sodium pyrophosphate solution.

Figure 3 shows the scanning electron microscopy (SEM) images of SBC and SP-SBC, which reflected the surface structural morphology. The SP-SBC surface (Figure 3(b)) was rougher than that of SBC (Figure 3(a)) and filled with many microparticles, which was caused by the introduction of sodium pyrophosphate. The results of FTIR spectra of SBC and SP-SBC (Figure 4) revealed peaks at around 790 and 1061 $\text{cm}^{-1}$, which were due to the aromatic C-H out-of-plane vibrations [61] and C-O stretching vibration, respectively [15, 62, 63]. The peak at around 1433 $\text{cm}^{-1}$ represented the C=C stretching vibration of aromatic hydrocarbons [64]. The peak at 1629 $\text{cm}^{-1}$ was associated with the –COOH stretching vibration [65]. The observed peak at around 2924 $\text{cm}^{-1}$ represented the C-H stretching vibration [66]. The intense peak at around 3405 $\text{cm}^{-1}$ was due to the -OH stretching vibration [67]. Overall, the peaks of the two biochars were consistent, suggesting that the categories of functional groups did not change before and after modification. However, for SP-SBC, the intensities of these peaks weakened. These results suggested that the amounts of the functional groups on the SP-BC surface (especially for –OH and –COOH) decreased. This finding was consistent with the above result that the alkalinity of SP-SBC was higher than that of SBC.

*3.2. Adsorption Capacities of SBC and SP-SBC for Cu(II).* The adsorption capacities of SBC and SP-SBC for Cu(II) varied with increased contact time (Figure 5). For SBC, the Cu(II)-adsorption capacity tended to be stable after 10 h. For SP-SBC, the Cu(II)-adsorption capacity tended to reach equilibrium at 12 h. At adsorption equilibrium, SP-SBC and SBC achieved the Cu(II)-adsorption capacities of 20.01 and 4.40 $\text{mg·g}^{-1}$, respectively. Results showed that SP-SBC had a higher Cu(II)-adsorption capacity (4.55 times) than SBC. First, the surface of SP-SBC was rougher than that of SBC (Figure 3), which helped in increasing the contact of Cu(II) with SP-SBC [68]. Second, for SP-SBC, the increased equivalent of sodium was greater than the sum of the decreased equivalents of potassium, calcium, and magnesium (Table 2), which enhanced the ion exchange with Cu(II) [52]. Third, the significant increase in the phosphorus and alkalinity of SP-SBC (Table 2) led to increased copper precipitation [69]. The above three reasons caused the significant improvement in the Cu(II)-adsorption capacity of SP-SBC.

For Cu(II) adsorption by biochar, the complexation and $\pi$ electron coordination of surface functional groups may be involved [6, 70, 71]. In the Section 3.1, compared with SBC, SP-SBC had fewer surface functional groups. However, the Cu(II)-adsorption capacity of SP-SBC was 4.55 times higher than that of SBC. This finding indicated that the increased Cu(II)-adsorption capacity of SP-SBC was independent of

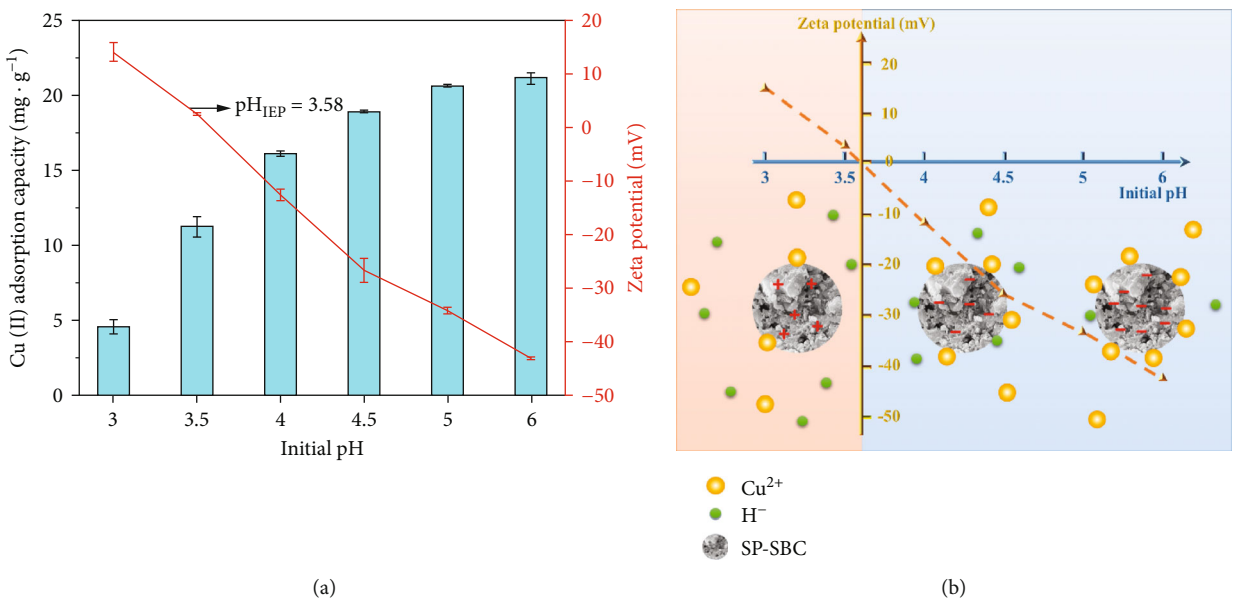


Figure 7: (a) Effect of initial pH on the adsorption capacity of SP-SBC for Cu(II), and (b) an illustration of the effect of initial pH on Cu(II) adsorption by SP-SBC.

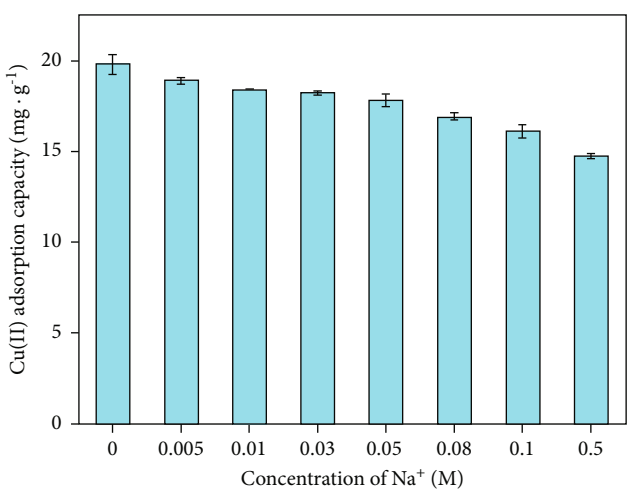


Figure 8: Effect of ionic strength on the adsorption capacity of SP-SBC for Cu(II).

surface functional groups. Thus, the complexion and $\pi$ electron coordination of surface functional groups may not be the main mechanism for the Cu(II) adsorption by SP-SBC. Additionally, the SP-SBC after Cu(II) adsorption (SP-SBC +Cu) was characterized by FTIR (Figure 4). We found inconspicuous changes in the positions and intensities of peaks between the FTIR spectra of SP-SBC and SP-SBC +Cu. These results suggested that surface functional groups had little effect on Cu(II) adsorption, which strongly supported the above discussion of surface functional group effects for Cu(II) adsorption.

Overall, modifying SBC with sodium pyrophosphate can effectively improve its Cu(II)-adsorption capacity.

*3.3. Effect of SP-SBC Dosage.* For the Cu(II)-adsorption capacity, the influence of SP-SBC dosage is shown in Figure 6. With increased SP-SBC dosage (from 0.5 g·L$^{-1}$ to 10 g·L$^{-1}$), the Cu(II)-adsorption capacity decreased ($p < 0.05$) from 26.06 mg·g$^{-1}$ to 4.983 mg·g$^{-1}$, in accordance with those of other reported biochars [71, 72]. This decrease in adsorption capacity for Cu(II) was associated with the following reasons: (i) the nonsaturated Cu(II) adsorption on SP-SBC caused by the excessive amount of SP-SBC [72] and (ii) the agglomeration and polymerization of SP-SBC at a high dosage [73].

*3.4. Effect of Initial pH.* To avoid the experimental interference caused by the extra precipitation of Cu(II) at the initial pH of >6 [6, 69], the initial pH was adjusted to 3–6. Figure 7(a) shows the effect of initial pH on the Cu(II) adsorption by SP-SBC. As shown in Figure 7, with increased initial pH from 3 to 5, the Cu(II)-adsorption capacity rapidly increased from 4.52 mg·g$^{-1}$ to 20.63 mg·g$^{-1}$ ($p < 0.05$). pH importantly influences the adsorption of metal ions because it usually determines the surface charge of the sorbent [3, 6, 12, 23]. Figure 7 also displays the zeta potentials of SP-SBC at different pH values. We found that the zeta potential gradually decreased with increased initial pH ($p < 0.05$), and the isoelectric point (pH$_{IEP}$) of SP-SBC was 3.58. These results suggested that the negative charges on the surface of SP-SBC increased with increased pH to >3.58. It enhanced the electrostatic attraction between Cu(II) and SP-SBC, leading to the increasing trend of Cu(II)-adsorption capacity from the initial pH of 3 to 5 [4, 15]. Moreover, the adsorption competition between Cu(II) and H$^{+}$ gradually weakened with increased initial pH within the range of 3–5, also resulting in increased Cu(II)-adsorption capacity of SP-SBC. These findings suggested that electrostatic attraction participated in the adsorption of Cu(II) by SP-SBC (Figure 7(b)). When the initial pH was above 5, the Cu(II)-

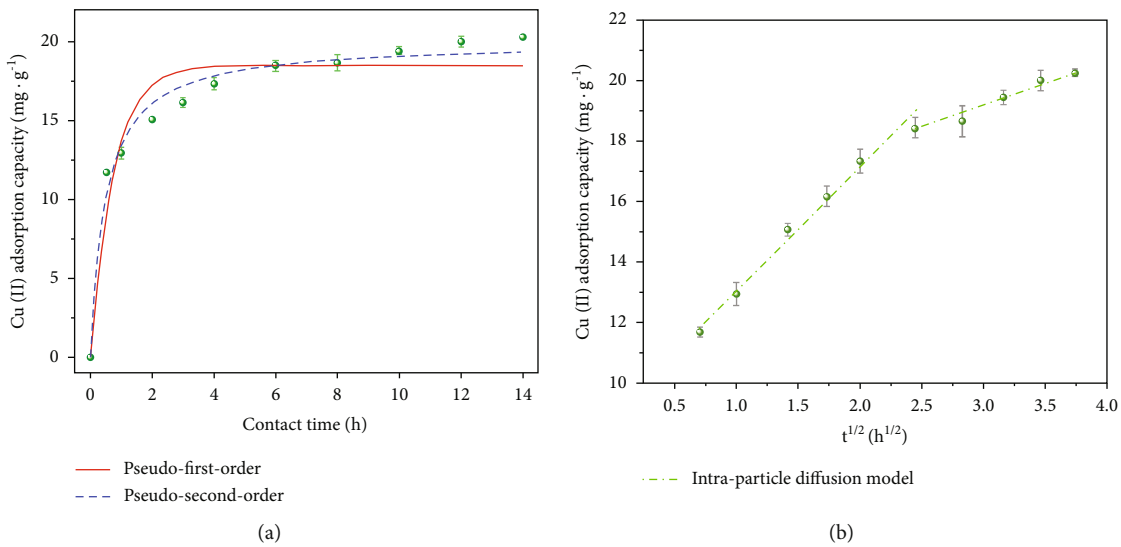


Figure 9: Effect of contact time on the adsorption capacity of SP-SBC for Cu(II) and fitting results of the PFO and PSO models (a) and the IPD model (b).

Table 3: Fitting parameters of three kinetic models.

| Pseudo-first order | | | Pseudo-second order | | |
|---|---|---|---|---|---|
| $Q_{et}$ (mg·g$^{-1}$) | $k_1$ (h$^{-1}$) | $R^2$ | $Q_{et}$ (mg·g$^{-1}$) | $k_2$ (g·mg$^{-1}$·h$^{-1}$) | $R^2$ |
| 18.50 | 1.348 | 0.931 | 20.02 | 0.103 | 0.980 |
| Intraparticle diffusion | | | | | |
| Step 1 | | | Step 2 | | |
| $C$ (mg·g$^{-1}$) | $k_i$ (mg·(g·min$^{0.5}$)$^{-1}$) | $R^2$ | $C$ (mg·g$^{-1}$) | $k_i$ (mg·(g·min$^{0.5}$)$^{-1}$) | $R^2$ |
| 8.91 | 4.12 | 0.98 | 14.91 | 1.43 | 0.95 |

adsorption capacity remained unchanged ($p > 0.05$), consistent with the results of Deng et al. [74].

*3.5. Effect of Ionic Strength.* Ionic strength usually has a significant effect on adsorption [75]. The effect of ionic strength ($Na^+$) on Cu(II) adsorption by SP-SBC is displayed in Figure 8. With increased ionic strength (0.005–0.5 M), the Cu(II)-adsorption capacity decreased significantly ($p < 0.05$). The reasons for this trend were as follows: (i) $Na^+$ competed with $Cu^{2+}$ in the adsorption [6]; (ii) a dense hydrating shell formed on the surface of SP-SBC once $Na^+$ was adsorbed [76], which prevented Cu(II) from making contact with the surface of SP-SBC; and (iii) the increase in ionic strength greatly reduced the activity coefficient of Cu(II), making it difficult for SP-SBC to capture Cu(II) [77]. In conclusion, ionic strength can significantly influence the Cu(II)-adsorption capacity of SP-SBC, especially under the high-ionic-strength condition. These results suggested that attention should be paid to the salinity control for the application of SP-SBC in high-salinity copper-containing wastewater.

*3.6. Effect of Contact Time and Adsorption Kinetics.* Figure 9 shows the effect of contact time on Cu(II) adsorption by SP-SBC. With increased contact time, the Cu(II)-adsorption capacity increased ($p < 0.05$) within the initial 12 h and then reached equilibrium ($p > 0.05$) (Figure 9). The Cu(II) adsorption by SP-SBC was fast within the initial 0.5 h, and the adsorption capacity at 0.5 h reached 58% of the adsorption capacity at equilibrium time. Then, the Cu(II)-adsorption rate gradually slowed down between 0.5 and 12 h, finally reaching stability after 12 h. The high initial Cu(II)-adsorption rate was due to the considerable amount of unsaturated adsorption sites on SP-SBC, whereas the decelerating adsorption rate was due to the adsorption sites being gradually saturated as adsorption proceeded [23].

Figure 9 exhibits the fitting curves of the PFO, PSO, and IPD models for Cu(II) adsorption by SP-SBC. The fitting curve of the PSO model showed a better approximation to the experimental data than those of the PFO and IPD models. The fitting parameters, i.e., $Q_{et}$, $k_1$, $k_2$, $k_i$, $C$, and correlation coefficient ($R^2$), are displayed in Table 3. Compared with the PFO and IPD models, the PSO model had the highest $R^2$ (0.980). Additionally, the simulated $Q_{et}$ (20.02 mg·g$^{-1}$) obtained by the PSO model better agreed with the $q_e$ (20.01 mg·g$^{-1}$) obtained in the experiment. Therefore, Cu(II) adsorption by SP-SBC was better depicted by the PSO model. The result implied that the number of active sites of the SP-SBC surface restricted the Cu(II)-adsorption rate of SP-SBC; i.e., chemical adsorption was the rate-limiting step for Cu(II) adsorption by SP-SBC [15, 78, 79]. Thus,

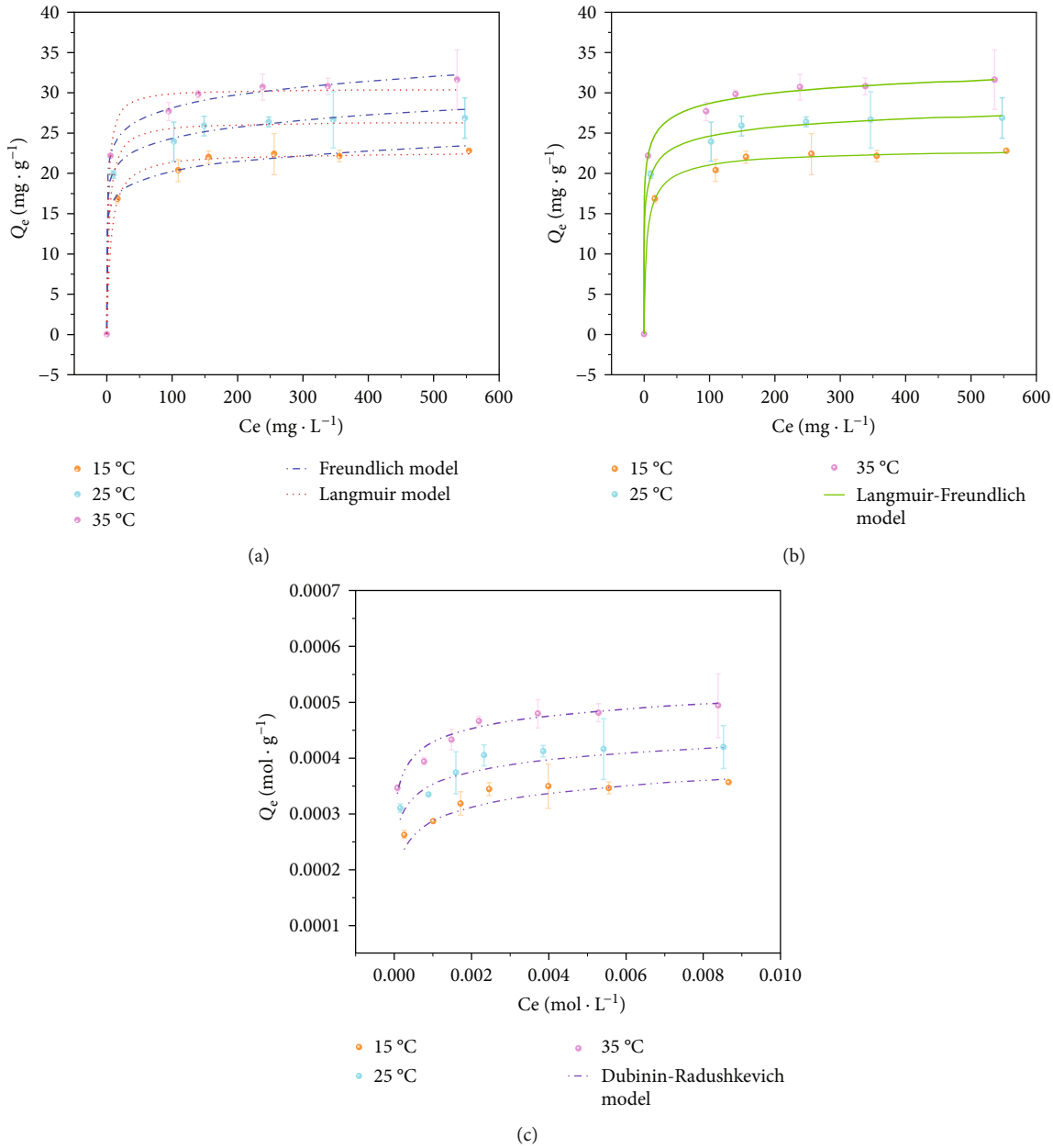


Figure 10: Effect of temperature on the adsorption capacity of SP-SBC for Cu(II), and fitting results of the F and L (a), L-F (b), and D-R (c) models.

chemical adsorption may be a key mechanism in this study [11, 13, 71], consistent with the discussion in Section 3.2. Meanwhile, Figure 9(b) shows that the adsorption process of Cu(II) by SP-SBC can be divided two stages: boundary-layer diffusion with fast diffusion speed and intraparticle diffusion with relatively slow diffusion speed. Notably, the fitting curves of the above two stages did not pass through the original point, indicating that intraparticle diffusion was not the only rate-limiting step to control the Cu(II)-adsorption process of SP-SBC [11, 13].

*3.7. Effect of Temperature and Adsorption Isotherms.* The Cu(II) equilibrium adsorption capacities of SP-SBC ($Q_e$) at different initial Cu(II) concentrations and temperatures are shown in Figure 10. At the same initial concentration, $Q_e$ increased with increased temperature (15–35°C). This result was due to the increased contact between Cu(II) and SP-SBC at a high temperature. At the same temperature, $Q_e$ increased sharply within the range of low initial Cu(II) concentration (i.e., <200 mg·L$^{-1}$) ($p < 0.05$) and then gradually reached equilibrium.

To further ascertain the Cu(II)-adsorption behavior of SP-SBC, the experimental data were simulated by the L, F, L-F, and D-R models. Table 4 lists the fitting values of $K_L$, $Q_m$, $K_f$, $1/n$, $K_a$, $n'$, $Q_{mD}$, $E$, and correlation coefficient obtained using the four models. For the L model, $K_L$ can

Table 4: Fitting parameters of four isotherm models.

| Temperature | Langmuir | | | Freundlich | | |
|---|---|---|---|---|---|---|
| | $K_L$ (L·mg$^{-1}$) | $Q_m$ (mg·g$^{-1}$) | $R^2$ | $K_f$ (mg$^{(1-n)}$·L$^n$·g$^{-1}$) | $1/n$ | $R^2$ |
| 15°C | 0.17 | 22.59 | 0.996 | 13.63 | 0.085 | 0.995 |
| 25°C | 0.28 | 26.44 | 0.994 | 16.80 | 0.081 | 0.996 |
| 35°C | 0.45 | 30.52 | 0.992 | 19.53 | 0.080 | 0.998 |

| Temperature | Langmuir-Freundlich | | | | Dubinin-Radushkevich | | |
|---|---|---|---|---|---|---|---|
| | $K_a$ (L·mg$^{-1}$) | $Q_m$ (mg·g$^{-1}$) | $n'$ | $R^2$ | $E$ (kJ·mol$^{-1}$) | $Q_{mD}$ (mol·g$^{-1}$) | $R^2$ |
| 15°C | 0.21 | 23.22 | 0.74 | 0.998 | 17.51 | 4.48 | 0.91 |
| 25°C | 0.48 | 31.50 | 0.33 | 0.998 | 21.13 | 4.89 | 0.74 |
| 35°C | 0.52 | 38.49 | 0.27 | 0.999 | 23.17 | 5.73 | 0.91 |

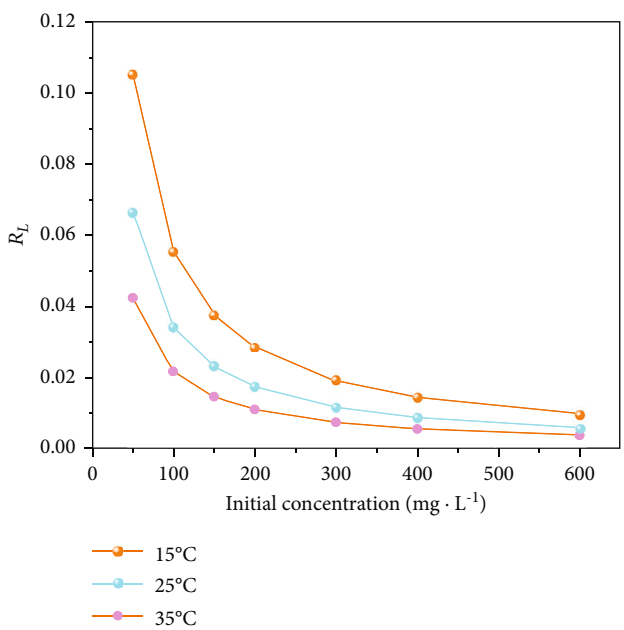


Figure 11: Separation parameters ($R_L$) for Cu(II) adsorption by SP-SBC at different temperatures and initial Cu(II) concentrations.

be used to calculate the separation parameter ($R_L$) and reflect the type of isotherm [4, 12], as shown in the following equation.

$$R_L = \frac{1}{1 + C_0 K_L}. \quad (17)$$

Figure 11 shows the $R_L$ values at different temperatures and initial Cu(II) concentrations. The values of $R_L$ were all less than 1, implying that Cu(II) adsorption by SP-SBC was a favorable process [3, 4, 13]. Moreover, with increased the temperature and Cu(II) initial concentration, the $R_L$ value continuously decreased. This result suggested that the Cu(II) adsorption was more favorable at a higher concentration and temperature [80]. For the F model, $1/n$ can reflect the adsorption intensity [56]. If $1/n < 0.5$, the adsorption of the adsorbate is easy, whereas if $1/n > 2$, the adsorption of the adsorbate is difficult [80]. As shown in Table 4, for the different temperatures, the calculated $1/n$ was always less than 0.5, demonstrating that Cu(II) was easily absorbed by SP-SBC. With increased temperature, the value of $K_f$ also increased. A larger value of $K_f$ implies a higher adsorption capacity [79]. Thus, a high temperature was favorable for Cu(II) adsorption; i.e., the Cu(II)-adsorption capacity strengthened with increased the temperature. For the L-F model, the $n'$ values at three temperatures ranged within 0–1, and a higher temperature corresponded with a higher $K_a$ value in this work. The results also demonstrated that Cu(II) adsorption by SP-SBC was a favorable process [81], and the adsorption capability of SP-SBC for Cu(II) was enhanced with increased temperature [82]. For the D-R model, the values of $E$ at all experimental temperatures exceeded 16 kJ·mol$^{-1}$, indicating that Cu(II) adsorption by SP-SBC involved chemical adsorption [83–85].

Figure 10 shows that the experimental data were matched better by the L-F model than the other three models. Furthermore, the L-F model had the highest $R^2$ among all models (Table 4). Thus, the L-F model was better adapted to fit the isotherms, suggesting that both processes (i.e., the Langmuir and Freundlich processes) were involved in Cu(II) adsorption by SP-SBC. In other words, Cu(II) adsorption was controlled by multiple mechanisms [86], such as ion exchange, precipitation (in Section 3.2) and electrostatic attraction (in Section 3.4). Additionally, the maximum Cu(II)-adsorption capacity of 38.49 mg·g$^{-1}$ was achieved for SP-SBC at 35°C by the L-F model. Table 5 summarizes the Cu(II)-adsorption capacities of different biochars. Compared with these sorbents, SP-SBC had a moderate adsorption capacity. The Cu (II)-adsorption equilibrium time of SP-SBC was also less than those of most adsorbents. Notably, the adsorption capacity of SP-SBC exceeded those of reported commercial activated carbons in Table 5. Overall, SP-SBC is a desirable and effective sorbent for Cu(II) removal from aqueous solutions.

*3.8. Fixed-Bed Column Adsorption.* Fixed-bed column adsorption can be used to understand the application

Table 5: Cu(II)-adsorption capacities of different biochars.

| Biochar | Conditions | Cu(II) maximum adsorption capacity ($mg \cdot g^{-1}$) | References |
|---|---|---|---|
| Corn straw biochar | pH = 5, $t$ = 24 h, $T$ = 22 ∘ C | 12.52 | [87] |
| Composted swine manure biochar | pH = 5, $t$ = 24 h, $T$ = 25 ∘ C | 21.94 | [88] |
| *S. hermaphrodita* biochar | pH = 5.5, $t$ = 24 h, $T$ = 22 ∘ C | 33.33 | [89] |
| Date seed-derived biochar | pH = 6, $t$ = 24 h, $T$ = 23 ∘ C | 26.94 | [90] |
| Miscanthus giganteus biochar | pH = 6, $t$ = 1 h, $T$ = 25 ∘ C | 19.72 | [91] |
| Sewage sludge biochar | pH = 5.2, $t$ = 20 h, $T$ = 25 ∘ C | 7.32 | [36] |
| Municipal sewage sludge biochar | pH = /, $t$ = 24 h, $T$ = 25 ∘ C | 5.34 | [37] |
| Steam-activated giant *Miscanthus* biochar | pH = 6, $t$ = 48 h, $T$ = 20 ∘ C | 15.4 | [92] |
| Amino-modified sawdust biochar | pH = 5, $t$ = 200 min, $T$ = 30 ∘ C | 17.01 | [25] |
| KOH-activated brewers draft biochar | pH = 5, $t$ = 24 h, $T$ = / | 10.30 | [93] |
| $KMnO_4$-modified loofah biochar | pH = 5.5, $t$ = 10 h, $T$ = / | 47.64 | [71] |
| Modified date seed biochar with HCl pretreatment | pH = 6, $t$ = 24 h, $T$ = 23 ∘ C | 45.12 | [24] |
| NaOH-modified *Opuntia ficus-indica*-activated biochar | pH = 6, $t$ = /, $T$ = 30 ∘ C | 49.36 | [94] |
| Commercial activated carbon | pH = 5, $t$ = /, $T$ = 25 ∘ C | 19.21 | [95] |
| Commercial activated carbon | pH = 4, $t$ = 4 h, $T$ = 25 ∘ C | 6.9 | [96] |
| Commercial activated carbon | pH = 6.5, $t$ = 1 h, $T$ = 22 ∘ C | 13.7 | [97] |
| SP-SBC | pH = 5, $t$ = 12 h, $T$ = 35 ∘ C | 38.49 | This study |

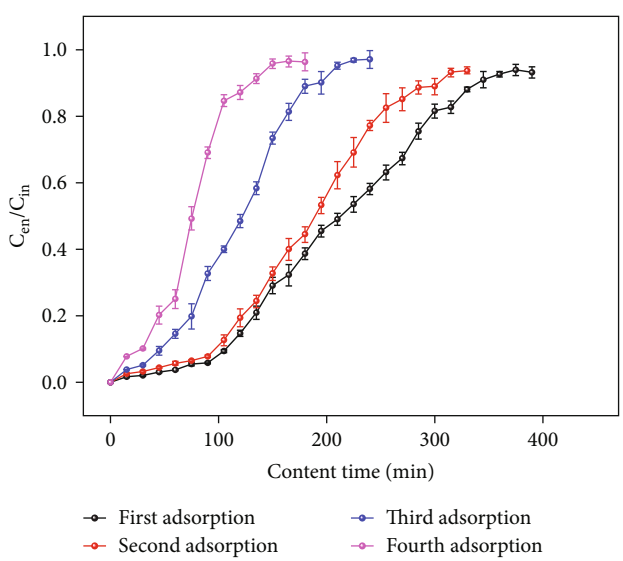


Figure 12: Breakthrough curves of four adsorption–desorption cycles in the fixed-bed column experiment.

potential of SP-SBC and offer support for the large-scale treatment of real copper-containing wastewater by SP-SBC [98]. Figure 12 and Table 6 show the breakthrough curves and the corresponding calculated parameters of four adsorption–desorption cycles in the fixed-bed column experiment, respectively. The values of $q_{ec}$, $M'$, and $V_{eff}$ in the first cycle were 8.528 $mg \cdot g^{-1}$, 153.5 mg, and 5175 mL, respectively, indicating that SP-SBC can be used for fixed-bed column

Table 6: Adsorption parameters acquired by fixed-bed column adsorption in four adsorption–desorption cycles.

| Cycle | $t_b$* (min) | $t_e$ (min) | $V_{eff}$ (mL) | $M$ (mg) | $M'$ (mg) | $q_{ec}$ ($mg \cdot g^{-1}$) |
|---|---|---|---|---|---|---|
| 1 | 110 | 345 | 5175 | 258.75 | 153.5 | 8.528 |
| 2 | 95 | 310 | 4650 | 232.50 | 133.71 | 7.428 |
| 3 | 50 | 195 | 2925 | 146.25 | 82.49 | 4.583 |
| 4 | 30 | 125 | 1875 | 93.75 | 50.29 | 2.794 |

*$t_b$ is the breakthrough time (min), which is the corresponding time when $C_t/C_0 = 0.1$.

adsorption. With the number of cycles increasing, the slope of the breakout curve increased gradually, indicating that the breakthrough ($C_t/C_0 = 0.1$) and saturation ($C_t/C_0 = 0.9$) points came earlier, and the values of $M$, $M'$, $V_{eff}$, and $q_{ec}$ decreased. These changes may be due to the inactivation of adsorption sites on the surface of SP-SBC during the adsorption–desorption cycles. After four adsorption–desorption cycles, $q_{ec}$ was still 2.794 $mg \cdot g^{-1}$, indicating that SP-SBC can be reused at least four times. Considering the large sewage sludge production in China ($>3 \times 10^7$ *tons per year*), the relatively simple preparation procedures, and the desired adsorption performance in the fixed-bed column adsorption, SP-SBC has a good application potential to treat copper-containing wastewater. Nevertheless, to effectively guide the practical application of SP-SBC, the following works need to be carried out: (i) optimization of adsorption-operating parameters to determine the optimum adsorption

conditions; (ii) evaluation of the desorption effect of various desorbents, such as $H_2SO_4$, $HNO_3$, and EDTA, to select the effective desorbents; and (iii) design of feasible preparation procedures of SP-SBC from the perspective of industrial production to provide technical guidance for the market promotion of SP-SBC.

## 4. Conclusions

$Na_4P_2O_7$-modified biochar (SP-SBC) was successfully prepared by a simple one-pot method. Compared with SBC, the Cu(II)-adsorption capacity of SP-SBC improved 4.55 times. The Cu(II)-adsorption process of SP-SBC can be better described by the pseudo-second-order and Langmuir-Freundlich models. Cu(II) adsorption by SP-SBC involved ion exchange, electrostatic attraction, and precipitation. For Cu(II) adsorption, SP-SBC gained the maximum adsorption capacity of 38.49 $mg \cdot g^{-1}$ at 35°C, which was higher than those of some reported commercial activated carbons. The fixed-bed column experiment indicated that SP-SBC can be used at least four times and had a good application potential for the treatment of copper-containing wastewater. Overall, SP-SBC can serve as an alternative sorbent to effectively remove Cu(II) from aqueous solutions. For the practical application of SP-SBC, the optimization of adsorption-operation parameters, evaluation of the desorption effect of various desorbents, and design of a feasible industrial-production scheme are required.

## Data Availability

All data generated or analyzed during this study are included in this published article.

## Conflicts of Interest

The authors have no competing interests to declare that are relevant to the content of this article.

## Authors' Contributions

Liangqian Fan, Xianda Wang, and Jiaxin Miao contributed equally to this work and should be considered as co-first authors.

## Acknowledgments

This work was financially supported by the Scientific Research Innovation Team Project of Sichuan Provincial Department of Education (No. 16TD0006).

## References

[1] R. R. Karri, G. Ravindran, and M. H. Dehghani, "Wastewater–sources, toxicity, and their consequences to human health," in *Soft computing techniques in solid waste and wastewater management*, pp. 3–33, Elsevier, 2021.

[2] M. H. Dehghani, G. A. Omrani, and R. R. Karri, "Solid waste–sources, toxicity, and their consequences to human health," in *Soft computing techniques in solid waste and wastewater management*, pp. 205–213, Elsevier, 2021.

[3] K. L. Bhowmik, A. Debnath, R. K. Nath, and B. Saha, "Synthesis of $MnFe_2O_4$ and $Mn_3O_4$ magnetic nano-composites with enhanced properties for adsorption of Cr(VI): artificial neural network modeling," *Water Science and Technology*, vol. 76, no. 12, pp. 3368–3378, 2017.

[4] A. Debnath, A. Bera, K. K. Chattopadhyay, and B. Saha, "Facile additive-free synthesis of hematite nanoparticles for enhanced adsorption of hexavalent chromium from aqueous media: kinetic, isotherm, and thermodynamic study," *Inorganic and Nano-Metal Chemistry*, vol. 47, no. 12, pp. 1605–1613, 2017.

[5] Y. Yan, X. Liang, J. Ma, and J. Shen, "Rapid removal of copper from wastewater by Fe-based amorphous alloy," *Intermetallics*, vol. 124, article 106849, 2020.

[6] Q. Wang, L. Li, L. Kong et al., "Compressible amino-modified carboxymethyl chitosan aerogel for efficient Cu(II) adsorption from wastewater," *Separation and Purification Technology*, vol. 293, article 121146, 2022.

[7] H. Zhang, J. Chen, S. Ni, C. Bie, H. Zhi, and X. Sun, "A clean process for selective recovery of copper from industrial wastewater by extraction-precipitation with p-tert-octyl phenoxy acetic acid," *Journal of Environmental Management*, vol. 304, article 114164, 2022.

[8] Y. Li, B. Pan, H. Miao, H. Xu, X. Liu, and G. Shi, "Single and binary dye adsorption of methylene blue and methyl orange in alcohol aqueous solution via rice husk based activated carbon: kinetics and equilibrium studies," *Chemical Research in Chinese Universities*, vol. 36, no. 6, pp. 1272–1278, 2020.

[9] M. Feng, S. Yu, P. Wu, Z. Wang, S. Liu, and J. Fu, "Rapid, high-efficient and selective removal of cationic dyes from wastewater using hollow polydopamine microcapsules: isotherm, kinetics, thermodynamics and mechanism," *Applied Surface Science*, vol. 542, article 148633, 2021.

[10] W. Tala and S. Chantara, "Use of spent coffee ground biochar as ambient PAHs sorbent and novel extraction method for GC-MS analysis," *Environmental Science and Pollution Research*, vol. 26, no. 13, pp. 13025–13040, 2019.

[11] L. P. Lingamdinne, R. R. Karri, M. R. Khan, Y. Chang, and J. R. Koduru, "Evaluation of surface phenomena of magnetic biomass for dye removal via surface modeling," *Journal of Environmental Chemical Engineering*, vol. 105953, no. 5, article 105953, 2021.

[12] B. Saha, A. Debnath, and B. Saha, "Fabrication of PANI@Fe–Mn–Zr hybrid material and assessments in sono-assisted adsorption of methyl red dye: uptake performance and response surface optimization," *Journal of the Indian Chemical Society*, vol. 99, no. 9, article 100635, 2022.

[13] P. Das and A. Debnath, "Fabrication of $MgFe_2O_4$/polyaniline nanocomposite for amputation of methyl red dye from water: isotherm modeling, kinetic and cost analysis," *Journal of Dispersion Science and Technology*, vol. 43, pp. 1–12, 2022.

[14] B. Saha, A. Debnath, and B. Saha, "Evaluation of Fe–Mn–Zr trimetal oxide/polyaniline nanocomposite as potential adsorbent for abatement of toxic dye from aqueous solution," in *Polymer Technology in dye-Containing Wastewater*, pp. 15–37, Springer Nature Singapore, Singapore, 2022.

[15] L. P. Lingamdinne, J. Choi, G. K. R. Angaru et al., "Magnetic-watermelon rinds biochar for uranium-contaminated water treatment using an electromagnetic semi-batch column with removal mechanistic investigations," *Chemosphere*, vol. 286, article 131776, Part 2, 2022.

[16] M. N. Hairuddin, N. M. Mubarak, M. Khalid, E. C. Abdullah, R. Walvekar, and R. R. Karri, "Magnetic palm kernel biochar potential route for phenol removal from wastewater," *Environmental Science and Pollution Research*, vol. 26, no. 34, pp. 35183–35197, 2019.

[17] Z. Meng, T. Xu, S. Huang, H. Ge, W. Mu, and Z. Lin, "Effects of competitive adsorption with Ni(II) and Cu(II) on the adsorption of Cd(II) by modified biochar co-aged with acidic soil," *Chemosphere*, vol. 293, article 133621, 2022.

[18] X. Wang, X. Li, G. Liu et al., "Mixed heavy metal removal from wastewater by using discarded mushroom-stick biochar: adsorption properties and mechanisms," *Environmental Science: Processes & Impacts*, vol. 21, no. 3, pp. 584–592, 2019.

[19] T. Chi, J. Zuo, and F. Liu, "Performance and mechanism for cadmium and lead adsorption from water and soil by corn straw biochar," *Frontiers of Environmental Science & Engineering*, vol. 11, no. 2, p. 15, 2017.

[20] Z. Mahdi, Q. J. Yu, and A. El Hanandeh, "Competitive adsorption of heavy metal ions ($Pb^{2+}$, $Cu^{2+}$, and $Ni^{2+}$) onto date seed biochar: batch and fixed bed experiments," *Separation Science and Technology*, vol. 54, no. 6, pp. 888–901, 2019.

[21] Z. Zhou, Z. Xu, Q. Feng et al., "Effect of pyrolysis condition on the adsorption mechanism of lead, cadmium and copper on tobacco stem biochar," *Journal of Cleaner Production*, vol. 187, pp. 996–1005, 2018.

[22] F. Wu, L. Chen, P. Hu, Y. Wang, J. Deng, and B. Mi, "Industrial alkali lignin-derived biochar as highly efficient and low-cost adsorption material for Pb(II) from aquatic environment," *Bioresource Technology*, vol. 322, article 124539, 2021.

[23] R. Katiyar, A. K. Patel, T. Nguyen, R. R. Singhania, C. Chen, and C. Dong, "Adsorption of copper (II) in aqueous solution using biochars derived from *Ascophyllum nodosum* seaweed," *Bioresource Technology*, vol. 328, article 124829, 2021.

[24] Z. Mahdi, A. E. Hanandeh, and Q. J. Yu, "Preparation, characterization and application of surface modified biochar from date seed for improved lead, copper, and nickel removal from aqueous solutions," *Journal of Environmental Chemical Engineering*, vol. 7, no. 5, article 103379, 2019.

[25] G. Yang and H. Jiang, "Amino modification of biochar for enhanced adsorption of copper ions from synthetic wastewater," *Water Research*, vol. 48, pp. 396–405, 2014.

[26] H. Wang, B. Gao, S. Wang, J. Fang, Y. Xue, and K. Yang, "Removal of Pb(II), Cu(II), and Cd(II) from aqueous solutions by biochar derived from $KMnO_4$ treated hickory wood," *Bioresource Technology*, vol. 197, pp. 356–362, 2015.

[27] F. Wang, L. Jin, C. Guo et al., "Enhanced heavy metals sorption by modified biochars derived from pig manure," *Science of the Total Environment*, vol. 786, article 147595, 2021.

[28] S. Bashir, J. Zhu, Q. Fu, and H. Hu, "Comparing the adsorption mechanism of Cd by rice straw pristine and KOH-modified biochar," *Environmental Science and Pollution Research*, vol. 25, no. 12, pp. 11875–11883, 2018.

[29] J. Xiong, M. Zhou, C. Qu et al., "Quantitative analysis of Pb adsorption on sulfhydryl-modified biochar," *Biochar*, vol. 3, no. 1, pp. 37–49, 2021.

[30] Y. Wang and R. Liu, "$H_2O_2$ treatment enhanced the heavy metals removal by manure biochar in aqueous solutions," *Science of the Total Environment*, vol. 628-629, pp. 1139–1148, 2018.

[31] J. Song, S. Zhang, G. Li, Q. Du, and F. Yang, "Preparation of montmorillonite modified biochar with various temperatures and their mechanism for Zn ion removal," *Journal of Hazardous Materials*, vol. 391, article 121692, 2020.

[32] G. Zhou, Y. Gu, H. Yuan, Y. Gong, and Y. Wu, "Selecting sustainable technologies for disposal of municipal sewage sludge using a multi-criterion decision-making method: a case study from China," *Resources Conservation and Recycling*, vol. 161, article 104881, 2020.

[33] S. Zhang, F. Wang, Z. Mei, L. Lv, and Y. Chi, "Status and development of sludge incineration in China," *Waste and Biomass Valorization*, vol. 12, no. 7, pp. 3541–3574, 2021.

[34] K. Bondarczuk, A. Markowicz, and Z. Piotrowska-Seget, "The urgent need for risk assessment on the antibiotic resistance spread via sewage sludge land application," *Environment International*, vol. 87, pp. 49–55, 2016.

[35] T. Chen, Y. Zhang, H. Wang et al., "Influence of pyrolysis temperature on characteristics and heavy metal adsorptive performance of biochar derived from municipal sewage sludge," *Bioresource Technology*, vol. 164, pp. 47–54, 2014.

[36] T. Shen, Y. Tang, X. Lu, and Z. Meng, "Mechanisms of copper stabilization by mineral constituents in sewage sludge biochar," *Journal of Cleaner Production*, vol. 193, pp. 185–193, 2018.

[37] Z. Dan, L. Dan, G. Fengxiang, L. Mengke, and L. Xianping, "Effects of biochar-derived sewage sludge on heavy metal adsorption and immobilization in soils," *International Journal of Environmental Research and Public Health*, vol. 14, no. 7, p. 681, 2017.

[38] L. Gao, J. Deng, G. Huang et al., "Relative distribution of $Cd^{2+}$ adsorption mechanisms on biochars derived from rice straw and sewage sludge," *Bioresource Technology*, vol. 272, pp. 114–122, 2019.

[39] T. Chen, Z. Zhou, S. Xu, H. Wang, and W. Lu, "Adsorption behavior comparison of trivalent and hexavalent chromium on biochar derived from municipal sludge," *Bioresource Technology*, vol. 190, pp. 388–394, 2015.

[40] M. Wu, B. Liu, J. Li, X. Su, W. Liu, and X. Li, "Influence of pyrolysis temperature on sludge biochar: the ecological risk assessment of heavy metals and the adsorption of Cd(II)," *Environmental Science and Pollution Research*, 2022.

[41] M. Zhao, Y. Dai, M. Zhang et al., "Mechanisms of Pb and/or Zn adsorption by different biochars: biochar characteristics, stability, and binding energies," *Science of the Total Environment*, vol. 717, article 136894, 2020.

[42] Y. Chen, M. Li, Y. Li et al., "Hydroxyapatite modified sludge-based biochar for the adsorption of $Cu^{2+}$ and $Cd^{2+}$: adsorption behavior and mechanisms," *Bioresource Technology*, vol. 321, article 124413, 2021.

[43] K. M. Smith, G. D. Fowler, S. Pullket, and N. J. D. Graham, "Sewage sludge-based adsorbents: a review of their production, properties and use in water treatment applications," *Water Research*, vol. 43, no. 10, pp. 2569–2594, 2009.

[44] C. Santhosh, E. Daneshvar, K. M. Tripathi et al., "Synthesis and characterization of magnetic biochar adsorbents for the removal of Cr(VI) and acid orange 7 dye from aqueous solution," *Environmental Science and Pollution Research*, vol. 27, no. 26, pp. 32874–32887, 2020.

[45] W. Zuo, C. Chen, H. Cui, and M. Fu, "Enhanced removal of Cd(II) from aqueous solution using $CaCO_3$ nanoparticle modified sewage sludge biochar," *RSC Advances*, vol. 7, no. 26, pp. 16238–16243, 2017.

[46] N. Zhao, B. Li, H. Huang, X. Lv, M. Zhang, and L. Cao, "Modification of kelp and sludge biochar by TMT-102 and NaOH

for cadmium adsorption," *Journal of the Taiwan Institute of Chemical Engineers*, vol. 116, pp. 101–111, 2020.

[47] L. Yang, L. He, J. Xue et al., "Highly efficient nickel (II) removal by sewage sludge biochar supported $\alpha$-$Fe_2O_3$ and $\alpha$-FeOOH: sorption characteristics and mechanisms," *PLoS One*, vol. 14, no. 6, article e218114, 2019.

[48] J. Wang, T. Wang, Q. Zhu et al., "Preparation of a novel sludge-derived biochar by $K_2FeO_4$ conditioning to enhance the removal of $Pb^{2+}$," *Colloid and Interface Science Communications*, vol. 42, article 100417, 2021.

[49] I. I. Shahib, J. Ifthikar, D. T. Oyekunle et al., "Influences of chemical treatment on sludge derived biochar; physicochemical properties and potential sorption mechanisms of lead (II) and methylene blue," *Journal of Environmental Chemical Engineering*, vol. 10, no. 3, article 107725, 2022.

[50] K. Phoungthong and T. Suwunwong, "Magnetic biochar derived from sewage sludge of concentrated natural rubber latex (CNRL) for the removal of $Al^{3+}$ and $Cu^{2+}$ ions from wastewater," *Research on Chemical Intermediates*, vol. 46, no. 1, pp. 385–407, 2020.

[51] S. Tang, N. Shao, C. Zheng, F. Yan, and Z. Zhang, "Amino-functionalized sewage sludge-derived biochar as sustainable efficient adsorbent for Cu(II) removal," *Waste Management*, vol. 90, pp. 17–28, 2019.

[52] L. Fan, J. Miao, J. Yang et al., "Invasive plant-crofton weed as adsorbent for effective removal of copper from aqueous solution," *Environmental Technology & Innovation*, vol. 26, article 102280, 2022.

[53] N. Delgado, A. Capparelli, A. Navarro, and D. Marino, "Pharmaceutical emerging pollutants removal from water using powdered activated carbon: study of kinetics and adsorption equilibrium," *Journal of Environmental Management*, vol. 236, pp. 301–308, 2019.

[54] N. Slyusarenko, M. Gerasimova, M. Atamanova, A. Plotnikov, and E. Slyusareva, "Adsorption of eosin Y on polyelectrolyte complexes based on chitosan and arabinogalactan sulfate," *Colloids and Surfaces A: Physicochemical and Engineering Aspects*, vol. 610, article 125731, 2021.

[55] R. R. Karri, J. N. Sahu, and B. C. Meikap, "Improving efficacy of Cr (VI) adsorption process on sustainable adsorbent derived from waste biomass (sugarcane bagasse) with help of ant colony optimization," *Industrial Crops and Products*, vol. 143, article 111927, 2020.

[56] R. R. Karri, J. N. Sahu, and N. S. Jayakumar, "Optimal isotherm parameters for phenol adsorption from aqueous solutions onto coconut shell based activated carbon: error analysis of linear and non-linear methods," *Journal of the Taiwan Institute of Chemical Engineers*, vol. 80, pp. 472–487, 2017.

[57] F. Wang, J. Yu, Z. Zhang, Y. Xu, and R. Chi, "An amino-functionalized ramie stalk-based adsorbent for highly effective $Cu^{2+}$ removal from water: adsorption performance and mechanism," *Process Safety and Environmental Protection*, vol. 117, pp. 511–522, 2018.

[58] A. Abdolali, H. H. Ngo, W. Guo et al., "Application of a breakthrough biosorbent for removing heavy metals from synthetic and real wastewaters in a lab-scale continuous fixed-bed column," *Bioresource Technology*, vol. 229, pp. 78–87, 2017.

[59] J. Jin, Y. Li, J. Zhang et al., "Influence of pyrolysis temperature on properties and environmental safety of heavy metals in biochars derived from municipal sewage sludge," *Journal of Hazardous Materials*, vol. 320, pp. 417–426, 2016.

[60] S. Ho, Y. Chen, Z. Yang, D. Nagarajan, J. Chang, and N. Ren, "High-efficiency removal of lead from wastewater by biochar derived from anaerobic digestion sludge," *Bioresource Technology*, vol. 246, pp. 142–149, 2017.

[61] F. Ma, J. Dai, Z. Fu et al., "Biochar for asphalt modification: a case of high-temperature properties improvement," *Science of the Total Environment*, vol. 804, article 150194, 2022.

[62] W. Wu, M. Yang, Q. Feng et al., "Chemical characterization of rice straw-derived biochar for soil amendment," *Biomass and Bioenergy*, vol. 47, pp. 268–276, 2012.

[63] N. Hagemann, E. Subdiaga, S. Orsetti et al., "Effect of biochar amendment on compost organic matter composition following aerobic composting of manure," *Science of the Total Environment*, vol. 613-614, pp. 20–29, 2018.

[64] C. He, X. He, J. Li et al., "The spectral characteristics of biochar-derived dissolved organic matter at different pyrolysis temperatures," *Journal of Environmental Chemical Engineering*, vol. 9, no. 5, article 106075, 2021.

[65] S. Chellappan, V. Nair, V. Sajith, and K. Aparna, "Synthesis, optimization and characterization of biochar based catalyst from sawdust for simultaneous esterification and transesterification," *Chinese Journal of Chemical Engineering*, vol. 26, no. 12, pp. 2654–2663, 2018.

[66] F. V. Hackbarth, F. Girardi, S. M. A. G. de Souza, A. D. Souza, R. Boaventura, and V. Vilar, "Marine macroalgae *Pelvetia canaliculata* (*Phaeophyceae*) as a natural cation exchanger for cadmium and lead ions separation in aqueous solutions," *Chemical Engineering Journal*, vol. 242, pp. 294–305, 2014.

[67] L. Zhao, X. Cao, O. Masek, and A. Zimmerman, "Heterogeneity of biochar properties as a function of feedstock sources and production temperatures," *Journal of Hazardous Materials*, vol. 256-257, pp. 1–9, 2013.

[68] Y. Chen, Y. Liu, Y. Li et al., "Novel magnetic pomelo peel biochar for enhancing Pb(II) and Cu(II) adsorption: performance and mechanism," *Water, Air, & Soil Pollution*, vol. 231, no. 8, p. 404, 2020.

[69] S. Zhao, N. Ta, and X. Wang, "Absorption of Cu(II) and Zn(II) from aqueous solutions onto biochars derived from apple tree branches," *Energies*, vol. 13, no. 13, p. 3498, 2020.

[70] H. H. Han, A. Kim, T. Kim, and Y. Bae, "Facile Cu(I) loading for adsorptive $C_3H_6/C_3H_8$ separation through double Cu(II) salts incorporation within pores with unsaturated Fe(II) sites," *Bulletin of the Korean Chemical Society*, vol. 42, no. 3, pp. 471–476, 2021.

[71] F. Zhao, R. Shan, J. Gu, Y. Zhang, H. Yuan, and Y. Chen, "Magnetically recyclable loofah biochar by $KMnO_4$ modification for adsorption of Cu(II) from aqueous solutions," *ACS Omega*, vol. 7, no. 10, pp. 8844–8853, 2022.

[72] K. Jung, S. Y. Lee, and Y. J. Lee, "Hydrothermal synthesis of hierarchically structured birnessite-type $MnO_2$/biochar composites for the adsorptive removal of Cu(II) from aqueous media," *Bioresource Technology*, vol. 260, pp. 204–212, 2018.

[73] Z. Lu, H. Zhang, A. Shahab et al., "Comparative study on characterization and adsorption properties of phosphoric acid activated biochar and nitrogen-containing modified biochar employing eucalyptus as a precursor," *Journal of Cleaner Production*, vol. 303, article 127046, 2021.

[74] J. Deng, Y. Liu, S. Liu et al., "Competitive adsorption of Pb(II), Cd(II) and Cu(II) onto chitosan-pyromellitic dianhydride modified biochar," *Journal of Colloid and Interface Science*, vol. 506, pp. 355–364, 2017.

[75] V. Bernal, L. Giraldo, and J. C. Moreno-Piraján, "Thermodynamic analysis of acetaminophen and salicylic acid adsorption onto granular activated carbon: importance of chemical surface and effect of ionic strength," *Thermochimica Acta*, vol. 683, article 178467, 2020.

[76] Y. Xiao, Y. Xue, F. Gao, and A. Mosa, "Sorption of heavy metal ions onto crayfish shell biochar: effect of pyrolysis temperature, pH and ionic strength," *Journal of the Taiwan Institute of Chemical Engineers*, vol. 80, pp. 114–121, 2017.

[77] Y. Chen, B. Wang, J. Xin, P. Sun, and D. Wu, "Adsorption behavior and mechanism of Cr(VI) by modified biochar derived from *Enteromorpha prolifera*," *Ecotoxicology and Environmental Safety*, vol. 164, pp. 440–447, 2018.

[78] G. Tan, W. Sun, Y. Xu, H. Wang, and N. Xu, "Sorption of mercury (II) and atrazine by biochar, modified biochars and biochar based activated carbon in aqueous solution," *Bioresource Technology*, vol. 211, pp. 727–735, 2016.

[79] Z. Chen, T. Liu, J. Tang et al., "Characteristics and mechanisms of cadmium adsorption from aqueous solution using lotus seedpod-derived biochar at two pyrolytic temperatures," *Environmental Science and Pollution Research*, vol. 25, no. 12, pp. 11854–11866, 2018.

[80] S. Fan, Y. Wang, Z. Wang, J. Tang, J. Tang, and X. Li, "Removal of methylene blue from aqueous solution by sewage sludge-derived biochar: adsorption kinetics, equilibrium, thermodynamics and mechanism," *Journal of Environmental Chemical Engineering*, vol. 5, no. 1, pp. 601–611, 2017.

[81] R. Marouf, N. Khelifa, K. Marouf-Khelifa, J. Schott, and A. Khelifa, "Removal of pentachlorophenol from aqueous solutions by dolomitic sorbents," *Journal of Colloid and Interface Science*, vol. 297, no. 1, pp. 45–53, 2006.

[82] Z. Zhao, S. Wang, Y. Yang, X. Li, J. Li, and Z. Li, "Competitive adsorption and selectivity of benzene and water vapor on the microporous metal organic frameworks (HKUST-1)," *Chemical Engineering Journal*, vol. 259, pp. 79–89, 2015.

[83] J. Li, G. Yu, L. Pan et al., "Study of ciprofloxacin removal by biochar obtained from used tea leaves," *Journal of Environmental Sciences*, vol. 73, pp. 20–30, 2018.

[84] H. Yan, W. Zhang, X. Kan et al., "Sorption of methylene blue by carboxymethyl cellulose and reuse process in a secondary sorption," *Colloids and Surfaces A: Physicochemical and Engineering Aspects*, vol. 380, no. 1-3, pp. 143–151, 2011.

[85] Ş. S. Bayazit, E. Kurtulbaş, M. Bilgin, and S. Şahin, "Decontamination of endocrine disruptors from water by graphene nanoplatelet/UiO-66 nanocomposites," *Environmental Nanotechnology, Monitoring & Management*, vol. 18, article 100733, 2022.

[86] M. Zhang, J. Yang, H. Wang, Q. Lv, and J. Xue, "Enhanced removal of phosphate from aqueous solution using Mg/Fe modified biochar derived from excess activated sludge: removal mechanism and environmental risk," *Environmental Science and Pollution Research*, vol. 28, no. 13, pp. 16282–16297, 2021.

[87] X. Chen, G. Chen, L. Chen et al., "Adsorption of copper and zinc by biochars produced from pyrolysis of hardwood and corn straw in aqueous solution," *Bioresource Technology*, vol. 102, no. 19, pp. 8877–8884, 2011.

[88] J. Meng, X. Feng, Z. Dai, X. Liu, J. Wu, and J. Xu, "Adsorption characteristics of Cu(II) from aqueous solution onto biochar derived from swine manure," *Environmental Science and Pollution Research*, vol. 21, no. 11, pp. 7035–7046, 2014.

[89] A. Bogusz, P. Oleszczuk, and R. Dobrowolski, "Application of laboratory prepared and commercially available biochars to adsorption of cadmium, copper and zinc ions from water," *Bioresource Technology*, vol. 196, pp. 540–549, 2015.

[90] Z. Mahdi, Q. J. Yu, and A. E. Hanandeh, "Investigation of the kinetics and mechanisms of nickel and copper ions adsorption from aqueous solutions by date seed derived biochar," *Journal of Environmental Chemical Engineering*, vol. 6, no. 1, pp. 1171–1181, 2018.

[91] A. Cibati, B. Foereid, A. Bissessur, and S. Hapca, "Assessment of *Miscanthus × giganteus* derived biochar as copper and zinc adsorbent: study of the effect of pyrolysis temperature, pH and hydrogen peroxide modification," *Journal of Cleaner Production*, vol. 162, pp. 1285–1296, 2017.

[92] T. Shim, J. Yoo, C. Ryu, Y. Park, and J. Jung, "Effect of steam activation of biochar produced from a giant Miscanthus on copper sorption and toxicity," *Bioresource Technology*, vol. 197, pp. 85–90, 2015.

[93] L. Trakal, R. Šigut, H. Šillerová, D. Faturíková, and M. Komárek, "Copper removal from aqueous solution using biochar: effect of chemical activation," *Arabian Journal of Chemistry*, vol. 7, no. 1, pp. 43–52, 2014.

[94] M. Choudhary, R. Kumar, and S. Neogi, "Activated biochar derived from *Opuntia ficus-indica* for the efficient adsorption of malachite green dye, $Cu^{+2}$ and $Ni^{+2}$ from water," *Journal of Hazardous Materials*, vol. 392, article 122441, 2020.

[95] M. L. Huang, C. Wang, and S. Q. Liu, "Adsorption of Cu and Ni ions from aqueous solutions by commercial activated carbon and the reutilization in glass coloration," *Journal of Wuhan University of Technology-Materials Science*, vol. 34, no. 1, pp. 41–46, 2019.

[96] E. Pehlivan and S. Cetin, "Application of fly ash and activated carbon in the removal of $Cu^{2+}$ and $Ni^{2+}$ ions from aqueous solutions," *Energy Sources Part A-Recovery Utilization and Environmental Effects*, vol. 30, no. 13, pp. 1153–1165, 2008.

[97] E. Safaei, N. S. Langeroodi, and E. Baher, "Investigation of removal of Cu(II) ions by commercial activated carbon: equilibrium and thermodynamic studies," *Protection of Metals and Physical Chemistry of Surfaces*, vol. 55, no. 1, pp. 28–33, 2019.

[98] M. Zhang, M. Ahmad, M. I. Al-Wabel et al., "Adsorptive removal of trichloroethylene in water by crop residue biochars pyrolyzed at contrasting temperatures: continuous fixed-bed experiments," *Journal of Chemistry*, vol. 2015, Article ID 647072, 6 pages, 2015.

Hindawi
Adsorption Science & Technology
Volume 2023, Article ID 1532660, 17 pages
https://doi.org/10.1155/2023/1532660

*Research Article*

# Remediation of Methyl Red Dye from Aqueous Solutions by Using Biosorbents Developed from Floral Waste

**Abdelfattah Amari**,[1,2] **Virendra Kumar Yadav**,[3] **Sabir Khan Pathan**,[4] **Bijendra Singh**,[5] **Haitham Osman**,[1] **Nisha Choudhary**,[6] **Khaled Mohamed Khedher**,[7,8] **and Anup Basnet**[9]

[1]*Department of Chemical Engineering, College of Engineering, King Khalid University, Abha 61411, Saudi Arabia*
[2]*Research Laboratory of Processes, Energetics, Environment and Electrical Systems, National School of Engineers of Gabes, Gabes University, 6072, Tunisia*
[3]*School of Liberal Arts & Sciences, Mody University of Science & Technology, Sikar, Lakshmangarh, Rajasthan 332311, India*
[4]*Department of Chemistry, School of Sciences, P P Savani University, Surat, Kosamba, Gujarat 394125, India*
[5]*School of Chemical Sciences, Central University of Gujarat, Gandhinagar, Gujarat 382030, India*
[6]*Department of Environment Sciences, School of Sciences, P P Savani University, Kosamba, Surat, Gujarat 394125, India*
[7]*Department of Civil Engineering, College of Engineering, King Khalid University, Abha 61421, Saudi Arabia*
[8]*Department of Civil Engineering, High Institute of Technological Studies, Mrezgua University Campus, Nabeul 8000, Tunisia*
[9]*Department of Microbiology, Saint Xavier's College, Maitighar, Tribhuvan University, Kathmandu, Nepal*

Correspondence should be addressed to Anup Basnet; basnet.a@sxc.edu.np

Received 17 June 2022; Revised 5 November 2022; Accepted 24 November 2022; Published 24 January 2023

Academic Editor: Chinenye Adaobi Igwegbe



The disposal of biological waste into water bodies is a major global concern as it leads to water pollution resulting in the loss of plenty of revenue in the cleaning of water bodies. Here, in the present research work, sacred flowers were collected, segregated, sun-dried, and powdered. The dried floral powders (marigold and rose) were characterized by field emission scanning electron microscopy (FESEM), electron diffraction spectroscopy (EDS), Fourier transforms infrared spectroscopy (FT-IR), and X-ray diffraction (XRD). The microscopy revealed the irregular spherical shape of the sheet-like structure whose size varies in microns. The EDS revealed the elemental composition which was dominated by mainly carbon and oxygen. The XRD shows the presence of carbon (10-25$^{\boxtimes}$) in the amorphous form and the absence of any crystalline phase in the biosorbents. The FT-IR showed peaks that conformed to the presence of functional groups like -OH and a carbonyl group. The dried powders were used as an economical and eco-friendly biosorbent for the removal of methyl red (MR) dye from the aqueous solutions by batch adsorption study. After 60 minutes of contact time, the marigold powder (MGP) and rose petal powder (RPP) showed decolorization of 61.16% and 56.08% for 2 ppm of MR dye. The kinetic revealed that the dye removal reaction does not follow the pseudo-first-order as well as the pseudo-second-order. The utilization of such waste-based biosorbents will minimize solid waste and also will provide an economical biosorbent for the removal of environmental pollutants.

## 1. Introduction

Since ancient times only, India is known as the land of temples, especially in cities like Haridwar, Varanasi, Dwarka, and Mathura. [1]. Besides this, India is also having a large number of mosques, churches, and other religious places where every day, a huge number of flowers are offered by the devotees [2]. In addition, these flowers are also used in huge amounts in various marriage events, funerals, last-rite, and other social gatherings. Every year, all these major religious places dispose of millions of tonnes of dried flowers into the river or other water bodies or are dumped as solid

municipal waste [3, 4]. The disposal of tonnes of dried or semidried flowers in important rivers, like the Ganga, and the Yamuna leads to water pollution [5, 6]. Every year, various government organizations like "Namami Gangae," national river conservation plan (NRCP), Yamuna action plan (YAP), River Development and Ganga Rejuvenation (MOWR), and Atal mission for rejuvenation and urban transformation (Amrut), spend a huge amount of money for cleaning the important and sacred rivers of the country. Besides this, there are several nongovernmental organizations (NGOs) like "The ISHA foundation" and "Jeevitnadi-Living River Foundation" which are involved in cleaning rivers in India. The disposal of flowers in the rivers increases pollution by increasing the biological oxygen demand (BOD), nitrogen content, and other parameters of the water [7], hence affecting the flora and fauna of the river or the aquatic ecosystem. As per reports in 2019, every year, about $8 \times 10^9$ kilogram of flowers is dumped into river Ganga alone which leads to water pollution [8].

To date, various techniques like precipitation, adsorption, filtration, nanofiltration, and absorption are applied for the removal of both organic and inorganic pollutants from the wastewater [9]. Most of these techniques are quite simple and economical but less effective and energy intensive. So, the utilization of such biological waste as an adsorbent for the remediation of dyes, pesticides, etc. may reduce the cost of wastewater treatment. The adsorption method is easy to implement, reliable, less expensive, and has no formation of any toxic product at any step [10]. So, adsorption is the most preferred technique. Moreover, being organic in nature, the bioadsorbents easily get degraded or mineralized in the environment. There are several investigators which have reported the utilization of the abovementioned techniques for wastewater treatment and other environmental cleanups. Elgarahy et al. reported the sorption of cationic and anionic dyes from wastewater by using an untapped sepia-based composite [11]. Further, Elwakeel et al. reported the remediation of chromate ions from the wastewater by a magnetic Schiff's base sorbent which was based on the waste peels of shrimps [12]. Further, recently, Elwakeel et al. developed a product named 2-mercaptobenzimidazole which was functionalized with chitosan. The functionalized product was used for the effective remediation of methylene blue in a batch and column experiment. The authors have reported MB dye removal percentage of up to 94.5% [13]. Another approach by Tsuchiai et al., Ishizuka et al., and Shi et al. remediated the MB dye by using beach bivalve shells collected from the Port Said coastal area (Egypt) as an adsorbent. The dye removal percentage with this adsorbent reached 93.6% [14–16].

Biosorbents are biological materials used to passively remove contaminants from a solution [17, 18]. Activated carbon is widely used in sorbent matter in biosorption practice due to its great physicochemical structural properties. One major drawback of this activated carbon is its low regeneration capacity and expensive manufacturing [19]. Biological waste is one of the best substitutions for activated carbon as an adsorbent due to its low-cost, environmental friendly, high yield, biodegradable nature, high regeneration capacity, high abundance, and renewable nature [20]. The effective transformation of biological waste into a biosorbent reduces the ecological risk imposed by dumping such waste into the natural environment. Moreover, such practices also minimize the cost of solid waste management [21]. There are several types of biosorbents [22–24] such as (1) tea-industry waste [25], (2) sugar industry waste (bagasse) [26], (3) peach and apricot stones, (4) antibiotic waste, (5) sludge, (6) waste green sands, (7) fly ash [6, 27, 28], and incense sticks ash [4, 29–31].

El-Azazy et al. utilized green tea waste (GTW) as an absorbent for the removal of methylene blue (MB) from the wastewater where the investigators achieved a maximum adsorption capacity of 96.58% MB dye by using about 68.28 mg/g GTW [25]. Kerrou et al. used sugarcane bagasse (SB) to remove organic dyes from the wastewater. The removal rate of MB dye was 80.27% to 98.49% with the increase of the mass of absorbent from 0.05 g to 5 g due to an increase in a specific area [26]. Abatal et al. utilized pitahaya fruit (*Hylocereus* spp.) peels for the remediation of Pb(ll), Cd(ll), Co(ll), and Ni(ll) from the wastewater where the biosorption capacity of pitahaya peel was 77%, 72%, 74%, and 74% for Pb(ll), Cd(ll), Co(ll), and Ni(ll), respectively [32]. Saranya et al. developed biosorbents from floral waste for the removal of lead ions from the aqueous solutions [33].

A large number of heavy metals, pesticides, dyes [34], etc. are pollutants that cause environmental threats all over the world [35]. Nowadays, heavy metals are the most threatening environmental pollutants which affect public health due to their nonbiodegradable nature. The increase in the use of pesticides for controlling pests to ensure food security causes environmental pollution [36]. Dye is used in large amounts in textiles, paper, leather, cosmetics, food, plastics, rubber, and the pharmaceutical industry. The discharge of dyes in water bodies adversely affects the overall ecosystem [37]. Therefore, there is an immediate requirement for the remediation of environmental pollutants including dyes from the environment by using low-cost, eco-friendly, and biodegradable biosorbents such as flowers [38].

These flowers are mainly consisting of carbon, which can be used in its natural form for the development of various value-added materials. The value-added materials developed from such floral waste will be economical and eco-friendly. Moreover, the development of such value-added products from floral waste will also help in the reduction of the solid waste arising from the disposal of sacred flowers into the rivers [21]. There are several examples where *Rosa damascena* mill sacred flowers were used for the manufacturing of value-added materials like an essential oil. Adeel et al. reported the extraction of dye pigment from such sacred flowers offered at religious places [39]. Vankar et al. utilized the residue left after dye extraction from the *Hibiscus rosa-sinensis* flower. Here, investigators have used such floral residue for the removal of heavy metals from the aqueous solutions [40]. Elangovan et al. also reported the remediation of hexavalent and trivalent chromium by using biosorbent prepared from palm flower (*Borassus aethiopum*) [41]. Waghmode et al. formulated a media for the growth of an actinomycete, i.e., *Microbisspora* sps from the floral extracts of *Madhuca latifolia L* [3]. Luis et al. utilized marigold

flowers for the extraction of xanthophyll pigments under optimized conditions [42]. Pu et al. evaluated the chemical properties and other parameters of safflowers [43]; while Sato et al. developed safflower yellow B and carthamin red pigment from the same flower [44]. So, from the literature, it is evident that floral waste has been used as a source of value-added material. Davamani et al. utilized flower waste for the removal of chromium ions from the tannery effluent. Here, flower waste biomass absorbed around 70% chromium from the tannery effluent [45]. Aman et al. used rose biomass for the removal of chromium, mercury, and zinc from the contaminated waters. The absorption capacity of 100 ppm of chromium, mercury, and zinc was 5.26, 6.76, and 4.07 mg/g, respectively [46]. Mondal et al. also utilized the waste marigold flower powder for the removal of heavy metals, i.e., Cd (II) and Cr (VI) from aqueous solutions [47]. Tolcha et al. used the flower of *Typha latifolia* for the uptake of multiclass pesticide residues from contaminated water. These studies show the removal of diazinon, atrazine, chlorothalonil, ametrine, chlorpyrifos, and dimethametryn pesticides from the wastewater using a batch experiment [48]. Elango and Govindasamy used temple waste flowers for the removal of color from textile dyeing effluent. The maximum color removal efficiency of activated carbon was 98.17% at a 200 mg dose of biosorbent, and color removal was high at 95.83% at 100 min [49]. From the above piece of literature work, it is evident that floral waste could act as a potential biosorbent for the removal of both organic and inorganic pollutants from wastewater [36]. Generally, *Tegetes erecta* (TE) is used as garlands in prayer, *C. infundibuliformis* (CI) while bowing heads, and *P. tuberosa* are used at religious places to worship Gods, which is evident from the literature. So, the majority of the literature available in the scientific domain is based on these flowers only [3].

Methyl Red ($C_{15}H_{15}N_3O_2$) is an azo-dye compound having a molecular weight of 269.31 g/mol. It is chiefly used as a pH indicator in laboratories as its color changes with solution pH. The dye imparts red color in acidic solutions having a pH of 4.4, yellow color in solutions having a pH higher than 6.2, whereas orange color in the solutions having a pH range of 4.4-6.2. MR is generally used as a model dye for various experimental studies due to its intense color in aqueous systems. The dye has low biodegradability because of the presence of benzene rings in its structure. Methyl red is a toxic organic compound and is known to cause respiratory problems, digestive tract infections, skin and eye irritation, carcinogenesis, mutagenesis, and teratogenesis. Hence, wastewater containing such toxic organic contaminants has to be treated prior to its disposal or discharge into the aquatic systems [50–52]. The utilization of floral waste from religious places as an adsorbent will solve the flower-based waste disposal problems and environmental pollution [3].

Recently, various investigators have used different metallic/nonmetallic nanoparticles, biosorbents, clay, etc. for the remediation of methyl orange dyes from the wastewater. Bhowmik et al. developed a new magnetic nanoparticle having a mixed phase of $CaFe_2O_4$ and $MnFe_2O_4$ magnetic nanocomposite (CaF-MnF-MNC) by coprecipitation method. Further, the MR dye was removed from the aqua matrix by using this nanocomposite. The authors achieved very high efficiency for the dye remediation, i.e., 99.88% [53]. In another work reported by Bhowmik et al. developed a magnetic nanocomposite ($Fe_2O_3/Mn_3O_4$) for the increased remediation of MO dyes from the aqueous solutions. They performed neural network modelling and response surface methodology optimization. Further, Bhowmik et al. reported the development of magnetic $CaFe_2O_4/MnFe_2O_4$ nanocomposite and utilized for the remediation of Eriochrome Black-T (an anionic dye) from the aqua matrix by simple adsorption technique. Here, the investigators reported the dye remediation by simple shaking condition, batch stirring, and sonoassisted, and out of which, the latter technique was most efficient which removed the EBT dye up to 98% [54]. In another work by Bhowmik et al. where the investigators developed a nanocomposite of calcium ferrite and zirconia and utilized them further for the remediation of MO dyes from the aqua matrix. Here, the investigators have mainly focused on the optimization parameters for the remediation. Under optimized conditions, investigators reported the removal of MO dye from the aqua matrix of up to 98.92% [54].

Yadav et al. extracted ferrous particles from incense sticks ash and modified them into iron oxide nanoparticles (IONPs). Further, the investigator utilized the synthesized IONPs for the remediation of methylene blue from the aqueous solution and the efficiency attained was about 70% [55]. Modi et al. also provided descriptive information about the utilization of zinc oxide nanoparticles for the removal of methylene blue from wastewater [56].

Several investigators have used metallic particles as an adsorbent for the removal of MR dye and other pollutants. For instance, Elwakeel et al. provided detailed information about metal/mineral-incorporating materials for water treatment. The authors have mainly focused on the remediation of Cr (VI) from wastewater using metallic particles [57]. Mashabi et al. provided detailed information about the remediation of dyes by using adsorbents made from chitosan or glycidyl methacrylate [58]. One more article by Elwakeel reported descriptive information about the detailed information for the applications of chitosan resins in wastewater treatment. The chitosan was used as a bioadsorbent for the remediation of pollutant removal from wastewater [59].

There were several objectives for performing this experiment. Firstly, to suggest the utilization of floral waste as an economical and biodegradable bioadsorbent from various religious places. Secondly, to assess the potential of the recycled flowers-based bioadsorbents for the remediation of MR dye from the aqueous solutions. Thirdly, to minimize the solid waste arising from the disposal of flowers at rivers or other water bodies and in municipality areas. One final objective of this study was to suggest an economical and effective method to maintain the cleanliness of the river water.

In the current research work, authors have emphasized the utilization of sacred flowers offered at temples, mosques, and other religious places for the development of bioadsorbents. The current methods involve several steps like a

collection of flowers, segregation of flowers, sun-drying, and conversion into powder form. The developed biosorbents (marigold and rose flowers) were characterized by analytical instruments for detailed features. Finally, the potential of both types of floral-based biosorbents was assessed for the remediation of MR dye from the aqueous solutions. Such approaches for wastewater treatment are quite economical due for several reasons, firstly, less energy is required for the manufacturing of biosorbents, and secondly, biosorbents originated from the waste material. The current novel approach utilizes biological waste as an economical biosorbent without affecting the environment due to its biodegradable nature.

## 2. Materials and Methods

*2.1. Materials.* Flowers were collected from temples (Uttam Nagar, New Delhi, India) and mosques (Hazrat Nizamuddin, New Delhi, India), double distilled water (ddw), ceramic mortar pestle (Laboratory Scientific, Haryana, India), methyl red dye (99% purity, AR grade) (SRL, New Delhi, India), methanol (98% purity, AR grade) (SRL, New Delhi, India), potassium bromide, 99.98% IR grade (Sigma Aldrich, Darmstadt, Germany), pulverizer (Kudarat Enterprises, Rajkot, Gujarat, India), sieve sets (Laboratory Scientifics, Haryana, India), and 100 ml round bottom flask (Borosil, Gujarat, India).

### 2.2. Methods

*2.2.1. Processing of Sacred Recycled Flowers.* Sacred flowers were collected from the temples, mosques, and other events in plastic bags. The flowers were manually segregated to remove wrappers of incense sticks, incense cones, candles, paper pieces, and other items. Then, the rose flowers and petals were separated from the marigold flowers. The flower petals for both flowers were collected by detaching them with other flower parts like sepals, carpels, and sometimes leaves. The detached floral petals were then spread on a plastic sheet and kept under sunlight for several days. This ensures the complete drying and removal of moisture content from the floral petals. Once the sun-drying was over, the floral petals were collected in a plastic bag, which in turn was kept in an airtight container. Both marigold and rose petals were passed separately through a pulverizer machine for grinding. Both types of floral petal powders were collected separately. The floral petal powder was then sieved by using sieve sets to remove larger particles. The floral powder was then analyzed by using sophisticated instruments for detailed morphological and elemental properties. The floral petal powders were then stored for future use.

Figure 1 is showing the sequential steps involved in the development of biosorbents from floral waste. Figure 1(a) is the collected flowers from religious places, whereas Figure 1(b) is the segregated marigold flowers, which are free from all other parts of a flower. While Figure 1(c) is the powdered form of the sun-dried marigold flower petals. Figure 1(d) is showing dried rose petals while Figure 1(e) is showing the powdered form of rose petals obtained after passing through pulverizer. While Figure 2 is showing a mini pulveriser machine used in this experiment for grinding floral petals, here the powdered flowers are collected in the stainless-steel collecting drum placed at the bottom. Figure 3 is showing a schematic flow chart for the development of biosorbents from floral waste.

*2.2.2. Preparation of Aqueous Solution of Dyes.* About 3 mg of dye was dissolved in a 200 ml beaker and was continuously stirred on a magnetic stirrer at 500 rpm for the complete dissolution of the dye particles. Further, the aqueous solution of dye was filtered through a Whatman filter paper no 42 to remove the impurities. Finally, the methyl red (MR) dye stock solution was stored in a reagent bottle for future use.

*2.2.3. Remediation of Dyes by Using Bioadsorbents.* The flower powder obtained previously was used as an adsorbent for the remediation of dyes (methyl red) from the aqueous solution prepared in the above step. The stocks of an aqueous solution of MR dye were prepared by weighing about 0.2 mg of MR dye. The weighed quantity of the MR dye solute was both the dyes were mixed with the 100 mL distilled water. About 50 mL of MR dye solution was transferred to a 100 mL plastic beaker. About 1 mg of each bioadsorbent/flower powder was added to the aqueous solution of MR dye in two separate beakers. Further, an initial sample of MR dye aqueous solution was kept for analysis. Further, both the beakers containing an aqueous solution of dyes and rose petal powders and marigold petal powders were kept for stirring at 350 rpm at room temperature (RT). Further, an aliquot of about 5 mL was collected from both beakers after a regular interval of 10 minutes and kept in a centrifuge tube.

The dye adsorption study was carried out in the batch shake flask method in an incubator shaker under controlled conditions. The effect of time on the remediation of MR dye from the aqueous solution was analyzed. To settle down the bioadsorbents from the mixture, centrifugation of the sample was done at 5000 rpm for 10 minutes. Finally, the centrifuged samples were analyzed by using a Carry 60, UV-Vis spectrophotometer (Agilent Technologies, Santa Clara, USA). The spectral analysis was done to reveal the concentration of the MR dye in the various samples. The removal percentage of MR dye and adsorption capacity of MGP and RPP at any time ($q_t$) were calculated using the following equation.

$$\begin{aligned} \%\text{Decolorization} &= \frac{A_0 - A_t}{A_0} \times 100, \\ q_t(\text{mg}|g) &= \frac{(A_0 - A_t)V}{M}, \end{aligned} \tag{1}$$

where $A_0$ is the initial concentration of MR (mg $L^{-1}$), $A_t$ is the concentration of MR at a given time (mg $L^{-1}$), $V$ is the volume of solution (liter), and $M$ is the mass of bioadsorbents.

Figure 4 is showing the mechanism involved in the removal of methyl red dye from the aqueous solutions by using floral biosorbents.

*2.2.4. Characterization of the Bioadsorbents.* Both the bioadsorbents were analyzed by various sophisticated instruments like Fourier-transform infrared spectroscopy (FT-IR), Field

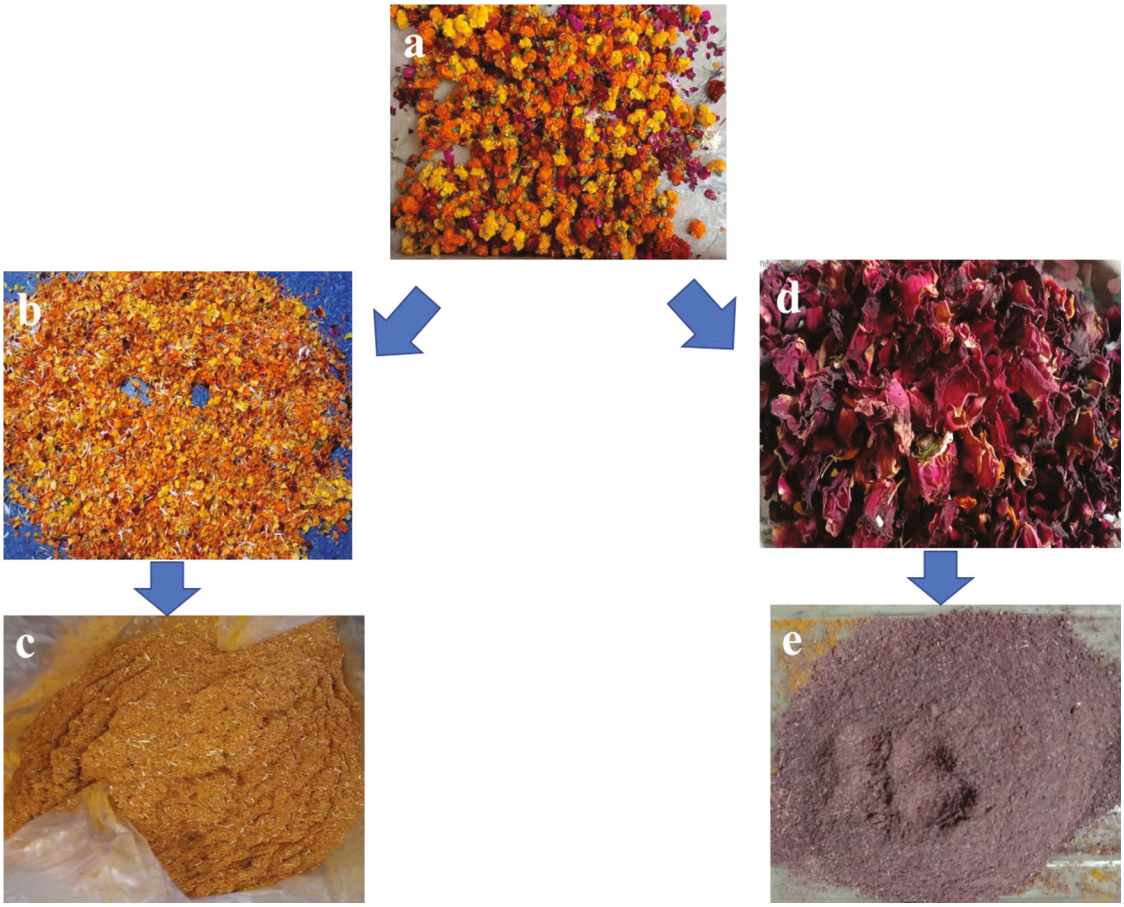


Figure 1: Steps involved in the processing and transformation of floral waste into biosorbents.

emission scanning electron microscopy (FESEM), and X-ray diffraction spectroscopy (XRD). The FT-IR analysis of both bioadsorbent powders was done by using the solid KBr pellet method, where KBr and each bioadsorbents were separately mixed in a ratio of 98 : 2 and mixed thoroughly in a mortar pestle. Preparation of the solid pellet of KBr and samples were done by using a hydraulic press for both samples separately. Finally, both pellets were analyzed by using a blank KBr pellet, and measurements were done by using Bruker Tensor 27 FT-IR Spectrometer (Billerica, Massachusetts, USA), instrument at a resolution of 2 $cm^{-1}$. To find the mineral phases, present in the biosorbent powder, both the powders were analyzed by the D-8 Advance Bruker (USA) made instrument. The scanning of the powder samples was done in the range of 10-80 degrees with a scanning rate of 5/sec. To find the morphological and elemental features, both powders were analyzed by using NOVA, NanoSEM, 450 FEI FESEM (USA). The powder samples were sprayed on the carbon tape which in turn adhered to the Al stub. The sample imaging was done in the variable range at 5 kev. The electron diffraction spectroscopy (EDS) was done by using the attached Oxford-made elemental analyzer in the FESEM. Finally, the different dye samples in aqueous solutions were analyzed by using a Carry 60, UV-Vis spectrophotometer (Agilent Technologies, Santa Clara, USA).

## 3. Results and Discussion

Figure 4 is showing the simplest possible mechanism of adsorption of MR dye molecules on the surface of the bioadsorbents. The dye molecules get adsorbed on the surface of the bioadsorbents due to the various functional groups like hydroxyl group and carboxyl group present in the bioadsorbents. The presence of these functional groups was confirmed by the FT-IR.

The FESEM analysis of both sorbents will in determining the size of the sorbents. From the literature, it is well established that the smaller the size of the particle, the more will be the surface area to volume ratio (SVR), so the more will the adsorption sites for the pollutants. This feature will increase the efficiency of the sorbents for the remediation of pollutants from the aqueous solutions. Moreover, the elemental analysis by the EDS analyzer will of the biosorbents reveals the purity as an impurity in the sorbent will minimize the efficiency of adsorption and ultimately the remediation of pollutants. FT-IR measurement of the biosorbents will reveal the various functional groups present on the surface of the biosorbents like hydroxyl and carbonyl which make them specific for the adherence of the pollutants like MR dyes. Methyl red is an azo dye, so the FT-IR analysis will reveal the possibility of adherence of azo dye on the biosorbents based on the functional groups. The selection of XRD


Figure 2: Showing the mini pulveriser machine, where the powdered flowers are collected in the stainless-steel collecting drum placed at the bottom.

analysis of the biosorbents was mainly used to find the amorphous or crystalline phase. Since the original of both biosorbents was biological plant material, so there is the possibility of carbon in an amorphous form.

### 3.1. FESEM-EDS of Flower Powders

*3.1.1. Marigold Flower Powder.* FESEM was carried out to reveal the morphological details of the developed bioadsorbents. The imaging was done at various magnification scales. Figures 5(a)–5(c) show FESEM micrographs of marigold petal powder at different magnifications. The size of the MGP is in microns where the size is irregular in shape and highly aggregated. The size of lumps is 20-70 microns, which are visible in the FESEM image. There are a few rectangular-shaped particles also surrounded by smaller irregular spherical lumps. The irregular shape indicates the high carbon in the sample, which is quite obvious due to the organic nature of the powder. The particles are porous in nature, which is evident from the FESEM image. The EDS analysis of the MGP shows the EDS spectra in Figure 4(d) and the elemental composition. The spectra have various elements like C, O, P, Na, Mg, Al, and Si which are dominated by mainly C and O. The carbon is present in the highest amount, i.e., 63.5% and O is 34.46%, which alone constitutes more than 97%; while remaining 2% is contributed by Si, Mg, Al, and Na which are present in trace amount in the MGP. The high percentage of carbon and oxygen proves the organic nature of the bioadsorbent.

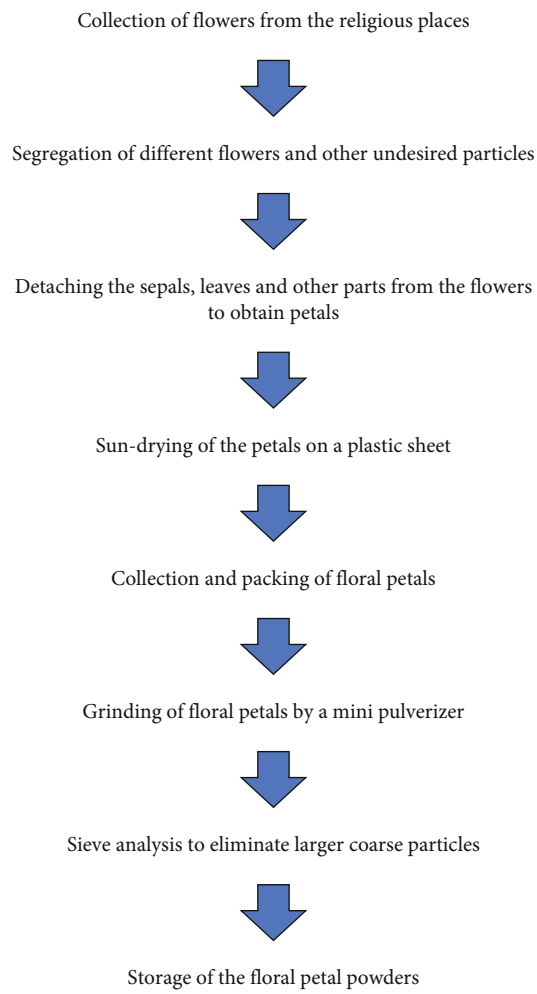


Figure 3: Schematic diagram for the development of floral petal powders/bioadsorbents.

Figures 6(a) and 6(b) show FESEM micrographs of rose petal powders that are obtained from pulverizing the dried rose petals. The particle's layered structure whose size is in the range of several microns, i.e., 8-17 microns. In Figure 6(a), there are several holes and spots in the structure. Such holes and spots were also reported by Saranya et al. in the floral powders of *Tegetis errata* and others [33]. The particles appear white in color, which indicates the carbon-rich region. While Figure 6(c) shows the EDS region of the RPP, analyzed for elemental detection. EDS spectra in Figure 4(d) and the elemental composition show that the powder is having mainly elements like C, O, Ca, Mg, P, Cl, and S. The major dominating element is C, i.e., 55.1% and O is 39.4%, while the remaining is in trace amounts. The percentage of C and O indicates the purity of the bioadsorbents. Several investigators have also reported similar properties of the RPP.

Among both MGP and RPP, the former is an irregular spherical shape while the latter is a layered sheet-like structure. MGPP has a slightly higher amount of carbon than the RPP, while O was marginally higher in MGPP. Besides this, both of them have traces of elements which constitutes 1-2% of the biosorbent. These elements may be present in the flowers from the soil via roots, etc.

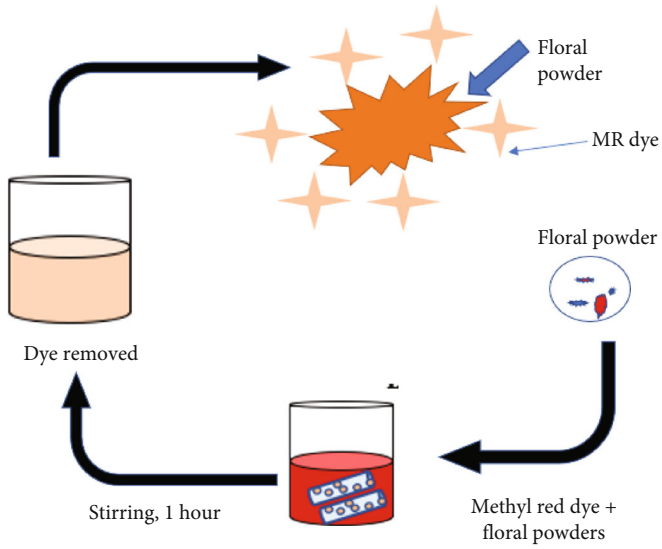


Figure 4: Steps involved in the floral waste based biosorbent development and dye removal from aqueous solutions.

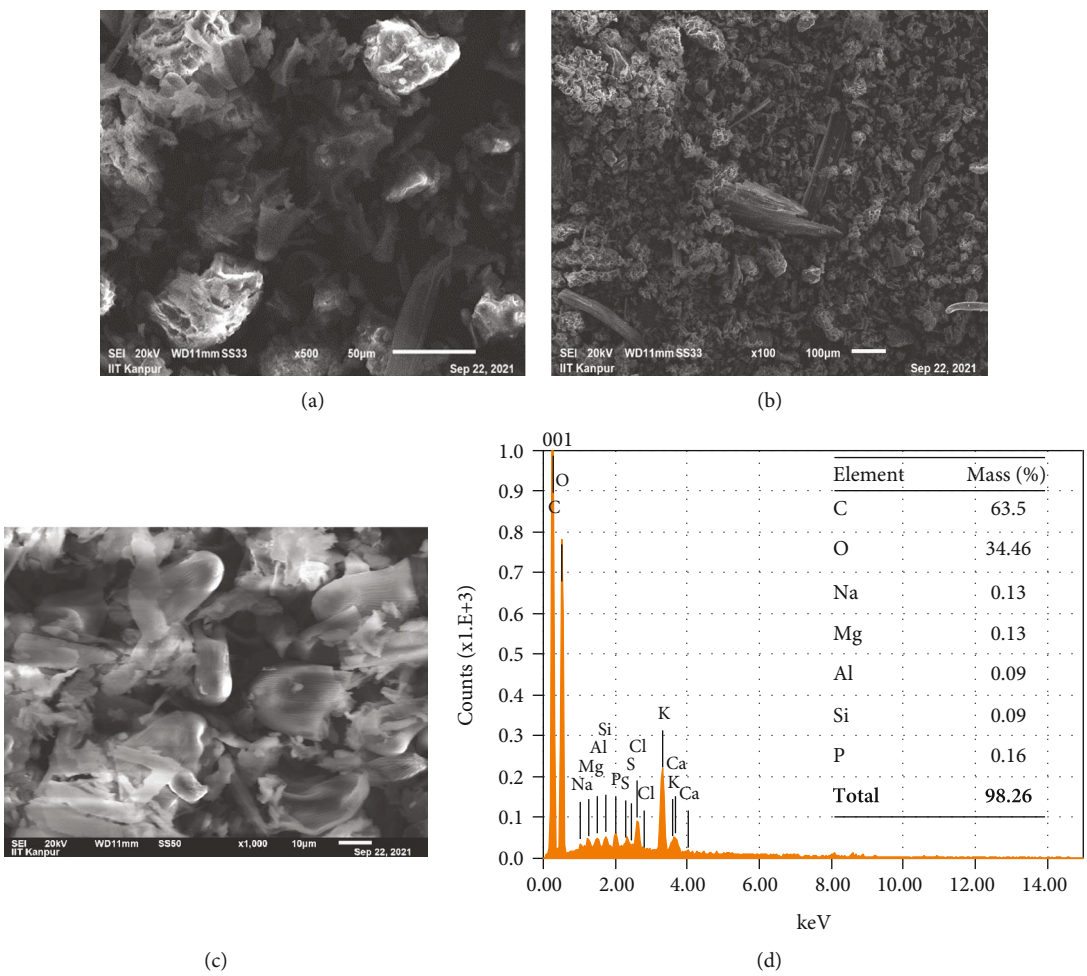


Figure 5: FESEM micrographs of marigold flowers (a, b), EDS spot (c), and EDS spectra (d).

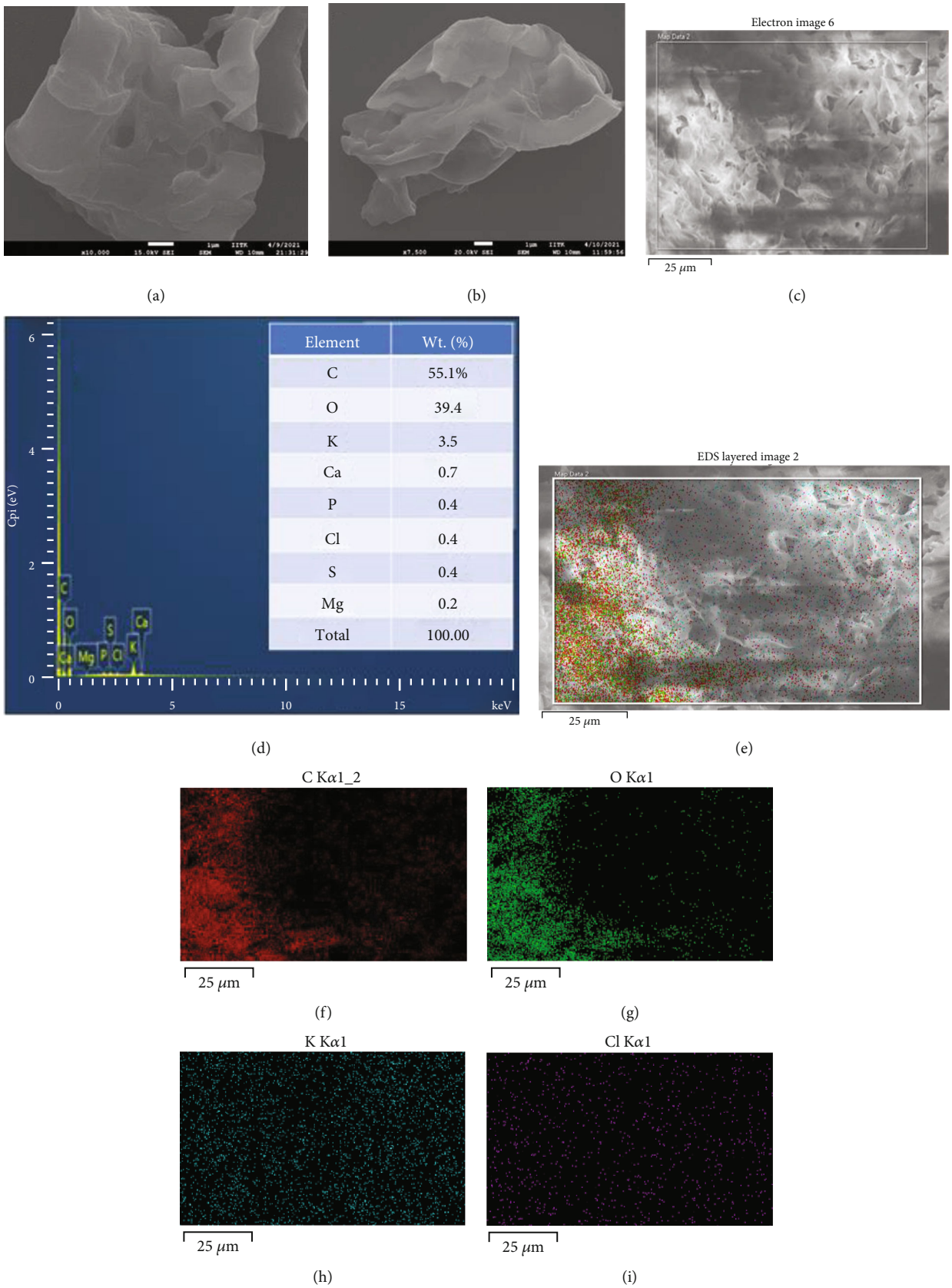


| Element | Wt. (%) |
|---|---|
| C | 55.1% |
| O | 39.4 |
| K | 3.5 |
| Ca | 0.7 |
| P | 0.4 |
| Cl | 0.4 |
| S | 0.4 |
| Mg | 0.2 |
| Total | 100.00 |

Figure 6: FESEM micrographs of rose petal powder (a, b), EDS spot (c), EDS spectra (d), and elemental mapping of rose powders (e–i).

Table 1: Comparative morphological and elemental studies of floral bioadsorbent by FESEM.

| Biosorbent | Shape | Size | Application | References |
|---|---|---|---|---|
| Flower waste | Irregular | Micron sized | $Pb^{2+}$ removal | [62] |
| *Acroptilon* response flower powder | Rectangular, sheet-shaped | Micron sized | Cr VI removal | [60, 61] |
| Crushed marigold flowers | Powder has pansy's stripes, fritillary's checks, or tiger-lily's dots | Micron sized | Compost preparation | [3] |
| Mixed floral waste | Heterogeneous surface, having cellulose, hemicellulose, and lignin | Micron sized | For biofuel and compost manufacturing | [63] |

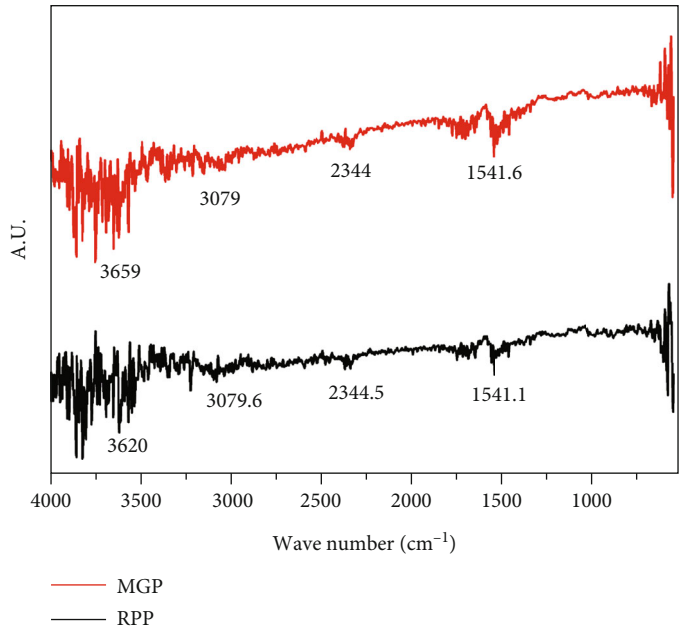


Figure 7: FT-IR spectrum of Rose Petal powder and Marigold flowers.

Table 2: FT-IR peak assignments of MGP and RPP along with previous work done.

| Peaks | Functional group | Attributions | References |
|---|---|---|---|
| 1735 | C=O, (in all plants) | Stretching vibrations (SV) | [33, 62] |
| 2851–2850 cm$^{-1}$ and 2920–2919 cm$^{-1}$ | Alkanes | SV of C–H. | [33, 62] |
| 3403.65–3421.19 cm$^{-1}$ | O-H, of the carboxylic group | SV | [33, 62] |
| 3409.63–3416.57 cm$^{-1}$ | Alcohol and phenol compound of O–H vibration | | [33, 62] |
| 3404.97–3414.65 cm$^{-1}$ | N–H of amides | Symmetric and asymmetric vibrations | [33, 47, 61] |
| 1297.74–1243.96 cm–1 and 1056–1054 cm$^{-1}$ | C–N of aliphatic amines | SV | [47, 61] |
| 1413.29–1419.33 cm$^{-1}$ | C–C of the aromatic ring | SV | [33, 47, 66] |
| 1337–1441 cm$^{-1}$ | C–H of alkanes group | Bending and rock vibration | [33, 47, 60] |
| 1,526 and 1,528 cm$^{-1}$ | COO and C=O groups | | [47, 61] |
| 571-605 cm$^{-1}$ | Aromatic compounds | Bending modes | [47] |

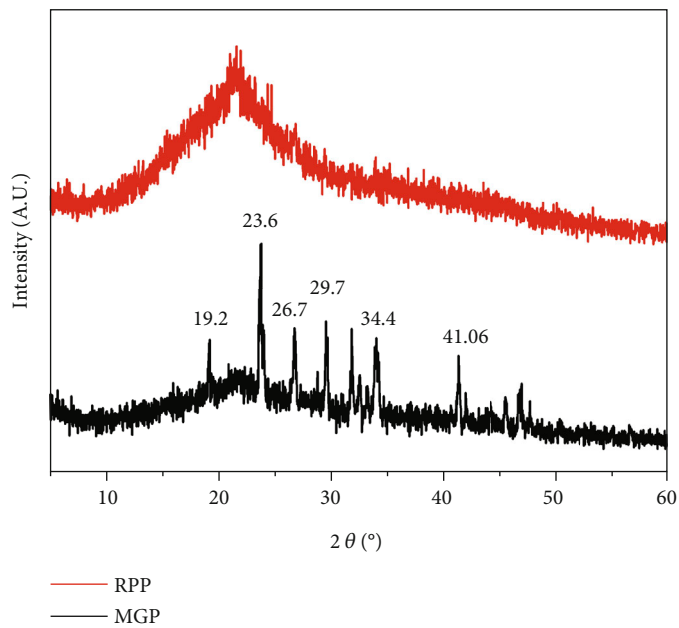


Figure 8: X-ray diffraction spectra of marigold and rose petal powders.

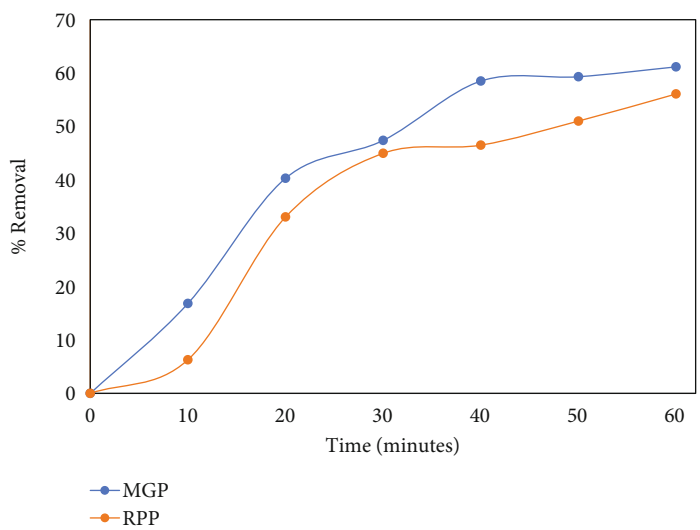


Figure 9: Removal percentage of methyl red dye by marigold and rose petal powder as biosorbents.

Figure 6(e) is showing the elemental mapping of RPP by EDS, and Figure 6(f) shows the mapping region of carbon in the EDS, while the green area is of oxygen (Figure 6(g)) while the blue zone is of potassium (Figure 6(h)). So, from the EDS elemental mapping, it is also confirmed that the bioadsorbent is highly pure in nature, i.e., made up of only carbon and oxygen along with traces of elements like K, etc.

Srinivasulu et al. also used flower-based bioadsorbent for the remediation of pollutants from the wastewater. The investigators have used the floral-based bioadsorbent for the removal of heavy metals. The size of the bioadsorbent was also in the micron range which was mainly rectangular and sheet-shaped [60]. Moreover, Ghaneian et al. also used floral-based bioadsorbents for the remediation of pollutants from the wastewater and reported almost similar morphology of the biobent [61].

Similar elemental mapping of flowers was also reported by investigators whose details are provided in Table 1.

*3.2. FT-IR Study of Flower Powders.* Figure 7 shows typical FT-IR spectra of floral powders as bioadsorbents where (a) rose powder and (b) marigold powder revealed that the presence of some functional groups like –OH, -NH, and C=O were identified by the peaks with specific band range. The functional groups in the floral powder samples help in the remediation of contaminants like heavy metals, dyes, and others. So, the presence of different functional groups in the floral powders makes them more suitable for the adsorption of different pollutants from wastewater. The functional

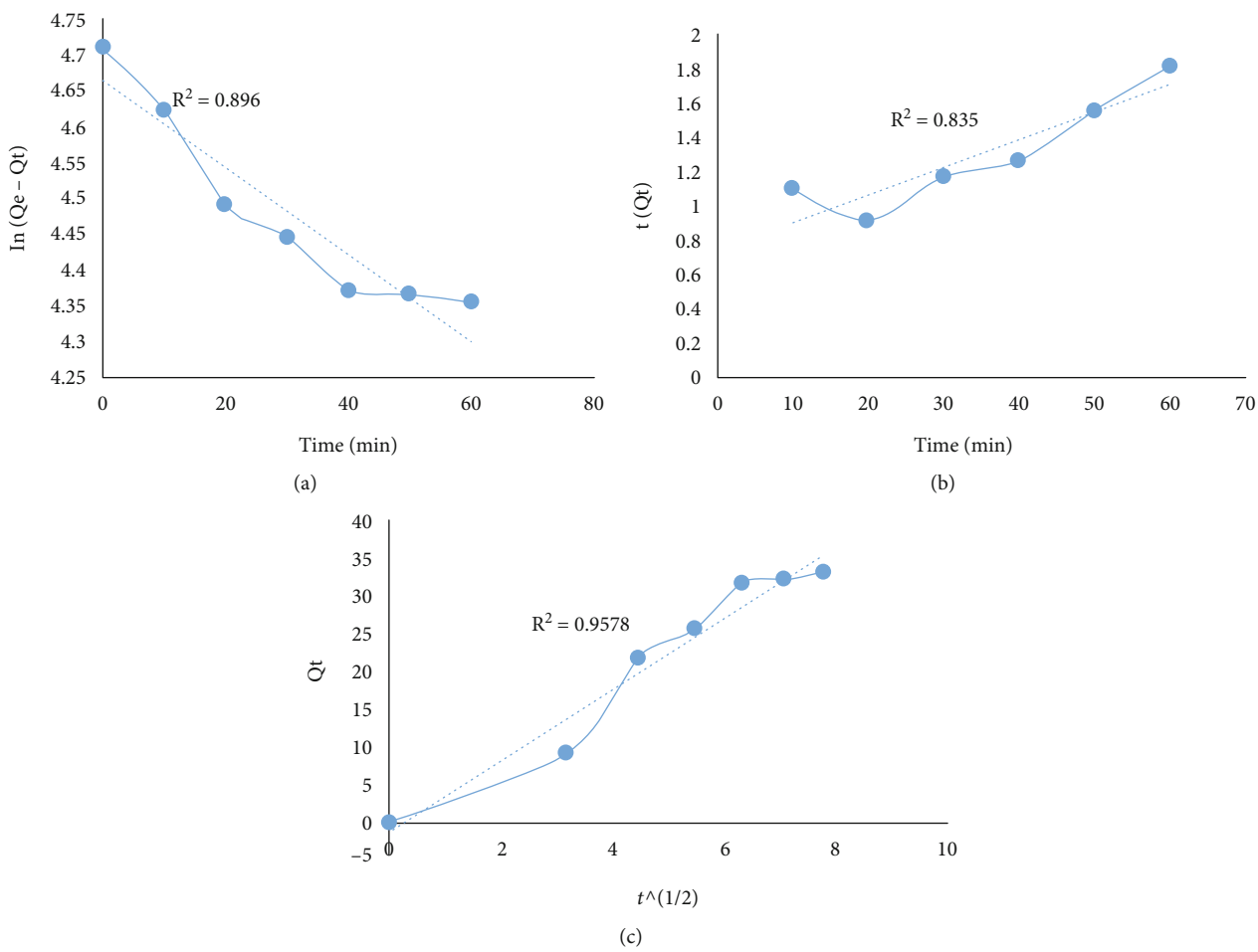


Figure 10: (a) Pseudo-first-order, (b) pseudo-second-order, and (c) intraparticle diffusion study of methyl red removal by MGP.

group-based removal of pollutants by floral wastes depends on the factors like the chemical state, accessibility, site quantity, and affinity among bioadsorbents surfaces and dyes or pollutants [64]. The variety of absorption bands was observed as overlapped and shifted so it was not feasible to confirm the specific stretching frequency for a functional group, due to their different environment and molecular structure. The factors which influence the shift of absorption bands are the electronic and mass effect of adjacent substitution, intra-molecular and intermolecular H-bonding, physical state, and conjugation and ring strain [65].

The weak and overlap bands do not provide much more data about the nature of the samples. The FT-IR spectrum of bioadsorbent revealed weak and overlap bands in the region of 550–4000 $cm^{-1}$, which specified the presence of C=O and –OH of carbonyl, -COOH, and phenols. The band near 1541 $cm^{-1}$ is attributed to the C=O stretching mode in -C=O and -COOH, while very weak and overlap bands between 1500–1400 $cm^{-1}$ were directed to the C – O stretching and O – H bending modes for instance phenolic and -COOH. The weak band around 3079 $cm^{-1}$ was assigned to aromatic stretching. The band near 3620–3659 $cm^{-1}$ is the N-H stretching of aromatic compounds. Besides this, the band near 3620–3659 $cm^{-1}$ is also attributed to the -OH group present in the samples. Mondal et al. also obtained bands at the same position and attributed it to the N-H stretching of amides [47].

Table 3: Kinetic parameters for methyl red removal by MGP.

| Kinetic | Parameter | Values |
|---|---|---|
| Pseudo-first-order | $Q_e$(mg/g) | 105.86 |
| | $k_1$($min^{-1}$) | $0.0338*10^{-7}$ |
| | $R^2$ | 0.896 |
| Pseudo-second-order | $Q_e$(mg/g) | 62.89 |
| | $k_2$(g/mg. Min) | $0.341*10^{-3}$ |
| | $R^2$ | 0.835 |
| Intraparticle diffusion | $k_{id}$(mg/g. $min^{3/2}$) | 4.7216 |
| | $C$ (mg/g) | 1.1332 |
| | $R^2$ | 0.957 |

Mondal et al. reported this while working on marigold petal powder as a bioadsorbent for the remediation of heavy metals (Cd (II) and Cr (VI)) from wastewater [47]. The higher bands were assigned to O – H vibrations of free hydroxyl groups and overtones by 3600 $cm^{-1}$ and above while some lower bands (under 800 $cm^{-1}$) could be assigned to nitrogen-containing sites in the bioadsorbent. So, it may

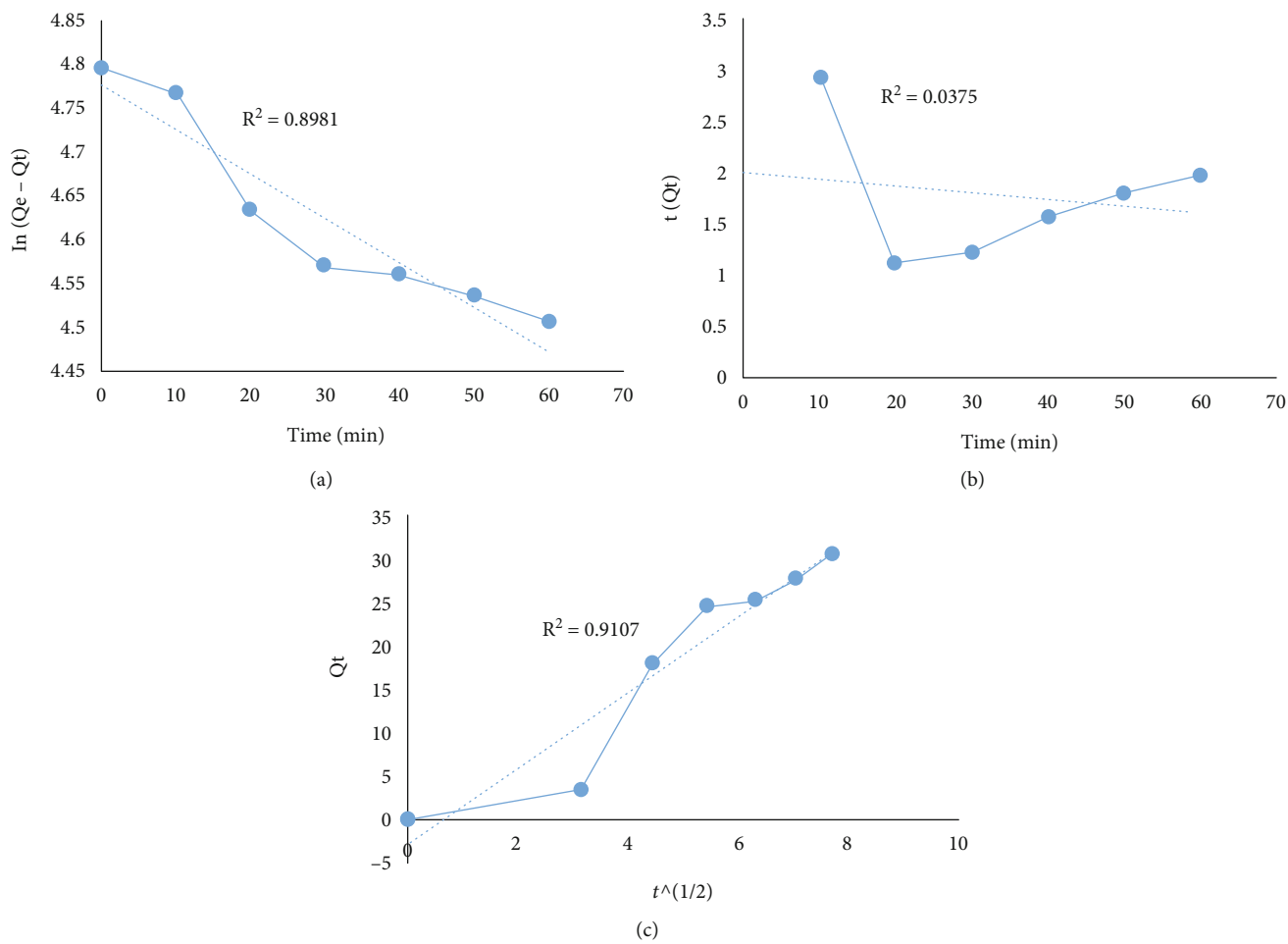


Figure 11: (a) Pseudo-first-order, (b) pseudo-second-order, and (c) intraparticle diffusion study of methyl red removal by RPP.

Table 4: Kinetic parameters for methyl red removal by rose petal powder.

| Kinetic | Parameter | Values |
|---|---|---|
| Pseudo-first-order | $Q_e$(mg/g) | 118.54 |
| | $k_1$(min$^{-1}$) | 2.78*10$^{-5}$ |
| | $R^2$ | 0.898 |
| Pseudo-second-order | $Q_e$(mg/g) | 147.058 |
| | $k_2$(g/mg. min) | 2.29*10$^{-5}$ |
| | $R^2$ | 0.0375 |
| Intraparticle diffusion | $k_{id}$(mg/g. min$^{3/2}$) | 4.3399 |
| | $C$ (mg/g) | 2.8001 |
| | $R^2$ | 0.910 |

be concluded from spectrum results that functional groups like –CO, -COO, -NH, and –OH are present in the bioadsorbent with a binding site. The dried floral powder from the marigold showed the presence of polymeric hydroxyl group, C-H, and carboxylic groups of polysaccharides [47]. The major FT-IR assignments of both the floral powders are given below in Table 2.

*3.3. XRD Study of Flower Powders.* The XRD patterns of the bioadsorbent are presented in Figure 8. The diffractogram of the bioadsorbent indicates the presence of a cellulose or carbon structure in the crystalline phase along with the presence of some amorphous material which is confirmed due to the peaks present at $2\theta \sim 19.2^\circ$, $23.6^\circ$, $26.7^\circ$, $29.7^\circ$, $34.4^\circ$, and $41.06^\circ$. This peak suggests the arrangement of cellulose molecules in ordered lattices where certain functional groups like -OH were available. Moreover, these peaks are absent at higher $2\theta$ values which confirmed a decrease in the degree of crystallinity, i.e., the presence of more amorphous than crystalline.

*3.4. Bioremediation of Methyl Red Dye by Using Bioadsorbents.* The removal of MR dye was observed against contact time for both types of biosorbents. The MR dye removal percentage by both types of biosorbents was calculated and is displayed in Figure 9. There was a continuous gradual increase in the percentage removal of MR dye by both types of biosorbents from initial to 60 minutes. After 60 minutes of contact time, the marigold powder (MGP) and rose petal powder (RPP) showed decolorization of 61.16% and 56.08% for 2 ppm of MR dye. There are several pieces of literature where MR dye removal was carried out

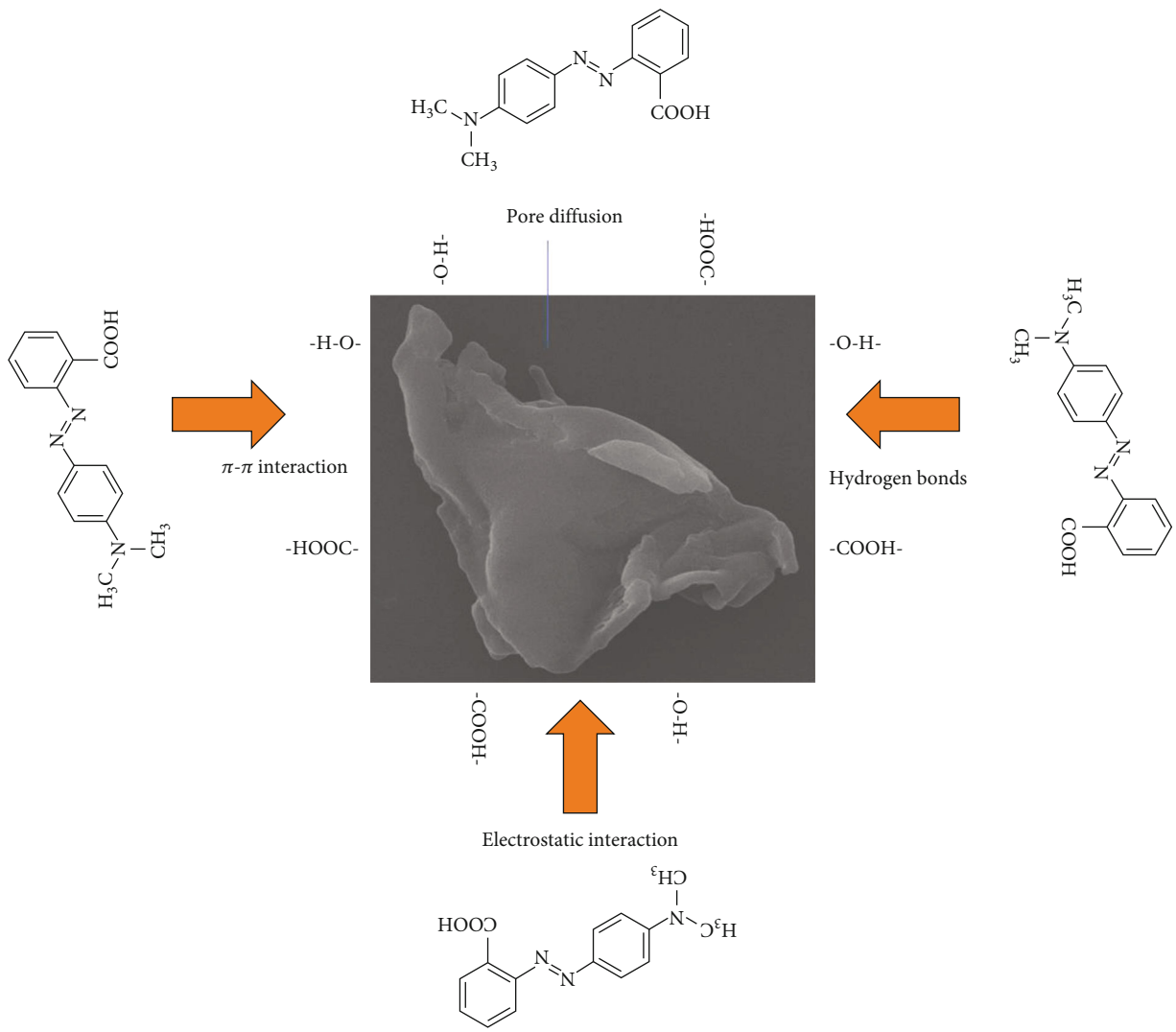


Figure 12: Summary of possible adsorption mechanism of methyl red dye on the floral waste powders.

by using different microorganisms like bacteria and mixed culture; for instance, Takkar et al. used actinobacterium *Zhihengliuella* sp. ISTPL4 for the remediation of MR dye [67]. Vijaya and Sandhya used mixed culture for the removal of MR dye from the wastewater [68].

Echavarria-Alvarez and Hormaza-Anaguano reported the utilization of floral waste as a low-cost adsorbent for the remediation of acid blue 19 dye from the aqueous solutions. The batch adsorption study was conducted at 2 pH, and removal efficiency was 90% when the concentration of acid blue 19 dye was 15.0 $mgL^{-1}$ and the dosage of bioadsorbent of 4.0 $gL^{-1}$ [69].

*3.5. Kinetic Studies of MGP and RPP.* To investigate the removal rate of the dye by MGP, different kinds of the kinetic model were used to perform the kinetic studies. Pseudo-first-order and pseudo-second-order kinetic model was examined on primary bases, which clearly showed that it does not follow pseudo-first-order as well as pseudo-second-order (Figures 10(a) and 10(b)). Intraparticle diffusion was applied for the same, it follows the intraparticle diffusion reaction (Figure 9(c)) as it followed a linear fitted curve ($R^2 = 0.96$). Table 3 depicts the kinetic parameters for the calculated pseudo-first- and second-order kinetics along with the intraparticle diffusion.

In addition, kinetic models were used to study the removal rate of dye by rose petal powder and plots are shown in Figures 11(a)–11(c). Both the pseudo-first and second-order kinetic models were examined on primary bases. This case also does not follow pseudo-first-order as well as second-order (Figures 11(a) and 11(b)), while intraparticle diffusion was found to be significant for the removal rate of dye, Figure 11(c). Intraparticle diffusion has also been mentioned by Igwegbe et al. while remediation of various dyes by using biosorbents [70]. Table 4 indicates the kinetic parameters for all models used in kinetics studies, where the intraparticle diffusion showed $R^2 = 0.910$.

Bhattacharjee et al. also reported kinetics and isotherms for the removal of dyes and heavy metal from the wastewater using watermelon rind as a bioadsorbent. The investigator concluded that the dyes are being adsorbed on the surface

of bioadsorbent due to the presence of carboxyl and hydroxyl groups in the watermelon rind [71].

*3.6. Adsorption Mechanism.* Figure 12 is showing the possible mechanism of uptake of MR dye on the surface of floral powders based on the findings of modelling studies. There are several reports where it has been proved that the dye uptake is because of both the chemisorption and physisorption processes. Based on the parameters, like pH and temperature, the properties of various functional groups present on the surface of biosorbents also changes. The pKa value of MR is 5.1, it is red in color in acidic conditions (4.4), and yellow in color over 6.2 pH. The MR gets protonated below pKa value, i.e., 5.1, and there is generally electrostatic interaction. The biosorbent has mainly negative charge due to OH, and COOH, which interacts with dye due to electrostatic attraction. There are several forces like pi-pi interactions among the functional groups on the sorbents and the dye molecule. Besides this, there are electrostatic interactions like London dispersion interactions, van der Waal forces, and dipole-induced dipole bonds. The MR dye has two benzene rings, which are electron-rich areas that can induce could induce a donor-acceptor relationship. This will lead to a stacking effect of the dyes onto the surface of biosorbent. Sometimes, the dye molecules get inside the biosorbent via pore diffusion since the biosorbents are highly porous, which was evident from the FESEM. Similarly, a group of investigators led by Igwegbe et al. and Balarak predicated similar types of possible adsorption mechanism dyes like Congo red, malachite green, acid orange 7, and AB92. Igwegbe et al. used carbon as a biosorbents developed from rubber seed shells (*Hevea brasiliensis*) and used them for the removal of Congo red and malachite green dye from aqueous solutions. Balarak et al. also shown the summary of adsorption mechanism of AB92 dye onto single walled carbon nanotubes (SWCNTs). Balarak et al. also shown the acid orange 7 dye removal from the aqueous solutions by using synthesized mesoporous goethite [70, 72, 73].

## 4. Conclusion

The processing of sacred flowers offered at religious places for the development of value-added materials can prove to be an eco-friendly approach. The developed bioadsorbents are carbon-rich, micron-sized, and free from other elements. The sacred flowers from religion can be utilized as an efficient and economical adsorbent for the remediation of methyl red dye. Out of both, rose petal powder and marigold petal powder, rose petal powder was found slightly efficient in comparison to the marigold petal powder. The development of value-added materials from waste sacred flowers will reduce solid waste as well as water pollution leading due to the dumping of flowers in the water bodies.

## Data Availability

All relevant data are included within the article.

## Conflicts of Interest

There are no conflicts to declare.

## Authors' Contributions

Abdelfattah Amari and Virendra Kumar Yadav contributed equally to this work.

## Acknowledgments

The authors extend their appreciation to the Deanship of Scientific Research at King Khalid University for funding this work through Research Groups Program under grant number RGP.2/57/43.

## References

[1] V. K. Yadav, N. Choudhary, D. Ali et al., "Experimental and computational approaches for the structural study of novel Ca-rich zeolites from incense stick ash and their application for wastewater treatment," *Adsorption Science & Technology*, vol. 2021, article 6066906, pp. 1–12, 2021.

[2] V. K. Yadav, K. K. Yadav, J. Alam et al., "Transformation of hazardous sacred incense sticks ash waste into less toxic product by sequential approach prior to their disposal into the water bodies," *Environmental Science and Pollution Research*, pp. 1–13, 2021.

[3] M. Waghmode, A. Gunjal, N. Nawani, and N. Patil, "Management of floral waste by conversion to value-added products and their other applications," *Waste and Biomass Valorization*, vol. 9, no. 1, pp. 33–43, 2018.

[4] V. K. Yadav, B. Singh, A. Gacem et al., "Development of novel microcomposite materials from coal fly ash and incense sticks ash waste and their application for remediation of malachite green dye from aqueous Solutions," *Water*, vol. 14, no. 23, p. 3871, 2022.

[5] B. Jamoussi, R. Chakroun, C. Jablaoui, and L. Rhazi, "Efficiency of *Acacia gummifera* powder as biosorbent for simultaneous decontamination of water polluted with metals," *Arabian Journal of Chemistry*, vol. 13, no. 10, pp. 7459–7481, 2020.

[6] V. K. Yadav, A. Gacem, N. Choudhary et al., "Status of coal-based thermal power plants, coal fly ash production, utilization in India and their emerging applications," *Minerals*, vol. 12, no. 12, p. 1503, 2022.

[7] E. E. Cordes, D. O. B. Jones, T. A. Schlacher et al., "Environmental impacts of the deep-water oil and gas industry: a review to guide management strategies," *Frontiers in Environmental Science*, vol. 4, p. 4, 2016.

[8] N. Gupta, V. K. Yadav, A. Gacem et al., "Deleterious effect of air pollution on human microbial community and bacterial flora: a short review," *International Journal of Environmental Research and Public Health*, vol. 19, no. 23, article 15494, 2022.

[9] N. Puri, A. Gupta, and A. Mishra, "Recent advances on nano-adsorbents and nanomembranes for the remediation of water," *Journal of Cleaner Production*, vol. 322, article 129051, 2021.

[10] N. A. A. Qasem, R. H. Mohammed, and D. U. Lawal, "Removal of heavy metal ions from wastewater: a comprehensive and critical review," *npj Clean Water*, vol. 4, no. 1, p. 4, 2021.

[11] A. M. Elgarahy, K. Z. Elwakeel, G. A. Elshoubaky, and S. H. Mohammad, "Untapped sepia shell–based composite for the sorption of cationic and anionic dyes," *Water, Air, and Soil Pollution*, vol. 230, no. 9, 2019.

[12] K. Z. Elwakeel, A. M. Elgarahy, and S. H. Mohammad, "Magnetic Schiff's base sorbent based on shrimp peels wastes for consummate sorption of chromate," *Water Science and Technology*, vol. 76, no. 1, pp. 35–48, 2017.

[13] K. Z. Elwakeel, A. S. Al-Bogami, and E. Guibal, "2-mercaptobenzimidazole derivative of chitosan for silver sorption - contribution of magnetite incorporation and sonication effects on enhanced metal recovery," *Chemical Engineering Journal*, vol. 403, article 126265, 2021.

[14] H. Tsuchiai, T. Ishizuka, H. Nakamura, T. Ueno, and H. Hattori, "Study of flue gas desulfurization absorbent prepared from coal fly ash: effects of the composition of the absorbent on the activity," *Industrial and Engineering Chemistry Research*, vol. 35, no. 7, pp. 2322–2326, 1996.

[15] T. Ishizuka, T. Ueno, A. Tatani, and S. Kotake, "Advanced flue gas treatment system using LILAC absorbent prepared from flyash," in *Coal Science and Technology*, J. A. Pajares and J. M. D. Tascón, Eds., pp. 1855–1858, Elsevier, 1995.

[16] B. Shi, J. Zhao, and Q. Chang, "Green synthesize of fly ash-based zeolite X: a potential microwave absorbent," *Journal of Materials Science: Materials in Electronics*, vol. 32, no. 21, pp. 26097–26104, 2021.

[17] V. K. Yadav, N. Choudhary, S. H. Khan et al., "Synthesis and characterisation of nano-biosorbents and their applications for waste water treatment," in *Handbook of Research on Emerging Developments and Environmental Impacts of Ecological Chemistry*, pp. 252–290, IGI Global, 2020.

[18] Y. G. Adewuyi, "Recent advances in fly-ash-based geopolymers: potential on the utilization for sustainable environmental remediation," *ACS Omega*, vol. 6, no. 24, pp. 15532–15542, 2021.

[19] J. Saleem, U. B. Shahid, M. Hijab, H. Mackey, and G. McKay, "Production and applications of activated carbons as adsorbents from olive stones," *Biomass Convers Biorefin*, vol. 9, no. 4, pp. 775–802, 2019.

[20] H. Hamada, A. Alattar, B. Tayeh, F. Yahaya, and A. Adesina, "Sustainable application of coal bottom ash as fine aggregates in concrete: a comprehensive review," *Case Studies in Construction Materials*, vol. 16, article e01109, 2022.

[21] A. Kumari, A. R. Aich, S. Kumari, and S. Mohanty, "Greenways for solid waste management," in *Handbook of Solid Waste Management: Sustainability through Circular Economy*, C. Baskar, S. Ramakrishna, S. Baskar, R. Sharma, A. Chinnappan, and R. Sehrawat, Eds., pp. 1–40, Springer Singapore, Singapore, 2021.

[22] W. Liu, H. An, C. Qin et al., "Performance enhancement of calcium oxide sorbents for cyclic CO2capture—a review," *Energy & Fuels*, vol. 26, no. 5, pp. 2751–2767, 2012.

[23] S. Scaccia, G. Vanga, D. M. Gattia, and S. Stendardo, "Preparation of CaO-based sorbent from coal fly ash cenospheres for calcium looping process," *Journal of Alloys and Compounds*, vol. 801, pp. 123–129, 2019.

[24] F. Yan, J. Jiang, K. Li et al., "Green synthesis of nanosilica from coal fly ash and its stabilizing effect on CaO sorbents for $CO_2$ capture," *Environmental Science & Technology*, vol. 51, no. 13, pp. 7606–7615, 2017.

[25] M. El-Azazy, A. S. El-Shafie, and B. A. S. Yousef, "Green tea waste as an efficient adsorbent for methylene blue: structuring of a novel adsorbent using full factorial design," *Molecules*, vol. 26, no. 20, 2021.

[26] M. Kerrou, N. Bouslamti, A. Raada, A. Elanssari, D. Mrani, and M. S. Slimani, "The use of sugarcane bagasse to remove the organic dyes from wastewater," *Journal of Analytical Chemistry*, vol. 2021, article 5570806, 11 pages, 2021.

[27] N. Choudhary, V. K. Yadav, P. Malik et al., "Recovery of natural nanostructured minerals," in *Handbook of Research on Emerging Developments and Environmental Impacts of Ecological Chemistry*, pp. 450–470, IGI Global, 2020.

[28] D. Singh, V. K. Yadav, D. Ali et al., "Isolation and characterization of siderophores producing chemolithotrophic bacteria from the coal samples of the aluminum industry," *Geomicrobiology Journal*, pp. 1–7, 2022.

[29] V. K. Yadav, G. Gnanamoorthy, D. Ali et al., "Cytotoxicity, removal of Congo red dye in aqueous solution using synthesized amorphous iron oxide nanoparticles from incense sticks ash waste," *Journal of Nanomaterials*, vol. 2022, Article ID 5949595, 12 pages, 2022.

[30] V. K. Yadav, N. Choudhary, V. Tirth et al., "A short review on the utilization of incense sticks ash as an emerging and overlooked material for the synthesis of zeolites," *Crystals*, vol. 11, no. 10, p. 1255, 2021.

[31] V. K. Yadav, G. Gnanamoorthy, K. K. Yadav et al., "Utilization of incense stick ash in hydrometallurgy methods for extracting oxides of Fe, Al, Si, and Ca," *Materials*, vol. 15, no. 5, p. 1879, 2022.

[32] M. Abatal, E. C. Lima, D. A. Giannakoudakis et al., "Pitahaya fruit (Hylocereus spp.) peels evaluation for removal of Pb (II), Cd (II), Co(II), and Ni(II) from the waters," *Sustainability*, vol. 14, no. 3, p. 1685, 2022.

[33] S. Saranya, A. D. Gandhi, G. Suriyakala et al., "A biotechnological approach of Pb(II) sequestration from synthetic wastewater using floral wastes," *SN Applied Sciences*, vol. 2, no. 8, p. 1357, 2020.

[34] H. Patel, V. K. Yadav, K. K. Yadav et al., "A recent and systemic approach towards microbial biodegradation of dyes from textile industries," *Water*, vol. 14, no. 19, p. 3163, 2022.

[35] M. T. Amin, A. A. Alazba, and U. Manzoor, "A review of removal of pollutants from water/wastewater using different types of nanomaterials," *Advances in Materials Science and Engineering*, vol. 2014, Article ID 825910, 24 pages, 2014.

[36] A. L. Srivastav and A. Kumar, "An endeavor to achieve sustainable development goals through floral waste management: a short review," *Journal of Cleaner Production*, vol. 283, article 124669, 2021.

[37] R. Al-Tohamy, S. S. Ali, F. Li et al., "A critical review on the treatment of dye-containing wastewater: ecotoxicological and health concerns of textile dyes and possible remediation approaches for environmental safety," *Ecotoxicology and Environmental Safety*, vol. 231, article 113160, 2022.

[38] A. Acosta-Dacal, M. E. Hernández-Marrero, C. Rial-Berriel et al., "Comparative study of organic contaminants in agricultural soils at the archipelagos of the Macaronesia," *Environmental Pollution*, vol. 301, article 118979, 2022.

[39] S. Adeel, N. Amin, A. T. Fazal-ur-Rehman, F. Batool, and A. Hassan, "Sustainable isolation of natural dyes from plant wastes for textiles," in *Recycling from Waste in Fashion and Textiles*, pp. 363–390, Publisher: Wiley online library(2020 Scrivener Publishing LLC), 2020.

[40] P. S. Vankar, R. Sarswat, and D. S. Malik, "Biosorption of lead and cadmium ions from aqueous solutions onto natural dye

waste of Hibiscus rosa sinensis," *Environmental Progress & Sustainable Energy*, vol. 29, no. 4, pp. 421–427, 2010.

[41] R. Elangovan, L. Philip, and K. Chandraraj, "Biosorption of hexavalent and trivalent chromium by palm flower (*Borassus aethiopum*)," *Chemical Engineering Journal*, vol. 141, no. 1-3, pp. 99–111, 2008.

[42] N.-B. J. Luis, J.-I. Hugo, B.-A. Enrique, R.-M. Ramiro, and P.-L. Octavio, "An optimization study of solid-state fermentation: xanthophylls extraction from marigold flowers," *Applied Microbiology and Biotechnology*, vol. 65, no. 4, pp. 383–390, 2004.

[43] Z. J. Pu, S. J. Yue, G. S. Zhou et al., "The comprehensive evaluation of safflowers in different producing areas by combined analysis of color, chemical compounds, and biological activity," *Molecules*, vol. 24, no. 18, p. 24, 2019.

[44] S. Sato, T. Kusakari, T. Suda et al., "Efficient synthesis of analogs of safflower yellow B, carthamin, and its precursor: two yellow and one red dimeric pigments in safflower petals," *Tetrahedron*, vol. 61, no. 40, pp. 9630–9636, 2005.

[45] S. Davamani, E. Arulmani, T. Parameswari, T. Anitha, T. Thangaselvabai, and T. N. Balamohan, "Flower waste: a novel candidate for the removal of chromium from tannery effluent," *Acta Hortic*, vol. 1, no. 1241, pp. 663–672, 2019.

[46] A. Aman, D. Ahmed, N. Asad, R. Masih, and H. M. Abd ur Rahman, "Rose biomass as a potential biosorbent to remove chromium, mercury and zinc from contaminated waters," *International Journal of Environmental Studies*, vol. 75, no. 5, pp. 774–787, 2018.

[47] M. K. Mondal, G. Mishra, and P. Kumar, "Adsorption of cadmium (II) and chromium (VI) from aqueous solution by waste marigold flowers," *Journal of Sustainable Development of Energy, Water and Environment Systems*, vol. 3, no. 4, pp. 405–415, 2015.

[48] T. Tolcha, T. Gemechu, and N. Megersa, "Flower of typha latifolia as a low-cost adsorbent for quantitative uptake of multiclass pesticide residues from contaminated waters," *South African Journal of Chemistry*, vol. 73, 2020.

[49] G. Elango and R. Govindasamy, "Analysis and utilization of temple waste flowers in Coimbatore district," *Environmental Science and Pollution Research*, vol. 25, no. 11, pp. 10688–10700, 2018.

[50] Z. Zaheer, A. al-Asfar, and E. S. Aazam, "Adsorption of methyl red on biogenic [email protected] nanocomposite adsorbent: isotherms, kinetics and mechanisms," *Journal of Molecular Liquids*, vol. 283, pp. 287–298, 2019.

[51] M. A. Ahmad, N. B. Ahmed, K. A. Adegoke, and O. S. Bello, "Sorption studies of methyl red dye removal using lemon grass (*Cymbopogon citratus*)," *Chemical Data Collections*, vol. 22, article 100249, 2019.

[52] S. Rajoriya, V. K. Saharan, A. S. Pundir, M. Nigam, and K. Roy, "Adsorption of methyl red dye from aqueous solution onto eggshell waste material: kinetics, isotherms and thermodynamic studies," *Current Research in Green and Sustainable Chemistry*, vol. 4, article 100180, 2021.

[53] M. Bhowmik, M. Kanmani, A. Debnath, and B. Saha, "Sono-assisted rapid adsorption of anionic dye onto magnetic $CaFe_2O_4/MnFe_2O_4$ nanocomposite from aqua matrix," *Powder Technology*, vol. 354, pp. 496–504, 2019.

[54] M. Bhowmik, A. Debnath, and B. Saha, "Fabrication of mixed phase calcium ferrite and zirconia nanocomposite for abatement of methyl orange dye from aqua matrix: optimization of process parameters," *Applied Organometallic Chemistry*, vol. 32, no. 12, article e4607, 2018.

[55] V. K. Yadav, N. Choudhary, D. Ali et al., "Determination of adsorption of methylene blue dye by incense stick ash waste and its toxicity on RTG-2 cells," *Adsorption Science and Technology*, vol. 2022, article 8565151, pp. 1–10, 2022.

[56] S. Modi, V. K. Yadav, A. Gacem et al., "Recent and emerging trends in remediation of methylene blue dye from wastewater by using zinc oxide nanoparticles," *Water*, vol. 14, no. 11, p. 1749, 2022.

[57] K. Z. Elwakeel, A. M. Elgarahy, Z. A. Khan, M. S. Almughamisi, and A. S. Al-Bogami, "Perspectives regarding metal/mineral-incorporating materials for water purification: with special focus on Cr (vi) removal," *Materials Advances*, vol. 1, no. 6, pp. 1546–1574, 2020.

[58] R. A. Mashabi, Z. A. Khan, and K. Z. Elwakeel, "Chitosan- or glycidyl methacrylate-based adsorbents for the removal of dyes from aqueous solutions: a review," *Materials Advances*, vol. 3, no. 14, pp. 5645–5671, 2022.

[59] K. Z. Elwakeel, "Environmental application of chitosan resins for the treatment of water and wastewater: a review," *Journal of Dispersion Science and Technology*, vol. 31, no. 3, pp. 273–288, 2010.

[60] D. Srinivasulu, "*Senna auriculata* L. flower petal biomass: an alternative green biosorbent for the removal of fluoride from aqueous solutions," *Acta Ecologica Sinica*, vol. 43, no. 1, 2023.

[61] M. T. Ghaneian, M. H. Ehrampoush, A. M. Arany, B. Jamshidi, and M. Dehvari, "Equilibrium and kinetic studies of Cr (VI) removal from synthetic wastewater by acroptilon repense flower powder," *Polish Journal of Chemical Technology*, vol. 15, no. 2, pp. 40–47, 2013.

[62] H. Khoshsang and A. Ghaffarinejad, "Rapid removal of lead (II) ions from aqueous solutions by saffron flower waste as a green biosorbent," *Journal of Environmental Chemical Engineering*, vol. 6, no. 5, pp. 6021–6027, 2018.

[63] S. Dutta and M. S. Kumar, "Characterization of floral waste as potential candidates for compost and biofuel production," *Biomass Convers Biorefin*, 2022.

[64] S. Nigam, P. S. Vankar, and K. Gopal, "Biosorption of arsenic from aqueous solution using dye waste," *Environmental Science and Pollution Research*, vol. 20, no. 2, pp. 1161–1172, 2013.

[65] Y. W. Mak, L. O. Chuah, R. Ahmad, and R. Bhat, "Antioxidant and antibacterial activities of hibiscus (*Hibiscus rosa- sinensis* L.) and *cassia* (*Senna bicapsularis* L.) flower extracts," *Journal of King Saud University - Science*, vol. 25, no. 4, pp. 275–282, 2013.

[66] L. P. Lingamdinne, J. R. Koduru, R. K. Jyothi, Y.-Y. Chang, and J.-K. Yang, "Factors affect on bioremediation of Co(II) and Pb(II) ontoLonicera japonicaflowers powder," *Desalination and Water Treatment*, vol. 57, no. 28, pp. 13066–13080, 2016.

[67] S. Takkar, B. Tyagi, N. Kumar et al., "Biodegradation of methyl red dye by a novel actinobacterium *Zhihengliuella* sp. ISTPL4: kinetic studies, isotherm and biodegradation pathway," *Environmental Technology and Innovation*, vol. 26, article 102348, 2022.

[68] P. P. Vijaya and S. Sandhya, "Decolorization and complete degradation of methyl red by a mixed culture," *Environmentalist*, vol. 23, pp. 145–149, 2003.

[69] A. M. Echavarria-Alvarez and A. Hormaza-Anaguano, "Flower wastes as a low-cost adsorbent for the removal of acid blue 9," *Dyna*, vol. 81, no. 185, p. 132, 2014.

[70] C. A. Igwegbe, J. O. Ighalo, K. K. Onyechi, and O. D. Onukwuli, "Adsorption of Congo red and malachite green using H3PO4 and NaCl-modified activated carbon from rubber (Hevea brasiliensis) seed shells," *Sustainable Water Resources Management*, vol. 7, no. 4, p. 63, 2021.

[71] C. Bhattacharjee, S. Dutta, and V. K. Saxena, "A review on biosorptive removal of dyes and heavy metals from wastewater using watermelon rind as biosorbent," *Environmental Advances*, vol. 2, article 100007, 2020.

[72] D. Balarak, R. Raju, C. A. Igwegbe, and J. O. Ighalo, "Ultimate eradication of acid orange 7 from contaminated liquid via synthesized mesoporous goethite," *Turkish Chemical Society*, vol. 4, pp. 13–26, 2021.

[73] D. Balarak, M. Zafariyan, C. A. Igwegbe, K. K. Onyechi, and J. O. Ighalo, "Adsorption of acid blue 92 dye from aqueous solutions by single-walled carbon nanotubes: isothermal, kinetic, and thermodynamic studies," *Environmental Processes*, vol. 8, no. 2, pp. 869–888, 2021.

Hindawi
Adsorption Science & Technology
Volume 2023, Article ID 8943198, 17 pages
https://doi.org/10.1155/2023/8943198

*Research Article*

# Trinary Component Adsorption of Methylene Blue, Methyl Orange, and Methyl Red from Aqueous Solution Using $TiO_2$/Activated Carbon

**Nguyen Thi Thanh Tu,[1] Tran Si Thanh,[2,3] Phan Tu Quy,[4] Tran Thi Minh Ha,[4] Phan Thi Kim Thu,[4] Nguyen Hong Bich,[2] Le Van Thanh Sơn,[5] Vo Thang Nguyen,[5] Dao Ngoc Nhiem,[6] Pham Khac Lieu,[7] and Dinh Quang Khieu[2]**

[1]*Faculty of Applied Technology, School of Engineering and Technology, Van Lang University, 700000, Vietnam*
[2]*University of Sciences, Hue University, 530000, Vietnam*
[3]*Dak Nong Department of Education and Training, 640000, Vietnam*
[4]*Tay Nguyen University, 630000, Vietnam*
[5]*University of Education and Science, The University of Danang, 500000, Vietnam*
[6]*Institute of Materials Sciences, VAST, 100000, Vietnam*
[7]*Hue University, 530000, Vietnam*

Correspondence should be addressed to Nguyen Thi Thanh Tu; tu.ntt@vlu.edu.vn
and Dinh Quang Khieu; dqkhieu@hueuni.edu.vn

Received 18 May 2022; Revised 26 August 2022; Accepted 13 October 2022; Published 20 January 2023

Academic Editor: Anjani Ravi Kiran Gollakota



Porous $TiO_2$/activated carbon (AC) material was synthesized by grafting peroxo-hydro titanium complexes to rice husk-derived activated carbon. It was found that the morphology of $TiO_2$/AC consists of $TiO_2$ fine particles highly dispersed on the AC matrix. The obtained $TiO_2$/AC composites with high surface area and a red shift exhibit an excellent adsorption performance in both single and trinary system toward methylene blue (MB), methyl orange (MO), and methyl red (MR). The isotherm models including extended Langmuir, P-factor, ideal adsorbed solution theory (IAST) for Langmuir, Freundlich, and Sips models were applied to study the adsorption equilibrium data of trinary solutions. It was found that IAST for Freundlich and Langmuir models were the most suitable one to describe the adsorption of the three dyes on $TiO_2$/AC material. The high maximum adsorption capacities (mmol $g^{-1}$) in single/trinary mixture were found as 0.452/0.340 for MB; 0.329/0.321 for MO; and 0.806/2.04 for MR. Moreover, the recyclability experiments showed that the adsorbent could be reused through photocatalytic self-cleaning for at least three cycles with stable capacity. Thus, the $TiO_2$/AC can be effectively employed for the removal of dyes from industrial textile wastewater.

## 1. Introduction

Dye pollutants in wastewater are a critical environmental issue due to their nonbiodegradable and toxic nature which can generate serious threats to human being and marine organism. The dyeing wastewater discharged from industrial textiles is highly visible and undesirable even at low concentrations of dyes. Hence, the dyes must be effectively eliminated from the dyestuff wastewater to clear up the biological, ecological, and industrial issues. Therefore, various physical-chemistry treatment methods, including chemical ion exchange [1], membrane filtration [2], physical adsorption [3], photocatalytic [4], and biological approaches [5], have been developed to remove dyestuff from effluents. Among these, the adsorption approach has been considered as a promising method for treatment of discharged wastewater due to its easy operation, high efficiency, and economic feasibility. The nature of the adsorbent is one of the

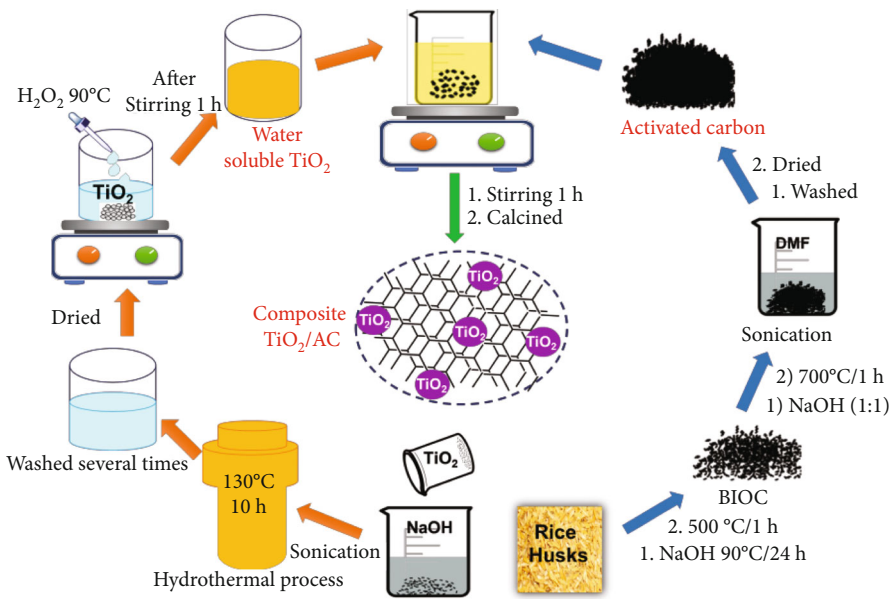


Scheme 1: The diagram of synthesis of $TiO_2$/AC from soluble-water titanium and rice husk-derived activated carbon.

important factors deciding the effectiveness of any adsorption processes. The adsorbents with low cost, high adsorption capacity, and easy recyclability are desirable in the adsorption removal of dye molecules. The use of activated carbon prepared from rich-carbon biomasses for removing pollutants from wastewater has been intensively investigated because of its high synthesis yield, cheapness, eco-friendliness, and great adsorption efficiency [6]. However, the recycling of activated carbon material for further use usually involves organic solvents, resulting in secondary pollutants. A more eco-friendly strategy to recycle these adsorbents is photocatalytic self-cleaning activities through grafting other catalytically reactive species such as metal halides, metal oxides, and metal sulfides on various carbon matrixes. $TiO_2$ nanoparticles is a well-known photocatalyst in advanced oxidation process which can mineralize organic pollutants under UV irradiation. However, there are some disadvantages of using $TiO_2$ in powder form during the photocatalytic process: (i) titanium sources such as titanium alkoxides and titanium chlorides are difficult to handle due to its instability in moisture atmospheres; (ii) the fine powder $TiO_2$ is likely to aggregate to form larger particles. These issues can be solved by using soluble-water titanium complexes instead of traditional easily hydrolyzed titanium sources. Therefore, the construction of heterojunctions by hybridizing activated carbon with water-soluble titanium complexes derived catalytically reactive $TiO_2$ is an effective method to improve for recycling through photocatalytic self-cleaning.

Although there is a great availability of research information on single-component adsorption [7–10] or binary-component adsorption [11, 12], that for complex mixture is more limited which leaves the adsorption of most industries discharge wastewater containing several components unexplainable. Gurav et al. presented the adsorption of the binary mixture containing bisphenol-A and solvent black-3 dye mixtures onto biochar by using Langmuir isotherm model [13]. Adsorption of safranine O and methylene blue dyes from single and binary systems using Langmuir, Freundlich, Temkin, and Dubinin–Radushkevich model was also reported [14]. According to our best knowledge, the study on adsorption isotherms of trinary component system is less available.

In this study, we synthesized a three-dimensional $TiO_2$/activated carbon ($TiO_2$/AC) via peroxo-hydroxo titanium (IV) complexes and activated carbon derived from rice husks for eliminating the pollutants from aqueous solution. Three organic compounds including methylene blue (MB), methyl orange (MO), and methyl red (MR) were used as model pollutants to investigate their adsorption on $TiO_2$/activated carbon ($TiO_2$/AC) in single/trinary component systems using extended Langmuir, P-factor model, ideal adsorbed solution theory for Langmuir, Freundlich, and Sips models. The main objective of this work is to investigate the simultaneous removal of both anionic and cationic dyes from the single/trinary systems. Furthermore, the recyclability of the $TiO_2$/AC was performed by the photocatalytic self-cleaning.

## 2. Experimental Methods

*2.1. Materials.* Rice husks were collected from local area (Hue city, Vietnam). All chemicals were used as received without any further purification. Anatase ($TiO_2$; Merck, Germany, 99%), sodium (NaOH; Guangzhou, China, 97%), acid chlohydride (HCl; Guangzhou, China, 36%), hydroperoxide ($H_2O_2$ 30% Guangzhou, China), methylene blue (MB, $C_{16}H_{18}ClN_3S$), methyl orange (MO, $C_{14}H_{14}N_3NaO_3S$), methyl red (MR, $C_{15}H_{15}N_3O$), and N,N- Dimethyformamide (DMF) were used in this work.

*2.2. Synthesis of the Peroxo-Hydroxo Titanium Complexes and Activated Carbon.* $TiO_2$ was synthesized by ultrasonically assisted hydrothermal method. 0.25 grams of $TiO_2$

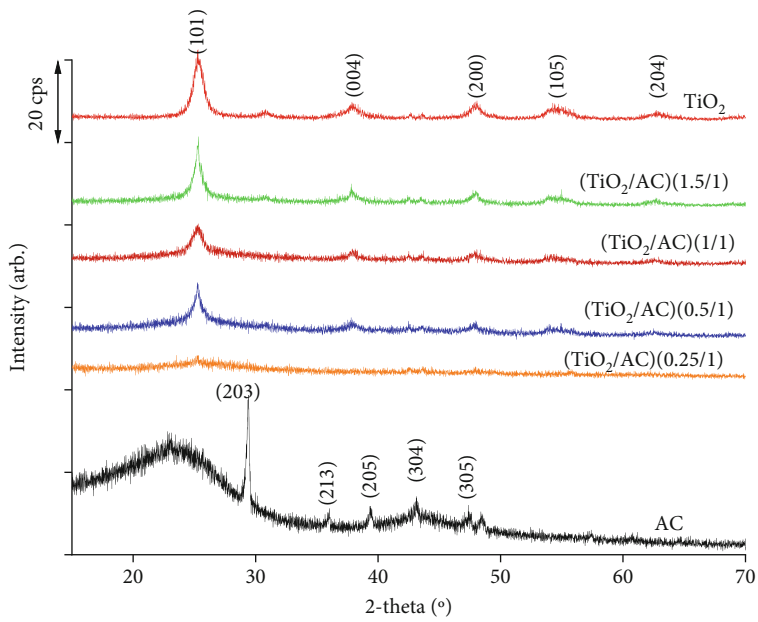


(a)

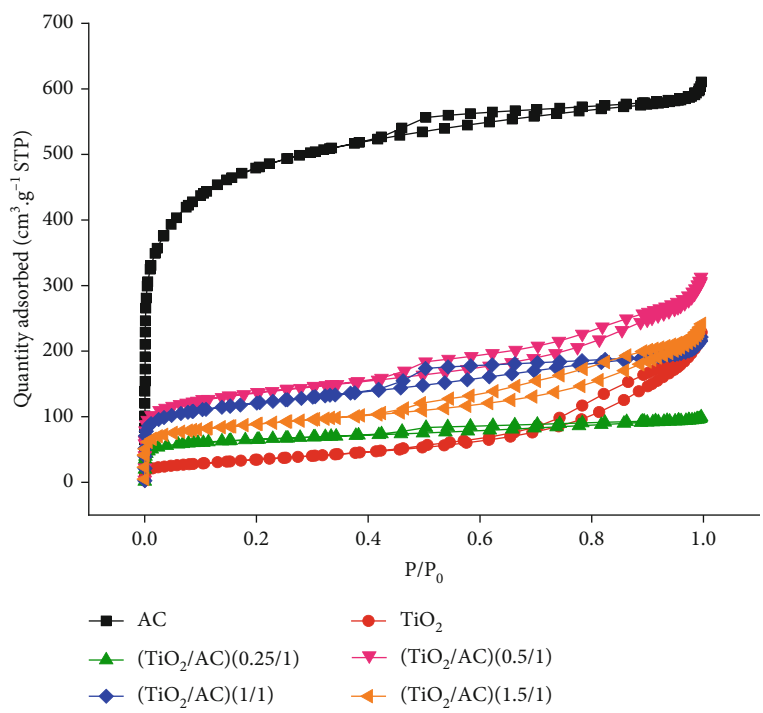


(b)

Figure 1: Continued.

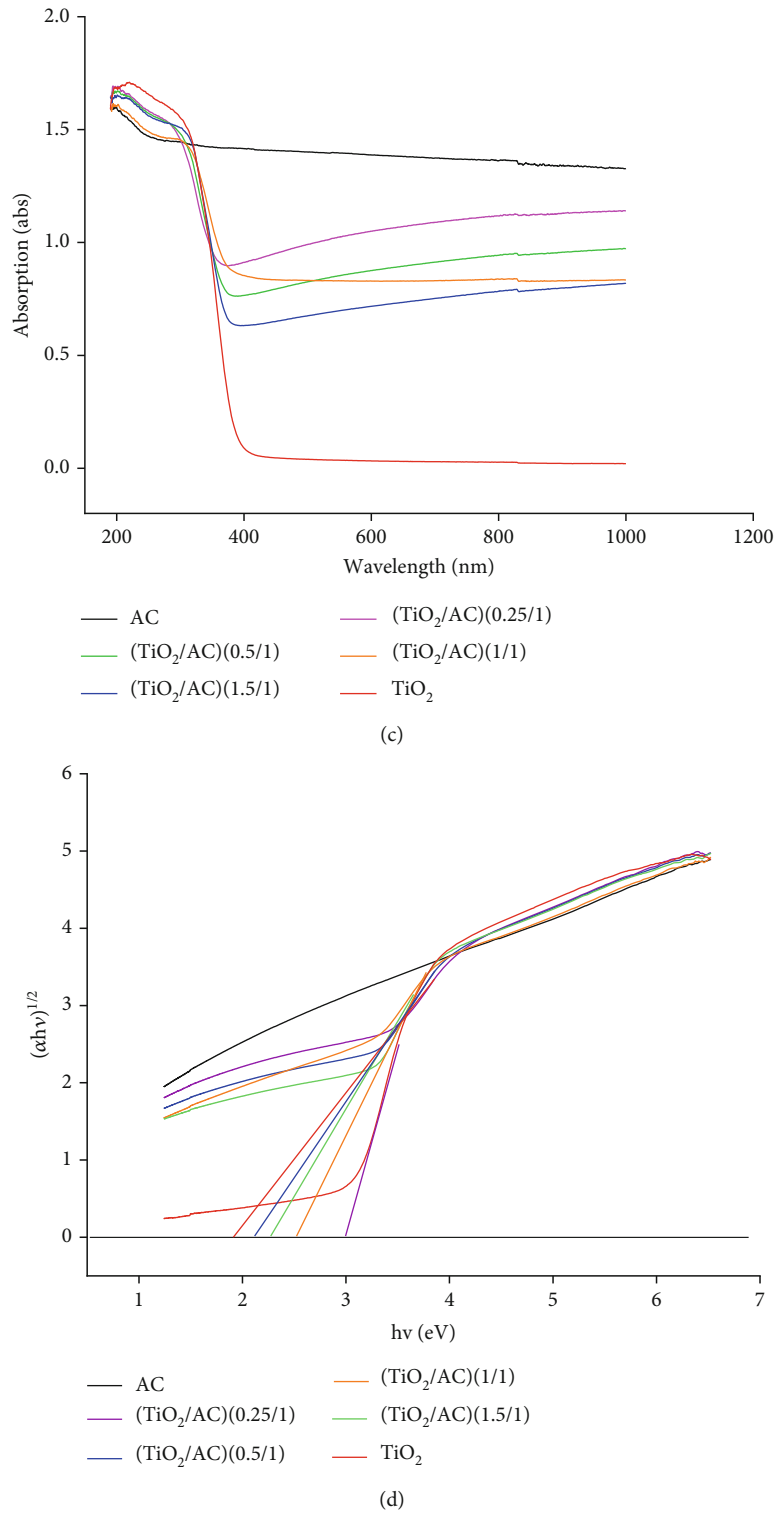


Figure 1: (a) XRD patterns, (b) nitrogen adsorption/desorption isotherms, (c) UV-Vis diffuse reflectance spectroscopy, and (d) Tauc's plots of AC, $TiO_2$/AC (0.25/1), $TiO_2$/AC (0.5/1), $TiO_2$/AC (1/1), $TiO_2$/AC (1.5/1), and $TiO_2$.

powder was dispersed into a teflon flask containing 12.5 mL of 20 M NaOH solution before being processed by ultrasonic for 30 minutes. The teflon bottle was then inserted in the autoclave and kept at 130°C for 10 h. After the hydrothermal process, the autoclave was naturally cooled to room temperature. The mixture was then washed several times with 0.1 M HCl and distilled water until the pH of supernatant was neutral. The product was dried in vacuum at 100°C for 6 h. 0.25 grams obtained product was mixed with 35 mL of $H_2O_2$ at 90°C with magnetic stirring for an hour to form a yellow

Table 1: Textural properties of AC, $TiO_2$, and $TiO_2$/AC composites.

| Materials | Surface area based on BET model ($m^2 g^{-1}$) | Porous volume ($cm^3/g$) | Mesoarea ($m^2 g^{-1}$) | Microarea ($m^2 g^{-1}$) |
|---|---|---|---|---|
| AC | 1713 | 610 | 333 | 1380 |
| $TiO_2$ | 124 | 228 | 94 | 31 |
| $TiO_2$/AC (0.25/1) | 238 | 100 | 108 | 131 |
| $TiO_2$/AC (0.5/1) | 494 | 313 | 206 | 288 |
| $TiO_2$/AC (1/1) | 436 | 222 | 193 | 243 |
| $TiO_2$/AC (1.5/1) | 320 | 241 | 182 | 138 |

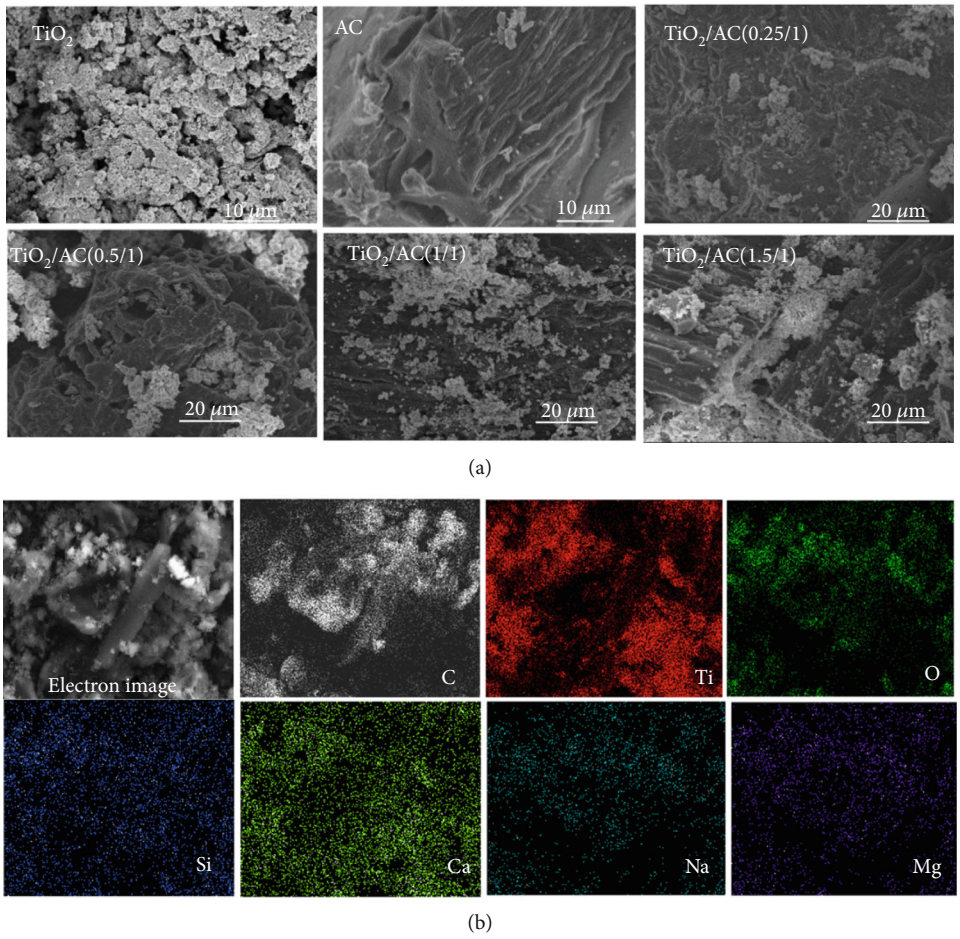


Figure 2: (a) SEM observation of $TiO_2$/AC composites and (b) EDX mapping of $TiO_2$/AC (0.5/1).

transparent peroxo-hydroxo titanium complex solution (0.25 grams $TiO_2$/35 mL).

The preparation of activated carbon from rice husk consists of two steps: firstly 60 grams of rice husks was soaked in 800 mL of 1 M NaOH and placed in an oven at 90°C for 24 h. The rice husks were then collected, washed, and calcined at 500°C for an hour to obtain the biochar. After that, 2 grams of biochar was mixed with 2 grams of NaOH in a Ni crucible and heated at 700°C for 2 h. The resulting product was washed with distilled water to completely remove all the excess NaOH, followed by ultrasonic treatment in DMF for 1 hour. The solid was separated by the centrifugation and dried at 100°C for 24 h to obtain the activated carbon (denoted as AC).

The $TiO_2$/AC composites with different $TiO_2$/AC mass ratio were prepared through ultrasonic mixing of a specific volume of titanium complex solution (17.5, 35.0, 70.0, and 105.0 mL equivalent to 0.125, 0.250, 0.500, and 0.750 grams of $TiO_2$, respectively) and 0.5 grams of AC, after sonication for 1 h the mixture is dried at 80°C for 6 hours. The resultant powders were calcined at 350°C for 2 hours in oxygen-free atmosphere. The $TiO_2$/AC composites was denoted as $TiO_2$/AC (0.25/1), $TiO_2$/AC (0.5/1), $TiO_2$/AC (1/1), and $TiO_2$/AC (1.5/1) with the numbers in parenthesis presenting

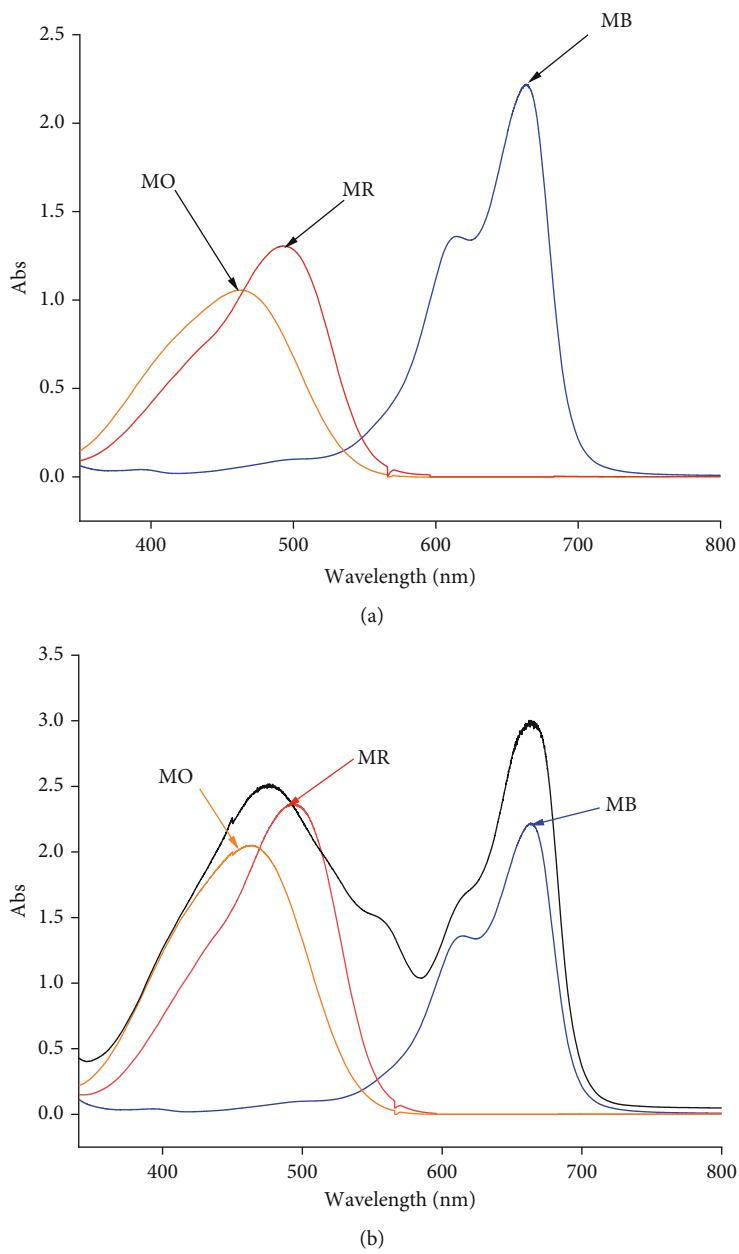


Figure 3: (a) The UV-Vis spectra of MB, MO, and MR individual (0.0625 mM MB, 0.061 mM MO, and 0.111 mM MR) and (b) UV-Vis spectrum of trinary mixture of MB, MO, and MR as well as corresponding UV-Vis deconvulated spectra (Trinary component mixture of 0.0625 MB, 0.061 MO, and 0.111 MR, mass of adsorbent).

the ratio of $TiO_2$/AC in weight. The schematic diagram of $TiO_2$/AC synthesis is illustrated in the Scheme 1.

### 2.3. Adsorption Experiments

#### 2.3.1. Adsorption Isotherm in Single Component Solution

*(1) Determination of the Isoelectric Point of $TiO_2$/AC.* 10 mg $TiO_2$/AC was dispersed into 100 mL conical flasks containing 25 mL 0.1 M NaCl, and the $pH_i$ of solution was adjusted in the range of 2-12 by adding 0.01 M HCl and 0.01 M NaOH solution. The sample was shaken in the dark for 24 h at a constant speed of 200 rpm and the $pH_f$ of the supernatant was then measured. The pH of point of zero charge was derived from the plot of $\Delta pH = pH_f - pH_i$ versus $pH_i$ where $\Delta pH = 0$.

*(2) Single Component Isotherm Studies.* To study isotherm adsorption in the single component system, 0.1, 0.2, 0.3, 0.4, 0.5, 0.6, and 0.7 grams of $TiO_2$/AC were added into a series of seven flasks containing 200 mL solution of individual dyes at concentration of 0.0469 mM, 0.0458 mM, and 0.0743 mM for MB, MO, and MR, respectively. These flasks were shaken in the dark for 24 hours to ensure adsorption/desorption equilibrium. The dye concentration in the supernatant was measured by UV-Vis spectrophotometry at its corresponding adsorption maxima.

Table 2: The parameters of adsorption isotherms of Langmuir, Freundlich, and Temkin models for $TiO_2$/AC (0.5/1), $TiO_2$, and AC in single component system of MB, MO, and MR.

| Adsorbent | Dyes | Langmuir isotherm model | | | Freundlich isotherm model | | | Temkin isotherm model | | |
|---|---|---|---|---|---|---|---|---|---|---|
| | | $q_m$ (mmol g$^{-1}$) | $a_L$ (L g$^{-1}$) | $R^2$ | $b_F$ | $K_F$ (L g$^{-1}$) | $R^2$ | $K_T$ (L g$^{-1}$) | $b_T$ (KJ.mol$^{-1}$) | $R^2$ |
| AC | | 0.865 | 0.139 | 0.989 | 1.737 | 49.854 | 0.993 | 589.03 | 13.39 | 0.986 |
| $TiO_2$/AC | MB | 0.452 | 0.094 | 0.997 | 1.744 | 18.683 | 0.998 | 256.19 | 23.51 | 0.997 |
| $TiO_2$ | | 0.200 | 0.084 | 0.999 | 1.932 | 9.072 | 0.999 | 205.23 | 49.17 | 0.999 |
| AC | | 0.532 | 0.539 | 0.993 | 4.706 | 87.207 | 0.991 | 4682.30 | 28.00 | 0.992 |
| $TiO_2$/AC | MO | 0.329 | 0.390 | 0.988 | 2.686 | 37.545 | 0.995 | 1366.62 | 35.12 | 0.991 |
| $TiO_2$ | | 0 | 0 | — | 0 | 0 | — | 0 | 0 | — |
| AC | | 1.219 | 0.152 | 0.979 | 2.129 | 64.512 | 0.951 | 359.84 | 8.82 | 0.982 |
| $TiO_2$/AC | MR | 0.806 | 0.305 | 0.998 | 3.116 | 75.239 | 0.908 | 0.80 | 5.48 | 0.823 |
| $TiO_2$ | | 0 | 0 | — | 0 | 0 | — | 0 | 0 | — |

The adsorption capacity ($q_t$) at a certain time and ($q_e$) at the equilibrium time for each dye are expressed as follows:

$$q_t = \frac{(C_i - C_f)V}{m}, \quad (1)$$

$$q_e = \frac{(C_i - C_e)V}{m}, \quad (2)$$

where $C_i$ (mM) and $C_e$ (mM) are the concentration of dyes at a certain and equilibrium time in the solution, respectively; $V$ and $m$ are the solution volume (L) and mass of adsorbent (g).

Three isotherms were used to investigate the adsorption of three dyes onto $TiO_2$/AC, namely, Langmuir [15], Freundlich [16], Sips [17], and Temkin [18] isotherms as expressed in

$$q_e = \frac{K_L.C_e}{1 + a_{L,i}C_e} \text{ Langmuir isotherm}, \quad (3)$$

$$q_e = a_F.C_e^{b_F} \text{ Freudlich isotherm}, \quad (4)$$

$$q_e = \frac{K_S.C_e^{1/b_S}}{1 + a_S C_e^{1/b_S}} \text{ Sips isotherm}, \quad (5)$$

$$q_e = \frac{RT}{b_T} \ln R_T.C_e \text{ Tempkin isotherm}, \quad (6)$$

where $q_e$ and $C_e$ present adsorption capacity (mmol g$^{-1}$) and concentration (mM) at equilibrium, and $K_L$ (L.g$^{-1}$) and $a_L$ (L.mM$^{-1}$), $a_F$ and $b_F$,$K_S$, $a_S$ (L.mM$^{-1}$), and $b_S$, and $A_T$ (L.g$^{-1}$), $b_T$, R (8.314 x 10$^{-3}$J.mM$^{-1}$.K$^{-1}$), $T$ (298 K), and B = RT/$b_T$ are the constants of Langmuir, Freudlich, Sips, and Tempkin models, respectively.

*2.3.2. Adsorption Study of Multicomponent System*

*(1) Effect of pH on the Simultaneous Adsorption of the Mixture of Three Chosen Dyes onto $TiO_2$/AC Adsorbent.* The influence of pH on dye absorption of $TiO_2$/AC was studied by determining the dye uptake in a mixture of three dyes at different pH. The experiments were conducted on 200 mL solution containing 0.0469 mM MB, 0.0458 mM MO, and 0.0743 mM MR with the presence of 10 mg of $TiO_2$/AC. The pH of solution was adjusted from 2 to 12 by adding 0.01 M HCl and 0.01 M NaOH solution. The samples were keep in the dark and were shaken at a constant speed of 200 rpm for 4 h to achieve adsorption equilibrium conditions. Afterwards, the samples were centrifuged at 4500 rpm for around 15 min to separate the supernatant for UV-Vis measurement at corresponding maximum absorbance wavelength to determine the residual concentrations of each dye.

*(2) Multicomponent Isotherm Studies.* The adsorption equilibrium of multicomponent system was investigated in a similar manner in a 200 mL mixtures of 0.0469 mM MB, 0.0458 mM MO, and 0.0743 mM MR.

The extended Langmuir, P-factor models, and ideal adsorbed solution theory (IAST) incorporating three different isotherm models of Langmuir, Freundlich, and Sips equations were used to examine the trinary dye system. Theory of these models is presented in detail in references [10, 11].

A model for competitive sorption based on the Langmuir equation (extended Langmuir (EL)) was first proposed by Butler and Ockrent [19] to express the adsorption equilibrium in multicomponent systems. This isotherm is applicable as each component obeys Langmuir behavior in a single-solute system.

$$q_{e,i} = \frac{K_{L,i}.C_{e,i}}{1+\sum a_{L,i}C_{e,i}}, \quad (7)$$

where $q_{e,i}$ and $C_{e,i}$ present adsorption capacity (mmol.g$^{-1}$) and concentration (mM) of component $i$ at equilibrium, and $K_{L,i}$ (L.g$^{-1}$) and $a_{L,i}$ (L.mM$^{-1}$) are Langmuir constants of component $i$.

The P-factor method can be employed to investigate the competitive adsorption behavior of dyes in the trinary component system. This model presumed a simplified approach to correlate and compare between single- and multicomponents systems through the introduction of factor (P)

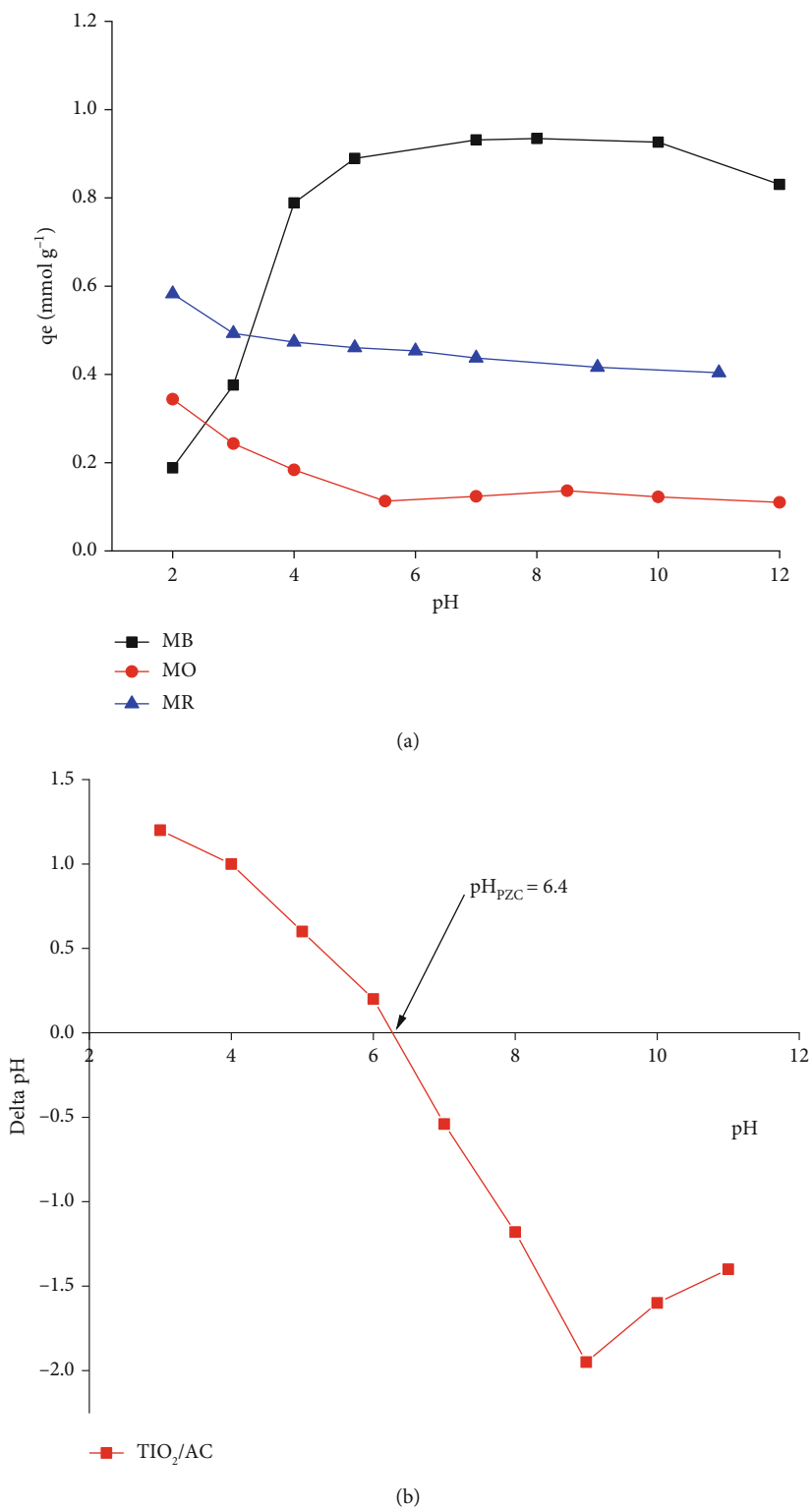


Figure 4: (a) pH effect on dye adsorption capacity; (b) The point of zero charge estimated by pH drift method.

(Equation (7)) proposed by Mckay and Al Duri [20].

$$P_i = \frac{K_{L,i}/a_{L,i,\text{single}}}{K_{L,i,\text{mul}}/a_{L,i,\text{trinary}}}, \quad (8)$$

where $K_{L,i}/a_{L,i,\text{single}} = q^0_{L,i,\text{single}}$ and $K_{L,i,\text{trinary}}/a_{L,i,\text{trinary}} = q^0_{L,i,\text{trinary}}$ are the maximum monolayer adsorption capacity for component $i$ in a single and trinary systems.

If P – factor < 1, the adsorption is enhanced by the existence of other components; P – factor = 1, there is no

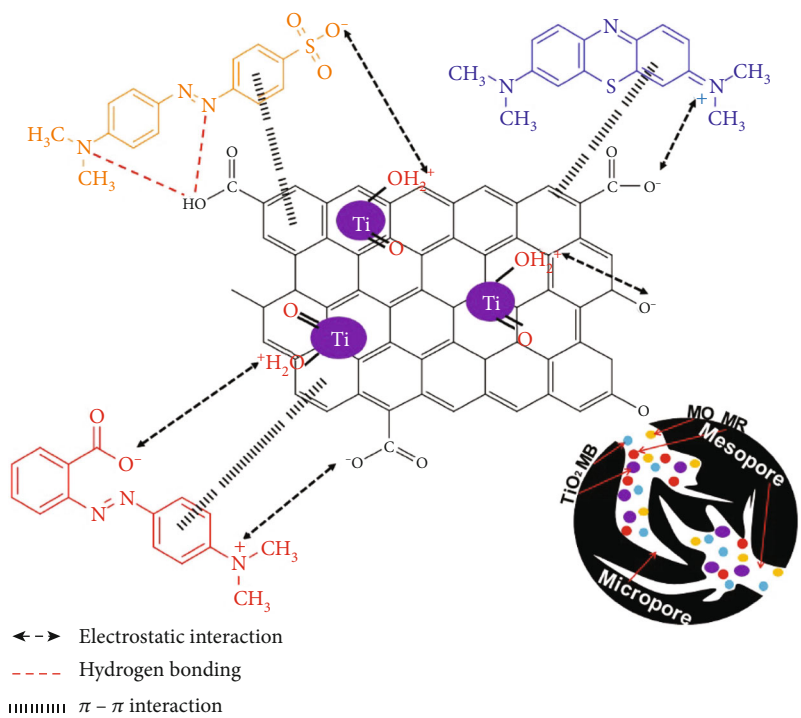


Scheme 2: The diagram of interaction mechanisms of MB, MR, and MO with $TiO_2$/AC.

noticeable interaction; and P – factor > 1 indicates that the adsorption is suppress with the existence of other dyes. This model assumes that a Langmuir isotherm for each component ($i$), the multicomponent isotherm equation can be defined as:

$$q_{e,i,\text{trinary}} = \frac{1}{P_{,i}} \frac{K_{\text{L,i}}.C_{e,i,\text{single}}}{1 + a_{L,i}.C_{\text{e,i,trinary}}}, \tag{9}$$

where $a_{L,i}$ is the Langmuir isotherm constants calculated from single solute system.

The IAST is an approach to predict the adsorption isotherms of multiple components solution based on the isotherm data of each individual component considering the thermodynamic consistency of the system. [21]

The Langmuir isotherm in the IAST is developed by using the spreading pressure of component, $i$, and $\psi$ in integral form proposed by McKay and Al Duri [20].

$$\psi = \frac{\pi.A}{\text{RT}} = \int_0^{C_o} \frac{q_e}{C_e} dC_e = \frac{K_L}{a_L} \ln\left(1 + a_L\right). \tag{10}$$

Rearranging Equations (3) and (9) [22] to obtain Equations (10) and (11).

$$C^0_{e,i} = \frac{\exp\left(\psi\left(a^0_L/K^0_{L,i}\right)\right) - 1}{a^0_{L,i}}, \tag{11}$$

$$q^0_{e,i} = \frac{K^0_{L,i}}{a^0_{L,i}} \left[1 - \exp\left(-\psi\left(\frac{a^0_L}{K^0_{L,i}}\right)\right)\right]. \tag{12}$$

Equation (11) describes the Langmuir isotherm in the IAST at the specified spreading pressure.

The Freundlich isotherm in the IAST is performed by using the spreading pressure in the form of the integral proposed by Kidnay and Myers [23] as in Equation (12).

$$\psi = \frac{\pi.A}{RT} = \int_0^{C_o} \frac{dlnC_e(q_e)}{dlnq_e} dq_e = \frac{q_e}{b_F}, \tag{13}$$

$$q^0_{e,j} = \psi.b_{F,j} \frac{K^0_{L,i}}{a^0_{L,i}}. \tag{14}$$

The Freundlich isotherm in the IAST is as follows:

$$C^0_{e,j} = \left(\frac{q^0_{e,j}}{a_{F,j}}\right)^{1/b_{F,j}}. \tag{15}$$

By applying the Sips isotherm, the spreading pressure, $\psi$, can be expressed by [22].

$$\psi = \frac{\pi.A}{RT} = \int_0^{C_o} \frac{q_e}{C_e} dC_e = \frac{q_e}{b_F} \ln\left(1 + a_S.C_e^{b_S}\right), \tag{16}$$

$$C_{e,j} = \left(\frac{\exp\left(\left(\psi a^0_{S,i} b^0_{S,i}\right)/K^0_{S,i}\right) - 1}{a^0_{S,i}}\right)^{1/b_{S,i}}. \tag{17}$$

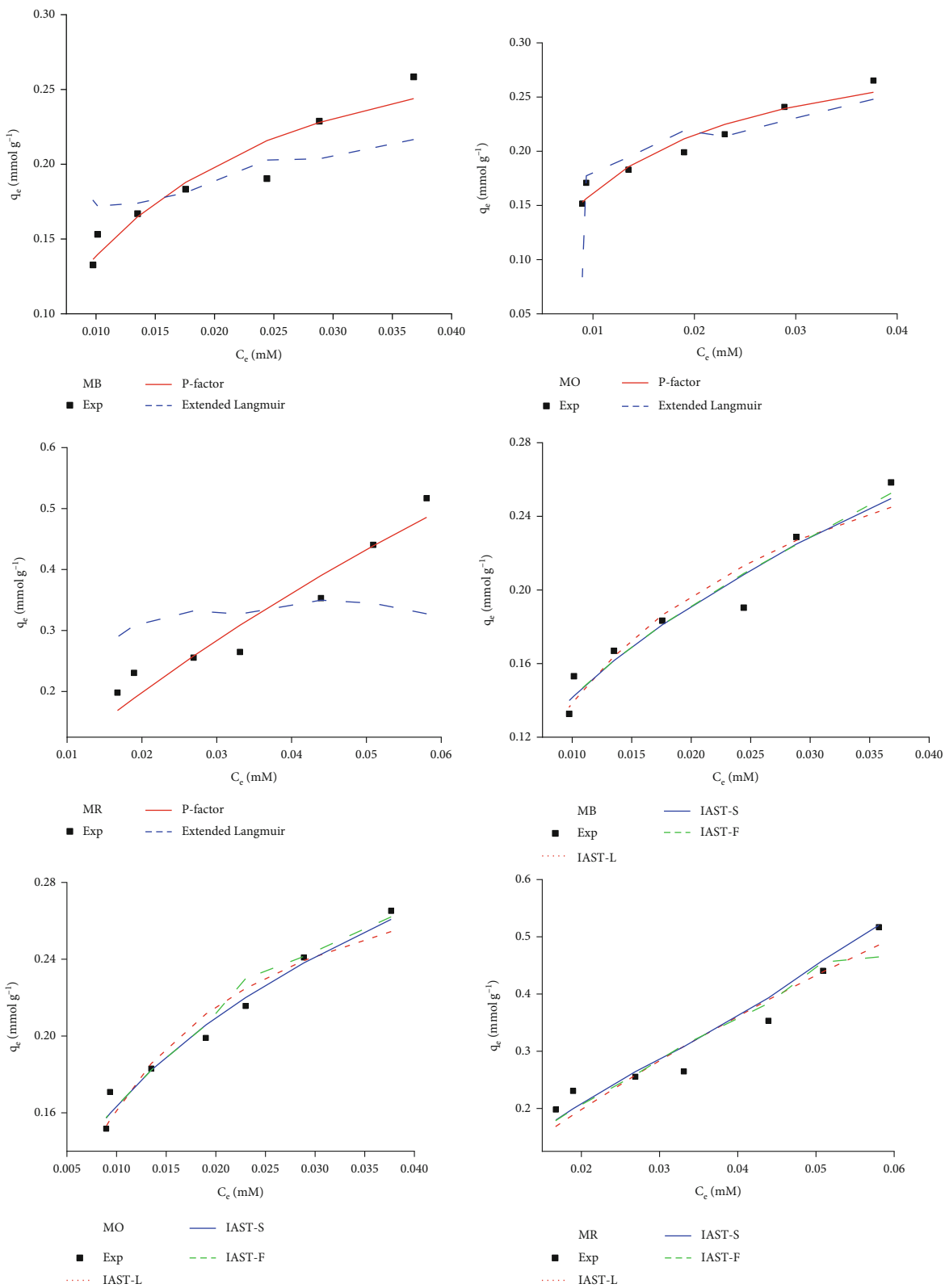


Figure 5: The plot of adsorption isotherms for different models.

Table 3: The parameters of EL, P-factor, and IAST-sorption isotherm (Langmuir, Freundlich, and Sips), $R^2$, and $AIC_c$ values.

| Extended-Langmuir model | | | | | | | | | | | |
|---|---|---|---|---|---|---|---|---|---|---|---|
| Dye | $q^0_{L,MB}$ (mmol g$^{-1}$) | $q^0_{L,MO}$ (mmol g$^{-1}$) | $q^0_{L,MR}$ (mmol g$^{-1}$) | $K^0_{L,MB}$ (L.g$^{-1}$) | $K^0_{L,MO}$ (L.g$^{-1}$) | $K^0_{L,MR}$ (L.g$^{-1}$) | $a^0_{L,MB}$ (L.mM$^{-1}$) | $a^0_{L,MO}$ (L.mM$^{-1}$) | $a^0_{L,MR}$ (L.mM$^{-1}$) | $R^2$ | AICs |
| MB | 2.274 | | | 68.82 | | | 30.263 | | | 0.576 | -48.16 |
| MO | | 0.60 | | | 77.03 | | | 127.95 | | 0.900 | -37.04 |
| MR | | | 0.80 | | | 65.98 | | | 82.08 | 0.674 | -29.50 |
| P-factor-Langmuir model | | | | | | | | | | | |
| Dye | $q^0_{L,MB}$ (mmol g$^{-1}$) | $q^0_{L,MO}$ (mmol g$^{-1}$) | $q^0_{L,MR}$ (mmol g$^{-1}$) | $K^0_{L,MB}$ (L.g$^{-1}$) | $K^0_{L,MO}$ (L.g$^{-1}$) | $K^0_{L,MR}$ (L.g$^{-1}$) | $a^0_{L,MB}$ (L.mM$^{-1}$) | $a^0_{L,MO}$ (L.mM$^{-1}$) | $a^0_{L,MR}$ (L.mM$^{-1}$) | $R^2$ | AICs |
| MB | 0.394 | | | 26.65 | | | 67.63 | | | 0.916 | -54.34 |
| MO | | 0.324 | | | 33.10 | | | 101.9 | | 0.996 | -57.86 |
| MR | | | 1.281 | | | 6.90 | | | 5.40 | 0.918 | -40.47 |
| IAST-Langmuir model | | | | | | | | | | | |
| Dye | $q^0_{L,MB}$ (mmol g$^{-1}$) | $q^0_{L,MO}$ (mmol g$^{-1}$) | $q^0_{L,MR}$ (mmol g$^{-1}$) | $K^0_{L,MB}$ (L.g$^{-1}$) | $K^0_{L,MO}$ (L.g$^{-1}$) | $K^0_{L,MR}$ (L.g$^{-1}$) | $a^0_{L,MB}$ (L.mM$^{-1}$) | $a^0_{L,MO}$ (L.mM$^{-1}$) | $a^0_{L,MR}$ (L.mM$^{-1}$) | $R^2$ | AICs |
| MB | 0.340 | | | 23.22 | | | 67.63 | | | 0.917 | -55.34 |
| MO | | 0.321 | | | 32.67 | | | 101.86 | | 0.998 | -58.86 |
| MR | | | 2.04 | | | 10.99 | | | 5.40 | 0.919 | -41.47 |
| IAST-Freudlich model | | | | | | | | | | | |
| Dye | $a_{F,MB}$ | $a_{F,MO}$ | $a_{F,MR}$ | $b_{F,MB}$ | $b_{F,MO}$ | $b_{F,MR}$ | | | | $R^2$ | AICs |
| MB | 1.05 | | | 0.43 | | | | | | 0.996 | -58.37 |
| MO | | 0.843 | | | 0.35 | | | | | 0.998 | -61.23 |
| MR | | | 6.40 | | | 0.89 | | | | 0.987 | -40.92 |
| IAST-Sips model | | | | | | | | | | | |
| Dye | $K^0_{S,MB}$ | $K^0_{S,MO}$ | $K^0_{S,MR}$ | $a^0_{S,MB}$ | $a^0_{S,MO}$ | $a^0_{S,MR}$ | $b^0_{S,MB}$ | $b^0_{S,MO}$ | $b^0_{S,MR}$ | $R^2$ | AICs |
| MB | 1.27 | | | 0.44 | | | 0.466 | | | 0.943 | -50.99 |
| MO | | 1.11 | | | 0.60 | | | 0.40 | | 0.999 | -57.76 |
| MR | | | 16.65 | | | 17.5 | | | 0.95 | 0.945 | -37.24 |

The Sips isotherm in the IAST is as follows:

$$q^0_{e,i} = \frac{K^0_{S,i}}{a^0_{S,i}}\left[1 - \exp\frac{-\psi a^0_{S,i} b^0_{S,i}}{K^0_{S,i} - 1}\right]. \quad (18)$$

The model's parameters åe by the least square method by minimizing the sum of squared deviations, $SSE_S$, by means of the numerical optimization techniques using the Solver function in Microsoft Excel. The function for minimization is

$$SSE_S = \sum_1^N \left(y_{exp} - y_{est}\right)^2, \quad (19)$$

where $y_{exp}$ is the experimental response, and $y_{est}$ is the response calculated from the model.

The determination coefficient $R^2$ is obtained according to the expression

$$R^2 = \frac{1 - SSE_S}{SSE_T}, \quad (20)$$

where $SSE_T$ is the total sum of squares equal to $(\sum_1^N (y_{exp} - y_{mean})^2$ (where $y_{mean}$ is the mean value of $y$).

The AIC (Akaike's information criteria) is used to compare two models. AIC is calculated for each model from Equation (20) [24].

$$AIC = N \cdot \ln\left(\frac{SSE_T}{N}\right) + 2 \cdot N_p + \frac{2 \cdot N_p \cdot (N_p + 1)}{N - N_p - 1}, \quad (21)$$

where $N$ is the number of data points; $N_p$ is the number of parameters fit by the regression.

AIC decides how well the data fit each model. The value of AIC can be positive or negative. The model with the lowest $AIC_c$ score is considered the most likely correct [25].

*2.3.3. Recycling of Adsorbent.* The recyclability of $TiO_2$/AC was performed by photocatalytic self-cleaning. After adsorption experiments in 200 mL solution of each dyes at a concentration of 0.0469 mM for MB, 0.0458 mM for MO, and 0.0743 mM for MR in the presence of 0.2 g adsorbent, the used adsorbent, obtained from centrifugation, was desorbed by magnetic stirring under halogen lamp illumination for 2

Table 4: A comparison of maximum adsorption capacity based on Langmuir isotherm model of $TiO_2$/AC with those of other adsorbents reported.

| Adsorbents | Adsorption capacity for MB ($mmol\,g^{-1}$) | Adsorption capacity for MO ($mmol\,g^{-1}$) | Adsorption capacity for MR ($mmol\,g^{-1}$) | References |
|---|---|---|---|---|
| Walnut shell-derived activated carbon | 0.251 | | | [37] |
| Kaolinite | 0.062 | | | [38] |
| Wasted biomass-derived activated carbon | 0.048 | | | [34] |
| Pistachio shell-derived activated carbon | 0.430 | | | [39] |
| $TiO_2$/rice husk-derived activated carbon* | **0.452/0.340** | | | The present work |
| Multiwalled carbon nanotubes | | 0.157 | | [40] |
| Diaminoethane sporopollenin biopolymer | | 0.014 | | [41] |
| Hypercrosslinked polymeric adsorbent | | 0.217 | | [42] |
| Calcined-layered double hydroxides | | 0.611 | | [43] |
| $TiO_2$/rice husk-derived activated carbon* | | **0.329/0.321** | | The present work |
| Apple fruit shell-derived activated carbon | | | 1.615 | [44] |
| Ag@Fe nanoparticles | | | 0.646 | [45] |
| MIL-53(Fe) | | | 0.680 | [46] |
| $TiO_2$/rice husk-derived activated carbon* | | | **0.806/2.04** | The present work |

*adsorption capacity in single system/trinary system.

hours. The adsorbent was then washed with distilled water and dried at 100°C for further use.

## 3. Results and Discussion

*3.1. Characterization of Materials.* Crystal structures of the obtained materials were studied by XRD patterns (Figure 1(a)). XRD patterns of AC exhibit the peaks at 2 theta angles of 29.45, 36.49, 39.49, 43.03, and 47.56° corresponding to (203), (213), (205), (304), and (305) Miller indexes of carbon (JCPDS-00-022-1069). XRD patterns of $TiO_2$ and composite $TiO_2$/AC show the characteristic peaks of anatase at 25.25, 38.15, 47.85, 54.65, and 62.75° corresponding to the diffraction plane of (101), (004), (200), (105), and (204) (JCPDS -21-1272). With increasing amount of $TiO_2$, the intensity of diffraction peaks of anatase increases indicating that two phases of activated carbon and anatase are coexisted. The composition of titanium and carbon elements estimated by EDX is presented in Figure S1. It is found that $TiO_2$/carbon atomic ratio in product increases with the increase of $TiO_2$ in initial mixture, indicating that the composition of $TiO_2$/AC could be controlled by adjusting the reaction composition. Figure 1(b) and Table 1 presents the nitrogen adsorption and desorption isotherms of AC, $TiO_2$, and $TiO_2$/AC composites. All the isotherms exhibit a hysteresis loop which is characteristic for type IV isotherm, confirming the existence of mesoporous materials. The hysteresis loop occurs at relatively high pressures illustrating that the mesoporous structure formed between the particles. The surface area calculated based on the BET model is 1713 $m^2.g^{-1}$ for AC, 124 $m^2.g^{-1}$ for $TiO_2$, and 436 $m^2.g^{-1}$ for $TiO_2$/AC. The surface areas of $TiO_2$ and AC are relatively large compared with previously reported studies [26, 27] showing that the structure of $TiO_2$ in this study is highly porous. Furthermore, the combination of $TiO_2$ on AC matrix significantly increased the surface area of $TiO_2$ itself.

Figures 1(c) and 1(d) show the UV-Vis-DRS and their Tauc's plot for calculating band gap energy derived from UV-Vis-DRS. No energy absorption edge of AC which can be considered as a conductor was observed. The band gap energy of $TiO_2$ is 3.2 eV which is equivalent to previous report in the range of 3.1-3.2 eV [28]. The combination of $TiO_2$ with AC gives rise to a red shift in the energy adsorption spectrum, corresponding a band gap energy of 1.9 -2.5 eV illustrating that these composites might have photocatalytic activity in the visible region.

The morphology of $TiO_2$ prepared from peroxo-hydroxo titanium (IV) complexes consists of fine particles of around 10 nM which can be seen to agglomerate to form larger particles, while AC exhibits the typical layered-structure. In the composite structure, $TiO_2$ agglomerates are highly dispersed

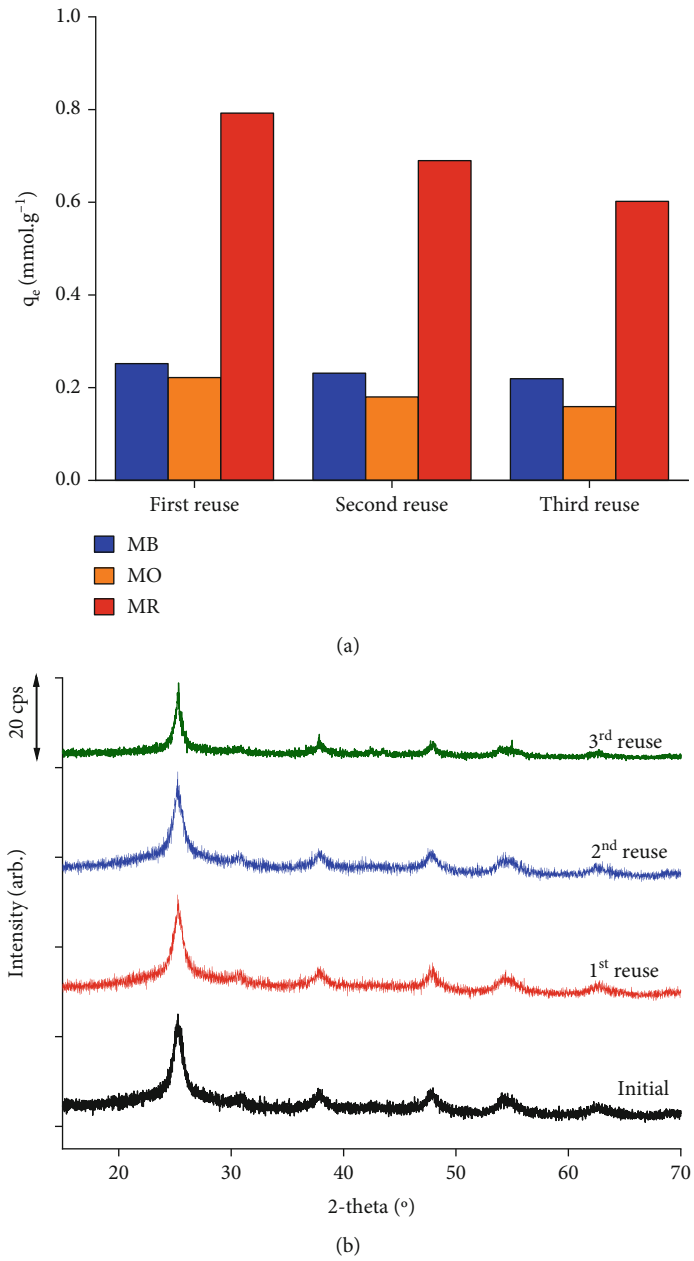


Figure 6: (a) Variation of adsorption capacity and (b) XRD patterns of $TiO_2$/AC and reused $TiO_2$/AC.

on the AC matrix. The higher $TiO_2$ content leads to a better coverage of $TiO_2$ on AC matrix. The distribution of $TiO_2$ on AC was also studied by EDX mapping. Figure 2 illustrates the elementary mapping of $TiO_2$/AC (0.5/1) sample. The extensive dispersion of Ti, C, and O elements confirms that $TiO_2$ was well-distributed on the surface of AC. EDX spectrum also shows some impurity of Mg, Si, Na, and Ca element (of around 0.2-1% w) which might present in rice husks.

### 3.2. Adsorption Studies

*3.2.1. Simultaneous Determination of MB, MO, and MR by UV-Vis Spectroscopy.* The dye concentration in solution was determine by UV-Vis spectroscopy at maximum wavelength of 664 nm for MB, 464 nm for MO, and 500 nm for MR. However, the spectra of three dyes are overlapped resulting in larger error for simultaneous determination of these dyes (Figure 3(a)). In the work, the peaks were deconvoluted by means of OriginPro19/Deconvolution Software as illustrated in Figure 3(b). The deconvoluted UV-Vis spectrum was used to estimate the linear calibration range for dye determination. The linear range of each dye was found to be 0.0063-0.094 mM for MB, 0.015-0.138 mM for MO, and 0.019-0.167 mM for MR. The limit of detections (LODs) for MB, MO, and MR are 0.0007 mM, 0.002 mM, and 0.009 mM, respectively, which are suitable for the detection of these dyes in the adsorption study. Standard addition

method is used to determine the dye in the trinary mixture. The recovery was found to be in the range of 0.9-0.99 indicating that the proposed method could be used for simultaneous determination of MB, MO, and MR (Table S1).

*3.2.2. Adsorption Studies of Single Component System of MB, MO, and MR over $TiO_2$, AC, and $TiO_2$/AC.* The adsorption kinetics of $TiO_2$, AC, and $TiO_2$/AC composites at different concentrations of dyes (0.0306–0.0743 mM) are performed in Figure S2 and Table S2. All of samples exhibit the high adsorption towards MB, MO, and MR expect only $TiO_2$ which can adsorb MB. As can be seen from the figure, the higher the dye concentration, the greater the adsorption capacity. This can explain by the fact that the high dye concentration enhances the driving force that overcomes all the mass transfer resistance of dye between the aqueous solution and the surface of absorbent. The adsorption of dyes is fast in the earlier stage (0–100 minutes) and gradually reached the equilibrium. It is found that the time required to obtain the adsorption/desorption equilibrium was around 120 minutes for all of cases. The kinetics data were applied to the pseudo-first-order and pseudo-second-order kinetic models. The kinetic parameters of the models and $R^2$ are presented in Table S2. The regression equation based one pseudo-first-order model provides the high values of determination coefficient ($R^2 = 0.88 - 0.98$) and the equilibrium adsorption capacity calculated by this model ($q_{e,cal}$) agrees with equilibrium adsorption capacity obtained by the experiment ($q_{e,exp}$). Hence, the experimental results fit the pseudo-first-order model.

In order to select the $TiO_2$/AC composite for further study, the removal of MB using $TiO_2$/AC as a dye model was conducted (Figure S3). The AC exhibits the highest adsorption capacity for MB; whereas, $TiO_2$ presents a very poor adsorption capacity. The adsorption capacity and the regeneration of spent adsorbent by the photocatalytic self-cleaning are significantly dependent on the composition of $TiO_2$ in AC. The adsorption capacity was found to be 0.865 mmol $g^{-1}$ for AC, 0.211 mmol $g^{-1}$ for $TiO_2$/AC (0.25/1), 0.452 mmol $g^{-1}$ for $TiO_2$/AC (0.5/1), 0.301 mmol $g^{-1}$ for $TiO_2$/AC (1/1), 0.251 mmol $g^{-1}$ for $TiO_2$/AC (1.5/1), and only 0.2 mmol $g^{-1}$ for $TiO_2$. However, after the first recycle, the adsorption capacity of $TiO_2$/AC(0.5/1) was the highest. Based on the balance between adsorption capacity and visible-light derived photocatalytic self-cleaning, $TiO_2$/AC (0.5/1) catalyst was selected for further experiments. Figure S4 and Figure S5 present the relationship of equilibrium concentration and adsorption capacity of AC, $TiO_2$/AC, and $TiO_2$. Either Langmuir, Freundlich, or Tempkin models describe well the equilibrium data with high determination coefficients ($R^2 = 0.823 - 0.999$) (Table 2) indicating the monolayer adsorption with different energy. The differences between the adsorption capacities of the three dyes may results from different adsorption mechanisms, which might depend on the molecular size and their electron affinities toward adsorbent surface.

*3.2.3. Adsorption Isotherms of Trinary Component System for MB, MO, and MR over $TiO_2$/AC (0.5/1)*

*(1) Effect of pH on the Adsorption of $TiO_2$/AC (0.5/1).* The pH effect on the adsorption of trinary component mixture by $TiO_2$/AC is presented in Figure 4(a). The MB uptake was found to increase from 0.188 to 0.889 mmol $g^{-1}$ for an increase in pH from 2 to 5. At higher pH values (5–11), the MB uptake remains almost constant. The point of zero charge of $TiO_2$/AC obtained by the pH drift method was found at pH = 6.4 (Figure 4(b)). At higher pH (>6.4), the surface of $TiO_2$/AC may become negatively charged, which promoted the adsorption of the positively charged MB cations (pKa of MB = 3.8 [29]) through electrostatic attraction. This, however, cannot explain its constant adsorption by $TiO_2$/AC at all the studied pH values. There might be another mode of adsorption, e.g., ion exchange which is similar to the adsorption of MB onto wheat shells [30] or malachite green onto treated sawdust [31].

In contrast, the uptake of MO and MR decreases with the rise of pH. When pH increases from 2 to around 6, the adsorption capacity decreases from 0.344 to 0.124 mmol $g^{-1}$ for MO and from 0.582 mmol $g^{-1}$ to 0.452 mmol $g^{-1}$ for MR. The MO or MR uptake keep unchanged with further pH increasing. Higher adsorptions at lower pH values could be due to protonation properties of the $TiO_2$/AC. At pH below the point of zero charge (pHs < 6.4), the positive charges at the surface of $TiO_2$/AC favoured the adsorption of anionic MO and MR (pKa of MO = 3.8 [32] and pKa of MR = 5.1 [33]). A similar trend of adsorption behavior has also been reported with some different adsorbents [34].

In general, the mechanism of dye adsorption is related to the interaction between the adsorbent and the adsorbate in solution. This interaction can occur in many different ways such as hydrogen bonding, electrostatic interaction, $\pi$-$\pi$ stacking interaction, ion-exchange, hydrophobic bonding, and pores and chemical bonding [16, 25, 37, 62, 63] as illustrated in the Scheme 2.

*3.2.4. Equilibrium Studies.* The equilibrium data of trinary component system were fitted to the extended Langmuir model (EL), the Langmuir model using P-factor models (P-Langmuir model) and Langmuir, Freundlich, and Sips models using IAST (denoted L-IAST, F-IAST, and S-IAST, respectively) as shown in Figure 5. As can be seen, except EL model, the other four models are able to adequately correlate the equilibrium data. Although, the determination coefficient ($R^2$) is widely used to estimate the goodness of fit for the models with an equal number of experimental points and of the fitting parameters, Akaike information criterion (AIC) is preferred for comparing the models with different parameters. The smaller AICs are, the better the model fit the data. As can be seen from Table 3, it is little difficult to estimate how the AICs are small because there are three values of AICs for each model. Relatively, it can be seen from Table 3 that the AICs are possibly rearranged from low to high based on the sum of AICs as follows: -160.92 (-58.37, -61.23, and -40.92) for F-IAST; -155.67 (-55.34, -58.86, and -41.47) for L-IAST; -152.67 (-54.34, -57.86, and -40.47) for P-factor-Langmuir model; -145.99 (-50.99, -57.76, and -37.24) for S-IAST; and –39.1(-22.96,

-11.83, and -4.31) for EL suggesting both F-IAST model were the best to fit experimental data of all three chosen dyes followed by L-IAST. The Langmuir maximum sorption capacities based on L-IAST model in trinary dyes system were found to be lower than those obtained from the single-dye system, due to the presence of competing dyes. The influence of competitive dyes on the sorption of specific dyes onto the $TiO_2$/AC is analyzed by using P-factor. The ratios of $q^0_{L,MR,}/q^0_{L,MB}$ and $q^0_{L,MR,}/q^0_{L,MO}$ are >1, indicating the predominant MR adsorption over MB and MO in both single and trinary systems. The P-values of $Q^0_{L,MR,\text{single}}/Q^0_{L,MR,\text{trinary}} = 0.806/2.04 < 1$ prove that the sorption process of MR was promoted by the existence of other dyes, while that of $q^0_{L,MB,\text{single}}/q^0_{L,MB,\text{trinary}} = 0.450/0.340 > 1$ presents that the MB adsorption was hindered by the existence of competing dyes. The ratio of $q^0_{L,MO,single}/q^0_{L,MO,trinary} = 0.329/0.321 = \sim 1$ reveals that the MO adsorption is independent on the existence of other dyes. The presence of MB and MO seems to enhance significantly the adsorption capacity of $TiO_2$/AC toward MR to ~2.5 times. MB contains a positively charged amine group while MR and MO contain negatively charged carboxyl and sulfite groups, respectively. It is possible that the MB moleculars adsorbed on $TiO_2$/AC promote the MR adsorption via electrostatic interaction and $\pi$-$\pi$ stacking interaction. The mechanism of completive adsorption of the components is not clear and need to study further.

Table 3 reveals that $TiO_2$/AC can adsorb as much as approximately two third its own weight (total 763.77 mg (MB + MO + MR)/1000 mg) at ambient temperature. The adsorption capacity of $TiO_2$/AC was compared with the reported materials for the dye adsorption. The adsorption of MB, MO, or MR in the literature is mostly in single component system (Table 4). One can see that the reported adsorbents include carbon nanotubes, activated carbon, and biopolymers as well as one metal organic framework. However, most of these materials only exhibited lower adsorption capacities than the $TiO_2$/AC adsorbent or even the MOF, MIL-53(Fe), just possessed an adsorption capacity of 0.668 $mM.g^{-1}$. Meanwhile, the adsorption capacity in single system/trinary system of $TiO_2$/AC is 0.452/0.340 for MB, 0.329/0.321 for MO, and 0.806/2.04 for MR. This indicates that the potential using $TiO_2$/AC to remove dyes is indeed promising.

*3.2.5. Recyclability of Adsorbent.* The regeneration and reuse of the adsorbent are one of critical criteria for its application in practice. Conventional recycle process is progressed by resining the used adsorbents with organic solvents (ethanol, benzene, and methanol) [35] and heating in limited oxygen environment [36] to elute dyes, resulting in the secondary pollutants and extra cost. Since $TiO_2$/AC could act as a photocatalytic material, the used $TiO_2$/AC could be regenerated by self-cleaning when exposed to visible light. Figure 6(a) shows the change in the adsorption capacity of $TiO_2$/AC after three regenerations by photocatalytic self-cleaning. It can be seen that after the first-cycle regeneration, $TiO_2$/AC still possessed a comparable adsorption capacity, suggesting that the photocatalytic self-cleaning was a feasible and effective technique to remove dyes from the used $TiO_2$/AC. After three reused cycles, $TiO_2$/AC could still exhibit 96% of its initial adsorption capacity. Figure 6(b) presents the XRD patterns of the reused $TiO_2$/AC. It was found that there is a slight decrease in intensity but the characteristic peaks of anatase phase still remain unchanged after the recycle process indicating that $TiO_2$/AC is stable for three recycles.

## 4. Conclusions

$TiO_2$/AC materials were synthesized from water soluble titanium hydroperoxide complex and activated carbon from rice husks. The obtained material has high surface area and excellent adsorption capacity to methylene blue, methyl orange, and methyl red compared to the other materials reported. The Freundlich model and Langmuir model in the ideal adsorbed solution theory provide the best prediction to the trinary mixture data in comparison to the extended Langmuir model; Langmuir model using P-factor and Sips model in ideal-adsorbed solution theory. The $TiO_2$/AC exhibits the excellent reusability by visible light-driven photocatalytic self-cleaning, and their adsorption efficiency was maintained even after three cycles; the change in structure and adsorption capacity of $TiO_2$/AC was insignificant, proving that this material is durable and has potential for practical applications.

## Data Availability

The data used to support the findings of this study are available from the corresponding authors upon request.

## Conflicts of Interest

The authors declare that they have no conflicts of interest.

## Acknowledgments

This research was financially supported by the Van Lang University, Vietnam, and partially supported by the Hue University under the Core Research Program No. NCM.DHH.2019.08.

## Supplementary Materials

Table 1: the recovery in the range of 0.9-0.99 is acceptable indicating that the proposed method could be used for simultaneous determination of MB, MO, and MR. Figure S1: $TiO_2$/carbon atomic ratio in product analyzed by EDX increases with the increase of $TiO_2$ in initial mixture, suggesting that the composition of $TiO_2$/AC could be controlled by adjusting the reaction composition. Figure S2 and Table S2: all of samples present the high adsorption towards MB, MO, and MR expect only $TiO_2$, which can adsorb MB. The adsorption of dyes is fast in the earlier stage (0–100 minutes) and gradually reached the equilibrium. The experimental data fit the pseudo-first-order model. Figure S3: based on the balance between adsorption capacity and visible-light derived photocatalytic self-cleaning, $TiO_2$/AC (0.5/1)

catalyst was selected for next experiments. Figure S4: relationship of equilibrium concentration and adsorption capacity of AC, $TiO_2$/AC, and $TiO_2$ using Langmuir, Freundlich, or Tempkin models. Figure S5: adsorption isotherms of single component system for MB, MO, and MR over $TiO_2$/AC (0.5/1). *(Supplementary Materials)*

## References


[1] M. A. Khan, M. I. Khan, and S. Zafar, "Removal of different anionic dyes from aqueous solution by anion exchange membrane," *Membrane Water Treatment*, vol. 8, no. 3, pp. 259–277, 2017.

[2] V. Vatanpour, H. Karimi, S. Imanian Ghazanlou et al., "Antifouling polyethersulfone nanofiltration membranes aided by amine- functionalized boron nitride nanosheets with improved separation performance," *Journal of Environmental Chemical Engineering*, vol. 8, no. 6, article 104454, 2020.

[3] L. Bulgariu, L. B. Escudero, O. S. Bello et al., "The utilization of leaf-based adsorbents for dyes removal: a review," *Journal of Molecular Liquids*, vol. 276, pp. 728–747, 2019.

[4] A. George, D. Magimai Antoni Raj, X. Venci et al., "Photocatalytic effect of CuO nanoparticles flower-like 3D nanostructures under visible light irradiation with the degradation of methylene blue (MB) dye for environmental application," *Environmental Research*, vol. 203, article 111880, 2022.

[5] D. Bhatia, N. R. Sharma, J. Singh, and R. S. Kanwar, "Biological methods for textile dye removal from wastewater: a review," *Critical Reviews in Environmental Science and Technology*, vol. 47, no. 19, pp. 1836–1876, 2017.

[6] S. Ragupathy, V. Manikandan, S. Devanesan, M. Ahmed, M. Ramamoorthy, and A. Priyadharsan, "Enhanced sun light driven photocatalytic activity of Co doped $SnO_2$ loaded corn cob activated carbon for methylene blue dye degradation," *Chemosphere*, vol. 295, article 133848, 2022.

[7] P. Das, P. Debnath, and A. Debnath, "Enhanced sono-assisted adsorptive uptake of malachite green dye onto magnesium ferrite nanoparticles: Kinetic, isotherm and cost analysis," *Environmental Nanotechnology, Monitoring & Management*, vol. 16, article 100506, 2021.

[8] P. Das, S. Nisa, A. Debnath, and B. Saha, "Enhanced adsorptive removal of toxic anionic dye by novel magnetic polymeric nanocomposite: optimization of process parameters," *Journal of Dispersion Science and Technology*, vol. 43, no. 6, pp. 880–895, 2022.

[9] A. Deb, A. Debnath, and B. Saha, "Sono-assisted enhanced adsorption of eriochrome black-T dye onto a novel polymeric nanocomposite: kinetic, isotherm, and response surface methodology optimization," *Journal of Dispersion Science and Technology*, vol. 42, no. 11, pp. 1579–1592, 2021.

[10] P. Das and A. Debnath, "Reactive orange 12 dye adsorption onto magnetically separable CaFe2O4 nanoparticles synthesized by simple chemical route: kinetic, isotherm and neural network modeling," *Water Practice Technology*, vol. 16, no. 4, pp. 1141–1158, 2021.

[11] A. Deb, A. Debnath, K. L. Bhowmik, S. Rudra Paul, and B. Saha, "Application of polyaniline impregnated mixed phase Fe2O3, MnFe2O4 and ZrO2 nanocomposite for rapid abatement of binary dyes from aqua matrix: response surface optimisation," *International Journal of Environmental Analytical Chemistry*, pp. 1–19, 2021.

[12] W. Tian, J. Lin, H. Zhang et al., "Kinetics and mechanism of synergistic adsorption and persulfate activation by N-doped porous carbon for antibiotics removals in single and binary solutions," *Journal of Hazardous Materials*, vol. 423, article 127083, 2022.

[13] R. Gurav, S. K. Bhatia, T. R. Choi et al., "Adsorptive removal of synthetic plastic components bisphenol-A and solvent black-3 dye from single and binary solutions using pristine pinecone biochar," *Chemosphere*, vol. 296, article 134034, 2022.

[14] S. Yadav, A. Yadav, N. Bagotia, A. K. Sharma, and S. Kumar, "Novel composites of pennisetum glaucum with CNT: preparation, characterization and application for the removal of safranine O and methylene blue dyes from single and binary systems," *Biomass Convers Biorefinery*, 2022.

[15] I. Langmuir, "The adsorption of gases on plane surfaces of glass, mica and platinum," *Journal of the American Chemical Society*, vol. 40, no. 9, pp. 1361–1403, 1918.

[16] H. Freundlich, "Über die adsorption in lösungen," *Zeitschrift für Physikalische Chemie*, vol. 57U, no. 1, pp. 385–470, 1907.

[17] R. Sips, "On the structure of a catalyst surface," *The Journal of Chemical Physics*, vol. 16, no. 5, pp. 490–495, 1948.

[18] M. J. Tempkin and V. Pyzhev, "Kinetics of ammonia synthesis on promoted iron catalyst," 2022, https://www.researchgate.net/publication/306535741_Kinetics_of_ammonia_synthesis_on_promoted_iron_catalyst.

[19] J. A. V. Butler and C. Ockrent, "Studies in electrocapillarity. III," *The Journal of Physical Chemistry*, vol. 34, no. 12, pp. 2841–2859, 1930.

[20] G. McKay and B. Al Duri, "Ein vereinfachtes modell fur das adsorptionsgleichgewicht von mischungen aus farbstoffen an aktivkohle," *Chemical Engineering and Processing Process Intensification*, vol. 22, no. 3, pp. 145–156, 1987.

[21] A. Myers and J. Praunitz, "Thermodynamics of photosynthesis," *Biophysics (Oxf)*, vol. 9, no. 3, pp. 316–321, 1964.

[22] K. K. H. Choy, J. F. Porter, and G. McKay, "Single and multicomponent equilibrium studies for the adsorption of acidic dyes on carbon from effluents," *Langmuir*, vol. 20, no. 22, pp. 9646–9656, 2004.

[23] A. J. Kidnay and A. L. Myers, "A simplified method for the prediction of multicomponent adsorption equilibria from single gas isotherms," *AICHE Journal*, vol. 12, no. 5, pp. 981–986, 1966.

[24] H. Motulsky and A. Christopoulos, *Fitting Models to Biological Data Using Linear and Nonlinear Regression. Fitting Curves with GraphPad Prism*, GraphPad Prism Softw. Inc, San Diego, California, 2003.

[25] N. T. Thanh Tu, T. V. Thien, P. D. Du, V. T. Thanh Chau, T. X. Mau, and D. Q. Khieu, "Adsorptive removal of Congo red from aqueous solution using zeolitic imidazolate framework–67," *Journal of Environmental Chemical Engineering*, vol. 6, no. 2, pp. 2269–2280, 2018.

[26] N. Yalçin and V. Sevinç, "Studies of the surface area and porosity of activated carbons prepared from rice husks," *Carbon N. Y*, vol. 38, no. 14, pp. 1943–1945, 2000.

[27] S. Xiong, Y. Tang, H. S. Ng et al., "Specific surface area of titanium dioxide ($TiO_2$) particles influences cyto- and photo-toxicity," *Toxicology*, vol. 304, pp. 132–140, 2013.

[28] S. K. S. K. S. Saranya, V. Vellora Thekkae Padil, C. Senan et al., "Green synthesis of high temperature stable anatase titanium dioxide nanoparticles using gum kondagogu: characterization

and solar driven photocatalytic degradation of organic dye," *Nanomaterials*, vol. 8, no. 12, p. 1002, 2018.

[29] J. R. Kim and E. Kan, "Heterogeneous photo-Fenton oxidation of methylene blue using CdS-carbon nanotube/$TiO_2$ under visible light," *Journal of Industrial and Engineering Chemistry*, vol. 21, pp. 644–652, 2015.

[30] Y. Bulut and H. Aydin, "A kinetics and thermodynamics study of methylene blue adsorption on wheat shells," *Desalination*, vol. 194, no. 1–3, pp. 259–267, 2006.

[31] V. K. Garg, R. Gupta, A. B. Yadav, and R. Kumar, "Dye removal from aqueous solution by adsorption on treated sawdust," *Bioresource Technology*, vol. 89, no. 2, pp. 121–124, 2003.

[32] S. G. Richard, H. Gary, W. Robert, and E. Edwåd, "Knintics of Acid disociation ion recombination of aqueous methyl orange," vol. 2240, no. 26, pp. 2–4, 1989.

[33] R. K. Srour and L. M. McDonald, "Determination of the acidity constants of methyl red and phenol red indicators in binary methanol– and ethanol-water mixtures," *Journal of Chemical & Engineering Data*, vol. 53, no. 1, pp. 116–127, 2008.

[34] N. Mohammadi, H. Khani, V. K. Gupta, E. Amereh, and S. Agarwal, "Adsorption process of methyl orange dye onto mesoporous carbon material- kinetic and thermodynamic studies," *Journal of Colloid and Interface Science*, vol. 362, no. 2, pp. 457–462, 2011.

[35] K. Y. A. Lin and H. A. Chang, "Ultra-high adsorption capacity of zeolitic imidazole framework-67 (ZIF-67) for removal of malachite green from water," *Chemosphere*, vol. 139, pp. 624–631, 2015.

[36] D. Guo, Y. Li, B. Cui et al., "Natural adsorption of methylene blue by waste fallen leaves of _Magnoliaceae_ and its repeated thermal regeneration for reuse," *Journal of Cleaner Production*, vol. 267, p. 121903, 2020.

[37] M. Liu, X. Li, Y. Du, and R. Han, "Adsorption of methyl blue from solution using walnut shell and reuse in a secondary adsorption for Congo red," *Bioresource Technology Reports*, vol. 5, pp. 238–242, 2019.

[38] D. Ghosh and K. G. Bhattacharyya, "Adsorption of methylene blue on kaolinite," *Applied Clay Science*, vol. 20, no. 6, pp. 295–300, 2002.

[39] A. A. Attia, B. S. Girgis, and S. A. Khedr, "Capacity of activated carbon derived from pistachio shells by H3PO4 in the removal of dyes and phenolics," *Journal of Chemical Technology and Biotechnology*, vol. 78, no. 6, pp. 611–619, 2003.

[40] Y. Yao, H. Bing, X. Feifei, and C. Xiaofeng, "Equilibrium and kinetic studies of methyl orange adsorption on multiwalled carbon nanotubes," *Chemical Engineering Journal*, vol. 170, no. 1, pp. 82–89, 2011.

[41] M. Küçükosmanoğlu, O. Gezici, and A. Ayar, "The adsorption behaviors of methylene blue and methyl orange in a diaminoethane sporopollenin-mediated column system," *Separation and Purification Technology*, vol. 52, no. 2, pp. 280–287, 2006.

[42] J. H. Huang, K. L. Huang, S. Q. Liu, A. T. Wang, and C. Yan, "Adsorption of Rhodamine B and methyl orange on a hypercrosslinked polymeric adsorbent in aqueous solution," *Colloids and Surfaces A: Physicochemical and Engineering Aspects*, vol. 330, no. 1, pp. 55–61, 2008.

[43] Z. M. Ni, S. J. Xia, L. G. Wang, F. F. Xing, and G. X. Pan, "Treatment of methyl orange by calcined layered double hydroxides in aqueous solution: adsorption property and kinetic studies," *Journal of Colloid and Interface Science*, vol. 316, no. 2, pp. 284–291, 2007.

[44] E. A. Khan and T. A. K. Shahjahan, "Adsorption of methyl red on activated carbon derived from custard apple *Annona squamosa* fruit shell: equilibrium isotherm and kinetic studies," *Journal of Molecular Liquids*, vol. 249, pp. 1195–1211, 2018.

[45] Z. Zaheer, A. AL-Asfar, and E. S. Aazam, "Adsorption of methyl red on biogenic [email protected] nanocomposite adsorbent: isotherms, kinetics and mechanisms," *Journal of Molecular Liquids*, vol. 283, pp. 287–298, 2019.

[46] E. Yilmaz, E. Sert, and F. S. Atalay, "Synthesis, characterization of a metal organic framework: MIL-53 (Fe) and adsorption mechanisms of methyl red onto MIL-53 (Fe)," *Journal of the Taiwan Institute of Chemical Engineers*, vol. 65, pp. 323–330, 2016.

Hindawi
Adsorption Science & Technology
Volume 2022, Article ID 5664344, 13 pages
https://doi.org/10.1155/2022/5664344

*Research Article*

# Synthesis of $ZrO_2$:$Dy^{3+}$ Nanoparticles: Photoluminescent, Photocatalytic, and Electrochemical Sensor Studies

**K. Gurushantha,[1] K. S. Anantharaju,[2] Nagaraju Kottam,[1] K. Keshavamurthy,[3] C. R. Ravikumar,[4] B. S. Surendra,[2] A. Murugan,[5] and H. C. Ananda Murthy[6,7]**

[1]*Department of Chemistry, M.S. Ramaiah Institute of Technology, Bengaluru 560054, India*
[2]*Department of Chemistry, Dayananda Sagar College of Engineering, Bengaluru 560111, India*
[3]*Department of Physics, Vivekananda Institute of Technology, Bangalore 560074, India*
[4]*Research Center, Department of Science, East West Institute of Technology, Bangalore 560091, India*
[5]*Department of Chemistry, North Eastern Regional Institute of Science & Technology, Nirjuli, Itanagar, 791109 Arunachal Pradesh, India*
[6]*Department of Applied Chemistry, School of Applied Natural Sciences, Adama Science and Technology University, P.O. Box 1888, Adama, Ethiopia*
[7]*Department of Prosthodontics, Saveetha Dental College & Hospital, Saveetha Institute of Medical and Technical Science (SIMAT), Saveetha University, Chennai, 600077 Tamil Nadu, India*

Correspondence should be addressed to C. R. Ravikumar; ravicr128@gmail.com
and H. C. Ananda Murthy; anandkps350@gmail.com

Received 8 April 2022; Revised 21 July 2022; Accepted 2 August 2022; Published 16 August 2022

Academic Editor: Hesham Hamad



Solution combustion was employed to create a series of $ZrO_2$:$Dy^{3+}$ (1-11 mol percent) nanoparticles (NPs) using oxalyl dihydrazide (ODH) as the fuel. $ZrO_2$:$Dy^{3+}$ NPs were subjected to calcination at about 700°C. $ZrO_2$:$Dy^{3+}$ NPs comprised of 1 to 11 mol% of $Dy^{3+}$ were characterized by employing the X-ray diffraction (XRD), transmission electron microscopic (TEM), UV-visible, and X-ray photoelectron spectroscopic (XPS) techniques. The crystallite diameters of 1 to 11 mol% $ZrO_2$:$Dy^{3+}$ NPs were observed to range from 8.1 nm to 16.3 nm, exhibiting spherical shape. According to BET tests, the pore volume of $ZrO_2$:$Dy^{3+}$ NPs was determined to be 100.129 $cm^3$/g. The mean pore diameter of $ZrO_2$:$Dy^{3+}$ NPs was determined to be 4.803 nm from the Barrett-Joyner-Halenda (BJH) plot. The photoluminescence and photocatalytic dye degradation properties of $ZrO_2$:$Dy^{3+}$ NPs were investigated. The acid red 88 (AR88) dye was applied to appraise the photocatalytic activities of the NPs under UV irradiation. $ZrO_2$:$Dy^{3+}$ NPs with 3 mol% $Dy^{3+}$ exhibited improvised photocatalytic activity due to the operative departure of charge carriers. The electrochemical examination of $ZrO_2$:$Dy^{3+}$ NP modified carbon paste electrode in 0.1 N HCl demonstrated considerable redox potential output, as evidenced by cyclic voltammetric and amperometric measurements. The electrochemical sensor studies on $ZrO_2$:$Dy^{3+}$ NPs exhibited potentiality towards sensing of highly toxic metals like mercury and lead.

## 1. Introduction

Because of its outstanding optical and electrical properties, such as strong thermal stability, huge dielectric constant, broad band gap (5–7 eV), and high melting point, zirconium oxide ($ZrO_2$) was subjected to investigation extensively over the last two decades [1, 2]. Due to its outstanding optical properties, including a high band gap value, a large refractive index, a low optical cost, and improved transparency in the near-infrared and visible ranges, it is a common material in many optical applications [3, 4]. It exhibits a broad band gap and emits photoluminescent (PL) light at short

wavelengths [5]. Materials made of rare-earth-doped oxides have unique optical properties like luminescence efficiency and photochemical stability [6, 7].

Tetragonal, monoclinic, and cubic crystal forms are all found in zirconia. The temperature at which each structure is formed is determined by the synthesis method used and the presence of a dopant of any kind; zirconia produced using the sol–gel process, for example, has an amorphous structure, but it can be transformed into tetragonal zirconia after heat treatment at 500°C. The monoclinic structure begins to appear at 800°C, and at 1300°C, the cubic structure emerges. Zirconia can be utilized in biocomposites, combustible cells, catalytic supports, oxygen detectors, and oxygen sensors [8]. Many researchers have looked into the optical characteristics of Dy-doped $ZrO_2$. For low concentrations of Dy dopant, zirconia has been reported to have improved photoluminescence (3 mol percent). Gu et al. [9] investigated the consequence of calcinations and doping of $Dy^{3+}$ on $ZrO_2$ nanoparticle luminescence. They discovered that a concentration of 2% Dy in $ZrO_2$ produces the extreme comparative luminescence intensity having wavelength of 480 nm. The effective photoluminescence in nanocrystalline zirconia was reported at low Dy concentrations [10].

For the production of $ZrO_2$:$Dy^{3+}$ in this study, the combustion solution method was used (1-11 mol). The crystalline nature and morphological characteristics of the material were studied using a variety of characterization techniques.

The significant and amazing method of removing contaminants from water and wastewater has been photocatalysis. Under UV light illumination, the produced nanomaterial's catalytic activity for the destruction of acid red 88 (AR88) was evaluated. The photocatalytic activities were explained in relation to the photoluminescence studies and crystallite size, and their applicability in display applications was examined in depth. In 0.1 N HCl solution, cyclic voltammetric and amperometric investigations were also carried out employing electrodes modified with $ZrO_2$ and $ZrO_2$:$Dy^{3+}$ (3 mol). Under the detection limit of $2.3602 \times 10^{-3}$ mol/L, the material demonstrated outstanding catalytic activity for mercury and lead sensing.

## 2. Experimental

Zr and Dy were obtained from the basic precursors, zirconium (IV) oxynitrate hydrate ($ZrO(NO_3)_2 \cdot H_2O$: 99.9 percent, S D Fine) and dysprosium (III) oxide ($Dy_2O_3$: 99.9 percent, Merck). The fuel was made in our lab and is called oxalyl dihydrazide (ODH: $C_2H_6N_4O_2$). For synthesis, oxalic acid, glycine, urea, citric acid, and other fuels were used. ODH with a low ignition temperature produces low molecular weight, innocuous gases as compared to other fuels. Oxide materials produced using ODH as a fuel can be used for a variety of purposes [11, 12]. Initially, $Dy_2O_3$ is converted to dysprosium nitrate by the dissolution of required quantity of $Dy_2O_3$ in $HNO_3$ (1 : 1) for the synthesis of $ZrO_2$:$Dy^{3+}$ (1–11 mol percent). After the reaction on a sand bath at 80°C was finished, the excess nitric acid was evaporated to produce a transparent terbium nitrate solution.

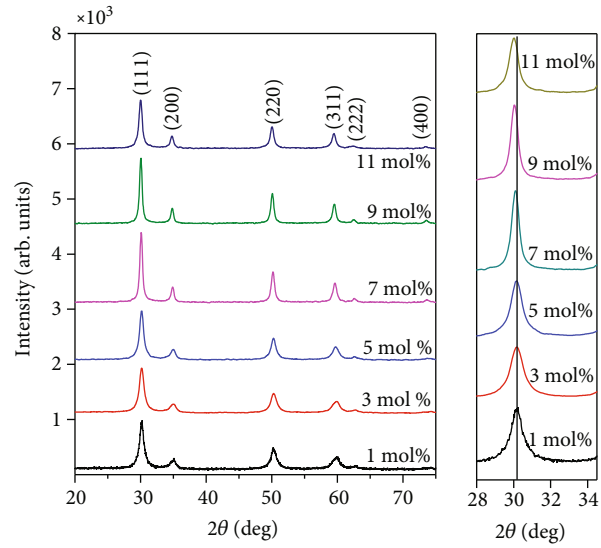


Figure 1: X-ray diffraction pattern of $Dy^{3+}$-doped (1-11 mol%) $ZrO_2$ NPs.

The required amounts of ODH and zirconium (IV) oxynitrate hydrate solution were added to the dysprosium nitrate solution while being continuously stirred to achieve smooth mixing. This heterogeneous mixture (redox) was placed on a Petri plate and introduced into a muffle furnace set to 400°C. The decomposition of the mixture eventually unfolds, culminating in the release of large volumes of gases such as $CO_2$, $H_2O$, and $N_2$. The entire procedure consumes about 5 minutes and leads to the production of $ZrO_2$:$Dy^{3+}$ nanophosphor.

## 3. Results and Discussion

*3.1. Powder X-Ray Diffraction Analysis.* XRD experiments were conducted in order to understand the crystalline nature and true crystallite size of Dy-doped $ZrO_2$ NPs. PXRD patterns of as-synthesised $ZrO_2$:$Dy^{3+}$ NPs have been found to be very similar to the pattern as per standard JCPDS card no. 81-1551. The cubic phase of $ZrO_2$ was used to index all of the diffraction patterns (Figure 1). Cubic, monoclinic, and tetragonal polymorphs of $ZrO_2$ exist in three different crystalline forms. The cubic/tetragonal phase [13] is the most suitable for technological uses among these. Only the peak associated to $ZrO_2$ was found after doping $ZrO_2$ with $Dy^{3+}$. There were no other peaks corresponding to Dy $(NO_3)_3$ or other contaminants, showing that $Zr^{4+}$ ions in the $ZrO_2$ matrix were replaced by $Dy^{3+}$ ions. A slight peak shift has been observed for $ZrO_2$ upon Dy doping, which is possibly due to lattice modification and corresponding strain.

Using full width at half maximum (FWHM) data, $D = k/\cos\theta$ [10], the average crystallite size ($D$) was deduced by applying Scherrer's formula, where $k$ is a constant (approximately 0.90), the X-ray wavelength is 0.15418 nm, and $\theta$ is the diffraction angle. The diameters of $ZrO_2$ crystallite $Dy^{3+}$ (1-11 mol percent) NPs were observed to be between 8.3 and 13.8 nm in size (Table 1).

Table 1: Crystallite sizes of $ZrO_2$:$Dy^{3+}$ (1-11mol%) NPs.

| Samples | Crystallite size (nm) | | Strain ($\varepsilon$) $\times 10^{-3}$ | SF | $\delta$ ($10^{16}$ lin $m^{-2}$) |
|---|---|---|---|---|---|
| | Scherrer's formula | W–H plot | | | |
| $ZrO_2$:$Dy^{3+}$ (1mol%) | 8.3 | 9.3 | 14.3 | 0.3973 | 1.451 |
| $ZrO_2$:$Dy^{3+}$ (3mol%) | 9.3 | 6.4 | 15.1 | 0.3971 | 1.156 |
| $ZrO_2$:$Dy^{3+}$ (5mol%) | 10.2 | 6.9 | 9.61 | 0.3974 | 0.961 |
| $ZrO_2$:$Dy^{3+}$ (7mol%) | 14.9 | 9.1 | 4.47 | 0.3979 | 0.450 |
| $ZrO_2$:$Dy^{3+}$ (9mol%) | 16.3 | 5.3 | 3.73 | 0.3982 | 0.376 |
| $ZrO_2$:$Dy^{3+}$ (11mol%) | 13.8 | 6.6 | 5.20 | 0.3984 | 0.525 |

Additionally, Dy doping induces a gradual loss of crystallinity of $ZrO_2$, due to lattice instability and induced strain on the lattice. Previously, the FWHM was assumed to represent a linear combination of crystallite size and lattice strain components [14]. Equation (1) can be used to express the influence of crystallite size and strain on the FWHM.

$$\beta \cos\theta = \varepsilon(4 \sin\theta) + \frac{\lambda}{D}, \quad (1)$$

where $\beta$, $\theta$, $\lambda$, and $\varepsilon$ are FWHM in radians, Bragg angle, wavelength, and strain associated with the NPs, respectively.

A straight line between 4 sin ($x$-axis) and cos ($y$-axis) is shown in equation (1) (Figure 2).

The line's intercept (0.90/$D$) on the $y$-axis is determined by the crystallite size, and the strain ($\varepsilon$) determines the line's slope ($D$). The tiny variations in the numbers were attributable to Scherrer's calculation assuming that the strain component was minimal, and the observed broadening of the diffraction peak was credited only to grain size reduction. With a rise in $Dy^{3+}$ concentration, the strain alters. Table 1 lists the results for other structural features such as dislocation density ($\delta$) and stacking fault (SF) using the following equations [15]:

$$\delta = \frac{1}{D^2}, \quad (2)$$

$$\mathrm{SF} = \left[\frac{2\pi^2}{45(3\tan\theta)^{1/2}}\right], \quad (3)$$

$$\sigma_{\mathrm{stress}} = \frac{\text{microstrain}}{2} \times E, \quad (4)$$

where $E$ is the elastic constant (Young's modulus) of the nanomaterial = 186.21 GPa [16].

The presence of the estimated microstrain in the majority of the planes in the current study suggested the presence of tensile stress on the particle's surface. The residual stress was tensile, with a positive microstrain, causing the PXRD patterns to move to the lower angle side.

*3.2. Morphological Studies.* Figure 3 depicts the SEM images of $ZrO_2$:$Dy^{3+}$ (1-11 mol percent) NPs. Because of the large number of gasses generated during combustion, the surface morphology of $ZrO_2$:$Dy^{3+}$ NPs reveals the presence particle agglomeration which rises with increasing Dy concentration.

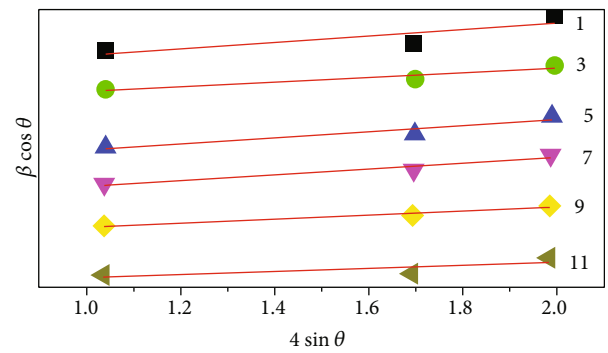


Figure 2: W–H plots of as-formed $ZrO_2$:$Dy^{3+}$ (1–11 mol%) NPs.

Figure 4(a) depicts the TEM micrograph of $ZrO_2$:$Dy^{3+}$ (3 mol percent) NM with considerable aggregation of nearly spherical nanocrystals. The recorded crystallite size matched the PXRD data perfectly. A HRTEM image captured from a specific location in Figure 4(b) showed the (111) plane crystal facet of cubic zirconia. The interplanar spacing values of 0.294 nm displayed the (111) plane of cubic zirconia. SAED pattern of $ZrO_2$:$Dy^{3+}$ (Figure 4(c)) (3 mol%) NM represents cubic $ZrO_2$ diffraction rings generated from planes (111), (200), (220), and (311) due to cubic zirconia polycrystalline diffraction (Figure 4(b)). The single and pure crystalline cubic $ZrO_2$ serves as evidence of the value of the current synthesis procedure in producing cubic $ZrO_2$ NM with good compact size, high purity, and high crystallinity.

Figure 5 shows the nitrogen adsorption-desorption isotherms of BET and BJH plots (inset), respectively. The IUPAC classifications' type IV adsorption isotherms are conformed to by the BET plot for the substance [14]. Type IV adsorption isotherms are frequently produced by mesoporous materials, showing the presence of layer-by-layer adsorption on smooth surfaces [15, 16]. The materials' specific surface area, commonly performed within the linear plots, approximately ranging from $0.05 < P/P0 < 0.3$ [17] is 100.129 $m^2$/g. Besides, the materials also have H2 type hysteresis loop in accordance with the IUPAC classification [17]; the H2 type hysteresis loop indicates the presence of narrow pore cavity distribution with wide neck size [15]. The BJH plots also confirm the mesoporous nature of the materials with the pore volume and pore diameter values of 0.151 cc/g and 4.803 nm, respectively.

The XPS technique was used to evaluate the elemental composition, chemical states, and elemental bonding for

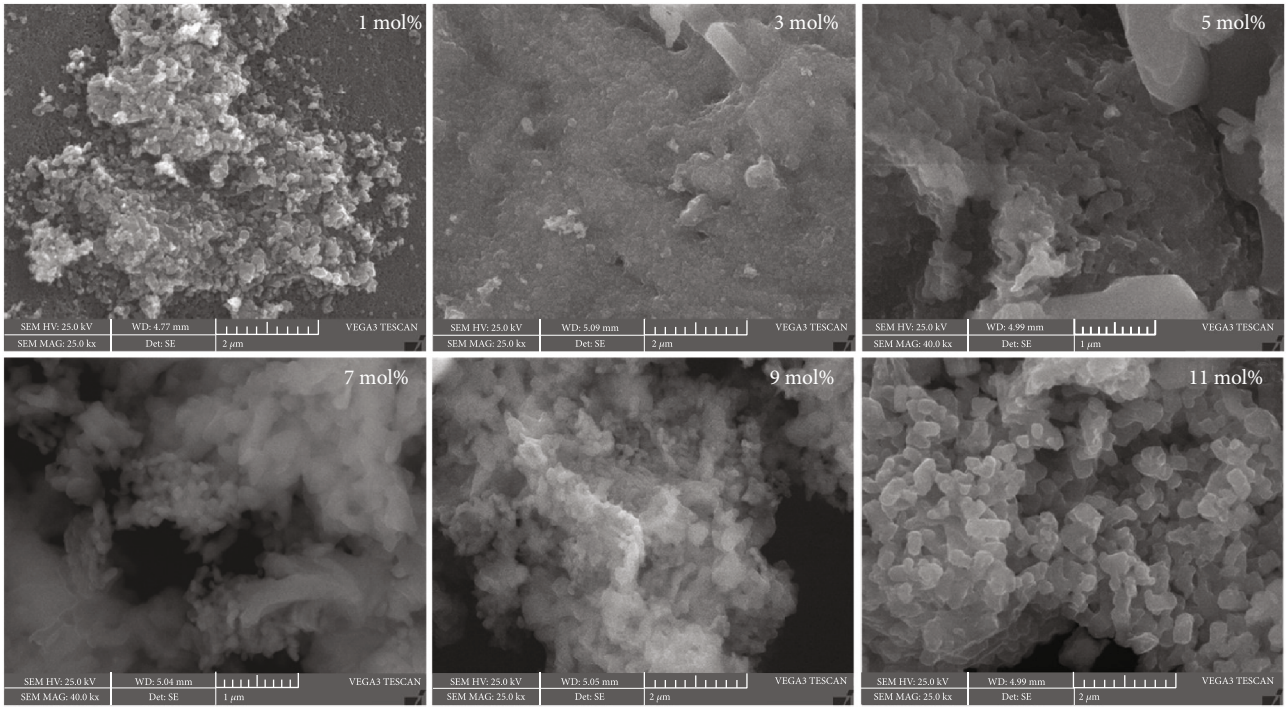


Figure 3: SEM images of $ZrO_2$:$Dy^{3+}$ (1–11 mol%) NPs.

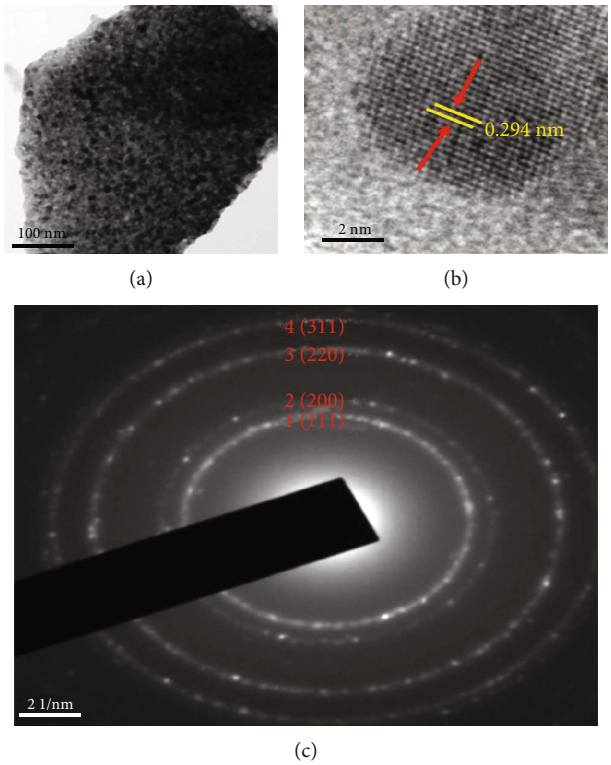


Figure 4: (a) TEM image, (b) HRTEM image, and (c) SAED pattern of $ZrO_2$:$Dy^{3+}$ (3 mol%) NPs.

the produced $ZrO_2$:$Dy^{3+}$ (3 mol percent), as shown in Figure 6. The recorded wide spectrum of the NM displayed the existence of binding energies ~1072, ~537.6, ~292.2, and~186.3 eV which corroborates to Dy 3d, O 1s, C 1s, and Zr 3d peaks, respectively.

*3.3. Photoluminescence (PL) Studies.* Exploration of the energy levels inside the band gap positions yielded crucial knowledge from PL research. PL emission can be used to analyse the effectiveness of migration, charge carrier entrapment, and the destiny of photogenerated electron-hole pairs

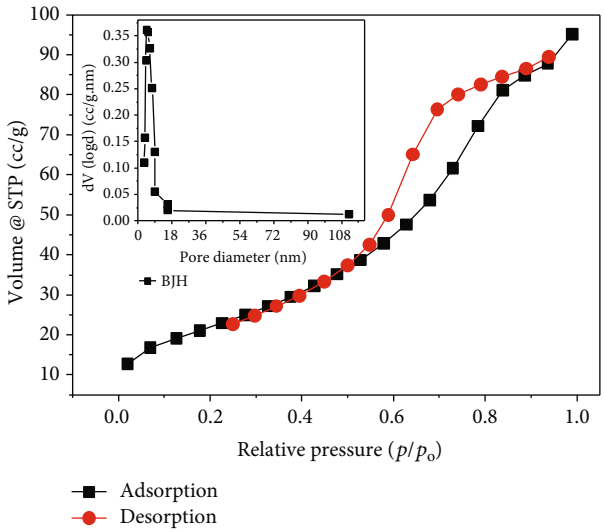


Figure 5: Adsorption-desorption measurements showing BJH plot (inset: pore size distribution).

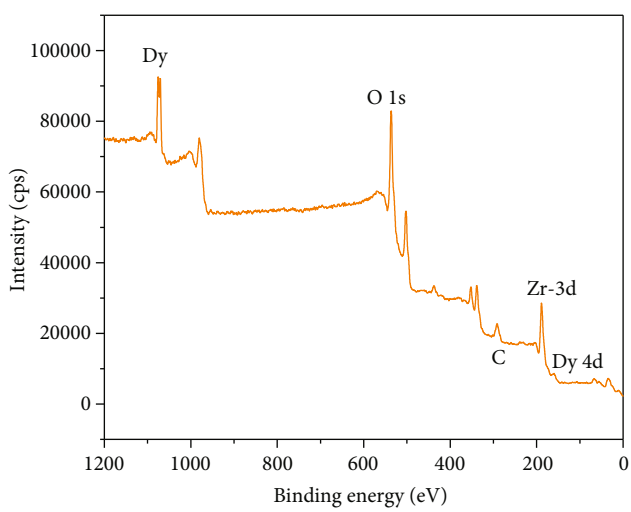


Figure 6: XPS spectra of Dy-doped (3 mol%) ZrO+ NPs.

in semiconductors [18–20]. Because PL emission caused excited electron-hole pairs to recombine, effective separation of charge carrier resulted in a decrease in PL intensity [21, 22].

A PL excitation (PLE) spectrum of 3 mol% $Dy^{3+}$-doped $ZrO_2$ nanophosphor measured at a fixed emission wavelength of 580 nm corresponds to the electronic transition ($^4F_{9/22} \rightarrow {}^6H_{13/2}$). The PLE bands at 320, 353, 367, 386, 393, and 416 nm were considered to the electronic transitions of $^6H_{15/2} \rightarrow {}^4H_{11/2}$, $^4M_{17/2}$, $^4G_{11/2}$, $^4I_{5/2}$, $^4F_{9/2}$, and $^4I_{13/2}$, respectively. The energy transfer between central oxygen and the f-f transitions of the $Dy^{3+}$ ions are what causes the former band and are attributed to the host's absorption bands. It proves that the phosphor may be effectively activated by near-UV wavelengths, enabling its use in the creation of white LEDs. Figure 7 displays the emission spectra of $ZrO_2$:$Dy^{3+}$ phosphors stimulated at 353 nm with 1 to 11 mol percent of $Dy^{3+}$.

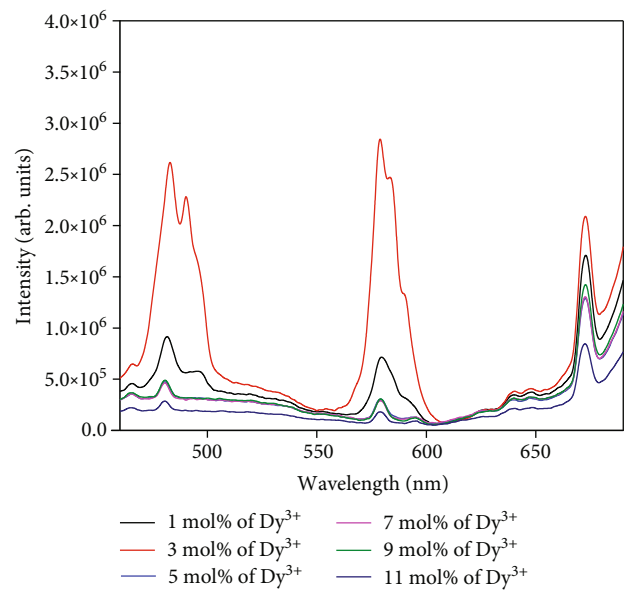


Figure 7: PL emission spectrum of $ZrO_2$:$Dy^{3+}$ (1–11 mol%) NMs excited at 353 nm.

Table 2: Kinetic studies under UV light for ZrO2:$Dy^{3+}$ (1–11mol%) photocatalysts.

| Photocatalysts | Under UV light $k \times 10^{-3} min^{-1}$ | $\%D$ |
|---|---|---|
| $ZrO_2$:$Dy^{3+1}$mol% | 10.95 | 73.42 |
| ZrO2:$Dy^{3+3}$mol% | 21.57 | 82.65 |
| ZrO2:$Dy^{3+5}$mol% | 22.76 | 75.55 |
| ZrO2:$Dy^{3+7}$mol% | 23.9 | 79.45 |
| ZrO2:$Dy^{3+9}$mol% | 31.67 | 80.52 |
| ZrO2:$Dy^{3+1}$1mol% | 20.09 | 84.00 |

When activated with 352 nm, all of the peaks were observed to be $Dy^{3+}$'s emission peaks, exhibiting energy efficient transfers from the host to $Dy^{3+}$. The luminescence centers stimulated by $Dy^{3+}$ ions were thought to be responsible for the PL spectrum [23]. With the exception of the PL emission intensity, there were essentially insignificant changes in the emission spectra as the $Dy^{3+}$ doping concentration was raised. The peaks observed at 483 nm (blue), 580 nm (yellow), and 672 nm (red) consist of $Dy^{3+}$ transitions corresponding to $^4F_{9/2} \rightarrow {}^6H_{15/2}$, $^4F_{9/2} \rightarrow {}^6H_{13/2}$, and $^4F_{9/2} \rightarrow {}^6H_{11/2}$, respectively. The blue emission corresponding to $^4F_{9/2} \longrightarrow {}^6H_{15/2}$ is due to the magnetic dipole (MD) transition which adheres to the selection rule $\Delta J = 0, \pm 1$ and $0 \leftrightarrow 0$ is a forbidden transition. Meanwhile, the yellow ($^4F_{9/2} \longrightarrow {}^6H_{13/2}$) emission corresponds to the forced electric dipole (ED) transition, which follows the selection rule of $\Delta L = \pm 2$ and $\Delta J = \pm 2$. This transition is significantly impacted by the surrounding environment, and its intensity is decided by the host and also observed that the feeble red emission for ($^4F_{9/2} \longrightarrow {}^6H_{11/2}$) transition belongs to the electric dipole transition. $Dy^{3+}$ ion transitions from the $^4F_{9/2}$ energy level to the overlying energy levels $^6H_{15/2}$, $^6H_{13/2}$,

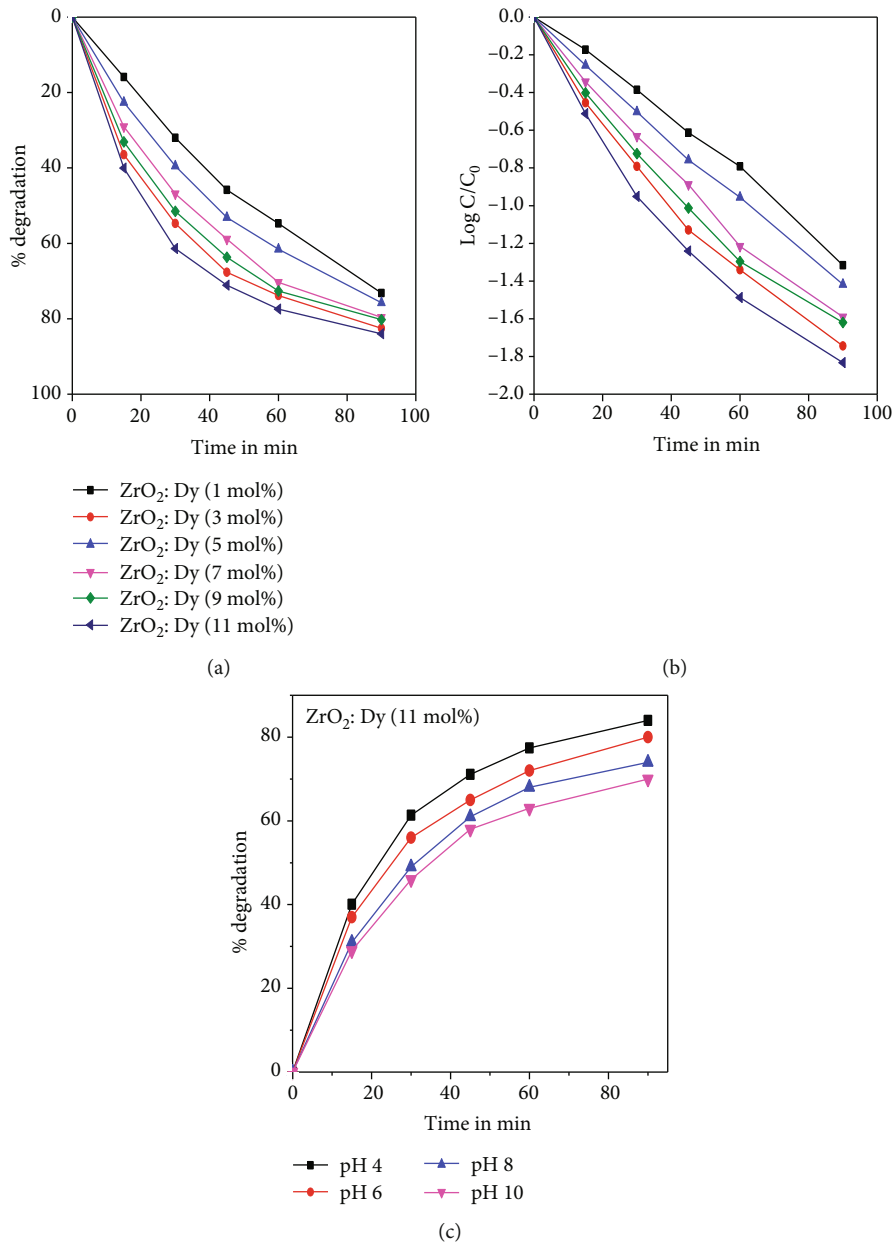


Figure 8: (a) Percentage degradation and (b) C/CO for the decolorization of acid red 88 dye under UV light illumination. (c) Effect of pH on photocatalytic degradation of $ZrO_2$:Dy (11 mol%) catalyst.

and $^6H_{11/2}$ emit PL. The $Dy^{3+}$ ion's crystal field strength has little effect on the MD transition, while the ED transition can only occur when the $Dy^{3+}$ ion has low symmetry and no inversion center. The intensity of emission increases up to 3 mol percent with an increase in $Dy^{3+}$ concentration from 1 to 11 mol percent before decreasing as a result of concentration quenching. This will clearly show how the PL emission is impacted by the concentration of dopant ions. In fact, luminescence quenching is caused by energy migration, ionic interactions, and cross relaxation to ground energy states, all of which are due to higher concentration of dopant, resulting in the reduction in the mean distance between dopant ions and, in some cases, the creation of dopant clusters. Nevertheless, the excellent emission property of $ZrO_2$:$Dy^{3+}$ sample shows that it can be used for display application [24].

*3.4. Photocatalytic Activity of Acid Red 88 (AR88) Dye under UVA/Sunlight.* To investigate the photodegradation activity of $Dy^{3+}$-doped $ZrO_2$ (1-11 mol percent) NPs, the decolorization of hazardous azo acid red 88 dye was conducted under UV light irradiation for 90 minutes. Acid red 88 degradation was found to be minimal in the absence of $ZrO_2$:$Dy^{3+}$ and under dark condition. As a consequence, the photocatalytic activity of the excited semiconductors is primarily responsible for the decolorization of the dye.

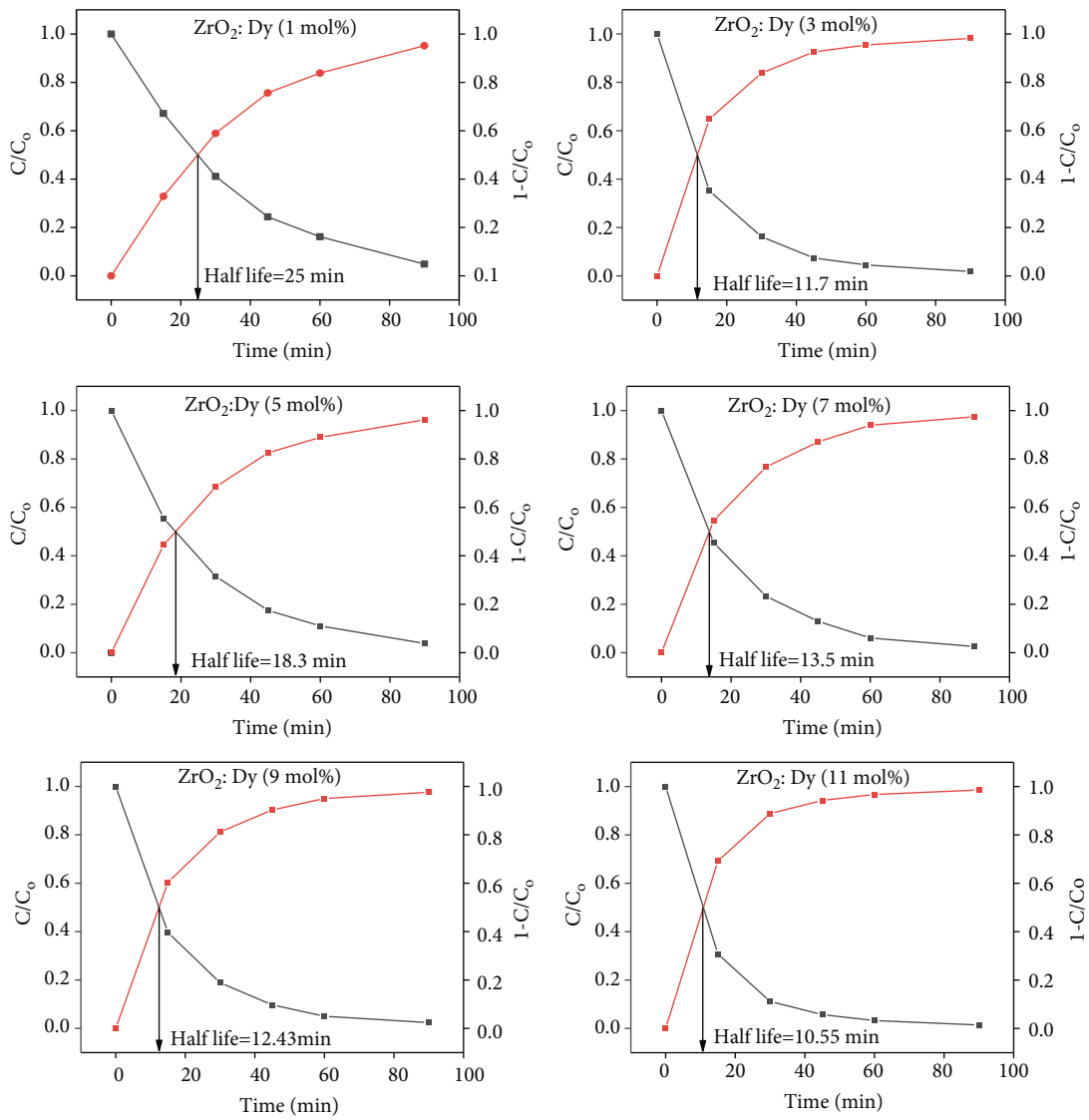


Figure 9: Half-life plot for the AR88 dye under UV irradiation in the presence of $ZrO_2$:$Dy^{3+}$ (1-11 mol%) photocatalyst.

Table 3: Summary of the photocatalytic degradation of various photocatalysts and dyes.

| Photocatalysts | Light | Dye | Degradation | Ref. |
|---|---|---|---|---|
| TaON/$Bi_2MoO_6$ | Visible light | Levofloxacin | 92.7% (75min) | [29] |
| $SiO_2$-$Bi_2MoO_6$ | Visible light | Methyl blue | 86.3% (4.5 hours) | [30] |
| WNR/TNB | Solar light | Rhodamine B (RhB) | 96% (80min) | [31] |
| SCNT6 | Xenon lamp irradiation | Congo red | 96.2% (60min) | [32] |
| $Ag_2O/TiO_2$ (4 : 10) | UV | Methyl orange | 93% (6min) | [33] |
| $ZrO_2$-doped $TiO_2$ | UV | Rhodamine B | 96.3% (60min) | [34] |
| $ZrO_2$-doped $TiO_2$ at 1%wt | UV | Methyl orange and rhodamine B | 78.1 and 75.5% | [35] |
| $ZrO_2$:$Fe^{3+}$ (2 mol%) | UV | Acid orange 7 | 98% (90min) | [18] |
| $ZrO_2$:$Sm^{3+11}$mol% | Solar light | Acid green G | 83.8% (90min) | [36] |
| ZrO2:$Dy^{3+11}$mol% | UV | Acid red 88 | 84% (90min) | Present work |

Under UV light, the percentage of acid red 88 decolorization catalyzed by $ZrO_2$:$Dy^{3+}$ photocatalysts is shown in Table 2. Acid red 88 decolorization rises with increasing dopant concentration up to 11 mol% under UV light, implying that 11 mol% Dy-doped NPs were efficient in separating photo-emitted electron-hole pairs to enhance

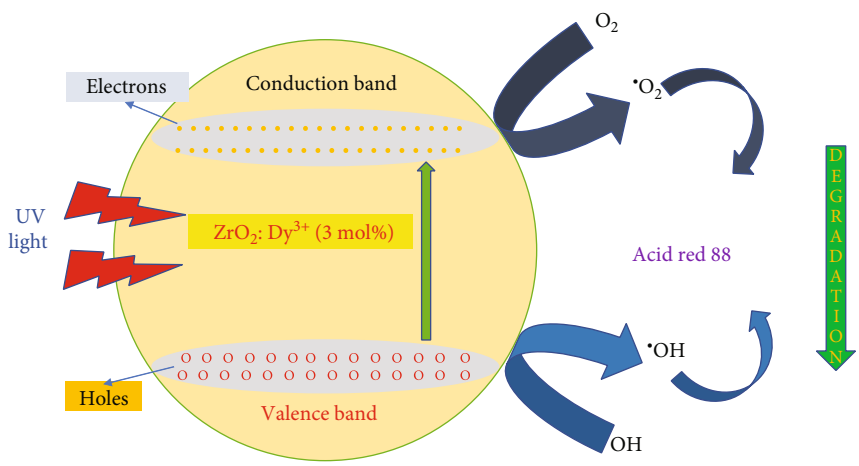


Figure 10: Proposed mechanism for the photocatalytic decolorization of AR88 dye over the $ZrO_2$:$Dy^{3+}$ photocatalyst.

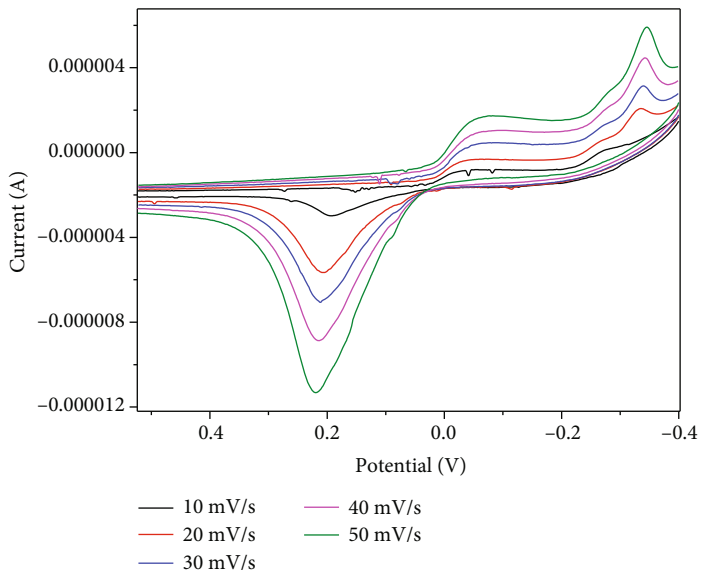


(a)

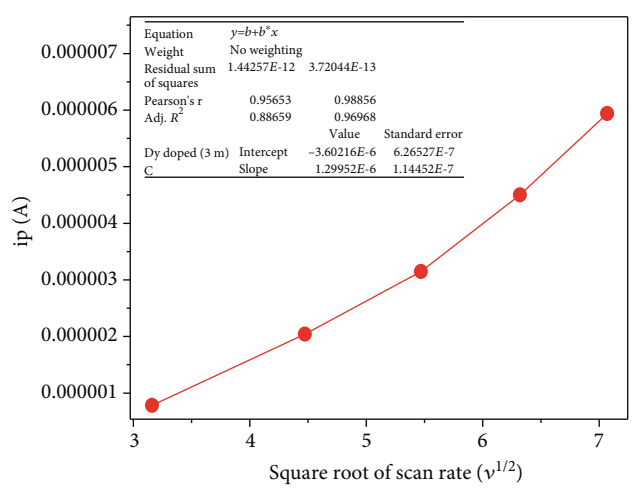


(b)

Figure 11: Cyclic voltammogram of Dy-doped (3 mol%) $ZrO_2$ sample at different scan rates v/s silver-silver chloride electrode. (b) A plot of cathodic peak current (ip) and the square root of scan rate ($v_{1/2}$) for $Dy^{3+}$-doped (3 mol%) $ZrO_2$ electrode.

Table 4: Oxidation potential ($E_O$), reduction potential ($E_R$), the difference between $E_O$ and $E_R$, diffusion coefficient of $Dy^{3+}$-doped $ZrO_2$ (1–11 mol%) electrodes.

| Name of the sample | $E_O$ (V) | $E_R$ (V) | $E_O$ (V) – $E_R$ (V) |
|---|---|---|---|
| 1% $Dy^{3+}$-doped $ZrO_2$ | 0.3732 | 0.0204 | 0.3528 |
| 3% $Dy^{3+}$-doped $ZrO_2$ | 0.4536 | 0.3824 | 0.0712 |
| 5% $Dy^{3+}$-doped $ZrO_2$ | 0.4812 | 0.3741 | 0.1071 |
| 7% $Dy^{3+}$-doped $ZrO_2$ | 0.1808 | -0.0792 | 0.2600 |
| 9% $Dy^{3+}$-doped $ZrO_2$ | 0.2048 | -0.0436 | 0.2484 |
| 11% $Dy^{3+}$-doped $ZrO_2$ | 0.2039 | -0.0511 | 0.2550 |

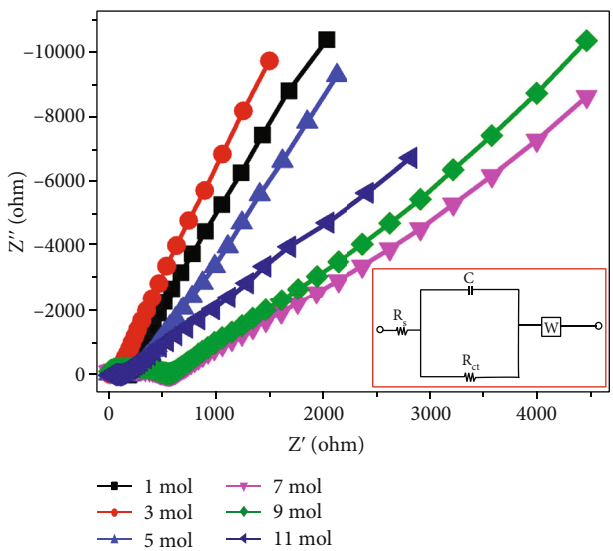


Figure 12: Nyquist plots of $Dy^{3+}$-doped $ZrO_2$ (1–11 mol%) electrodes.

the photocatalytic degradation efficiency. Acid red 88 was decolorized under solar light with $ZrO_2$:$Dy^{3+}$ catalysts in the following order: $ZrO_2$ : $Dy^{3+}$ (11 mol%) > ZrO2 : $Dy^{3+}$ (3 mol%) > ZrO2 : $Dy^{3+}$ (9 mol%) > ZrO2 : $Dy^{3+}$ (7 mol%) > ZrO2 : $Dy^{3+}$ (5 mol%) > ZrO2 : $Dy^{3+}$ (1 mol%) and is shown in Figures 8(a) and 8(b) and Table 2.

These findings imply that in the $ZrO_2$ lattice, an optimal dopant concentration of $Dy^{3+}$ exists, resulting in effective charge carrier separation. To check the performance of photocatalyst under the effect of pH, 11 mol% ZrO2:$Dy^{3+}$ NPs were assessed on the removal of acid red 88 at different values of pH. As the pH decreases, degradation of AR88 increases as shown in Figure 8(c). In acidic medium, photocatalytic activity increases due to the anionic nature of AR88 dye. An electrostatic force is generated between protonated surface of the catalyst $ZrO_2$:Dy in acidic medium and anionic dye AR88. Hence, dye adsorption on the catalyst surface is enhanced and photodegradation increases. In alkaline medium, there is repulsion between the negatively charged $ZrO_2$:Dy and anionic dye AR88 molecule; hence, percentage of degradation is less in alkaline medium compared to acidic medium.

Table 5: EIS data of $Dy^{3+}$-doped $ZrO_2$ (1–11 mol%) electrodes.

| Name of the sample | $R_S$ (V) | $R_{ct}$ (V) | $C_{dl}$ (F) |
|---|---|---|---|
| 1% $Dy^{3+}$-doped $ZrO_2$ | 1.948 | 161.34 | 0.000226 |
| 3% $Dy^{3+}$-doped $ZrO_2$ | 0.862 | 79.32 | 0.01512 |
| 5% $Dy^{3+}$-doped $ZrO_2$ | 1.594 | 94.43 | 0.003541 |
| 7% $Dy^{3+}$-doped $ZrO_2$ | 2.595 | 99.64 | 0.000865 |
| 9% $Dy^{3+}$-doped $ZrO_2$ | 2.578 | 110.52 | 0.000642 |
| 11% $Dy^{3+}$-doped $ZrO_2$ | 4.691 | 194.46 | 0.000835 |

Increasing the amount of $Dy^{3+}$ in the catalyst structure resulted in a greater surface barrier and a narrower space charge area, allowing the generated electron-hole pairs to be separated efficiently. Increases in $Dy^{3+}$ concentration up to a certain point cause the space charge layer to be breached, allowing light to penetrate deeper into ZrO2:$Dy^{3+}$ nanoparticles are a type of $Dy^{3+}$ nanoparticle [25]. The half-life of the degradation was calculated for each dopant, and it was found to be 25 min, 11.7 min, 18.3 min, 13.5 min, 12.43 min, and 10.55 min for 1, 3, 5, 7, 9, and 11 mol%, respectively. The respective results are shown in Figure 9. In comparison to the other dopants as mentioned in Table 3, the half-life required for degradation by 3 mol% and 11 mol% was substantially shorter. Hence, it can be concluded that the best suitable dopant for the degradation was 11 mol%.

According to the proposed mechanism, when light energy strikes the catalyst's surface, the electron in the valence band (VB) is stimulated to the empty conduction band (CB) (Figure 10), resulting in the production of electron-hole, which further react with the pollutant causing the formation of hydroxyl radicals or singlet oxygen radicals or holes which are responsible for the pollutant degradation [26–28].

When the migration occurs, these electron-hole pairs will be involved in the redox reaction. When holes combine with the hydroxide ion, it results in the formation of hydroxyl radicals, whereas the superoxide and hydrogen peroxide were produced due to the interaction of electrons with oxygen in the system. The produced superoxide and hydrogen peroxide react together by producing the hydroxyl radicals. In the final step, the produced radicals will react with the pollutant on the metal surface by forming the intermediate compounds in a short time. Finally, these radicals will help in the breakdown of the pollutant to form $CO_2$ and $H_2O$.

The 11mol% ZrO2:$Dy^{3+}$ NP reusability test was carried out with an AR88 concentration of 10 ppm, a photocatalyst dosage of 60 mg, and a reaction period of 90 min. To calculate the degrading efficiency loss after each run, six consecutive runs were made. The percentage of degradation for six cycles is 84%, 84%, 83.1%, 82.9%, 82.8%, and 82%, respectively. Even after the sixth run, the degrading efficiency barely decreased may be due to the loss of catalyst during filtration of the catalyst for the next cycle. It was shown that 11 mol% ZrO2:$Dy^{3+}$ NPs can be an effective photocatalyst with high reusability potential for the degradation of AR88 [37–44].

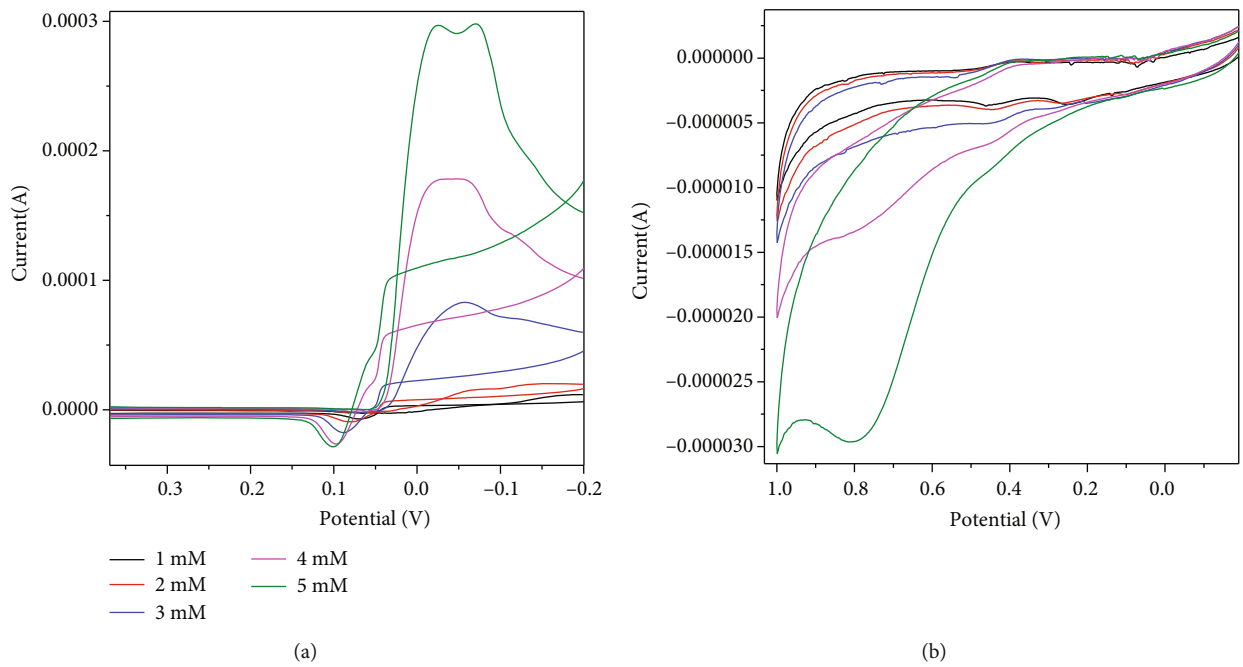


Figure 13: Cyclic voltammogram of $ZrO_2$:$Dy^{3+}$ (3 mol%) NP detection of (a) mercury and (b) lead of concentration range 1-5 mM.

### 3.5. Electrochemical Sensor Study

*3.5.1. Carbon Paste Electrode.* To make a carbon paste electrode, a mixture of the prepared sample $Dy^{3+}$-doped $ZrO_2$, graphite powder, and silicon oil (mass ratio of 15 : 70 : 15) was crushed in a mortar for 20 minutes. This powder was then gently pressed into a Teflon hollow tube (0.3 mm surface area) for further research [45].

*3.5.2. Electrochemical Studies.* Cyclic voltammetric measurements were performed using the three-electrode assembly in a 50 mL beaker chamber at room temperature. The energetic electrode material $ZrO_2$ undergoes a few strong Faradaic reactions that lead to a few strong redox peaks [46]. The CV activity of a (3 mol percent) sample in 1 N HCl at different moles using -0.4 to 0.6 V potentials and scan rates of 10 to 50 mV (Figure 11(a)) has been investigated. The observed capacitance was far from that of a typical double-layer electrical conductor, which typically displays a rectangular CV curve.

The linear connection between cathodic peak current (ip) and scan rate ($v_{1/2}$) (Figure 11(b)) demonstrates that hydrogen diffusion limits the electrode reaction of $Dy^{3+}$-doped $ZrO_2$ electrodes. The constructed electrode's hydrogen diffusion coefficient ($D$) was calculated using the slope of the fitted line in Figure 11(b). The value of $D$ is $1.299 \times 10^{-6}\ cm^2 s^{-1}$.

The greatest potential difference between the anodic ($E_O$) and cathodic ($E_R$) peaks for particular moles is a good predictor of redox reversibility. From Table 4, the $ZrO_2$ sample with 3 mol% $Dy^{3+}$ dopant has the lowest value, 0.0712 V, which is small when compared to other doped samples, indicating that it is more reversible [47].

Figure 12 shows the electrochemical impedance spectra of $Dy^{3+}$-doped $ZrO_2$ (1–11 mol percent) electrodes with a frequency range varying from 1 Hz to 1 MHz and a 5 mV amplitude. The spectra show a high-frequency load transfer resistance and a low-frequency slope associated with the Warburg resistance. The resistance of the $ZrO_2$ electrode with $Dy^{3+}$-doped (3 mol%) additive is substantially lower than that of other $Dy^{3+}$-doped $ZrO_2$ electrodes, suggesting that the 3 mol% additional electrode's electrochemical reaction is stronger than that of other electrodes [48]. A high-frequency zone marked by a semicircle depicts charge transport at the electrode/electrolyte interface, as well as a low-frequency zone denoted by a straight line that represents electrode capacitance. The diameter of the semicircle arc on the real axis can be used to calculate the charge transfer resistance $R_{ct}$ [49]. The sample's $R_{ct}$ value is lower because the semicircle arc has a smaller circumference. As the linear curve moves closer to the $y$-axis, it indicates that the sample has a high capacitance [50].

Additionally, this circumstance is associated to the ideals of $R_{ct}$ and $C$ yielded by circuit fitting (inset of Figure 12). As illustrated in the Nyquist plots, the resistance gauges the high-frequency semicircle of charge transfer ($R_{ct}$) and the capacitance ($C$) of the double layer.

Table 5 includes values that were obtained by fitting simulation data with an equivalency circuit and relate to the catalytic properties of active materials, such as solution resistance ($R_s$), charge transfer resistance ($R_{ct}$), and double-layer capacitance ($C_{dl}$). The charge transfer resistance is low due to the surface catalytic activity of the generated electrodes; when $ZrO_2$:$Dy^{3+}$ is used, the electrode double-layer capacitance is at its highest (3 mol percent) [34].

The cyclic voltammograms of $Dy^{3+}$-doped $ZrO_2$ (3 mol%) utilized for mercury and lead sensing are shown in Figure 13. As a consequence, peak position variation due to oxidation and reduction was justified. The

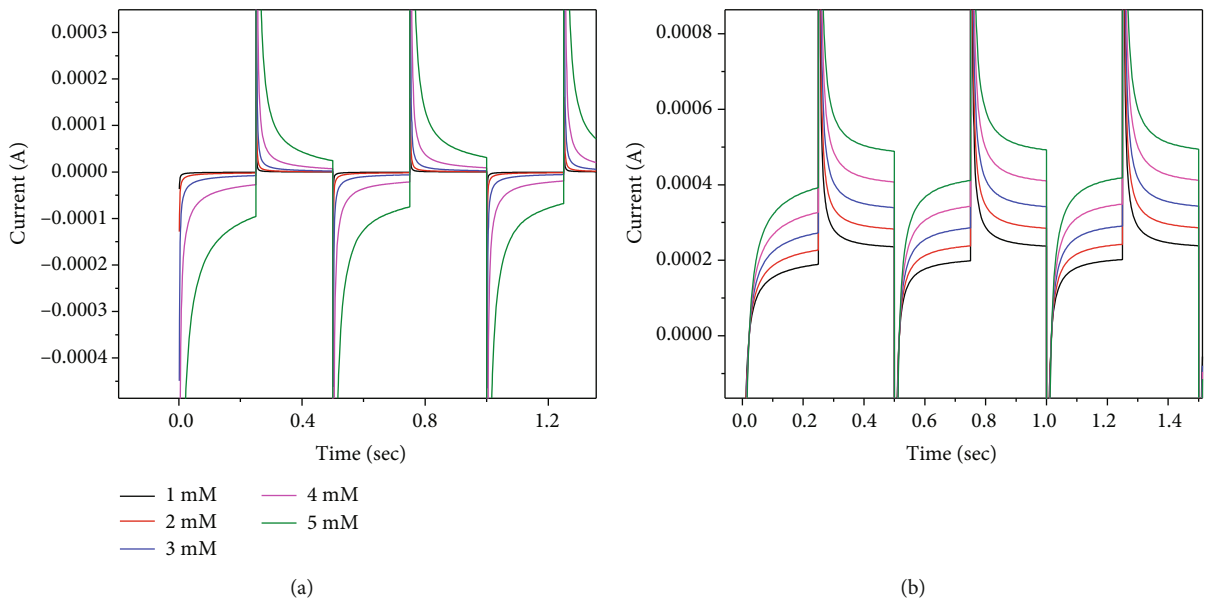


FIGURE 14: Amperometric $i-t$ curve for determination of mercury and lead using $ZrO_2$:$Dy^{3+}$ (3 mol%).

development of an anodic oxidation peak at 0.1 V and a cathodic reduction peak at -0.05 V during sensing, as well as the disappearance of the oxidation peak at 0.2 V, shows that the manufactured carbon paste electrode is successful in sensing approach for amounts 1-5 mM.

Nevertheless, the cyclic voltammogram of a lead sensor reveals that the entire voltammogram form changes, including the elimination of the oxidation and reduction peaks, but the introduction of an oxidation peak at 0.8 V. For 0 mM mercury and lead, the constructed electrode showed an initial current response of 60 s. Furthermore, the current response increases with continuous introduction of 1 mM mercury and lead (Figure 14), and within the brief time frame of 4 seconds, it approaches a steady current.

This result indicates that the sensor reacts quickly to mercury (0.0003 A) and lead (0.0008 A) oxidation. Finally, the positions of the reduction and oxidation peaks were determined to be considerably different, indicating that the electrodes produced are suitable for sensor applications without impacting other compounds in the sample.

## 4. Conclusion

A variety of nanoparticles ZrO2:$Dy^{3+}$ (1-11 mol percent) were prepared in this study using a simple and cheap propellant combustion process. The cubic phase of $Dy^{3+}$-doped $ZrO_2$ NPs was confirmed by PXRD and HRTEM. The average crystallite size, as determined by Debye Scherrer's and W–H techniques, was found to be between 8.1 and 16.3 nm. The results were very similar to those of the TEM. Under UV light, the photocatalytic activity of ZrO2:$Dy^{3+}$ increased as the concentration of $Dy^{3+}$ rose. All of the photocatalysts displayed increased activity for the breakdown of acid red 88 dye when exposed to UV light. The successful separation of charge carriers was related to the increased activity for the decolorization of acid red 88 under UV radiation. The reversibility of the carbon paste electrode made with $Dy^{3+}$-doped $ZrO_2$ NPs was excellent (lower value of $E_O - E_R$). Electrochemical impedance measurements revealed a low charge-transfer resistance, confirming its excellent conductivity. The proton diffusion coefficient ($D$) value of the $Dy^{3+}$-doped $ZrO_2$ electrode material was found to be $1.299 \times 10^{-6}\,cm^2s^{-1}$. These electrodes were particularly successful in sensing heavy metals like mercury and lead in acidic media, according to CV and amperometric studies. The electrode material's quick reaction (3 s) for sensing medicines at concentrations as low as 1 mM was the study's highlight. The study shows that $Dy^{3+}$-doped $ZrO_2$ is a viable and economical electrode material for upcoming sensing applications, which might be scaled up for commercialization.

## Data Availability

The data used to support the findings of this study are included within the article.

## Conflicts of Interest

The authors declare no conflict of interest.

## Acknowledgments

We would like to express our deepest regards for the Centre for Advanced Materials & Technology, M.S. Ramaiah Institute of Technology, Bangalore, India, for their support and help toward characterization analysis.

## References

[1] L. Liao, J. W. Bai, Y. C. Lin, Y. Q. Qu, Y. Huang, and X. F. Duan, "High-performance top-gated graphene-nanoribbon transistors using zirconium oxide nanowires as high-dielectric-constant gate dielectrics," *Advanced Materials*, vol. 22, pp. 1941–1945, 2010.

[2] M. F. Hanafi and N. Sapawe, "The potential of $ZrO_2$ catalyst toward degradation of dyes and phenolic compound," *Materials Today: Proceedings*, vol. 19, pp. 1524–1528, 2019.

[3] I. John Berlin, J. S. Lakshmi, S. Sujatha Lekshmy, G. P. Daniel, P. V. Thomas, and K. Joy, "Effect of sol temperature on the structure, morphology, optical and photoluminescence properties of nanocrystalline zirconia thin films," *Journal of Sol-Gel Science and Technology*, vol. 58, no. 3, pp. 669–676, 2011.

[4] I. John Berlin, L. V. Maneeshya, K. Jijimon, P. V. Thomas, and K. Joy, "Enhancement of photoluminescence emission intensity of zirconia thin films via aluminum doping for the application of solid state lighting in light emitting diode," *Journal of Luminescence*, vol. 132, no. 11, pp. 3077–3081, 2012.

[5] I. John Berlin, V. S. Anitha, P. V. Thomas, and K. Joy, "Influence of oxygen atmosphere on the photoluminescence properties of sol–gel derived $ZrO_2$ thin films," *Journal of Sol-Gel Science and Technology*, vol. 64, no. 2, pp. 289–296, 2012.

[6] T. Ninjbadgar, G. Garnweitner, A. Borger, L. M. Goldenberg, O. V. Sakhno, and J. Stumpe, "Synthesis of luminescent $ZrO_2$: $Eu^{3+}$ nanoparticles and their holographic submicrometer patterning in polymer composites," *Advanced Functional Materials*, vol. 9, pp. 1819–1825, 2009.

[7] H. Hobbs, S. Briddon, and E. Lester, "The synthesis and fluorescent properties of nanoparticulate $ZrO_2$ doped with Eu using continuous hydrothermal synthesis," *Green Chemistry*, vol. 11, no. 4, pp. 484–491, 2009.

[8] S. D. Meetei and S. D. Singh, "Hydrothermal synthesis and white light emission of cubic $ZrO_2$:$Eu^{3+}$ nanocrystals," *Journal of Alloys and Compounds*, vol. 587, pp. 143–147, 2014.

[9] F. Gu, S. F. Wang, M. K. Lu et al., "Effect of $Dy^{3+}$ doping and calcination on the luminescence of $ZrO_2$ nanoparticles," *Chemical Physics Letters*, vol. 380, no. 1-2, pp. 185–189, 2003.

[10] L. A. D. Torres, E. D. la Rosa, P. Salas, V. H. Romero, and C. A. Chavez, "Efficient photoluminescence of $Dy_3$+ at low concentrations in nanocrystalline $ZrO_2$," *Journal of Solid State Chemistry*, vol. 181, no. 1, pp. 75–80, 2008.

[11] S. T. Fardood, F. Moradnia, R. Forootan et al., "Facile green synthesis, characterization and visible light photocatalytic activity of $MgFe_2O_4$@$CoCr_2O_4$ magnetic nanocomposite," *Journal of Photochemistry and Photobiology A: Chemistry*, vol. 423, article 113621, 2022.

[12] M. Muthuraman, N. A. Dhas, and K. C. Patil, "Combustion synthesis of oxide materials for nuclear waste immobilization," *Bulletin of Materials Science*, vol. 17, no. 6, pp. 977–987, 1994.

[13] A. Khataee, R. D. C. Soltani, Y. Hanifehpour, M. Safarpour, H. G. Ranijbar, and S. W. Joo, "Synthesis and characterization of dysprosium-doped ZnO nanoparticles for photocatalysis of a textile dye under visible light irradiation," *Industrial and Engineering Chemistry Research*, vol. 53, no. 5, pp. 1924–1932, 2014.

[14] M. Thommes, K. Kaneko, A. V. Neimark et al., "Physisorption of gases, with special reference to the evaluation of surface area and pore size distribution (IUPAC technical report)," *Chem*, vol. 87, no. 9-10, pp. 1051–1069, 2015.

[15] K. A. Cychosz and M. Thommes, "Progress in the physisorption characterization of nanoporous gas storage materials," *Engineering*, vol. 4, no. 4, pp. 559–566, 2018.

[16] M. Fan, X. Zeng, X. Yang, X. Zhang, and B. Ren, "Rational design of asymmetric supercapacitorsviaa hierarchical core–shell nanocomposite cathode and biochar anode," *RSC Advances*, vol. 9, no. 72, pp. 42543–42553, 2019.

[17] K. S. Walton and R. Q. Snurr, "Applicability of the BET method for determining surface areas of microporous metal –organic frameworks," *American Chemical Society*, vol. 129, no. 27, pp. 8552–8556, 2007.

[18] K. Gurushantha, K. S. Anantharaju, H. Nagabhushana et al., "Facile green fabrication of iron-doped cubic $ZrO_2$ nanoparticles by _Phyllanthus acidus_ : structural, photocatalytic and photoluminescent properties," *Journal of Molecular Catalysis A: Chemical*, vol. 397, pp. 36–47, 2015.

[19] D. Prakashbabu, R. H. Krishna, B. M. Nagabhushana et al., "Low temperature synthesis of pure cubic $ZrO_2$ nanopowder: structural and luminescence studies," *Spectrochimica Acta Part A: Molecular and Biomolecular Spectroscopy*, vol. 122, pp. 216–222, 2014.

[20] R. Suresh, V. Ponnuswamy, and R. Mariappan, "Effect of annealing temperature on the microstructural, optical and electrical properties of $CeO_2$ nanoparticles by chemical precipitation method," *Applied Surface Science*, vol. 273, pp. 457–464, 2013.

[21] L. X. Lovisa, J. Andres, L. Gracia et al., "Photoluminescent properties of $ZrO^2$: $Tm^{3+}$, $Tb^{3+}$, $Eu^{3+}$ powders- a combined experimental and theoretical study," *Journal of Alloys and Compounds*, vol. 695, pp. 3094–3103, 2017.

[22] A. A. Nashivochnikov, A. I. Kostyukov, A. V. Zhuzhgov, M. I. Rakhmanova, S. V. Cherepanova, and V. N. Snytnikov, "Shaping the photoluminescence spectrum of $ZrO_2$: $Eu^{3+}$ phosphor in dependence on the Eu concentration," *Optical Materials*, vol. 121, article 111620, 2021.

[23] A. King, R. Singh, R. Anand, S. K. Behera, and B. B. Nayak, "Dopant concentration induced tuning of emission in $Eu^{3+}$-doped zirconia nanoparticles," *Journal of Physics and Chemistry of Solids*, vol. 163, article 110575, 2022.

[24] R. K. Tamrakar, D. P. Bisen, and K. Upadhyay, "Photoluminescence behavior of $ZrO_2$: $Eu^{3+}$ with variable concentration of $Eu^{3+}$ doped phosphor," *Journal of Radiation Research and Applied Sciences*, vol. 8, no. 1, pp. 11–16, 2015.

[25] A. Martínez-Hernández, J. Guzmán-Mendoza, T. Rivera-Montalvo et al., "Synthesis and cathodoluminescence characterization of $ZrO_2$:$Er^{3+}$ films," *Journal of Luminescence*, vol. 153, pp. 140–143, 2014.

[26] A. Naveen Kumar, D. M. Jnaneshwara, H. Nagabhushana et al., "Enhanced photoluminescence, electrochemical and photocatalytic activity of combustion synthesized $La_{10}Si_6O_{27}$: $Dy^{3+}$ nanophosphors," *Journal of Science: Advanced Materials and Devices*, vol. 6, pp. 49–57, 2021.

[27] B. N. Lakshminarasappa, S. C. Prashantha, and F. Singh, "Ionoluminescence studies of combustion synthesized $Dy^{3+}$ doped nano crystalline forsterite," *Current Applied Physics*, vol. 11, pp. 1274–1277, 2011.

[28] L. G. Devi, S. G. Kumar, K. M. Reddy, and C. Munikrishnappa, "Effect of various inorganic anions on the degradation of Congo Red, a di azo dye, by the photo-assisted Fenton process using zero-valent metallic iron as a catalyst," *Desalination and Water Treatment*, vol. 4, no. 1-3, pp. 294–305, 2009.

[29] L. Renuka, K. S. Anantharaju, Y. S. Vidya et al., "A simple combustion method for the synthesis of multi-functional $ZrO_2$/CuO nanocomposites: excellent performance as sunlight photocatalysts and enhanced latent fingerprint detection," *Applied Catalysis. B, Environmental*, vol. 210, pp. 97–115, 2017.

[30] C. Gionco, S. Hernández, M. Castellino et al., "Synthesis and characterization of Ce and Er doped $ZrO_2$ nanoparticles as

solar light driven photocatalysts," *Journal of Alloys and Compounds*, vol. 775, pp. 896–904, 2019.

[31] C. Pratapkumar, S. C. Prashantha, V. G. Dileep Kumar et al., "Structural, photocatalytic and electrochemical studies on facile combustion synthesized low-cost nano chromium (III) doped polycrystalline magnesium aluminate spinels," *Journal of Science: Advanced Materials and Devices*, vol. 6, no. 3, pp. 462–471, 2021.

[32] S. Li, C. Wang, M. Cai et al., "Facile fabrication of TaON/$Bi_2MoO_6$ core–shell S-scheme heterojunction nanofibers for boosting visible-light catalytic levofloxacin degradation and Cr (VI) reduction," *Chemical Engineering Journal*, vol. 428, article 131158, 2022.

[33] X. Liu, G. Shaonan, Y. Zhao, G. Zhou, and W. Li, "$BiVO_4$, $Bi_2WO_6$ and $Bi_2MoO_6$ photocatalysis: a brief review," *Journal of Materials Science & Technology*, vol. 56, pp. 45–68, 2020.

[34] Z. Jun-Yu, L. Hong-Gang, and S. Shi-Gang, "Construction of 1D/1D$WO_3$nanorod/$TiO_2$ nanobelt hybrid heterostructure for photocatalytic application," *Chinese Journal of Structural Chemistry*, vol. 39, no. 6, pp. 1019–1028, 2020.

[35] J. Wang, G. Wang, B. Cheng, J. Yu, and J. Fan, "Sulfur-doped g-$C_3N_4$/$TiO_2$ S-scheme heterojunction photocatalyst for Congo Red photodegradation," *Chinese Journal of Catalysis*, vol. 42, no. 1, pp. 56–68, 2021.

[36] C. H. E. N. Yi-Lan, X. U. Yu-Xian, L. I. N. Dai-Feng, L. U. O. Yong-Jin, X. U. E. Hun, and C. H. E. N. Qing-Hua, "Insight into superior visible light photocatalytic activity for degradation of dye over corner-truncated cubic $Ag_2O$ decorated $TiO_2$ hollow nanofibers," *Chinese Journal of Structural Chemistry*, vol. 39, no. 3, pp. 588–597, 2020.

[37] J. Zhao, S. Ge, D. Pan et al., "Solvothermal synthesis, characterization and photocatalytic property of zirconium dioxide doped titanium dioxide spinous hollow microspheres with sunflower pollen as bio-templates," *Journal of Colloid and Interface Science*, vol. 529, pp. 111–121, 2018.

[38] V. Ruíz-Santoyo, V. F. Marañon-Ruiz, R. Romero-Toledo, O. A. González Vargas, and A. Pérez-Larios, "Photocatalytic degradation of rhodamine B and methylene orange using $TiO_2$-$ZrO_2$ as nanocomposite," *Catalysts*, vol. 11, article 1035, 2021.

[39] K. Gurushantha, K. S. Anantharaju, S. C. Sharma et al., "Biomediated Sm doped nano cubic zirconia: photoluminescent, Judde Ofelt analysis, electrochemical impedance spectroscopy and photocatalytic performance," *Journal of Alloys and Compounds*, vol. 685, pp. 761–773, 2016.

[40] M. Ikram, R. Asghar, M. Imran et al., "Experimental and computational study of Zr and CNC-doped $MnO_2$ nanorods for photocatalytic and antibacterial activity," *ACS Omega*, vol. 7, no. 16, pp. 14045–14056, 2022.

[41] A. Ul-Hamid, M. Ikram, A. Haider et al., "In-situ phenylhydrazine chemical detection based on facile Zr-doped $MoS_2$ nanocomposites (NCs) for environmental safety," *Journal of the Taiwan Institute of Chemical Engineers*, vol. 120, pp. 267–277, 2021.

[42] M. Ikram, J. Hassan, A. Raza et al., "Photocatalytic and bactericidal properties and molecular docking analysis of $TiO_2$nanoparticles conjugated with Zr for environmental remediation," *RSC Advances*, vol. 10, no. 50, pp. 30007–30024, 2020.

[43] M. Ikram, R. Tabassum, U. Qumar et al., "Promising performance of chemically exfoliated Zr-doped $MoS_2$ nanosheets for catalytic and antibacterial applications," *RSC Advances*, vol. 10, no. 35, pp. 20559–20571, 2020.

[44] J. Kim, D. Rhee, O. Song et al., "All-solution-processed van der Waals heterostructures for wafer-scale electronics," *Advanced Materials*, vol. 34, no. 12, 2022.

[45] E. Kharatzadeh, S. R. Masharian, and R. Yousefi, "The effects of S-doping concentration on the photocatalytic performance of SnSe/S-GO nanocomposites," vol. 32, no. 2, pp. 346–357, 2021.

[46] M. R. Anil Kumar, B. Abebe, H. P. Nagaswarupa, H. C. Ananda Murthy, C. R. Ravikumar, and F. K. Sabir, "Enhanced photocatalytic and electrochemical performance of $TiO_2$-$Fe_2O_3$ nanocomposite: its applications in dye decolorization and as supercapacitors," *Scientific Reports*, vol. 10, no. 1, pp. 1–15, 2020.

[47] N. Montoya, P. Pardo, A. Doménech-Carbó, and J. Alarcón, "Structural stability and electrochemical properties of Gd-doped $ZrO_2$ nanoparticles prepared by sol–gel," *Journal of Sol-Gel Science and Technology*, vol. 69, no. 1, pp. 137–147, 2014.

[48] C. V. Reddy, I. N. Reddy, J. Shim, D. Kim, and K. Yoo, "Synthesis and structural, optical, photocatalytic, and electrochemical properties of undoped and yttrium-doped tetragonal $ZrO_2$ nanoparticles," *Ceramics International*, vol. 44, no. 11, pp. 12329–12339, 2018.

[49] K. Y. Zhang and Y. Zhai, "Preparation of Y-doped $ZrO_2$ coatings on $MnO_2$ electrodes and their effect on electrochemical performance for $MnO_2$ electrochemical supercapacitors," *RSC Advances*, vol. 6, pp. 1750–1759, 2016.

[50] N. Smirnova, Y. Gnatyuk, A. Eremenko et al., "Photoelectrochemical characterization and photocatalytic properties of mesoporous $TiO_2$/$ZrO_2$ films," *International Journal of Photoenergy*, vol. 2006, Article ID 85469, 6 pages, 2006.

Hindawi
Adsorption Science & Technology
Volume 2022, Article ID 6818348, 16 pages
https://doi.org/10.1155/2022/6818348

*Research Article*

# Evaluation of Zn Adenine-Based Bio-MOF for Efficient Remediation of Different Types of Dyes

**Eslam Salama,[1] Ali Hamdy,[2,3] Hassan S. Hassan,[4,5] Wael A. Amer,[2,6] El-Zeiny M. Ebeid,[2,7] Mona Ossman,[1] and Marwa F. Elkady[8,9]**

[1]*Environment and Natural Materials Research Institute (ENMRI), City of Scientific Research and Technological Applications (SRTA-City), New Borg El-Arab City, Alexandria 21934, Egypt*
[2]*Chemistry Department, Faculty of Science, Tanta University, Tanta 31527, Egypt*
[3]*Environmental Biotechnology Department, Genetic Engineering and Biotechnological Research Institute (GEBRI), City of Scientific Research and Technological Applications (SRTA-City), New Borg El-Arab City, Alexandria 21934, Egypt*
[4]*Electronic Materials Research Department, Advanced Technology and New Materials Research Institute (ATNMRI), City of Scientific Research and Technological Applications (SRTA-City), New Borg El-Arab City, Alexandria 21934, Egypt*
[5]*Environmental Engineering Department, Egypt-Japan University of Science and Technology, New Borg El-Arab City, Alexandria 21934, Egypt*
[6]*Department of Chemistry, College of Science, University of Bahrain, Sakhir 32038, Bahrain*
[7]*Center of Basic Sciences (CBS), Misr University for Science and Technology (MUST), 6th of October City 12563, Egypt*
[8]*Fabrication Technology Research Department, Advanced Technology and New Materials Research Institute (ATNMRI), City of Scientific Research and Technological Applications (SRTA-City), New Borg El-Arab City, Alexandria 21934, Egypt*
[9]*Chemical and Petrochemical Engineering Department, Egypt-Japan University of Science and Technology (E-JUST), New Borg El-Arab City, Alexandria 21934, Egypt*

Correspondence should be addressed to Eslam Salama; eslamsobhysalama@gmail.com

Received 6 January 2022; Revised 10 July 2022; Accepted 2 August 2022; Published 13 August 2022

Academic Editor: Adrián Bonilla-Petriciolet



As an eco-friendly material, Zn-adeninate bio-metal-organic framework (bio-MOF) was investigated as an efficient adsorbent for both anionic and cationic dyes. The adsorption capability of the synthesized Zn-adeninate bio-MOF was confirmed by its notable surface area of 52.62 $m^2 g^{-1}$ and total pore volume of 0.183 $cm^3 g^{-1}$. The bio-MOF adsorption profiles of anionic direct red 81 (DR-81) and cationic methylene blue (MB) dyes were investigated under different operating parameters. The optimum dosages of Zn-adeninate bio-MOF were 0.5 $g L^{-1}$ and 1 $g L^{-1}$ for MB and DR-81 decolorization, respectively. The $pH_{PZC}$ of Zn-adeninate bio-MOF was 7.2, and maximum monolayer adsorption capacity was 132.15 $mg g^{-1}$ for MB, which decreased to 82.54 $mg g^{-1}$ for DR-81 dye. Thermodynamic data indicated the spontaneous and endothermic nature of the decolorization processes. Additionally, the adsorption processes were in agreement with the Langmuir and pseudo-second-order kinetic models. The synthesized Zn-adeninate bio-MOF could be reused several times with high decolorization ability. These findings demonstrated that the synthesized Zn bio-MOF is an effective and promising adsorbent material for the removal of both cationic and anionic dyes from polluted water.

## 1. Introduction

Water accounts for approximately 70% of the Earth's surface, but only approximately 3% is freshwater. A large fraction of the freshwater is locked up in glacial ice caps or at great depths under the surface of the earth, which is difficult to extract and hence is not used by humans. Moreover, a high percentage of the freshwater has become highly polluted, leaving only 0.4% as usable, which is insufficient for the 7.80 billion people living on the earth [1]. The safety of water sources is the most challenging matter related to water sustainability that is faced by several countries worldwide.

Contamination of water with harmful materials, such as organic dyes and heavy metal ions, is a severe problem because of their toxic and carcinogenic nature [2].

Currently, a large number of fabricated dyes are produced annually around the globe, and approximately 10% of these are discharged into the environment as wastewater because they (50% concentration) do not strictly bind to the fibers and can act as liquid contaminants [3]. Additionally, the multifaceted aromatic structures of the synthetic dyes make them stable and difficult to decompose [4]. The aromatic amines created after the degradation of azo dyes, a type of synthetic dye, are highly toxic [5]. Moreover, approximately 40% of the dyes contain organically bound chlorine, which is a known carcinogen [6]. Further, the discharge of dye-polluted liquids into streams and rivers lowers dissolved oxygen and enables anaerobic media, which can destroy aquatic organisms [4].

Direct dyes are characterized by their affinity for bleached and unbleached chemical pulps and are primarily used in the pulp and textile industries. They usually contain sulfonic acid groups and at least one azo group that imparts water solubility to the dyes. Direct red-81 dye (DR-81) is one of the most famous anionic azo dyes used in industrial applications (Figure 1(a)) [7]. By contrast, methylene blue (3,7-bis(dimethylamino)-phenothiazin-5-ium chloride) (MB) or basic blue-9 is a univalent cationic dye with the molecular formula of $C_{16}H_{18}N_3ClS$, as shown in Figure 1(b), and is utilized for biological staining as well as coloring hair, papers, wool, and cotton [8]. However, the accumulation of MB in water has undesirable health effect, including eye burns, breathing problems, diarrhea, and nausea [9].

Accordingly, researchers have investigated various techniques for wastewater treatment, such as advanced oxidation processes [10], electrocoagulation, coagulation/flocculation [11], adsorption [12–14], activated sludge processes [15], filtration [16], ion exchange [17], photodegradation [18], membrane bioreactors [19], bed biofilm reactors [20], and constructed wetlands (CW) [21]. Among these techniques, adsorption is a very efficient removal technique because of its ease of operation, high removal efficiency, reusability of the adsorbents, and cost-effectiveness. Adsorption involves transition of solids from the solution to the adsorbent surface [22]. Several adsorbents, such as carbon-based nanoadsorbents, polymer-based adsorbents, biosorbents, transition metal-based oxides, and metal-organic frameworks (MOFs), have been employed to remove dyes from wastewater [1, 23–25]. Recent studies have found that MOFs are powerful adsorbents compared to other materials owing to their high surface areas and porous structures [1, 26].

MOFs are a category of hybrid materials that contain metal ion-based matrices and organic ligands that attach the vertices to form two- or three-dimensional periodic structures [1]. The appropriate choice of organic ligands and vertices results in the synthesis of MOFs with different pore sizes, topologies, and geometries. Several techniques, such as defect engineering, modulation of noncovalent interactions, and functionalization of organic ligands [26], have been developed to prepare porous frameworks for adsorbing organic dyes with high selectivity. Significant advancements have been made in the design of water-stable MOFs. MOFs can be soaked in water for extended periods at various pH values without changing their structures [27]. Consequently, MOFs are considered promising materials for wastewater remediation owing to their impressive properties and specific interactions with the pollutants, in addition to their catalytic activities against specific organic pollutants [28].

In recent years, bio-MOFs have attracted significant interest as green sustainable frameworks. Derived biomolecules that are usually readily biodegradable and nontoxic are combined to synthesize bio-MOFs [1, 29]. Biomolecules, such as polysaccharides, amino acids, nucleobases, and peptides, are combined with metal ions to synthesize bio-MOFs. Salamat et al. studied the combination of a polysaccharide with metal ions for MOF crystallization under biocompatible conditions. The hydroxyl groups present on the polysaccharide molecules were found to assist in the coordination interactions with the metal ions. Hence, functional polysaccharides trigger the formation of MOFs by controlling the morphological structure and particle size of the prepared MOFs [30]. Furthermore, the integration of the functionalized biopolymers with MOF materials can improve the biocompatibility, adsorption, and flexibility of the composite materials, which can extend their application in biocatalysis and biological sciences [31]. Zn-based bio-MOFs have been used for the wastewater remediation because of their high porosity, which simplifies the decontamination process of pollutants [1]. The existence of tunable chemical functions, such as $-NH_2$ groups, result in excellent removal capacities of the negative and positive dyes [32]. In this study, an eco-friendly reusable Zn-adeninate bio-MOF was synthesized and investigated as an effective adsorbent material for the anionic DR-81 and cationic MB dyes from polluted water.

## 2. Materials and Methods

*2.1. Materials.* Adenine and 4,4′-biphenyl dicarboxylic acid were purchased from Alfa Aesar and Acros Organics, respectively. Zinc acetate dihydrate and dimethylformamide (DMF, HPLC) were obtained from Fisher Scientific. DR-81 (MW = 675.60 g mol$^{-1}$) and MB (MW = 319.85 g mol$^{-1}$) were procured from Sigma-Aldrich. The chemicals were used as received.

*2.2. Synthesis of Zn-Adeninate Bio-MOF.* In a 25 mL screw-capped tube, 0.03378 g of adenine was dispersed in 5 mL of DMF. The dispersed adenine powder was sonicated at 70°C for 6 h in an isothermal sonicator to obtain a well-dispersed solution of the organic ligand. In another 25 mL screw-capped tube, 0.1097 g of zinc acetate dihydrate was dissolved in 10 mL of DMF. Additionally, 0.12111 g of 4,4′-biphenyl dicarboxylic acid was dispersed in 6 mL of DMF, and all the tubes were sonicated in an isothermal sonicator for 6 h. Zinc acetate dihydrate solution was added to the dispersed adenine solution, and the dispersed 4,4′-biphenyl dicarboxylic acid solution was added to the mixture. Subsequently, 4 mL of DMF, 2 mL of methanol, and 0.5 mL of nanopure water were added to the mixture. Finally, the reaction mixture was heated

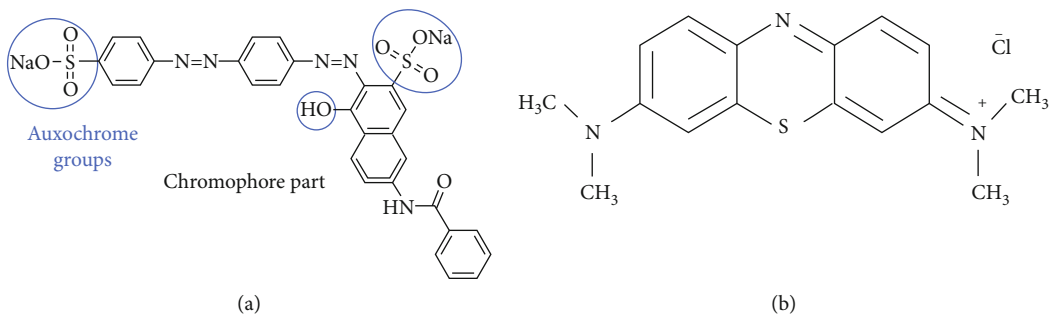


Figure 1: Structures of (a) direct red-81 and (b) methylene blue.

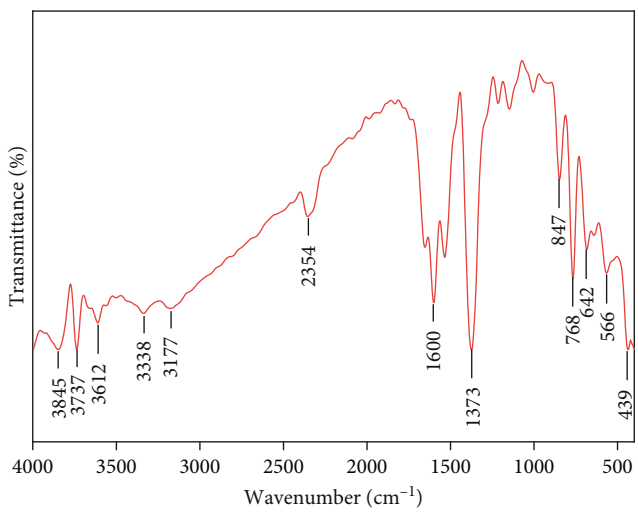


Figure 2: FTIR spectrum of the prepared Zn-adeninate bio-MOF.

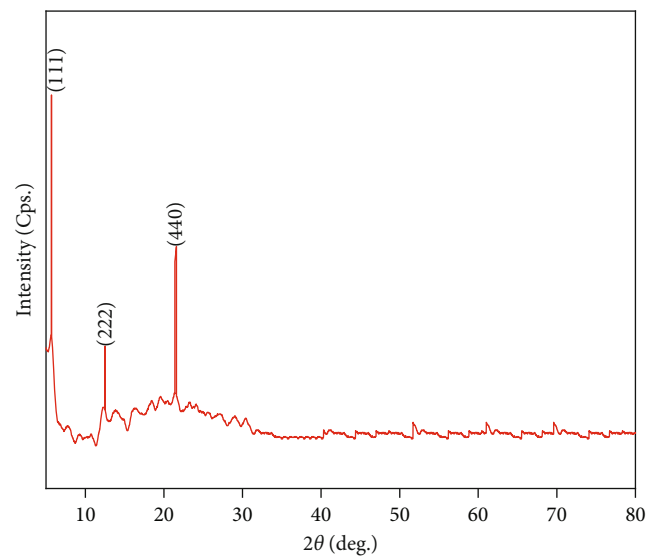


Figure 3: XRD pattern of the synthesized Zn-adeninate bio-MOF.

at 85°C for 24 h. After cooling to room temperature (23°C), the formed white precipitate was collected by centrifugation for 15 min at 6000 rpm, washed three times with 3 mL of DMF, and subsequently dried in an oven at 50°C overnight.

*2.3. Characterization of the Synthesized Zn Bio-MOF.* The functional groups of the synthesized Zn-adeninate bio-MOF were determined by analyzing its infrared absorption spectrum obtained using a Thermo Scientific Nicolet (USA). X-ray photoelectron spectroscopy (XPS, Thermo Fisher Scientific, USA) was used to evaluate the chemical states of the synthesized Zn-adeninate bio-MOF. To determine the crystal structure of the synthesized Zn-adeninate bio-MOF, X-ray diffraction (XRD) pattern of the synthesized sample was obtained by a Shimadzu XRD-6100 diffractometer with Cu-K$\alpha$ radiation at $\lambda = 1.54$ Å. Scanning electron microscopy (SEM, JEOL JSM-6010LV) was used to determine the morphology of the fabricated bio-MOFs. Transmission electron microscopy (TEM, JEOL JEM-2100F) was employed to obtain high-resolution images of the fabricated bio-MOF for investigating its bulk morphology. The pore size and surface area of the synthesized material were determined using a Belsorp-max automated apparatus via degassing of the fabricated Zn-adeninate MOF at 200°C for 6 h before detection. The thermal stability of the fabricated bio-MOF was investigated using a TGA-50 (Shimadzu), and the weight loss of the material was recorded in the temperature range of 28–800°C under nitrogen gas atmosphere. The gas flow and material heating rates were 40 mL min$^{-1}$ and 10°C min$^{-1}$, respectively.

*2.4. Decolorization of Cationic and Anionic Dyes using the Synthesized Bio-MOF.* The characteristic adsorption affinity of the prepared Zn-adeninate bio-MOF was investigated for different pollutant dyes, including cationic and anionic dyes, using a batch technique. Subsequently, 50 mg of the synthesized Zn-adeninate bio-MOF was shaken at 23°C with 50 mL of the dye solution at different initial concentrations. The influence of adsorption parameters, such as pH (1–11), contact time (0–180 min), initial dye concentration (5–100 mg L$^{-1}$), material dosage (0.1–2 g L$^{-1}$), and reaction temperature (23–85°C), were investigated. The adsorption experiments were performed in triplicate to confirm the results, and the mean values were used for the data analysis. After the adsorption experiment, the supernatant was separated from the adsorbent material by centrifugation and

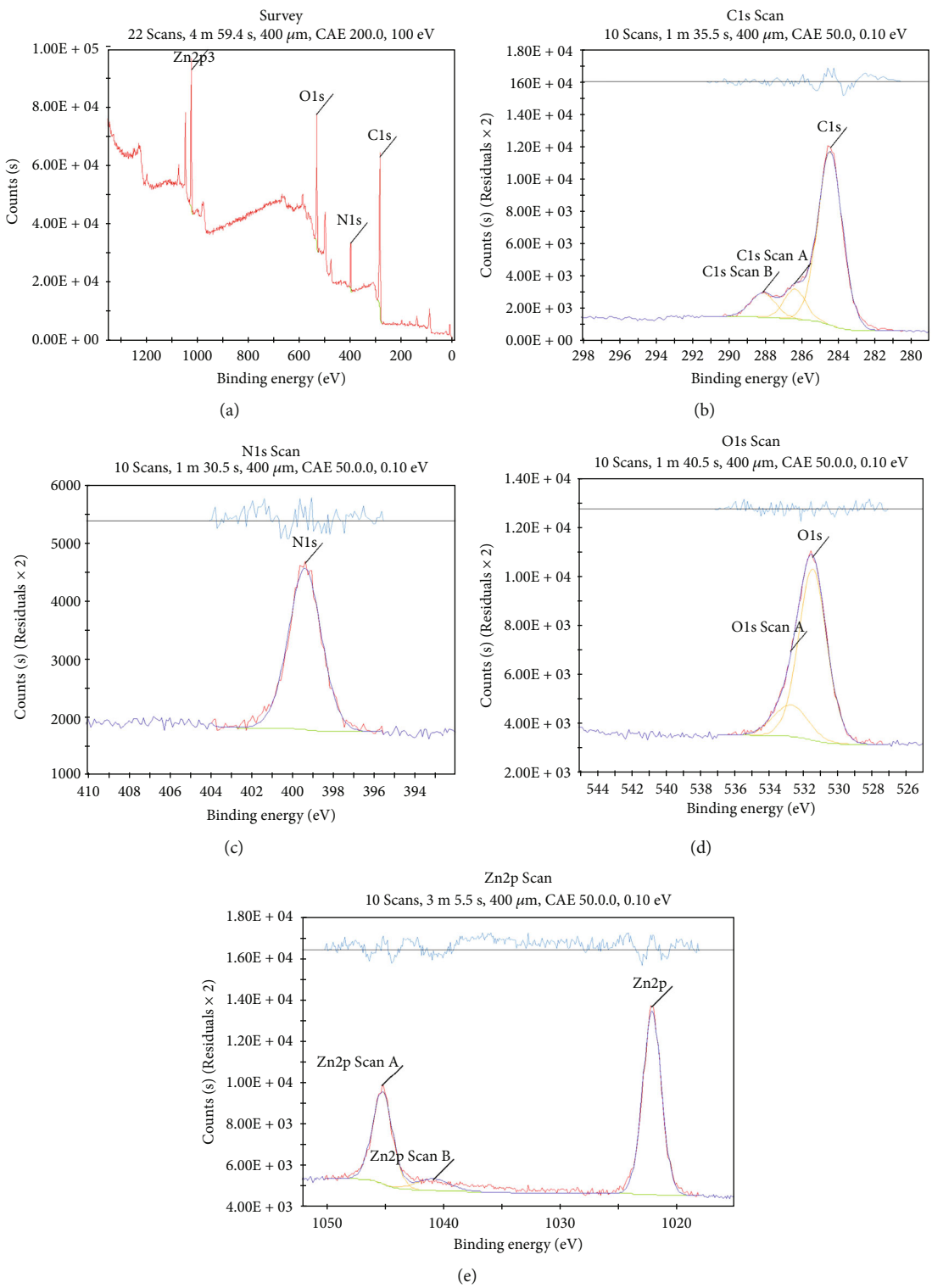


Figure 4: XPS spectra of the fabricated Zn-adeninate bio-MOF; (a) full spectrum, (b) C 1s spectrum, (c) N 1s spectrum, (d) O 1s spectrum, and (e) Zn 2p spectrum.

the absorbance of the supernatant was determined using a colorimetric method with a UV-visible spectrophotometer at 665 and 465 nm for MB and DR-81, respectively. The decolorization percentage of the dye by the synthesized Zn-adeninate bio-MOF was calculated using the following equation [33]:

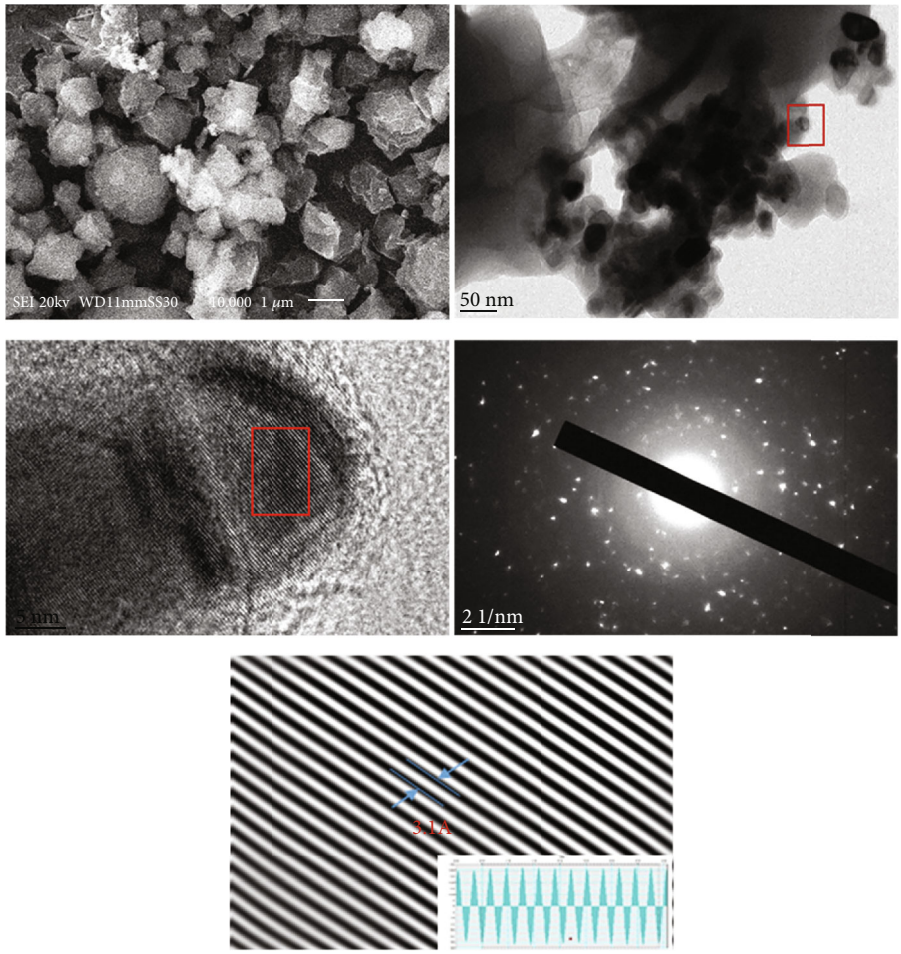


Figure 5: Morphological structures of the Zn-adeninate bio-MOF: (a) SEM and (b) TEM, HRTEM, fringe lattices, and SAED.

$$\text{Decolorization\%} = \left(\frac{C_o - C_e}{C_o}\right) \times 100, \quad (1)$$

where $C_e$ and $C_o$ refer to the equilibrium and initial pollutant concentrations ($\text{mg L}^{-1}$). The adsorption capacity ($\text{mg g}^{-1}$) was calculated using the following equation [13]:

$$q_e = \frac{V(C_o - C_e)}{m}, \quad (2)$$

where $V$ denotes the solution volume (L), $q_e$ denotes the adsorption capacity of the pollutant ($\text{mg g}^{-1}$), and $m$ denotes the mass of the fabricated Zn-adeninate bio-MOF (g).

The point of zero charge of the synthesized Zn-adeninate bio-MOF was determined by mixing 0.1 g of the adsorbent material with 25 mL of 0.01 molar NaCl. The pH of the solution was adjusted to 1–12 using 0.01 M NaOH and/or 0.01 M HCl. Equilibration was achieved by shaking the solution in a thermostatic bath at 25°C for 24 h. The powdered material was separated, and the final pH of the supernatant was determined. The pH of the final solution was plotted against the initial pH, and the pH value at which the curves intersected (pH (final) = pH (initial)) was the $\text{pH}_{\text{pzc}}$ of the fabricated Zn-adeninate bio-MOF [12].

*2.5. Thermodynamics, Equilibrium, and Kinetics of the Bio-MOF Adsorption Behavior.* The nature of the decolorization processes by the synthesized Zn-adeninate bio-MOF was evaluated by determining the thermodynamic parameters. The adsorption equilibrium was analyzed using the Langmuir, Freundlich, and Temkin isothermal models. Furthermore, the kinetics of the dye removal processes by the synthesized material were tested by applying the pseudo-first-order, pseudo-second-order, Elovich, and intraparticle kinetic models.

*2.6. Regeneration of the Prepared Zn Bio-MOF.* One gram of the used Zn-adeninate bio-MOF was recovered and washed three times with distilled water and 50 mL of methanol at 23°C, agitated at 150 rpm for 10 min, and dried at 150°C overnight for use in the subsequent adsorption experiments. Furthermore, the readsorption processes were performed at the following optimized removal conditions: *contact time* = 10 min for MB and 30 min for DR-81, *pH* = 7, bio-MOF *dosage* = $0.5\,\text{g L}^{-1}$ for MB and $1\,\text{g L}^{-1}$ for DR-

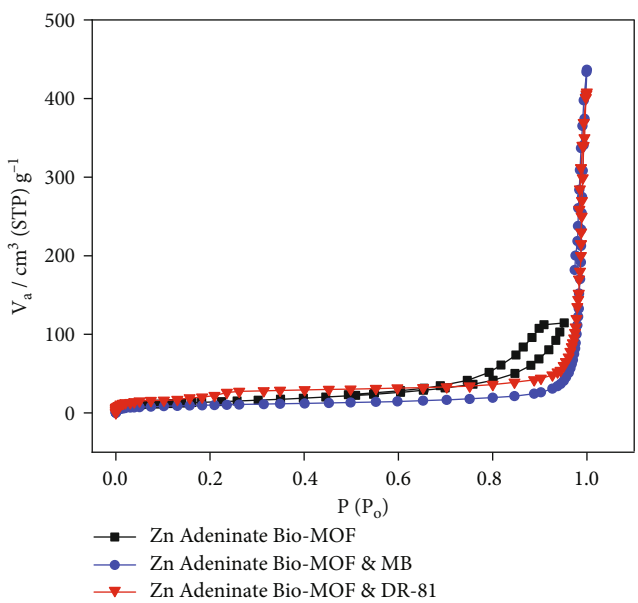


Figure 6: $N_2$ adsorption/desorption isotherm before and after decolorization of MB and DR-81 by the synthesized Zn-adeninate bio-MOF.

81, initial dye *concentration* = 10 ppm, agitation *speed* = 300 rpm, and solution *temperature* = 23°C.

## 3. Results and Discussion

*3.1. Characterization of the Fabricated Zn-Adeninate Bio-MOF.* The FT-IR spectrum of the prepared Zn-adeninate bio-MOF exhibited various characteristic peaks of both the organic framework ligands and metal. The C–O stretching peak of the carboxylic unit in the adeninate group was observed at 1600 $cm^{-1}$, as shown in Figure 2. The peak at 1373 $cm^{-1}$ accounts for the C–C stretching; additionally, most bands in the range of 3000–3800 $cm^{-1}$ were assigned to the OH unit of carboxylic acid [34]. The stretching frequencies of the N–H group of adenine are located in the range of 3117–3338 $cm^{-1}$ [35]. The peaks observed in the wavenumber range of 420–1000 $cm^{-1}$ are characteristic of the Zn–O bonds, confirming the presence of metal in the synthesized bio-MOF [36]. Therefore, the FT-IR spectrum contains the characteristic peaks of the synthesized Zn-adeninate bio-MOF.

The crystalline structure of the prepared Zn-adeninate bio-MOF was determined using XRD, as shown in Figure 3. The XRD pattern contains distinct Zn-adeninate bio-MOF peaks at 6.5°, 13.6°, and 21.8°, which can be attributed to the (111), (222), and (440) planes, respectively. These peaks are characteristic of the crystalline structure of bio-MOF and are completely different from the XRD patterns of ZnO [12, 37].

The chemical structure of the synthesized Zn-adeninate bio-MOF was investigated using XPS (Figure 4). The four peaks located at 284.2, 400, 531.6, and 1022.3 eV were assigned to C 1s, N 1s, O 1s, and Zn 2p, respectively. The C 1s spectra contained three peaks at binding energies (BE) of 284.2, 286.3, and 288.2 eV, which were related to the C=C, C=O, and $COO^-$/COOH functional groups, respectively [35]. The N 1s peak in the XPS spectrum of the synthesized Zn-adeninate bio-MOF indicated the presence of $-NH_2$ and $-NH_2/NH_3^+$ units [38]. Moreover, the N 1s peak characteristic of the $-NH_2$ species appeared at 399.3 eV, while the peaks corresponding to the H-bonded and/or quaternary ammonium structures were present at approximately 400 eV [1]. The O 1s spectrum contained the characteristic peak of the bridging hydroxyl ($\mu_3$-OH) group at 533 eV, while the Zn carboxylate and ($\mu_3$-O) in Zn–O peaks appeared at 531.6 eV and 531.4 eV, respectively [39]. The presence of Zn was confirmed by the appearance of Zn 2p peaks at 1022.3 and 1045.5 eV [35].

The morphology of the Zn-adeninate bio-MOF was analyzed using SEM, HRTEM, and SAED, as shown in Figure 5. The presence of large crystals in the SEM image was attributed to the agglomeration of the particles, which was proved *via* TEM. The SEM and TEM images confirmed the presence of uniform morphology with small nanoparticles in the synthesized Zn-adeninate bio-MOF sample, which was different from the extensive size distribution at the microscale observed in the previously prepared bio-MOFs. The reduction in the particle size of the synthesized sample can be attributed to the variations in the synthesis conditions, such as the long stirring time that results in the formation of smaller nanoparticles with a higher yield compared to the procedures previously described in the literature [40]. Moreover, the circular pattern observed in the SAED image revealed the homogeneous polycrystalline nature of the synthesized Zn-adeninate bio-MOF, which is in agreement with the XRD data.

The surface properties of the synthesized Zn-adeninate bio-MOF before and after the adsorption of different dyes were determined using the Brunauer-Emmett-Teller (BET) method and $N_2$ isotherms, as shown in Figure 6. The isotherms before and after adsorption were type III with relatively similar shapes, exhibiting an indistinct hysteresis loop related to $N_2$ condensation in the mesopores [41]. The specific surface area, mean pore diameter, and total pore volume of the prepared Zn-adeninate bio-MOF were approximately 52.62 $m^2 g^{-1}$, 14.454 nm, and 0.183 $cm^3 g^{-1}$, respectively. The large pore size and surface area of Zn-adeninate bio-MOF are appropriate for the utilization of the synthesized bio-MOF as an adsorbent for water pollutants [1]. After the adsorption process, the BET surface area of Zn-adeninate bio-MOF decreased to 34.06 $m^2 g^{-1}$ and 32.59 $m^2 g^{-1}$ for MB and DR-81, respectively. This was expected because of the agglomeration and blockage of pores in Zn-adeninate bio-MOF after the adsorption of MB and DR-81 ions [42].

The thermal profile of the synthesized Zn-adeninate bio-MOF was obtained in a nitrogen gas atmosphere to test its thermal stability. Multiple degradation stages are present in the thermogram of the synthesized bio-MOF, as shown in Figure 7. The first weight loss of approximately 17.5% occurred at 298°C, which can be assigned to the loss of gases and water molecules that penetrated the pores of bio-MOF [1, 33]. The second weight loss of stage is approximately 59% occurred in the temperature range of 298–510°C, which

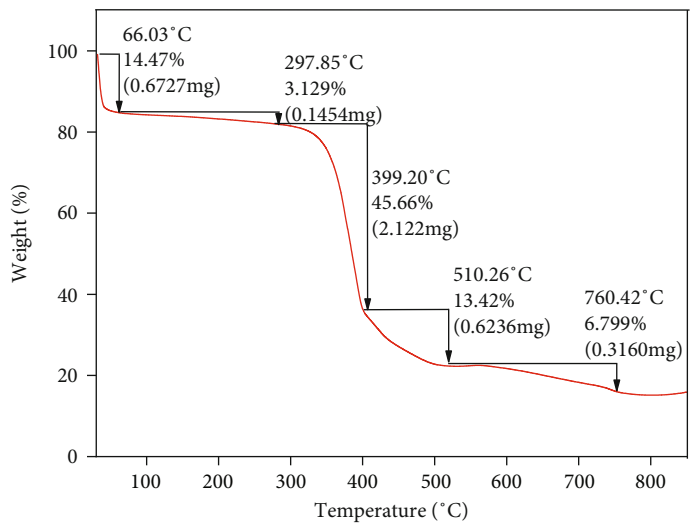


Figure 7: TGA plot of the synthesized Zn-adeninate bio-MOF.

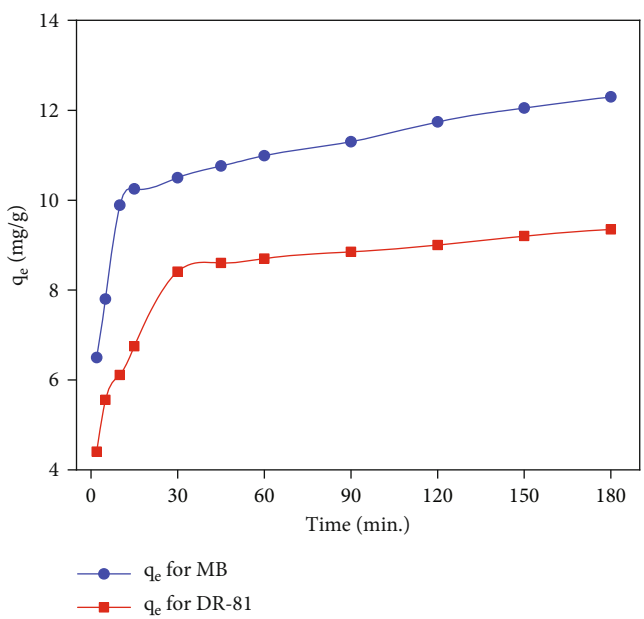


Figure 8: Effect of contact time on the adsorption capacity of the synthesized Zn-adeninate bio-MOF for the MB and DR-81 dyes (pH = 7, bio-MOF dosage = 1 g $L^{-1}$, initial concentration = 10 ppm, solution temperature = 23°C, and stirring speed = 300 rpm).

is related to the breakdown of the organic framework of the bio-MOF. These results demonstrated the excellent thermal stability of the prepared Zn-adeninate bio-MOF.

*3.2. Assessment of the Synthesized Zn-Adeninate Bio-MOF for Cationic and Anionic Decolorization from Wastewater.* The performance of the prepared Zn-adeninate bio-MOF was investigated for the decolorization of MB and DR-81 from the polluted synthetic solutions at room temperature via a batch technique.

*3.2.1. Influence of Contact Time on the Decolorization of Cationic and Anionic Dyes.* The effect of the contact time on the adsorption capacity of the synthesized Zn-adeninate bio-MOF for MB and DR-81 was evaluated at different time intervals of up to 180 min, as shown in Figure 8. The adsorption capacities increased with time until the equilibrium state was reached. The improvement in the adsorption capacities for the cationic and anionic dyes in the initial stage can be attributed to the functional groups that can bind with the target dyes and large surface area of the Zn-adeninate bio-MOF [1, 12]. The optimum contact time at neutral pH was 10 min for MB and 30 min for DR-81 with adsorption capacities of 9.88 and 8.41 mg $g^{-1}$ for MB and DR-81, respectively. After equilibrium was achieved, the active sites of the prepared adsorbent became saturated with MB and DR-81, limiting further removal [13]. These results demonstrated the high capacity of the synthesized Zn-adeninate bio-MOF to decolorize both anionic and cationic dyes in short contact times.

*3.2.2. Influence of Initial pH on the Decolorization of Cationic and Anionic Dyes.* The pH plays a significant role in the dye decolorization from wastewater. The pH directly affects the surface charge of the adsorbent and ionization degree of the pollutants [12, 43]. The $pH_{PZC}$ of Zn-adeninate bio-MOF was 7.2, as shown in Figure 9(a). This illustrates that the synthesized Zn-adeninate bio-MOF is positively charged till $pH = 7.2$ and negatively charged beyond this point [12]. The effect of pH on the decolorization process was studied at pH values ranging from 1 to 11. As shown in Figure 9(b), the acidic media were a promising candidate for decolorizing anionic DR-81 using Zn-adeninate bio-MOF. High decolorization values were recorded for the removal of DR-81 up to $pH = 7$, with an adsorption capacity of 8.41 mg $g^{-1}$, which then decreased to 3.13 mg $g^{-1}$ at $pH = 11$. By contrast, basic, neutral, and slightly acidic media favored MB decolorization. The adsorption capacity for MB decolorization was 9.89 mg $g^{-1}$ at $pH = 7$. As the pH of the solution increased to 11, the adsorption capacity of bio-MOF for MB reached 10.88 mg $g^{-1}$. Under alkaline conditions ($pH > 7$), more

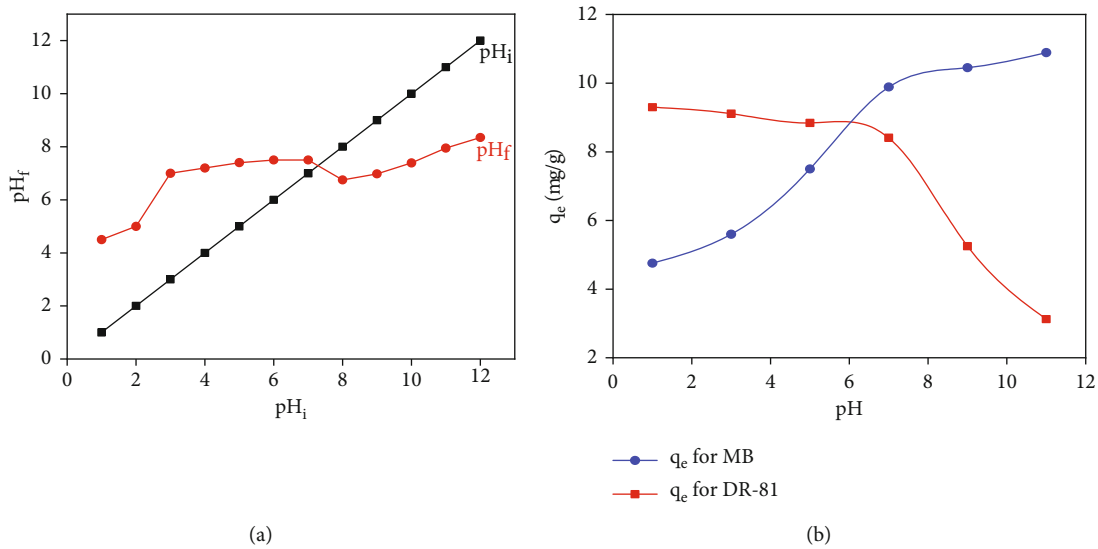


Figure 9: (a) The $pH_{pzc}$ of the synthesized Zn-adeninate bio-MOF and (b) the effect of pH on the adsorption capacity of the synthesized Zn-adeninate bio-MOF for MB and DR-81 (contact time = 10 min for MB and 30 min for DR-81, bio-MOF dosage = 1 g $L^{-1}$, initial dye concentration = 10 ppm, stirring speed = 300 rpm, and solution temperature = 23°C) (b).

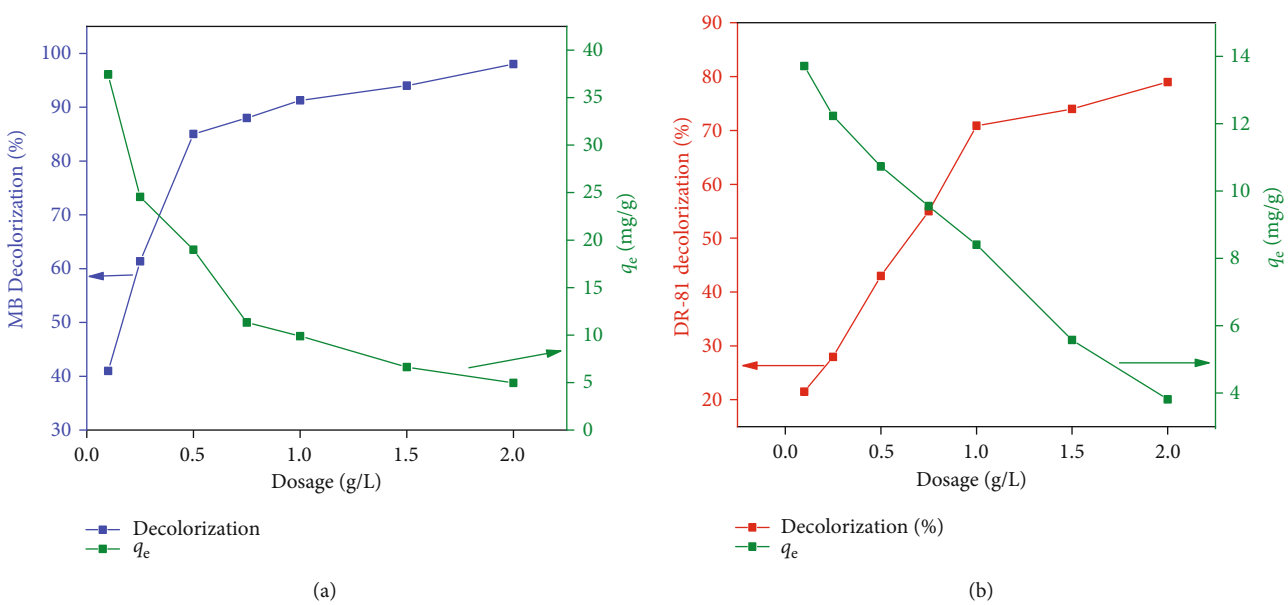


Figure 10: Influence of the dosage of the synthesized Zn-adeninate bio-MOF on the decolorization of (a) MB and (b) DR-81 (contact time = 10 min for MB and 30 min for DR-81, pH = 7, initial dye concentration = 10 ppm, stirring speed = 300 rpm, and solution temperature = 23°C).

negative ions are available in the solution; therefore, the electrostatic attractive forces between the negatively charged hydroxyl and carbonyl groups of the synthesized Zn-adeninate bio-MOF and the positively charged species of the cationic MB dye increase. Under similar conditions, repulsive forces exist between the negatively charged Zn-adeninate bio-MOF and anionic DR-81 [44]. Under acidic conditions ($pH < 7$), more protons are formed, which increase the competition with the active sites of bio-MOF, decreasing the removal of MB and increasing the removal of DR-81 [45, 46]. However, the decolorization rate of the MB dye by bio-MOF was limited to less than 8% when the solution pH was increased from 7 to 11. Therefore, a solution pH of 7 was selected as the optimum pH for removing both DR-81 and MB dyes using the prepared Zn-adeninate bio-MOF [47].

*3.2.3. Influence of the Synthesized Zn-Adeninate Bio-MOF Dosage on the Decolorization of Cationic and Anionic Dyes.* The adsorbent dosage is an important factor that controls the adsorbent capacity and, hence, the decolorization process [43]. The effect of the adsorbent dosage of the synthesized Zn-adeninate bio-MOF was tested after 10 and

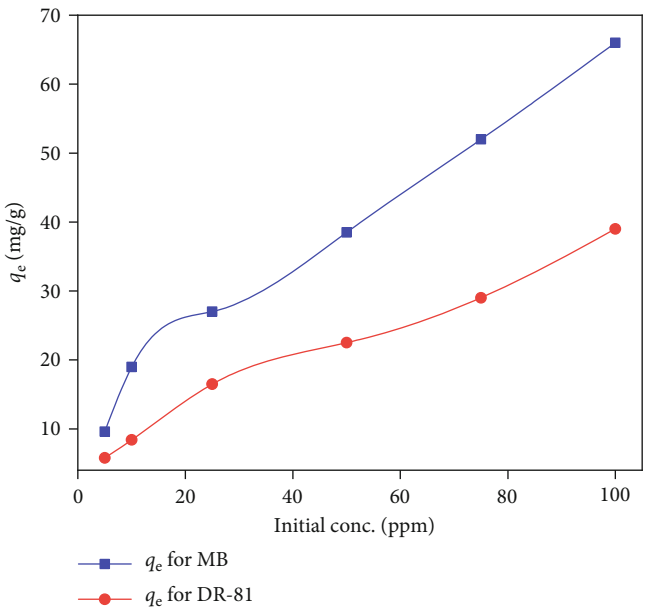


Figure 11: Effect of initial concentrations of the dyes on the adsorption capacity of the fabricated Zn-adeninate bio-MOF for MB and DR-81 (contact time = 10 min for MB and 30 min for DR-81, pH = 7, bio-MOF dosage = 0.5 g $L^{-1}$ for MB and 1 g $L^{-1}$ for DR-81, stirring speed = 300 rpm, and solution temperature = 23°C).

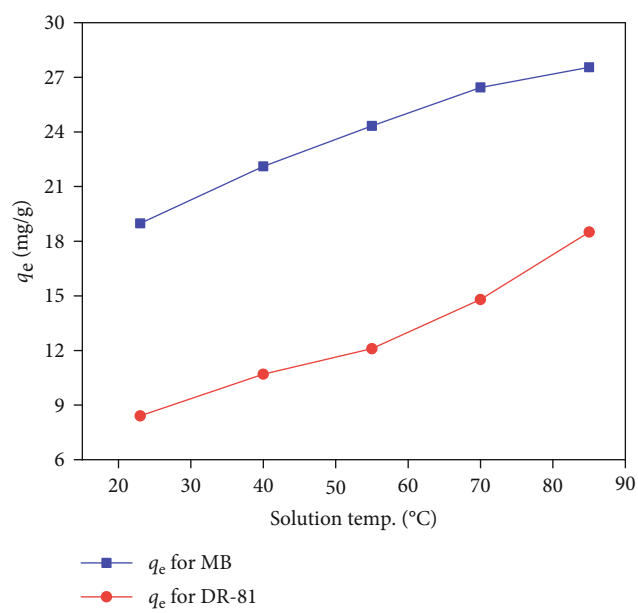


Figure 12: Effect of the solution temperature on the adsorption capacity of the synthesized Zn-adeninate bio-MOF for MB and DR-81 (contact time = 10 min for MB and 30 min for DR-81, pH = 7, bio-MOF dosage = 0.5 g $L^{-1}$ for MB and 1 g/L for DR-81, initial dye concentration = 10 ppm, and stirring speed = 300 rpm).

30 min for MB and DR-81, respectively. The decolorization of MB and DR-81 dyes by the synthesized Zn-adeninate bio-MOF was enhanced by increasing the material dosages from 0.1 g to 2 g $L^{-1}$, as shown in Figure 10. Furthermore, the decolorization capacity of the synthesized Zn-adeninate bio-MOF toward the two different dyes decreased with the increasing amounts of the synthesized adsorbent. The reduced decolorization capacity toward numerous types of dyes at high dosages of the prepared bio-MOF can be attributed to the unsaturated decolorization residual sites on the synthesized bio-MOF [1]. By contrast, increasing the dosage of the synthesized bio-MOF enabled the extra active sites available for dye decolorization, which in turn increased the removal percentage of the dyes from the wastewater. These findings can be attributed to the high surface area of the fabricated Zn-adeninate bio-MOF [48]. Therefore, the optimum dosages (or the economical dosages) of the synthesized Zn-adeninate bio-MOF were chosen as 0.5 and 1 g $L^{-1}$ for the decolorization of MB and DR-81 dyes, respectively.

Table 1: Thermodynamic parameters for the decolorization of MB and DR-81 by the synthesized Zn-adeninate bio-MOF.

| Dye | $\Delta G^\circ$ (kJ $mol^{-1}$) | $E_a$ (kJ $mol^{-1}$) | $\Delta H^\circ$ (kJ $mol^{-1}$) | $\Delta S^\circ$ (kJ $mol^{-1}$) |
|---|---|---|---|---|
| MB | −17.70 | 48.02 | 31.27 | 29.22 |
| DR-81 | −3.65 | 35.23 | 34.27 | 36.34 |

*3.2.4. Influence of Initial Concentrations of the Dyes on the Decolorization Processes.* The effect of the initial dye concentration on the decolorization process was investigated in the concentration range of 5 to 100 ppm at the optimum contact time, pH, and material dosage for each dye solution. Figure 11 shows that the adsorption capacity increased as the initial dye concentration increased from 5 to 100 ppm, which agrees with the results of the previous investigations [12, 49]. This may be attributed to the saturation of the surface-active sites of the adsorbent at high initial concentrations of the MB and DR-81 dyes. These results indicated that the synthesized Zn-adeninate bio-MOF possesses practical and effective ability to decolorize the cationic and anionic dyes from the wastewater at different initial dye concentrations.

*3.2.5. Influence of Solution Temperature on the Decolorization of Cationic and Anionic Dyes.* Figure 12 shows the influence of the solution temperature on the decolorization of the MB and DR-81 dyes by the synthesized Zn-adeninate bio-MOF. When the solution temperatures were increased from 23 to 85°C, the decolorization processes were enhanced, indicating a favorable decolorization process at high temperatures. These results indicated that the decolorization processes by the fabricated Zn-adeninate bio-MOF are endothermic [1].

*3.2.6. Thermodynamic Modeling of the Decolorization Processes.* The decolorization mechanism in terms of favorability, energy, and reversibility was studied and analyzed using the decolorization thermodynamics. To determine the thermodynamics of the decolorization process, the changes in enthalpy ($\Delta H^\circ$), entropy ($\Delta S^\circ$), and free energy

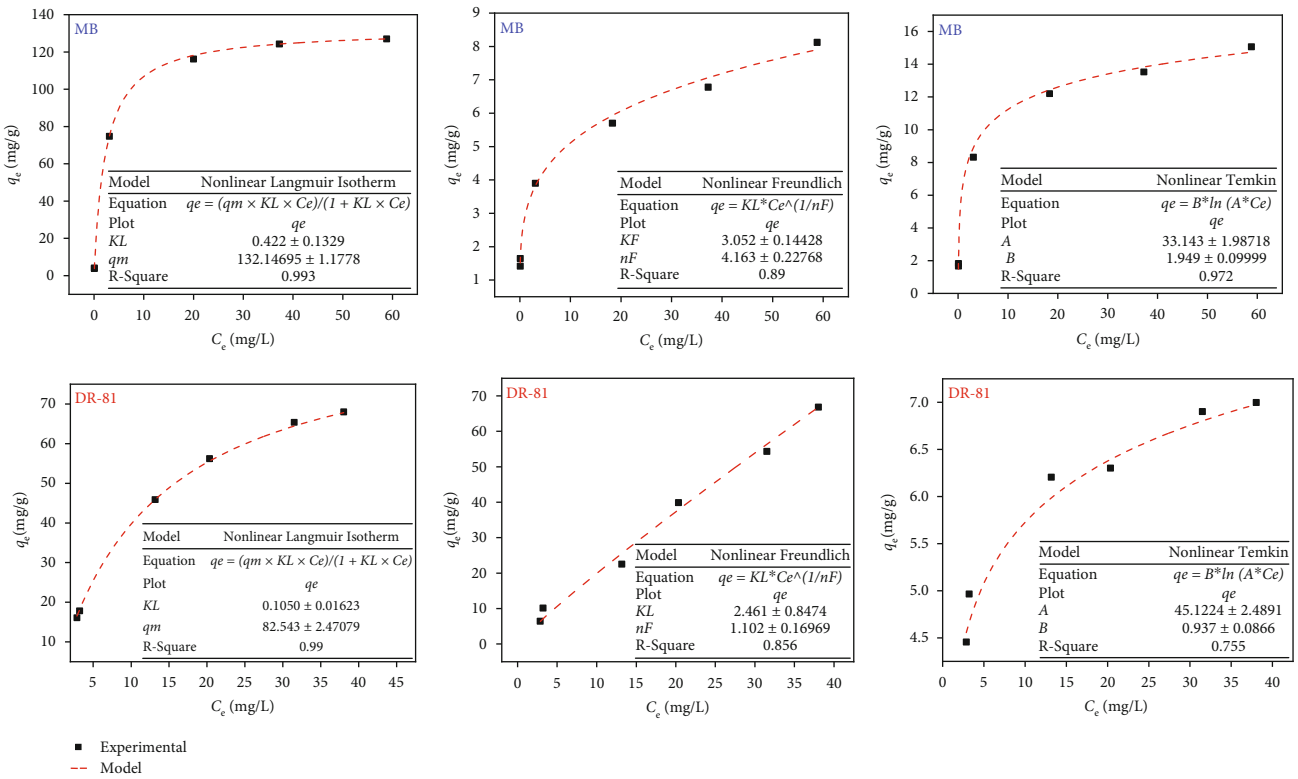


Figure 13: Adsorption isotherms for MB and DR-81 by the synthesized bio-MOF.

Table 2: Isotherm parameters of the Langmuir, Freundlich, and Temkin models for the decolorization of MB and DR-81 by the synthesized bio-MOF.

| Isotherm parameters | | MB | DR-81 |
|---|---|---|---|
| Langmuir parameters | $q_m$ (mg g$^{-1}$) | 132.147 | 82.543 |
| | $K_L$ (L mg$^{-1}$) | 0.422 | 0.105 |
| | $R_L$ | 0.056 | 0.079 |
| | $R^2$ | 0.993 | 0.990 |
| Freundlich parameters | $K_F$ (mg g$^{-1}$) | 3.052 | 2.461 |
| | $n_F$ | 4.163 | 1.102 |
| | $R^2$ | 0.890 | 0.856 |
| Temkin parameters | $A$ (L g$^{-1}$) | 33.143 | 45.1224 |
| | $B$ (J mol$^{-1}$) | 1.949 | 0.937 |
| | $R^2$ | 0.972 | 0.755 |

($\Delta G^\circ$) were determined in kilojoule per mole. The Gibbs free energy was calculated using the following equation:

$$\Delta G^\circ = -RT \ln K_c, \tag{3}$$

where $T$ denotes the temperature of the solution in Kelvin, $K_c$ denotes the fraction adsorbed at equilibrium, $K_c = F_e/(1 - F_e)$, $F_e = (C_o - C_e)/C_o$, and $R$ represents the universal gas constant (8.314 J mol$^{-1}$ K$^{-1}$).

The standard entropy and enthalpy values were calculated using the Van't Hoff equation as

$$\ln K_c = \frac{\Delta S^\circ}{R} - \frac{\Delta H^\circ}{RT}. \tag{4}$$

The Hoff plot for ln $K_c$ versus 1000/$T$ was a straight line with satisfactory values of $R^2$ for different concentrations of MB and DR-81. The $\Delta S^\circ$ and $\Delta H^\circ$ values were calculated from the intercept and slope of the plot, respectively. The activation energy ($E_a$) was estimated using the following equation [33]:

$$E_a = \Delta H^\circ + RT. \tag{5}$$

The values of the thermodynamic parameters ($E_a$, $\Delta G^\circ$, $\Delta S^\circ$, and $\Delta H^\circ$) for the decolorization of MB and DR-81 dyes by the synthesized Zn-adeninate bio-MOF at 396 K are listed in Table 1. The negative value of $\Delta G^\circ$ indicates that the decolorization of MB and DR-81 by the synthesized bio-MOF is thermodynamically spontaneous [14]. However, the positive value of enthalpy indicates that the decolorization processes were endothermic. Furthermore, enhanced disorder at the liquid/solid interface during the decolorization processes is reflected by the positive values of the entropy [12, 14].

*3.2.7. Equilibrium Isotherms of MB and DR-81 Decolorization.* To examine the decolorization behaviors of the MB and DR-81 dyes by the synthesized bio-MOF, three models, namely,

Table 3: Comparison of the monolayer decolorization capacities of MB and DR-81 for different nanoadsorbents.

| Pollutant | Adsorbents | Optimized conditions | Decolorization capacity ($mg\,g^{-1}$) | References |
|---|---|---|---|---|
| MB | Zn-adeninate bio-MOF | Time = 10 min<br>Dosage = 0.5 $g\,L^{-1}$<br>MB conc. = 10 ppm | 132.15 | Present study |
| | Activated carbon | Time = 120 min<br>Dosage = 0.5 $g\,L^{-1}$<br>MB conc. = 10 ppm | 53.90 | [47] |
| | MIP-202 bio-MOF | Time = 8 min<br>Dosage = 1.0 $g\,L^{-1}$<br>MB conc. = 10 ppm | 79.79 | [1] |
| | Cu-BTC MOF | Time = 20 min<br>Dosage = 0.5 $g\,L^{-1}$<br>MB conc. = 10 ppm | 15.28 | [54] |
| | UiO-66 MOF | Time = 20 min<br>Dosage = 0.1 $g\,L^{-1}$<br>MB conc. = 20 ppm | 13.2 | [55] |
| | Fe-BDC MOF | Time = 300 min<br>Dosage = 2.5 $g\,L^{-1}$<br>MB conc. = 5 ppm | 8.65 | [56] |
| DR-81 | Zn-adeninate bio-MOF | Time = 30 min<br>Dosage = 1.0 $g\,L^{-1}$<br>DR-81 conc. = 10 ppm | 82.54 | Current study |
| | Kaolinite | Time = 120 min<br>Dosage = 4 $g\,L^{-1}$<br>DR-81 conc. = 50 ppm | 26.55 | [57] |
| | MIP-202 bio-MOF | Time = 12 min<br>Dosage = 1.0 $g\,L^{-1}$<br>DR-81 conc. = 50 ppm | 36.07 | [1] |
| | Potato peel | Time = 50 min<br>Dosage = 0.25 $g\,L^{-1}$<br>DR-81 conc. = 50 ppm | 10.40 | [58] |
| | Neem bark | Time = 50 min<br>Dosage = 0.25 $g\,L^{-1}$<br>DR-81 conc. = 50 ppm | 8.40 | [58] |

Langmuir, Freundlich, and Temkin, were utilized. For nonlinear estimation, a trial-and-error method was developed to minimize the error distribution between the experimental and theoretical adsorption data using the Solver add-in of Microsoft Excel. The Langmuir nonlinearized plots exhibited good correlation coefficients ($R^2 = 0.993$ for MB and 0.990 for DR-81) [50].

$$q_e = \frac{q_m K_L C_e}{1 + K_L C_e}, \tag{6}$$

where $C_e$ refers to the adsorbate equilibrium concentration ($mg\,L^{-1}$), $q_e$ denotes the adsorbed amount of MB/DR-81 at equilibrium ($mg\,g^{-1}$), and $K_L$ and $q_m$ denote the Langmuir constants of the decolorization energy ($L\,mg^{-1}$) and maximum monolayer decolorization capacity ($mg\,g^{-1}$), respectively. Equation (7) was used to test the Freundlich model by plotting log $q_e$ against log $C_e$ [51].

$$q_e = K_F \times C_e^{1/n_f}, \tag{7}$$

where $K_F$ and $n_F$ denote the Freundlich constants related to the capacity and intensity of decolorization, respectively. Equation (8) was employed to verify the Temkin isotherm model for the adsorption data of the MB and DR-81 dyes on bio-MOF [52].

$$q_e = \left(\frac{RT}{b}\right) \ln (A \times C_e), \tag{8}$$

Table 4: Parameters of the kinetic models for MB and DR-81 removal by the synthesized Zn-adeninate bio-MOF.

| Kinetic model | Parameters | MB | DR-81 |
|---|---|---|---|
| Pseudo-first-order model | $q_{exp.}$ (mg g$^{-1}$) | 17.992 | 11.835 |
| | $q_{theor}$ (mg g$^{-1}$) | 1.842 | 6.328 |
| | $K_1$ (min$^{-1}$) | 0.274 | 0.250 |
| | $R^2$ | 0.531 | 0.463 |
| Pseudo-second-order model | $q_{exp.}$ (mg g$^{-1}$) | 17.992 | 11.834 |
| | $q_{theor}$ (mg g$^{-1}$) | 18.134 | 12.008 |
| | $K_2$ (g min mg$^{-1}$) | 0.437 | 0.111 |
| | $R^2$ | 0.996 | 0.989 |
| Elovich kinetic model | $\alpha$ (mg min g$^{-1}$) | 12.426 | 7.252 |
| | $\beta$ (g mg$^{-1}$) | 0.0921 | 0.447 |
| | $R^2$ | 0.800 | 0.679 |
| Intraparticle diffusion kinetic model | $C_1$ (mg g$^{-1}$ min$^{-1}$) | 19.751 | 10.341 |
| | $k_i$ (g mg$^{-1}$) | 0.022 | 0.362 |
| | $R^2$ | 0.700 | 0.790 |

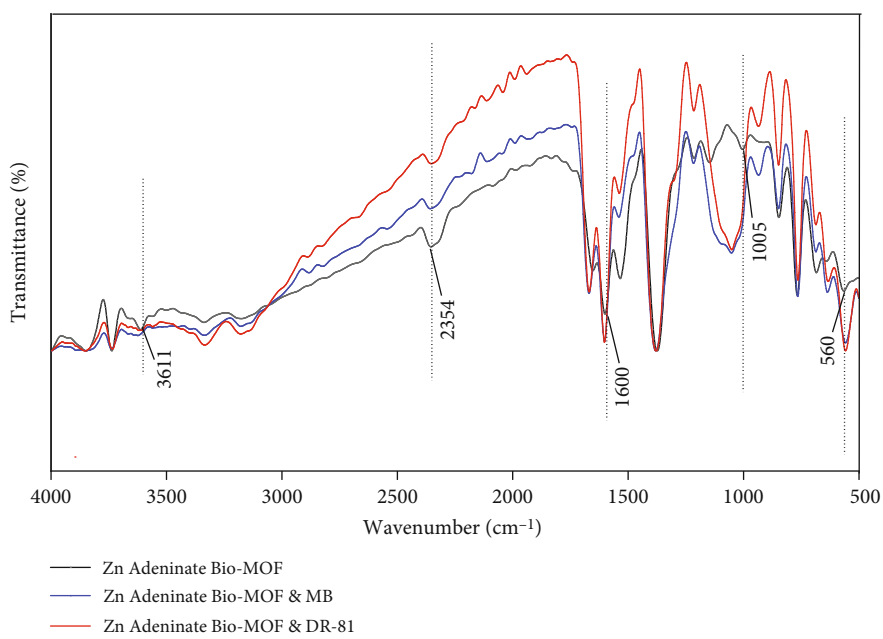


Figure 14: Comparison of the FT-IR spectra of (a) the synthesized Zn-adeninate bio-MOF, (b) Zn-adeninate bio-MOF and MB, and (c) Zn adeninate bio-MOF and DR-81.

where $B = RT/b$ is a constant that is related to the decolorization heat (J mol$^{-1}$) and $A$ is the Temkin isotherm constant (L g$^{-1}$).

A comparison of the nonlinear fittings of the Langmuir, Freundlich, and Temkin models is presented in Figure 13 and Table 2.

The Langmuir model was found to be the most appropriate for describing the dye removal processes of MB and DR-81 by the synthesized bio-MOF because this model showed the highest correlation coefficients. Additionally, the values of the separation factor $R_L$ were in the range of 0 to 1, which indicated that the Langmuir model is favorable for describing the dye removal procedures [53]. Meanwhile, the Freundlich decolorization intensities ($n_F$) were 4.163 and 1.102 for the decolorization of MB and DR-81, respectively, which was higher than unity, indicating the favorable nature of dye removal by the synthesized adsorbent [1, 53]. By contrast, the Temkin correlation coefficients had low values, indicating poor fitting of the equilibrium decolorization data of MB and DR-81 with the Temkin isothermal model.

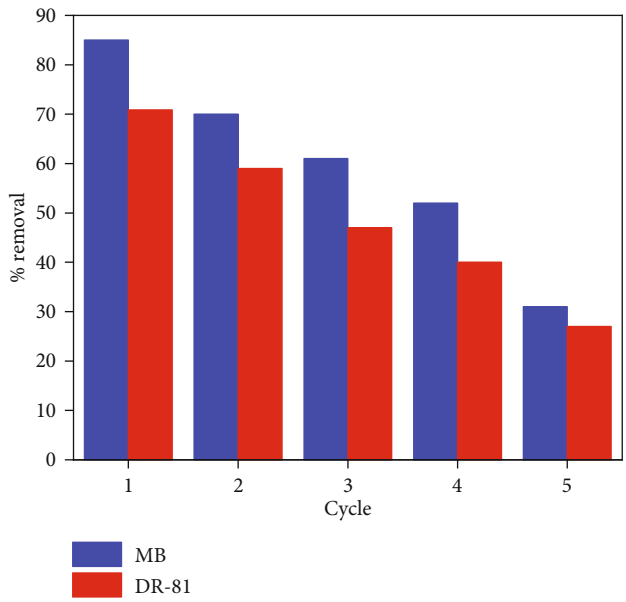


Figure 15: Reusability test of the synthesized Zn-adeninate bio-MOF against cationic and anionic dyes.

Hence, the Langmuir model was found to be the most suitable for describing the monolayer decolorization of MB and DR-81 by the synthesized bio-MOF surface [43].

*3.2.8. Comparison of the Decolorization Capacity of MB and DR-81 for the Synthesized Zn-Adeninate Bio-MOF with other Adsorbents.* The monolayer decolorizing capacities ($q_m$) of the MB and DR-81 dyes for Zn-adeninate bio-MOF were compared with the $q_m$ values of other reported nanoadsorbents (Table 3). The synthesized Zn-adeninate bio-MOF was found to have better decolorization results for MB and DR-81 compared to those of the previously reported nanoadsorbents.

*3.2.9. Decolorization Kinetic Analysis of the MB and DR-81 Dyes.* Pseudo-first-order and pseudo-second-order models were used to understand the decolorization kinetics of MB and DR-81 by the synthesized Zn-adeninate bio-MOF. The two nonlinear decolorization models can be described by Equations (9) and (10), respectively [59, 60]:

$$q_t = q_e\left(1 - e^{k_1 t}\right), \tag{9}$$

$$q_t = \frac{{q_e}^2 K_2 t}{q_e K_2 t + 1}, \tag{10}$$

where $q_t$ and $q_e$ (mg g$^{-1}$) denote the adsorbed amounts of dye at time $t$ and equilibrium, respectively, and $K_1$ (min$^{-1}$) and $K_2$ (g mg$^{-1}$ min$^{-1}$) define the rate constants of the pseudo-first-order and pseudo-second-order models, respectively. Additionally, the following nonlinear Elovich equation was used to decolorize the different water pollutants [61]:

$$q_t = \left(\frac{1}{\beta}\right) \ln\left(1 + \alpha\beta t\right), \tag{11}$$

where $\alpha$ denotes the initial decolorization rate (mg g$^{-1}$ min$^{-1}$) and $\beta$ is related to the degree of surface coverage and decolorization activation energy (g mg$^{-1}$). The intercept and slope of the linear plot of $q_t$ versus ln $t$ describe $\beta$ and $\alpha$, respectively. The intraparticle diffusion model was explored using the following equation proposed by Weber and Morris [62]:

$$q_t = k_i t^{1/2} + C, \tag{12}$$

where $k_i$ denotes the constant of the intraparticle diffusion rate and $C$ denotes the thickness of the border layer. The linear fitting of $q_t$ versus $t^{1/2}$ when the plot passes through the origin indicates intraparticle diffusion, in which the rate-limiting process is the only intraparticle diffusion process. If this was not obtained, other mechanisms along with the intraparticle diffusion would be included.

The correlation coefficients of the four kinetic models are listed in Table 4. The nonlinearity of $q_t$ versus time plots show high correlation coefficient values of 0.996 and 0.989 for the MB and DR-81 dyes, respectively. The computed $q_e$ values were in perfect agreement with the experimental data ($q_e$) for the pseudo-second-order kinetics. Hence, the decolorization of MB and DR-81 by the synthesized bio-MOF followed the pseudo-second-order kinetic model. According to the pseudo-second-order model, the decolorization processes become rapid and equilibrium times are very short, which is similar to the experimental results. Rapid adsorption of MB and DR-81 on Zn-adeninate bio-MOF occurred in the first 25 min, and then, it diminished in the subsequent 3 h. The rapid adsorption can be principally associated with boundary layer diffusion or macropore diffusion, while the reluctant decolorization is due to intraparticle diffusion or micropore diffusion with a low $R^2$ value [63]. The data confirmed that MB and DR-81 decolorization processes by the synthesized bio-MOF may be mainly controlled by a pseudo-second-order model for the studied pollutants [1, 14].

*3.2.10. Decolorization Mechanism of MB and DR-81 by the Synthesized Bio-MOF.* The FT-IR spectra before and after the decolorization of MB and DR-81 were compared, as shown in Figure 14. Following MB and DR-81 adsorption, the FT-IR spectra showed distinct changes due to the decolorization of the cationic and anionic dyes by the Zn-adeninate bio-MOF. The transition in the peak at 1005 cm$^{-1}$ may be due to the symmetric bending of S–O in MB with Zn bio-MOF. Furthermore, the variation in the characteristic peak at 1600 cm$^{-1}$ may be due to the chemical combination of C–C in Zn bio-MOF with the electrophilic $N^+$ groups of DR-81 and MB [1]. Furthermore, the Zn–O peak in the lower wavenumber region shifted, indicating the interaction between Zn–O and the positively charged groups in the dyes [64]. The characteristic peak of the asymmetric vibration at 3611 cm$^{-1}$ shifted, indicating chemical bonding between the $-NH_2$ group and positively charged

functional groups of the dyes [36]. These findings indicated that the decolorization mechanism of the MB and DR-81 dyes by the synthesized Zn-adeninate bio-MOF might be chemically controlled.

*3.2.11. Recyclability Study of the Synthesized Zn-Adeninate Bio-MOF.* The regeneration of the adsorbent is significant because it affects the cost of practical applications [1, 14]. The synthesized adsorbent was washed and reused to decolorize MB and DR-81 from wastewater. The decolorization-desorption cycles were repeated five times, as shown in Figure 15. The results indicated that the prepared Zn-adeninate bio-MOF could be reused several times with high decolorization performance for both MB and DR-81 [1].

## 4. Conclusions

In this study, a novel, efficient, environmentally benign, and nontoxic adsorbent of porous Zn-adeninate bio-MOF was reported for the decolorization of both cationic and anionic dyes from wastewater. The prepared Zn-adeninate bio-MOF was characterized using different techniques, such as XRD, FT-IR, BET, SEM, TEM, XPS, and TGA. The synthesized Zn-adeninate bio-MOF had a surface area of $52.62\,m^2\,g^{-1}$ and total pore volume of $0.183\,cm^3\,g^{-1}$. The decolorization processes of the MB and DR-81 dyes were in agreement with the Langmuir model, which represents monolayer decolorization by the prepared Zn bio-MOF. The best-fit kinetic model for the MB and DR-81 dye decolorization was the pseudo-second-order model. Furthermore, the maximum decolorization capacity of the synthesized Zn-adeninate bio-MOF against MB and DR-81 was 132.15 and $82.54\,mg\,g^{-1}$, respectively. The synthesized Zn-adeninate bio-MOF could be reused several times with a high decolorization performance. Accordingly, the prepared Zn-adeninate bio-MOF is a promising and effective adsorbent for MB and DR-81 from wastewater, with high stability and good reusability for numerous cycles.

## Data Availability

All the investigated data in this study are included in the submitted article.

## Conflicts of Interest

The authors declare no conflicts of interest.

## Acknowledgments

This work was supported by the Science, Technology & Innovation Funding Authority (STDF) (grant number 43565).

## References

[1] K. E. Diab, E. Salama, H. S. Hassan, A. Abd El-moneim, and M. F. Elkady, "Biocompatible MIP-202 Zr-MOF tunable sorbent for cost-effective decontamination of anionic and cationic pollutants from waste solutions," *Scientific Reports*, vol. 11, no. 1, pp. 1–13, 2021.

[2] X. Li, B. Wang, Y. Cao et al., "Water contaminant elimination based on metal–organic frameworks and perspective on their industrial applications," *ACS Sustainable Chemistry & Engineering*, vol. 7, no. 5, pp. 4548–4563, 2019.

[3] H. Yuan, L. Chen, Z. Cao, and F. F. Hong, "Enhanced decolourization efficiency of textile dye Reactive Blue 19 in a horizontal rotating reactor using strips of BNC-immobilized laccase: optimization of conditions and comparison of decolourization efficiency," *Biochemical Engineering Journal*, vol. 156, article 107501, 2020.

[4] S. Ledakowicz and K. Paździor, "Recent achievements in dyes removal focused on advanced oxidation processes integrated with biological methods," *Molecules*, vol. 26, no. 4, p. 870, 2021.

[5] A. Albahnasawi, E. Yüksel, E. Gürbulak, and F. Duyum, "Fate of aromatic amines through decolorization of real textile wastewater under anoxic-aerobic membrane bioreactor," *Journal of Environmental Chemical Engineering*, vol. 8, no. 5, article 104226, 2020.

[6] R. Kant, "Textile dyeing industry an environmental hazard," *Natural Science*, vol. 4, article 17027, p. 5, 2012.

[7] P. Bajpai, *Pulp and Paper Industry: Chemicals*, Elsevier, Amsterdam, 2015.

[8] V. Gupta, I. A. Suhas, and V. Saini, "Removal of rhodamine B, fast green, and methylene blue from wastewater using red mud, an aluminum industry waste," *Industrial & Engineering Chemistry Research*, vol. 43, no. 7, pp. 1740–1747, 2004.

[9] O. S. Bayomie, H. Kandeel, T. Shoeib, H. Yang, N. Youssef, and M. M. El-Sayed, "Novel approach for effective removal of methylene blue dye from water using fava bean peel waste," *Scientific Reports*, vol. 10, no. 1, pp. 1–10, 2020.

[10] A. Giwa, A. Yusuf, H. A. Balogun et al., "Recent advances in advanced oxidation processes for removal of contaminants from water: a comprehensive review," *Process Safety and Environmental Protection*, vol. 146, pp. 220–256, 2021.

[11] N. Nippatla and L. Philip, "Electrocoagulation-floatation assisted pulsed power plasma technology for the complete mineralization of potentially toxic dyes and real textile wastewater," *Process Safety and Environmental Protection*, vol. 125, pp. 143–156, 2019.

[12] M. F. Elkady, H. Shokry Hassan, and E. Salama, "Sorption profile of phosphorus ions onto ZnO nanorods synthesized via sonic technique," *Journal of Engineering*, vol. 2016, Article ID 2308560, 2016.

[13] M. F. Elkady, H. S. Hassan, W. A. Amer, E. Salama, H. Algarni, and E. R. Shaaban, "Novel magnetic zinc oxide nanotubes for phenol adsorption: mechanism modeling," *Materials*, vol. 10, no. 12, p. 1355, 2017.

[14] M. Elkady, E. Salama, W. A. Amer, E.-Z. M. Ebeid, M. M. Ayad, and H. Shokry, "Novel eco-friendly electrospun nanomagnetic zinc oxide hybridized PVA/alginate/chitosan nanofibers for enhanced phenol decontamination," *Environmental Science and Pollution Research*, vol. 27, no. 34, pp. 43077–43092, 2020.

[15] K. Meerbergen, S. Crauwels, K. A. Willems et al., "Decolorization of reactive azo dyes using a sequential chemical and activated sludge treatment," *Journal of Bioscience and Bioengineering*, vol. 124, no. 6, pp. 668–673, 2017.

[16] J. Meng, Y. Xie, Y.-H. Gu et al., "PVDF-CaAlg nanofiltration membranes with dual thin-film-composite (TFC) structure

and high permeation flux for dye removal," *Separation and Purification Technology*, vol. 255, article 117739, 2021.

[17] L. Cseri, F. Topuz, M. A. Abdulhamid, A. Alammar, P. M. Budd, and G. Szekely, "Electrospun adsorptive nanofibrous membranes from ion exchange polymers to snare textile dyes from wastewater," *Advanced Materials Technologies*, vol. 6, no. 10, article 2000955, 2021.

[18] M. Shaban, M. R. Abukhadra, A. Hamd, R. R. Amin, and A. A. Khalek, "Photocatalytic removal of Congo red dye using MCM-48/$Ni_2O_3$ composite synthesized based on silica gel extracted from rice husk ash; fabrication and application," *Journal of Environmental Management*, vol. 204, no. 1, pp. 189–199, 2017.

[19] B. Dong, H. Chen, Y. Yang, Q. He, and X. Dai, "Treatment of printing and dyeing wastewater using MBBR followed by membrane separation process," *Desalination and Water Treatment*, vol. 52, no. 22-24, pp. 4562–4567, 2014.

[20] O. Onukwuli, P. Nnaji, M. Menkiti et al., "Dual-purpose optimization of dye-polluted wastewater decontamination using bio-coagulants from multiple processing techniques via neural intelligence algorithm and response surface methodology," *Journal of the Taiwan Institute of Chemical Engineers*, vol. 125, pp. 372–386, 2021.

[21] M. Hartl, M. J. García-Galán, V. Matamoros et al., "Constructed wetlands operated as bioelectrochemical systems for the removal of organic micropollutants," *Chemosphere*, vol. 271, article 129593, 2021.

[22] C. Manera, A. P. Tonello, D. Perondi, and M. Godinho, "Adsorption of leather dyes on activated carbon from leather shaving wastes: kinetics, equilibrium and thermodynamics studies," *Environmental Technology*, vol. 40, no. 21, pp. 2756–2768, 2019.

[23] S. Dutta, B. Gupta, S. K. Srivastava, and A. K. Gupta, "Recent advances on the removal of dyes from wastewater using various adsorbents: a critical review," *Materials Advances*, vol. 2, no. 14, pp. 4497–4531, 2021.

[24] M. M. Ayad, W. A. Amer, S. Zaghlol, I. M. Minisy, P. Bober, and J. Stejskal, "Polypyrrole-coated cotton textile as adsorbent of methylene blue dye," *Chemical Papers*, vol. 72, no. 7, pp. 1605–1618, 2018.

[25] W. A. Amer, M. M. Omran, and M. M. Ayad, "Acid-free synthesis of polyaniline nanotubes for dual removal of organic dyes from aqueous solutions," *Colloids and Surfaces A: Physicochemical and Engineering Aspects*, vol. 562, pp. 203–212, 2019.

[26] V. K. M. Au, "Recent advances in the use of metal-organic frameworks for dye adsorption," *Frontiers in Chemistry*, vol. 8, p. 708, 2020.

[27] K. Wang, H. Huang, W. Xue et al., "An ultrastable Zr metal–organic framework with a thiophene-type ligand containing methyl groups," *CrystEngComm*, vol. 17, no. 19, pp. 3586–3590, 2015.

[28] M. S. Khan, M. Khalid, and M. Shahid, "What triggers dye adsorption by metal organic frameworks? The current perspectives," *Materials Advances*, vol. 1, no. 6, pp. 1575–1601, 2020.

[29] M. R. Saeb, N. Rabiee, M. Mozafari, and E. Mostafavi, "Metal-organic frameworks-based nanomaterials for drug delivery," *Materials*, vol. 14, no. 13, p. 3652, 2021.

[30] S. Salamat, M. Hadavifar, and H. Rezaei, "Preparation of nanochitosan-STP from shrimp shell and its application in removing of malachite green from aqueous solutions," *Journal of Environmental Chemical Engineering*, vol. 7, no. 5, article 103328, 2019.

[31] S. S. Nadar, L. Vaidya, S. Maurya, and V. K. Rathod, "Polysaccharide based metal organic frameworks (polysaccharide-MOF): a review," *Coordination Chemistry Reviews*, vol. 396, pp. 1–21, 2019.

[32] A. H. Ibrahim, W. A. El-Mehalmey, R. R. Haikal et al., "Tuning the chemical environment within the UiO-66-$NH_2$nanocages for charge-dependent contaminant uptake and selectivity," *Inorganic Chemistry*, vol. 58, no. 22, pp. 15078–15087, 2019.

[33] H. Shokry, M. Elkady, and E. Salama, "Eco-friendly magnetic activated carbon nano-hybrid for facile oil spills separation," *Scientific Reports*, vol. 10, no. 1, pp. 1–17, 2020.

[34] Q. Qian, A. X. Wu, W. S. Chi et al., "Mixed-matrix membranes formed from imide-functionalized UiO-66-$NH_2$for improved interfacial compatibility," *ACS Applied Materials & Interfaces*, vol. 11, no. 34, pp. 31257–31269, 2019.

[35] Y. Rachuri, J. F. Kurisingal, R. K. Chitumalla et al., "Adenine-based Zn(II)/Cd(II) metal–organic frameworks as efficient heterogeneous catalysts for facile $CO_2$fixation into cyclic carbonates: a DFT-supported study of the reaction mechanism," *Inorganic Chemistry*, vol. 58, no. 17, pp. 11389–11403, 2019.

[36] T. Hashem, A. H. Ibrahim, C. Wöll, and M. H. Alkordi, "Grafting zirconium-based metal–organic framework UiO-66-$NH_2$nanoparticles on cellulose fibers for the removal of Cr(VI) ions and methyl orange from water," *ACS Applied Nano Materials*, vol. 2, no. 9, pp. 5804–5808, 2019.

[37] J. An, O. K. Farha, J. T. Hupp, E. Pohl, J. I. Yeh, and N. L. Rosi, "Metal-adeninate vertices for the construction of an exceptionally porous metal-organic framework," *Nature Communications*, vol. 3, no. 1, pp. 1–6, 2012.

[38] N. Graf, E. Yegen, T. Gross et al., "XPS and NEXAFS studies of aliphatic and aromatic amine species on functionalized surfaces," *Surface Science*, vol. 603, no. 18, pp. 2849–2860, 2009.

[39] Y. Wang, L. Li, P. Dai et al., "Missing-node directed synthesis of hierarchical pores on a zirconium metal–organic framework with tunable porosity and enhanced surface acidity via a microdroplet flow reaction," *Journal of Materials Chemistry A*, vol. 5, no. 42, pp. 22372–22379, 2017.

[40] G. Han, Q. Qian, K. Mizrahi Rodriguez, and Z. P. Smith, "Hydrothermal synthesis of sub-20 nm amine-functionalized MIL-101(Cr) nanoparticles with high surface area and enhanced $CO_2$uptake," *Industrial & Engineering Chemistry Research*, vol. 59, no. 16, pp. 7888–7900, 2020.

[41] H. Hamad, E. Bailon-Garcia, S. Morales-Torres, F. Carrasco-Marin, A. F. Perez-Cadenas, and F. J. Maldonado-Hodar, "Physicochemical properties of new cellulose-$TiO_2$ composites for the removal of water pollutants: developing specific interactions and performances by cellulose functionalization," *Journal of Environmental Chemical Engineering*, vol. 6, no. 4, pp. 5032–5041, 2018.

[42] A. M. Omer, E. M. Abd El-Monaem, M. M. Abd El-Latif, G. M. El-Subruiti, and A. S. Eltaweil, "Facile fabrication of novel magnetic ZIF-67 [email protected] chitosan composite beads for the adsorptive removal of Cr(VI) from aqueous solutions," *Carbohydrate Polymers*, vol. 265, article 118084, 2021.

[43] M. Abd El-Latif, A. M. Ibrahim, and M. El-Kady, "Adsorption equilibrium, kinetics and thermodynamics of methylene blue from aqueous solutions using biopolymer oak sawdust composite," *Journal of American Science*, vol. 6, no. 6, pp. 267–283, 2010.

[44] K. Parida and A. C. Pradhan, "Removal of phenolic compounds from aqueous solutions by adsorption onto manganese nodule leached residue," *Journal of Hazardous Materials*, vol. 173, no. 1-3, pp. 758–764, 2010.

[45] E. M. El-Sayed, H. A. Hamad, and R. M. Ali, "Journey from ceramic waste to highly efficient toxic dye adsorption from aqueous solutions via one-pot synthesis of $CaSO_4$ rod- shape with silica," *Journal of Materials Research and Technology*, vol. 9, no. 6, pp. 16051–16063, 2020.

[46] A. Hamadi, N. Yeddou-Mezenner, A. Lounis, R. M. Ali, and H. Hamad, "Upgrading of agro-industrial green biomass residues from chocolate industry for adsorption process: diffusion and mechanistic insights," *Journal of Food Science and Technology*, vol. 58, no. 3, pp. 1081–1092, 2021.

[47] Y. Kuang, X. Zhang, and S. Zhou, "Adsorption of methylene blue in water onto activated carbon by surfactant modification," *Water*, vol. 12, no. 2, p. 587, 2020.

[48] M. El-Aassar, I. H. Alsohaimi, A. S. Ali, and A. A. Elzain, "Removal of phenol and Bisphenol A by immobilizedLaccaseon poly (acrylonitrile-co-styrene/pyrrole) nanofibers," *Separation Science and Technology*, vol. 55, no. 15, pp. 2670–2678, 2020.

[49] M. F. Elkady, M. R. El-Aassar, and H. S. Hassan, "Adsorption profile of basic dye onto novel fabricated carboxylated functionalized co-polymer nanofibers," *Polymers*, vol. 8, no. 5, p. 177, 2016.

[50] I. Langmuir, "The constitution and fundamental properties of solids and liquids. Part I. Solids," *Journal of the American Chemical Society*, vol. 38, no. 11, pp. 2221–2295, 1916.

[51] H. Freundlich, "Über die adsorption in lösungen," *Zeitschrift für Physikalische Chemie*, vol. 57U, no. 1, pp. 385–470, 1907.

[52] M. Temkin, "Kinetics of ammonia synthesis on promoted iron catalysts," *Acta physiochim. URSS*, vol. 12, pp. 327–356, 1940.

[53] O. Üner, Ü. Geçgel, and Y. Bayrak, "Adsorption of methylene blue by an efficient activated carbon prepared from Citrullus lanatus rind: kinetic, isotherm, thermodynamic, and mechanism analysis," *Water, Air, & Soil Pollution*, vol. 227, no. 7, pp. 1–15, 2016.

[54] S. Lin, Z. Song, G. Che et al., "Adsorption behavior of metal-organic frameworks for methylene blue from aqueous solution," *Microporous and Mesoporous Materials*, vol. 193, pp. 27–34, 2014.

[55] J. Qiu, Y. Feng, X. Zhang, M. Jia, and J. Yao, "Acid-promoted synthesis of UiO-66 for highly selective adsorption of anionic dyes: adsorption performance and mechanisms," *Journal of Colloid and Interface Science*, vol. 499, pp. 151–158, 2017.

[56] C. Arora, S. Soni, S. Sahu, J. Mittal, P. Kumar, and P. Bajpai, "Iron based metal organic framework for efficient removal of methylene blue dye from industrial waste," *Journal of Molecular Liquids*, vol. 284, pp. 343–352, 2019.

[57] T. A. Khan, S. Dahiya, and E. A. Khan, "Removal of direct red 81 from aqueous solution by adsorption onto magnesium oxide-coated kaolinite: isotherm, dynamics and thermodynamic studies," *Environmental Progress & Sustainable Energy*, vol. 36, no. 1, pp. 45–58, 2017.

[58] N. Sharma, D. Tiwari, and S. Singh, "Efficiency of chemically treated potato peel and Neem bark for sorption of Direct Red-81 dye from aqueous solution," *Rasayan Journal of Chemistry*, vol. 7, article 399e409, 2014.

[59] S. K. Lagergren, "About the theory of so-called adsorption of soluble substances," *Sven. Vetenskapsakad. Handingarl*, vol. 24, pp. 1–39, 1898.

[60] Y. Ho and G. McKay, "Kinetic model for lead (II) sorption on to peat," *Adsorption Science & Technology*, vol. 16, no. 4, pp. 243–255, 1998.

[61] S. Chien and W. Clayton, "Application of Elovich equation to the kinetics of phosphate release and sorption in soils," *Soil Science Society of America Journal*, vol. 44, no. 2, pp. 265–268, 1980.

[62] W. J. Weber Jr. and J. C. Morris, "Kinetics of adsorption on carbon from solution," *Journal of the Sanitary Engineering Division*, vol. 89, no. 2, pp. 31–59, 1963.

[63] N. Widiastuti, H. Wu, H. M. Ang, and D. Zhang, "Removal of ammonium from greywater using natural zeolite," *Desalination*, vol. 277, no. 1-3, pp. 15–23, 2011.

[64] K. Vikrant, V. Kumar, K.-H. Kim, and D. Kukkar, "Metal–organic frameworks (MOFs): potential and challenges for capture and abatement of ammonia," *Journal of Materials Chemistry A*, vol. 5, no. 44, pp. 22877–22896, 2017.

Hindawi
Adsorption Science & Technology
Volume 2022, Article ID 5455330, 18 pages
https://doi.org/10.1155/2022/5455330

*Research Article*

# Adsorption Properties of Modified ATP-RGO Composite Aerogel for Removal of Malachite Green and Methyl Orange from Unitary and Binary Aqueous Solutions

**Hong Ji Li, Jia Hui Xu, Liu Qing Wang, Dan Dan Hou, Zhi Ru Wang, and Hao Zhuo Li**

*School of Urban Planning and Municipal Engineering Xi'an Polytechnic University, Xi'an 710048, China*

Correspondence should be addressed to Hong Ji Li; lhj861106@126.com

Received 23 May 2022; Revised 24 June 2022; Accepted 19 July 2022; Published 2 August 2022

Academic Editor: Hesham Hamad



In this paper, the modified attapulgite-reduced graphene oxide composite aerogel (ATP-RGO CA) was prepared by sol-gel method using modified attapulgite as silica source. The removal of the cationic dye malachite green (MG) and azo dye methyl orange (MO) onto ATP-RGO CA from unitary and binary systems was investigated. Morphology and microstructure studies of ATP-RGO CA were investigated by Fourier transform infrared (FTIR), scanning electron microscopy (SEM), X-ray diffraction (XRD), and specific surface area and porosity analysis. Experiments were carried out as a function of pH, contact time, initial dye concentration, and temperature in unitary and binary systems. The adsorption kinetics, isotherms, thermodynamics, and dye desorption were studied in unitary and binary dye systems. The adsorption kinetics was modeled using the pseudo-first-order, pseudo-second-order, and intraparticle diffusion kinetics equations. The equilibrium adsorption data of MG and MO dyes on ATP-RGO CA were analyzed. Thermodynamic parameters of dye adsorption were obtained. In addition, the regeneration of ATP-RGO CA was studied using dye desorption in unitary and binary dye systems. The adsorption kinetics of the dyes followed pseudo-second-order kinetics. The results indicate that the Langmuir model provides the best correlation of the experimental data. The thermodynamic studies showed that the dye adsorption onto ATP-RGO CA was a spontaneous and endothermic reaction. High desorption of MG and MO showed the regeneration of ATP-RGO CA. It can be concluded that ATP-RGO CA is suitable as an adsorbent material to remove MG and MO dyes from unitary and binary systems.

## 1. Introduction

Dyes are widely used in various industries including textile, cosmetics, paper, plastics, rubber, and coating. Their discharge into water causes serious environmental and health problems [1]. Most of these dyes contain aromatic rings, which make them carcinogenic and mutagenic. Dyes can cause allergy, dermatitis, and skin irritation and also provoke cancer and mutation in humans [2]. At the same time, their complex molecular structure makes them very stable and difficult for biodegradation [3]. Therefore, the removal of color from waste effluents has become environmentally important. Many researchers have made considerable attempts to find suitable treatment systems to treat wastewater containing dyes from different industries, especially the textile industry.

Cationic dye malachite green (MG) and azo dye methyl orange (MO) are the representatives of dyes. MG and MO dyes have a negative impact on human health and increase the risk of cancer. Those used in the food industry are related to the appearance of allergy, asthma, dermatitis, and vascular edema [4], while the use in the pharmaceutical industry is alleged to cause skin irritation. MG rapidly metabolizes into fat-soluble colorless malachite green when it enters aquatic animals. MG has potential carcinogenic, teratogenic, and mutagenic effects. The wastewater formed by MO contains −N=N− components that are difficult to degrade, and carcinogens will be produced under certain

conditions. MG and MO dyes are toxic due to the presence of aromatic rings in their structures. Dye degradation is not easy and can induce the following diseases: dizziness, jaundice, burns, allergic problems, vomiting, diarrhea, nausea, and even affect development and mental health [4]. Due to the stable chemical properties and obvious toxicity of MG and MO, it is considered as a refractory organic wastewater by researchers [5]. The commonly used methods for dye removal from waste effluents are adsorption [6], coagulation [7, 8], biodegradation [9], membrane process, etc. [10, 11]. At present, the most common technique is adsorption technology, which is popular for its effectiveness, efficiency, economy, and absence of secondary pollution [12].

Recent studies have also confirmed that adsorption is a reliable and effective method for removing dyes from dye wastewater. Li et al. [13] prepared polyvinyl alcohol/graphene oxide adsorption sponge by crosslinking graphene oxide and polyvinyl alcohol. The adsorption sponge has ultralow density, good mechanical properties, and excellent continuous flow adsorption capacity. Sobhanardakani et al. [14] studied the adsorption of malachite green (MG), Nile blue A (NB), and Janus green B (JG) dyes on $NiFe_2O_4$ nanoparticles. Wu et al. [15] used ethyl silicate as the precursor, anhydrous ethanol as solvent, and $\gamma$-methacryloxypropyltrimethoxysilane as a modifier to prepare hydrophobic $SiO_2$ aerogel by sol-gel two-step catalytic method. The results show that the temperature resistance can reach 407°C, the specific surface area is 877.17 $m^2 \cdot g^{-1}$, the pore size distribution is 1.9~5 nm, and the particle size range is 10~50 nm. It is a typical nano-mesoporous material. These studies have shown that adsorption has a good effect on the removal of dyes from aqueous solutions, but few researchers pay attention to the cost and mechanical strength of the prepared adsorbents. Due to the use of expensive raw materials, the prepared adsorbents are unacceptable under large-scale production conditions. Moreover, if the mechanical strength of the adsorbent is not ideal, the potential cost generated in production activities is also immeasurable. Therefore, it is very important for researchers to find economical raw materials and prepare adsorbents with high mechanical strength and excellent adsorption performance to remove dyes from dye-polluted wastewater [16, 17].

In this manuscript, we used cheap natural attapulgite modified as silicon source to extract amorphous silicon oxides. The modified attapulgite-reduced graphene oxide composite aerogel (ATP-RGO CA) was synthesized by the sol-gel method. We report a detailed application of ATP-RGO CA as an adsorbent for the removal of dyes: methyl orange (MO) and malachite green (MG). The morphology features of ATP-RGO CA were characterized by Fourier transform infrared (FTIR), scanning electron microscopy (SEM), X-ray diffraction (XRD), and specific surface area and porosity analysis. The impact of external adsorption conditions such as pH value, contact time, and adsorption temperature on the adsorption process of unitary and binary dye systems was successfully achieved. To achieve the adsorption capacity and mechanisms of MG and MO adsorption onto ATP-RGO CA, the equilibrium kinetic, isotherm, and thermodynamic parameters were studied. The reusability test of ATP-RGO CA was performed by carrying out five cycles of adsorption-desorption studies. This study provides a useful reference for the preparation and application evaluation of dye adsorbents in the future.

## 2. Materials and Methods

*2.1. Chemicals and Materials.* Graphite powder, concentrated sulfuric acid, potassium permanganate, hydrochloric acid, and sodium nitrate are analytical pure, purchased from Tianjin Tianli Chemical Reagent Co., Ltd.; hydrogen peroxide, purchased from Tianjin Damao chemical reagent factory; ascorbic acid, concentration for analysis pure, purchased from Tianjin Tianxin Fine Chemical Development Center; malachite green, methyl orange, sodium hydroxide, sodium chloride, trimethylchlorosilane, and n-hexane are analytical pure, purchased from Tianjin Comiou Chemical reagent Co., Ltd. All the used chemicals are of analytical grade and without further purification. Attapulgite was collected from a real estate company in Gansu Province.

*2.2. Preparation of Graphene Aerogel and Composite Aerogel*

*2.2.1. Preparation of Graphene Oxide.* Add graphite powder and sodium nitrate at a ratio of 1 : 2 in 50 mL concentrated sulfuric acid and react for 40 min in the ice bath. Then, potassium permanganate was added in batches and fully reacted; heating, stirring at the same time, and then slowly dropping water, full reaction15 minutes, according to the water and ultrapure water volume ratio of 1 : 8 in the solution, after filtration. The filter cake was washed with dilute hydrochloric acid, dispersed with pure water, and centrifuged. The obtained graphene oxide sample was dried at 40°C [18].

*2.2.2. Preparation of Graphene Aerogel.* Graphene oxide solution of 4 mg·mL-1 was mixed uniformly by ultrasonic stirring. The graphene oxide and ascorbic acid were mixed according to the mass ratio of 1 : 2.5. The mixed solution after ultrasonic vibration treatment was put into a reaction kettle and heated in an oven at 90°C for 2 h to prepare the thermally reduced graphene hydrogel in the effluent [19]. Remove static to room temperature after multiple cleaning dialyzes in ethanol aqueous solution [20], after freeze-drying machine processing graphene aerogel.

*2.2.3. Preparation of Modified ATP-RGO Composite Aerogel.* Attapulgite was immersed in hydrochloric acid with a concentration of 9%. After shaking in a water bath shaker at 25°C and 30 rad/min for 30 min, it was moved to a water bath pot, stirred every 30 min at 70°C, cooled to room temperature after 8 h, and dried after filtration [21]. The 2.00 g acid-modified attapulgite was placed in a 50 mL small beaker, and hydrochloric acid with a concentration of 9% was added. The mixture was stirred evenly with a glass rod and moved to a hydrothermal crystallization reactor with polytetrafluoroethylene as the lining. The mixture was placed in an oven at 180°C and cooled to room temperature after 12 h. The mixture was filtered and dried with a circulating

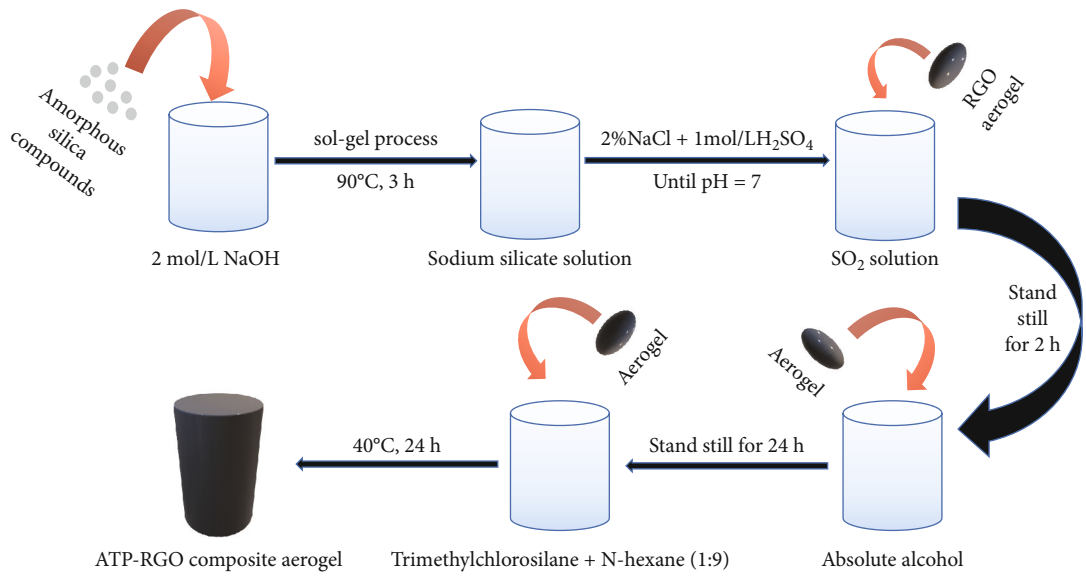


Figure 1: Preparation scheme of ATP-RGO composite aerogels.

vacuum pump to obtain a white powdered solid, which was the silicon source [22].

Add silicon source into 2 mol·L$^{-1}$ NaOH solution reacted at 90°C for 3 hours, and the solution was filtered to remove insoluble residues. Sodium chloride solution with a mass fraction of 4% and saturated sodium silicate solution with the same volume were mixed at room temperature, and dilute sulfuric acid solution with a mass fraction of 1 mol·L$^{-1}$ was added when stirring to form silica sol (pH = 7). Reduced graphene oxide (RGO) was impregnated in the sol and fully washed after solidification.

After standing for 2 h at room temperature, the water in the gel was washed and replaced with a 50% ethanol solution. After aging for 12 h at room temperature, the gel was further aged with anhydrous ethanol for 24 h. Trimethylchlorosilane and n-hexane were mixed evenly as modifiers according to the volume ratio of 1 : 9, and the sample was immersed in it for 24 h at 40°C for hydrophobic treatment. After modification, modified ATP-RGO composite aerogel was prepared by fully washing and drying with n-hexane. A brief preparation procedure of ATP-RGO composite aerogel is demonstrated in Figure 1.

### 2.3. Experimental Method

*2.3.1. Adsorption Experiment.* The concentration of 500 mg·L$^{-1}$ MG, MO solution 100 mL, adding 20 mg composite aerogel, shaking the water bath at 25°C for 6 hours, sampling every other time, and determination of MG, MO absorbance. The removal rate and adsorption amount of MG and MO dye systems by composite aerogel were calculated. Experimental design adjusted pH to 2, 4, 6, 8, and 10; the initial dye concentration was 200 mg·L$^{-1}$, 300 mg·L$^{-1}$, 400 mg·L$^{-1}$, and 500 mg·L$^{-1}$. The set temperature is 25°C, 35°C, and 45°C three temperatures; Langmuir and Freundlich's isothermal adsorption models were used to fit the adsorption experimental results of composite aerogel. The effect of contact time on dye removal rate was investigated by selecting a certain time node as the contact time. The calculation formulas of MG and MO removal rate $\eta$ and equilibrium adsorption capacity $q_e$ are as follows:

$$\eta = \frac{\rho_0 - \rho_e}{\rho_0} \times 100\%, \tag{1}$$

$$q_e = \frac{(\rho_0 - \rho_e)V}{m}, \tag{2}$$

where $\rho_0$ and $\rho_e$ are the dye concentration at the initial stage and equilibrium stage (mg/L), $V$ is the volume of reaction solution (L), and $m$ is the quality of adsorbent (g).

To better explain the adsorption mechanism in the adsorption process, several adsorption models were fitted in this study. Pseudo-first-order kinetic (Equation (3)), pseudo-second-order kinetic (Equation (4)), and intraparticle diffusion (Equation (5)) are three classical kinetic models that reveal the adsorption process. The equation is as follows:

$$\ln(q_e - q_t) = \ln q_e - k_1 t, \tag{3}$$

$$\frac{t}{q_t} = \frac{1}{k_2 q_e^2} + \frac{1}{q_e} t, \tag{4}$$

$$q_t = k_p\left(t^{1/2}\right), \tag{5}$$

where $q_e$ and $q_t$ are the adsorption capacity of composite aerogel at equilibrium and at different times (mg/g). $k_1$ (min$^{-1}$), $k_2$ (g·mg$^{-1}$·min$^{-1}$), and $k_p$ (g·mg$^{-1}$·min$^{-1/2}$) are the kinetic rate constants. $t$ (min) is the adsorption time.

Langmuir, Freundlich, and Temkin isothermal adsorption models are the three most commonly used adsorption models for wastewater treatment. Therefore, in this study, the Langmuir model (Equation (6)), Freundlich model

Table 1: L9 (34) orthogonal design and experimental results.

| Serial number | Combination | $A$ | $B$ | $C$ | Gelling time $T$ (min) | Mechanical strength $J$ (g) |
|---|---|---|---|---|---|---|
| 1 | $A_1B_1C_1$ | 1 : 10 | 25 | 40 | 10 | 93 |
| 2 | $A_1B_2C_2$ | 1 : 10 | 40 | 60 | 7 | 83 |
| 3 | $A_1B_3C_3$ | 1 : 10 | 55 | 80 | 3 | 97 |
| 4 | $A_2B_1C_2$ | 1 : 15 | 25 | 60 | 8 | 85 |
| 5 | $A_2B_2C_3$ | 1 : 15 | 40 | 80 | 9 | 91 |
| 6 | $A_2B_3C_1$ | 1 : 15 | 55 | 40 | 4 | 100 |
| 7 | $A_3B_1C_3$ | 1 : 20 | 25 | 80 | 5 | 92 |
| 8 | $A_3B_2C_1$ | 1 : 20 | 40 | 40 | 15 | 90 |
| 9 | $A_3B_3C_2$ | 1 : 20 | 55 | 60 | 6 | 95 |
| $T$ mean value 1 | $K_1$ | 20 | 23 | 29 | | |
| $T$ mean value 2 | $K_2$ | 21 | 31 | 19 | | |
| $T$ mean value 3 | $K_3$ | 26 | 13 | 17 | | |
| $T$ range | $R_j$ | 6 | 18 | 12 | | |
| $J$ mean value 1 | $Q_1$ | 263 | 270 | 283 | | |
| $J$ mean value 2 | $Q_2$ | 276 | 264 | 263 | | |
| $J$ mean value 3 | $Q_3$ | 277 | 292 | 280 | | |
| $J$ range | $R_j$ | 14 | 28 | 20 | | |

(Equation (7)), and Temkin model (Equation (8)) were used to fit the adsorption isotherms of MG and MO on composite aerogel. The equation is as follows:

$$\frac{C_e}{q_e} = \frac{1}{Q_{\max}k_L} + \frac{C_e}{Q_{\max}}, \tag{6}$$

$$\ln q_e = \ln k_F + \frac{\ln C_e}{n}, \tag{7}$$

$$q_e = k_T \ln (fC_e), \tag{8}$$

where $C_e$ (mg·L$^{-1}$) is the equilibrium concentration. $Q_{\max}$ (mg·g$^{-1}$) is the theoretical maximum adsorption capacity of composite aerogel. $k_L$ (L·mg$^{-1}$), $k_F$ (mg·g$^{-1}$), and $k_T$ (J/mol) are the constants of Langmuir, Freundlich, and Temkin isotherms. $n$ represents the adsorption intensity, and $f$ (L/mg) is the Temkin binding energy.

To further evaluate the adsorption process, one of the key parameters of the Langmuir equation $R_L$ was calculated (Equation (9)); $R_L$ is a dimensionless separation growth factor that examines whether the adsorption process is favorable.

$$R_L = \frac{1}{1 + K_L C_e}. \tag{9}$$

If $R_L > 1$, it indicates that the adsorption is not favorable; if $R_L = 1$, the adsorption is linear; if $0 < R_L < 1$, the adsorption is favorable, and if $R_L = 0$, it means that adsorption is irreversible [23].

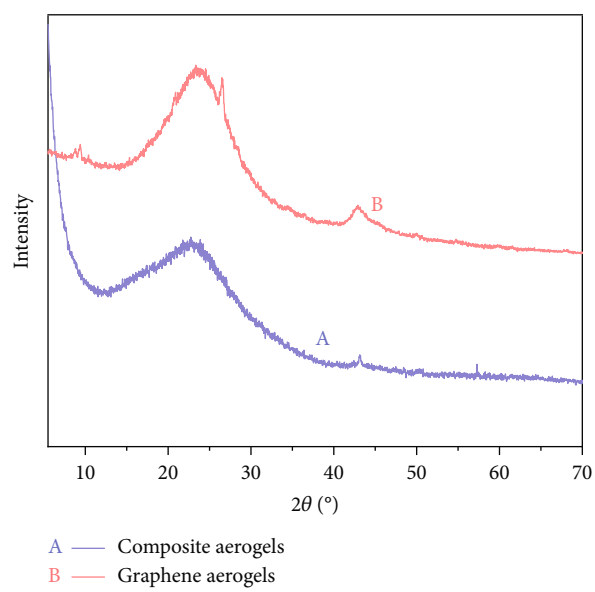


Figure 2: X-ray diffraction patterns of graphene aerogels and composite aerogels.

To study the dependency of the MG and MO adsorption process on the temperature, the equilibrium data were evaluated in terms of thermodynamics. The effects of different operating temperatures (298.15 K, 308.15 K, and 318.15 K) are investigated in this research. The thermodynamic parameters enthalpy ($\Delta H$), entropy ($\Delta S$), and free energy ($\Delta G$) alteration were studied to the determination of the thermodynamic behavior of the adsorption process. The

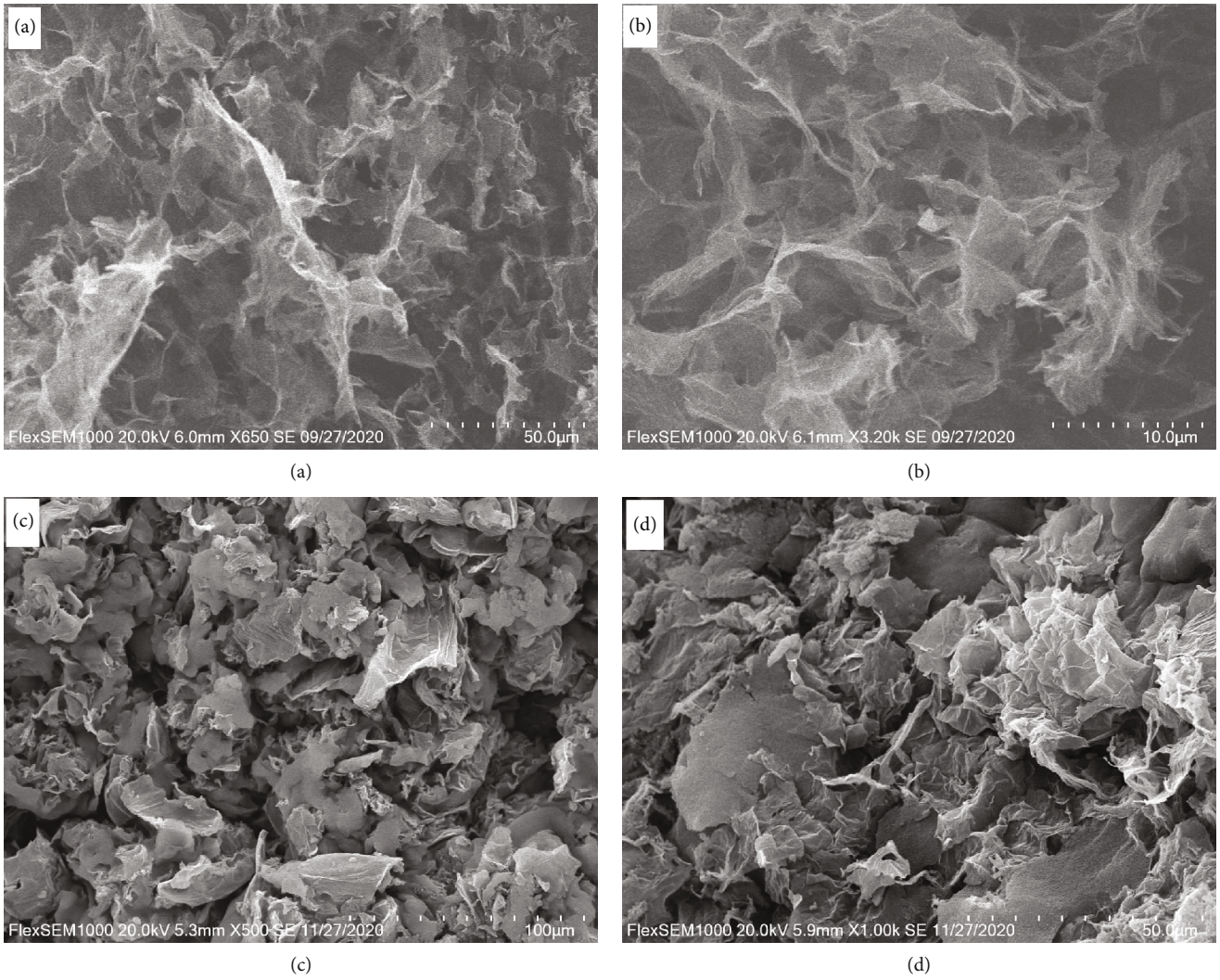


Figure 3: SEM of (a, b) graphene aerogel and (c, d) composite aerogel.

changes in the thermodynamic parameters were calculated with the following equation:

$$\Delta G^0 = -RT \ln k_d, \tag{10}$$

$$k_d = \frac{q_e}{c_e}, \tag{11}$$

$$\ln \mathrm{k_d} = \frac{\Delta \mathrm{S}}{\mathrm{R}} - \frac{\Delta \mathrm{H}}{\mathrm{RT}}, \tag{12}$$

$$\Delta G^0 = \Delta H^0 - T\Delta S^0, \tag{13}$$

where $K_d$, $q_e$, and $c_e$ are the equilibrium constant, the amount of dye adsorbed on the adsorbent of the solution at equilibrium (mol·L$^{-1}$), and the equilibrium concentration of dye in the solution (mol·L$^{-1}$), respectively. $\Delta G^0$ is the free energy change (kJ/mol), $\Delta H^0$ (kJ/mol) and $\Delta S^0$ (J/mol/K) are standard enthalpy and standard entropy. $R$ is the ideal gas constant (kJ/mol/K), and $T$ is the solution temperature (K) [24].

*2.3.2. Orthogonal Experiment.* As a kind of material with a controllable structure, the modified ATP-RGO composite aerogel has many variables in the preparation process, and each variable restricts the other. The change of a variable will directly affect the performance of the composite aerogel. Therefore, it is necessary to comprehensively analyze the influence of various factors on its performance. Therefore, the orthogonal test method can be used to analyze. The orthogonal experiment method is a design method to study multifactor and multilevel, which can improve the efficiency of the experiment and give the optimization analysis scheme. It is an efficient, rapid, and experimental design method [25]. In this experiment, the solid-liquid ratio of silicon source to alkali solution ($A$), aging temperature ($B$), and drying temperature ($C$) was used as variables to study the influence on the performance of modified ATP-RGO composite aerogel. The orthogonal table L9 (34) of three factors and three levels was selected for nine experiments. The gel time and mechanical strength were tested in the sample preparation process. The results of the orthogonal experiment and analysis are shown in Table 1.

It can be seen from the orthogonal experiment results that the gel of sample 3 ($A_1B_3C_3$) was the fastest. According to the analysis, the primary and secondary order of the factors affecting the gel time was $B$ (aging temperature) > $C$ (drying temperature) > $A$ (solid-liquid ratio), and the primary and secondary order of the factors affecting the mechanical strength was $B$ (aging temperature) > $C$ (drying temperature) > $A$ (solid-liquid ratio). It can be seen that regardless of gel time or mechanical strength, the aging temperature was the most important factor. After measurement, sample 6 ($A_2B_3C_1$) has the highest mechanical strength, which can withstand 100 g weight. It is the best sample in the orthogonal experimental group.

In summary, in the preparation of ATP-RGO CA, the aging temperature has the greatest influence on gelation time and mechanical strength. Analysis of experimental data, comprehensive factors, selected solid-liquid ratio 1 : 15, aging temperature 55°C, drying temperature 40°C, the best preparation process of modified ATP-RGO composite aerogel.

*2.3.3. Desorption Experiment.* To evaluate the reusability of the composite aerogel, adsorption and desorption tests were conducted using three eluents, namely, 0.01 M $CH_3COOH$, 0.01 M $C_5H_6O$, and 0.01 M HCl. Desorption (%) is estimated by

$$\text{desorption (\%)} = \frac{C_m}{C_e} \times 100\%, \tag{14}$$

where $C_m$ and $C_e$ (mg/L) refer to the concentration of MO and MG released in the solution and the initially adsorbed MO and MG concentration, respectively.

## 3. Discussion

### 3.1. Material Characterization

*3.1.1. X-Ray Diffraction Analysis.* XRD diffraction patterns of graphene aerogel and modified ATP-RGO composite aerogel are given in Figure 2. It can be found from the graphene aerogel that a broad diffraction peak appears at $2\theta = 25°$, sharp diffraction peaks disappear, the results showed that the oxygen-containing functional groups on reduced graphene oxide surface were removed by ascorbic acid reduction, and the crystal plane spacing was reduced and the hydrophobicity was enhanced [26]. It was found from the diffraction pattern of the composite aerogel that there was a diffraction peak with small intensity $2\theta = 15° \sim 30°$, and there was no graphene oxide diffraction peak reduced by ascorbic acid. According to JCPDS No. 75-0254, indicating that the composite of silicon oxide and graphene was successful, and it also reflected that in the composite aerogel, amorphous silicon oxide inhibits the natural accumulation of graphene sheets, resulting in an increase in the distance between graphene sheets and the disappearance of graphene diffraction peaks, reflecting the protective effect of amorphous silicon oxide particles [27].

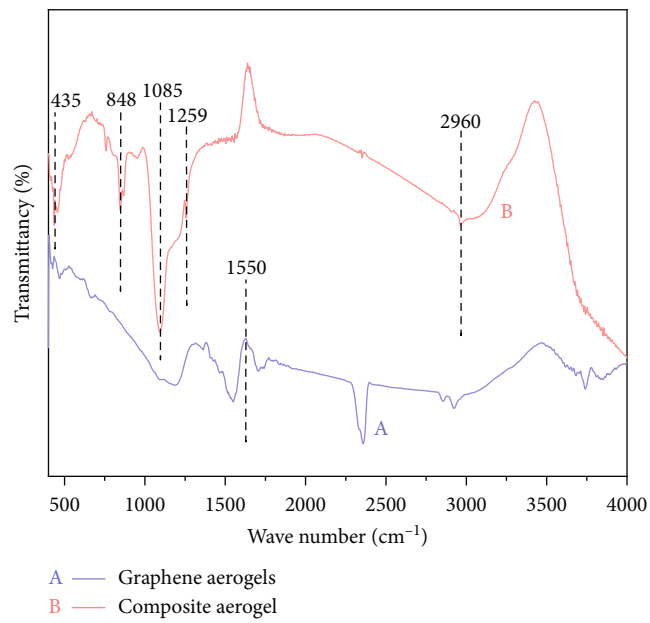


Figure 4: Infrared spectra of graphene aerogel and composite aerogel.

*3.1.2. Scanning Electron Microscopy.* SEM images were used to examine the morphology and structure of graphene aerogels and composite aerogel. Figures 3(a) and 3(b) show the SEM images of graphene aerogels; Figures 3(c) and 3(d) show SEM images of composite aerogel.

It can be seen from Figures 3(a) and 3(b) that the prepared graphene aerogel has a three-dimensional network structure, the graphene sheets overlap with each other, and its structure has a certain regularity. It can be seen from Figures 3(c) and 3(d) that the composite aerogel is also three-dimensional networks. White flake amorphous silicon oxide particles are uniformly distributed on the surface of graphene, indicating that silicon oxide is well loaded on the surface of graphene. These silicon oxide particles coated on the surface can effectively prevent the natural accumulation of graphene oxide sheets, which is another evidence of the protective effect of silicon oxide particles. The existence of a three-dimensional network structure greatly increased the specific surface area of aerogels [28] and provided a large number of adsorption sites, which showed great adsorption capacity.

*3.1.3. Infrared Spectroscopic Analysis.* From the infrared spectra of graphene aerogel (GA) and composite aerogel (CA) shown in Figure 4, there is no obvious absorption peak, which indicates that the oxygen-containing groups on the graphene aerogel sheet are reduced by ascorbic acid, and the new absorption peak at 1550 $cm^{-1}$ also indicates that the graphene aerogel with the new structure is successfully prepared [29]. The composite aerogel showed characteristic peaks of Si-O-Si at 1085 $cm^{-1}$, 848 $cm^{-1}$, and 435 $cm^{-1}$, indicating that silicon oxide was successfully loaded into the graphene aerogels [30]. Due to the modification of trimethylchlorosilane, the alkyl peak appeared at 2960 $cm^{-1}$. At 757 $cm^{-1}$ and 2960 $cm^{-1}$, the antisymmetric stretching

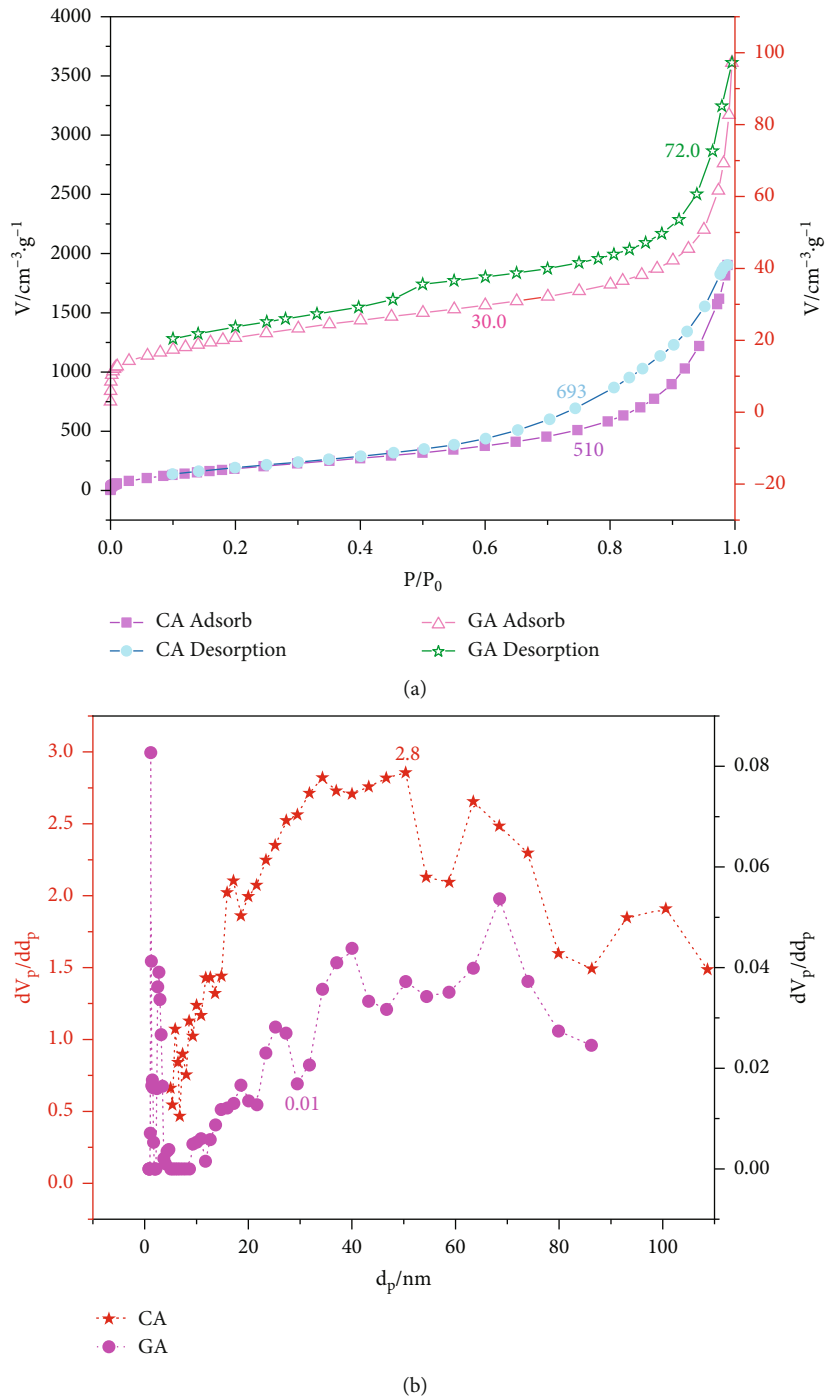


Figure 5: (a) $N_2$ adsorption-desorption isotherms and (b) pore size distribution of graphene aerogels and composite aerogels.

vibration peak and symmetric stretching vibration peak of C-H in -$CH_3$ were observed, respectively [31]. The absorption peak near 1259 $cm^{-1}$ was caused by Si-C vibration, which indicated that after the modification of trimethylchlorosilane, -$CH_3$ was connected to the end branch of the composite aerogel so that the aerogel was hydrophobic [32].

*3.1.4. Specific Surface Area and Pore Size Analysis.* The $N_2$ adsorption-desorption isotherms and pore size distribution curves of graphene aerogels and composite aerogel are displayed in Figures 5(a) and 5(b), respectively. From Figure 5(a), it is obvious that all isotherms are type IV, indicating typical mesoporous materials. From Figure 5(b), when $P/P0 > 0.5$, there was an obvious H3 hysteresis loop, indicating that there is a mesoporous structure inside and the pore shape is slender. At this time, the specific surface areas of graphene aerogel and composite aerogel are 171.14 $m^2 \cdot g^{-1}$ and 781.57 $m^2 \cdot g^{-1}$, respectively. –Si–O–C– the

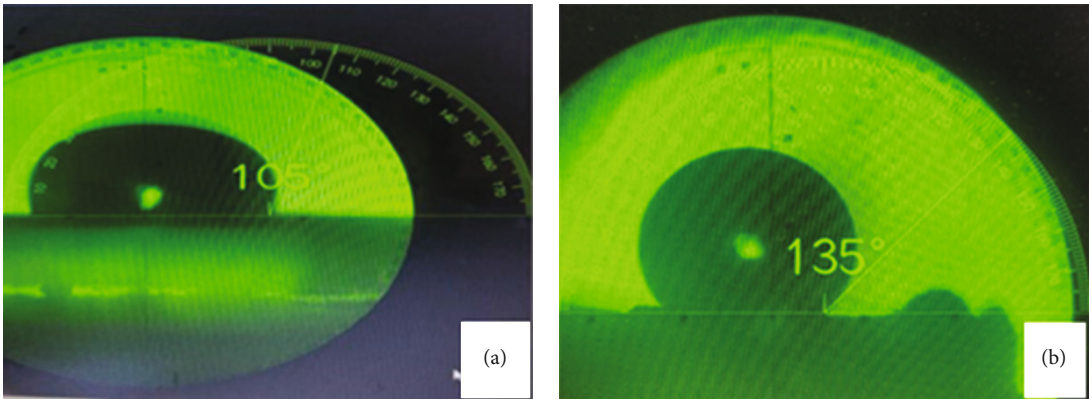


(a) (b)

Figure 6: Contact angle test diagram of (a) graphene aerogel and (b) composite aerogel.

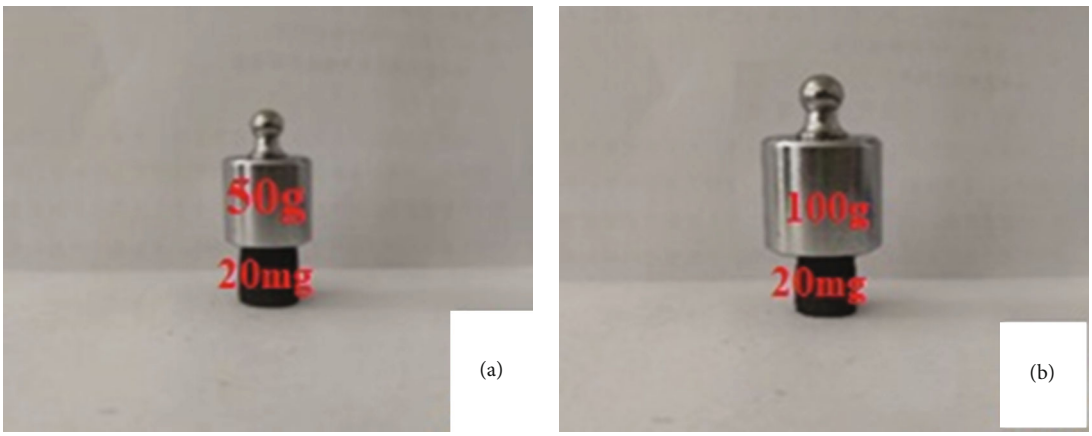


(a) (b)

Figure 7: Mechanical strength test diagram of graphene aerogel and composite aerogel.

bond between amorphous silica compounds and graphene can form via the condensation reaction between –Si–OH and –OH on the basal plane of graphene, where the basal plane of graphene can act as a barrier agent, being favorable to the dispersion of amorphous silica compounds nanoparticles and avoid the formation of large particles, thus resulting in the increase of the specific surface area of aerogels [33]. According to the BET method and BJH equation, the pore volumes of graphene aerogel and composite aerogel are $0.127\,cm^3 \cdot g^{-1}$ and $2.94\,cm^3 \cdot g^{-1}$, respectively, and the pore sizes are 2.34 nm and 31.81 nm, respectively. This is mainly due to the successful addition of silica compounds, increasing the spacing of graphene sheets, resulting in increased specific surface area and pore volume [34].

*3.1.5. Contact Angle Analysis.* The contact angle test diagram of graphene aerogel and composite aerogel is shown in Figures 6(a) and 6(b), respectively. When the contact angle is in the range of 90°~150°, the solid surface is difficult to be soaked in water, which is called the hydrophobic surface and reflects the hydrophobicity of the solid. As shown in the figure, the contact angle between graphene aerogel and pure water is 105°, showing a certain hydrophobicity. The contact angle between the composite aerogel and pure water is 135°, indicating that the sample has good hydrophobicity. Hydrophobicity enables aerogels to maintain nonwettability in water and to preferentially adsorb dyes in water, which is beneficial to the treatment of dye wastewater.

*3.1.6. Mechanical Strength Analysis.* Aerogels must have a certain mechanical strength, otherwise under the impact of the fluid will appear scattered, structural collapse, and so on. To this end, we tested the mechanical properties of graphene aerogels and composite aerogel, as shown in Figure 7. It indicates that 20 mg of graphene aerogel can support the 2500-fold weight (50 g) of its mass without deformation and damage. Figure 7(b) indicates that 20 mg composite aerogel can successfully support 100 g weight, which is 5000 times its weight. After removing the weight, the aerogel has no deformation and damage, showing excellent mechanical strength. The reason for the increase in the strength of the composite aerogel is that silicon oxide is added as an

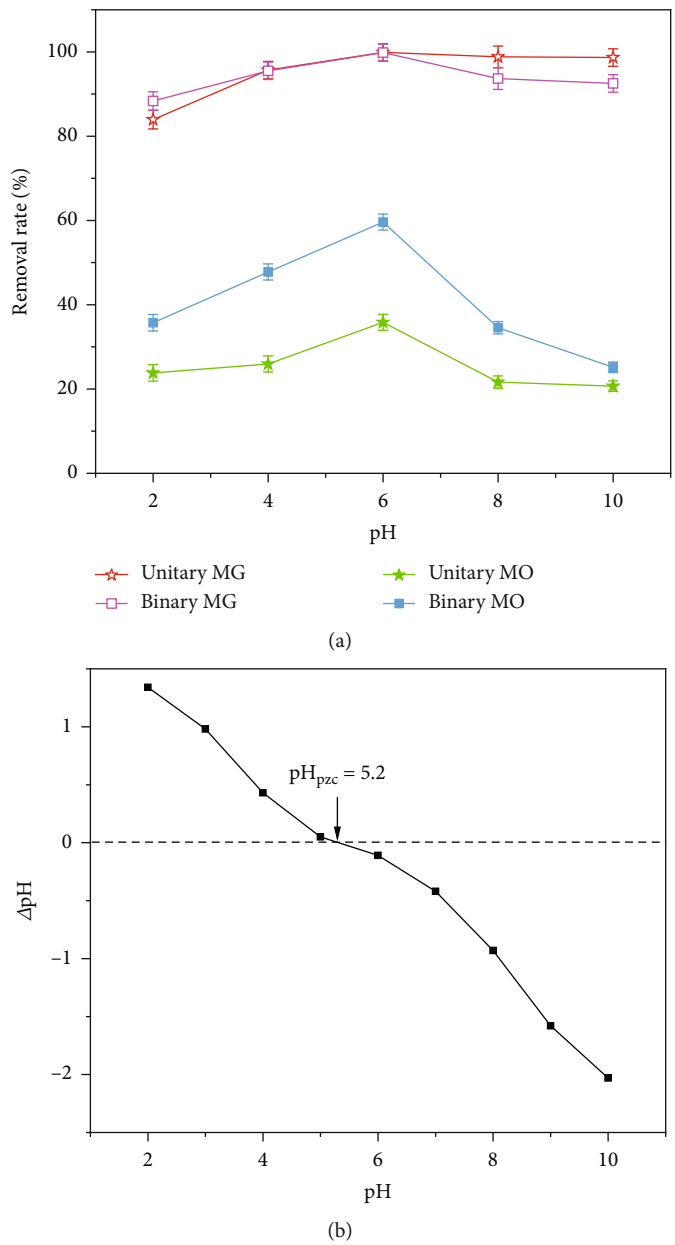


Figure 8: (a) Effect of pH on adsorption of MG and MO; (b) $pH_{pzc}$ of the adsorbent.

agglomeration inhibitor to curb the accumulation of graphene sheets, resulting in a more complete pore wall structure of the composite aerogel, enhancing the stability of its structure and thereby increasing the mechanical strength of the composite aerogel.

### 3.2. Adsorption Experiments

*3.2.1. Effect of pH on Adsorption of Malachite Green and Methyl Orange.* The pH is one of the important factors that affect the adsorption process of pollutants in wastewater. The pH influences the solubility of dyes in water, the activity of surface functional groups of the adsorbents, and ion competition for the adsorption centers [35]. To explore the effect of pH on the adsorption properties of composite aerogel, MG and MO monobasic and binary dye systems were adsorbed by composite aerogel under different pH (Figure 8(a)). Meanwhile, to better understand the effect of solution pH on the adsorbent itself, the point of zero charge ($pH_{pzc}$) of the composite aerogel was also studied. The results are shown in Figure 8(b). The removal rates of MG and MO reached the highest adsorption capacity at pH = 6. Since then, with the increase of pH, the removal rate of MO decreased, but the removal rate of MG remained at the highest point. When pH is lower than 4, the removal rate of MG in the unitary dye system is relatively low, because under acidic conditions, excessive $H^+$ and cationic dye MG produce competitive adsorption [36]. When pH

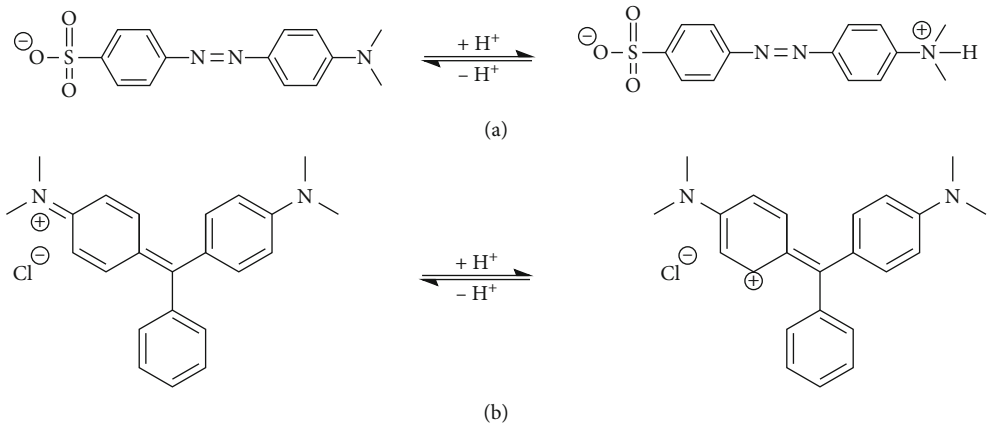


Figure 9: The MO structures in acidic solute (a); the MG structures in acidic solute (b).

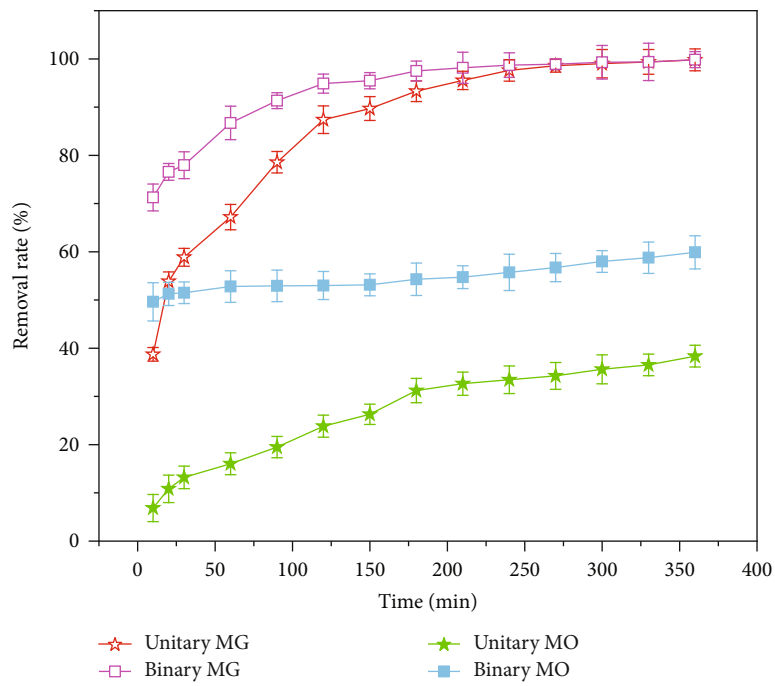


Figure 10: Effect of adsorption time on the adsorption of MG and MO by composite aerogel.

is less than 6, the removal rate of MO increases with the increase of pH. When pH is greater than 6, the removal rate decreases with the increase of pH. This is due to the quinoid structure of methyl orange in an acidic environment. The sulfonic acid end of the molecule is negatively charged, and it can form a chemical bond with $MOH_2^+$ (Figure 9(a)), which promotes the adsorption of methyl orange to a certain extent. In an alkaline environment, methyl orange is negatively charged and repels $MO^-$, which hinders the adsorption of methyl orange [37]. And as shown in Figure 8(b), the $pH_{pzc}$ of the composite aerogel is 5.2, which means that the surface of the composite aerogel is negatively charged when the solution pH is greater than 5.2 and positively charged when the solution pH is lower than 5.2. MO is a typical anionic dye with a negative charge. This means that when pH is greater than 5.2, there is electrostatic repulsion between the negatively charged surface and negatively charged MO, which is not conducive to the adsorption of MO [38]. Therefore, with the increase of pH, the removal rate of MO decreased. In contrast, MG is a typical cationic dye, and the increase of pH is beneficial to the adsorption of MG (Figure 9(b)).

Considering the practical application, the pH value was determined to be 6. Different from the monobasic system, the removal rate of MO by composite aerogel in the binary dye system has been greatly improved, indicating that the coexistence of the two dyes has a great role in promoting the adsorption of the two, and the two are synergistic adsorption.

*3.2.2. Effect of Adsorption Time on Adsorption of Malachite Green and Methyl Orange.* The composite aerogels were

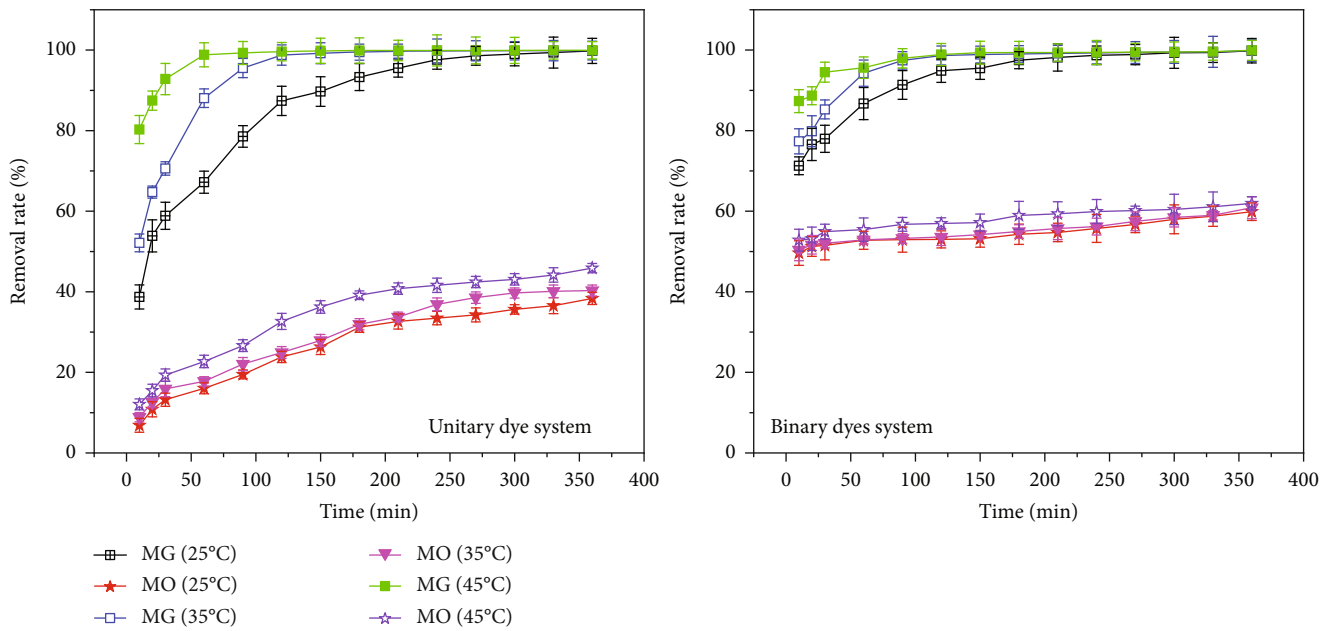


Figure 11: Effect of temperature on the adsorption of MG and MO by composite aerogel.

used to adsorb MG and MO monobasic and binary dye systems, and the results are shown in Figure 10. The removal rate of MG by composite aerogel in either monobasic or binary dye systems was high, indicating that the silica compounds were successfully composited into graphene aerogels, which increased the specific surface area of composite aerogel and improved their adsorption capacity. It can be seen that in the binary system, MG and MO reach the adsorption equilibrium after 180 and 60 minutes, respectively, while in the unitary system, MG and MO reach the adsorption equilibrium after 250 minutes. At the same time, the removal rates of MG and MO in the binary dye system were higher than those in the monadic system, which was due to the formation of dimers between MG and MO in the binary system to improve their aromaticity, thereby enhancing the $\pi$-$\pi$ interaction between themselves and the adsorbent and improving the adsorption performance of MG. When MG is adsorbed on the surface of the adsorbent, the electrostatic repulsion between the adsorbent surface and the MO molecule will be weakened. At the same time, the adsorbed MG forms hydrogen bonds or $\pi$-$\pi$ interactions with the MO in the solution, thereby enhancing the interaction between the two and thereby improving the removal rate of MO in the binary dye system [39].

*3.2.3. Effect of Adsorption Temperature on Adsorption of Malachite Green and Methyl Orange.* At different temperatures, MG and MO monobasic and binary dye systems were adsorbed to explore the effect of temperature on the adsorption properties of composite aerogel. The results are shown in Figure 11. The removal rate of MG and MO increased with the increase in temperature, indicating that the adsorption of dyes by composite aerogel was an endothermic reaction. It is obvious that in the binary system, the removal rate of MO by composite aerogel fluctuates little with time, and the removal rate is much higher than that of the monobasic dye system, which once again shows the synergistic adsorption of the two dyes. In addition, it can be observed that the removal rate of MG by composite aerogel in the binary dye system is higher than that in the unitary system, which also reflects that MG and MO form dimers to improve their aromaticity in the binary system, thereby enhancing the $\pi$-$\pi$ interaction between themselves and the adsorbent and improving the adsorption performance of MG [39].

*3.2.4. Adsorption Kinetics of Malachite Green and Methyl Orange on Modified ATP-RGO Composite Aerogel.* To explore the adsorption mechanism of MG and MO on composite aerogel, pseudo-first-order kinetic model, pseudo-second-order kinetic model, and intraparticle diffusion model were used to fit and analyze the experimental results of MG and MO adsorption on monobasic and binary dye systems. The obtained adsorption kinetics data are shown in Figure 12 and Table 2.

Table 2 shows the fitting of different kinetic equations to the test results. According to the data in the table, the correlation coefficient $R^2$ of the fitting quasi-second-order kinetic equation is greater than that of the fitting quasi-first-order kinetic equation and is greater than 0.999, indicating that the adsorption process of dyes on composite aerogel is more in line with the quasi-second-order kinetic equation. It indicates that adsorption is a chemical process, not a physical diffusion process. In addition, it can be seen from the quasi-second-order kinetic parameters that in the binary dye system, the parameter $q_e$ of MG is significantly smaller than that of the mono-dye system, while the parameter $q_e$ of MO is significantly higher than that of the mono-dye system. This is because, in the binary dye system, the presence of MG promotes the adsorption of MO by the composite aerogel. In the table, the linear correlation coefficient obtained by

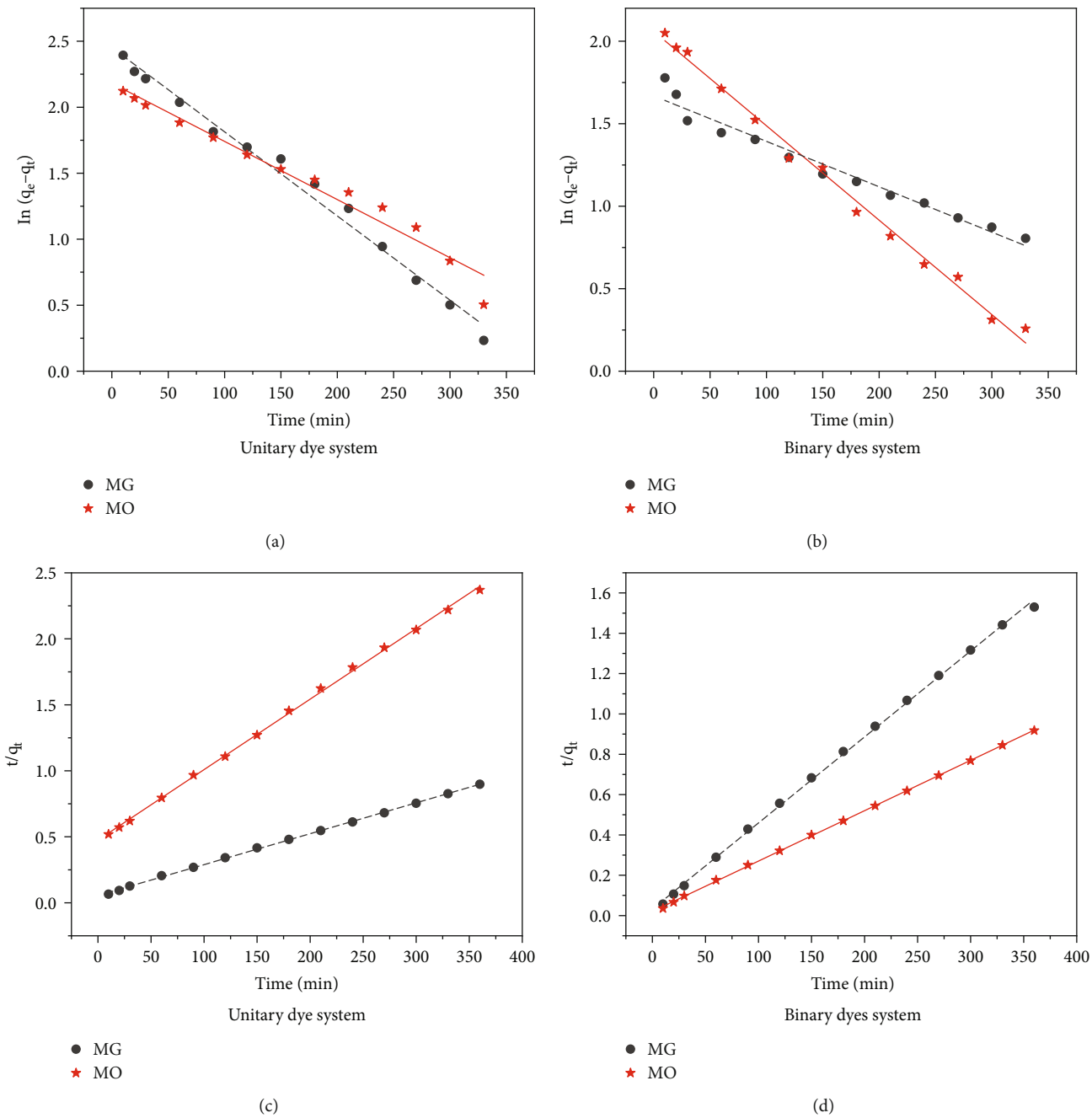


Figure 12: Continued.

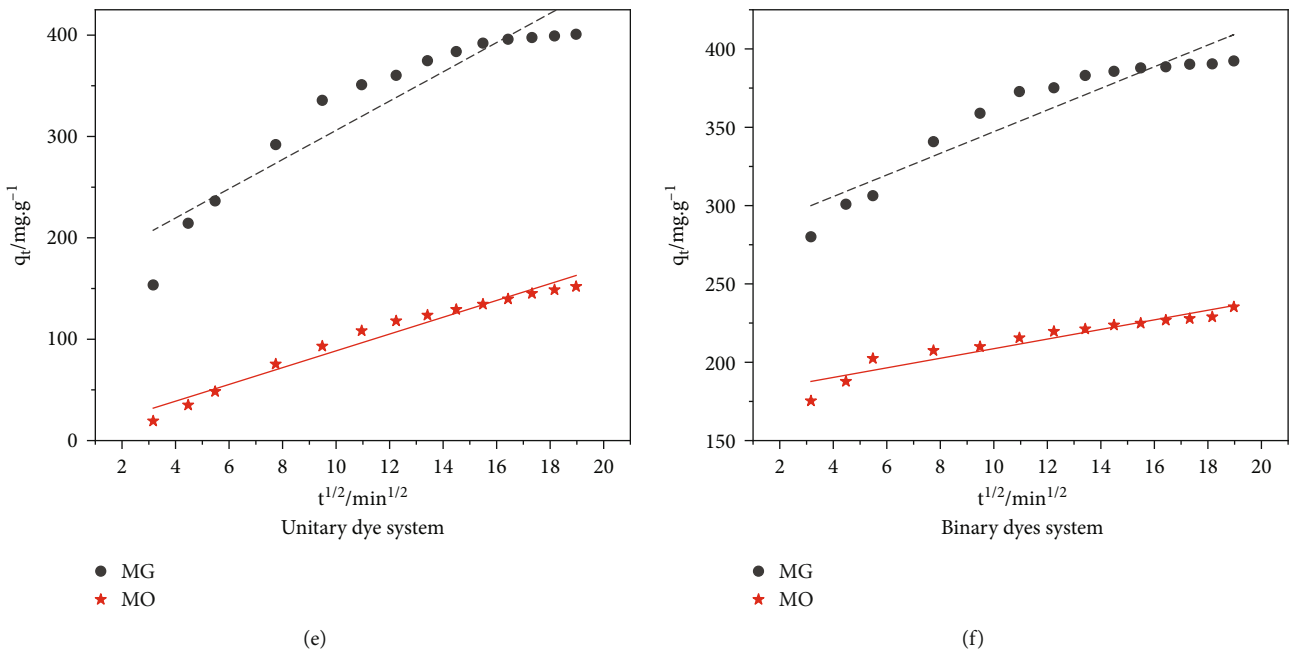


Figure 12: (a, b) Pseudo-first-order kinetic fitting curve, (c, d) pseudo-second-order kinetic fitting curve, and (e, f) intraparticle diffusion equation fitting curve of MG and MO adsorption on composite aerogel.

Table 2: Adsorption kinetic parameters of malachite green and methyl orange on composite aerogel.

| | | Pseudo-first-order kinetic equation | | | Pseudo-second-order kinetic equation | | | Intraparticle diffusion equation | |
|---|---|---|---|---|---|---|---|---|---|
| | | $K_1$ (min$^{-1}$) | $q_e$ (mg·g$^{-1}$) | $R^2$ | $K_2 \times 10^{-3}$ (g·mg$^{-1}$·min$^{-1}$) | $q_e$ (mg·g$^{-1}$) | $R^2$ | $K_p$ (mg·(g·s)$^{-1}$) | $R^2$ |
| MG | Unitary | 0.006 | 11.6 | 0.989 | 0.096 | 434.78 | 0.9994 | 14.4 | 0.894 |
| | Binary | 0.006 | 7.85 | 0.993 | 0.0003 | 400.00 | 0.9998 | 6.91 | 0.889 |
| MO | Unitary | 0.004 | 8.86 | 0.969 | 0.0592 | 188.68 | 0.9992 | 8.28 | 0.966 |
| | Binary | 0.003 | 5.30 | 0.964 | 0.0006 | 232.56 | 0.9991 | 3.07 | 0.907 |

particle diffusion fitting is very low, indicating that the particle diffusion equation cannot fully describe the whole adsorption process and should be controlled by the combination of particle diffusion and membrane diffusion [40, 41].

*3.2.5. Adsorption Isotherms of Malachite Green and Methyl Orange on Modified ATP-RGO Composite Aerogel.* To explore the interaction between composite aerogel and two dyes, unitary and binary dye systems with different initial concentrations were adsorbed at 25°C and an analysis of adsorption isotherm. The adsorption isotherm data fitted by Langmuir, Freundlich, and Temkin isotherm models are tabulated in Figure 13 and Table 3.

As shown in Table 3, based on the Langmuir isotherm model data, under the optimum experimental conditions (temperature = 25°C, initial concentration = 200 mg/L, adsorption time = 360 min), the maximum adsorption capacity of the binary dye system is better than that of unitary dye system, the maximum adsorption capacity of MG and MO in the binary dye system was 842.0 mg/g and 540.5 mg/g, respectively. In Table 4, we compared the maximum adsorption capacities of MG and MO on the adsorbents proposed in this study with those in other studies. The results show that the adsorbent proposed in this study has higher adsorption capacity for MG and MO.

It can be seen from Table 3 that the $R^2$ coefficient fitted by the Langmuir isothermal equation was higher than that fitted by the Freundlich isothermal and Temkin isothermal, which was greater than 0.99, indicating that the Langmuir isothermal adsorption equation was more in line with the adsorption process of composite aerogel for dyes, indicating that the adsorption process belonged to monolayer adsorption, and the surface structure of the adsorbent was uniform [46]. Meanwhile, the dimensionless separation factor $R_L$ of the Langmuir model can effectively reflect the adsorption process: when $R_L > 1$, it indicates that the adsorption is not favorable; when $R_L = 1$, the adsorption is linear; when $0 < R_L < 1$, the adsorption is favorable, and if $R_L = 0$, it means that adsorption is irreversible. As shown in Table 3, the $R_L$ values of the two dyes are all between 0 and 1 in both unitary and binary systems. It shows that the adsorption of two dyes on composite aerogel is favorable and reversible. In addition, in the Freundlich model values, $n < 1$ indicated that adsorbate was unfavorably adsorbed on an adsorbent, while $n >$

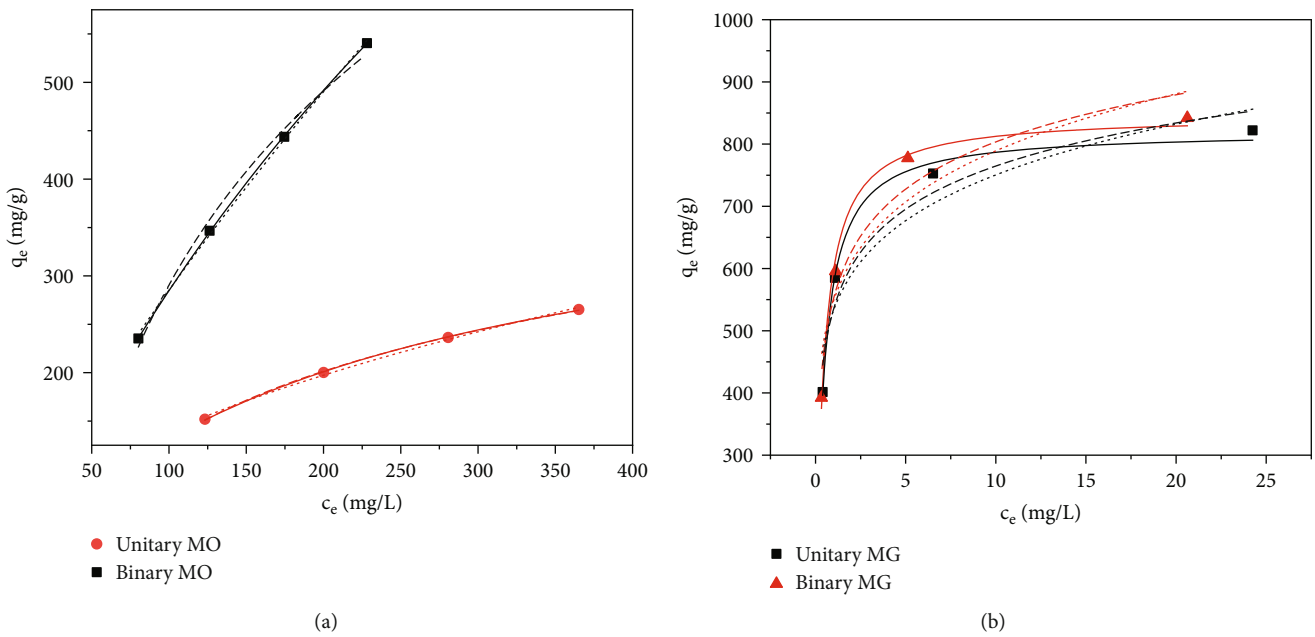


Figure 13: Isotherm fittings of (a) MO adsorption and (b) MG adsorption on the composite aerogels (Langmuir isotherm: solid line, Freundlich isotherm: point line, Temkin isotherm: scratch line).

Table 3: Adsorption isotherm parameters of MG and MO on composite aerogel.

| | | Langmuir isothermal | | | | Freundlich isothermal | | | Temkin isothermal | | |
|---|---|---|---|---|---|---|---|---|---|---|---|
| | | $Q_m$ | $k$ | $R_L$ | $R^2$ | $n$ | $K_F$ | $R^2$ | $k_T$ | $f$ | $R^2$ |
| MG | Unitary | 822.1 | 0.053 | 0.87 | 0.99 | 1.48 | 14.9 | 0.91 | 98.93 | 0.04 | 0.95 |
| | Binary | 842.0 | 0.024 | 0.17 | 0.99 | 1.46 | 1.68 | 0.90 | 105.5 | 0.03 | 0.92 |
| MO | Unitary | 365.3 | 0.004 | 0.55 | 0.99 | 1.69 | 13.1 | 0.99 | 104.3 | 0.21 | 0.99 |
| | Binary | 540.5 | 0.002 | 0.73 | 0.99 | 1.27 | 7.80 | 0.99 | 109.6 | 0.16 | 0.99 |

Table 4: Comparison of maximum adsorption capacities of different adsorbents for MG and MO.

| Dye | Adsorbent | Maximum adsorption capacity ($mg \cdot g^{-1}$) | Reference |
|---|---|---|---|
| MG | Cd $(OH)_2$-NW-AC | 80.64 | [42] |
| | NiO flowerlike nanoarchitectures | 142.1 | [43] |
| | $NiFe_2O_4$ NPs | 210.0 | [14] |
| | ATP-RGO CA | 842.0 | This study |
| MO | $CoFe_2O_4$ from binary solutions with CR | 117.5 | [35] |
| | Muscovite-supported $Fe_3O_4$ nanoparticles | 149.3 | [44] |
| | Multiwalled carbon nanotubes (MWCNTs) coated | 81.00 | [45] |
| | ATP-RGO CA | 540.5 | This study |

1 indicated that adsorbate was favorably adsorbed on an adsorbent [47]. In this study, the $n$ value was higher than 1, which indicated that adsorption intensity was good throughout the experimental concentration range. Finally, the fitted $R^2$ values of the Temkin model in unitary and binary systems of MG and MO are relatively high, suggesting that there is a strong electrostatic interaction between MG, MO, and composite aerogel which contributes to adsorptive removal of both dyes[48–52].

*3.2.6. Adsorption Thermodynamics Analysis of Malachite Green and Methyl Orange on Modified ATP-RGO Composite Aerogel.* The thermodynamic parameters of MG and MO adsorption by composite aerogel at 298.15 K, 308.15 K, and 318.15 K were obtained through the thermodynamic analysis of the adsorption process of MG and MO in the monobasic and binary dye systems. The results are shown in Table 5. All $\triangle G^0$ was less than 0 and greater than −20 kJ/mol, indicating that the adsorption reaction was

Table 5: Adsorption thermodynamic parameters of MG and MO on composite aerogel.

| | $T$ (K) | | $\triangle G^0$ (kJ·mol$^{-1}$) | | $\triangle H^0$ (KJ·mol$^{-1}$) | | $\Delta S^0$ (J·mol$^{-1}$·K$^{-1}$) | |
|---|---|---|---|---|---|---|---|---|
| | Unitary | Binary | Unitary | Binary | Unitary | Binary | Unitary | Binary |
| | 298.15 K | 298.15 K | -7.30 | -7.56 | | | | |
| MG | 308.15 K | 308.15 K | -8.33 | -8.39 | 23.4 | 17.2 | 102.81 | 83.1 |
| | 318.15 K | 318.15 K | -9.36 | -9.22 | | | | |
| | 298.15 K | 298.15 K | -0.20 | -1.16 | | | | |
| MO | 308.15 K | 308.15 K | -0.38 | -1.25 | 5.23 | 1.54 | 18.21 | 9.05 |
| | 318.15 K | 318.15 K | -0.56 | -1.34 | | | | |

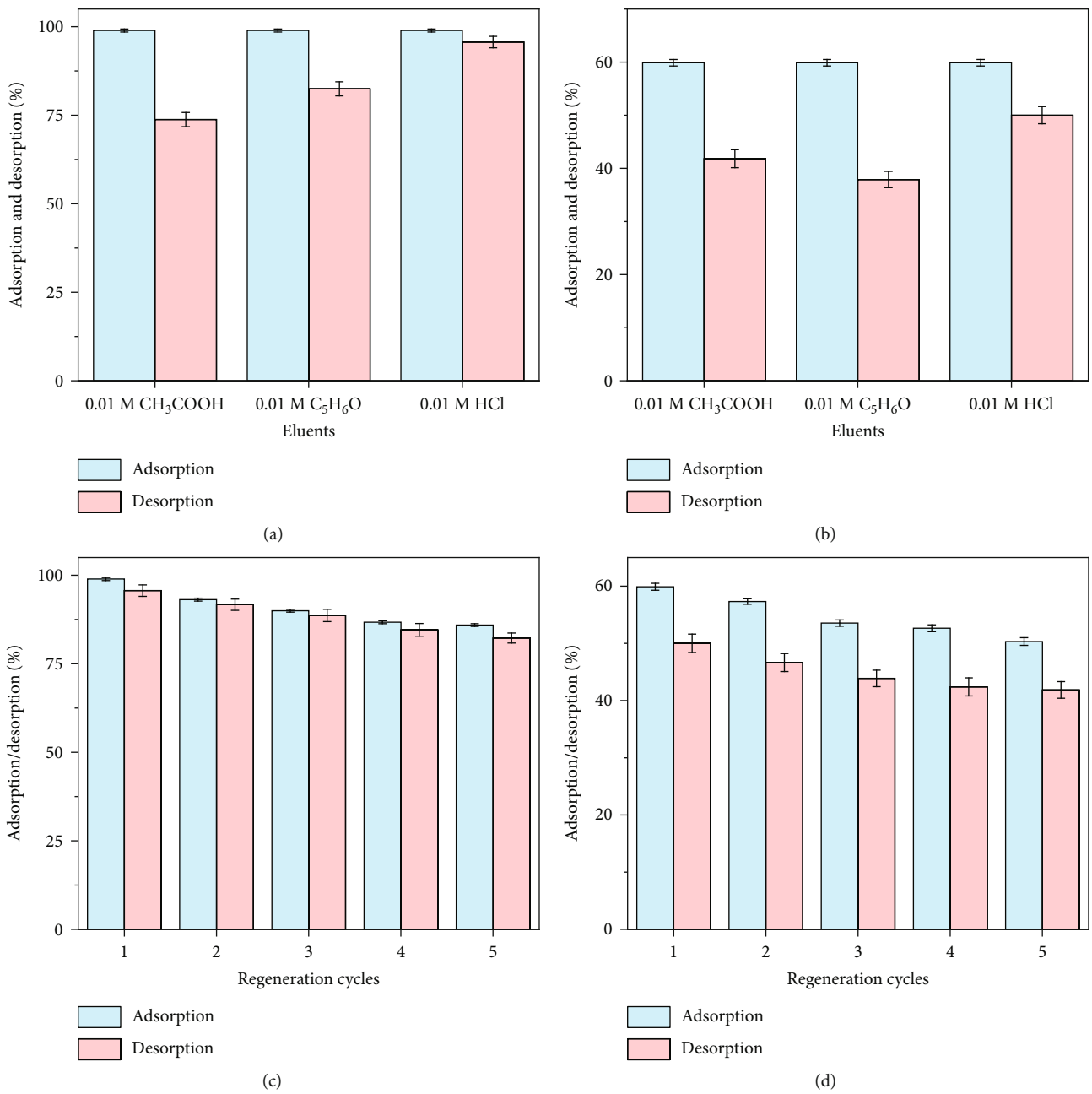


Figure 14: (a) Comparison of eluents for desorption of MG from composite aerogel surface, (b) comparison of eluents for desorption of MO from composite aerogel surface, and reusability of composite aerogel for (c) MG and (d) MO.

spontaneous [53]. The absolute value of $\Delta G^0$ increases with the increase of ambient temperature, indicating that the degree of spontaneity increases with the increase of temperature [54]. The positive value of $\Delta S^0$ indicates that the adsorption process is an entropy increase process, and the randomness at the solid-solution interface occurs in the internal structure of the adsorption of MG and MO dyes onto composite aerogel [55]. Table 5 also shows that $\triangle H^0$ of composite aerogel is greater than 0 in the either monobasic or binary system, indicating that the adsorption process is an endothermic reaction and $\triangle H^0$ of the binary dye system is less than that of the unitary dye system, which further confirms the existence of MG, promotes the adsorption of MO by composite aerogel, and reduces the difficulty of adsorption.

*3.2.7. Desorption Study.* Nowadays, the reproduction of adsorbents is one of the most challenging and important factors for industrial applications. At the same time, the reusability is also one of the criteria for evaluating the performance of an adsorbent. In this study, 0.01 M $CH_3COOH$, 0.01 M $C_5H_6O$, and 0.01 M HCl were designated as desorbing agents to test the reusability of composite aerogel in multiple dye adsorption-desorption cycles. Five adsorption-desorption cycles in ethanol, acetone, and HCl were applied to check the reusability of both adsorbents. The results of these experiments are presented in Figure 14.

As shown in Figure 14, the desorption process of MG and MO loaded on composite aerogel was performed by 0.01 M ethanol, 0.01 M acetone, and 0.01 M HCl as three eluents by an ultrasonic assistant. Readsorption process was carried out at the same optimum condition of experiments (pH = 6, adsorbent dosage = 0.02 g, initial concentration = 200 mg/L, and mixing time = 360 min). The composite aerogel was washed several times with eluent by ultrasonic aid until the most of dye molecules were extracted from the surface of the composite [35, 48]. At last, the recovered composite aerogel before being dried in a vacuum oven at 70°C was rinsed one more time with distilled water. It was found that 0.01 M HCl had the best desorption effect on MG and MO compared with the other two eluents, so HCl was selected as the eluent for subsequent cycle experiments.

After five cycles, the adsorption amount of MG on the composite aerogel decreased by 13.4%, and the final adsorption amount was 82.27%. The adsorption amount of MO decreased by 8.15%, and the final adsorption amount was 41.86% (Figures 12(c) and 12(d)). The results indicated that composite aerogel was a regenerable and reusable adsorbent.

## 4. Conclusions

The modified attapulgite-reduced graphene oxide composite aerogel (ATP-RGO CA) was synthesized by the sol-gel method to be used as effective adsorbents for the removal of malachite green (MG) and methyl orange (MO) dyes from unitary and binary aqueous solutions. The as-obtained composite materials prepared were characterized by X-ray diffraction, FTIR spectroscopy, SEM, and specific surface area and porosity analysis. The results confirmed the successful synthesis of composite materials. Moreover, the physical properties of the prepared composite aerogel were improved compared with those of the initial graphene aerogels. Kinetic, equilibrium, and thermodynamic studies were conducted for the adsorption of MG and MO from aqueous solutions onto ATP-RGO CA in unitary and binary systems. The results of adsorption showed that ATP-RGO CA can be effectively used as an adsorbent for the removal of dyes. The kinetic studies of dyes on ATP-RGO CA were performed based on pseudo-first-order, pseudo-second-order, and intraparticle diffusion rate mechanisms. The data indicated that the adsorption kinetics of dyes on ATP-RGO CA followed the pseudo-second-order model. The equilibrium data were analyzed using the Langmuir, Freundlich, and Temkin isotherms, and the characteristic parameters for each isotherm were determined. The results showed that the Langmuir isotherm best describes the adsorption on ATP-RGO CA and indicates that MG and MO adsorption occurs on the homogeneous surface of ATP-RGO CA as a monolayer. Thermodynamic studies show that the adsorption process of MG and MO onto ATP-RGO CA was endothermic and spontaneous. The reusability test of ATP-RGO CA exhibited that the adsorption capacity of ATP-RGO CA decreased slightly after five cycles, but the adsorption capacity was still good. The results of the study indicate that ATP-RGO CA is relevant as adsorbent to clean dye-containing wastewater.

## Data Availability

All relevant data in this article are available to the corresponding author.

## Conflicts of Interest

The authors state that there is no conflict of interest in the publication of this paper.

## Acknowledgments

This work was supported by the National Natural Science Foundation of China (No. 21573171), the Shaanxi Province Key Research and Development Plan of China (2021SF-438), the Natural Science Foundation of Shaanxi Province of China (No. 17JK0327), the Ph.D. Research Initiation Fund of Xi'an Polytechnic University (BS201932), and the Research and Innovation Training Project for Graduate in General Universities of China (201910709028).

## References

[1] J. Liu, Q. X. Zhu, X. W. Tan, Y. Yan, and H. P. Zhang, "Adsorption of methyl orange on modified activated carbon," *The Chinese Journal of Process Engineering*, vol. 16, pp. 222–227, 2016.

[2] L. G. Silva, R. Ruggiero, P. M. Gontijo, R. B. Pinto, and B. Royer, "Adsorption of Brilliant Red 2BE dye from water solutions by a chemically modified sugarcane bagasse lignin," *Chemical Engineering Journal*, vol. 168, no. 2, pp. 620–628, 2011.

[3] S. Liu, Y. Ding, P. Li et al., "Adsorption of the anionic dye Congo red from aqueous solution onto natural zeolites modified with N,N-dimethyl dehydroabietylamine oxide," *Chemical Engineering Journal*, vol. 248, pp. 135–144, 2014.

[4] K. G. Pavithra, P. S. Kumar, V. Jaikumar, and P. S. Rajan, "Removal of colorants from wastewater: a review on sources and treatment strategies," *Journal of Industrial and Engineering Chemistry*, vol. 75, pp. 1–19, 2019.

[5] H. Chen, Y. F. Liu, X. Q. Xu et al., "How does iron facilitate the aerated biofilter for tertiary simultaneous nutrient and refractory organics removal from real dyeing wastewater," *Water Research*, vol. 148, pp. 344–358, 2019.

[6] P. S. Kumar, S. Ramalingam, C. Senthamarai, M. Niranjanaa, P. Vijayalakshmi, and S. Sivanesan, "Adsorption of dye from aqueous solution by cashew nut shell: studies on equilibrium isotherm, kinetics and thermodynamics of interactions," *Desalination*, vol. 261, no. 1-2, pp. 52–60, 2010.

[7] A. Alinsafi, M. Khemis, M. N. Pons et al., "Electro-coagulation of reactive textile dyes and textile wastewater," *Chemical Engineering and Processing: Process Intensification*, vol. 44, no. 4, pp. 461–470, 2005.

[8] E. Sharifpour, M. Ghaedi, A. Asfaram, M. Farsadrooh, E. A. Dil, and H. Javadian, "Modeling and optimization of ultrasound-assisted high performance adsorption of Basic Fuchsin by starch-capped zinc selenide nanoparticles/AC as a novel composite using response surface methodology," *International Journal of Biological Macromolecules*, vol. 152, pp. 913–921, 2020.

[9] R. K. Sonwani, G. Swain, B. S. Giri, R. S. Singh, and B. N. Rai, "Biodegradation of Congo red dye in a moving bed biofilm reactor: performance evaluation and kinetic modeling," *Bioresource Technology*, vol. 302, article 122811, 2020.

[10] M. Cheng, G. Zeng, D. Huang et al., "Efficient degradation of sulfamethazine in simulated and real wastewater at slightly basic pH values using Co-SAM-SCS/$H_2O_2$ Fenton-like system," *Water Research*, vol. 138, pp. 7–18, 2018.

[11] B. Hameed and T. Lee, "Degradation of malachite green in aqueous solution by Fenton process," *Journal of Hazardous Materials*, vol. 164, no. 2-3, pp. 468–472, 2009.

[12] L. Ai and J. Jiang, "Removal of methylene blue from aqueous solution with self-assembled cylindrical graphene-carbon nanotube hybrid," *Chemical Engineering Journal*, vol. 192, pp. 156–163, 2012.

[13] X. Li, T. Liu, and D. Wang, "Superlight adsorbent sponges based on graphene oxide crosslinked with poly (vinyl alcohol) for continuous flow adsorption," *ACS Applied Materials & Interfaces*, vol. 10, no. 25, pp. 21672–21680, 2018.

[14] S. Sobhanardakani, R. Zandipak, H. Khoshsafar, and R. Zandipak, "Removal of cationic dyes from aqueous solutions using $NiFe_2O_4$ nanoparticles," *Journal of Water Supply: Research and Technology—AQUA*, vol. 65, pp. 64–74, 2015.

[15] H. J. Wu, H. Y. Hu, Q. L. Chen, J. Wang, and L. Xiang, "Preparation of low-density hydrophobic silica aerogels by controlling strength of alcogels," *CIESC Journal*, vol. 66, pp. 4281–4287, 2015.

[16] Y. Cheng, Q. X. Zhou, and Q. Y. Ma, "Progress in treating methods of wastewater containing dyes," *Techniques And Equipment for Environmental Pollution Control*, vol. 4, pp. 56–60, 2003.

[17] N. Q. Ren, X. J. Zhou, and W. Q. Guo, "A review on treatment methods of dye wastewater," *CIESC Journal*, vol. 64, pp. 84–94, 2013.

[18] S. Y. Li, F. Xiong, L. Wang, Y. Wang, and S. B. Xie, "Adsorption properties of graphene oxide/SiO2 composites for Cd(II)," *Acta Materiae Compositae Sinica*, vol. 34, pp. 1205–1211, 2017.

[19] C. Yang, Z. Du, M. Z. Li, and Y. Zhang, "Preparation and influencing factors of the 3-D graphene," *Micronanoelectronic Technology*, vol. 52, pp. 521–525, 2015.

[20] Y. Zhang, *Adsorption properties of graphene oxide composite aerogels for Cd and MB*, Northwest A&F University, China, 2019.

[21] H. J. Li, X. D. Zhou, H. B. Gao, and L. J. Chen, "Influence of different modification methods on pore structure and $Cr6^+$ adsorption of ATP," *Chemical Engineering*, vol. 45, pp. 29–33, 2017.

[22] X. Z. Zhou, *Synthesis of zeolites from attapulgite clay and its applications*, Zhejiang University, China, 2013.

[23] I. Bameri, J. Saffari, S. Baniyaghoob, and M. S. Ekrami-Kakhki, "Synthesis of magnetic nano-$NiFe_2O_4$ with the assistance of ultrasound and its application for photocatalytic degradation of Titan Yellow: kinetic and isotherm studies," *Colloid and Interface Science Communications*, vol. 48, article 100610, 2022.

[24] N. M. Mahmoodi, "Nickel ferrite nanoparticle: synthesis, modification by surfactant and dye removal ability," *Water, Air, and Soil Pollution*, vol. 224, no. 2, p. 1419, 2013.

[25] K. Chen, *Design and analysis of experiment*, Tsinghua University publishing house, China, 2005.

[26] M. Ren, Z. Q. Qu, X. Tan, and C. L. Jiao, "Preparation of PDMS/$Fe_3O_4$/graphene aerogel composite and its application in oil-water separation," *Research of Environmental Sciences*, vol. 34, pp. 2173–2181, 2021.

[27] J. C. Xu, B. Zhang, Y. K. Lu et al., "Adsorption desulfurization performance of PdO/$SiO_2$@graphene oxide hybrid aerogel: influence of graphene oxide," *Journal of Hazardous Materials*, vol. 421, article 126680, 2022.

[28] Y. Wu, H. Luo, H. Wang, C. Wang, J. Zhang, and Z. Zhang, "Adsorption of hexavalent chromium from aqueous solutions by graphene modified with cetyltrimethylammonium bromide," *Journal of Colloid and Interface Science*, vol. 394, pp. 183–191, 2013.

[29] T. T. P. N. Trinh, D. M. Nguyet, T. H. Quan et al., "Preparing three-dimensional graphene aerogels by chemical reducing method: investigation of synthesis condition and optimization of adsorption capacity of organic dye," *Surfaces and Interfaces*, vol. 23, article 101023, 2021.

[30] S. Caprarescu, C. Modrogan, V. Purcar, and A. M. Dancila, "Study of polyvinyl alcohol-$SiO_2$ nanoparticles polymeric membrane in wastewater treatment containing zinc ions," *Polymers*, vol. 13, no. 11, article 1875, 2021.

[31] J. A. Labinger and J. E. Bercaw, "Understanding and exploiting C-H bond activation," *ChemInform*, vol. 417, no. 6888, pp. 507–514, 2002.

[32] L. Pastewka, A. Klemenz, P. Gumbsch, and M. Moseler, "Screened empirical bond-order potentials for Si-C," *Physical Review B Condensed Matter*, vol. 87, no. 20, article 205410, 2013.

[33] J. Kim, L. J. Cote, F. Kim, W. Yuan, K. R. Shull, and J. Huang, "Graphene oxide sheets at interfaces," *Journal of the American Chemical Society*, vol. 132, no. 23, pp. 8180–8186, 2010.

[34] L. Liu, R. Bao, J. H. Yi, M. Xie, S. D. Guo, and P. Yang, "Preparation and properties of CNTs-graphene aerogel," *Acta Materiae Compositae Sinica*, vol. 34, pp. 2296–2303, 2017.

[35] C. M. Simonescu, A. Tătărus, D. C. Culită, N. Stănică, and I. A. Ionescu, "Comparative study of $CoFe_2O_4$ nanoparticles and $CoFe_2O_4$-chitosan composite for Congo red and methyl orange removal by adsorption," *Nanomaterials*, vol. 11, no. 3, article 711, 2021.

[36] C. R. Girish, "Multicomponent adsorption and the interaction between the adsorbent and the adsorbate: a review," *Interaction*, vol. 14, article 15, 2018.

[37] Q. K. Hu, "Removal of methyl orange from water with fly ash," *Shanghai Chemical Industry*, vol. 8, pp. 10–12, 2004.

[38] W. A. Khanday, M. J. Ahmed, P. U. Okoye, E. H. Hummadi, and B. H. Hameed, "Single-step pyrolysis of phosphoric acid-activated chitin for efficient adsorption of cephalexin antibiotic," *Bioresource Technology*, vol. 280, pp. 255–259, 2019.

[39] J. Ma, Y. Ma, and F. Yu, "A novel one-pot route for large-scale synthesis of novel magnetic CNTs/Fe@C hybrids and their applications for binary dye removal," *ACS Sustainable Chemistry & Engineering*, vol. 6, no. 7, pp. 8178–8191, 2018.

[40] D. Y. Song, H. Q. Guo, and L. S. Yan, "Adsorptive property of crystal violet on camellia oleifera shell in aqueous solution," *Chinese Journal of Environmental Engineering*, vol. 8, pp. 5129–5134, 2014.

[41] Z. Q. Huang, Y. X. Ding, and T. Q. Yang, "Preparation of magnetic microsphere containing quaternary ammonium salt of chitosan and methyl orange adsorption," *New Chemical Materials*, vol. 46, pp. 209–212, 2018.

[42] M. Ghaedi, G. Negintaji, H. Karimi, and F. Marahel, "Solid phase extraction and removal of brilliant green dye on zinc oxide nanoparticles loaded on activated carbon: new kinetic model and thermodynamic evaluation," *Journal of Industrial and Engineering Chemistry*, vol. 20, no. 4, pp. 1444–1452, 2014.

[43] A. Wei, B. Liu, H. Zhao et al., "Synthesis and formation mechanism of flowerlike architectures assembled from ultrathin NiO nanoflakes and their adsorption to malachite green and acid red in water," *Chemical Engineering Journal*, vol. 239, pp. 141–148, 2014.

[44] M. A. Barakat, R. Kumar, E. C. Lima, and M. K. Seliem, "Facile synthesis of muscovite supported $Fe_3O_4$ nanoparticles as an adsorbent and heterogeneous catalyst for effective removal of methyl orange: characterisation, modelling, and mechanism," *Journal of the Taiwan Institute of Chemical Engineers*, vol. 119, pp. 146–157, 2021.

[45] Y. Zhang and Z. Nan, "Preparation of magnetic $ZnLa_{0.02}$-$Fe_{1.98}O_4$/MWCNTs composites and investigation on its adsorption of methyl orange from aqueous solution," *Materials Research Bulletin*, vol. 66, pp. 176–185, 2015.

[46] Y. X. Ma, P. S. Jin, W. J. Shao, Y. L. Kou, and P. Q. La, "Adsorption behavior of Hg (II) on the hydroxyl-terminated-polyamidoamine-grafted magnetic graphene oxide," *Materials Review*, vol. 33, pp. 234–239, 2019.

[47] S. Sobhanardakani, M. Ghoochian, S. Jameh-Bozorghi, and R. Zandipak, "Assessing of removal efficiency of indigo carmine from wastewater using MWCNTs," *Iranian Journal of Science and Technology, Transaction A- Science*, vol. 41, no. 4, article 312, pp. 1047–1053, 2017.

[48] N. M. Mahmoodi, M. Taghizadeh, and A. Taghizadeh, "Activated carbon/metal-organic framework composite as a bio-based novel green adsorbent: preparation and mathematical pollutant removal modeling," *Journal of Molecular Liquids*, vol. 277, pp. 310–322, 2019.

[49] N. M. Mahmoodi, M. Oveisi, A. Taghizadeh, and M. Taghizadeh, "Synthesis of pearl necklace-like ZIF-8@chitosan/PVA nanofiber with synergistic effect for recycling aqueous dye removal," *Carbohydrate Polymers*, vol. 227, article 115364, 2019.

[50] R. Zandipak and S. Sobhanardakani, "Synthesis of $NiFe_2O_4$-nanoparticles for removal of anionic dyes from aqueous solution," *Desalination and Water Treatment*, vol. 57, no. 24, pp. 11348–11360, 2016.

[51] S. Sobhanardakani, R. Zandipak, and R. Sahraei, "Removal of Janus Green dye from aqueous solutions using oxidized multi-walled carbon nanotubes," *Toxicological & Environmental Chemistry*, vol. 95, no. 6, pp. 909–918, 2013.

[52] S. Sobhanardakani and R. Zandipak, "Removal of anionic dyes (direct blue 106 and acid green 25) from aqueous solutions using oxidized multi-walled carbon nanotubes," *Iranian Journal of Health Sciences*, vol. 3, pp. 48–57, 2015.

[53] S. Arivoli and M. Thenkuzgali, "Kinetic, mechanistic, thermodynamic and equilibrium studies on the adsorption of rhodamine B by acid activated low cost carbon," *E-Journal of Chemistry*, vol. 5, no. 2, article 437375, pp. 187–200, 2008.

[54] N. M. Mahmoodi, M. Taghizadeh, and A. Taghizadeh, "Mesoporous activated carbons of low-cost agricultural bio-wastes with high adsorption capacity: preparation and artificial neural network modeling of dye removal from single and multicomponent (binary and ternary) systems," *Journal of Molecular Liquids*, vol. 269, pp. 217–228, 2018.

[55] N. M. Mahmoodi, B. Hayati, and M. Arami, "Textile dye removal from single and ternary systems using date stones: kinetic, isotherm, and thermodynamic studies," *Journal of Chemical & Engineering Data*, vol. 55, no. 11, pp. 4638–4649, 2010.

Hindawi
Adsorption Science & Technology
Volume 2022, Article ID 4544611, 9 pages
https://doi.org/10.1155/2022/4544611

*Research Article*

# Removal of Chromium (VI) and Lead (II) from Aqueous Solution Using Domestic Rice Husk Ash- (RHA-) Based Zeolite Faujasite

**Rajesh Chanda,[1] Mukter Hosain,[1] Sumaia Aktar Sumi,[1] Marzia Sultana,[1] Saiful Islam,[2] and Biplob Kumar Biswas[1]**

[1]*Department of Chemical Engineering, Jashore University of Science and Technology, Jashore 7408, Bangladesh*
[2]*Department of Glass and Ceramic Engineering, Bangladesh University of Engineering and Technology, Dhaka 1000, Bangladesh*

Correspondence should be addressed to Biplob Kumar Biswas; bk.biswas@just.edu.bd

Received 6 June 2022; Accepted 13 July 2022; Published 31 July 2022

Academic Editor: Randa Khalifa



Rice husk ash (RHA), is a widely available biobased source for high purity silica. In this work, zeolite Faujasite (FAU) is synthesized using extracted silica from RHA (collected from a local region of Bangladesh). The synthesized zeolite FAU was used as an adsorbent for Cr(VI) and Pb (II) batch-wise adsorptive removal from respective aqueous solution. The synthesized zeolite FAU was characterized using X-ray diffraction (XRD), scanning electron microscopy (SEM), nitrogen-sorption, and Fourier transfer infrared (FT-IR) spectroscopy. Metal ion adsorption studies were performed by varying metal concentration (20–100 mg/L for Cr(VI) and 900–133 mg/L for Pb(II)), sorbent dosage (2–10 g/L for chromium and 0.5–1.5 g/L for lead), and contact time (10–120 min for both metal ions). The maximum adsorption capacity of RHA-based zeolite FAU was found to be 3.56 mg/g and 342.16 mg/g for Cr(VI) and Pb(II), respectively. Since the sorption data was found to match with Langmuir isotherm, a monolayer adsorption was occurred. The regeneration of the RHA-based zeolite FAU by NaCl solution showed the potential of repeated as well as continuous operation.

## 1. Introduction

Water contamination by heavy metals is a major concern for the environment and human health. Heavy metals such as chromium, lead, cadmium, mercury, nickel, copper, and zinc are nonbiodegradable and accumulate in the human body, posing health risks due to their toxicity [1]. Hence, it is necessary to treat metal-contaminated wastewater before its discharge into the environment. Chromium and lead are two of the most hazardous heavy metals for living beings and the environment. Various processes such as mining, leather tanning, electroplating, wood preservatives, paints, and textile dyeing deal with inorganic chemicals and pigments that discharge chromium and lead-based compounds as industrial wastewater [2]. Since Bangladesh is one of the leading textile product producers and has a considerable electroplating demand, contamination of chromium and lead in water is a growing concern here in this country.

From toxicological data, it is obvious that the degree of toxicity depends on the chemical form in which the element is present [3]. In the case of chromium, the trivalent form Cr(III) and the hexavalent form Cr(VI) are more prevalent in the environment and, therefore, are the two main chromium components of concern in respect to water pollution [4]. Cr(III) is supposed to be an essential micronutrient for human, plant, and animal metabolism. On the other hand, Cr(VI) is soluble in a wider pH range and has greater mobility and more toxic than Cr(III). Human can be exposed to excessive amount of Cr(VI) through different media such as food, drinking water, and inhaling air. The respiratory tract is supposed to be the major target organ for Cr(VI). For acute exposure of Cr(VI) coughing, breathing problem and wheezing can occur while for chronic exposure bronchitis, pneumonia, perforations, and ulceration of septum may happen. Chromium(VI) can be heavily lethal if the concentration reaches to 0.1 mg/g of a human weight [5]. Hexavalent

chromium (Cr(VI)) is a probable carcinogen that causes primary liver cancer. Moreover, Cr(VI) belongs to water hazard class 3, which means extremely hazardous. Hence, the maximum permitted concentration in wastewater for hexavalent chromium is 0.05 mg·dm$^{-3}$, which is ten times lower than the trivalent form (5 mg·dm$^{-3}$) [6].

In a similar fashion, lead contaminates groundwater through its usage in, for example, batteries, glass ceramics, mining, smelting, and plating industries [7] and in contact with biotic communities causes health problems. When lead builds up in a human body for a longer period (over months or years), lead poisoning can occur. Serious health problems may occur due to even a small amount of lead poisoning. Children are reported to be more vulnerable than adults to lead poisoning because lead poisoning may affect mental as well as physical development. Lead accumulates in muscles, bones, kidneys, and brain tissues and can result in anemia, nervous system disorders, and kidney diseases [8]. Therefore, it is extremely required to effectively remove Cr(VI) and Pb(II) from contaminated effluent of various industries.

An adsorption process is a widely reported technique for the removal of various hazardous pollutants from aqueous solution due the high efficiency [9] and economic viability [10]. It is also commonly used to remove heavy metals from wastewater compared to other techniques like chemical precipitation [11], ion flotation [12], and biological treatment [13]. Biosorbents [14], synthetic adsorbents [15], and bioresource-derived adsorbents [16] have been reported for the removal of such heavy metals from an aqueous solution. Among them, bioresource-derived sorbents for wastewater treatment provide a greener and sustainable alternative.

Bangladesh is the third-highest rice-producing country per annum in the world. According to the data from the Ministry of Agriculture, Bangladesh, in the fiscal year 2020-21, around 38.7 million metric tons (MMT) of rice were cultivated in Bangladesh [17]. The cultivated rice consists of 20 wt.% rice husk which composition is as follows: cellulose (50%), lignin (25–30%), silica (15–20%), and moisture (10–15%) [18]. Therefore, 1.6 MMT silica was produced in the fiscal year 2020-21 in Bangladesh. Typically, rice husk is used as burning fuel in the rice boiling process, and at the end, rice husk ash (RHA) is left over. Although such a burning process is an uncontrolled one, still around 60% of silica from RHA can be chemically extracted from it [19]. The extracted silica can be used in cement as additives, or as other forms of silica, or can be converted into other materials such as zeolites.

Zeolites are a porous aluminosilicate material. And silicon is an essential structural element for this material. Zeolite Faujasite-type is widely used as ion-exchange material due to its thermochemical stability, being easily tunable and its selective sorption properties, synthesizability using inexpensive elements, and environmental compatibility [20–22]. The inside cages or surface of 7.2 nm sized pore of zeolite FAU acts as sorption active sites for ion species due to the presence of positive aluminum in the framework [22]. Moreover, after completion of adsorption cycle, the zeolite can be regenerated with a simple ion exchange and be used for several sorption cycles resulting in longer service life.

Therefore, in this paper, an eco-friendly and sustainable pathway for removing Cr(VI) and Pb(II) from wastewater using zeolite FAU as adsorbent, which is synthesized from the local bio-sourced of RHA, is presented. The experimental work includes extraction of silica from locally collected waste RHA, its subsequent utilization in zeolite FAU synthesis, and batch-wise adsorptive removal of Cr(VI) and Pb(II) from aqueous solution.

## 2. Materials and Methods

*2.1. Chemicals.* Rice Husk Ash was collected from Khan Agro-Rice mill, Muktagachha, Mymensingh, Bangladesh. Other chemicals used were sodium aluminate (43-44% $Al_2O_3$, Sigma-Aldrich, Germany), potassium dichromate (99%, Sigma-Aldrich, USA), 1,5-diphenylcarbazide (99%, Sigma-Aldrich, USA), NaOH pellets (97%, Merck, India), $H_2SO_4$ (98% purity, Merck, India), and HCl (37%, Merck India).

*2.2. Silica Extraction.* Before silica extraction, RHA was washed with adequate distilled water until discarded water pH was at 7-8 and oven-dried. In a typical silica extraction process, 20 g of washed RHA was mixed with 120 mL 1 N NaOH and left for 5 hours with constant stirring at 75°C. Next, the filtrates (aqueous parts) were collected via filtration. The collected aqueous solution was allowed to cool to room temperature and titrated with adequate 1 N HCl with constant stirring until a gel was formed (typically at pH < 8 ). The obtained gels were aged for 18 h in room temperature, and by adding deionized water, a slurry was produced. Finally, the formed silica was separated via vacuum filtration and dried in an oven.

*2.3. Zeolite FAU Synthesis.* The zeolite FAU was synthesized hydrothermally using the seed gel method. First, a seed gel having a molar composition of 10.67 $Na_2O$ : 1 $Al_2O_3$ : 10 $SiO_2$ : 180 $H_2O$ was prepared. Typically, 1.2 g of NaOH pellet was dissolved in 3.43 g of $H_2O$, and then 6.24 g of sodium metasilicate was added under stirring. The formed seed gel was aged for 18 hr.

For synthesis, a mixer having a molar composition of 4.3 $Na_2O$ : 1 $Al_2O_3$ : 10 $SiO_2$ : 180 $H_2O$ was prepared. First, 4.97 g of NaOH was dissolved in 35.51 g of $H_2O$ under stirring for 15 minutes, and then 3.05 g of $NaAlO_2$ was added to the mixture and stirred for 30 minutes (mixture 1). In another beaker, an amount of 11.50 g of an extracted silica source was completely dissolved in 35.51 g of water via 15 minutes of stirring, and the resulted solution was then transferred into mixture 1. Finally, previously prepared seed gel was added to the fresh mixture in a mass ratio of 1 (seed gel): 9 (fresh mixture) and stirred for 2 hr. The resulting mixture was put into a polypropylene PP bottle and inserted into a preheated oven at 70°C for 48 hr. After the synthesis, the powder was collected via vacuum filtration and washed with abundant water.

*2.4. Cr(VI) and Pb(II) Adsorption Study and Analysis.* All batch Cr(VI) and Pd(II) adsorption studies conducted at pH 5 as point of zero charge of synthesized zeolite FAU were

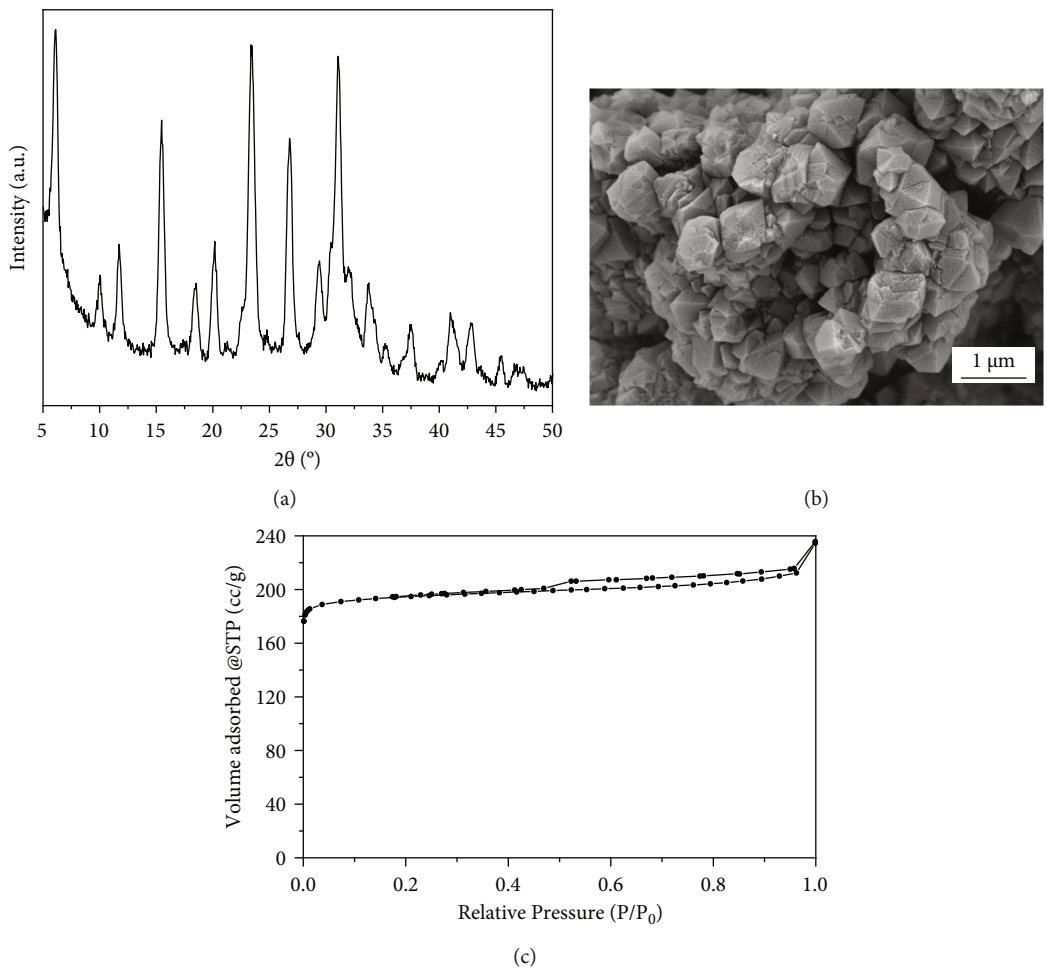


Figure 1: Textural properties of RHA silica-based zeolite FAU: (a) XRD pattern, (b) SEM image, and (c) $N_2$-sorption.

found to be pH 7.3 (Figure S1). The starting solutions were prepared by dissolving required potassium di-chromate and lead nitrate in deionized water, respectively. During the adsorption, the solution and adsorbent were put into a 200 rpm shaker for the required time. The Cr(VI) content in the solution was determined via the Di-phenyl carbazide (DPC) method using UV-vis 1900i (Shimadzu) at a detection range of 300-700 nm (Figure S2). Pb(II) content was determined using the AA-7000 (Shimadzu) AAS spectrometer.

*2.5. Regeneration of Adsorbent.* Regeneration tests of the adsorbent for Cr(VI) and Pb(II) removal was carried out by using sodium chloride (NaCl) solution. After the adsorption test, the adsorbent was collected and washed with NaCl solution to desorb or elute the adsorbed metal ions. Thus, the active sites of the adsorbent became unoccupied and the adsorbent became ready for adsorption again. Then, the adsorption experiment was done in the same fashion as before.

## 3. Characterization

XRD analysis was carried out using an Empyrean diffractometer (Malvern Panalytical) in the $2\theta$ range of 5-90°. SEM analysis was done using GeminiSEM 500 (Zeiss); $N_2$-Sorption was carried out at -196°C in a Quadrasorb™ SI gas sorption analyzed after the sample was pretreated at 250°C in a vacuum for 12 h. FT-IR analysis was carried out in the Nicolet iS20 FTIR spectrometer.

## 4. Results and Discussion

*4.1. RHA-Based Zeolite FAU Textural Properties.* XRD pattern (Figure 1(a)) of synthesized powders shows prominent peaks at $2\theta$ positions of 6.1°, 10.2°, 11.7°, 15.6°, 18.4°, 20.2°, 23.6°, 26.8°, 31.2°, and 33.9°, which match with zeolite Faujasite crystallography patterns. Scanning electron microscopy (SEM) images provide an insight into the morphology of the studied material. Figure 1(b) represents the SEM image of RHA-based zeolite FAU. It shows that the surface of the zeolite consists of an inhomogeneous crystalline structure (octahedral shape) with a particle size of around 1 $\mu$m. $N_2$-sorption analysis shows (Figure 1(c)) IUPAC type I isotherms, which indicates microporous material. The synthesized zeolite FAU has a specific surface area of 661.2 $m^2$/g.

*4.2. Cr(VI) and Pb(II) Adsorption on RHA-Based Zeolite FAU.* To know the insight into the metal ion sorption

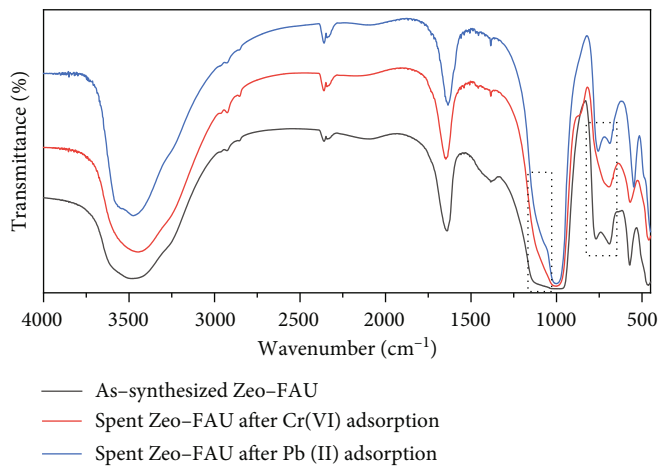


Figure 2: FT-IR spectra of synthesized RHA-based zeolite FAU before and after adsorption of Pb(II) and Cr(VI) ions.

mechanism by RHA-based zeolite FAU, FT-IR is a useful tool for material characterization. Figure 2 shows the FT-IR spectra of synthesized RHA-based zeolite FAU before and after adsorption of Pb(II) and Cr(VI) ions over a range of 400–4000 cm$^{-1}$. In the case of RHA-based zeolite FAU before adsorption of metal ions, strong broadband at 3500 cm$^{-1}$ was observed. This band indicated O-H stretching as well as Si-OH and Si-OH-Al. At 1640 cm$^{-1}$, a strong band was spotted which was supposed to be assigned for O-H bending vibration of adsorbed metal ion onto the adsorbent. A wide and broader band in the range 950–1150 cm$^{-1}$ was associated with Si-O-Al asymmetric stretching vibration. A double band around 685–770 cm$^{-1}$ was attributed to the symmetric stretching vibration of Si-O-Si or Si-O-Al. A sharp band at 570 cm$^{-1}$ was due to external linkage vibration, which is connected to sodalite cages (Si-O-Na). The comparison of spectra showed that characteristic peaks of RHA-based zeolite FAU have been slightly shifted toward high or low wavenumber after adsorption of metal ions. This might happen due to the introduction of cations into the framework of the adsorbent because the interaction between the adsorbent and the metal ion could change the IR spectra [23]. As in the case of Pb(II) adsorption, a narrow peak at 983 cm$^{-1}$ was observed. This peak originated from Pb-O vibrations [7]. On the other hand, a double band disappeared and a single band at 686 cm$^{-1}$ was observed. This might happen due to the adsorption of Cr(VI) by the zeolite.

### 4.3. Adsorption Parameters Study

*4.3.1. Effect of Contact Time.* Determining the optimum agitation time for obtaining better sorption performance is one of the key issues in the adsorption process. In this study, the percentage removal of chromium as well as lead using RHA-based zeolite FAU was investigated with varying agitation time (such as 10, 20, 40, 60, 90, and 120 min). Agitation speed and temperature were kept constant for both experiments. As depicted in Figure 3, the percent removal increases with increasing contact time. At the initial stage of the tests, the adsorption process was quite fast and maximum removal of metal ions occurred in 2 h. The figure shows that 88% lead removal occurred within 40 minutes, whereafter a very little lead removal (from 88% to 91%) was observed. However, equilibrium was achieved in 2 h time. A similar trend of adsorption was also observed for the adsorptive removal of chromium from an aqueous solution (Figure 3). Therefore, 2 h was selected as the optimum time for the adsorption process for the removal of both metal ions.

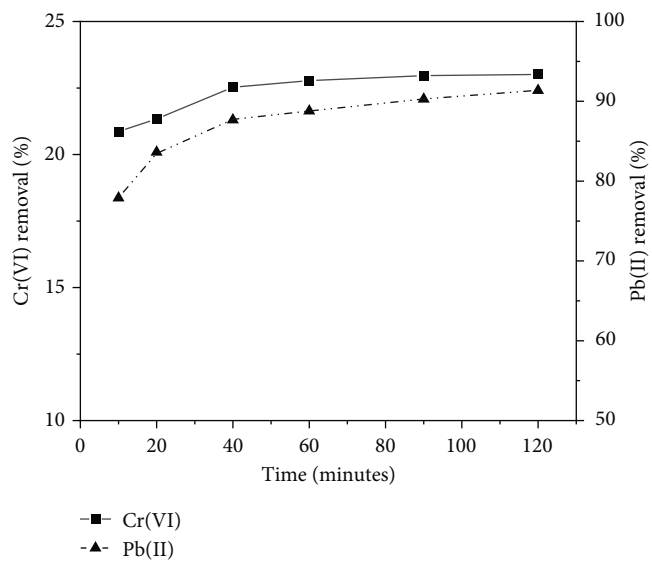


Figure 3: Removal of chromium and lead as a function of time by using RHA-based zeolite FAU.

At the beginning of the adsorption process, there were a large number of active sites available to take part in the adsorption process. That is the reason for the faster adsorption of the metal ion by the adsorbent. As the process goes on, the active binding sites become gradually occupied by the metal ion and the removal process slows down. Hence, fraction lessening of adsorbent surface and competition among metal ions are supposed to be responsible for decreasing metal ion removal. Similar findings were reported

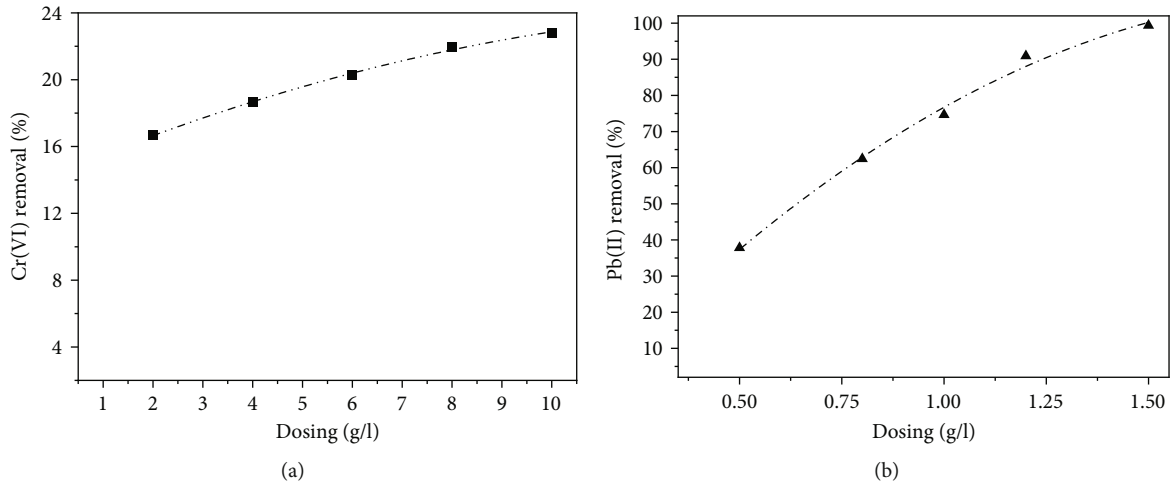


Figure 4: Effect of adsorbent dosing on the removal of (a) Cr(VI) and (b) Pb(II) from aqueous solution by using RHA-based zeolite FAU.

by Khalil et al. and Badessa et al. [24, 25] who removed Cr(VI) from aqueous solution by using different biobased sorbents.

*4.3.2. Effect of Adsorbent Dosing on Cr(VI) and Pb(II) Removal.* The adsorbent dose is one of the key parameters that should be known to select optimal conditions for the adsorption process. The variations of adsorbent dose were tested in this study by keeping adsorbate concentration, pH, agitation speed, and operating temperature constant. Figures 4(a) and 4(b) show the effect of the adsorbent dose for removal of Cr(VI) and Pb(II), respectively, by using the same adsorbent, namely, rice husk ash-based zeolite FAU. The percent of metal removal through adsorption was found to improve with rising adsorbent doses. Figures 4(a) and 4(b) show that chromium removal by RHA-based zeolite FAU rises from 17% to 23% for a rise in dosing from 2 g/L to 10 g/L. In the case of lead, the percent removal increases from 38% to almost 100% for a rise in adsorbent dose from 0.5 g/L to 1.5 g/L.

Because of the increase in adsorbent dose, the surface area of the adsorbent enhances resulting in increased binding sites for more metal ions to be adsorbed [26]. After a certain dose, the adsorption process reaches equilibrium whereafter the percent removal of metal ions is no more affected by the increase in dose. A similar pattern of dosing influence on the removal of lead from aqueous solution by using combination of oil shale ash and coal fly ash-derived zeolite FAU (X-type) was reported in the literature [27].

*4.3.3. Effect of Metal Ion Concentration.* The initial concentration of adsorbate is considered a crucial parameter because it provides the necessary driving force for the transport of adsorbate from the bulk solution to the surface of the adsorbent [24]. The adsorption capacity of RHA-zeolite was studied separately for the adsorption of chromium as well as for lead by varying initial adsorbate concentration and by keeping all other parameters (e.g. pH, agitation time, agitation speed, adsorbent dosage, and temperature) constant. Initial metal ion concentration for chromium was spanning from 20 to 100 mg/L while that for the lead was 900 to 1300 mg/L. For both metals, it was observed that when the metal ion concentration is low, the adsorption capacity of the adsorbent was at its minimum. But with the increase in metal ion level, the adsorptive process between the sorption sites and metal ions increased, which enhanced the metal ion uptake until an adsorption equilibrium was attained. The effect of metal ion concentration on adsorbent capacity has been shown in Figure 5 from where it is obvious that with the increase in ion concentrations (for both lead and chromium), the adsorption capacity increases. This phenomenon can be explained by the fact that all available active sites of the RHA-based zeolite FAU would be completely exposed to get filled by the metal ions of the solution [28]. With a further increase in Pb(II) concentration, the adsorption capacity does not significantly increase and eventually forms a plateau from where the maximum adsorption capacity can be determined. From the experimental data of this study, the maximum sorption capacity was determined to be 3.56 mg/g for Cr(VI) and 342.5 mg/g for Pb(II). The extent of adsorption capacity is quite comparable to other similar adsorbents. A comparison has been tabulated below in Table 1.

*4.4. Adsorption Isotherm Modeling.* When a solid-liquid adsorption system is concerned, it is required to know the isotherm model. The reason is that the adsorption isotherm model necessarily describes the adsorption behavior. The adsorption isotherm specifies the distribution of adsorbate molecules between the solid phase and liquid phase when the system is in equilibrium. Since it is significant to understand the adsorption behavior, the distribution of metal ions between the phases has been determined by two well-known adsorption isotherm models, namely, (i) Langmuir isotherm and (ii) Freundlich isotherm. The modeling has been accomplished by fitting the experimental data into the specific isotherm equations.

*4.4.1. Langmuir Isotherm.* The assumption of the Langmuir isotherm model includes a feature, which expresses that

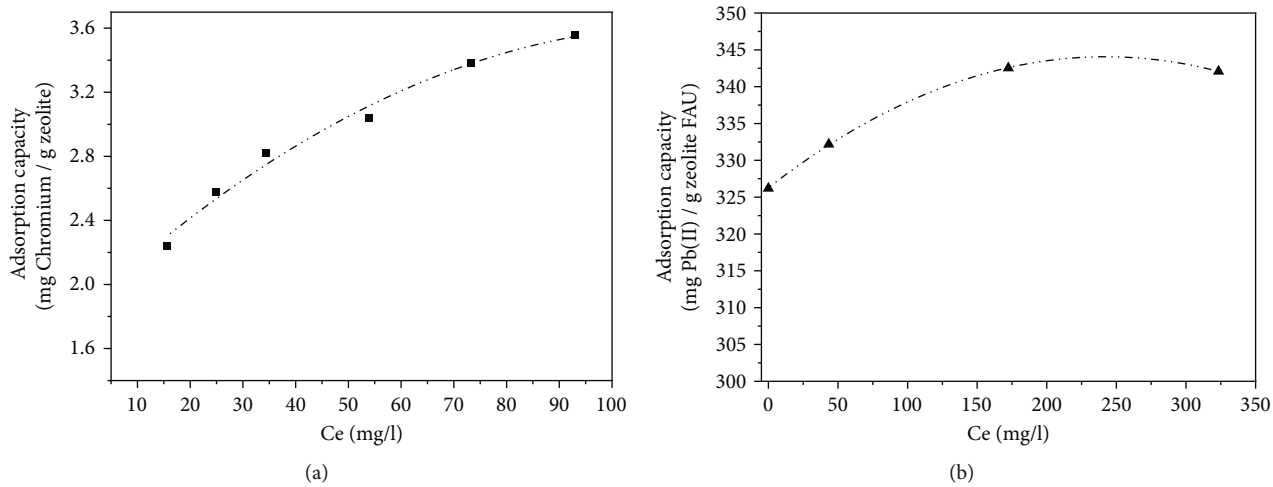


Figure 5: Effect of metal ion concentration on the removal of (a) Cr(VI) and (b) Pb(II) from aqueous solution by using RHA-based zeolite FAU.

Table 1: Comparison of notable aluminium-rich zeolites for Pb(II) and Cr(VI) removal from aqueous solution.

| Adsorbent | Silica source | Adsorbate | Capacity (mg/g) | Reference |
|---|---|---|---|---|
| Zeolite A | Red mud | Pb (II) | 100 | 29 |
| Zeolite X | Mixed of oil shale ash and coal fly ash | Pb (II) in mixed metal ion solution | 112.5 | 27 |
| Zeolite X | Coal fly ash | Pb (II) | 314 | 30 |
| Zeolite 13 X | Commercial | Cr (VI) | 3.92 | 28 |
| Natural zeolite | Not required | Cr (VI) | 3.2 | 31 |
| Zeolite NaP1 | Coal fly ash | Cr(VI) | 17.92 | 32 |
| Zeolite FAU | Rice husk ash | Pb(II) | 342.5 | This study |
| Zeolite FAU | Rice husk ash | Cr(VI) | 3.56 | This study |

monolayer adsorption (of the adsorbate molecule) occurs on the homogeneous surface of the adsorbent [33]. Langmuir isotherm can be expressed as the following equation (Equation (1)). This equation can be simplified by mathematical operation and can be rewritten as Equation (2).

$$q_e = \frac{q_m K_L C_e}{1 + K_L C_e}, \quad (1)$$

$$\frac{C_e}{q_e} = \frac{1}{q_m b} + \frac{C_e}{q_e}, \quad (2)$$

where $q_e$ stands for metal ion adsorbed per gram of adsorbent (mg/g), $q_m$ is the maximum adsorption capacity with the same unit of $q_e$, $C_e$ designates equilibrium concentration of metal ion (mg/L), and $K_L$ indicates Langmuir constant (L/mg).

From the simplified Langmuir equation, a plot of $C_e/q_e$ vs. $C_e$ has been depicted in Figure 6. Considering the value of the correlation coefficient ($R^2$), the experimental data was found to fit well with the linear Langmuir isotherm equation. The maximum adsorption capacity of RHA-based zeolite FAU and the value of equilibrium constant was calculated from the slope and the intercept of the straight line, respectively. The calculated sorption capacities were 3.95 mg-Cr(VI)/g and 342.46 mg Pb(II)/g, which were consistent with the experimental data (Tables 1 and 2). Therefore, it is perceived that a monolayer adsorption of metal ions has occurred. A dimensionless parameter, also called equilibrium separation factor ($R_L$), is considered one of the essential characteristics of the Langmuir isotherm. The equilibrium separation factor can be defined as follows:

$$R_L = \frac{1}{1 + K_L C_0}, \quad (3)$$

where $K_L$ (L/mg) and $C_0$ (mg/L) are designated as Langmuir constant and initial adsorbate concentration, respectively. The values of $R_L$ were calculated (for both chromium and lead ions) and found to remain between 0 and 1. This means that the adsorption was favorable under the studied conditions.

*4.4.2. Freundlich Isotherm.* Freundlich isotherm is an empirical mathematical model which represents the amount adsorbed per unit amount of adsorbent. The mathematical model of the Freundlich isotherm is based on the assumptions that both anions and cations can be adsorbed on the same surface simultaneously. It articulates multilayer

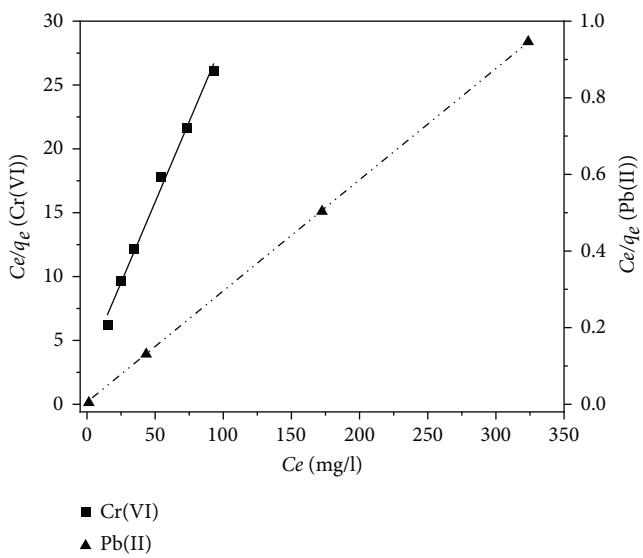


Figure 6: Langmuir isotherm plot for the removal of Cr(VI) and Pb(II) by RHA-based zeolite FAU.

Table 2: Parametric values of Langmuir and Freundlich isotherm data.

| Isotherm model | Parameters | Values | |
|---|---|---|---|
| | | Cr(VI) | Pb(II) |
| Langmuir isotherm | $K_L$ (L/mg) | 0.0784 | 1.7391 |
| | $q_m$ (mg/g) | 3.95 | 342.46 |
| | $R^2$ | 0.991 | 0.999 |
| Freundlich isotherm | $K_f$ (mg/g) | 1.3269 | 324.31 |
| | $1/n$ | 0.2146 | 0.0092 |
| | $R^2$ | 0.971 | 0.896 |

adsorption onto a heterogeneous surface. The Freundlich model can be defined as follows:

$$q_e = K_f C_e^{1/n}, \tag{4}$$

where $q_e$ (mg/g) is the amount of metal ion adsorbed at equilibrium, $C_e$ (mg/L) is the equilibrium concentration of a metal ion in the solution, and $K_f$ and $1/n$ are the Freundlich empirical parameters, which are related to adsorption capacity and adsorption intensity, respectively. The adsorption intensity may vary with the heterogeneity of the adsorbent surface. To determine the essential Freundlich parameters this equation can be made linear. The linearized form of this equation can be represented as follows:

$$\ln q_e = \ln K_f + \frac{1}{n} \ln C_e. \tag{5}$$

The value of $K_f$ and $1/n$ can be evaluated from the intercept and slope of the linear plot of $\ln q_e$ vs. $\ln C_e$. If $0.1 < 1/n < 1$ and if $K_f$ is larger, the adsorption system is thought to be favorable. The parameters obtained from Freundlich isotherm model have been presented in Table 2. It is seen from Table 2 that the value of $K_f$ is small for the removal of Cr(VI) and the value of $1/n$ is smaller than 0.1 for Pb(II) adsorption. Therefore, neither of the metal ion adsorption follows the Freundlich isotherm.

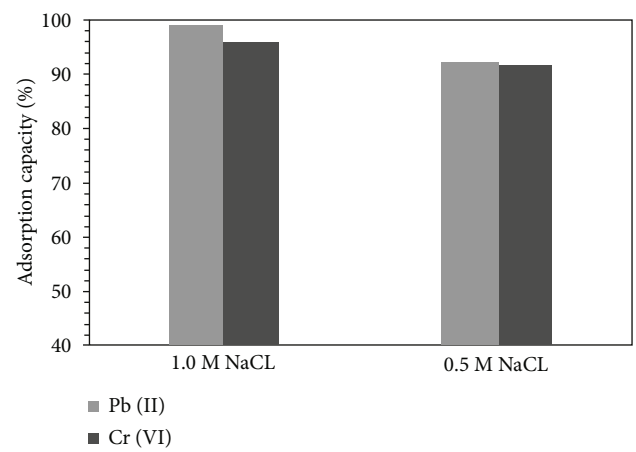


Figure 7: Regeneration of adsorbent with different concentration sodium chloride solution.

*4.5. Regeneration and Economical Analysis.* Although adsorption is widely used for remediation of water contamination, often, it cannot be used for commercial utilization because of its disposal problem as well as its incapability to reuse [34]. Therefore, the efficiency of regeneration of adsorbents is something that should be focused on. Moreover, regeneration is supposed to be an important feature because it controls the economy of the water treatment process to a huge extent. For the sake of material cycling, it is needed to remove the adsorbed metal ion from the metal ion-loaded adsorbent. Through the desorption process, the metal ion can be removed from the active binding sites of the adsorbent surface and thus the adsorbent becomes ready for further adsorption. This process (desorption) can also be termed as elution, where an appropriate chemical reagent (called eluent) can be used to desorb the metal ions that are already loaded on the adsorbent surface. For effective regeneration of adsorbent as well as heavy metal recovery, various acids, alkalis, complexing agents, salts, etc. are used [34, 35]. The choice of eluent largely depends on binding chemistry between adsorbent and metal ion, endurance, and tolerance of adsorbents towards the reagents, and so forth.

In this study, regeneration experiments were conducted by using one of the most abundant minerals on the earth, NaCl, rather than using acids and alkalis. Sodium chloride was chosen for this purpose to avoid acid-base consumption. Salt (NaCl) concentrations of 1.0 M and 0.5 M were used for regenerating the adsorbent. The results are presented in Figure 7, which shows that 99% and 92% regeneration of the RHA-based zeolite FAU adsorbent (in case of Pb(II) removal) was possible by using NaCl of 1.0 M and 0.5 M, respectively. Similarly, 95% and 91% regeneration of the RHA-based zeolite FAU (for Cr(VI) removal) was found to

occur by using sodium chloride concentrations of 1.0 M and 0.5 M, respectively. The result indicated that regeneration of rice husk ash-based zeolite FAU adsorbent is very much possible by using an inorganic chloride salt, namely, sodium chloride.

The economical perspective of any process is a key factor [36] to consider. The commercial zeolite FAU is relatively cheap materials costing around $ 0.3-0.4 per kilogram. As one of the building elements (silica) of the synthesized zeolite FAU in this study was extracted from the relatively abundant and cheap materials (rice husk), the final cost will be lower than those of commercial ones. The high sorption capacity of regenerated adsorbent (99% and 92% for Pb(II) and Cr(VI), respectively) makes the material economically more attractive.

## 5. Conclusion

Zeolite Faujasite was successfully prepared from an agroindustrial waste precursor, namely, rice husk ash. It was applied for the removal of pollutants (lead and nickel ions) from contaminated water. Batch-wise experiments were conducted to establish the most favorable conditions for Pb(II) and Cr(VI) removal. SEM image exhibited the morphology of the adsorbent where a crystalline structured octahedral shape was observed. From BET surface analysis, the surface area of the adsorbent was found to be 661.2 $m^2$/g. Characterization of the adsorbent displayed that there was change in FTIR spectra before and after adsorption of metal ions, which was the proof of metal ion adsorption by rice husk ash-based zeolite-FAU as sorbent. The percentage removal of Pb(II) as well as Cr(VI) ion increased with the increase in adsorbent dose and contact time. During an adsorption process, equilibrium was achieved in 120 min. The adsorption process of Cr(VI) and Pb(II) followed the Langmuir isotherm model. Maximum sorption capacity of the adsorbent was 3.56 mg-Cr(VI)/g and 342.5 mg-Pb(II)/g. Regeneration, using different concentration of NaCl solution, indicated a potency to reuse the RHA-based zeolite-FAU. This process could be well-integrated into a waste treatment plant where the water is contaminated with heavy metals like Pb(II) and Cr(VI).

## Data Availability

The data used to support the findings of this study are available from the corresponding author upon request.

## Conflicts of Interest

The authors declared there are no conflicts of interest with respect to the research, publication of this article, and authorship.

## Acknowledgments

The authors are grateful to Jashore University of Science and Technology for granting the research fund.

## Supplementary Materials

*Supplementary 1.* Figure S1 exhibits the point of zero charge ($pH_{pzc}$) of the surface of the adsorbent (RHA-based zeolite FAU). The $pH_{pzc}$ is the pH at which the net surface charge of the adsorbent is zero. The extent of $pH_{pzc}$ was found to be 7.3 in this study. The concept of $pH_{pzc}$ has drawn much attention because the adsorption of many substances is extremely dependent on the solution pH.

*Supplementary 2.* Figure S2 demostrates a calibration curve for Cr(VI) detection via UV-vis DPC method. A detailed detection process was provided in the supplementary data. The sample was analyzed at 300-800 nm range UV-vis spectroscopy (a peak at 553 nm).

## References

[1] R. Vinoth Kumar and G. Pugazhenthi, "Removal of chromium from synthetic wastewater using MFI zeolite membrane supported on inexpensive tubular ceramic substrate," *Journal of Water Reuse and Desalination*, vol. 7, no. 3, pp. 365–377, 2017.

[2] T. Ai, X. Jiang, and Q. Liu, "Chromium removal from industrial wastewater using phyllostachys pubescens biomass loaded Cu-S nanospheres," *Open Chemistry*, vol. 16, no. 1, pp. 842–852, 2018.

[3] L. Rafati, A. H. Mahvi, A. R. Asgari, and S. S. Hosseini, "Removal of chromium (VI) from aqueous solutions using lewatit fo36 nano ion exchange resin," *International journal of Environmental Science and Technology*, vol. 7, no. 1, pp. 147–156, 2010.

[4] R. Leyva-Ramos, A. Jacobo-Azuara, P. E. Diaz-Flores, R. M. Guerrero-Coronado, J. Mendoza-Barron, and M. S. Berber-Mendoza, "Adsorption of chromium(VI) from an aqueous solution on a surfactant-modified zeolite," *Colloids and Surfaces A: Physicochemical and Engineering Aspects*, vol. 330, no. 1, pp. 35–41, 2008.

[5] B. Kakavandi, R. R. Kalantary, M. Farzadkia et al., "Enhanced chromium (VI) removal using activated carbon modified by zero valent iron and silver bimetallic nanoparticles," *Journal Of Environmental Health Science and Engineering*, vol. 12, pp. 1–10, 2014.

[6] M. Pang, N. Kano, and H. Imaizumi, "Adsorption of chromium (VI) from aqueous solution using zeolit/chitosan hybrid composite," *J. Chem. Chem. Eng.*, vol. 9, no. 7, pp. 433–441, 2015.

[7] N. Bu, X. Liu, S. Song et al., "Synthesis of NaY zeolite from coal gangue and its characterization for lead removal from aqueous solution," *Advanced Powder Technology*, vol. 31, no. 7, pp. 2699–2710, 2020.

[8] S. A. Kim, S. Kamala-Kannan, K. J. Lee et al., "Removal of Pb(II) from aqueous solution by a zeolite–nanoscale zero-valent iron composite," *Chemical Engineering Journal*, vol. 217, pp. 54–60, 2013.

[9] S. Soni, P. K. Bajpai, J. Mittal, and C. Arora, "Utilisation of cobalt doped iron based MOF for enhanced removal and recovery of methylene blue dye from waste water," *Journal of Molecular Liquids*, vol. 314, p. 113642, 2020.

[10] A. Patel, S. Soni, J. Mittal, A. Mittal, and C. Arora, "Sequestration of crystal violet from aqueous solution using ash of black turmeric rhizome," *Desalination and Water Treatment*, vol. 220, pp. 342–352, 2021.

[11] A. Pohl, "Removal of heavy metal ions from water and wastewaters by sulfur-containing precipitation agents," *Water, Air, and Soil Pollution*, vol. 231, no. 10, 2020.

[12] M. Taseidifar, F. Makavipour, R. M. Pashley, and A. F. M. M. Rahman, "Removal of heavy metal ions from water using ion flotation," *Environmental Technology and Innovation*, vol. 8, pp. 182–190, 2017.

[13] A. M. Hamdan, H. Abd-El-Mageed, and N. Ghanem, "Biological treatment of hazardous heavy metals by Streptomyces rochei ANH for sustainable water management in agriculture," *Scientific Reports*, vol. 11, no. 1, pp. 1–12, 2021.

[14] B. R. Chanda, A. H. Mithun, M. A. Hasan, and B. K. Biswas, "Nickel removal from aqueous solution using chemically treated mahogany sawdust as biosorbent," *Journal of Chemistry*, vol. 2021, pp. 1–10, 2021.

[15] X. Zhang, J. Gao, S. Zhao et al., "Hexavalent chromium removal from aqueous solution by adsorption on modified zeolites coated with Mg-layered double hydroxides," *Environmental Science and Pollution Research*, vol. 26, no. 32, pp. 32928–32941, 2019.

[16] I. V. Joseph, L. Tosheva, and A. M. Doyle, "Simultaneous removal of Cd(II), Co(II), Cu(II), Pb(II), and Zn(II) ions from aqueous solutions via adsorption on FAU-type zeolites prepared from coal fly ash," *Journal of Environmental Chemical Engineering*, vol. 8, no. 4, p. 103895, 2020.

[17] U. S. Agriculture, "Department of Bangladesh: Grain and Feed Annual," https://www.fas.usda.gov/data/bangladesh-grain-and-feed-annual-6.

[18] B. Singh, "Rice husk ash," in *Waste and Supplementary Cementitious Materials in Concrete*, Woodhead Publishing, 2018.

[19] K. Kordatos, S. Gavela, A. Ntziouni, K. N. Pistiolas, A. Kyritsi, and V. Kasselouri-Rigopoulou, "Synthesis of highly siliceous ZSM-5 zeolite using silica from rice husk ash," *Microporous and Mesoporous Materials*, vol. 115, no. 1-2, pp. 189–196, 2008.

[20] C. S. Cundy and P. Cox, "The hydrothermal synthesis of zeolites: Precursors, intermediates and reaction mechanism," *Microporous Mesoporous Mater*, vol. 82, pp. 1–78, 2005.

[21] R. Chanda, L. Wang, and W. Schwieger, "Heat and mass transfer properties of zeolite coatings: comparison of reactive- and spray-coated systems," *Chemie Ingenieur Technik*, vol. 90, no. 5, pp. 708–712, 2018.

[22] L. F. De Magalhães, G. R. Da Silva, and A. E. C. Peres, "Zeolite application in wastewater treatment," *Adsorption Science and Technology*, vol. 2022, pp. 1–26, 2022.

[23] M. Król, W. Mozgawa, W. Jastrzębski, and K. Barczyk, "Application of IR spectra in the studies of zeolites from D4R and D6R structural groups," *Microporous and Mesoporous Materials*, vol. 156, pp. 181–188, 2012.

[24] U. Khalil, M. B. Shakoor, S. Ali, and M. Rizwan, "Tea waste as a potential biowaste for removal of hexavalent chromium from wastewater: equilibrium and kinetic studies," *Arabian Journal of Geosciences*, vol. 11, no. 19, p. 573, 2018.

[25] T. S. Badessa, E. Wakuma, and A. M. Yimer, "Bio-sorption for effective removal of chromium(VI) from wastewater using Moringa stenopetala seed powder (MSSP) and banana peel powder (BPP)," *BMC Chemistry*, vol. 14, no. 1, p. 71, 2020.

[26] D. Song, K. Pan, A. Tariq et al., "Adsorptive removal of toxic chromium from waste-water using wheat straw and Eupatorium adenophorum," *PLoS One*, vol. 11, no. 12, article e0167037, 2016.

[27] S. Bai, M. Chu, L. Zhou, Z. Chang, C. Zhang, and B. Liu, "Removal of heavy metals from aqueous solutions by X-type zeolite prepared from combination of oil shale ash and coal fly ash," *Energy Sources, Part A: Recovery, Utilization, and Environmental Effects*, pp. 1–11, 2019.

[28] Y. Jin, Y. Wu, J. Cao, and Y. Wu, "Adsorption behavior of Cr(VI), Ni(II), and Co(II) onto zeolite 13x," *Desalination and Water Treatment*, vol. 54, no. 2, pp. 511–524, 2015.

[29] W. M. Xie, F. P. Zhou, X. L. Bi et al., "Accelerated crystallization of magnetic 4A-zeolite synthesized from red mud for application in removal of mixed heavy metal ions," *Journal of Hazardous Materials*, vol. 358, pp. 441–449, 2018.

[30] R. Panek, M. Medykowska, M. Wiśniewska, K. Szewczuk-Karpisz, K. Jędruchniewicz, and M. Franus, "Simultaneous removal of $Pb^{2+}$ and $Zn^{2+}$ heavy metals using fly ash Na-X zeolite and its carbon Na-X(C) composite," *Materials (Basel)*, vol. 14, no. 11, p. 2832, 2021.

[31] M. Akbari Binabaj, S. M. Nowee, and N. Ramezanian, "Comparative study on adsorption of chromium(VI) from industrial wastewater onto nature-derived adsorbents (brown coal and zeolite)," *International journal of Environmental Science and Technology*, vol. 15, no. 7, pp. 1509–1520, 2018.

[32] Y. Zhang, L. Zhou, L. Chen et al., "Synthesis of zeolite Na-P1 from coal fly ash produced by gasification and its application as adsorbent for removal of Cr(VI) from water," *Frontiers of Chemical Science and Engineering*, vol. 15, no. 3, pp. 518–527, 2021.

[33] I. Langmuir, "The constitution and fundamental properties of solids and liquids. Part I. Solids," *Journal of the American chemical society*, vol. 38, no. 11, pp. 2221–2295, 1916.

[34] S. Lata, P. K. Singh, and S. R. Samadder, "Regeneration of adsorbents and recovery of heavy metals: a review," *International journal of Environmental Science and Technology*, vol. 12, no. 4, pp. 1461–1478, 2015.

[35] B. K. Biswas, J. I. Inoue, K. Inoue et al., "Adsorptive removal of As(V) and As(III) from water by a Zr(IV)-loaded orange waste gel," *Journal of Hazardous Materials*, vol. 154, no. 1-3, pp. 1066–1074, 2008.

[36] S. Soni, P. K. Bajpai, D. Bharti, J. Mittal, and C. Arora, "Removal of crystal violet from aqueous solution using iron based metal organic framework," *Desalination and Water Treatment*, vol. 205, pp. 386–399, 2020.

Hindawi
Adsorption Science & Technology
Volume 2022, Article ID 3669652, 16 pages
https://doi.org/10.1155/2022/3669652

*Research Article*

# Removal of Toxic Metal Ions from Aqueous Solutions in Integrated Clay Adsorption and Electroflotation

**Raimundo Nonato Pereira Teixeira,[1] Vicente Oliveira Sousa Neto,[2] Juliene Tomé Oliveira,[3] Lucas Fontenele Amorim,[3] Eliezer Fares Abdala Neto,[3] Diego de Quadros Melo,[4] Henrique Douglas Melo Coutinho,[1] Bonglee Kim,[5] Jorge Marcell Coelho Menezes,[1] and Ronaldo Ferreira do Nascimento[3]**

[1]*Department of Biological Chemistry, Laboratory of Research in Natural Products, Regional University of Cariri (URCA), 63100-000 Crato, CE, Brazil*
[2]*State University of Ceara, Center of Education, Sciences and Technology of Region of Inhamuns-CECITEC, BR 116, s/n, Bairro Bezerra e Souza, Tauá, Ceará, Brazil*
[3]*Department of Analytical Chemistry and Physico-Chemistry, Federal University of Ceará, Rua do Contorno, S/N, Campus do Pici, Bl. 940 CEP:, 60451-970 Fortaleza, CE, Brazil*
[4]*Department of Physical, Federal University of Ceará, Fortaleza, Ceara 60455-900, Brazil*
[5]*Department of Pathology, College of Korean Medicine, Kyung Hee University, Seoul 02447, BK, Republic of Korea*

Correspondence should be addressed to Henrique Douglas Melo Coutinho; hdmcoutinho@gmail.com and Bonglee Kim; bongleekim@khu.ac.kr

Received 20 February 2022; Revised 16 May 2022; Accepted 2 July 2022; Published 20 July 2022

Academic Editor: Randa Khalifa



Most galvanic process industries treat their effluents by chemical precipitation methods. Such a method produces an amount of galvanic sludge that is often disposed of inappropriately to the environment, causing major environmental damage. These rejects present high concentrations of toxic metallic ions, such as copper (Cu(II)), lead (Pb(II)), nickel (Ni(II)), and cadmium (Cd(II)). Several alternatives have been proposed to contribute in a cheaper and efficient way to treat these effluents. This study aimed to describe the results obtained in the removal of the concentrations of Cu(II), Ni(II), Cd(II), and Pb(II) ions, present in an aqueous solution, by the use of a hybrid system combining the adsorption and electroflotation processes simultaneously. The adsorbent materials used were two Brazilian soil clays classified as sodium clay (SC) and ferric clay (FC). For the electroflotation process, aluminum, iron, and stainless-steel electrodes were used. The obtained data showed good efficiency in the removal of the four metallic ion concentrations. The best results presented a reduction in the concentration of Cu(II), Ni(II), Cd(II), and Pb(II) ions of 50.11%, 36.71%, 21.59%, and 23.43%, respectively, when it was used the hybrid system formed by the ferrous clay as adsorbent and the aluminum electrode for the electroflotation process.

## 1. Introduction

Highly acidic heavy metal laden effluents, originating from electroplating industry, are of major concern and increasingly subjected to stringent regulations in the way that they must be treated prior to their discharge into the environment. In electroplating units, water is used for various processes, thus eventually forming electroplating wastewaters (EWW), which are highly enriched in acid contents and heavy metals (Zn, Fe, Cr, Ni, Cd, Au, and Cu), which render them severely corrosive and polluting in nature. According to Nagajyoti et al. [1], the accumulation of heavy metals in soils causes concern for agricultural production, because it has adverse effects on commercialization and food safety and its phytotoxicity affects the growth of the crop and also on the environmental health of soil organisms.

Their adverse effect on the environment can be neutralized by the application of purification methods. Various techniques have been employed so far, including adsorption, physicochemical treatment, membrane filtration, ion exchange, and electrochemical treatment [2].

Electrochemical methods have been shown so far as a good alternative to the traditional physicochemical methods in water treatment [3]. In this context, electroflotation-coagulation has played an important role among the techniques for the treatment of industrial wastewater. And this is due to its versatility, in an operational mode as the efficiency of contaminant removal. Electroflotation-coagulation is a process based on the electrodissolution of the metal ions of anodes by electrolytic oxidation. Aluminum and iron metals have been commonly used as electrodes as they are cheap and easily available. The reactions occurring in an electrochemical cell for an aluminum electrode are shown below.

At the cathode:

$$2H_2O + 2e^- \longrightarrow H_2\,(g) + 2OH^-, \tag{1}$$

At the anode:

$$\mathrm{Al(s)} \longrightarrow Al^{+3}(aq) + 3e^-, \tag{2}$$

In the solution:

$$Al^{+3}\,(aq) + 3H_2O \longrightarrow \mathrm{Al(OH)_3}(s) + 3H^+(aq). \tag{3}$$

The aluminum hydroxide flakes act as adsorbents for toxic metal ions. Furthermore, the toxic metal ions combine with the electrogenerated $OH^-$ ions at the cathode and precipitate in the form of their insoluble hydroxides. Both phenomena act synergistically leading to a rapid removal of toxic metal pollutants from the aqueous solution [4].

According to Gupta, Nayak, and Agarwal [5] and Saleh and Gupta [6], the adsorption has been developed as an efficient method for the removal of toxic metals from contaminated water and soil. A variety of adsorbents have been used for the removal of metal ions, such as clays [7–10], zeolites [11, 12], dried plant parts [13, 14], and activated carbon [15, 16].

The reactors used to removal of pollutants by electroflotation are small and compact and present low maintenance and operation costs when compared to other flotation processes.

Some works have proposed systems using two or more processes for removing toxic metal ions from aqueous solutions [17]. Among these hybrid processes are included microfiltration-electrocoagulation [18] adsorption-microfiltration processes [19], and adsorption-ion exchange [20].

The hybrid system that combines adsorption and electrocoagulation has been shown to be effective for the removal of organic and inorganic pollutants. Many studies report on the treatment of effluents contaminated by organic pollutants using this hybrid system. Pekka et al. (2018) [21] tested the efficiency of this system in removing total carbon from an electrocoagulation system accompanied by adsorption with activated carbon. However, some researchers have tried to investigate the hybrid system in the removal of inorganic pollutants, and some studies report on the use of the two techniques combined in the treatment of effluents contaminated by metals. Sohail et al. (2020) [22] showed that the hybrid system was efficient for the removal of Cr, Cu, and Zn, obtaining a maximum removal capacity of 97.44% for Cr, 97.45% for Cu, and 74.18% for Zn. Elbert et al. (2020) [23] tested the efficiency of this hybrid system that showed a calcium removal capacity of 88% ($6.0\,mg.L^{-1}$) and 72% of strontium ($0.4\,mg.L^{-1}$).

The results found that a combined hybrid system is very promising. Thereby, the objective of this paper is to investigate the use of a hybrid system which associates the process of adsorption onto clays with electroflotation-coagulation for removal of Cu(II), Ni(II), Cd(II), and Pb(II) in aqueous systems.

## 2. Materials and Methods

*2.1. Adsorbents.* The clays samples used in this study were given from the Bentonisa Company in Campina Grande, Paraíba, Brazil. The sodium and ferric clays were used in their raw form, without any prior treatment. The clays were sieved, and the material was separated in a range of 0.074-0.105 mm.

*2.2. Characterization Methods.* X-ray diffraction (XRD) patterns were recorded at a Philips X'Pert X-ray diffractometer, with a CuKa radiation for crystalline phase with a routine power of 1600 W (40 kV and 40 mA). A wavelength dispersive X-ray fluorescence spectrometer (model ZMS Mini II, Rigaku) was used to obtain the X-ray fluorescence spectra. The surface area analysis was determined by isotherms of adsorption/desorption of $N_2$ (isotherms Brunauer, Emmett and Taller - BET) and held in a porosimeter (brand: Quantachrome, Model: NOVA 1200), and the data was exported using the Autosorb software. Sample preparation was performed for 12 hours under vacuum at 110 °C. The pore size distribution (PSD) was determined using the BJH method, which is a method to determine pore size distribution of a mesoporous solid based on the Kelvin equation and provides a much more informative result for a pore size distribution. These exchange capacities (EC) were conventionally expressed in meq/100 g [24], which is numerically equal to centimoles of charge per kilogram of exchanger (cmol(+)/kg). These values were estimated using the ammonium acetate method. The soil sample is extracted with a 1 M $NH_4OAc$ solution at pH = 7.00. The soil-solution slurry is shaken for 2 h, and the solution is separated from the solid by centrifugation The addition of $NH_4^+$ in excess to the soil displaces the rapid exchangeable alkali and alkaline cations from the exchange sites of the soil particles [25].

*2.3. Batch Adsorption Experiments.* Analytical-grade chemicals and ultrapure water (Millipore Direct Q3 Water Purification System) were used to prepare the solutions.

Monoelement and multielement stock solutions of Ni(II), Cu(II), Cd(II), and Pb(II) (500 mg·L$^{-1}$) were prepared with $Ni(NO_3)_2{\cdot}6H_2O$, $Cu(NO_3)_2{\cdot}3H_2O$ $Cd(NO_3)_2{\cdot}4H_2O$, and $Pb(NO_3)_2$ (Merck, São Paulo, Brazil), respectively. The acetate buffer solution pH 5.5 was prepared with sodium acetate and glacial acetic acid. NaOH (0.10 mol·L$^{-1}$) and HCl (0.10 mol·L$^{-1}$) solutions were used for pH adjustments. Erlenmeyers (50.0 mL) and an orbital shaker device (Marconi, Brazil) operating at 150 rpm and 28 ± 2°C were used in the experiments. The adsorbents (50.0 mg) and the respective solutions (25.0 mL) containing the analytes were added to each flask. Equilibrium concentrations of the toxic metals were determined by using an atomic absorption spectrophotometer (VARIAN model AA240FS) with an air acetylene flame.

The equilibrium adsorption capacity of the adsorbent is calculated as follows:

$$q_e = \frac{(C_0 - C_{eq})}{w} * V, \tag{4}$$

where $q$ (mg g$^{-1}$) is the metal uptake of metal ion, $C_o$ is the initial concentration, $C_{eq}$ is the equilibrium concentration, $V$ is the volume in L, and $w$ is the mass of adsorbent in grams.

*2.4. Adsorption Isotherms.* To study adsorption isotherm, an orbital shaker table was used at a speed kept at 150 rpm. An adsorbent mass (50 mg) was mixed with solutions (25.0 mL) of each metal ion solution, at concentrations ranging from 40 to 300 (mg.L$^{-1}$). All experiments were performed in triplicate. The optimum pH used was 5.5 acetate-acid acetic buffer with an equilibration time of 1 h at 28 ± 2° C. At the end of the adsorption process, the supernatant was filtered, and the residual metal ion concentrations were determined by atomic absorption spectrophotometer (AAS). The amounts of adsorbed metals (mg g$^{-1}$) were determined from the concentrations before and after the equilibration time using Equation (4).

For an evaluation of the adsorption isotherms, the following statistical tools were used: $R^2$ (Equation (5))), Radj$^2$ (Equation (6))), SSE (Equation (7)), Hybrid (Equation (8)), and %Error (Equation (9)), where $z$: number of experimental points; $q_{exp}$: experimental adsorption capacity (mg g$^{-1}$); $q_{exp}$ ∗: average of experimental adsorption capacity values (mg g-1); $q_{calc}$: calculated adsorption capacity (mg g$^{-1}$); and $q_{max\_exp}$: maximum experimental adsorption capacity (mg g$^{-1}$).

To be considered adequate, the model must present the highest values of $R^2$ and Radj$^2$ and the lowest values of SSE, Hybrid, and %Error [26, 27]:

$$R^2 = \frac{\sum_i^z \left(q_{calc} - q_{\exp}*\right)2}{\sum_i^z \left(q_{calc} - q_{\exp *}\right)2 + \sum_i^z \left(q_{calc} - q_{\exp}\right)^{Ç}}, \tag{5}$$

$$R^2_{adj} = 1 - \frac{z-1}{z-(k-1)}\left(1 - R^2\right), \tag{6}$$

$$SSE = \sum_{i=1}^{z} \left(q_{\exp} - q_{calc}\right)^{Ç}, \tag{7}$$

$$Hybrid = \frac{100}{z-k}\sum_{i=1}^{z}\left(\frac{\left(q_{\exp} - q_{calc}\right)^{Ç}}{q_{\exp}}\right), \tag{8}$$

$$\%Error = \left|\frac{q_{max\_\exp} - q_{max}}{q_{max}}\right|100, \tag{9}$$

*2.5. Adsorption Kinetics.* Adsorption kinetics studies allow the evaluation of the extent of adsorbate removal, as well as the identification of the predominant mechanisms involved in the adsorption process. For this, a multielement solution (100.0 mg·L$^{-1}$) was continuously shaken (150 rpm) at pH 5.5. The metal ion equilibrium concentrations were analyzed for adequate time interval (2, 4, 6, 8 10, 15, 20, 30, 40, and 60 min). Adsorption capacities were calculated, using the Equation (4), for each studied time.

*2.6. Adsorption Electroflotation-Coagulation Experiments.* In the studies with the hybrid system adsorption (electroflotation-coagulation), a series of tests were initially performed with the clays (3 g) associated with the hybrid system of electroflotation-coagulation using multielement solution (300 mg L$^{-1}$) with four ions (Ni(II), Cu(II), Cd(II), and Pb(II)) at pH 5.5. The operating conditions of the apparatus used in the testing of hybrid systems with adsorption (electroflotation-coagulation) are shown in Figure 1.

The electroflotation-coagulation process was performed on conditions as follows: 500.0 mL of synthetic effluent into 1000 mL cubic reactor. The electroreduction conditions were carried out with stainless steel, iron, and aluminum electrode plates (total area for a set of electrodes 50 cm$^2$ (10 × 5 cm), amount of electrodes per compartment of 2 units, and distance between plates of 1.5 mm. Voltage and electrical current were measured by supplies (Hayama® HY-125™, 220-12 V/5A, and total power 200 W) for an average current applied to a set of electrodes of 0.9 A, current density of 18 mA cm$^{-2}$, and consumption of 0.02 KWh L$^{-1}$ for 20 minutes. The treatment procedure was run in duplicate. To evaluate the removal capacity for each hybrid system, we used the equation proposed for Grigorov and Alexandrova [28]:

$$\%Removal = \left(1 - \frac{C_f}{C_i}\right)x100, \tag{10}$$

where $C_f$ is the final concentration and $C_i$ is the initial concentration of the metal ion present in the solution.

*2.6.1. Effect of Time of Operation and Initial Concentration in Removal of Toxic Metal Ion Monoelement System.* The experiments were done using monoelementary solutions with concentrations of approximately 300 mg L$^{-1}$ for times

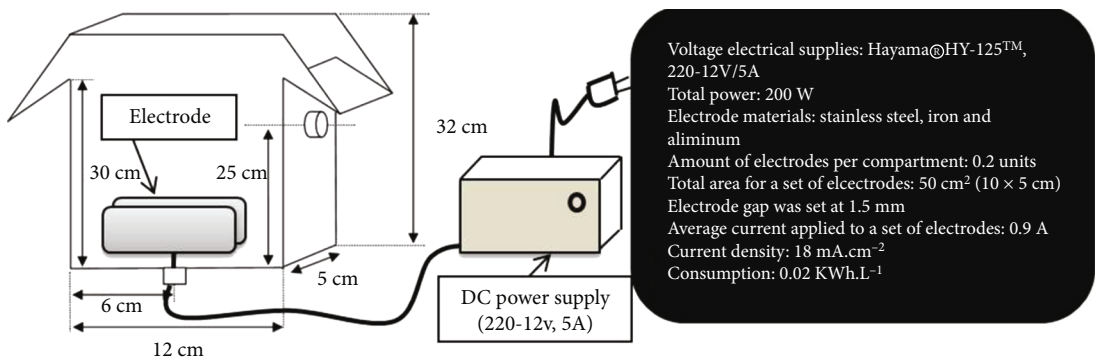


Figure 1: Electroflotation-coagulation reactor in laboratory scale used in the experiments and WRD patterns of the samples.

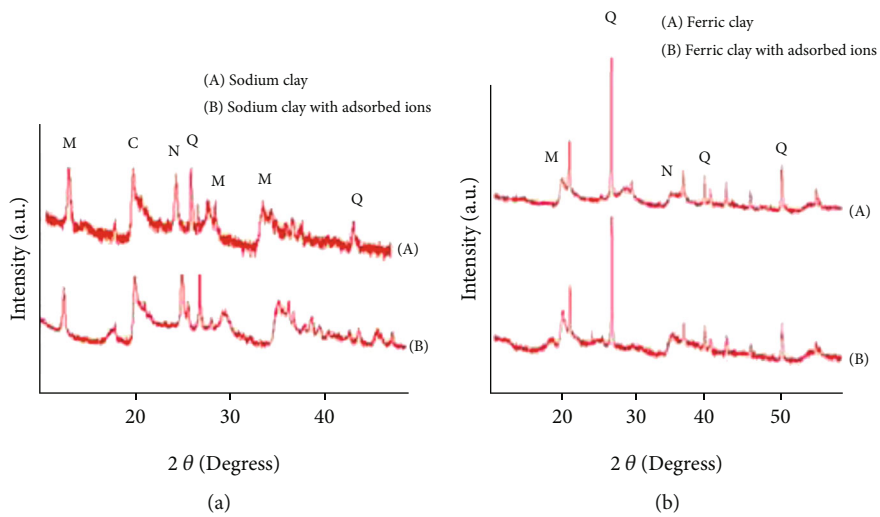


Figure 2: X-ray diffractogram of the clays before (a) and after (b) the four metal ions adsorption. 2 (a) Sodium clay and 2 (b) ferric clay. Ckaolinite ($Al_2H_4O_9Si_2$), M montmorillonite (Na, Ca), (Al,Mg) $2Si_4O_{10}$ $(OH)_2.xH_2O$), N-nontronite ($Fe_2H_{10}Na_{0,30}O_{16}Si_4$), Q-quartz ($SiO_2$).

of 2, 4, 6, 8, and 10 minutes. According to Sahu [29], many studies evaluate the influence of the initial concentration. To evaluate the effect of the initial concentration of metal ions, three different concentrations were prepared with the values 100, 250, and 500 mg $L^{-1}$.

*2.6.2. Removal of Toxic Metal Ion Multielement Systems.* The concentration of toxic metal ions ranges from 40 to 500 mg $L^{-1}$. Initially, tests using only the electrodes were performed without the addition of clays to evaluate the effect of the techniques separately, and experiments were then done with the hybrid system adsorption electrocoagulation-coagulation.

## 3. Results and Discussion

### *3.1. Clay Sample Characterizations*

*3.1.1. X-Ray Diffractograms.* The X-ray diffractograms of sodium and ferric clays, before and after the adsorption of the four metallic ions, are shown in Figures 2(a) and 2(b), respectively. Characteristics of an amorphous material with broad peaks can be observed. This follows from the fact that the clay minerals have not undergone any previous treatment and the analysis was done with the sample in the raw state. Nevertheless, one can check some typical patterns of bentonite, with the presence of clay minerals from the group of montmorillonites with interplanar distance (d001) in 14.053 Å [30], as well the presence of quartz with interplanar distance (D101) at 3.34 Å [31] and kaolinite (D002) 3.59 Å [32]. It is observed by the XRD pattern (Figure 2(a)) that there were no changes in the clay mineral structure after adsorption of the four ions. This is to be expected since the chemical species present in the clay mineral (such as quartz, kaolinite, and montmorillonite) do not suffer any transformation with the presence of these four new ions. The structures of clay minerals are usually affected by processes such as calcination, acid, alkaline attack, or pillarization [33].

XRD of the ferric clay, before and after the adsorption of the four ions (Figure 2(b)), present the existence of characteristic peaks of quartz (D100) with a basal spacing of 4.26 Å [29], in montmorillonite 13.60 Å [30], and nontronite at 13.30 Å [34]. There were also no changes in the structures of clay after adsorption of the four metal ions as shown in curve B.

Table 1: Chemical composition (% by weight) obtained for X-ray fluorescence..

| Clay | %Si | %Al | %Ca | %Fe | % K | %Zn | %Cu | %Ni | %Cd | %Pb | %Mn | %Ti |
|---|---|---|---|---|---|---|---|---|---|---|---|---|
| SC | 56.6 | 20.9 | 9.80 | 6.33 | 5.97 | 0.287 | — | — | — | — | — | — |
| | 4 | 6 | 5 | 2 | 1 | | | | | | | |
| SC/AD | 41.3 | 14.6 | 4.87 | 5.07 | 4.07 | 0.174 | 0.82 | 2.05 | 1.86 | 23.7 | 0.440 | 0.776 |
| S | 5 | 6 | 6 | 6 | 2 | | 4 | 1 | 9 | 2 | | |
| FC | 59.1 | 6.37 | 5.93 | 25.2 | 0.74 | — | — | — | — | — | 0.184 | 1.819 |
| | 6 | 7 | 1 | 7 | 0 | | | | | | | |
| FC/AD | 38.0 | 10.0 | 2.12 | 21.6 | 0.73 | — | 10.9 | 6.51 | 1.32 | 6.76 | — | 1.527 |
| S | 9 | 6 | 5 | 3 | 2 | | 9 | 2 | 3 | 4 | | |

CS: sodium clay; CS/ADS: sodium clay with adsorbed ions; CF: ferric clay; CF/ADS: ferric clay with adsorbed ions.

*3.1.2. X-Ray Fluorescence.* Table 1 presents the results obtained by the X-ray fluorescence for two clays before and after the metal ion adsorption. It can be seen that the two clays before the adsorption process are predominantly of Si and Al elements in the form of oxides. Sodium clay has a higher content of $Al_2O_3$ than ferric clay. The amount of $SiO_2$ is due to silicates such as feldspars and micas. Titanium and manganese oxides appear in small amount in the ferric clay, but they were not detected in sodium clay. The occurrence of calcium in the two types of clays can be due to cation exchange, since the difratograms of these clays do not show the presence of calcite, dolomite, or gypsum. On other hand, the presence of K in clays is almost entirely due to feldspar or exchangeable cations.

In general, the chemical composition of the clays tends to vary due to two main factors such as the different smectite and isomorphic substitutions in the presence of associated impurities. The results presented in Table 2 confirm the incorporation of the four metal ions in both clays after the adsorption process. Sodium clay showed that the highest amount of Pb(II) retained (23.72%). This is due to the fact that clay contains (in its chemical composition) the montmorillonite mineral, which has more negative adsorption sites found that of other clay minerals. In clay, ferric ion which had a higher amount retained is Cu(II), about 10.99%.

The average size of the clay particles was about $8.8 \times 10^{-3}$ cm. The surface area of sodium clay was 8.48 and for the ferric clay 59.2 $m^2\,g^{-1}$, by means of BET method using nitrogen. The exchange capacities (EC) were 13.6 meq/100 g to sodium clay and 11.9 meq/100 g to ferric clay.

*3.1.3. BET and EC.* Figure 3 presents the BET surface area and pore size distribution. The values of the specific surface areas of the clays samples were 8.478 and 59.2 $m^2.g^{-1}$ for sodium and ferric clays, respectively. It was observed that the ferric clay presented a specific area about seven times larger than the sodium clay. A total pore volume of $9.858 \times 10^{-2}\,cm^3.g^{-1}$ was observed for the sodium clay and $1.009 \times 10^{-1}\,cm^3.g^{-1}$ for the ferric clay, respectively.

It is noted that the curves presented for any two clays exhibit hysteresis and are similar to type IV isotherm, characterized by the presence of mesopores, with pores of intermediate diameters of between 20 and 500 Å [35], in which formation multilayer adsorption is possible, but with limited size of the porosity of the material. The predominance of mesopores with average diameters of 42.32 Å was observed in sodium clay and 48.25 Å in ferric clay. The exchange capacities (EC) were 13.6 meq/100 g in sodium clay and 11.9 meq/100 g in ferric clay.

### 3.2. Batch Adsorption

*3.2.1. Adsorption Isotherm Models.* The Langmuir adsorption model [36] has been successfully used to explain the metal's adsorption from aqueous solutions and is based that the maximum adsorption corresponds to a saturated monolayer of solute molecules on the adsorbent surface with no lateral interaction between the adsorbed metal ions. The Freundlich isotherm [37] is an empirical equation employed to describe heterogeneous systems.

Temkin and Pyzhev [38] considered the effects of some indirect sorbate/adsorbate interactions on adsorption isotherms and suggested that because of these interactions, the heat of adsorption of all the molecules in the layer would decrease linearly with coverage.

Comparing the experimental results and the parameters obtained by the models used, it was realized that they were similar to other results obtained by other researchers. Rybicka et al. [39] studied the adsorption capacity of Cu(II), Pb(II), Ni(II), Cd(II), and Zn(II) in three clays and observed that montmorillonite adsorbs the following descending order Pb > Cd ~ Cu > Zn. Potgieter et al. [40] studied the adsorption capacity of Pb(II), Ni(II), Cr(II), and Cu(II) by the paligorsquita adsorbent and obtained the following descending order for adsorption capacity Pb > Cr > Ni > Cu.

Figure 4 presents the experimental curves in comparison with the applied models.

Table 3 shows the results obtained in this study compared with other obtained by the literature.

*3.2.2. Sorption Kinetics.* The following kinetic models were studied in this work: pseudo-second order proposed by Ho and Mckay [41] and Elovich equation [42].

Analyzing the data presented in Tables 4 and 5, it is possible to observe that the pseudo-second-order model presented a better approximation of the experimental value ($R^2$), compared to the Elovich model.

Table 2: Langmuir, Freundlich, and Temkin isotherm models' constants and coefficients of determination for adsorption of Cu(II), Ni(II), Cd(III), and Pb(III) onto sodium clay (SC) and ferric clay (FC).

| Íons | Clay | Langmuir model | | | | | | | Freundlich model | | | Temkin model | | |
|---|---|---|---|---|---|---|---|---|---|---|---|---|---|---|
| | | Qmax ± SD | $K_L$ | $R^2$ | %Error | $R^2_{adj}$ | SSE | *Hybrid* | *N* | $K_F$ | $R^2$ | B | $K_T$ | $R^2$ |
| Cu(II) | SC | 35.71 ± 1.2 | 0.065 | 0.994 | 12.5 | 0.974 | 12.4 | 6.8 | 6.261 | 15.39 | 0.979 | 7.613 | 0.515 | 0.842 |
| | FC | 34.72 ± 1.2 | 0.036 | 0.986 | 5.4 | 0.956 | 9.5 | 4.3 | 3.098 | 5.583 | 0.988 | 6.076 | 0.690 | 0.977 |
| Ni(II) | SC | 26.84 ± 0.7 | 0.035 | 0.990 | 4.7 | 0.972 | 13.8 | 6.9 | 2.785 | 3.705 | 0.959 | 4.917 | 0.582 | 0.961 |
| | FC | 15.94 ± 0.4 | 0.198 | 0.986 | 4.1 | 0.961 | 14.4 | 7,5 | 8.682 | 8.654 | 0.622 | 1.366 | 523.8 | 0.591 |
| Cd(II) | SC | 26.81 ± 0.6 | 0.044 | 0.983 | 5.4 | 0.957 | 15.5 | 8.7 | 2.840 | 2.815 | 0.887 | 5.593 | 0.283 | 0.949 |
| | FC | 10.93 ± 0.4 | 0.259 | 0.989 | 8.9 | 0.954 | 18.4 | 8,9 | 7.716 | 5.476 | 0.787 | 1.189 | 47.09 | 0.740 |
| Pb(II) | SC | 50.76 ± 1.8 | 0.017 | 0.978 | 9.1 | 0.969 | 21.9 | 9.7 | 1.862 | 2.531 | 0.928 | 10.26 | 0.211 | 0.967 |
| | FC | 11.61 ± 0.3 | 0.093 | 0.995 | 4.2 | 0.975 | 7.4 | 3.8 | 4.249 | 3.358 | 0.828 | 1.891 | 2.133 | 0.841 |

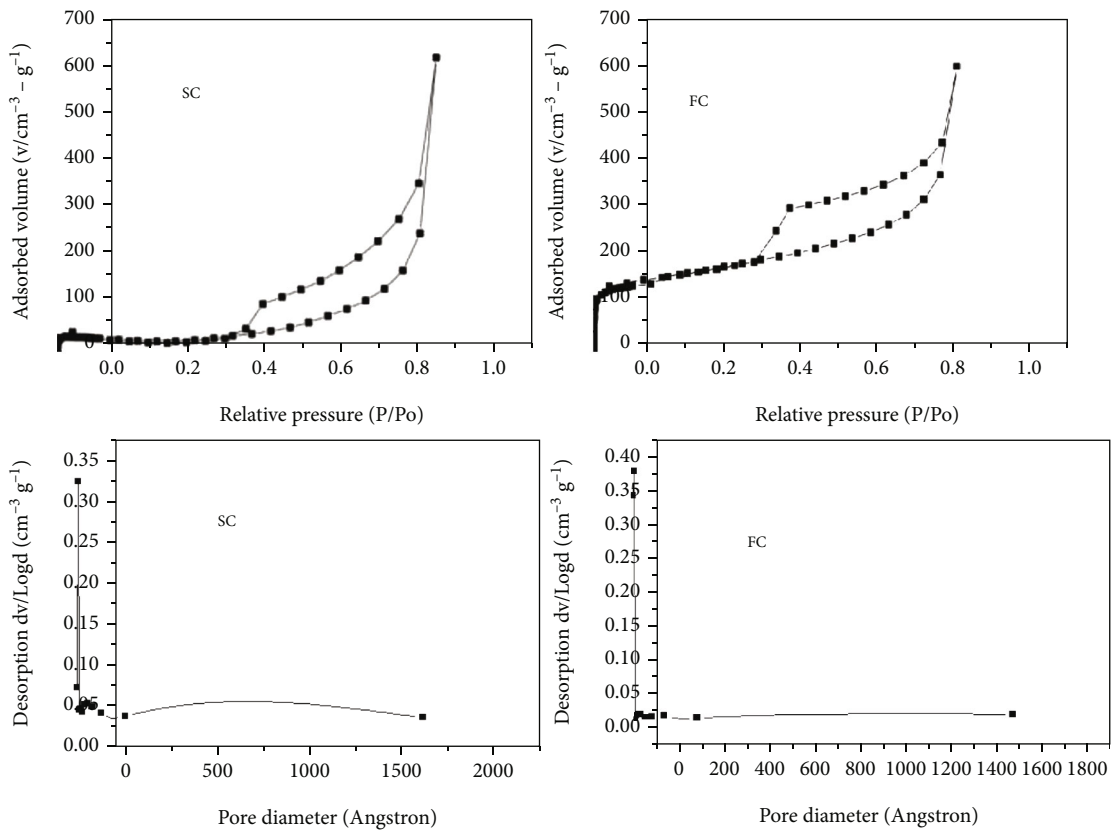


Figure 3: BET surface area plots and pore size distribution of the sodium clay (SC) and ferric clay (FC).

The fact that the second-order kinetics is the best fit model for the adsorption of metal ion onto clay indicates that the adsorption rate of all metal ion depends on the concentration of ions at the adsorbent surface and the behavior over a whole range of adsorption is in agreement with chemical adsorption being the rate controlling step [43, 44].

The $K_2$ results indicate that the adsorption of the four ions is favorable in both clays. The values only confirm this because the values were low in all systems studied.

*3.2.3. Diffusion Models.* The mechanisms and rate controlling steps that affect the kinetics of adsorption can be determined by fitting the kinetic experimental results to the Weber's intra-particle diffusion [45] and Boyd et al.'s [46] models.

Figures 5–12 present the experimental and theoretical curves for Cu(II), Ni(II), Cd(II), and Pb(II) ions from sodium and ferric clays.

These results can be explained because the clays have a very great swelling capacity by the incorporation of water

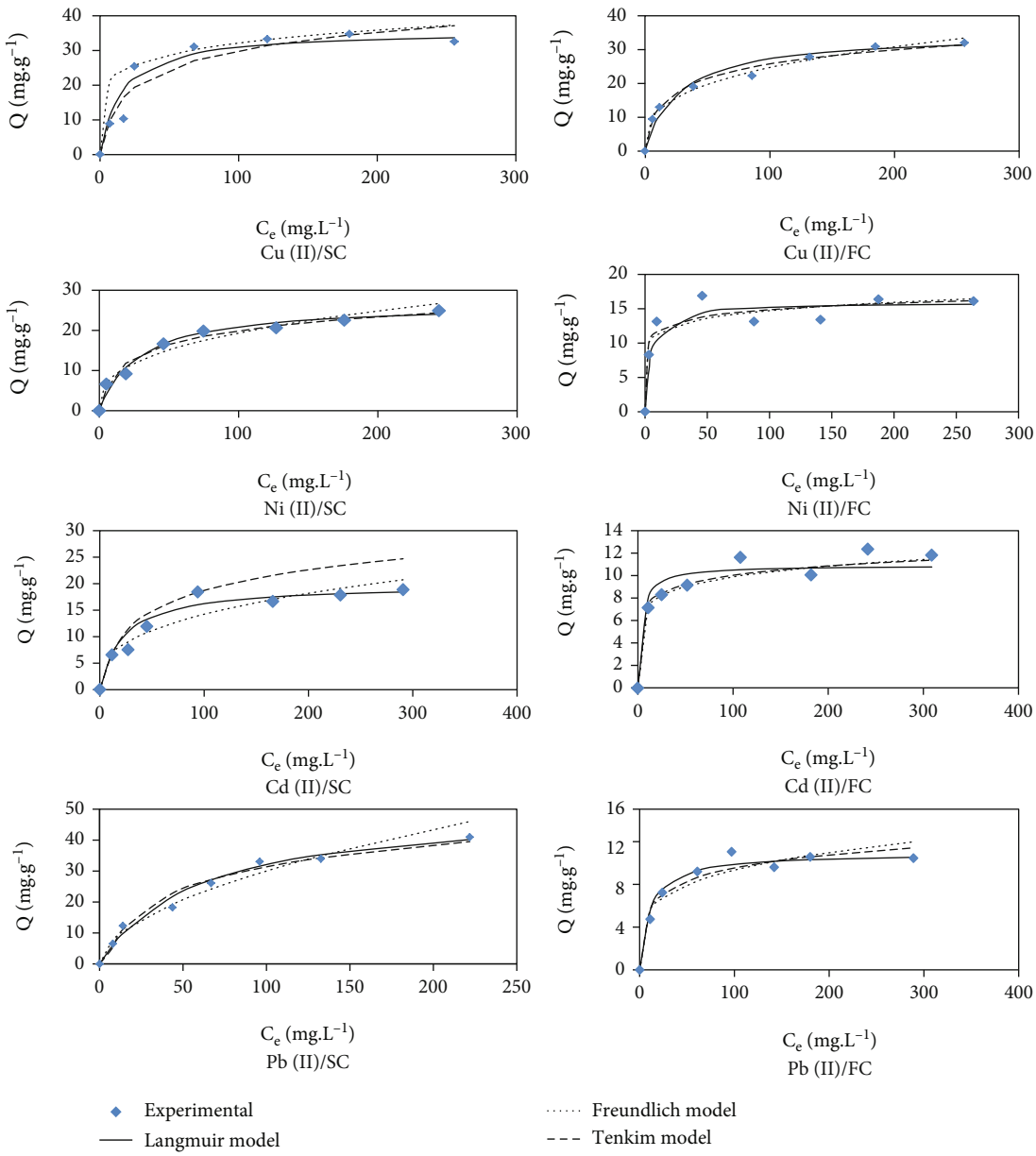


Figure 4: Experimental results of the adsorption equilibrium of Cu(II), Ni(II), Cd(II), and Pb(II) in SC and FC clays and theoretical curves from Langmuir, Freundlich, and Tenkim models at pH 5.5, T = 28°C, and stirring speed of 150 rpm.

in its structure. The clays which have interlayer cations present the properties well in the presence of water, increasing to several times its initial volume; this is because interlayer cations allow multiple water molecules and are adsorbed by increasing the distance between the layers and thus separating the clay particles from each other [47]. According to Glendening and Feller [48], the chemical mechanism of hydration of interlayer cations for these types of clay minerals is mainly through electrostatic interactions that maximize charge-dipole attraction and minimize water-water repulsion.

*3.3. Hybrid System Adsorption Electroflotation-Coagulation.* Initially, tests were conducted to discover the best operating conditions for hybrid systems. In order to do this, three types of electrodes were tested. The electrodes which were tested were as follows: an aluminum electrode, a stainless-steel electrode, and an iron electrode. The percentage of removal of ions in solution was calculated. The results for the removal percentages are presented in Table 6.

In Table 6, it is possible observe that the stainless-steel electrode combination with clays showed a lower removal capacity compared with the other two systems evaluated. The results of four systems were evaluated: (aluminum electrode/sodium clay), (iron electrode/sodium clay), (iron electrode/ferric clay), and (iron electrode/ferric clay). The assessments made with these systems note the operation time and the effect of the initial concentration.

To evaluate the contact time in the adsorption test, aliquots were removed at two-minute intervals, and the

Table 3: Comparison of Langmuir parameters on the adsorption of the ions Cu(II), Ni(II), Cd(II), and Pb(II) in these work clays and the literature.

| Metal ion | Adsorbent | Qmax (mg/g) | KL (L/mg) | Reference |
|---|---|---|---|---|
| Cu(II) | Natural montmorillonite | 31.8 | 192.8 | Gupta and Bhattacharyya, (2011) |
| | Clays containing montmorillonite | 30.9 | 0.0147 | Oubagaranadin and Murthy, (2010) |
| | Sodium clay | 35.71 | 0.065 | This study |
| | Ferric clay | 34.72 | 0.036 | This study |
| Ni(II) | Calcined montmorillonite | 21.14 | 137.54 | Bhattacharyya and Gupta (2006) |
| | Paligorsquita with acid activation | 93.02 | 0.0016 | Chen and Wang (2007) |
| | Sodium clay | 26.84 | 0.035 | This study |
| | Ferric clay | 15.948 | 0.198 | This study |
| Cd(II) | Turkish illitic clay | 13.09 | 0.0065 | Ozdes et al., (2011) |
| | Ca-montmorillonite modified with humic acid | 14.14 | 0.030 | Wu et al. (2011) |
| | Sodium clay | 26.81 | 0.044 | This study |
| | Ferric clay | 10.93 | 0.259 | This study |
| Pb(II) | Clay mixture containing boron | 79.4 | 0.11 | Olgun and Atar (2012) |
| | Turkish illitic clay | 53.76 | 0.069 | Ozdes et al. (2011) |
| | Sodium clay | 50.76 | 0.017 | This study |
| | Ferric clay | 11.614 | 0.093 | This study |

Table 4: Parameters of kinetic models for adsorption of Cu(II), Ni(II), Cd(II), and Pb(II) in clays: sodium (SC) and ferric (FC). Experimental conditions: acetate buffer pH = 5.5, T = 28°C. Initial concentration of ions = 100 mg $L^{-1}$.

| Ion | Clay | Ho model | | | | Elovich model | | | |
|---|---|---|---|---|---|---|---|---|---|
| | | Qexp | Qcal | K2 | R2 | Qcal | $\alpha$ | $\beta$ | R2 |
| Cu(II) | SC | 27.93 | 28.16 | 0.084 | 0.999 | 28.38 | 3.97 × 1027 | 2.37 | 0.722 |
| | FC | 21.24 | 21.50 | 0.195 | 0.999 | 22.12 | 4.42 × 1020 | 2.39 | 0.670 |
| Ni(II) | SC | 20.90 | 20.70 | 0.044 | 0.993 | 20.40 | 2.4 × 105 | 0.818 | 0.713 |
| | FC | 17.29 | 17.12 | 0.270 | 0.999 | 17.71 | 1.6 × 106 | 1.035 | 0.782 |
| Cd(II) | SC | 16.41 | 16.66 | 0.065 | 0.999 | 16.86 | 2.3 × 103 | 0.720 | 0.898 |
| | FC | 18.82 | 18.83 | 0.184 | 0.999 | 19.35 | 2.5 × 107 | 1.087 | 0.515 |
| Pb(II) | SC | 33.87 | 33.55 | 0.056 | 0.999 | 34.66 | 1.4 × 103 | 0.357 | 0.931 |
| | FC | 32.80 | 33.11 | 0.760 | 0.999 | 43.74 | 1.3 × 106 | 0.539 | 0.537 |

$Q_{cal}$ (mg $g^{-1}$); $K_2$ (g $mg^{-1}$ $min^{-1}$); $\alpha$ (mg $g^{-1}$ $min^{-1}$); and $\beta$ (mg $g^{-1}$).

amounts of the remaining metal ions in solutions were determined.

In all the systems studied, it was verified that very long times were not required for the system to remove the maximum amount of metal ions. This result is important, since the power consumed is one of the factors that must be taken into consideration to assess the operation of the system. Another fact that can be noted is that longer the system running the greater, amount of coagulants that are formed in situ from aluminum and iron electrodes. The faster the operation for removing ions, the lower the amount of iron and aluminum that will be added to the media.

This speed at which the removal of ions occurred was mainly due to the presence of clay in the solution. As discussed earlier, the clay minerals showed fairly rapid adsorption kinetics, compared with metal ions. Thus, there is an advantage to having removal processes using hybrid systems with very short times.

*3.3.1. Effect of Initial Concentration of Metal Ions.* The results of the effect of the initial concentration obtained from systems using only electroflotation-coagulation with aluminum and iron electrodes and hybrid adsorption electroflotation-coagulation systems are shown in the graphs of Figures 13 and 14.

From an analysis of the graphs, it can be seen that all systems showed a similar behavior when the initial concentration of metal ions was increased. It is possible to observe

Table 5: Parameters of diffusion mechanisms from Webber-Morri model and Boyd model in adsorption of Cu(II), Ni(II), Cd(II), and Pb(II) onto sodium clay (SC) and ferric clay (FC). Experimental conditions: acetate buffer pH = 5.5, T = 28°C. Initial concentration of ions = 100 mg $L^{-1}$.

| | Metal | Cu | | Ni | | Cd | | Pb | |
|---|---|---|---|---|---|---|---|---|---|
| | Clay | SC | FC | SC | FC | SC | FC | SC | FC |
| Webber-Morri | $K_1$ ($mg.g^{-1}.min^{-1}$) | 1.150 | 1.412 | 2.648 | 1.782 | 2.291 | 0.101 | 4.100 | 4.695 |
| | $C_1$ ($mg.g^{-1}$) | 25.73 | 17.53 | 12.28 | 10.50 | 8.676 | 17.98 | 18.774 | 19.83 |
| | $D_1$ ($cm^2.min^{-1}$) | 0.028 | 0.025 | 0.081 | 0.025 | 0.039 | $9.8x10^{-5}$ | 0.52 | 0.65 |
| | $R_1^2$ | 0.842 | 0.739 | 0.932 | 0.736 | 0.843 | 0.853 | 0.931 | 0.895 |
| | $K_2$ ($mg.g^{-1}.min^{-1}$) | 0.213 | 0.019 | 0.206 | 0.388 | 0.335 | — | 0.661 | 0.218 |
| | $C_2$ ($mg.g^{-1}$) | 26.79 | 21.23 | 19.24 | 14.33 | 13.9 | — | 28.68 | 21.02 |
| | D2 ($cm^2.min^{-1}$) | $9.8 \times 10-6$ | $4.5 \times 10-6$ | $4.9 \times 10-4$ | $1.2 \times 10-3$ | $8.4 \times 10-4$ | — | $1.3 \times 10-2$ | $1.4 \times 10-3$ |
| | $R_2^2$ | 0.764 | 0.978 | 0.967 | 0.926 | 0.974 | — | 0.789 | 0.822 |
| Boyd | B1 | 0.360 | 0.374 | 0.242 | 0.107 | 0.143 | 0.033 | 0.042 | 0.169 |
| | D1 ($cm^{-2}\,min^{-1}$) | $2.8 \times 10-6$ | $2.9 \times 10-6$ | $1.9 \times 10-6$ | $8.5 \times 10-7$ | $1.1 \times 10-6$ | $2.6 \times 10-7$ | $3.3 \times 10-7$ | $1.3 \times 10-6$ |
| | $R_1^2$ | 0.974 | 0.974 | 0.988 | 0.884 | 0.911 | 0.934 | 0.986 | 0.987 |
| | B2 | 0.018 | 0.023 | 0.051 | 0.024 | 0.031 | — | 0.026 | 0.005 |
| | D2 ($cm^{-2}\,min^{-1}$) | $1.4 \times 10-7$ | $1.8 \times 10-7$ | $4.0 \times 10-7$ | $1.9 \times 10-7$ | $2.5 \times 10-7$ | — | $2.1 \times 10-7$ | $4.5 \times 10-8$ |
| | $R_2^2$ | 0.758 | 0.976 | 0.924 | 0.932 | 0.958 | — | 0.583 | 0.629 |

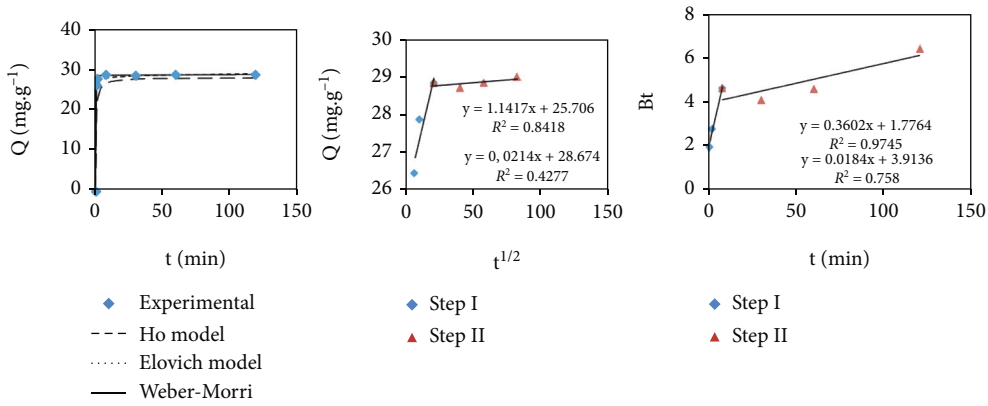


Figure 5: Experimental curves and the Ho, Elovich, and Webber-Morri models of the kinetic study of Cu(II) ion adsorption in sodium clay.

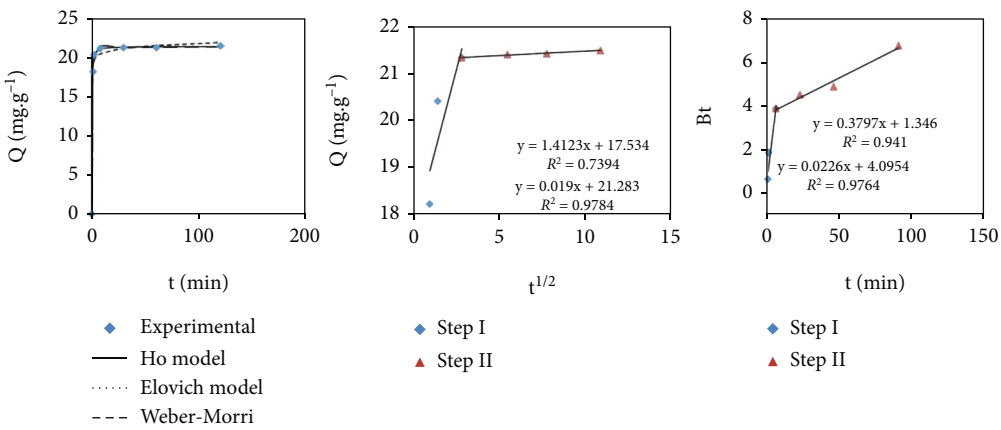


Figure 6: Experimental curves and the models of Ho, Elovich, and Webber-Morri models of the kinetic study of adsorption of the Cu(II) ion in ferric clay.

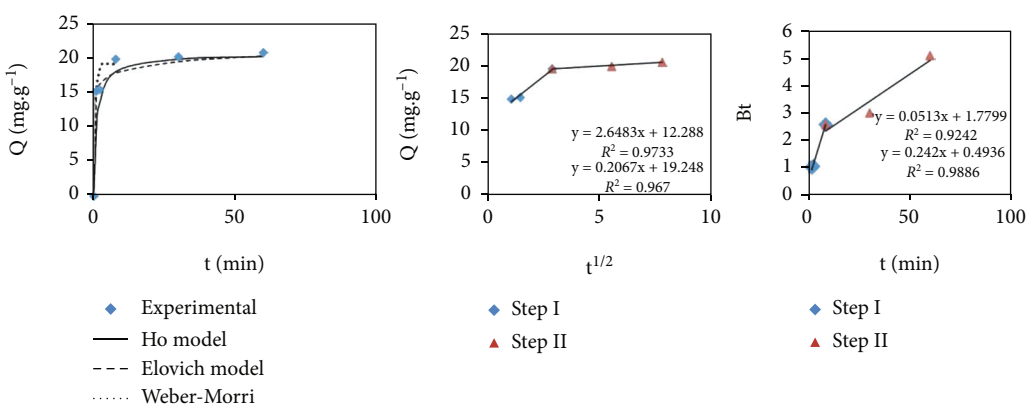


Figure 7: Experimental curves and the Ho, Elovich, and Webber-Morri models of the kinetic study of Ni(II) ion adsorption on sodic clay.

that the removal capabilities diminish when working with higher concentrations. This result is consistent, since the removal percentages are calculated from the remaining concentrations of metal ions in the solution by initial concentrations. All clays have a maximum capacity of saturation of their adsorption sites. At higher concentrations, saturation occurs after the adsorption capacity, and a greater number of ions remain in the solution than remain when working at lower concentrations. The percentage of ions that are removed is calculated from the amount that was not retained (Cf) of the initial amount (C), and at higher concentrations, these values decrease because the values (Ci) greatly increase, whereas the values of (Cf) do not decrease proportionately.

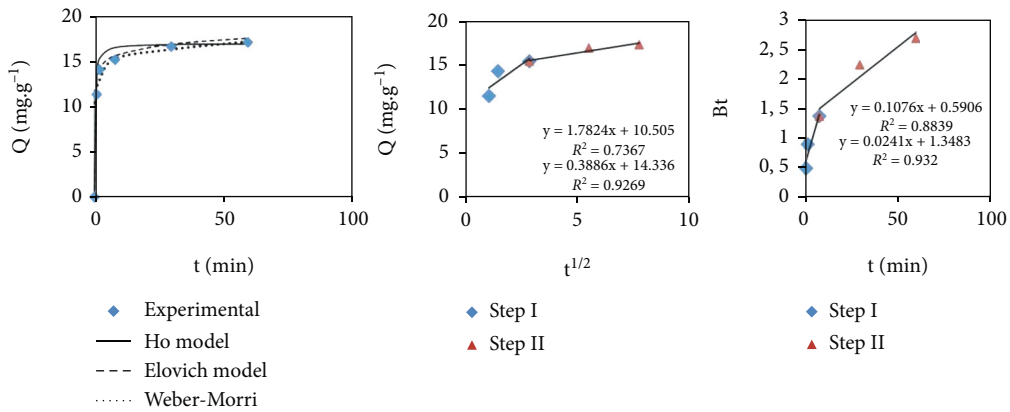


Figure 8: Experimental curves and the Ho, Elovich and Webber-Morri models of the kinetic study of Ni(II) ion adsorption in ferric clay.

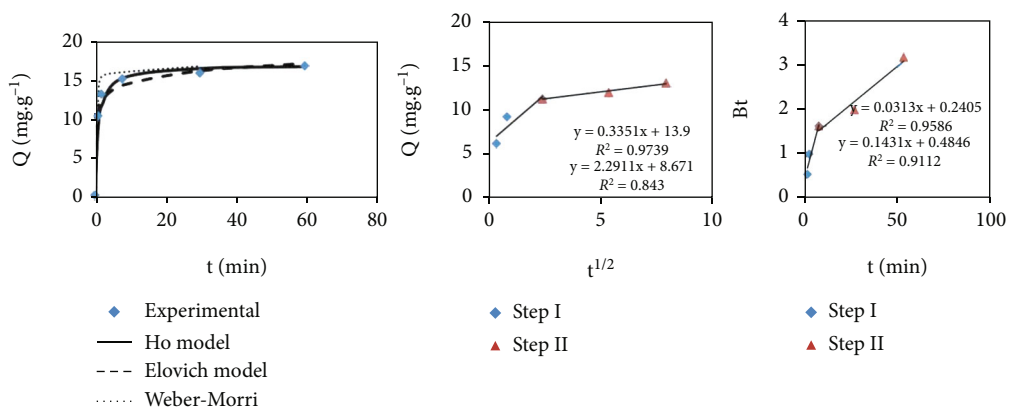


Figure 9: Experimental curves and the Ho, Elovich, and Webber-Morri models of the kinetic study of the adsorption of the Cd(II) ion in sodic clay.

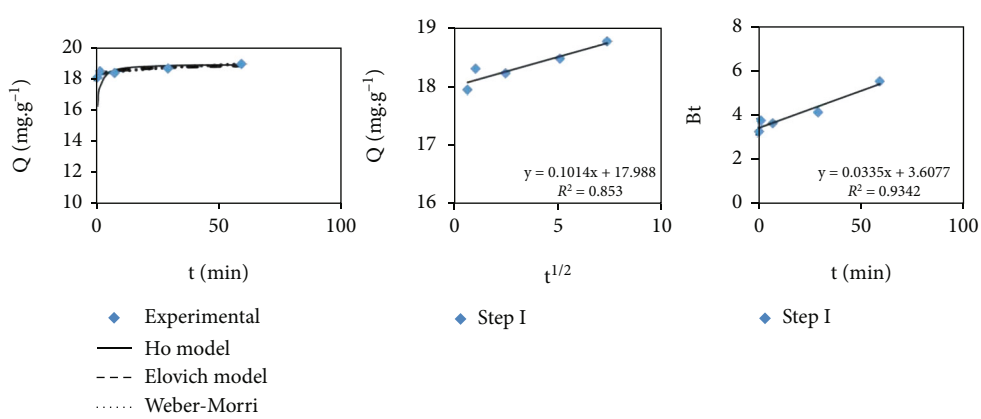


Figure 10: Experimental curves and the Ho, Elovich, and Webber-Morri models of the kinetic study of the adsorption of the Cd(II) ion in ferric clay.

In all cases, the hybrid systems promote greater removal capacity when compared to systems which use only electrodes. When using only the electrodes, the processes involved in the removal of metal ions occur from the formation of coagulants in situ agents, predominantly the electrocoagulation process [49]. Increased removal capability is noticeable when aluminum and carbon electrodes steel are utilized and then when compared to stainless steel electrode. However, when the same procedure is done with the addition of clay to the solution, there are two phenomena that

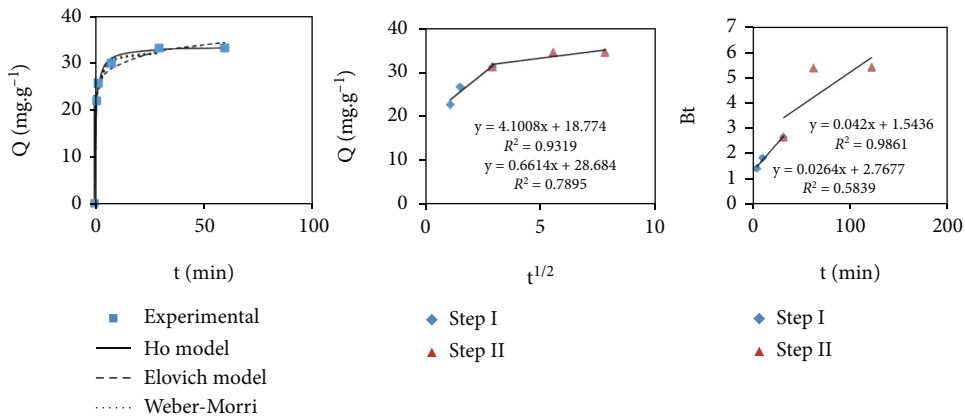


Figure 11: Experimental curves and the Ho, Elovich, and Webber-Morri models of the kinetic study of Pb(II) ion adsorption in sodic clay.

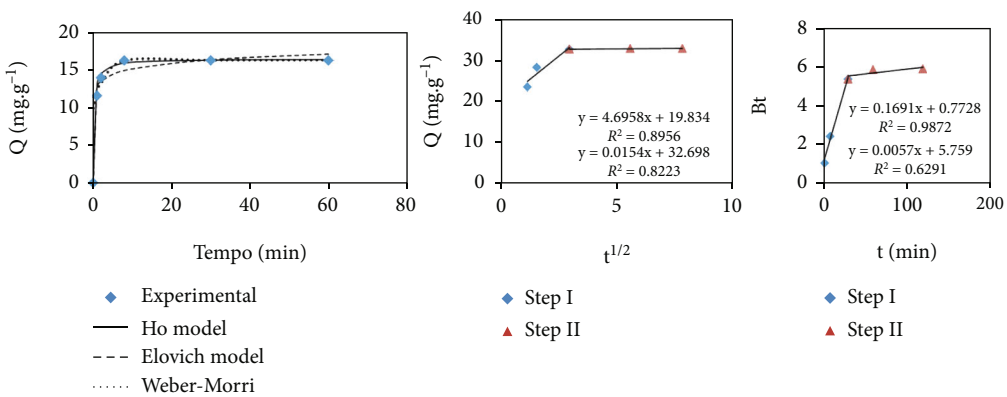


Figure 12: Experimental curves and the Ho, Elovich, and Webber-Morri models of the kinetic study of Pb(II) ion adsorption in ferric clay.

Table 6: Numerical results of tests to assess removal percentages of Cu(II), Ni(II), Cd(II), and Pb(II) from combinations clay x electrode.

| | Clay | Removal percentage | | | |
|---|---|---|---|---|---|
| | | Cu | Ni | Cd | Pb |
| Aluminum electrode | SC | 46.88 ± 3.2 | 32.95 ± 2.9 | 16.14 ± 1.2 | 32.54 ± 1.5 |
| | FC | 50.11 ± 3.4 | 36.71 ± 2.6 | 21.59 ± 2.2 | 23.43 ± 1.3 |
| Iron electrode | SC | 32.32 ± 1.4 | 31.61 ± 1.0 | 10.32 ± 1.6 | 29.82 ± 1.3 |
| | FC | 33.43 ± 2.3 | 30.43 ± 1.6 | 15.94 ± 2.2 | 29.82 ± 1.1 |
| Stainless steel electrode | SC | 16.50 ± 0.4 | 17.56 ± 1.2 | 11.06 ± 1.1 | 26.78 ± 1.5 |
| | FC | 20.81 ± 0.4 | 15.26 ± 1.7 | 10.23 ± 1.3 | 23.43 ± 2.4 |

help the separation of ions from solution. There are phenomena of electroflotation-coagulation of metal ions and simultaneously the adsorption of ions in the structure of clay minerals.

Other studies have obtained similar results when used only electroflotation-coagulation processes in the removal of other ions. Aji et al. [50] studied the removal of Cu(II), Mn(II), Zn(II), and Ni(II) using an iron electrode and showed a decrease in ability removal of these ions such as increased concentration. Adhoum and Monser [51] evaluated the use of electrocoagulation for the removal of Cu(II), Zn(II), and Cr(II) using aluminum electrode and observed that higher initial concentrations of metal ions in solution will be residual remaining in the solution after a certain time of operation. Golder et al. [52] removed the ion Cr(III) by electrocoagulation with a stainless-steel electrode and showed that the percentage removal of this ion falls from 60.0 to 47.2% when the concentrations of Cr(III) is increased

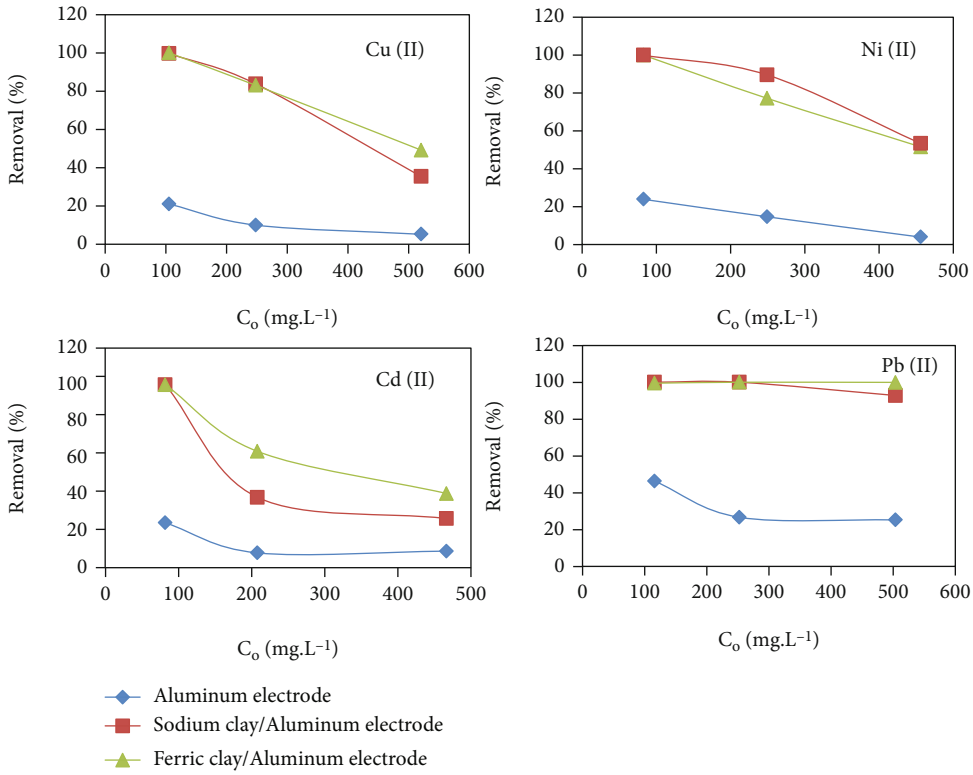


Figure 13: Percentage of removal of Cu(II), Ni(II), Cd(II), and Pb(II) ions in different systems using aluminum electrode. pH = 5.5, T = 28°C.

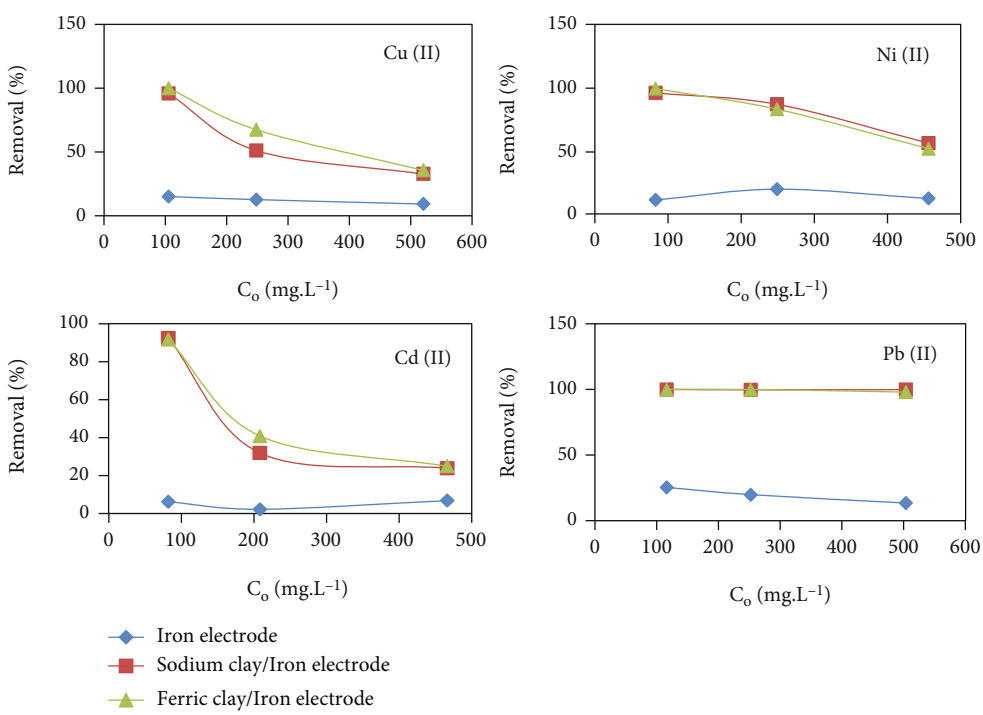


Figure 14: Percentage of removal of Cu(II), Ni(II), Cd(II), and Pb(II) ions in different systems using Iron electrode. pH = 5.5 , T = 28°C.

from 1700 to 3000 mg L$^{-1}$. Merzouk et al. [53] studied the removal of Cd(II), Fe(II), Ni(II), and Zn(II) using aluminum electrode and also showed a decrease in the removal capacity with increasing the initial concentrations of ions in solution.

## 4. Conclusion

The clays showed the fast adsorption kinetics and their good adsorption capacity. The analysis of the isotherms showed

that the experimental data were best described by the Langmuir model.

Hybrid system adsorption and electroflotation-coagulation presented itself as a good alternative association by using clay as adsorbents. This system showed that the main advantage is the possibility of working continuously with industrial wastewater purification processes, since the electrocoagulation process is more effective and produces a rapid separation of the clay from the aqueous solution. Moreover, the junction of electrocoagulation-coagulation processes to the processes of the adsorptive clays by increasing the amounts of the metal ion removal percentages.

Aluminum and iron electrodes were the ones which promoted a better removal rate when compared to stainless steel electrode. This was verified by the fact that these two types of electrodes release into the medium a greater amount of the coagulating agents than is released by the stainless steel electrode in a same time interval.

The operating times, for the removal of metal ions using the hybrid system, were very short. All maximum adsorption capacities were hit before the first ten minutes. The removal percentages varied according to the initial concentration of metal ions. The ion removal percentages for Pb(II), with iron electrode for sodium clays and ferric, were between 97 and 100%.

For the application of this technology in the industrial sector, some adjustments must be made with the operating conditions. In addition, the tailings produced after the removal of metal ions should be tested for other industrial purposes, for example, in catalysis studies and as fillers in the manufacture of materials such as ceramics.

## Data Availability

The data used to support the findings of this study are available from the corresponding author upon request.

## Conflicts of Interest

The authors have no conflict of interest to disclose.

## Acknowledgments

This research was supported by the Basic Science Research Program through the National Research Foundation of Korea (NRF) funded by the Ministry of Education (NRF2020R1I1A2066868) and the National Research Foundation of Korea (NRF) grant funded by the Korean government (MSIT) (No. 2020R1A5A2019413). This work was financially supported by the Cearense Foundation for Support to Scientific and Technological Development e FUNCAP.

## References

[1] P. C. Nagajyoti, K. D. Lee, and T. V. M. Sreekanth, "Heavy metals, occurrence and toxicity for plants: a review," *Environmental Chemistry Letters*, vol. 8, no. 3, pp. 199–216, 2010.

[2] T. A. Kurniawan, G. Y. Chan, W. H. Lo, and S. Babel, "Physico–chemical treatment techniques for wastewater laden with heavy metals," *Chemical Engineering Journal*, vol. 118, no. 1-2, pp. 83–98, 2006.

[3] H. Särkkä, B. Amit, and S. Mika, "Recent developments of electro-oxidation in water treatment—a review," *Journal of Electroanalytical Chemistry*, vol. 754, pp. 46–56, 2015.

[4] H. Chenik, M. Elhafdi, A. Dassaa, A. H. Essadki, and M. Azzi, "Removal of real textile dyes by electrocoagulation/electroflotation in a pilot external-loop airlift reactor," *Journal of Water Resource and Protection*, vol. 5, no. 10, pp. 1000–1006, 2013.

[5] V. K. Gupta, A. Nayak, and S. Agarwal, "Bioadsorbents for remediation of heavy metals: current status and their future prospects," *Environmental Engineering Research*, vol. 20, no. 1, pp. 1–018, 2015.

[6] T. A. Saleh and V. K. Gupta, "Processing methods, characteristics and adsorption behavior of tire derived carbons: a review," *Advances in Colloid and Interface Science*, vol. 211, pp. 93–101, 2014.

[7] M. Addy, B. Losey, R. Mohseni, E. Zlotnikov, and A. Vasiliev, "Adsorption of heavy metal ions on mesoporous silica-modified montmorillonite containing a grafted chelate ligand," *Applied Clay Science*, vol. 59-60, pp. 115–120, 2012.

[8] S. Lukman, M. H. Essa, N. Mu'azu, A. Bukhari, and C. Basheer, "Adsorption and desorption of heavy metals onto natural clay material: influence of initial pH," *Environmental Science & Technology*, vol. 6, no. 1, pp. 1–15, 2012.

[9] D. Ozdes, C. Duran, and H. B. Senturk, "Adsorptive removal of Cd (II) and Pb (II) ions from aqueous solutions by using Turkish illitic clay," *Journal of Environmental Management*, vol. 92, no. 12, pp. 3082–3090, 2011.

[10] E. Padilla-Ortega, R. Leyva-Ramos, and J. V. Flores-Cano, "Binary adsorption of heavy metals from aqueous solution onto natural clays," *Chemical Engineering Journal*, vol. 225, pp. 535–546, 2013.

[11] V. Hernández-Montoya, M. A. Pérez-Cruz, D. I. Mendoza-Castillo, M. R. Moreno-Virgen, and A. Bonilla-Petriciolet, "Competitive adsorption of dyes and heavy metals on zeolitic structures," *Journal of Environmental Management*, vol. 116, pp. 213–221, 2013.

[12] H. Merrikhpour and M. Jalali, "Comparative and competitive adsorption of cadmium, copper, nickel, and lead ions by Iranian natural zeolite," *Clean Technologies and Environmental Policy*, vol. 15, no. 2, pp. 303–316, 2013.

[13] D. Q. Melo, C. B. Vidal, T. C. Medeiros et al., "Biosorption of metal ions using a low cost modified adsorbent (*Mauritia Flexuosa*): experimental design and mathematical modeling," *Environmental Technology*, vol. 37, no. 17, pp. 2157–2171, 2016.

[14] A. G. Oliveira, J. Ribeiro, D. Q. Melo et al., "Evaluation of two biosorbents in the removal of metal ions in aqueous using a pilot scale fixed-bed system. Orbital: electron," *Chem*, vol. 6, pp. 47–55, 2014.

[15] T. Depci, A. R. Kul, and Y. Önal, "Competitive adsorption of lead and zinc from aqueous solution on activated carbon prepared from Van apple pulp: study in single-and multi-solute systems," *Chemical Engineering Journal*, vol. 200-202, pp. 224–236, 2012.

[16] S. F. Lo, S. Y. Wang, M. J. Tsai, and L. D. Lin, "Adsorption capacity and removal efficiency of heavy metal ions by Moso and Ma bamboo activated carbons," *Chemical Engineering Research and Design*, vol. 90, no. 9, pp. 1397–1406, 2012.

[17] M. A. Barakat, "New trends in removing heavy metals from industrial wastewater," *Chem*, vol. 4, no. 4, pp. 361–377, 2011.

[18] V. V. Keerthi and N. Balasubramanian, "Removal of heavy metals by hybrid electrocoagulation and microfiltration processes," *Environmental Technology*, vol. 34, no. 20, pp. 2897–2902, 2013.

[19] F. Han, G. H. Zhang, and P. Gu, "Removal of cesium from simulated liquid waste with countercurrent two-stage adsorption followed by microfiltration," *Journal of Hazardous Materials*, vol. 225-226, pp. 107–113, 2012.

[20] J. Charles, C. Bradu, N. Morin-Crini et al., "Pollutant removal from industrial discharge water using individual and combined effects of adsorption and ion-exchange processes: chemical abatement," *Journal of Saudi Chemical Society*, vol. 20, no. 2, pp. 185–194, 2016.

[21] P. Myllymäki, R. Lahti, H. Romar, and U. Lassi, "Removal of total organic carbon from peat solution by hybrid method—electrocoagulation combined with adsorption," *Journal of water process engineering*, vol. 24, pp. 56–62, 2018.

[22] S. Ayub, A. A. Siddique, M. S. Khursheed et al., "Removal of heavy metals (Cr, Cu, and Zn) from electroplating wastewater by electrocoagulation and adsorption processes," *Water Treat*, vol. 179, no. 1, pp. 263–271, 2020.

[23] E. M. Nigri, A. L. A. Santos, and S. D. F. Rocha, "Removal of organic compounds, calcium and strontium from petroleum industry effluent by simultaneous electrocoagulation and adsorption," *Journal of Water Process Engineering*, vol. 37, article 101442, 2020.

[24] P. Rengasamy and G. J. Churchman, *Cation exchange capacity, exchangeable cations and sodicity*, CSIRO Publishing, 1999.

[25] A. N. Oo, C. B. Iwai, and P. Saenjan, "Soil properties and maize growth in saline and nonsaline soils using cassava-industrial waste compost and vermicompost with or without earthworms," *Land Degradation and Development*, vol. 26, no. 3, pp. 300–310, 2015.

[26] V. B. Bagdonavicius and M. S. Nikulin, "Chi-squared goodness-of-fit test for right censored data," *The International Journal of Applied Mathematics and Statistics*, vol. 24, 2011.

[27] R. R. Karri, J. N. Sahu, and N. S. Jayakumar, "Optimal isotherm parameters for phenol adsorption from aqueous solutions onto coconut shell based activated carbon: error analysis of linear and non-linear methods," *Journal of the Taiwan Institute of Chemical Engineers*, vol. 80, pp. 472–487, 2017.

[28] L. Alexandrova and L. Grigorov, "Precipitate and adsorbing colloid flotation of dissolved copper, lead and zinc ions," *International Journal of Mineral Processing.*, vol. 48, no. 1-2, pp. 111–125, 1996.

[29] O. Sahu, B. Mazumdar, and P. K. Chaudhari, "Treatment of wastewater by electrocoagulation: a review," *Environmental Science and Pollution Research*, vol. 21, no. 4, pp. 2397–2413, 2014.

[30] G. W. Brindley and M. Nakahira, "The kaolinite-mullite reaction series: I, a survey of outstanding problems," *Journal of the American Ceramic Society*, vol. 42, no. 7, pp. 311–314, 1959.

[31] G. A. Lager, J. D. Jorgensen, and F. J. Rotella, "Crystal structure and thermal expansion of $\alpha$-quartz $SiO_2$ at low temperatures," *Journal of Applied Physics*, vol. 53, no. 10, pp. 6751–6756, 1982.

[32] J. D. Hanawalt, H. W. Rinn, and L. K. Frevel, "Chemical analysis by X-Ray diffraction," *Industrial & Engineering Chemistry Analytical Edition*, vol. 10, no. 9, pp. 457–512, 1938.

[33] E. Teixeira-Neto and A. A. Teixeira-Neto, "Modificação química de argilas: desafios científicos e tecnológicos para obtenção de novos produtos com maior valor agregado," *Química Nova*, vol. 32, no. 3, pp. 809–817, 2009.

[34] H. E. Swanson, E. Tatge, and R. K. Fuyat, *Standard x-ray diffraction powder patterns*, U.S. Department of commerce, 1953.

[35] S. K. Sing, D. H. Everett, R. Haul et al., "Reporting physisorption data for gas/solid system," *Pure and Applied Chemistry*, vol. 57, pp. 603–619, 2008.

[36] J. Langmuir, "The adsorption of gases on planes of glassmica and platinium," *Journal of the American Chemical Society*, vol. 40, no. 9, pp. 1361–1403, 1918.

[37] H. M. F. Freundlich, "Über die adsorption in Lösungen," *The Journal of Physical Chemistry*, vol. 57U, no. 1, pp. 385–470, 1907.

[38] M. J. Temkin and V. Pyzhev, "Recent modifications to Langmuir isotherms," *Acta physicochimica*, vol. 12, pp. 217–222, 1940.

[39] H. E. Rybicka, W. Calman, and A. Breeger, "Heavy metals sorption/desorption on competing clay minerals; an experimental study," *Applied Clay Science*, vol. 9, no. 5, pp. 369–381, 1995.

[40] J. H. Potgieter, S. S. Potgieter-Vermaak, and P. D. Kalibantonga, "Heavy metals removal from solution by palygorskite clay," *Minerals Engineering*, vol. 19, no. 5, pp. 463–470, 2006.

[41] Y. S. E. Ho and G. Mckay, "Sorption of dye from aqueous solution by peat," *Chemical Engineering Journal*, vol. 70, no. 2, pp. 115–124, 1998.

[42] S. Z. Roginsky and J. Zeldovich, "An equation for the kinetics of activated adsorption," *Acta Physicochimica*, vol. 1554, pp. 554–559, 1934.

[43] D. Q. Melo, C. B. Vidal, A. L. Silva et al., "Removal do $Cd^{+2}$, $Cu^{+2}$, $Ni^{+2}$ and $Pb^{+2}$ ions from aqueous solutions using Tururi fibers as an adsorbent," *Journal of Applied Polymer Science*, vol. 131, no. 20, 2014.

[44] H. Chen and A. Wang, "Kinetic and isothermal studies of lead ion adsorption onto palygorskite clay," *Journal of Colloid and Interface Science*, vol. 307, no. 2, pp. 309–316, 2007.

[45] W. J. Weber Jr. and J. C. Morris, "Kinetics of adsorption on carbon from solution," *Proceedings of the American Society of Civil Engineers*, vol. 89, no. 2, pp. 31–59, 1963.

[46] G. E. Boyd, J. Schubert, and A. W. Adamson, "The exchange adsorption of ions from aqueous solutions by organic zeolites, I: Ion exchange equilibria," *Journal of the American Chemical Society*, vol. 69, no. 11, pp. 2818–2829, 1947.

[47] F. Salles, J. M. Douillard, O. Bildstein et al., "Diffusion of interlayer cations in swelling clays as a function of water content: case of montmorillonites saturated with alkali cations," *The Journal of Physical Chemistry*, vol. 119, no. 19, pp. 10370–10378, 2015.

[48] E. D. Glendening and D. Feller, "Cation-water interactions: the $M^{+}(H_2O)_n$ clusters for alkali metals, M= Li, Na, K, Rb, and Cs," *The Journal of Physical Chemistry*, vol. 99, no. 10, pp. 3060–3067, 1995.

[49] M. Mollah and A. Yousuf, "Electrocoagulation (EC)- science and applications," *Journal of Hazardous Materials*, vol. 84, no. 1, pp. 29–41, 2001.

[50] A. B. Aji, Y. Yavuz, and A. S. Koparal, "Electrocoagulation of heavy metals containing model wastewater using monopolar iron electrodes," *Separation and Purification Technology*, vol. 86, pp. 248–254, 2012.

[51] N. Adhoum and L. Monser, "Decolourization and removal of phenolic compounds from olive mill wastewater by electrocoagulation," *Chemical Engineering and Processing*, vol. 43, no. 10, pp. 1281–1287, 2004.

[52] A. K. Golder, A. N. Samanta, and S. Ray, "Removal of trivalent chromium by electrocoagulation," *Separation and Purification Technology*, vol. 53, no. 1, pp. 33–41, 2007.

[53] B. Merzouk, B. Gourich, A. Sekki, K. Madani, and M. Chibane, "Removal turbidity and separation of heavy metals using electrocoagulation–electroflotation technique: a case study," *Journal of Hazardous Materials*, vol. 164, no. 1, pp. 215–222, 2009.

Hindawi
Adsorption Science & Technology
Volume 2022, Article ID 4148765, 15 pages
https://doi.org/10.1155/2022/4148765

*Research Article*

# Combined Effect of Zinc Oxide Nanoparticles and Bacteria on Osmolytes and Antioxidative Parameters of Rice (*Oryza sativa* L.) Plant Grown in Heavy Metal-Contaminated Water

**Nazneen Akhtar,[1] Sehresh Khan,[1] Shafiq Ur Rehman,[2] Eui Shik Rha,[3] and Muhammad Jamil[1]**

[1]*Department of Biotechnology and Genetic Engineering, Kohat University of Science & Technology (KUST), Kohat 26000, Pakistan*
[2]*Department of Biology, University of Haripur, Haripur, Pakistan*
[3]*Department of Well-Being Resources, Sunchon National University, Suncheon 540-742, Republic of Korea*

Correspondence should be addressed to Eui Shik Rha; euishik@scnu.ac.kr and Muhammad Jamil; dr.jamil@kust.edu.pk

Received 12 April 2022; Revised 9 June 2022; Accepted 18 June 2022; Published 29 June 2022

Academic Editor: Hesham Hamad



With the advancement in nanotechnology, the use of nanoparticles has been enhanced dramatically in biomedical, agriculture, and industrial processes. However, the combined effect of nanoparticles and bacteria on plant growth in heavy metal (Cd, Cr, Cu, and Pb)-contaminated wastewater is greatly limited. Therefore, the recent work was designed to determine the synergistic impact of green synthesized zinc oxide nanoparticles (ZnO-NPs) (5-10 mg/L) and *Bacillus* spp. (*Bacillus cereus* and *Lysinibacillus macroides)* on the physiological and biochemical activities of rice seedlings under heavy metal- (HM-) contaminated water. The results revealed that germination percentage (36%), root-shoot length (5.11 and 3.41 cm), fresh shoot-root weight (0.05 and 0.011 g), dry shoot-root weight (0.008 and 0.009 g), Chl a, Chl b, and carotenoid (5.4, 3.2 mg/g, and 4.3 $\mu$g/g), total soluble sugar (TSS) (26.44 mg/g), and total soluble protein (TSP) (21.99 mg/g) content considerably reduced in the plant tissues while combined impact of bacteria and ZnO NPs alleviates HM stress in contaminated water and improved seed germination (70%), root-shoot length (9.93 and 11.82 cm), fresh shoot-root weight (0.125 and 0.131 g), dry shoot-root weight (0.0532 and 0.042 g), Chl a, Chl b, and carotenoid (18.8, 13.9 mg/g, and 17.1 $\mu$g/g), TSS (57.651 mg/g), and TSP (47.990 mg/g) content. Lipid peroxidation induced by HM stress increased the amount of thiobarbituric acid reactive substances (TBRAS) (17.321 nM/mg) and hydrogen peroxide ($H_2O_2$) content (14.5 $\mu$M/g), stress markers such as glycine betaine (GB) (40.731 mg/g) and proline (Pro) (38.812 $\mu$mol/g) and antioxidant enzymes (SOD, POD, CAT, and APX) (180.87 U/mg, 450.677, 0.1066, and 0.631 $\mu$m/min/mg) under HM stress while the combined effect of ZnO NPs and bacteria reduced TBRAS (5.431 nM/mg), $H_2O_2$ content (2.25 $\mu$M/g), stress markers such as GB (24.731 mg/g) and Pro (18.811 $\mu$mol/g), and SOD, POD, CAT, and APX (187.53, 194.88, 0.061, and 0.271 $\mu$m/min/mg) contents. The present study suggested a potential role of combined impact of nanoparticles and bacteria in remediation of heavy metals from wastewater by improving plant growth.

## 1. Introduction

Seedling growth has an important role in plant development. Metabolic and antioxidative changes during growth are strongly related to the survival of seedlings which consequently affect plant yield and quality [1]. Abiotic stresses potentially affect growth through many factors including a reduction in water availability, imbalance in growth hormones, and effect on the metabolic and antioxidative activity [2]. Hydrogen peroxide accumulation and associated oxidative damages cause a decrease in antioxidant mechanisms that may suppress plant growth [3]. Bacteria-mediated seed priming is aimed at controlling seed hydration by way of decreasing outside water potential or shortening the hydration period at some stage in pressure. Several species of microorganism which include *Bacillus* spp. were said to solubilize the zinc ions in the course

of the growth by way of forming the complex with protons [4] and satisfy the requirement of nutrients by means of the use of zinc ions as a cofactor in their metabolic mechanism [5].

Bacteria can also increase the growth by utilizing minerals consisting of iron, phosphate, and nitrogen and prevent the plant from disease [6]. Conventional fertilizers were used to fulfil the demand of a rapidly growing population, but many fertilizers stay unavailable due to leaching, degradation by photolysis, hydrolysis, and decomposition [7]. Therefore, it is necessary to lower the nutrient losses in fertilization and improve plant growth [8]. Zinc oxide nanoparticles are used as nonfertilizers that act as important adsorbents for remediation, due to the fact that they carry various functional hydroxyl groups and protons on their surfaces [9]. ZnO nanoparticles (ZnO NPs) alter synthesis of many hormone, chlorophyll, and carbohydrate metabolism in the course of plant growth [10]. It has been shown that zinc can work as micronutrient and cofactor for metabolic processes, activating enzymes and organic solutes such as osmolytes or compatible solutes, amides, or betaine and amino acids [11]. Furthermore, zinc protects the plant cellular organelles from reactive oxygen species (ROS) and acts as a defense agent [4]; Various studies have shown that HMs can cause metabolic and antioxidative changes during plant growth [5]. Biopriming of seeds (seed priming with bacterial inoculation) grown in zinc oxide nanoparticle solution is an emerging, simple, and easily adaptable strategy to mitigate stress and improve the germination of seeds. Bacterial priming enhances the seed growth by improving gibberellin hormones that increase the amylase enzymes for development [12, 13].

Biopriming of seeds is not enough to increase the seed growth in toxic surroundings.It has been observed that solubilized form of HMs in water which cannot be removed by microorganism, so heavy metals easily bind with adsorbents of higher efficacy to bind with metals and increased the seed growth. Bio-nanotechnology has developed a relation between microorganism and nanoparticles, so nanoparticle at lower concentration improved the resistance level of microorganism against the toxic metals at low cost and high efficiency. Bacterial priming gave the protective coat around the seeds to prevent the entry by (1) producing auxin (IAA) hormones and activating cell division, (2) stabilizing the biomembrane integrity, (3) phospholipid formation, (4) increasing the protein synthesis, (5) remediating the oxidative stress, (6) transformation of nutrients towards new cells, and (7) lowering the uptake [4]. Furthermore, ZnO NPs at lower concentrations are more stable so dissolute into $Zn^{+2}$ ions, which might be solubilized by bacterial cells by using secreting certain metabolites and organic acid in media [9]. These zinc ions also played a significant role in plant growth by stabilizing the membrane, macromolecules, extraordinary steroid receptors, and carbohydrate metabolism [10], further remediating the toxic effect of HMs from water. It was also reported [12, 13] that hormones such as auxin and IAA which synthesized nanoparticles also enhanced the growth of roots against stress as compared with plants grown in control. The hormone-stabilized nanoparticle has accumulated in the treated area and slowly gets oxidized to release rooting hormone and ion, which facilitates prolonged root promoting activity and protects root inhibition activity from soil inoculated phytopathogens. Individual effect of nanoparticles and bacteria under heavy metals has been studied extensively, but no data is available about the synergistic effect of ZnO NP- and bacteria-primed seeds on the improvement of growth, metabolic, and antioxidative parameters of rice under contaminated water. Therefore, it was hypothesized that the synergistic treatments of bacteria and nanoparticles may significantly improve plant growth in the toxic environment and further enhance the metabolic and antioxidative mechanism of plant. The current study investigated the significance of combined treatments of bacteria and nanoparticles on plant growth by alleviating the toxicity on rice plant by enhancing their metabolic and antioxidative activity.

## 2. Material and Methods

Wastewater samples were collected from the Hayatabad industrial estate (HIE) present near the suburban town of Hayatabad Peshawar, Pakistan. The samples were collected in clean bottles, stored at 4°C until analyzed for the physicochemical properties. Physicochemical properties and heavy metal (Pb, Cd, Cr, and Cu) concentration of wastewater were analyzed to investigate the toxic metals and then compared it with the standard value of the National Environmental Quality Standards (NEQS, 2000) [14] (Table 1). NEQS is the uniform standard applicable to all kinds of industrial and municipal effluents. The stock solution of nanoparticles was stabilized at pH 10 to maintain their activity. Rice (*Oryza sativa* L. cv Super Basmati) seeds were obtained from Islamabad, Pakistan. Seeds were surface sterilized with 1% solution of sodium hypochlorite (NaOCl) and rinsed thoroughly with deionized distilled water.

ZnO nanoparticles were collected from Pir Mehr Ali Shah (PMAS) Arid Agriculture University, Pakistan. It was synthesized by coprecipitation method by Amara et al. [15]. ZnO nanoparticles were prepared by mixing 0.05 M zinc acetate Zn $(NO_3)$ $2.6H_2O$ (25 mL) solution with 4 mL of plant extract. Solution was heated and continuously stirred. The solution was centrifuged at 12,000 rpm for 15 min. Supernatant was discarded, and the isolated pellet was again suspended in deionized water. The solution was again centrifuged for 5 min and repeated the process three times to remove impurities. Synthesized ZnO NPs were white in color. The stock solution of nanoparticles was stabilized at pH 10 to maintain their activity. ZnO NPs were characterized by field emission scanning electron microscopy (FESEM), transmission electron microscopy (TEM), Fourier transform infrared spectroscopy (FTIR), and X-ray diffraction (XRD). ZnO NPs ranged from 30 to 50 nm in size [16].

*2.1. Biopriming of Seeds and Bacteria Growth.* Two heavy metal-resistant bacteria strains *Bacillus* strains (*B. cereus* (PMBL-3) and *L. macroides* (PMBL-7)) were previously isolated from Gadoon industrial estate's effluent [17] and were collected from the Plant and Microbial Biotechnology Lab, Kohat University of Science & Technology (KUST), Kohat, Pakistan. Strains were cultured for 24 hours at 37°C to

Table 1: Physicochemical parameters of water collected from Hayatabad industrial estate (HIE). The water was analyzed to evaluate the pollution load and heavy metal concentration.

| Physicochemical parameters | HIE wastewater standard | Standard (NEQS)* |
|---|---|---|
| Temperature | 24.5°C | 40.0°C |
| pH | 7.23 pH | 6-10 pH |
| EC | 682 ($\mu$S/m) | 500 ($\mu$S/m) |
| Odor | Bad | Bad |
| TSS | 400 mg/L | 150 mg/L |
| TDS | 4485 mg/L | 3500 mg/L |
| BOD | 250 mg/L | 80 mg/L |
| COD | 400 mg/L | 150 mg/L |
| Lead | 2.84 mg/L | 0.5 mg/L |
| Cadmium | 2.26 mg/L | 1.0 mg/L |
| Chromium | 2.40 mg/L | 1.0 mg/L |
| Iron | 1.19 mg/L | 0.2 mg/L |
| Manganese | 1.36 mg/L | 1.5 mg/L |
| Nickle | 1.83 mg/L | 1.0 mg/L |

*NEQS (National Environment Quality Standard) for industrial effluents.

increase cells up to $10^7$ to $10^9$ CFU/mL in cell suspension. After that, rice seeds were primed with *B. cereus* and *L. macroides* strains by adding 2% sucrose to bind seeds with bacteria and placed it for 10 hours in dark condition [18].

*2.2. Experimental Work.* Bacterial primed seeds were germinated in Petri plates supplemented with 5 and 10 mg/L of ZnO NP solution [18]. The young seedlings were exposed to sunlight after 5 days. Subsequently, after 10 days, young seedling were immediately transplanted in trays (3 L volume) containing one-fourth strength Hoagland solution [19]. Trays were covered with packing material to keep the root area dark [12, 13]. The experiment consisted of 9 treatments such as control (distilled water grown seedlings) seeds primed with *B. cereus* and *L. macroides* grown seedlings, seedlings grown in 5 and 10 mg/L ZnO NPs, and their combined treatments (*B.cereus*+5 mg/L ZnO NPs, *B.cereus* +10 mg/L ZnO NPs, *L.macroides*+5 mg/L ZnO NPs, and *L.macroides*+10 mg/L ZnO NPs). After 21 days, seedlings were then transferred from Hoagland solution to a new tray, which was filled with solutions containing 5 and 10 mg/L ZnO NPs along with HM-contaminated wastewater (w.w) of Hayatabad industrial estate (HIE). ZnO NPs at 5 and 10 mg/L have been used in several previous studies without showing any phytotoxic effect on plant seedlings [14, 15]. The hydroponic system was used to inhibit the adsorption of ZnO NPs to the soil surface and ensure that NPs and HMs are fully available [16]. Plants were grown in three replicates for each treatment and control. Plants were rotated and relocated to ensure equal light exposure during the exposure period. After the HM/ZnO NP exposure, the pH of the growth medium was measured with a pH meter. Seedlings were uprooted and analyzed for biochemical analysis. The synergistic data were subjected to one-way ANOVA by using statistic 9 software version (v.10) (Informer Technologies, Inc., United States).

### 2.3. Oxidative Damage to the Membrane

*2.3.1. Cell Injury.* Cell injuries in rice (root, shoot, and leaf) were examined by following the protocol of Hamim et al. [20]. Briefly, fresh plant materials were cut in 20 fine strips (1 cm each) and incubated at 25°C. After incubation, the first electrical conductance ($C_1$) was measured with an Electro Conductive (EC) meter (BMS EC-4001), and then, these mixtures were warmed for 40 min in a hot oven (121°C) to measure the electrical conductivity ($C_2$).

*2.3.2. Malondialdehyde (MDA).* Malondialdehyde (MDA) contents were determined by using the protocol of Velikova et al. [21]. Reaction mixture was made in 500 mL deionized water by adding trichloroacetic acid (TCA) (25 mg) and thiobarbituric acid (TBA) (2.5 mg). Enzyme extract (1.5 mL) was added in reaction substrate (2.5 ml) and incubated at 95°C for 15 min in water bath. Reaction was terminated on ice bath (35 min) and then vortexed for 10 minutes. Solution was centrifuged at 1300 rpm (15 min) until the clear solution formed. Record the absorbance at 532 nm while the (nonspecific) absorbance was measured at 600 nm. MDA-TBA value was calculated by coefficient 155 $nM^{-1}$ $cm^{-1}$.

*2.3.3. Hydrogen Peroxide ($H_2O_2$).* Hydrogen peroxide contents were determined by using the protocol of Nankano and Asada [22]. Make the substrate (3 mL) by adding PBS buffer (1 mL), potassium iodide (KI) (2 mL), and enzyme extract (1 mL). Hydrogen peroxide content was then determined by the absorbance at 390 nm.

*2.4. Photosynthetic Pigment.* Photosynthetic pigments were determined as discussed previously by Li et al. [23]. In a falcon tube, the equal amount of plant materials (25 mg) and magnesium oxide (25 mg) was taken. Methanol (5 mL) was added in the mixture and shake at 200 rpm for 2 hours for pigment extraction. The sample was centrifuged at 400 rpm for 5 min to extract the supernatant. After that, the supernatant (3 mL) was added in cuvette. The absorbance was recorded at 470, 653, and 666 nm by using a spectrophotometer (BMS, Biotechnology Medical Services).

### 2.5. Osmolyte Contents

*2.5.1. Proline (Pro) and Glycine Betaine (GB) Content.* The proline (Pro) content was measured by following the protocol of Bates et al. [24]. Sample (100 mg) was mixed by adding 3% solution of 5 mL sulfosalicylic acid and then centrifuged at 4000 rpm for 30 min. Afterwards, 1 mL mixture was mixed with 1 mL of acid ninhydrin followed by addition of 30 mL of glacial acetic acid along with 6 M phosphoric acid (20 mL) and heated at 100°C for 60 minutes. The two layers were separated by adding toluene (2 mL) in reaction mixture, and then, toluene was calculated at 520 nm in a spectrophotometer. Proline content was calculated by following formula:

$$\frac{((\mu\text{gproline/mL}) \times (2/115.5))}{(0.1/5)}. \quad (1)$$

Glycine betaine (GB) content was determined by using the methodology of Shtisarnit et al. [25]. Plant material (50 mg) was crushed and mixed with 4 mL of deionized water. Sample was mixed and then filtered by filter paper to isolate the extract. After filtration, extract (1 mL) was mixed with 2 N $H_2SO_4$ (1 mL) and kept the solution on ice for 1 hour. After that, potassium triiodide ($Kl_3$) was added and then cooled the solution with occasional shaking (2 hours). Centrifuge the mixture and two layers were separated. The upper phase contains crystals which were then dissolved in 1,2-dicholorethane. Glycine betaine (GB) content was estimated by measuring the absorbance at 365 nm by using the glycine betaine (GB) standard curve.

*2.5.2. Total Soluble Sugars (TSS) and Total Soluble Protein (TSP).* The phenol-sulfuric acid method was followed to find the total soluble sugars (TSS) [26]. Plant sample (50 mg) was digested in 3 mL prewarmed ethanol solution (90%) and then incubate the solution for 1 hour at 80°C. Extracted plant mixture (1 mL) was mixed with 1 mL of 5% phenol solution. Concentrated 5 mL of sulfuric acid was added in the mixture and then added 10 mL of distilled water, mixed vertically and heated for 30 min. Measure the absorbance at 485 nm by taking distilled water (DW) as blank. The glucose-soluble sugar standard curve was used to find the TSS in sample. Bradford assay was used to determine the total soluble protein [27]. Fresh plant material was grinded in liquid nitrogen and mixed with 10 mL of potassium phosphate buffer (PPB) (pH 7.8) solution. The mixture was centrifuged at 14,000 rpm for 20 minutes (4°C) to extract the protein. The reaction mixture was taken in a falcon tube by adding enzyme extract (20 $\mu$L), Bradford reagent (500 $\mu$L), and DW (2 mL). The mixture was shaken well and placed at 37°C. Absorbance was recorded at 595 nm by using DW as blank. Protein was estimated by known protein (bovine serum albumin) BSA curve [28].

*2.6. Extraction of Protein and Antioxidant Determination.* Antioxidative parameters were determined as previously described by Vasconcelos et al. [28]. Briefly, fresh plant material (500 g) was crushed in liquid nitrogen and mixed with 10 mL precooled phosphate buffer (50 Mm potassium phosphate buffer). The extract was centrifuged at 20,000 rpm for 20 min. Total protein content was estimated by Bradford assay using bovine serum albumin (BSA) as standard.

*2.6.1. Antioxidant Enzymes.* Super oxidase (SOD) enzymes were determined by using the protocol as described earlier [29]. In a reagent bottle (250 mL), substrate solution was prepared by adding NBT (nitro-blue-tetrazolium) (15.5 mg) along with 2 mg of riboflavin, Na-EDTA (100 mg), and methionine (485 mg). After that, reaction solution (3 mL) was prepared by adding 2.725 mL of substrate, 25 mL of hydrogen peroxide, and 0.025 mL of enzyme extract. Place the mixture at 4000 lux under light for 20 minutes and then observe at 560 nm. Peroxidase (POD) content was measured by using the protocol of Liu et al. [23]. Substrate (3 mL) was prepared by mixing enzyme extract (1 mL), guaiacol (1.5%) along with PBS (2.7 mL) and 4% of hydrogen peroxide (0.1 mL). After 2 min, record the absorbance at 470 nm. Catalase (CAT) content was determined by the methodology as described by Aebi [30]. Reaction mixture (3 mL) was formed by adding 25 mM of potassium phosphate buffer (2.8 mL), enzyme extract (100 $\mu$L), and 30 Mm of $H_2O_2$ (100 $\mu$L) and recorded the absorbance at 240 nm. APX content was determined by using the protocol of Sofo et al. [31]. Briefly, reaction mixture was made by adding 100 mM potassium phosphate buffer (PPB) (pH 7.0), sodium EDTA (ethylenediaminetetraacetic acid) (1 mM), ascorbic acid (3 mM), $H_2O_2$ (hydrogen peroxidase) (0.06 mm), and enzyme extract (100 $\mu$L) and recorded the absorbance at 290 nm.

*2.7. Statistical Analysis.* The data were subjected to one-way ANOVA by using statistic 9 software version (v.10) (Informer Technologies, Inc., United States). Difference between means was determined by the least significance difference (LSD) at $P \leq 0.05$.

## 3. Results

*3.1. Germination Percentage and Rate.* Results indicated that seeds grown in the Petri plate under stress showed significantly decreased percentage (36%) than distilled water (60%) (Figure 1(a)). Synergistic treatment of bioprimed seeds with *B. cereus* and *L. macroides* along with ZnO nanoparticle solution improved the germination percentage at 5 mg/L (90 and 86%) and 10 mg/L (76 and 70%) in distilled water and 5 mg/L (70 and 63%) and 10 mg/L (62 and 30%) in wastewater as compared with control distilled water and wastewater (60% and 36%), respectively. Synergistic effect of bioprimed seeds with *B. cereus* and *L. macroides* along with ZnO nanoparticles showed enhanced germination rate ($1/t_{50}$) at 5 mg/L (0.342 and 0.321) and 10 mg/L (0.29 and 0.28) in distilled water and 5 mg/L (0.275 and 0.273) and 10 mg/L (0.264 and 0.253) in wastewater as compared with control distilled water and wastewater (0.21 and 0.143), respectively (Figure 1(b)).

*3.2. Seedling Growth.* Combined impact of ZnO NPs along with seeds primed with *B. cereus* and *L. macroides* significantly increased the length of shoot (Supplementary Figure 1) at 5 (14.21 and 12.5 cm) and 10 mg/L (11.73 and 9.745 cm) in distilled water and 5 (11.82 and 9.75 cm) and 10 mg/L (9.485 and 6.375 cm) in wastewater as compared with control distilled water and wastewater (7.7 and 3.4 cm) grown plant, respectively (Figure 2). Results showed that root length was significantly increased (Supplementary Figure 1) in bioprimed seed treatments with *B. cereus* and *L. macroides* at 5 mg/L (12.57 and 12.45 cm) and 10 ppm (11.17 and 9.995 cm) in distilled water and 5 mg/L (9.93 and 9.45 cm) and 10 mg/L (8.27 and 8.59 cm) in wastewater as compared with control distilled water and wastewater (8.72 and 5.1 cm), respectively (Figure 2). Result showed that fresh shoot and root weight were significantly enhanced in *B.*

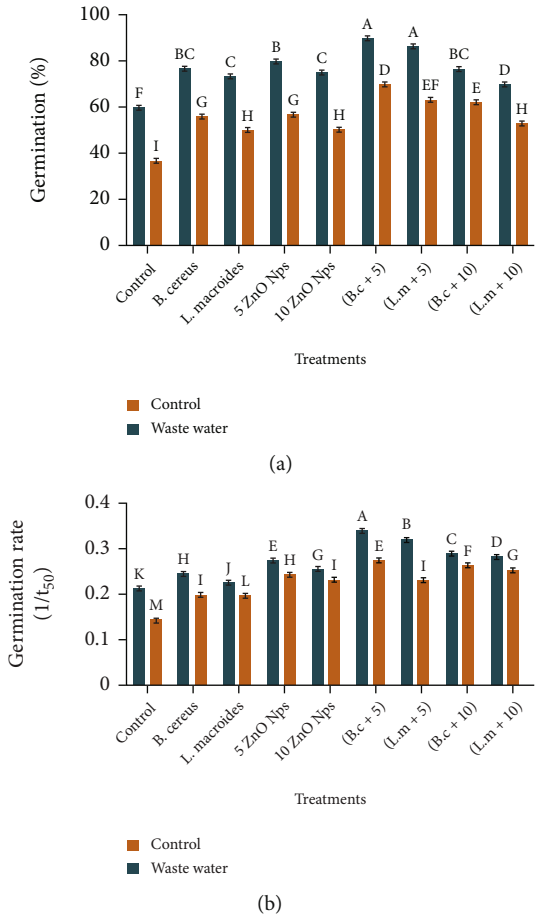


Figure 1: Synergistic effect of bacterial strains (*Bacillus cereus* and *Lysinibacillus macroides*) and ZnO NPs (5 and 10 mg/L) treatments on (a) germination % and (b) germination rate of rice grown in heavy metal-contaminated water. Error bars showed means of standard error (±SE) of three replicates ($n = 3$) followed by different alphabetic letters showing statistical significance at 5% probability level. Control (distilled water), B.C+5 (*Bacillus cereus* +5 mg/L ZnO NPs), L.M+5 (*Lysinibacillus macroides*+5 mg/L ZnO NPs), B.C+10 (*Bacillus cereus*+10 mg/L ZnO NPs), and L.M +10 (*Lysinibacillus macroides*+10 mg/L ZnO NPs).

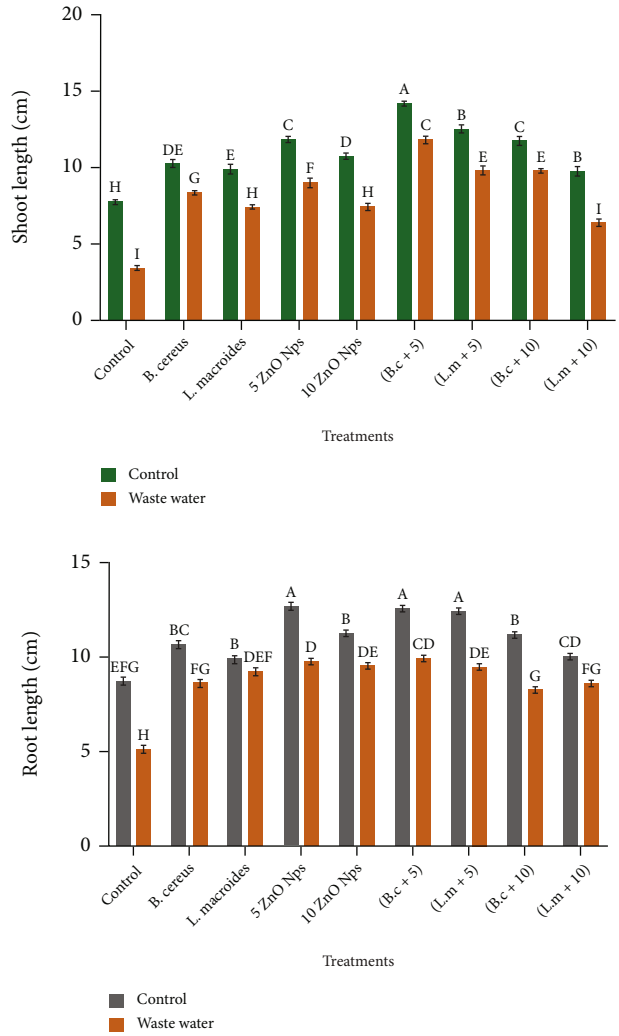


Figure 2: Synergistic effect of bacteria strain *Bacillus cereus* and *Lysinibacillus macroides* and ZnO NP (5 mg/L and 10 mg/L) treatments on shoot and root length of rice grown in heavy metal-contaminated water. Error bars showed means of standard error (±SE) of three replicates ($n = 3$) followed by different alphabetic letters showing statistical significance at 5% probability level. Control (distilled water), B.C+5 (*Bacillus cereus*+5 mg/L ZnO NPs), L.M+5 (*Lysinibacillus macroides*+5 mg/L ZnO NPs), B.C+10 (*Bacillus cereus*+10 mg/L ZnO NPs), and L.M+10 (*Lysinibacillus macroides*+10 mg/L ZnO NPs).

*cereus* and *L. macroides* primed seed treatments along with ZnO nanoparticles (Supplementary Figure 2) at 5 mg/L (0.147, 0.131, 0.031, and 0.028 g) and 10 mg/L (0.133, 0.115, 0.026, and 0.022 g) in distilled water and 5 mg/L (0.125, 0.131, 0.031, and 0.028 g) and 10 mg/L (0.106, 0.105, 0.026, and 0.022 g) in wastewater than control distilled water (0.065 and 0.0145 g) and wastewater (0.05 and 0.011 g), respectively (Figures 3 and 4). Results showed that dry shoot and root weight increased due to the synergistic effect of bioprimed seeds with *B. cereus* and *L. macroides* along with ZnO NP treatments at 5 mg/L (0.064, 0.0532, 0.0637, and 0.616 g) and 10 mg/L (0.0415, 0.035, 0.052, and 0.044 g) in distilled water and 5 (0.0532, 0.042, 0.051, and 0.047 g) and 10 mg/L (0.033, 0.031, 0.033, and 0.315 g) in wastewater than distilled water (0.024 and 0.042 g) and wastewater (0.012 and 0.014 g), respectively (Figures 4(c) and 4(d)).

### 3.3. Oxidative Damage to the Membrane

*3.3.1. Cellular Injury.* In addition to seedling growth, it was found that maximum cell injury (62.651) was measured in wastewater treatment, than control (distilled water)-treated plant (53.812 $\mu$S/cm). Surprisingly, the synergistic effect of bioprimed seeds with *B. cereus* and *L. macroides* along with 5 mg/L ZnO nanoparticle solution in wastewater showed lower cell injury (33.561 and 38.22 $\mu$S/cm) as compared with only bioprimed seeds (46.441 and 52.661) and 5 mg/L ZnO nanoparticles (54.702 $\mu$S/cm) (Figure 4).

*3.3.2. Malondialdehyde (MDA) and Hydrogen Peroxide ($H_2O_2$).* Current findings revealed that MDA content was

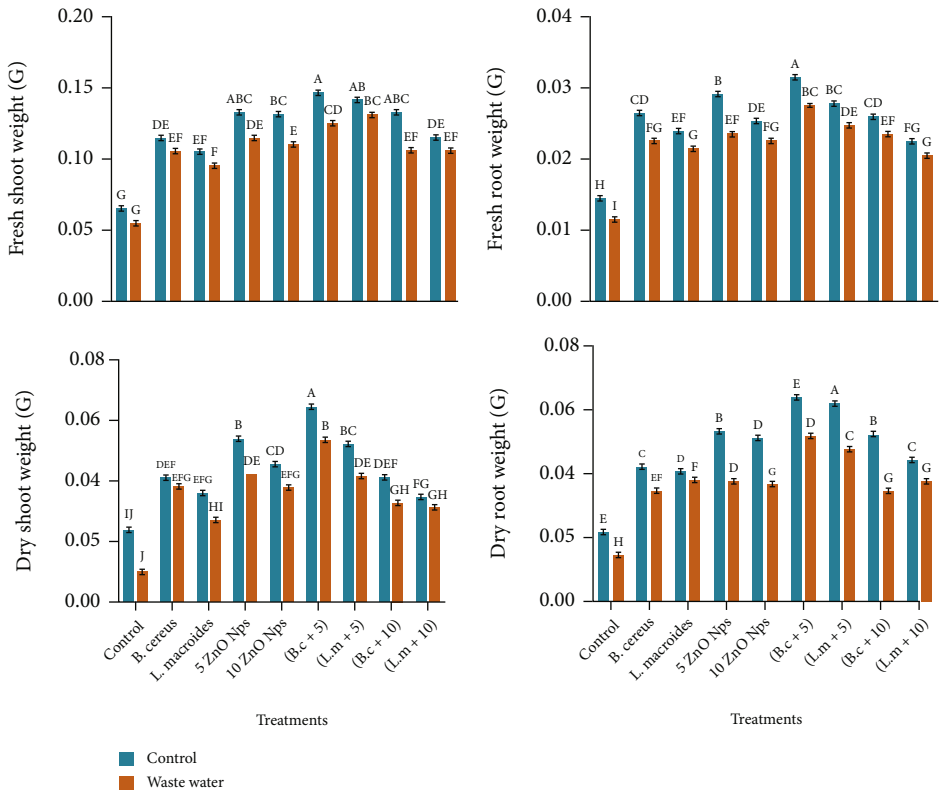


Figure 3: Synergistic effect of bacteria strains (*Bacillus cereus* and *Lysinibacillus macroides*) and ZnO NP (5 mg/L and 10 mg/L) treatments on (a) fresh shoot weight (FSW), (b) fresh root weight (FRW), (c) dry shoot weight (DSW), and (d) dry root weight of rice grown in heavy metal-contaminated water. Error bars showed means of standard error (±SE) of three replicates ($n = 3$) followed by different alphabetic letters showing statistical significance at 5% probability. Control (distilled water), B.C+5 (*Bacillus cereus*+5 mg/L ZnO NPs), L.M+5 (*Lysinibacillus macroides*+5 mg/L ZnO NPs), B.C+10 (*Bacillus cereus*+10 mg/L ZnO NPs), and L.M+10 (*Lysinibacillus macroides*+10 mg/L ZnO NPs).

enhanced in leaf, shoot, and root as compared to control (distilled water) (Figure 5(e)). Under stress, the MDA contents in leaf, shoot, and root were decreased in bioprimed seeds (4.096 and 5.368) and 5 mg/L ZnO nanoparticles (4.75 $\mu$m/g f.w). Significant decrease was observed in MDA content by synergistic effect of bioprimed seeds with *B. cereus* and *L. macroides* along with 5 mg/L ZnO nanoparticles under contaminated water in leaf, shoot, and root (2.241 and 2.71). $H_2O_2$ content was also increased in leaf, shoot, and root (6.34 $\mu$m/g f.w) than control (distilled water) (4.26 $\mu$m/g f.w) (Figure 5(f)). In addition, our results revealed that under stress, the MDA contents in leaf, shoot, and root were decreased in bioprimed seeds (3.41 and 4.54) and 5 mg/L ZnO nanoparticles (3.16 $\mu$m/g f.w). Maximum $H_2O_2$ content was observed in synergistic treatments of bioprimed seeds with *B. cereus* and *L. macroides* along with 5 mg/L ZnO nanoparticles under stress in leaf, shoot, and root (2.22 and 2.24 $\mu$m/g f.w).

*3.4. Photosynthetic Pigments.* Mean data revealed that chlorophylls (a, b, total pigments) and carotenoid contents were lowered in wastewater (5.4, 3.2, and 8.6) 4.3 $\mu$g/g than plant germinated in DW (12.4, 5.6, and 18.1 mg/g) 8.5 $\mu$g/g. Combined impact of *B. cereus* and *L. macroides* bioprimed seeds along with 5 mg/L ZnO NPs showed significant increase in photosynthetic pigments 21.2 (25.3, 16.3, and 41.6) and 17.2 (22.3, 14.3, and 36.7) as compared with alone bioprimed seeds 7.3 (9.3, 5.5, and 14.8) and 7.3 (8.1, 5.1, and 13.2) and 5 mg/L ZnO nanoparticles 14.3 $\mu$g/g (19.2, 11.2, and 30.2 mg/g) (Table 2).

### 3.5. Osmolyte Contents

*3.5.1. Proline and Glycine Betaine.* Higher contents of proline were observed in wastewater-treated leaf, shoot, and root (26.311 $\mu$mol/g) as compared with plant grown in control (distilled water) (12.881 $\mu$mol/g) (Figure 6(c)). In contaminated water, proline was decreased in *B. cereus* and *L. macroides* primed seeds (15.387 and 15.387) and 5 mg/L ZnO nanoparticles (11.890 $\mu$mol/g). Additionally, our results showed significant decrease in proline content in contaminated water when treated with *B. cereus* and *L. macroides* along with 5 mg/L ZnO nanoparticles in leaf, shoot, and root (4.315 and 6.735 $\mu$mol/g). The glycine betaine content was inecreased in plant tissues grown in wastewater while it was decreased in synergistic treatments of bacteria and ZnO nanoparticles (Figure 6(d)). GB content was enhanced in contaminated wastewater in leaf, shoot, and root (23.735 mg/g) than plant grown in control (distilled water) (10.041 mg/g). In

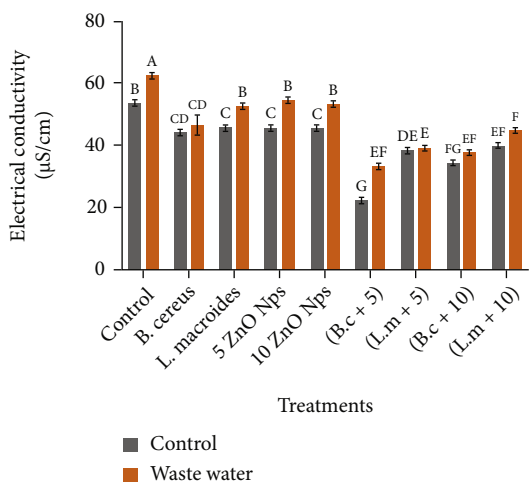


Figure 4: Synergistic effect of bacteria strains (*Bacillus cereus* and *Lysinibacillus macroides*) and ZnO NP (5 mg/L and 10 mg/L) treatments on cellular injury of rice grown in heavy metal-contaminated water. Error bars showed means of standard error (±SE) of three replicates ($n = 3$) followed by different alphabetic letters showing statistical significance at 5% probability level. Control (distilled water), B.C+5 (*Bacillus cereus*+5 mg/L ZnO NPs), L.M+5 (*Lysinibacillusmacroides*+5 mg/L ZnO NPs), B.C+10 (*Bacillus cereus*+10 mg/L ZnO NPs), and L.M+10 (*Lysinibacillusmacroides*+10 mg/L ZnO NPs).

contaminated water, glycine betaine was decreased in *B. cereus* and *L. macroides* primed seeds (14.725 and 13.618) and 5 mg/L ZnO nanoparticles (14.631 mg/g). Significant decrease in glycine betaine content was observed in synergistic treatments of *B. cereus* and *L. macroides* primed seeds along with 5 mg/L ZnO nanoparticles under treatments in leaf, shoot, and root (9.543 and 13.618 mg/g).

*3.5.2. Total Soluble Sugar (TSS) and Total Soluble Protein (TSP).* Total soluble sugar (TSS) content was significantly reduced (9.984 mg/g) in contaminated water as compared with plant grown in control (distilled water) (16.415 mg/g) (Figure 6(a)). In contaminated water, TSS was increased in *B. cereus* and *L. macroides* primed seed treatments (17.91 and 17.575 mg/g) and 5 mg/L ZnO nanoparticles (17.575 mg/g). Subsequent increase in TSS was determined in seeds treated with *B. cereus* and *L. macroides* along with 5 mg/L ZnO nanoparticles under contaminated water (32.311 and 31.251 mg/g). Similarly, TSP was significantly decreased (2.845 mg/g) in contaminated water as compared with (control) distilled water (2.845 mg/g), respectively (Figure 6(b)). In contaminated water, TSP was increased in combined treatment of *B. cereus* and *L. macroides* primed rice seeds (11.890 and 10.890) and 5 mg/L ZnO nanoparticles (10.890 mg/g). Maximum total soluble protein was determined in combined treatment of bioprimed seeds with *B. cereus* and *L. macroides* along with 5 mg/L ZnO nanoparticles under contaminated water (23.790 and 25.835 mg/g).

*3.6. Antioxidant Enzymes.* Synergistic effect of bioprimed seed and ZnO NPs on antioxidant enzymes was also tested. Data showed that superoxide dismutase (SOD) activity was increased in contaminated water (248.09 $\mu$g/g f.w) as compared with control (distilled water) (115.62 $\mu$g/g f.w) (Figure 5(a)). Similarly, our result revealed that under stress, the SOD content in leaf, shoot, and root was decreased in bioprimed seeds (63.73 and 158.05) and 5 mg/L ZnO nanoparticles (95.2 $\mu$g/g f.w). Maximum reduction in SOD content was observed in combined impact of bioprimed seeds with *B. cereus* and *L. macroides* along with 5 mg/L ZnO nanoparticles under stress (144.78 and 74.26 $\mu$g/g f.w). Result showed that POD content in leaf, shoot, and root was increased in contaminated water (197.23) as compared with control (distilled water) (126.32 $\mu$g/g f.w) (Figure 5(b)). Under stress, the POD content in leaf, shoot, and root was decreased in bioprimed seeds as compared with alone bioprimed seeds (100.21 and 112.5) and 5 mg/L ZnO nanoparticles (96.22 $\mu$g/g f.w). Significant reduction in POD content was observed in combined *B. cereus* and *L. macroides* along with 5 mg/L ZnO nanoparticles in contaminated water (62.07 and 68.03). Catalase activity (CAT) was increased in contaminated water (0.05 $\mu$g/g f.w) as compared with control (distilled water) (0.078 $\mu$g/g f.w), respectively (Figure 5(c)). It was observed that under stress, the CAT content in leaf, shoot, and root was decreased in bioprimed seeds (0.0431 $\mu$g/g f.w, 0.0431 $\mu$g/g f.w) and 5 mg/L ZnO nanoparticles (0.0404 $\mu$g/g f.w). Maximum reduction of CAT content was observed in bioprimed seeds with *B. cereus* and *L. macroides* along with 5 mg/L ZnO nanoparticles under stress in leaf, shoot, and root (0.0227 $\mu$g/g f.w, 0.0237 $\mu$g/g f.w). Ascorbate peroxidase (APX) activity in leaf, shoot, and root increased in plant grown in HMs (0.541) as compared with control (distilled water) (0.333 $\mu$g/g f.w) (Figure 5(d)). Additionally, we showed that under stress, the APX content in leaf, shoot, and root was decreased in bioprimed seeds (0.287 $\mu$g/g f.w, 0.172 $\mu$g/g f.w) and 5 mg/L ZnO nanoparticles (0.254 $\mu$g/g f.w). APX content was decreased in synergistic treatments of bioprimed seeds with *B. cereus* and *L. macroides* along with 5 mg/L ZnO nanoparticles in leaf, shoot, and root (0.152 $\mu$g/g f.w, 0.172 $\mu$g/g f.w) as compared in contaminated water.

## 4. Discussion

Plants are strongly influenced by metabolic and antioxidative mechanisms. Seed priming is an efficient strategy applied to improve plant growth and metabolic processes under stressful conditions. In the past, seed treatments with bacteria and application of NPs have been described as efficient strategies to improve plant growth under stress [32]. However, the synergistic treatments of ZnO NPs and *Bacillus* spp. on plant development have not been reported yet. Therefore, the present study was initiated to reveal the combined impact of ZnO NPs and bacteria on metabolic and antioxidative parameters of rice plant in heavy metal-contaminated water. *Bacillus* spp. release amino cyclopropane (1-carboxylic acid (ACC)) deaminase and bioactive metabolites (surfactant and lipopeptides) that covered the seed toxicity [33]. Furthermore, $Zn^{+2}$ ions are essential for bacterial enzymes (dehydrogenase, thiol peroxidase, and glutathione reductase) that enhanced the growth by uptake

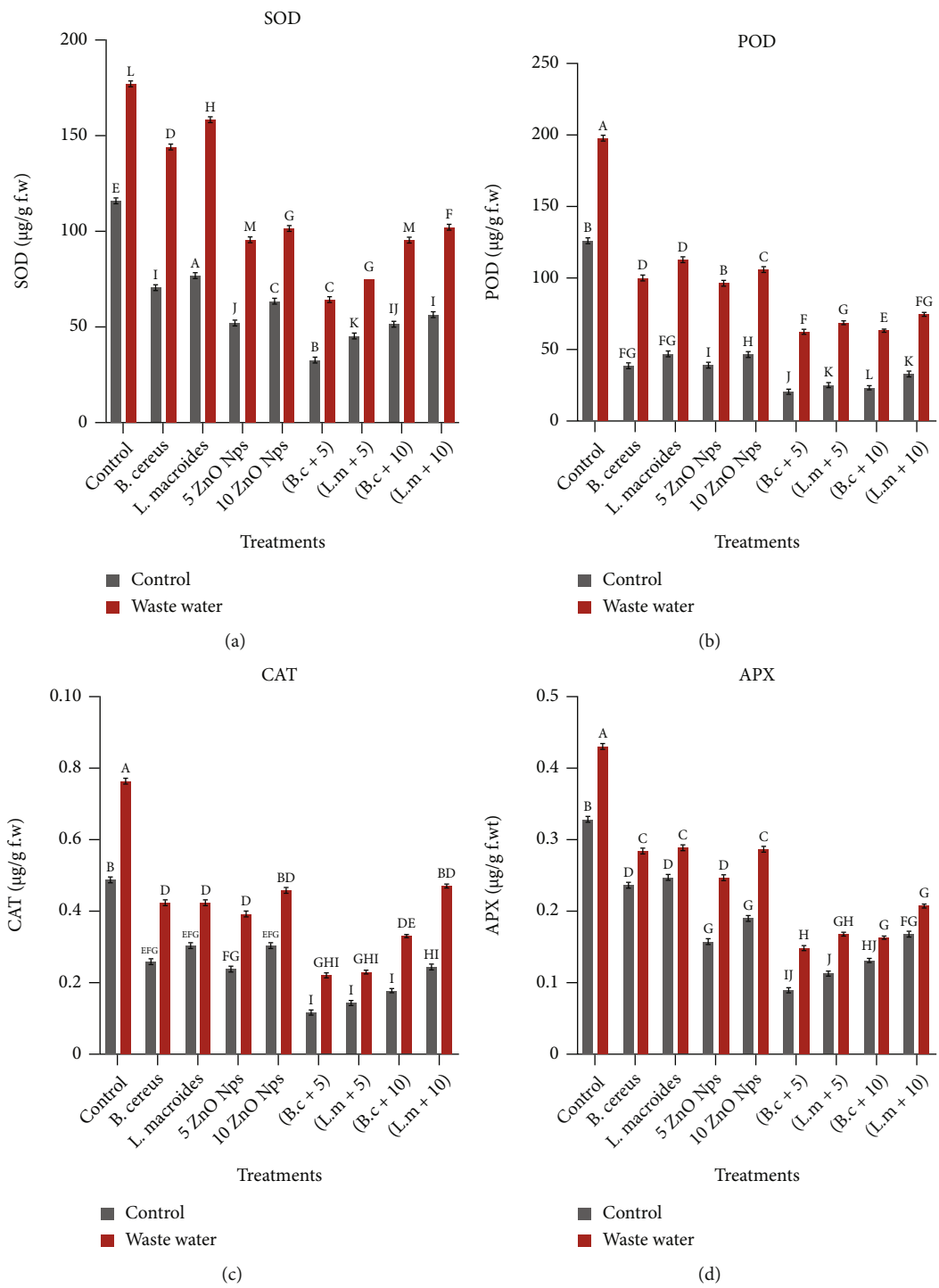


Figure 5: Continued.

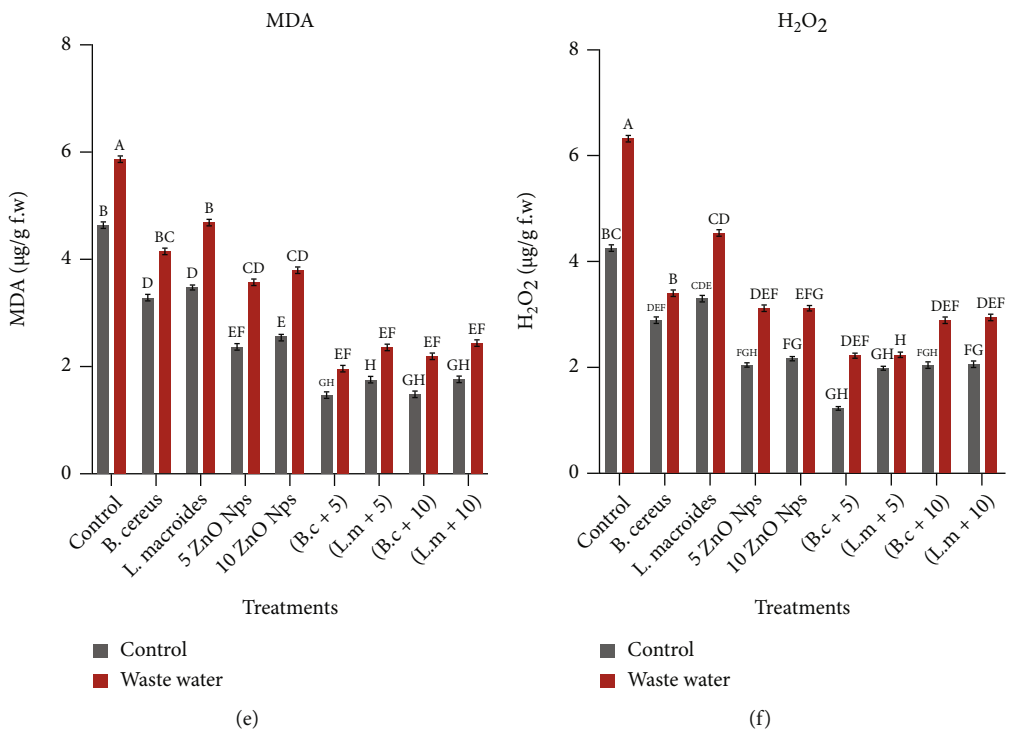


Figure 5: Synergistic effect of bacteria strains (*Bacillus cereus* and *Lysinibacillus macroides*) and ZnO NP (5 mg/L and 10 mg/L) treatments on (a) superoxide dismutase, (b) peroxidase, (c) catalase, (d) ascorbate peroxidase, (e) malondialdehyde, and (f) hydrogen peroxide on rice grown in heavy metal-contaminated water. Error bars showed means of standard error (±SE) of three replicates ($n = 3$) followed by different alphabetic letters showing statistical significance at 5% probability level. Control (distilled water), B.C+5 (*Bacillus cereus*+5 mg/L ZnO NPs), L.M+5 (*Lysinibacillus macroides*+5 mg/L ZnO NPs), B.C+10 (*Bacillus cereus*+10 mg/L ZnO NPs), and L.M+10 (*Lysinibacillus macroides* +10 mg/L ZnO NPs).

of nutrient reserves and metabolic and antioxidative activities [34]. Zinc ions also increased the cell stability by the nutrition uptake, water molecules, and translocation in plant tissues and enhanced the resistance level of plant against toxicity [35].

In this study, it was observed that stress reduced the germination of seeds by lowering the water potentials and nutrient uptake in seeds (Figure 1). Heavy metals inhibit seed germination by reduction in water availability and growth hormones and stop the metabolic and antioxidative activities [8]. These results are similar with other studies [32] in which they have shown that HMs create oxidative stress in the rice seed coat thus leading to the changes in microtubules during growth. The combined impact of bacteria and nanoparticles showed significant increase in germination under contaminated water (Figure 1). Overall, these can partially be attributed to the facts that ZnO NPs can potentially act as nanofertilizers at lower concentrations (<50 ppm) significantly enhanced seed germination [36]. These results are followed by other researcher data [12] that biopriming of rice seeds with bacteria enhances germination under heavy metal stress, while lower concentrations of ZnO NPs improved germination. It was observed that [32] the interaction of Si and PGPB seems an auspicious technique and eco-friendly approach to enhance metal tolerance in crop plants. Yan et al. [35] documented that zinc oxide nanoparticles improved the germination of wheat seeds at lower concentrations. It was reported that ZnO nanoparticles at lower concentrations act as a micronutrient and fertilizer for mung bean (*Vigna radiata*) chickpea (*Cicer arietinum*), ryegrass [37] (*Lolium perenne*), buckwheat (*Fagopyrum esculentum*), wetland plant (*softstem bulrush*, *Schoenoplectus tabernaemontani*) [1], and *Cucumis sativus* under drought stress [38]. Recently, it was reported [7] that the use of ZnO NPs (60 and 50 ppm) increased biochemical and nutritional quality of red radish plant.

Heavy metals affected the seedling biomass under toxic metals while combined impact of bacteria and ZnO nanoparticles enhanced the germination (Figures 2 and 3). The current study showed that bacteria primed seeds germinate in harsh environment; subsequently, ZnO NPs at lower concentrations act as micronutrients and remediate the HMs for better growth of the plant. Heavy metals drastically affect the seedling growth of rice [38]. Rizwan et al. [39] observed that phytohormonal seed priming protects the plant from toxicity by enhancing the tolerance mechanism such as causing the ROS detoxification, disrupting the photosynthetic activity and protein homeostasis. Seed priming also regulates the molecular mechanism by changing the stress inducible gene expression, transcriptional factors, and posttranslational modification. The current research [40] provides a novel insight into the potential mechanism of *B. megaterium* OSR-3 and putrescine in mitigation of hydrocarbon stress in *N. tabacum* plants. Moreover, these findings are further supported by earlier study [36] that ZnO NPs at lower concentration enhanced the enzyme production, synthesis of

Table 2: Synergistic effect of primed seeds with bacteria strains (*Bacillus cereus* and *Lysinibacillus macroides*) along with ZnO NP (5 and 10 mg/L) treatments on photosynthetic pigments of rice grown in heavy metal-contaminated water.

| Treatments | Chl (a) (mg/g) | Chl (b) (mg/g) | Chl (a)+Chl (b) (mg/g) | Carotenoids ($\mu$g/g) |
|---|---|---|---|---|
| Distilled water | $12.4 + 0.350^{ab}$ | $5.6 + 0.503^{cd}$ | $18.1 + 3.212^{ab}$ | $8.5 + 0.423^{d}$ |
| Wastewater (w.w) | $5.4 + 0.173^{a}$ | $3.2 + 0.432^{cd}$ | $8.6 + 2.12^{ac}$ | $4.3 + 0.321^{ad}$ |
| *Bacillus cereus* | $18.8 + 1.043^{abc}$ | $11.3 + 1.102^{abc}$ | $30.1 + 1.231^{abc}$ | $14.3 + 0.543^{cd}$ |
| (B.C+w.w) | $9.3 + 0.157^{ab}$ | $5.5 + 0.231^{cd}$ | $14.8 + 1.32^{ab}$ | $7.3 + 0.231^{abc}$ |
| *Lysinibacillus macroides* | $16.2 + 0.321^{ab}$ | $9.2 + 0.321^{ab}$ | $25.4 + 1.43^{bc}$ | $12.4 + 0.432^{ab}$ |
| (L.M+w.w) | $8.1 + 1.173^{ab}$ | $5.1 + 0.153^{ab}$ | $13.2 + 1.21^{abc}$ | $7.3 + 0.221^{ab}$ |
| 5 mg/L ZnO NPs | $22.2 + 0.323^{ab}$ | $15.4 + 0.421^{cd}$ | $37.6 + 3.231^{de}$ | $17.2 + 0.543^{abc}$ |
| (5+w.w) | $19.2 + 0.132^{bc}$ | $11.2 + 0.231^{cd}$ | $30.2 + 1.03^{a}$ | $14.3 + 0.543^{ab}$ |
| 10 mg/L ZnO NPs | $25.4 + 0.432^{d}$ | $19.2 + 0.421^{cd}$ | $44.6 + 3.12^{ab}$ | $20.1 + 0.231^{ab}$ |
| (10+w.w) | $21.23 + 0.132^{bc}$ | $15.4 + 0.142^{ab}$ | $36.6 + 1.21^{a}$ | $17.2 + 0.312^{abc}$ |
| B.C+5 mg/L ZnO NPs | $27.6 + 0.243^{b}$ | $19.2 + 1.12^{abc}$ | $46.8 + 2.32^{bd}$ | $22.3 + 0.432^{ab}$ |
| (B.C+5+w.w) | $25.3 + 0.121^{bcd}$ | $16.3 + 0.134^{ab}$ | $41.6 + 1.05^{ab}$ | $21.2 + 0.321^{ac}$ |
| L.M+5 mg/L ZnO NPs | $24.9 + 0.32^{abc}$ | $18.2 + 0.321^{ab}$ | $43.1 + 2.12^{bc}$ | $20.4 + 0.32^{abd}$ |
| (L.M+5+w.w) | $22.3 + 0.102^{ab}$ | $14.2 + 0.121^{abc}$ | $36.5 + 1.01^{ac}$ | $17.2 + 0.243^{ad}$ |
| B.C+10 mg/L ZnO NPs | $32.5 + 0.341^{bc}$ | $25.2 + 0.342^{bd}$ | $57.7 + 1.23^{abc}$ | $24.2 + 0.212^{ac}$ |
| (B.cereus+10+w.w) | $23.4 + 0.121^{ab}$ | $12.3 + 0.123^{abc}$ | $35.7 + 1.11^{ab}$ | $19.2 + 0.254^{ab}$ |
| L.M+10 mg/L ZnO NPs | $30.4 + 0.231^{ab}$ | $21.2 + 0.321^{ab}$ | $51.5 + 1.11^{a}$ | $25.3 + 0.341^{abc}$ |
| (L.M+10 w.w) | $21.3 + 0.142^{abc}$ | $13.3 + 0.113^{ab}$ | $34.2 + 1.21^{ab}$ | $18.2 + 0.232^{ac}$ |

Control (distilled water), B.C+5 mg/L (*Bacillus cereus*+5 mg/L ZnO NPs), L.M+5 mg/L (*Lysinibacillus macroides*+5 mg/L ZnO NPs), B.C+10 mg/L (*Bacillus cereus*+10 mg/L ZnO NPs), and L.M+10 mg/L (*Lysinibacillus macroides*+10 mg/L ZnO NPs). Data are statistically analyzed by statistic 9 software, and the numbers are mean of three replicates ($n = 3$) followed by standard deviation showed as (±) sign and analyzed by ANOVA test. Subsequently, different alphabetic letters appeared on each number showing statistical significance at 5% probability level and analyzed by Duncan's multiple range test (DMTR).

proteins, biomembrane stability, and growth regulation. A significant increase was observed in the root and shoot of the wheat plant by applying the different concentrations of ZnO nanoparticles [41]. It is also clear from the current findings that lower concentrations of ZnO NPs had no inhibitory effect on plant weight. These results were further supported by other experiments [35]; they showed that silver nanoparticles significantly increased the biomass and fresh and dry weight of plants. An earlier study showed that shoot-root elongation, fresh-dry weight was influenced in application of various doses of ZnO nanoparticles [42].

Plant cell membrane stability has a significant role in plant development while plant growth by bacteria and ZnO nanoparticle solution showed lowered cell injury than individual effect (Figure 4). Bioprimed treatment protects the seeds from toxic effect by using mineral (such as iron, phosphate, and nitrogen) from surrounding environment and enhanced the germination while ZnO NPs removed the HMs from water which caused cell stability. It has been shown previously that toxicity causes cellular deformation in plant tissues and damages the membrane structure [42]. ZnO NPs at lower concentration have an important function in enzyme productions, protein synthesis, biomembrane stability, and growth regulation in the plant [1]. Zinc ions enhanced the cell membrane stability by directly improving the nutrition uptake, water molecule conduction from roots to upper parts of the plant and vascular bundle tissue cells [36].

Photosynthetic pigments are bioindicators in plants for stress, for example, heavy metals change the sulfa-hydroxyl group, chlorophyllase, and pheophytinase enzymes by disturbing the nutrition uptake activities and $Mg^{+2}$ ion [3]. HM contents increased the MDA contents and affect the membrane-bound organelles (chloroplast) and photosynthetic pigments, damage the chloroplast structure by closing the stomata [43, 44], and change the chloroplast, electron transport chain (ETC), and metabolic functions of the plant [8]. It was revealed that plants germinated by bacteria nanoparticle interaction increased the photosynthetic pigments than the individual treatments of bioprimed seeds and 5 mg/L ZnO nanoparticles (Table 2). Bacteria-nanoparticle combined treatment increased the photosynthesis process in plants by enhancing different enzymes involved in photosynthesis. These findings are confirmed by other reports [18] that chlorophyll pigments were enhanced in leaves of *Leucaena leucocephala* under ZnO NP treatments because Zn ions enhanced the chlorophyll enzyme function and carbohydrate production. Moreover, ZnO NP treatments have a significant impact on the chlorophyll content, plant height, and fresh weight of peanut plants [35]. Furthermore, bacteria priming of seeds has also been shown to improve the photosynthesis of *faba* bean plant under cadmium stress [45].

Total soluble sugar (TSS) and protein (TSP) content have function in osmoregulation, energy production, and stress resistance. Heavy metal stress increased the catalytic activity and protein hydrolysis in plants (Figure 6). Plants stabilize the sugar and protein level by balancing the osmotic potential and degradation of biomolecules and membranes. ZnO NPs act as zinc ions which subsequently increase the sugar content, protein metabolism and hormones, and growth and biomass [46]. ZnO nanoparticles have been

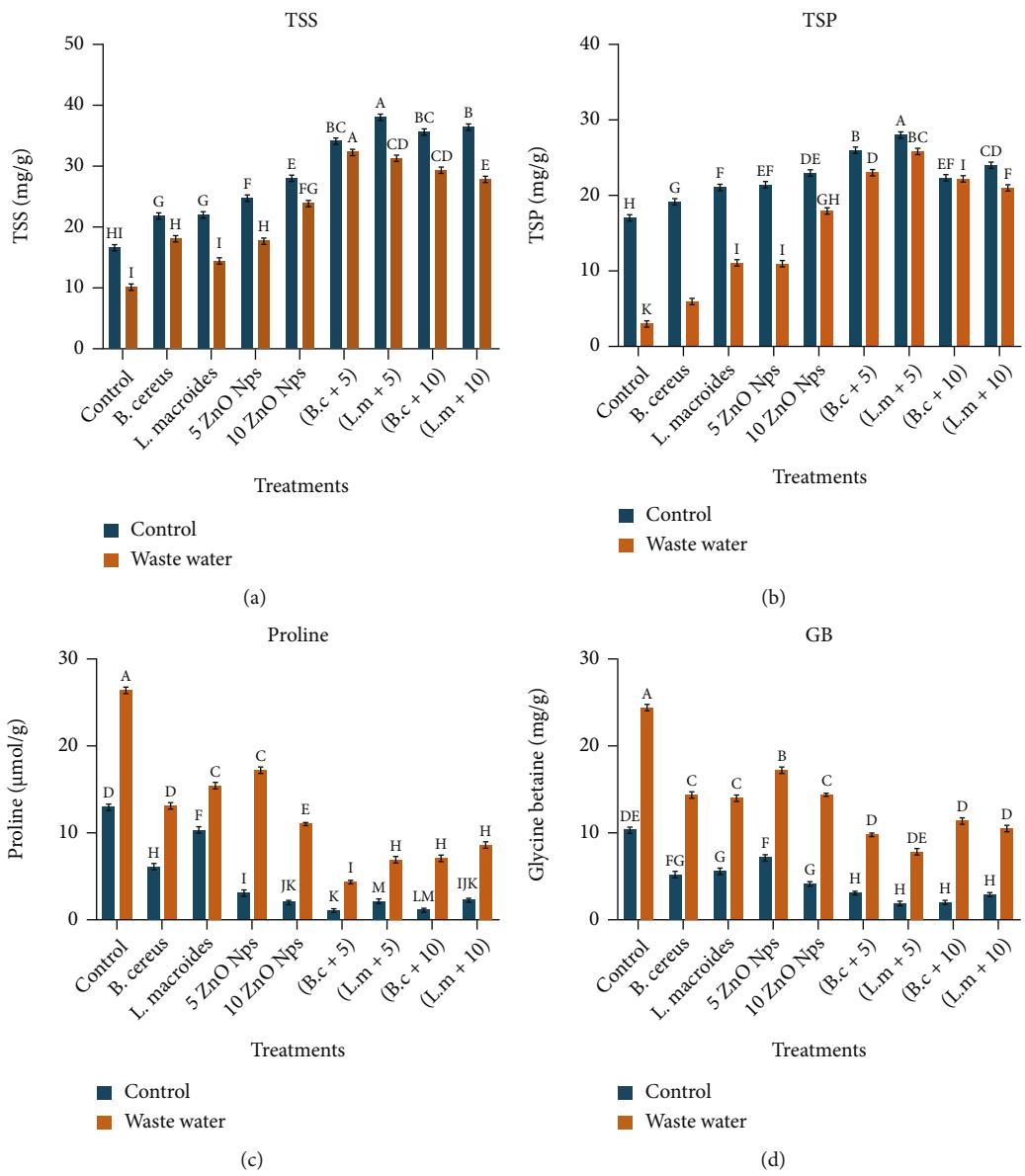


Figure 6: Synergistic effect of bacteria strains (*Bacillus cereus and Lysinibacillus macroides*) and ZnO NP (5 mg/L and 10 mg/L) treatments on (a) total soluble sugar, (b) total soluble protein, (c) total proline, and (d) glycine betaine content of rice grown in heavy metal-contaminated water. Error bars showed means of standard error (±SE) of three replicates ($n = 3$) followed by different alphabetic letters showing statistical significance at 5% probability level. Control (distilled water), B.C+5 (*Bacillus cereus*+5 mg/L ZnO NPs), L.M+5 (*Lysinibacillus macroides*+5 mg/L ZnO NPs), B.C+10 (*Bacillus cereus*+10 mg/L ZnO NPs), and L.M+10 (*Lysinibacillus macroides*+10 mg/L ZnO NPs).

shown to increase the protein content in cabbage followed by the increase in chlorophyll and carotenoids [47]. It was observed by Ahmad [14] that ZnO NPs lowered down the arsenic (As) stress in soybean plant by the synthesis of osmolytes, enzymatic and nonenzymatic antioxidant, enhanced the glyoxalase system in plants.

Proline (Pro) and glycine betaine (GB) are osmolytes that play important role in osmotic adjustment and growth of seeds. Proline has a specific role in protein denaturation and lipid peroxidation and scavenges the reactive oxygen species [48] while glycine betaine act as a phytoprotectant and its amount is increased in the plant under stress [35]. Bacterial treatments enhanced the sugar and protein content in seeds while zinc oxide nanoparticles give nutrients and remove the toxic metals, so proline and glycine betaine content was decreased in plants (Figure 6(c)). It has been noticed that ZnO NPs activate GB pathways and prevent the toxicity in *L. leucocephala* [18]. Similarly, it was revealed that silicon NPs increased the proline content in pea seedlings and protect the binding of HMs to functional groups of root cell wall [35].

Oxygen ($O_2$) is the basic element of metabolic processes in plant while oxidative stress caused many abnormalities in plants and damaged the biomolecules (proteins, lipids,

enzymes, and nucleic acid) [46]. Antioxidative enzymes in plant were enhanced under HM stress while the combined treatment of bacteria-nanoparticles lowered down the antioxidant enzymes (Figure 5). Superoxidase (SODs) is a multimeric metalloenzyme and in stress condition removed the superoxide free radicals and scavenges $H_2O_2$ into $O_2$. These results were further supported by other scientists [47]. He observed that the superoxidase level in rice seedlings increased by enzymatic protein de novo synthesis under stress condition. It was observed that in *Pisum sativum* plants, SOD activity increased under stress [48]. Bacteria priming may activate the oxidative stress resistance mechanism in seeds while zinc oxide nanoparticles may interact with the metals by cell surface metal retention and decreasing their permeability in the plant. These results were supported by another study that SOD level in rice seedlings increased under stress by enzymatic protein de novo synthesis [49]. In *Pisum sativum* plants, it was noticed that SOD activity increased under stress [35]. Foliar spray of zinc oxide nanoparticles in sunflower plants under salt stress showed an enhanced SOD activity [50]. It was also observed that combined application of ZnO-NPs and *B. fortis* IAGS-223 considerably changes the activity of antioxidant enzymes besides upgradation of the biochemicals and growth parameters of Cd-stressed plants. In cauliflower, enhanced concentration of ZnO nanoparticles (9.0 M) has been observed to stabilize the SOD, CAT, and sugar content [43]. Plant contains some metabolites and nonenzymatic components such as ascorbic acid and glutathione that act as ROS scavengers. These components are involved in many cellular processes and cause the detoxification of ROS due to its ability to donate electrons in a wide range of enzymatic and nonenzymatic reactions.

POD enzymes dismutase the $H_2O_2$ content under HM stress in plants by gaining electrons. Bacteria removed the HMs from media by making complex with metals and decreased the amount of SOD and POD while the low content of ZnO NPs changed into zinc ions that act as micronutrients for plant growth and essential cofactor for enzymes in the metabolic process. Increased activities of superoxidase and peroxidase have been documented in pigeon pea under stress [46]. Investigation [26] revealed that under Pb stress (800 mg $kg^{-1}$ soil), *Athium wardii* specie, soybean, and rice seedlings showed an increase in POD content. It was recently reported that ZnO NPs reduced drought-related damages to cell organelles, increased melatonin content, and decreased antioxidative enzymes under drought stress in maize plant [47]. It is further confirmed [48] that seed priming of pearl millet plant with silver NPs enhances salinity tolerance by increasing physiological and biochemical responses in plants. Silver NPs reduced the oxidative stress by improving antioxidant enzyme, decreased the sodium ($Na^+$), and increased the potassium ($K^+$), total phenolic, and flavonoid content, so priming with NPs increased the crop production in salt-contaminated lands. It was reported [51] that the combined application of Ca and Bd could effectively relieve individual and combined Cd stress and DDT toxicity in *B. alboglabra*.

It has been documneted [51] that a high amount of CAT content in biomass may be due to scavenging of $H_2O_2$ and toxic peroxidase under metal stress. Higher CAT content was measured in plant *Jatropha curcas* cotyledons at a high concentration of metals [35]. The result showed that the synergistic effect of bacteria and zinc oxide nanoparticles may remove the stress by decreasing the oxidative stress in plant and generates lower activity of CAT enzymes (Figure 5). *Bacillus* spp. increased the lignin production and activated defense mechanisms and decreased the CAT, SOD, and guaiacol peroxidase level [46]. It was observed that ZnO NPs change into zinc ions which is necessary for metabolic enzymes [52]. Ascorbate peroxidases (APX) scavenge the harmful effect of $H_2O_2$ in the plant by utilizing the ascorbic acid and maintain the ROS of chloroplast and other organelles. These results showed similarity with findings of other report [49], who observed increased content of APX in *Allium cepa* and rice plants at higher concentrations of metals. It was reported that *Wolffia arrhiza* and *Talinum triangulare* plant roots under Pb and Cd stress showed enhanced activities of reduced nicotinamide adenine dinucleotide (NADH), CAT, APX, glutathione, and ascorbate [49]. Bacteria reduced the level of HMs from water by increasing the level of APX and reducing the oxidative stress while ZnO nanoparticles remediate metals from water and lower the antioxidative enzymes. These findings are confirmed by other studies [39] that bacterial treatments increased the plant germination in oxidative stress. ZnO NPs act as a cofactor for different enzymes used in metabolic mechanism in plants [10] It was also recently reported that higher concentrations of zinc oxide nanoparticles such as 50 and 100 mg/L in hydroponics culture cause the upregulation of genes encoding antioxidant enzymes [14]. The current research [32] reveals that Si and K may improve gladiolus growth by decreasing the oxidative stress and Cd uptake and by increasing the activity of antioxidant defense enzymes and the quantity of secondary metabolites and plant nutrition.

ROS generate hydroxyl radicals in the plant and produce lipid hydrogen peroxide by Fenton-like reaction and formed aldehydes (malondialdehyde) during stress condition. $H_2O_2$ content in plants binds with thiol-containing proteins and generates various signaling pathways, activating gene expression, cell cycle, and transcription of protein [39]. These findings are confirmed by other researchers [14], who revealed that under Cr stress the MDA content was increased in leaf and other parts of *Kandelia obovata* and *Acanthus ilicifolius* plant. The synergistic effect of bioprimed seeds with microbes along with ZnO NPs enhanced the growth of rice and lowered the MDA and $H_2O_2$ content by remediating the metals from media and enhanced the photosynthetic pigments. It was observed [53] that seed inoculation with *B. siamensis* removes the oxidative stress under Cd stress in wheat plants, by decreasing the MDA level, increasing the antioxidant enzyme activities and nitrogen and mineral nutrition by reducing the uptake of Cd metal and ultimately increasing the growth of plants. In plants, zinc prevents the cell organelles from ROS and acts as a defense system for cell organelles [9]. These results are

confirmed by other scientist [54],they revealed higher $H_2O_2$ content under HM stress. It was reported that priming of seeds with salicylic acid (SA) decreased the stress of metals [47]. Biopriming with microbes along ZnO nanoparticles treatments showed decreased $H_2O_2$ content by alleviating the stress from media. It was reported [1] that ZnO NPs remediate the toxic stress which reduced $H_2O_2$ content and enhanced the growth. However, melatonin combined with nitric oxide scavenger increased MDA and $H_2O_2$ and decreases antioxidative enzymes. Hydrogen peroxide accumulation and associated oxidative damages decreased metabolic and antioxidative changes during seed germination [49]. Similar findings were observed by Akhtar et al. [55]; they confirmed the importance of the combined effect of *Bacillus* spp. and ZnO NPs on protein and gene profiles of rice plants under HM stress.

## 5. Conclusions

Current findings revealed that HM-contaminated wastewater significantly lowered down the plant biomass, chlorophyll content, soluble sugar, and protein contents and enhanced antioxidative metabolism and stress biomarkers (proline and glycine betaine content). However, ZnO NPs and bacteria individually had low potential to enhance the biochemical aspects of plants in HM-contaminated water. Importantly, the combined impact of bacteria-nanoparticles enhanced the plant growth, chlorophyll contents, total soluble sugar, and protein (TSP). Moreover, the synergistic effect of both factors has lowered antioxidative parameters than the individual effect. Subsequently, the notion that ZnO NPs may be used at lowered content acting as nanofertilizer is helpful to enhance the metabolic and antioxidative activities in HM-contaminated water. It is highly recommended to check the effect of ZnO NPs with bacteria in field condition which are ultimately required for sustainable environmental protection. Further research is needed to elaborate the actual mechanism of toxicity in plants at the molecular level and to determine the different cell signaling pathways involved in the alleviation of HM stress in rice plants.

## Data Availability

The data used to support the findings of this study are included within the article.

## Conflicts of Interest

The authors have no potential conflicts of interest.

## Supplementary Materials

Figure 1: synergistic effect of bacteria strains (Bacillus cereus and Lysinibacillus macroides) primed seeds along with ZnO NP (5 and 10 mg/L) treatments on shoot and root length in heavy metal-contaminated water. Figure 2: hydroponic culture experiment of plant grown from seeds primed with bacteria strains (Bacillus cereus and Lysinibacillus macroides) in 5 and 10 mg/L of ZnO NPs alone or in combination with heavy metal-contaminated water. *(Supplementary Materials)*

## References


[1] A. Wiszniewska, "Priming strategies for benefiting plant performance under toxic trace metal exposure," *Plants*, vol. 10, no. 4, pp. 623–645, 2021.

[2] Z. Zakaria, N. S. Zulkafflee, N. A. Mohd Redzuan et al., "Understanding potential heavy metal contamination, absorption, translocation and accumulation in rice and human health risks," *Plants*, vol. 10, no. 6, pp. 1070–1090, 2021.

[3] R. Kaur, S. Das, S. Bansal et al., "Heavy metal stress in rice: uptake, transport, signaling, and tolerance mechanisms," *Physiologia Plantarum*, vol. 173, no. 1, pp. 430–448, 2021.

[4] D. Mitra, R. Mondal, B. Khoshru, S. Shadangi, P. K. D. Mohapatra, and P. Panneerselvam, "Rhizobacteria mediated seed bio-priming triggers the resistance and plant growth for sustainable crop production," *Current Research in Microbial Sciences*, vol. 2, no. 1, pp. 100071–100071, 2021.

[5] O. S. Devika, S. Singh, D. Sarkar, P. Barnwal, J. Suman, and A. Rakshit, "Seed priming: a potential supplement in integrated resource management under fragile intensive ecosystems," *Frontiers in Sustainable Food Systems*, vol. 5, no. 1, pp. 209–219, 2021.

[6] J. Li, M. Zhang, J. Sun et al., "Heavy metal stress-associated proteins in rice and arabidopsis: genome-wide identification, phylogenetics, duplication, and expression profiles analysis," *Frontiers in Genetics*, vol. 11, no. 1, pp. 477–485, 2020.

[7] H. Sadiq, F. Sher, S. Sehar et al., "Green synthesis of ZnO nanoparticles from *Syzygium cumini* leaves extract with robust photocatalysis applications," *Journal of Molecular Liquids*, vol. 335, no. 1, pp. 116567–116567, 2021.

[8] V. D. Rajput, T. Minkina, A. Fedorenko et al., "Effects of zinc oxide nanoparticles on physiological and anatomical indices in spring barley tissues," *Nanomaterials*, vol. 11, no. 7, pp. 1722–1730, 2021.

[9] S. Awan, K. Shahzadi, S. Javad, A. Tariq, A. Ahmad, and S. Ilyas, "A preliminary study of influence of zinc oxide nanoparticles on growth parameters of *Brassica oleracea* var italic," *Journal of the Saudi Society of Agricultural Sciences*, vol. 20, no. 1, pp. 18–24, 2021.

[10] P. Zoufan, M. Baroonian, and B. Zargar, "ZnO nanoparticles-induced oxidative stress in *Chenopodium murale* L, Zn uptake, and accumulation under hydroponic culture," *Environmental Science and Pollution Research*, vol. 27, no. 10, pp. 11066–11078, 2020.

[11] N. Priyanka, N. Geetha, T. Manish, S. V. Sahi, and P. Venkatachalam, "Zinc oxide nanocatalyst mediates cadmium and lead toxicity tolerance mechanism by differential regulation of photosynthetic machinery and antioxidant enzymes level in cotton seedlings," *Toxicology Reports*, vol. 8, no. 1, pp. 295–302, 2021.

[12] M. Rafique, M. Sohaib, R. Tahir, M. Bilal Tahir, and M. Rizwan, "Plant-mediated green synthesis of zinc oxide nanoparticles using peel extract of Citrus reticulate for boosting seed germination of Brassica nigraseeds," *Journal of Nanoscience and Nanotechnology*, vol. 21, no. 6, pp. 3573–3579, 2021.

[13] R. M. Thangavelu, D. Gunasekaran, M. I. Jesse, S. U. Mohammed Riyaz, D. Sundarajan, and K. Krishnan, "Nanobiotechnology approach using plant rooting hormone synthesized silver nanoparticle as "nanobullets" for the dynamic applications in horticulture - An *in vitro* and *ex vitro* study," *Arabian Journal of Chemistry*, vol. 11, no. 1, pp. 48–61, 2018.

[14] N. Akhtar, S. Khan, S. U. Rehman et al., "Synergistic effects of zinc oxide nanoparticles and bacteria reduce heavy metals toxicity in rice (*Oryza sativa* L.) plant," *Toxics*, vol. 9, no. 5, pp. 113–120, 2021.

[15] U. Amara, S. Shad, N. Ilyas, A. Manaf, and N. I. Raja, "In vitro germination and biochemical profiling of *Brassica napus* in response to biosynthesized zinc nanoparticles," *IET Nanobiotech*, vol. 13, no. 1, pp. 46–51, 2018.

[16] N. Akhtar, S. Khan, S. U. Rehman et al., "Zinc oxide nanoparticles enhance the tolerance and remediation potential of *Bacillus spp.* against heavy metal stress," *Adsorption Science & Technology*, vol. 2021, article 1774528, 16 pages, 2021.

[17] M. R. Khattak, G. Shah, R. Naeem et al., "Assessment of heavy metal tolerance and reduction potential of bacillus sp. isolated from the soils contaminated with industrial effluents," *Fresenius Environmental Bulletin*, vol. 30, no. 1, pp. 4391–4401, 2021.

[18] I. Ashraf, F. Ahmad, A. Sharif, A. R. Altaf, and H. Teng, "Heavy metals assessment in water, soil, vegetables and their associated health risks via consumption of vegetables, district Kasur, Pakistan," *SN Applied Sciences*, vol. 3, no. 5, pp. 1–16, 2021.

[19] F. Delrue, M. Ribeiro de Jesus Cerqueira, A. Compadre et al., "Hydroponic farm wastewater treatment using an indigenous consortium," *Processes*, vol. 9, no. 3, p. 519, 2021.

[20] H. Hamim, M. Miftahudin, and L. Setyaningsih, *Cellular and ultrastructure alteration of plant roots in response to metal stress*, vol. 1, no. 1, 2018, Intech Open, London, 2018.

[21] V. Velikova, I. Yordanov, and A. Edreva, "Oxidative stress and some antioxidant systems in acid rain-treated bean plants," *Plant Science*, vol. 151, no. 1, pp. 59–66, 2000.

[22] Y. Nankano and K. Asada, "Hydrogen-peroxide is scavenged by ascorbate-specific peroxidase in spinach chloroplasts," *Plant & Cell Physiology*, vol. 1, no. 22, pp. 867–877, 1980.

[23] Y. Li, L. Liang, W. Li et al., "ZnO nanoparticle-based seed priming modulates early growth and enhances physio-biochemical and metabolic profiles of fragrant rice against cadmium toxicity," *Journal of Nanobiotechnology*, vol. 19, no. 1, pp. 1–19, 2021.

[24] L. S. Bates, R. P. Waldren, and I. D. Teare, "Rapid determination of free proline for water-stress studies," *Plant and Soil*, vol. 39, no. 1, pp. 205–207, 1973.

[25] S. Shtisarnit, P. Harinasut, S. Pornbunlualap, S. Cha-Um, P. Carillo, and Y. Gibon, "Extraction and determination of glycine betaine," *Kasetsart Journal - Natural Science*, vol. 1, no. 1, pp. 1–12, 2009.

[26] S. P. Dhas, P. J. Shiny, S. Khan, A. Mukherjee, and N. Chandrasekaran, "Toxic behavior of silver and zinc oxide nanoparticles on environmental microorganisms," *Journal of Basic Microbiology*, vol. 54, no. 9, pp. 916–927, 2014.

[27] M. M. Bradford, "A rapid and sensitive method for the quantitation of microgram quantities of protein utilizing the principle of protein-dye binding," *Analytical Biochemistry*, vol. 72, no. 1-2, pp. 248–254, 1976.

[28] A. C. F. de Vasconcelos, X. Zhang, E. H. Ervin, and J. de Castro Kiehl, "Enzymatic antioxidant responses to biostimulants in maize and soybean subjected to drought," *Scientia Agricola*, vol. 66, no. 3, pp. 395–402, 2009.

[29] C. Beauchamp and I. Fridovich, "Superoxide dismutase: improved assays and an assay applicable to acrylamide gels," *Analytical Biochemistry*, vol. 44, no. 1, pp. 276–287, 1971.

[30] H. Aebi, "[13] Catalase in vitro," *Methods in Enzymology*, vol. 105, no. 1, pp. 121–126, 1984.

[31] A. Sofo, A. Scopa, M. Nuzzaci, and A. Vitti, "Ascorbate peroxidase and catalase activities and their genetic regulation in plants subjected to drought and salinity stresses," *International Journal of Molecular Sciences*, vol. 16, no. 12, pp. 13561–13578, 2015.

[32] M. M. Zaheer, N. A. Yasin, S. R. Ahmad et al., "Amelioration of cadmium stress in gladiolus (Gladiolus grandiflora L.) by application of potassium and silicon," *Journal of Plant Nutrition*, vol. 41, no. 4, pp. 461–476, 2018.

[33] S. Rastogi and R. Kumar, "Remediation of heavy metals using non-conventional adsorbents and biosurfactant-producing bacteria," *Environmental Degradation: Causes and Remediation Strategies*, vol. 1, no. 1, pp. 23–45, 2020.

[34] W. A. Mohammad, S. M. Ali, N. Farhan, and S. M. Said, "The toxic effect of zinc oxide nanoparticles on the terrestrial slug Lehmannia nyctelia (*Gastropoda-Limacidae*)," *The Journal of Basic and Applied Zoology*, vol. 82, no. 1, pp. 1–9, 2021.

[35] S. Yan, F. Wu, S. Zhou, J. Yang, X. Tang, and W. Ye, "Zinc oxide nanoparticles alleviate the arsenic toxicity and decrease the accumulation of arsenic in rice (*Oryza sativa* L.)," *BMC Plant Biology*, vol. 21, no. 1, pp. 1–11, 2021.

[36] M. Yin, G. Pan, J. Tao et al., "Genome-wide identification of MYB gene family reveals their potential functions in cadmium stress response and the regulation of cannabinoid biosynthesis in hemp (*Cannabis sativa* L.)," *Industrial Crops and Products*, vol. 1, no. 1, pp. 1–29, 2021.

[37] H. Nawaz, N. Hussain, M. Jamil et al., "Seed bio-priming mitigates terminal drought stress at reproductive stage of maize by enhancing gas exchange attributes and nutrient uptake," *Turkish Journal of Agriculture and Forestry*, vol. 44, no. 3, pp. 250–261, 2020.

[38] N. Akhtar, S. Khan, I. Malook, S. Rehman, and M. Jamil, "Pb-induced changes in roots of two cultivated rice cultivars grown in lead-contaminated soil mediated by smoke," *Environmental Science and Pollution Research*, vol. 24, no. 26, pp. 21298–21310, 2017.

[39] M. Rizwan, S. Ali, M. Z. Rehman et al., "Effects of nanoparticles on trace element uptake and toxicity in plants: a review," *Ecotoxicology and Environmental Safety*, vol. 221, no. 1, article 112437, 2021.

[40] M. Tariq, A. A. Shah, N. A. Yasin, A. Ahmad, and M. Rizwan, "Enhanced performance of Bacillus megaterium OSR-3 in combination with putrescine ammeliorated hydrocarbon stress in Nicotiana tabacum," *International Journal of Phytoremediation*, vol. 23, no. 2, pp. 119–129, 2021.

[41] O. V. Moshynets, L. M. Babenko, S. P. Rogalsky et al., "Priming winter wheat seeds with the bacterial quorum sensing signal N-hexanoyl-L-homoserine lactone (C6-HSL) shows potential to improve plant growth and seed yield," *PLoS One*, vol. 14, no. 2, article e0209460, 2019.

[42] M. S. Sadak and B. A. Bakry, "Physiological and biochemical responses of soybean *(Glycine max* L.) to cysteine application under sea salt stress," *Bulletin of the National Research Centre*, vol. 44, no. 1, pp. 1–12, 2020.

[43] P. I. Angulo-Bejarano, J. Puente-Rivera, and R. Cruz-Ortega, "Metal and metalloid toxicity in plants: an overview on molecular aspects," *Plants*, vol. 10, no. 4, pp. 635–640, 2021.

[44] F. Tariq, X. Wang, M. H. Saleem et al., "Risk assessment of heavy metals in basmati rice: implications for public health," *Sustainability*, vol. 13, no. 15, pp. 8513–8521, 2021.

[45] S. E. Jin and H. E. Jin, "Antimicrobial activity of zinc oxide nano/microparticles and their combinations against pathogenic microorganisms for biomedical applications: from physicochemical characteristics to pharmacological aspects," *Nanomaterials*, vol. 11, no. 2, pp. 263–274, 2021.

[46] M. Kasahun, A. B. Alemayhu Yadate, Z. Belay, and M. Ramalingam, "Antimicrobial activity of chemical, thermal and green route-derived zinc oxide nanoparticles: a comparative analysis," *Nano Biomedicine and Engineering*, vol. 12, no. 1, pp. 47–56, 2020.

[47] A. Tymoszuk and J. Wojnarowicz, "Zinc oxide and zinc oxide nanoparticles impact on in vitro germination and seedling growth in *Allium cepa* L," *Materials*, vol. 13, no. 12, p. 2784, 2020.

[48] I. Khan, M. A. Raza, S. A. Awan et al., "Amelioration of salt induced toxicity in pearl millet by seed priming with silver nanoparticles (AgNPs): the oxidative damage, antioxidant enzymes and ions uptake are major determinants of salt tolerant capacity," *Plant Physiology and Biochemistry*, vol. 156, no. 1, pp. 221–232, 2020.

[49] D. F. Fiol, M. C. Terrile, J. Frik, F. A. Mesas, V. A. Álvarez, and C. A. Casalongué, "Nanotechnology in plants: recent advances and challenges," *Journal of Chemical Technology & Biotechnology*, vol. 96, no. 8, pp. 2095–2108, 2021.

[50] S. Hossain, S. Hossain, M. R. Islam et al., "Bioremediation of hexavalent chromium by chromium resistant bacteria reduces phytotoxicity," *International Journal of Environmental Research and Public Health*, vol. 17, no. 17, pp. 6013–6019, 2020.

[51] A. A. Shah, S. Aslam, M. Akbar et al., "Combined effect of *Bacillus fortis* IAGS 223 and zinc oxide nanoparticles to alleviate cadmium phytotoxicity in *Cucumis melo*," *Plant Physiology and Biochemistry*, vol. 158, pp. 1–12, 2021.

[52] S. Mubeen, I. Shahzadi, W. Akram et al., "Calcium nanoparticles impregnated with benzenedicarboxylic acid: a new approach to alleviate combined stress of DDT and cadmium in Brassica alboglabra by modulating bio-acummulation, anti-oxidative machinery and osmoregulators," *Frontiers in Plant Science*, vol. 13, pp. 825829–825829, 2022.

[53] N. Akhtar, N. Ilyas, H. Yasmin et al., "Role of *Bacillus cereus* in improving the growth and phytoextractability of *Brassica nigra* (l.) k. koch in chromium contaminated soil," *Molecules*, vol. 26, no. 6, pp. 1569–1569, 2021.

[54] E. Y. Shaba, J. O. Jacob, J. O. Tijani, and M. A. T. Suleiman, "A critical review of synthesis parameters affecting the properties of zinc oxide nanoparticle and its application in wastewater treatment," *Applied Water Science*, vol. 11, no. 2, pp. 1–41, 2021.

[55] N. Akhtar, S. Khan, M. Jamil, S. U. Rehman, Z. U. Rehman, and E. S. Rha, "Combine effect of ZnO NPs and bacteria on protein and gene's expression profile of rice (*Oryza sativa* L.) plant," *Toxics*, vol. 10, no. 6, p. 305, 2022.

Hindawi
Adsorption Science & Technology
Volume 2022, Article ID 8341279, 12 pages
https://doi.org/10.1155/2022/8341279

*Research Article*

# Concentrations of Lead in Groundwater and Human Blood in the Population of Palosai, a Rural Area in Pakistan: Human Exposure and Risk Assessment

**Yu Shuang Ren**,[1,2] **Muhammad Ilyas**,[3] **Rui Ze Xu**,[2] **Waqas Ahmad**,[4] **and Rui Wang**[2]

[1]*Post Doctoral Station of Theoretical Economics, Northeast Normal University, Chang Chun 130117, China*
[2]*School of Economics and Management, Jilin Jianzhu University, Chang Chun 130117, China*
[3]*Department of Environmental Sciences, University of Peshawar, Peshawar 25120, Pakistan*
[4]*Institute of Chemical Sciences, University of Peshawar, Peshawar 25120, Pakistan*

Correspondence should be addressed to Yu Shuang Ren; rysmiracle@126.com and Muhammad Ilyas; sirfilyas@yahoo.com

Received 5 January 2022; Revised 14 February 2022; Accepted 5 April 2022; Published 14 May 2022

Academic Editor: Hesham Hamad



Lead (Pb) is a toxic environmental contaminant, which enters water bodies from natural and anthropogenic activities. The present study investigates the Pb concentration in groundwater sources and evaluates their potential health risks in Palosai area, Peshawar, Khyber Pakhtunkhwa, Pakistan. Groundwater samples were collected from different groundwater sources in the area where the human blood samples were from the dependent residents. Pb concentration was analyzed using an atomic absorption spectrophotometer and compared with the permissible limits set by Pakistan Environmental Protection Agency and World Health Organization (WHO). The levels of physicochemical parameters were observed within the said safe limits, while the levels of Pb in different groundwater sources (tube wells and wells) showed a little bit variation. Health risk indicators such as chronic daily intake (CDI) and hazard quotient (HQ) were calculated for Pb. The calculated value of CDI and HQ for Pb via groundwater consumption was 0.001 mg/kg·day and $2.8E-02$ mg/kg·day, respectively; however, the overall HQ values of Pb in the groundwater were less than 1, indicating no health risk to the local depending community.

## 1. Introduction

Water is considered an important resource in the environment [1–3]. Water is an essential constituent of living beings; life of living beings without water is not possible. Total bodily water accounts for 60% of an adult human's body weight [4]. What is more, water contamination with heavy metals, for example, zinc (Zn), lead (Pb), nickel (Ni), manganese (Mn), copper (Cu), chromium (Cr), and cadmium (Cd), is an overall environmental issue [5, 6]. A variety of contaminants finds its way to the human body through different routes such as ingestion, inhalation, or direct skin contact. Heavy metals enter the human body through a variety of routes, including drinking contaminated water, eating contaminated food, and inhaling dust. Human exposure to heavy metals may be occupational and nonoccupational, living near, or working in an industrial site may increase human health risk [7]. When heavy metals contaminate food and water, they degrade their quality and induce toxicity [8]. Digestive issues, joint and muscle discomfort, high blood pressure, concentration and memory issues, nerve abnormalities, cataracts, and damage to sperm-producing organs in males are just a few of the damaging impacts of heavy metals [9, 10].

In both rural and urban areas of the world, the main source for drinking is groundwater. It is also an essential water source for the industrial and agricultural sectors. Lately, aquatic environmental contamination with metals has pulled in worldwide considerations inferable from its persistence, abundance, and environmental toxicity. Waste from anthropogenic activities, for example, agriculture waste, industrial effluents and urban waste, and additionally

natural process, for example, mineral weathering, erosion, and atmospheric deposition, degrade surface and groundwater and impair their utilization for drinking, industrial, agricultural or other purposes [11]. The groundwater quality differs from region to region contingent on the topographical development. The trace metal concentrations and distribution vary from one place to another relying upon factors, i.e., hydrogeometry of aquifers, redox potential, geological location, and pH [12]. Heavy metal carcinogenicity and toxicity depends upon the amount of ingestion, individual body immunity, and duration of exposure [13]. Pb is a possible human carcinogen and can affect every system and organ of the human body [7]. Lead (Pb) is one of the most common elements that occur in the environment and accounts for about 13 mg/kg of the total earth crust [14]. Contamination of drinking water may be natural or anthropogenic [15], among the anthropogenic sources, mining, manufacturing, use of fertilizers, fossil fuel combustion, and industrial activities [7] are the most common sources of Pb contamination. Similarly, Pb and its compounds are used to produce ammunition, metal products, batteries, and X-ray shielding devices. Pb is also used in several products like paints and gasoline [7]. Pb is a component of the pipes and plumbing system used in water distribution channels [16]. The concentration of Pb in drinking water as a result of dissolution and leaching from pipelines is affected by pH, hardness, temperature, dissolved oxygen, and chloride concentration [17]. There are certain metals, i.e., K, Na, Mg, Ca, Zn, Fe, Cu, and Co, which are essential for the growth and function of normal human body. However, many are toxic and nonessential such as Pb, Ni, As, and Cd which causes health risk when ingested in sufficient quantity [6, 15].

Globally, environmental researchers have a prime focus on human health risk assessment associated with drinking water [18]. Many examinations have researched the heavy metals occurrence in surface and groundwater. In Bangladesh, Frisbie et al. [19] have analyzed toxic elements and arsenic concentrations in drinking water and results of the investigation affirmed that drinking water is polluted with other poisonous and arsenic that may influence human well-being and additionally the health of the biological community in Bangladesh. In Jharkhand, India, Giri et al. [20] have examined in groundwater the content of heavy metals in the proposed region of two uranium mining areas and the aftereffects of the examination demonstrated that the determined concentration of elements was inside the measures for drinking water of the WHO and Indian measures. Muhammad et al. [6] investigated heavy metal levels in drinking water in Kohistan, northern Pakistan, and found that most heavy metal levels were within the Pak EPA and WHO acceptable limits. In Jammu and Kashmir, India, Kumar et al. [21] have determined trace metal concentrations in drinking water and the results of water samples demonstrated that the metal concentrations were below the permissible level. Due to the lack of awareness, the general public thinks that groundwater is safe for drinking and it is free from contamination; hence, no treatment is required for groundwater. The present study investigates the assessment of lead concentration in groundwater in the Peshawar. The potential health risk of the occurrence of lead in groundwater has also been investigated by determining the concentration of lead in the blood samples of the inhabitants of the study area. The exploration work will give a base for the awareness campaign with respect to the significance of safe and pure potable water quality.

## 2. Materials and Methods

*2.1. Study Area.* The study area is located in district Peshawar, Khyber Pakhtunkhwa, Pakistan. Its geographical coordinates are 34° 2′ 29″ North, 71° 29′ 19″ East [22]. In summer, the mean maximum and minimum temperatures are over 40°C (104°F) and 25°C (77°F), respectively, while in winter the mean minimum and maximum temperature is 4°C (39°F) and 18.35°C (65.03°F), respectively. Unlike other regions of the country, Palosai is nonmonsoon region. Canal is the major source of irrigation originated from River Shalam. The stream water used for irrigation in the peripherals of Palosai is highly polluted by the effluents discharged from Hayatabad industrial zone. The major source of drinking water is groundwater obtained from tube wells, bore wells, hand pumps, and open wells. The sites for collection of water and blood samples are shown in the map of the study area (Figure 1).

*2.2. Collection of Water Samples.* Groundwater samples ($n = 13$) were collected from various sources such as tube wells ($S_1$ to $S_8$) and open wells ($S_9$ to $S_{13}$) in clean polythene bottles using the standard procedure of Khan et al. [9], [10] and Ilyas et al. [2] for sample collection. Separate bottles were used for the collection of samples for physicochemical and Pb analysis. A few drops of nitric acid ($HNO_3$) were added to the samples for Pb analysis to avoid changes in the Pb concentration. The samples were transported to the laboratory for physicochemical and Pb analysis.

*2.3. Blood Sampling.* Blood samples ($n = 40$) were collected from the local volunteers of the area belonging to different age groups, which included 1–12 years (children), 12–18 years (adolescents), 18–45 years (adults), and above 45 (old) both male and female [23]. Blood samples from all volunteers were collected upon their permission and the permission of the local committee was constituted by the residents. 2 mL of blood sample was collected from each individual in precleaned clean polypropylene tubes, and the samples were transported to the laboratory in ice cold conditions [24].

*2.4. Instrumental Analysis*

*2.4.1. Water Samples.* Analyses of physiochemical parameters of water samples including pH, electrical conductivity (EC), dissolved oxygen (DO), and salinity was carried out at the sample collection site, according to the standard procedure of Machado and Bordalo [25], using portable instruments (HI9828, Hanna Instruments, Woonsocket, RI, USA). Alkalinity and chloride ($Cl^-$) concentration was determined by titration methods using the standard procedure [26]. Concentration of sulphate ($SO_4^{-2}$) was determined by electrothermal

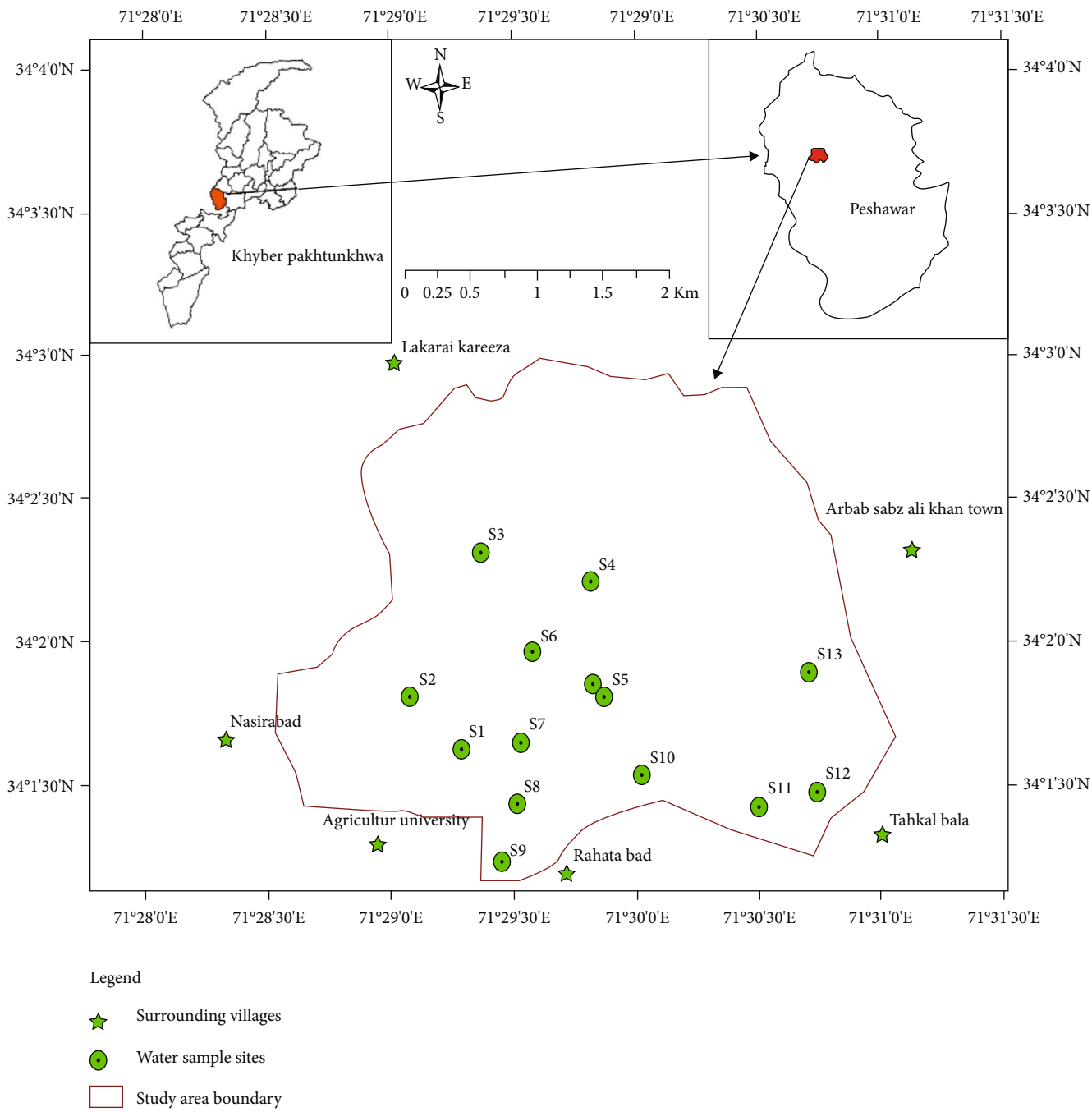


Figure 1: Location map of the study area showing the sampling sites in Peshawar, Pakistan.

atomic ultraviolet spectrophotometer, HACH-2800 [26]. Pb concentration was determined using atomic absorption spectrophotometer (Perkins Elmer-650), at the Centralized Resource Laboratories (CRL), University of Peshawar.

*2.4.2. Blood Samples.* For the determination of Pb concentration in blood samples using atomic absorption spectrophotometry (Perkins Elmer-650), blood and acid mixtures were used in different proportions to optimize the method. Standard reference materials (SRMs, Human blood, Batch 1701-3) were used to check the accuracy and precession of the analysis. Analytical grade concentrated percholric acid and nitric acid was used to wet digest 3 mL of blood sample. Briefly, in a conical flask, blood sample of 3 mL was put and then added percholric acid and nitric acid in 1 : 4 ratio. They were reserved immediately and then warmed at various standard temperatures on hot plates for obtaining a transparent solution. Subsequent to cooling, the extracts were separated and utilized exceedingly purified deionized water for dilution up to a volume of 100 mL [23].

*2.5. Questionnaire Survey.* A questionnaire survey was carried out to find the impacts of contaminated water on public health. The important information collected through

a questionnaire proforma from the local residents ($n = 13$) included their socioeconomic conditions, major diseases, and water supply source-related information such as source of water, depth of well, drainage system, pollution sources, and water treatment facility.

*2.6. Health Risk Assessment*

*2.6.1. Chronic Daily Intake.* Heavy metals and other toxic substances enter our body through various routs including inhalation, dermal contact, and ingestion; among all these exposure pathways, oral intake is the most common [7]. The CDI of contaminants through water intake was calculated using the modified equation of US EPA [27]:

$$\mathrm{CDI} = \mathrm{Cmx}\frac{\mathrm{Ir}}{\mathrm{Bw}}, \quad (1)$$

where CDI is the chronic daily intake, Cm is the metal concentration (mg/L), Ir is the water ingestion rate (2 L/day), and Bw is the weight of the body (66 kg) [6].

*2.6.2. Hazard Quotient (HQ).* Human health risk assessment (HQ) was done using the standard equation reported elsewhere [28]

$$\mathrm{HQ} = \frac{\mathrm{CDI}}{\mathrm{RfD}}, \quad (2)$$

where RfD represents the oral reference dose. The oral toxicity reference dose value (RfD) of Pb is $3.6E - 02$ mg/kg·day according to US EPA database [29]. Exposed population is considered safe when HQ < 1 [6, 28].

*2.7. Statistical Analysis.* All the data was statistically analyzed, and for all the result ranges, mean and standard deviations were calculated using Excel 2010 (Microsoft Office). The location map of the study area was prepared by the Arc geographic information system (Arc GIS).

## 3. Results and Discussion

*3.1. Physical Parameters.* Physiochemical characteristics of the water samples collected from any source, including springs, streams, well, and tube well, give a picture of the quality of water. These parameters can significantly affect the water quality and have a deep relation with environmental pollution and associated health hazards [30]. The levels of various physicochemical parameters of water samples collected from different sources are shown in Figure 2, and their mean concentrations are given in Table 1. Results indicate that the value of pH for all samples occurs in the range of 6.98 to 7.57. The minimum pH value of 6.98 was noted for the sample of tube well, while the maximum value of 7.57 was noted for the sample of open well at Palosai area; the rest of the samples showed no significant difference in pH values (Figure 2). It is clear from the data that the pH values of all the water samples are within the permissible limits according to WHO and Pak-EPA. These results are in agreement with the findings of Ullah et al. [31]. According to Hanipha and Hussain et al. [32], pH can be used as a tool to measure the degree of basicity and acidity of water. Literature shows that pH does not affect human health but indirectly it can affect human health by conferring better taste to drinking water [15] and affecting pathogen survival and solubility of different ions. pH is a good indicator to measure the degree of pollution of drinking water [33].

The levels of dissolved oxygen (DO) in water in different samples were found to be ranging between 3.08 and 3.23 mg/L, and the difference among sampling sites for DO was of slightest significance (Figure 2). The minimum and maximum values were noted for the tube well samples. The values of DO were within the permissible limits 8 mg/L [27]. Level of dissolved oxygen of water plays an important role in supporting aquatic life; it is a main factor in indicating the freshness of an aquatic system [34].

The EC values for different samples showed great variation ranging between 152 and 710 $\mu$S/cm. The maximum value of EC was observed for the sample collected from the tube well at Palosai (Sample S6), whereas the lowest value was noted for the sample of the open well from Palosai (Figure 2). EC is defined as the measure of the conductance of the water sample. Since the ability of electrical conductance depends upon the mobility of ions at a certain temperature, hence, it indicates the concentration of ions in the water sample. In other words, EC of water gives us an idea of total dissolved salts [35]. However, the toxicological effects can be determined from the nature of the ions through chemical analysis.

The values of salinity were found to be ranging from below the detection limit (BDL) to as high as 0.02%. The minimum values noted were for samples of well and tube well in the area, while the maximum value was also for the sample of tube well. Values of salinity determined in the groundwater samples collected from the area show no great variation (Figure 2). All of the physicochemical parameters are influenced upon the nature and concentration of dissolved minerals, which primarily depends upon the geological strata of the area [36]. The above results show that mostly the water samples collected from tube wells are rich in dissolved minerals, which is an indication of the fact that the deep geological strata of the area contain various types of soluble minerals. The value of physical parameters was in agreement with the findings of Giammanco et al. [36] and Neal et al. [37].

*3.2. Chemical Parameters.* Various chemical parameters examined for the water samples collected from different sources of the selected area included alkalinity, hardness, chloride, sulphate, and total dissolved solids (TDS). The results of the chemical parameters are graphically presented in Figure 3, while the mean concentrations of these parameters are shown in Table 2. Results indicated that the values of alkalinity for water samples collected from various sources were ranging between 75.3 and 191.45 mg/L. The data show that in the case of water samples collected from tube wells, the alkalinity was lower, ranging from 75 to 165 mg/L, with a mean value of 120.11, whereas for water samples collected from open wells the alkalinity was higher ranging from 128

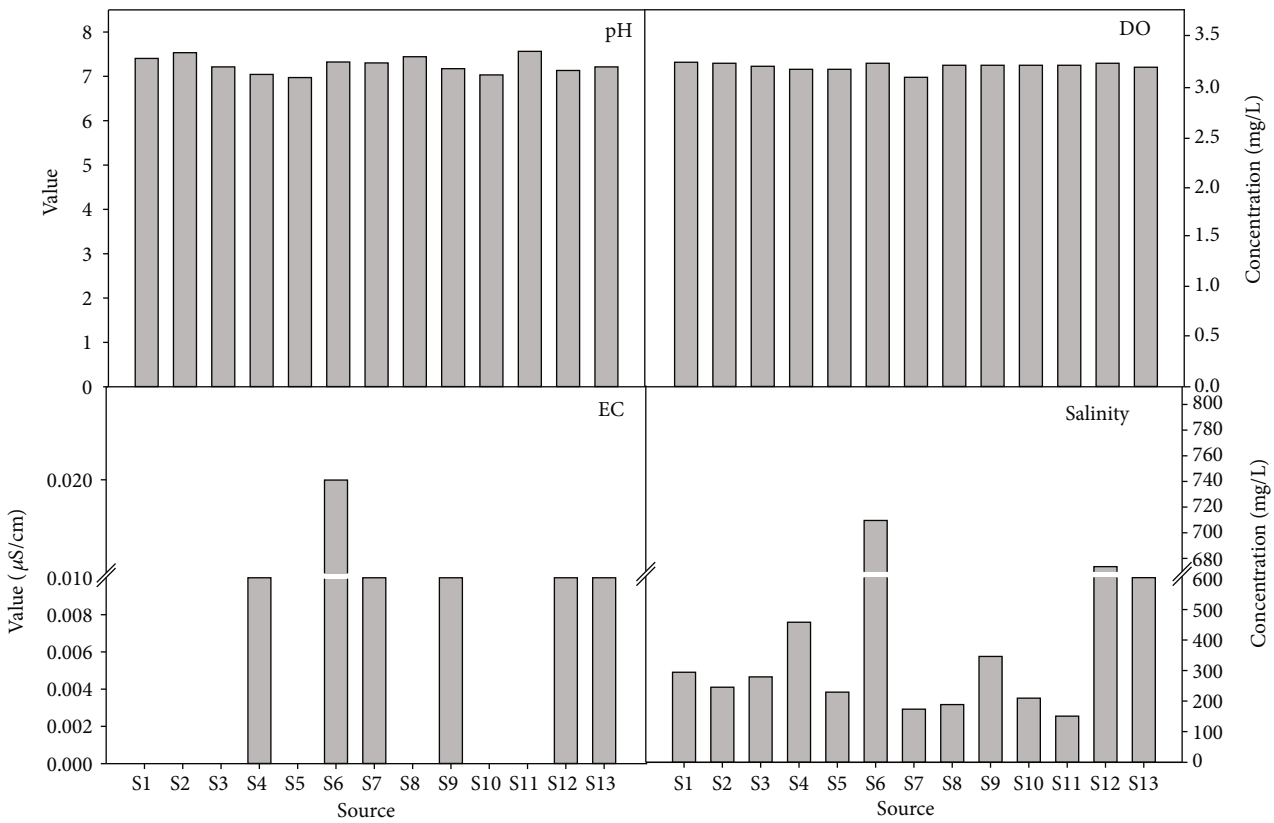


Figure 2: Physical parameters of the different water sources in the study area.

Table 1: Mean concentrations of physical parameters in the groundwater samples.

| Parameters | Tube wells | | Wells | | Pak-EPA[a] | WHO[b] |
|---|---|---|---|---|---|---|
| | Ranges | Mean value | Ranges | Mean values | | |
| pH | 6.98-7.54 | 7.29 | 7.04-7.57 | 7.23 | 6.5-8.5 | 6.5-8.5 |
| DO (mg/L) | 3.08-3.23 | 3.18 | 3.18-3.22 | 3.2 | 4 | 4 |
| EC ($\mu$s/cm) | 175-710 | 323.75 | 152-674 | 398.2 | 1500 | 1500 |
| Salinity (%) | *BDL-0.02 | 0.005 | BDL-0.01 | 0.006 | — | — |

[a]Pakistan Environmental Protection Agency (2008), [b]World Health Organization (2008). *BDL: below detection limit.

to 191 mg/L with a mean value of 157.3. Among the different sites, the alkalinity shows a great variation; at S7 and S8, it has a lower value, while in S11, they show a significant higher value (Figure 3). The alkalinity represents the acid neutralizing capacity of the water sample, which depends upon the concentration of various anionic components of water, i.e., bicarbonate, sulphate, chloride, and carbonate. There is no specific guideline for the permissible limits of alkalinity; however, according to some researchers it is from 50 to 500 mg/L [38]. High alkalinity in drinking water may lead to the formation of kidney stones and irritation of skin and eyes, besides such water can damage the metallic pipes [39].

The values of TDS in water samples of various sources and sites were found to be ranging between 230 and 586 mg/L. Higher TDS values were observed for tube well samples (290-586 mg/L) with mean value of 380 mg/L, whereas for the well sample, TDS values were lower (230-428 mg/L) with a mean value of 291.4 mg/L. The permissible limit for TDS is 1000 mg/L according to WHO guidelines. The water samples with TDS levels higher than the permissible limit are harmful for human health causing damage to kidneys, irritation of gastrointestinal tract, and heart diseases [40]. Higher TDS in the water system increases the chemical and biological oxygen demand and ultimately depletes the dissolved oxygen level in water. TDS of the water sample represents all dissolved organic and inorganic substances; these may include sodium, potassium, calcium, magnesium, manganese, and chloride.

The values of hardness as $CaCO_3$ were ranging between 132.8 and 340 mg/L and except two samples where the hardness was higher than 400 mg/L. In the case of water samples from tube wells, the hardness levels ranged between 130.8 and 471 mg/L with a mean value of 273.9 mg/L, and in the

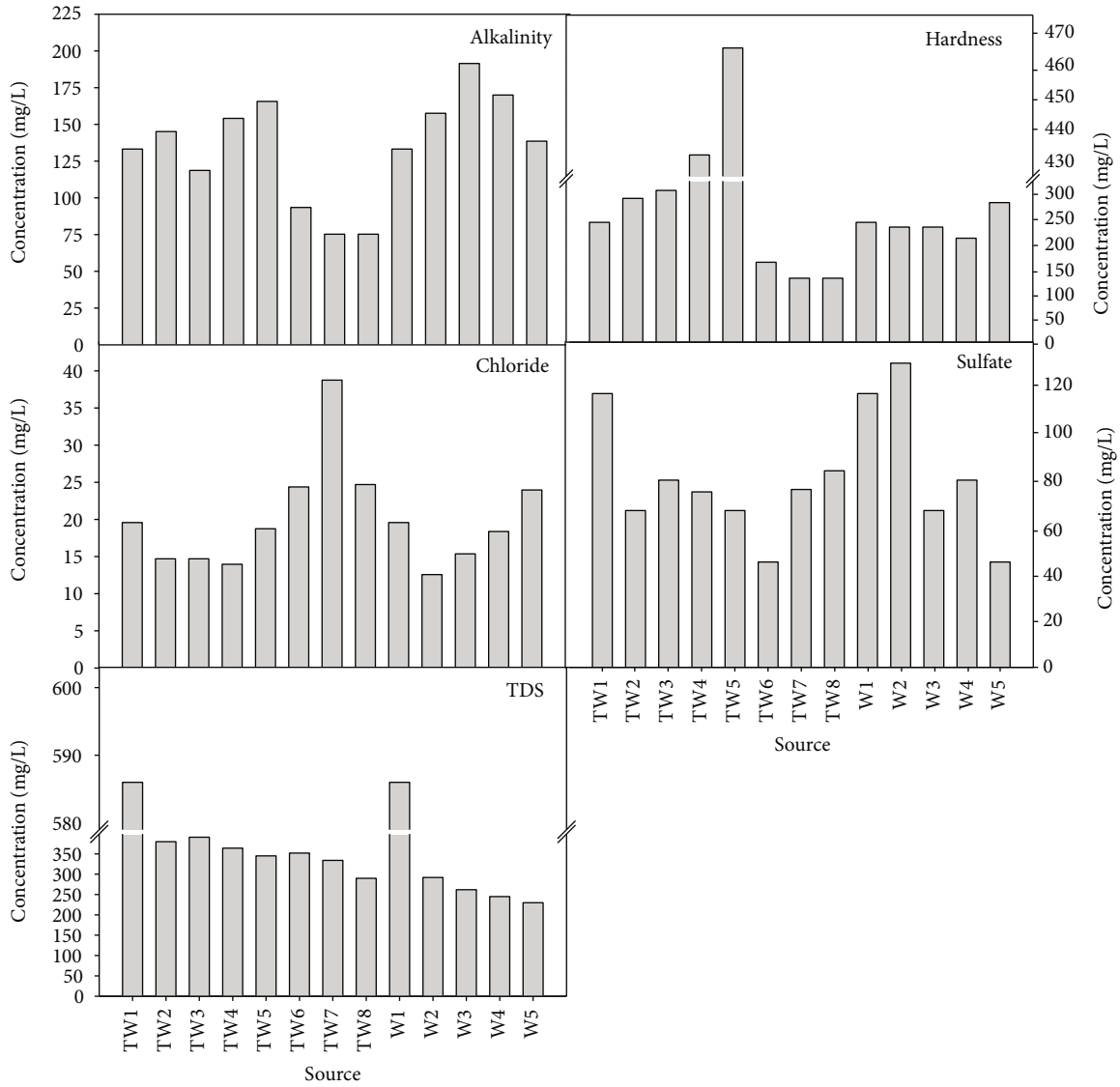


Figure 3: Chemical parameters of different water sources in the study area.

Table 2: Mean concentrations of chemical parameters in the groundwater samples.

| Parameters | Tube wells | | Wells | | Pak-EPA[a] |
|---|---|---|---|---|---|
| | Ranges | Mean values | Ranges | Mean values | |
| Alkalinity (mg/L as $CaCO_3$) | 75.3-165.65 | 120.11 | 128-191.45 | 157.13 | 500 |
| TDS (mg/L) | 290-586 | 380.75 | 230-428 | 291.4 | 1000 |
| Hardness (mg/L as $CaCO_3$) | 132.8-471 | 273.9 | 216-300.4 | 256.88 | 500 |
| Chloride (mg/L) | 13.96-38.75 | 21.18 | 9.7-23.96 | 15.99 | 250 |
| Sulphate (mg/L) | 45-117 | 76.38 | 45-130 | 76.4 | 1000 |

[a]Pakistan Environmental Protection Agency (2008).

case of water from open well, the hardness values were ranging between 216 and 300.4 mg/L with a mean value of 256.88 mg/L (Figure 3). The data shows that on overall basis the hardness level was high in samples collected from open wells, which are relatively shallow compared to tube wells in the case of which the hardness level was lower. Hardness of water is because of the presence of calcium and magnesium ions with bicarbonate, chloride, and sulphate. Most calcium comes in water from lime stone, industrial waste, and leaching from its minerals in rocks. Hardness of water causes no major harm to human health but may create digestive disorders. Results of hardness in the groundwater

of the selected area were in consistence with the finding of Ullah et al. [41] at Konhaye Stream, Lower Dir (131 mg/L).

The level of chloride in water samples ranged between 9.7 and 38.75 mg/L and was within the permissible limits shown by Pak-EPA (250 mg/L). The maximum value of 38.75 mg/L and a minimum value of 9.57 mg/L were noted in the sample of tube well and well in the area, respectively. As for the concentration of chloride is concerned, it shows significant variation among the samples of various sites, the highest values were observed at S7 while the lowest value at S10 (Figure 3). Higher value of chloride is an indicator of pollution (Rakesh 2012). Chloride concentration in water increases due to domestic waste and industrial effluents. Soil permeability and porosity play a key role in building up the chloride concentration [42]. Chloride values higher than the acceptable limits harm metallic pipes and agricultural crops. It can also cause kidney and heart diseases in human [43]. Similarly, the concentration of sulphate was observed to be in the range of 45 to 130 mg/L. The results show that the water samples of the well contain high sulphate concentration compared to the tube well in the Palosai area. The highest values were observed at S6 and S13 while the lowest value at S10 (Figure 3).

*3.3. Lead Concentration in Groundwater.* Lead is a toxic element distributed worldwide which is continuously added to the environment in large amounts as a result of anthropogenic activities [44]. The results of Pb concentration determined in groundwater samples are given in Table 3. The data shows that in all the water samples collected from tube wells of different sites, the concentration of lead occurs in the range of 0.022-0.067 mg/L, whereas in the case of samples of open wells the lead was found to be in the range of 0.004-0.015 mg/L. According to WHO and Pak-EPA, the permissible limit for lead in water is 0.05 mg/L; this shows that in the case of tube wells at few sites, the lead concentration exceeds the permissible limit. Hence, the water of the open wells is safe for health whereas that of tube wells poses a potential health risk due to excess of lead (Figure 4). The major uses of Pb include radioactive emissions and making safety shields from X-rays and other radiations. Pb is found everywhere like other contaminants and can occur as inorganic ions, salts, and metallic lead [45]. Pb has no vital role in the human body. The most common routes for intake of Pb include drinking water, food, and air. Plant absorbs Pb from soil, and thus, Pb enters the food chain and finally finds its way to the human body. The use of lead-based pottery glazes is also a source of ingestion of lead [46]. Generally, ingestion accounts for 5 to 15% of lead intake while 20 to 50% through inhalation, whereby inorganic lead is absorbed [47]. Pb is distributed among mineralizing tissue, soft tissue, and blood [46]. Pb is the most toxic and hazardous metal found in the environment. Pb toxicity has more effects on children compared to adults and may cause memory problems, behavioral disturbances, and anemia. Lead may also some time cause toxic effects like headache, hypertension, abdominal pain, irritability, kidney damage, stomach cancer, lung cancer, and nerve damage [48]. The present study and some of the earlier studies show that drinking water sources contaminated chemically and with other heavy metals are the main causes of health risk to human [6, 8–10, 15]. In the study area, Pb concentrations in water were observed lower than those reported in drinking water by Muhammad et al. [6] from the Kohistan region, Pakistan.

Table 3: Lead concentrations (mg/L) in the groundwater samples.

| Samples | Mean | Range | SD± | [a]Pak-EPA | [b]WHO |
|---|---|---|---|---|---|
| Tube wells | 0.039 | 0.022-0.067 | 0.00 | 0.05 | 0.05 |
| Wells | 0.004 | 0.004-0.015 | 0.01 | | |

[a]Pakistan Environmental Protection Agency (2008), [b]World Health Organization (2008); SD: std. deviation.

*3.4. Distribution of Lead in the Blood Samples.* The levels of Pb in human blood samples from Palosai area were determined. Pb concentrations ($\mu$g/L) in blood samples collected from peoples of different age groups of Peshawar are given in Table 4. From Table 4, it is clear that the mean concentration of Pb in blood samples of children were 0.01 $\mu$g/L for both males and females. In adolescent, mean concentration of Pb was 0.05 $\mu$g/L in males and 0.03 $\mu$g/L, in female. In adults, the mean concentrations of Pb were 0.10 $\mu$g/L in males and 0.06 $\mu$g/L in females. While in old age peoples, the mean concentration of Pb in blood was 0.16 $\mu$g/L in males and 0.10 $\mu$g/L in females. Overall concentration of Pb was higher in males compared to female; this may be attributed to body mass, diet habits, and some other factors related to the male community. In the study area, Pb concentration in blood samples of all the inhabitants was lower than the permissible levels [49]. However, on the overall basis, the above results reveal that the Pb concentration in the blood of old individuals is higher compared to children and adolescent, and this may be because of the slow accumulation of Pb in the body of old individuals over time. The cause of the Pb detected in the blood of human in the Palosai area may be associated to bioaccumulation from consumption of water from the tube well. The value of Pb of Palosai area determined in blood was in agreement with the result of Jan et al. [50]. The trace and heavy elements (i.e., Ni, Cr, Pb, Cu, Co, Fe, and Cd) in the waters of Peshawar area are within the acceptable concentration but Ni, Fe, Cr, and Pb concentrations are too high in certain areas which are a threat to people health. The possible source of contaminations in the area is both geogenic and anthropogenic sources. Industrial estates waste, underground pipes corrosion, and tannery industries are the anthropogenic sources, while ultramafic and mafic rocks in the northeast and northwest and sulphide seams are the geogenic sources of contamination [51]. Inam Ullah and Alam [52] collected groundwater samples from Peshawar in which the Pb and Mn quantities (2.97 and 8.26 mg/L) were high. These concentrations were high because of lack of awareness, lack of treatment facilities, lack of regulation of waste disposal, and mismanagement in the infrastructure of water distribution [52].

The use of plumbing materials and substandard pipes is one of the professed reasons for Pb contamination in the

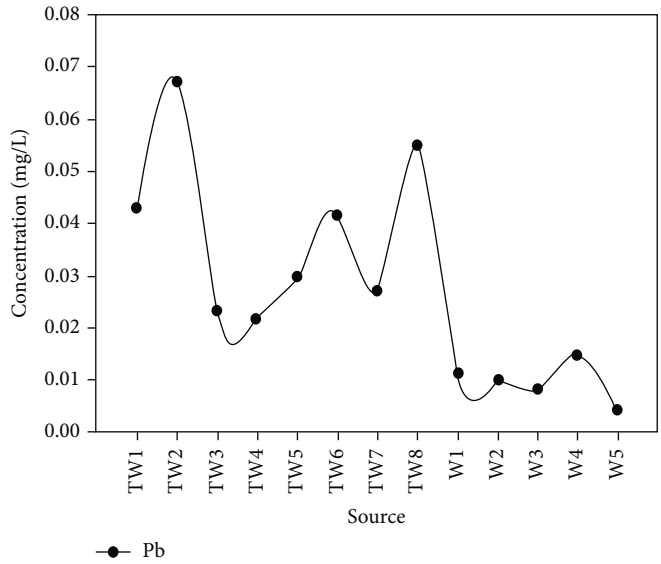


Figure 4: Pb concentrations of different water sources in the study area.

Table 4: Lead concentrations ($\mu$g/L) in the human blood of different age groups of people.

| Mean | Range | SD± | Mean | Range | SD± |
|---|---|---|---|---|---|
| Children (male), $n = 10$ | | | | Children (female), $n = 10$ | |
| 0.01 | 0.00-0.06 | 0.00 | 0.01 | 0.00-0.35 | 0.00 |
| Adolescent (male), $n = 10$ | | | | Adolescent (female), $n = 10$ | |
| 0.05 | 0.00-0.16 | 0.00 | 0.03 | 0.00-0.14 | 0.00 |
| Adults (male), $n = 10$ | | | | Adults (female), $n = 10$ | |
| 0.1 | 0.00-0.20 | 0.00 | 0.06 | 0.00-0.64 | 0.00 |
| Old age (male), $n = 10$ | | | | Old age (female), $n = 10$ | |
| 0.16 | 0.00-0.32 | 0.00 | 0.1 | 0.00-0.10 | 0.00 |

$n$: number of samples; SD±: standard deviation.

area. Under various climatic conditions, substandard pipes and uncovered water delivery systems are prone to corrosion. Quinn and Sherlock [16] stated that Pb is an essential part of plumbing materials. Pb in very small concentrations is found in natural water. Concentrations of Pb occur in home pipes or water distribution system. Thus, it can be concluded from the current study that at household levels, the pollution of Pb concentration is more because the water carries Pb through other distribution installations and pipes to the households.

*3.5. Chronic Daily Intake (CDI) Indices and Hazard Quotient (HQ).* CDI and HQ values for lead in water samples of both tube wells and wells were calculated. Results are shown in Table 5 for groundwater consumption. The CDI and HQ values of tube wells ranged from 0.01 to 0.002 $\mu$g/kg·day and $2.5E-02$ to $5.00E-02$ mg/kg·day for Pb, respectively. However, the CDI and HQ values were negligible for wells.

In the environment, e.g., water, soil, and atmosphere, Pb is found at various concentrations. Pb is found in food as residues due to their occurrence in the environment, as a result of anthropogenic activities such as from contamination during storage and processing of food, car exhaust, industry, or farming. Human are exposed to Pb by ingesting contaminated water or food or from the environment. Harmful effects are caused over time in the human body due to their accumulation [53]. Food contains metals such as Ca, Mg, K, Na, B, Fe, Se, Zn, and Cu. These metals are required in trace quantities for cellular processes maintenance. Other metals can be harmful found in the body if regularly consumed in the diet. In the earth's crust, most of the metals are found. Other elements and metals as a result of anthropogenic activities such as agricultural or industrial processes can enter food or occur in food naturally. Metals can exist chemically as pure, e.g., Pb or Sn or compounds formed by the combination of a nonmetallic element with a metallic element, e.g., chlorine in combination with sodium giving sodium chloride salt or an oxide giving by oxygen [54].

Pb, As, Cd, Hg, and Sn cause harmful effects in the body and are of major concern. Pb and Hg due to high atomic weight are considered as "heavy metals." Uranium and chromium are also found in water or food as contaminants and are potentially toxic. In the workplace, individuals are often

Table 5: Chronic daily intake (CDI) and hazard quotient (HQ) of Pb through ground water consumption.

| Chromic risk assessment | Tube wells | | Wells | |
|---|---|---|---|---|
| | Ranges | Mean | Ranges | Mean |
| CDI[c] (mg/kg-day) | 0.01-0.002 | 0.001 | BDL | BDL |
| HQ[d] (mg/kg-day) | $2.5E-02-5.00E-02$ | $2.80E-02$ | BDL | BDL |

[c]Chronic daily intake. [d]Hazard quotient.

Table 6: Disease wise representation of different age group below 18 years old.

| S. no. | Family strength | Under eighteen | Nervous system and kidney damage | Learning disabilities | Speech, language and behavior problems | Poor muscle coordination | Decreased muscle and bone growth | Hearing damage |
|---|---|---|---|---|---|---|---|---|
| 1 | 19 | 6 | No | Yes | No | No | No | Yes |
| 2 | 10 | 5 | No | No | No | No | No | No |
| 3 | 12 | 4 | No | No | No | No | No | No |
| 4 | 9 | 4 | No | No | No | No | No | No |
| 5 | 10 | 3 | No | No | No | No | No | No |
| 6 | 13 | 0 | No | No | No | No | No | No |
| 7 | 12 | 0 | No | No | No | No | No | No |
| 8 | 16 | 6 | No | Yes | No | No | No | No |
| 9 | 28 | 5 | No | Yes | No | No | No | No |
| 10 | 20 | 7 | No | Yes | No | No | No | No |
| 11 | 12 | 4 | No | Yes | No | No | No | No |
| 12 | 8 | 3 | No | Yes | No | No | No | No |
| 13 | 8 | 3 | No | Yes | No | No | No | No |

exposed to metals such as nickel and beryllium, which causes harmful effects in their body. The damaging effects of the latter group of metals are usually associated with metal dust inhalation, causing injury to the lung, and are not found in food at concentrations that could cause toxicity [55].

Exposure of children to Pb can affect children's behavior and development. Blood having Pb levels 0.1 mg/L are associated with delayed puberty, postnatal height or growth, cognitive performance, decreases in hearing, and increased behavioral effects. Blood having Pb levels less than 0.05 mg/L, including decreased academic achievement, increases in both attention related behaviors and behavioral problems, and lower IQ scores [56]. A number of health problems are caused in adults when exposed to Pb. As a common rule, the more health problems you will have, the more Pb you have in your body. Blood having high Pb levels greater than 0.15 mg/L are linked with decreased kidney function, nerve disorders, cardiovascular effects, and fertility problems, including delayed conception and adverse effects on semen and sperm, such as lower sperm motility and counts. Pb levels below 0.1 mg/L in blood are associated with hypertension, decreased kidney function, and incidence of essential tremor. There is also evidence of decreased kidney function in adults having a blood Pb levels less than 0.15 mg/L. Particularly, pregnant women require being careful about lead. Less than 0.05 mg/L of Pb in maternal blood is associated with reduced fetal growth [57]. Renal system, nervous system, and blood forming system are most sensitive to lead. Enzymatic systems in children are inhabited when the Pb levels are from 0.008 to 0.01 mg/L [58].

*3.6. Questionnaire Survey.* The information about the health problems commonly associated with Pb intake was collected through a questionnaire survey from the local residents of the area; summary of the data is presented in Tables 6 and 7. The tables represent two different age groups, i.e., age group below 18 years and above 18 years of peoples of Peshawar. Pb causes different diseases in young and adult peoples. Pb effect varies in both of these groups; it affects young children (under eighteen) more compared to adult peoples (above eighteen). In the study area, the diseases which were common in young individuals were learning disabilities and some with hearing damage, while no such problems were found in young individuals. As far as the adults were concerned, all had high blood pressure, muscle and joint pain, digestive problems, and some have memory and concentration problems. It is clear from the above table that the diseases caused by Pb were more in adults compared to young individuals. It is because of the chronic exposure of young individuals to Pb that accumulate in their body and show late effects on their body.

In the study area, majority of the population has low income level and they are residing in small villages. The people have no excess to pure and clean drinking water. The major sources from which the locals get their drinking water are tube well and well; however, the tube wells and their

Table 7: Disease wise representation of different age groups above 18 years olds.

| S. no. | Family strength | Above eighteen | High blood pressure | Muscle and joint pain | Digestive problems | Nerve disorders | Memory and concentration problems | Damage to sperm-producing organs in men | Cataracts |
|---|---|---|---|---|---|---|---|---|---|
| 1 | 19 | 13 | Yes | No | Yes | No | Yes | No | No |
| 2 | 10 | 5 | Yes | No | Yes | No | No | No | No |
| 3 | 12 | 8 | Yes | Yes | Yes | No | No | No | No |
| 4 | 9 | 5 | Yes | No | Yes | No | No | No | No |
| 5 | 10 | 7 | Yes | No | Yes | No | No | No | No |
| 6 | 13 | 13 | Yes | No | Yes | No | No | No | No |
| 7 | 12 | 12 | Yes | No | Yes | No | No | No | No |
| 8 | 16 | 10 | Yes | No | Yes | No | No | No | No |
| 9 | 28 | 23 | Yes | No | Yes | No | No | No | No |
| 10 | 20 | 13 | Yes | Yes | Yes | No | No | No | No |
| 11 | 12 | 8 | Yes | Yes | Yes | No | No | No | No |
| 12 | 8 | 5 | Yes | Yes | Yes | No | No | No | No |
| 13 | 8 | 5 | Yes | Yes | Yes | No | No | No | No |

ability to provide water to the households are in a very low quantity because of miss management. Because of the very low education level and due to lack of awareness, people are of the opinion that groundwater is safe. Some people even think that water lying below the gravel (underground rocks) is free from contamination. Therefore, they do not feel the need of any type of treatment for their groundwaters. The majority of the population is of low-income class and also the government and is not spending much in the field of safe drinking water provision to the community, and so, the bad transportation condition of water supply is leading to so many problems. Ilyas et al. [1] determined the heavy metals including lead (Pb), chromium (Cr), nickel (Ni), and zinc (Zn) in drinking water in the selected area of Lower Dir, Pakistan. The heavy metal results showed that all the metals were within the permissible limit except Cr (0.18 mg/L) and Pb (0.04 mg/L).

## 4. Conclusion

In this study, the groundwater quality and associated health risks was carried out in Palosai area, Peshawar, Khyber Pakhtunkhwa, Pakistan. The groundwater samples were analyzed for physicochemical parameters based on standard guidelines. Results revealed that the physiochemical parameters were within the permissible limits. Pb result shows that in the case of tube wells at few sites the lead concentration exceeds the permissible limits. It can be concluded from the current study that consumption of groundwater increases the concentration of lead in the blood of human. However, the overall HQ values of Pb in the groundwater were less than 1, indicating no health risk to the local depending community.

## 5. Recommendations

Provision of clean and safe water for domestic purposes, banning of water from contaminated sites, treatment of rural and wastewater, and good transportation condition of drinking water supply in the study area are recommended.

## Data Availability

All relevant data are included in the paper.

## Conflicts of Interest

The authors state no conflict of interest.

## Acknowledgments

The authors acknowledge the funding offered by the University of Peshawar, Khyber Pakhtunkhwa, Pakistan.

## References

[1] M. Ilyas, S. Khan, A. Khan, R. Amin, A. Khan, and M. Aamir, "Analysis of drinking water quality and health risk assessment-a case study of Dir Pakistan," *Journal of Himalayan Earth Sciences*, vol. 50, pp. 100–110, 2017.

[2] M. Ilyas, W. Ahmad, H. Khan, S. Yousaf, M. Yasir, and A. Khan, "Environmental and health impacts of industrial wastewater effluents in Pakistan: a review," *Reviews on Environmental Health*, vol. 34, no. 2, pp. 171–186, 2019.

[3] S. Yousaf, M. Shakil, A. Khan et al., "Seasonal characterization and potential human health risk of heavy metals contamination in sediments of the river Jindi," *Pakistan. Journal of Himalayan Earth Science*, vol. 53, no. 1, 2020.

[4] L. Petraccia, G. Liberati, S. G. Masciullo, M. Grassi, and A. Fraioli, "Water, mineral waters and health," *Clinical Nutrition*, vol. 25, no. 3, pp. 377–385, 2006.

[5] M. Ilyas, W. Ahmad, H. Khan, and S. Yousaf, "Potentially poisonous elements removal from vehicle-wash wastewater and aqueous solutions using composite adsorbents," *Desalination and Water Treatment*, vol. 224, pp. 331–342, 2021.

[6] S. Muhammad, M. T. Shah, and S. Khan, "Health risk assessment of heavy metals and their source apportionment in

drinking water of Kohistan region, northern Pakistan," *Microchemical Journal*, vol. 98, no. 2, pp. 334–343, 2011.

[7] ATSDR, *Agency for toxic substances disease registry toxicological profile for arsenic*, U.S. Department of Health & Human Services, Atlanta, Georgia, 2000.

[8] M. T. Shah, J. Ara, S. Muhammad, S. Khan, and S. Tariq, "Health risk assessment via surface water and sub-surface water consumption in the mafic and ultramafic terrain, Mohmand agency, northern Pakistan," *Journal of Geochemical Exploration*, vol. 118, pp. 60–67, 2012.

[9] S. Khan, M. Shahnaz, N. Jehan, S. Rehman, M. T. Shah, and I. Din, "Drinking water quality and human health risk in Charsadda district, Pakistan," *Journal of Cleaner Production*, vol. 60, pp. 93–101, 2013.

[10] K. Khan, Y. S. Lu, A. A. Khan, L. Wei, and T. Wang, "Health risks associated with heavy metals in the drinking water of Swat, northern Pakistan," *Journal of Environmental Sciences*, vol. 25, no. 10, pp. 2003–2013, 2013.

[11] M. S. Islam, M. K. Ahmed, M. Raknuzzaman, M. Habibullah-Al-Mamun, and M. K. Islam, "Heavy metal pollution in surface water and sediment: a preliminary assessment of an urban river in a developing country," *Ecological Indicators*, vol. 48, pp. 282–291, 2015.

[12] S. G. Donaldson, J. Van Oostdam, C. Tikhonov et al., "Environmental contaminants and human health in the Canadian Arctic," *Science of the Total Environment*, vol. 408, no. 22, pp. 5165–5234, 2010.

[13] G. Goyer, *Issue paper on the human health effects of metals*, US Environmental Protection Agency, Risk Assessment Forum, Washington, DC, USA, 2004.

[14] WHO, "World Health Organization guidelines for drinking water quality," in *Recommendations, vol 1.*, WHO, Geneva, Switzerland, 4th edition, 2011.

[15] S. Muhammad, M. T. Shah, and S. Khan, "Arsenic health risk assessment in drinking water and source apportionment using multivariate statistical techniques in Kohistan region, northern Pakistan," *Food and Chemical Toxicology*, vol. 48, no. 10, pp. 2855–2864, 2010.

[16] M. J. Quinn and J. C. Sherlock, "The correspondence between U.K. 'action levels' for lead in blood and in water," *Food Additives and Contaminants*, vol. 7, no. 3, pp. 387–424, 1990.

[17] M. R. Schock, "Causes of temporal variability of lead in domestic plumbing systems," *Environmental Monitoring and Assessment*, vol. 15, no. 1, pp. 59–82, 1990.

[18] S. E. Spayd, M. G. Robson, R. Xie, and B. T. Buckley, "Importance of arsenic speciation in populations exposed to arsenic in drinking water," *Human and Ecological Risk Assessment*, vol. 18, no. 6, pp. 1271–1291, 2012.

[19] S. H. Frisbie, R. Ortega, D. M. Maynard, and B. Sarkar, "The concentrations of arsenic and other toxic elements in Bangladesh's drinking water," *Environmental Health Perspectives*, vol. 110, no. 11, pp. 1147–1153, 2002.

[20] S. Giri, M. K. Mahato, G. Singh, and V. N. Jha, "Risk assessment due to intake of heavy metals through the ingestion of groundwater around two proposed uranium mining areas in Jharkhand, India," *Environmental Monitoring and Assessment*, vol. 184, no. 3, pp. 1351–1358, 2012.

[21] A. Kumar, R. Vij, M. Gupta, S. Sharma, and S. Singh, "Risk assessment of exposure to radon concentration and heavy metal analysis in drinking water samples in some areas of Jammu & Kashmir, India," *Journal of Radioanalytical and Nuclear Chemistry*, vol. 304, no. 3, pp. 1009–1016, 2015.

[22] D. N. Ali, *District health profile (District Peshawar)*, P. Pakistan Initiative for Mothers and Newborns Islamabad o. Document Number, 2009.

[23] F. A. Jan, M. Ishaq, S. Khan et al., "Bioaccumulation of metals in human blood in industrially contaminated area," *Journal of Environmental Sciences (China)*, vol. 23, no. 12, pp. 2069–2077, 2011.

[24] K. Khan, H. Khan, Y. Lu et al., "Evaluation of toxicological risk of foodstuffs contaminated with heavy metals in Swat, Pakistan," *Ecotoxicology and Environmental Safety*, vol. 108, no. 1, pp. 224–232, 2014.

[25] A. Machado and A. A. Bordalo, "Analysis of the bacterial community composition in acidic well water used for drinking in Guinea-Bissau, West Africa," *Journal of Environmental Sciences*, vol. 26, no. 8, pp. 1605–1614, 2014.

[26] APHA, *Standard Methods for the Examination of Water and Wastewater*, American Public Health Association and Water Environmental Foundation EPS Group, Inc., Maryland, USA, 18th ed. edition, 1992.

[27] USEPA (US Environmental Protection Agency), "United States Environmental Protection Agency, Arsenic, inorganic integrated risk information system (IRIS), (CASRN 7440–38–2)," 1998, http://www.epa.gov/iris/subst/0278.htm.

[28] S. Khan, Q. Cao, Y. M. Zheng, Y. Z. Huang, and Y. G. Zhu, "Health risks of heavy metals in contaminated soils and food crops irrigated with wastewater in Beijing, China," *Environmental Pollution*, vol. 152, no. 3, pp. 686–692, 2008.

[29] USEPA (US Environmental Protection Agency), *Guidelines for carcinogen risk assessment. EPA/630/P-03/001F.*, Risk Assessment Forum, Washington, DC, USA, 2005.

[30] A. Mora, A. C. Mac-Quhae, M. Calzadilla, and L. Sanchez, "Survey of trace metals in drinking water supplied to rural populations in the eastern Llanos of Venezuela," *Journal of Environmental Management*, vol. 90, no. 2, pp. 752–759, 2009.

[31] H. Ullah, I. Khan, and I. Ullah, "Impact of sewage contaminated water on soil, vegetables, and underground water of peri-urban Peshawar, Pakistan," *Environmental Monitoring and Assessment*, vol. 184, no. 10, pp. 6411–6421, 2012.

[32] M. M. Hanipha and Z. A. Hussain, "Study of ground water quality at Dindigul town, Tamilnadu, India," *International Research Journal of Environment Sciences*, vol. 2, no. 1, pp. 68–73, 2013.

[33] S. B. Jonnalagadda and G. Mhere, "Water quality of the Odzi River in the eastern highlands of Zimbabwe," *Water Research*, vol. 35, no. 10, pp. 2371–2376, 2001.

[34] S. O. Fakayode, "Impact assessment of industrial effluent on water quality of the receiving Alaro in Ibandan, Nigeria," *Ajeam-Ragee*, vol. 10, pp. 1–13, 2005.

[35] WHO, *Guidelines for drinking-water quality. Vol. 2*, Health criteria and other supporting information, World Health Organization, Geneva, 1995.

[36] S. Giammanco, M. Ottaviani, M. Valenza et al., "Major and trace elements geochemistry in the ground waters of a volcanic area: Mount Etna (Sicily, Italy)," *Water Research*, vol. 32, no. 1, pp. 19–30, 1998.

[37] C. Neal, W. A. House, H. P. Jarvie, M. Neal, L. Hill, and H. Wickham, "Phosphorus concentrations in the River Dun, the Kennet and Avon Canal and the River Kennet, southern England," *Science of the Total Environment*, vol. 344, no. 1-3, pp. 107–128, 2005.

[38] M. Jaffar, M. Ashraf, and M. Saleem, "A comparative study of physico-chemical parameters and trace metal contents of holy water zamzam and local potable as well as hot spring waters," *Pakistan Journal of Scientific and Industrial Research*, vol. 30, no. 3, 1986.

[39] G. R. Chhatwal, T. Katyal, M. Katlyal, M. C. Mehra, M. Satake, and T. Nagahiro, *Environmental Water Pollution and Control*, Anmol Publications, New Delh, 1989.

[40] C. K. Jain, C. P. Kumar, and M. K. Sharma, "Ground water qualities th of Ghataprabha command area Karnataka," *Indian Journal of Environment and Ecoplanning*, vol. 7, no. 2, pp. 251–262, 2003.

[41] S. Ullah, N. Ullah, K. Rahman, T. M. Khan, M. A. Jadoon, and T. Ahmad, "Study on physicochemical characterization of Konhaye Stream District Dir Lower, Khyber Pakhtunkhwa Pakistan," *World Journal of Fish and Marine Sciences*, vol. 6, no. 5, pp. 461–470, 2014.

[42] C. K. Jain, K. K. Bhatio, and S. R. Kumar, "Ground water quality in Malaprabha sub-basin Karnataka," *International Journal of Environmental Protection*, vol. 23, no. 3, pp. 321–329, 2005.

[43] A. D. Chapolikar and M. B. Ubale, "A correlation study on physico- chemical characteristics of ground water in Thane-Belapur industrial area, Mumbai," *Current World Environment*, vol. 5, no. 1, pp. 67–71, 2010.

[44] J. Oehlenschläger, "Identifying heavy metals in fish In," in *Safety and Quality Issues in Fish Processing*, H. A. Bremner, Ed., pp. 95–113, Woodhead Publishing Limited, Cambridge, 2002.

[45] N. Harrison, "Inorganic contaminantsin food," in *In: Food Chemical Safety Contaminants*, D. H. Watson, Ed., pp. 148–168, Woodhead Publishing, Cambridge, 2001.

[46] Y. Ming-Ho, *Environmental Toxicology: Biological and Health Effects of Pollutants, Chap. 12*, CRC Press LLC, Boca Raton, USA, 2nd Edition edition, 2005.

[47] A. Ara and J. A. Usmani, "Lead toxicity: a review," *Interdisciplinary toxicology*, vol. 8, no. 2, pp. 55–64, 2015.

[48] K. Steenland and P. Boffetta, "Lead and cancer in humans: where are we now?," *American Journal of Industrial Medicine*, vol. 38, no. 3, pp. 295–299, 2000.

[49] WHO, *Trace elements in human nutrition and health*, World Health Organization, Geneva, Switzerland, 1996.

[50] F. A. Jan, M. Ishaq, S. Khan, I. Ihsanullah, I. Ahmad, and M. Shakirullah, "A comparative study of human health risks via consumption of food crops grown on wastewater irrigated soil (Peshawar) and relatively clean water irrigated soil (lower Dir)," *Journal of Hazardous Materials*, vol. 179, no. 1-3, pp. 612–621, 2010.

[51] S. Nasreen, *Monitoring of surface water ground water air and soil in Peshawar basin against time the 3rd dimension*, Higher Education commission Pakistan, 2006.

[52] E. Inam Ullah and A. Alam, "Assessment of drinking water quality in Peshawar, Pakistan," *Bulgarian Journal of Agricultural Science*, vol. 20, no. 3, pp. 595–600, 2014.

[53] M. R. Moore, "Prenatal exposure to lead and mental retardation," in *Low Level Lead Exposure: The Clinical Implications of Current Research*, H. L. Needleman, Ed., pp. 53–65, Raven Press, New York, 1980.

[54] W. Yule and R. Landsdown, "Lead and children's development: recent findings," in *Heavy Metals in the Environment*, pp. 912–916, CEP Consultants Ltd, Edinburgh, Heidelberg, 1983.

[55] H. Hussein, S. Farag, K. Kandil, and H. Moawad, "Tolerance and uptake of heavy metals by _Pseudomonads_," *Process Biochemistry*, vol. 40, no. 2, pp. 955–961, 2005.

[56] F. W. Alexander, H. T. Delves, and B. E. Clayton, "The uptake and excretion by children of lead and other contaminants," in *Environmental Health Aspects of Lead. Commission of the European Communities Directorate General for Dissemination of Knowledge Centre for Information and Documentation*, pp. 319–330, Luxembourg, 1973.

[57] J. Lin-Fu, *Lead poisoning and undue lead exposure in. Children: History and Current Status*, Raven Press, New York, 1980.

[58] H. S. Peavy, D. R. Rowe, and G. Tchobanoglous, *Environmental Engineering*, 1985.

Hindawi
Adsorption Science & Technology
Volume 2022, Article ID 7138770, 13 pages
https://doi.org/10.1155/2022/7138770

*Research Article*

# Synthesis and Characterization of New Catalysts Grains Based on Iron(Oxy)Hydroxides supported on Zirconium for the Degradation of 4-Nitrophenol in Aqueous Solution

**Hafsa Loumi,[1,2] Faiza Zermane,[1,2] Benamar Cheknane,[1,2] Naima Bouchenafa,[1] Omar Bouras,[2] and Adrián Bonilla-Petriciolet[3]**

[1]*Laboratoire Chimie Physique Des Interfaces Des Matériaux Appliqués à l'Environnement, Département de Génie Des Procédés, Université Saad Dahlab Blida 1, 09000 Blida, Algeria*
[2]*Laboratoire Eau Environnement et Développement Durable, Département de Génie Des Procédés, Université Saad Dahlab Blida 1, 09000 Blida, Algeria*
[3]*Instituto Tecnológico de Aguascalientes, Aguascalientes 20256, Mexico*

Correspondence should be addressed to Adrián Bonilla-Petriciolet; petriciolet@hotmail.com

Received 22 December 2021; Revised 21 January 2022; Accepted 21 April 2022; Published 14 May 2022

Academic Editor: Hesham Hamad



This study reports the preparation of catalyst grains based on oxyhydroxides of iron and zirconium via the coprecipitation method and their application in the degradation of 4-nitrophenol. The morphology, microstructure, and surface composition of these catalysts were characterized by scanning electron microscopy, X-ray diffraction, nitrogen physisorption, and Fourier transform infrared spectroscopy. The catalytic activity of the grains was assessed in the degradation of 4-nitrophenol in a heterogeneous system at different operating conditions. Degradation rates up to 93% were obtained after 4 h of contact time where the catalytic activity of tested materials was higher at pH 7 than in acidic and basic conditions. Amorphous iron hydroxide with a ratio of 75% Zr+25%Fe showed the best catalytic properties. These novel materials are an interesting alternative for facing the water pollution caused by organic compounds.

## 1. Introduction

The environment has been impacted seriously by a variety of pollutants generated by both anthropogenic and geogenic sources [1]. In particular, the presence of organic matter from the discharge of untreated industrial wastewaters is an important source of environmental pollution. 4-Nitrophenol (4-NP) is an organic pollutant commonly found in wastewaters and contaminated soils [2]. It is used as a chemical intermediate for the preparation of insecticides (e.g., methyl parathion), the production of azo and sulfur dyes, rubber chemicals, lumber preservatives, and other industrial applications [3]. This phenolic compound is considered toxic and harmful for human health [4]. Literature indicates that the chronic exposure to this and other phenolic compounds can be associated to several health problems such as impairment of pancreas, liver and kidney and can also cause the paralysis of the central nervous system [5, 6]. The Environmental Protection Agency of United States (US-EPA) has classified 4-NP in the first category of dangerous products that pollutes the environment through the improper disposal of industrial and agricultural wastewaters thus affecting the soils and water sources and generating the conditions for its accumulation in the food chain [7].

Phenolic compounds in wastewaters can be removed by various physical and chemical techniques [8, 9]. Therefore, the complete degradation and/or mineralization of these chemicals via effective and low-cost processes is a challenging task [10–14]. The treatment of water polluted by organic compounds via oxidation processes is an effective and low cost solution. These oxidation processes utilize catalyst to improve the degradation performance [15]. In particular,

heterogeneous catalysts can be employed in the removal of organic compounds. These materials not only preserve the activity and selectivity offered by homogeneous catalysts but also allow their facile recovery and reuse in subsequent oxidation processes [15].

Several studies showed that a variety of heterogeneous catalysts can be utilized for the degradation of organic compounds in wastewater treatment. Zirconia and Fe-supported zirconia have been used as heterogeneous catalysts in photocatalytic advanced oxidation processes [16–20]. For instance, the wet oxidation of phenol via heterogeneous catalysis using materials based on iron and copper and hydrogen peroxide was carried out under normal conditions of temperature and pressure [21]. Results of this study showed a great stability of tested catalysts in the aqueous medium. Saeed and Ilyas [6] demonstrated that the nickel hydroxide was more effective to degrade phenolic compounds. The application of iron-based catalysts (e.g., Fe-$TiO_2$ and Fe-C-$TiO_2$) played an important role to accelerate the oxidation rate of phenol [6]. Espinosa et al. [22] studied the wet oxidation of phenol on metallic catalysts (Ru, Pt) supported on $TiO_2$-$CeO_2$ and showed that platinum-based catalysts were more effective than those based on ruthenium. Idrissi et al. [23] used a manganese-based catalyst supported on a bentonite for the oxidation reaction of phenol in a diluted aqueous solution. Catalytic tests showed that the solids based on Mn at 5% were more active but they were unstable in the aqueous solution compared to bentonite alone. However, the reduction in total organic carbon remained low for all the studied catalysts. The degradation of 4-NP was also analyzed by Gaffour and Mokhtari [2] using the advanced oxidation processes at room temperature where the mineralization of this compound was effective. On the other hand, the Fenton process showed that the degradation and reduction rates increased with the catalyst ratio and treatment time where the best oxidation process used UV/$H_2O_2/Fe^{2+}$ [2]. Sable et al. [4] synthesized heterogeneous catalysts from 4% Fe impregnated with $ZrO_2$, which were used in the Fenton-like process for the phenol degradation. Othman et al. [24] demonstrated the catalytic activity of copper and nickel in an aqueous medium. These metallic species were very effective in the oxidation reaction of phenol. Results also showed that phosphate coated $CuFe_2O_4$ were competitive Fenton-type catalysts for phenol degradation [24]. Although significant advances have been achieved in the preparation of photocatalysts for the degradation of organic compounds, there are still several challenges to be resolved with the aim of reducing the operational costs of this treatment technology for large-scale applications. Herein, it is convenient to remark that different synthesis procedures can be utilized and optimized to tailor the properties of catalytic materials including the application of biopolymers to obtain composites with improved properties for the removal of organic pollutants [25–27]. For instance, various nanocomposites of TiO2–ZnO, TiO2–ZnO/CS, and TiO2–ZnO/CS–Gr were synthesized by Patehkhor et al. [28] using sol–gel and ultrasound-assisted methods. These materials were utilized to enhance the photocatalytic degradation of tetracycline under UV irradiation where the best material showed 97% of efficiency in the degradation of tetracycline after 3 h. On the other hand, it is also important to analyze the kinetic and thermodynamic parameters related to the removal of organic pollutants using catalytic materials [25].

Considering this background, the main objective of this study was to synthesize catalysts in the form of grains based on a mixture of iron(oxy)hydroxides, especially amorphous iron hydroxide (HFO) and goethite, and zirconium for the catalytic oxidation of 4-NP under the presence of hydrogen peroxide. Degradation tests are reported in this paper including the physicochemical characterization of tested catalyst. The novelty of this study relied on the preparation of hybrid catalytic materials using iron (oxy)hydroxides supported by zirconium where their powders were shaped into grains of different sizes using the wet granulation method. Results reported in this study showed that this catalyst was effective for the 4-NP degradation from aqueous solution.

## 2. Materials and Methods

*2.1. Preparation of Catalysts.* Two (oxy)hydroxides iron solids (i.e., goethite and HFO) were used in this study. The catalysts were obtained via the coprecipitation method with different Fe/Zr ratios. Specifically, these materials were prepared following the next protocol. First, the synthesis of HFO was carried out according to the method reported by Jiang et al. [29]. This protocol consisted of dissolving slowly, with stirring and bubbling $N_2$, 60 g of NaOH pellets in 500 mL of a solution of $Fe(NO_3)_3.9H_2O$ (0.5 M) (>98%, Prolabo) and $ZrO(NO_3)_2.H_2O$ (>99%). This mixture reacted to form a solid product. After removing the supernatant, the solid was separated by centrifugation, washed twice with double-distilled water, and dried in an oven at 25°C. After grinding, the powder (goethite-Zr) was recovered in a dark bottle and protected against possible pollution by organic products.

The preparation of goethite-based catalyst was performed as follows. Goethite, $\alpha$-FeO(OH), was synthesized according to the protocol of Wu et al. [30]. It implied the rapid mixing of 100 mL of $Fe(NO_3)_3.9H_2O$ (1 M) (>98%, Prolabo) and $ZrO(NO_3)_2.H_2O$ (>99%) with 180 mL of NaOH (5 M) (>98%, Prolabo) under stirring and bubbling $N_2$ to avoid carbonation with atmospheric $CO_2$. The mixture was then diluted to 2 L with double-distilled water and placed in an oven at 70°C for 60 h. The final precipitate was washed several times with 500 mL of double-distilled water to remove the excess of nitrates. After drying at 60°C for 24 h, the solid was grounded until a homogeneous powder was obtained and the final product was stored in a dark bottle.

HFO-Zr and goethite-Zr catalysts with different compositions were prepared where Table 1 provides the sample labels and their characteristics. On the other hand, the preparation of uniform catalyst grains was carried out using a granulator with a high shear rate, see Figure 1. Table 2 provides the operating conditions of the granulation process, which were optimized by Cheknane [31]. First, 20 g of powder catalyst were introduced into the high shear mixer with a

rotation speed of 600 rpm to homogenize at the dry state. This step was followed by wet granulation that consisted of spraying the binder solution (industrial grade silicone) on the powder bed by varying the mixer speed from 100 to 1000 rpm for 6 min. At the end of granulation, the grains were collected carefully and placed on a plate and dried in a tray oven at 60°C. This temperature was chosen to allow the evaporation of wetting agent (water), while the main characteristics of the binding agent (industrial grade silicone) and catalyst were retained [29]. The final product was then calcined at 500°C for 3 h with a heating rate of 5°C/min.

*2.2. Physicochemical Characterization of Catalysts.* Different characterization techniques were used to analyze the morphology and surface properties of catalysts where the results were used to explain their performance and selectivity. In particular, XRD analysis was carried out with a X-ray diffractometer (Model Rigaku) with scanning rate of 5°/min from 5° to 80°, ceramic tube with copper and generator power at RX: 40 mA, 40 kV. XRD results were obtained with an angular step of 0.05° at 2 s per step and sample rotation with 0.02°. These results were utilized to identify the crystalline phases and the presence of (oxy)hydroxides. Fourier transform infrared spectroscopy (Perkin-Elmer FTIR spectrometer 310) was used to analyze the functional groups present on the catalyst surface. FTIR spectra were recorded at 400-4000 $cm^{-1}$ with resolution of 2 $cm^{-1}$. The measurements were made via diffuse reflection. Catalyst samples were analyzed in the form of fine pellets using KBr. BET areas of tested samples were measured by a model Quantachrome NOVA WIN 2 automated gas sorption system. Surface morphology of samples were analyzed with a scanning electron microscopy (SEM) Quanta 650 (FEI). The pH of point of zero charge (PZC) was determined for catalyst samples. First, 0.03 g of catalyst were added to 30 mL Erlenmeyer flasks containing a solution of potassium nitrate (0.1 M) adjusted to different pH values (from 2 to 12). The initial pH of solution (pHi) was adjusted by 0.1 M KOH and 0.1 M $HNO_3$. This solution was stirred at 225 rpm for 24 h at 24°C, and the final pH of supernatant liquid (pHf) was measured after filtration with a 0.45 $\mu$m filter paper. PZC was associated to the value of initial pH when the $\Delta$pH equals to zero.

Finally, some mechanical properties of the catalyst grains were also analyzed. First, the friability is a property that describes the mechanical resistance of grains subjected to impact and/or abrasion. Therefore, the friability measurements of catalyst samples were carried out by introducing 1 g of sample ($P1$) in a friabilimeter (Roche ERWEKA TA3R, Germany) for 10 min at a speed of 25 rpm. After a rotation of 250 turns, the grains were weighed (P2), and the friability index ($F$%) was calculated with the following equation:

$$F(\%) = \frac{P1 - P2}{P1}.100. \quad (1)$$

The settlement of powders reflects the ability of particles to rearrange spontaneously (under the effect of gravity) and then under the effect of mechanical stresses (under the effect of successive falls). Therefore, the test described in the European Pharmacopoeia was used to study the behavior of powders, placed in a test tube, and subjected to successive and standardized falls. In a 250 mL graduated cylinder, a sufficient amount of grain, not more than 100 g, was introduced without packing and the apparent volume ($V_0$) was recorded. Then, the sample was submitted to 50 and 100 strokes and the apparent volumes corresponding to $V_{50moy}$ and $V_{100moy}$ were also recorded. The compaction capacity ($V$) was calculated as follows:

$$V = V50 - V100. \quad (2)$$

The settling ability was associated to the Carr index (IC) by the following expressions:

$$\mathrm{IC} = \frac{V50 - V100}{V50}.100 = \frac{\text{settlement}}{V5O}.100. \quad (3)$$

Catalytic studies for the degradation of 4-nitrophenol.

The activity of catalysts was tested in the oxidation reaction of 4-NP under the presence of $H_2O_2$. 4-NP oxidation reaction was performed in a discontinuous system using 0.2 g of catalyst, 200 mL of 11 mg/L solution of 4-NP and 10 mL of hydrogen peroxide. This 4-NP concentration was selected considering that some discharges in Algeria showed concentrations lower than 20 mg/L. Degradation experiments were performed under the bubbling of $N_2$ and proper agitation at room temperature. Liquid samples were taken regularly in order to follow the evolution of 4-NP oxidation. The oxidation products were analyzed by high-performance liquid chromatography (HPLC) with a C18 column.

The conversion of 4-NP during the catalytic degradation was estimated and calculated using the next equation:

$$\text{Conversion} = 100\left(1 - \frac{Cr}{C0}\right), \quad (4)$$

where $C0$ and $Cr$ are the initial and final concentrations of 4-NP in the corresponding degradation study.

Table 1: Composition of catalysts prepared for the degradation of 4-nitrophenol in water.

| Catalyst composition | Precursor | Sample |
|---|---|---|
| 75%Fe + 25%Zr | Goethite | 75GFe25Zr |
| 50%Fe + 50%Zr | Goethite | 50GFe50Zr |
| 25%Fe + 75%Zr | Goethite | 25GFe75Zr |
| 75%Fe + 25%Zr | HFO | 75HFe25Zr |
| 50%Fe + 50%Zr | HFO | 50HFe50Zr |
| 25%Fe + 75%Zr | HFO | 25HFe75Zr |

## 3. Results and Discussion

*3.1. Characterization of Catalysts.* X-ray diffraction patterns of analyzed samples are given in Figure 2. They showed

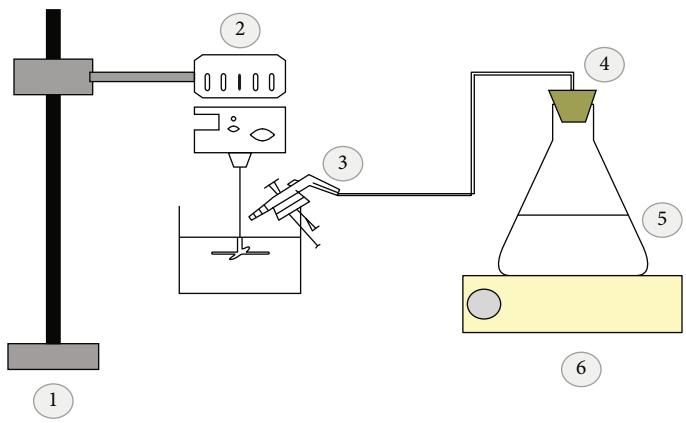


Figure 1: Configuration of mixer granulator used in the preparation of catalyst for the degradation of 4-nitrophenol. (1) Support, (2) mechanical stirrer, (3) sprayer, (4) plug, (5) Erlenmeyer flask, and (6) magnetic stirrer.

Table 2: Operating conditions used in the granulation process of catalyst.

| | |
|---|---|
| Mass of the powder, g | 20 |
| Rotation speed of the studied mixer, rpm | 100 to 1000 |
| Concentration of the binder solution, % | 40 |
| Duration of the process, min | 6 |

peaks located at $2\theta \geq 20^\circ$ attributed to the different iron (oxy)hydroxides. These iron species were present with percentages varying from 8 to 11% mainly for $\alpha$-FeOOH and HFO. Note that these findings agreed with results reported by other authors [32]. All XRD patterns exhibited two peaks at $2\theta$ ranges of 15°-40° and 40°-70°, thus indicating the amorphous nature of solids [33]. It was found that zirconia existed mainly in the monoclinic phase and only a very small peak was associated to the tetragonal phase according to JCPDS No. 42-1164. XRD results also showed the disappearance of the peaks in the diffraction pattern of HFO and $\alpha$-FeOOH-based materials that were initially present in the raw feedstock, and it was also identified the intensification of certain peaks located at $2\theta = 22$, 34, and 37° related to goethite. XRD pattern of the former catalyst showed peaks at $2\theta = 28.5$ and 31.8, thus indicating the retention of monoclinic phase of zirconium. However, the monoclinic phase of zirconia was lost in the catalyst, which was probably due to the presence of water. Debye-Scherrer equation was utilized to estimate the size of iron oxide aggregates, which ranged from 25 to 34 nm.

FTIR spectra of tested catalysts are reported in Figure 3. The coexistence between zirconium and ferric (oxy)hydroxides was associated to the intense absorption bands at 4000-3500 $cm^{-1}$ as well as those located at 1500 $cm^{-1}$ that were characteristic of (oxy) iron hydroxides, i.e., the bands located at 4000 and 3630 $cm^{-1}$ (wide) and 1630 up to 1480 $cm^{-1}$ (small). The (oxy)hydroxides were related to the absorption band at 1635 $cm^{-1}$ that was attributed to the deformation vibrations of $H_2O$ molecules. The band located at 3625 $cm^{-1}$ of the goethite spectrum corresponded to the vibration of OH bond. The absorption bands identified at 3320 and 1640 $cm^{-1}$ were assigned to the asymmetric stretching and bending modes of OH groups while the weak absorption band at 837 $cm^{-1}$ was attributed to Zr-O stretching mode.

BET surface areas of all the materials are reported in Table 3. Overall, the HFO-based catalysts showed higher specific surface areas than goethite. Note that this textural parameter partially explained the results of oxidation reaction for the catalysts prepared with HFO and zirconium. For illustration, Figure 4 shows the $N_2$ adsorption-desorption isotherm at 77 K of the catalyst 25HFe75Zr. This isotherm can be considered as type IV according to the IUPAC classification, which is characterized of a monolayer adsorption with the presence of mesopores. Calculated BET surface area of this sample was 267.66 $m^2/g$ with a pore volume of 0.262 $cm^3/g$.

SEM images were used to examine the morphology of supports, the presence of grains, and porosity in the goethite and HFO-based catalysts. SEM images of goethite and HFO showed rather opaque and nonregular structures, thus reflecting the existence of these (oxy)hydroxides in the form of a precipitate, see Figure 5(a). Catalyst samples with different compositions also presented a regular and orderly morphology where spherical-like forms were observed. The results of elemental analysis of tested samples confirmed the presence of iron, zirconium, and some traces of silica and aluminum, see Figure 5(b).

Table 4 reports the PZC values for different materials studied, which ranged from 4.1 to 10.42 in powder form and from 6.07 to 11.12 in grain form. As stated, PZC corresponds to the pH value where the net surface charge of a solid surface is zero. Surface charge of solids can be positive, negative, or zero depending on the solution pH. At pH < PZC, the surface charge of the material is positive and otherwise is negative if pH > PZC. Therefore, this property contributes to understand the phenomena that can occur during the catalytic process and helps to interpret the influence of solution pH on the pollutant degradation. Finally, Table 5 shows the results for the mechanical tests performed on the grains. The compaction capacity of all the grains ranged from 5 to 17 mL, which was consistent with standard

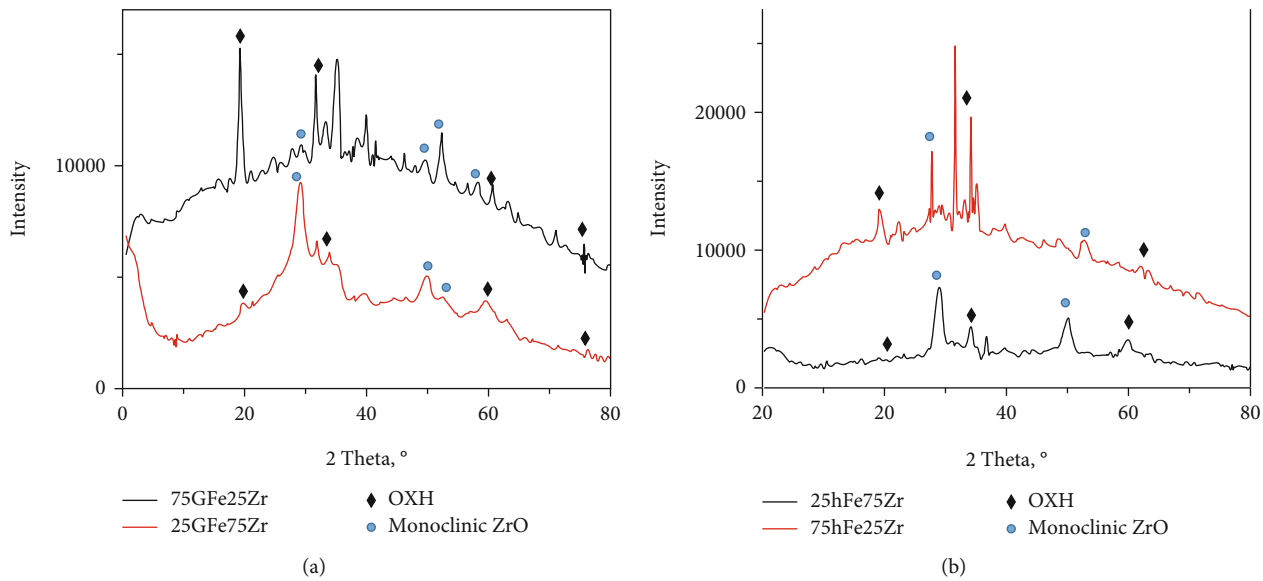


Figure 2: X-ray diffraction patterns of catalyst samples used in the degradation of 4-nitrophenol.

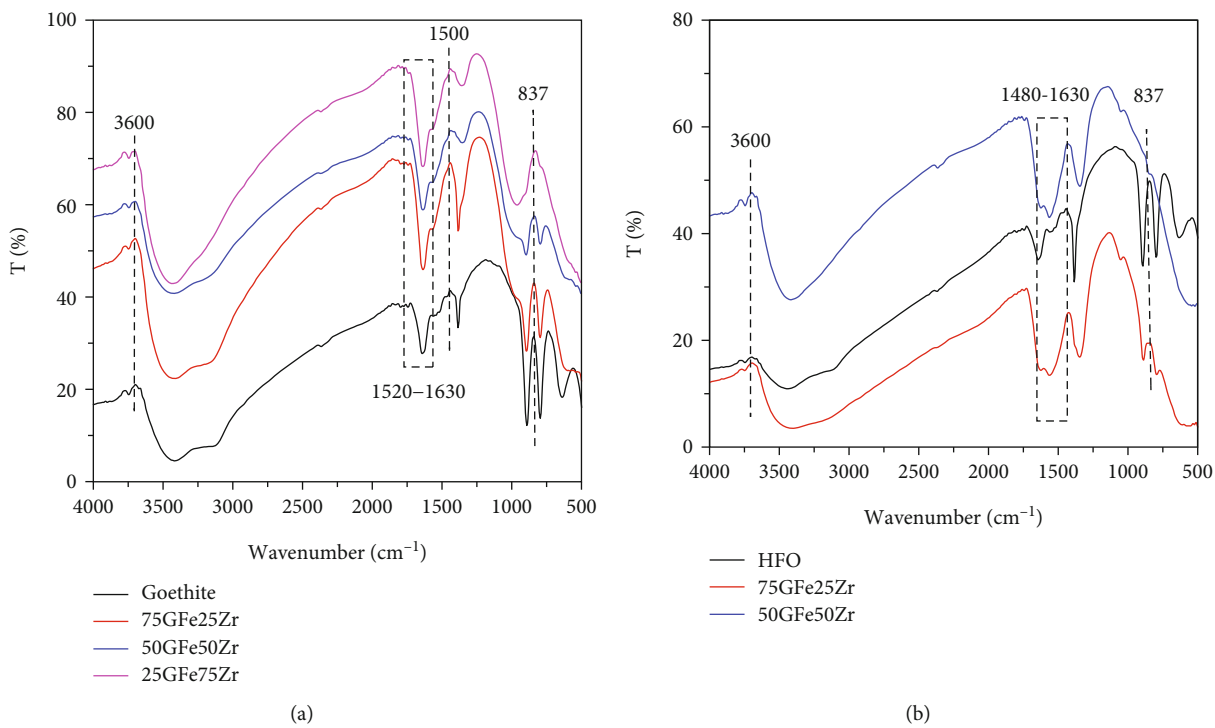


Figure 3: FTIR spectra of catalyst samples used in the degradation of 4-nitrophenol.

Table 3: Main textural parameters of catalysts prepared in this study.

| Sample | BET surface area, $m^2/g$ | Pore volume, cc/g |
|---|---|---|
| 75HFe25Zr | 213.911 | 0.159 |
| 50HFe50Zr | 236.418 | 0.2567 |
| 25HFe75Zr | 267.661 | 0.261 |
| 50GFe50Zr | 232.551 | 0.1682 |
| 75GFe25Zr | 114.809 | 0.12 |
| 25GFe75Zr | 188.496 | 0.1464 |

values (European pharmacy). The friability of catalyst grains was lower than 1%.

*3.2. Impact of Operating Conditions on the 4-NP Degradation.* The results of the effect of contact time on the conversion rate of 4-NP are given in Figure 6(a). A rapid degradation rate of 4-NP was observed at <30 minutes followed by a significant slower 4-NP degradation between 50 to 90 min. 4-NP removal rates were stabilized at

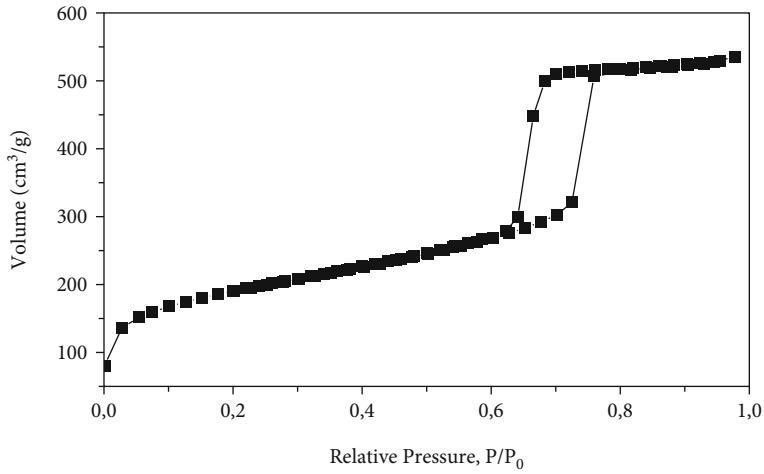


Figure 4: $N_2$ adsorption-desorption isotherms at 77 K of catalyst sample 25HFe75Zr.

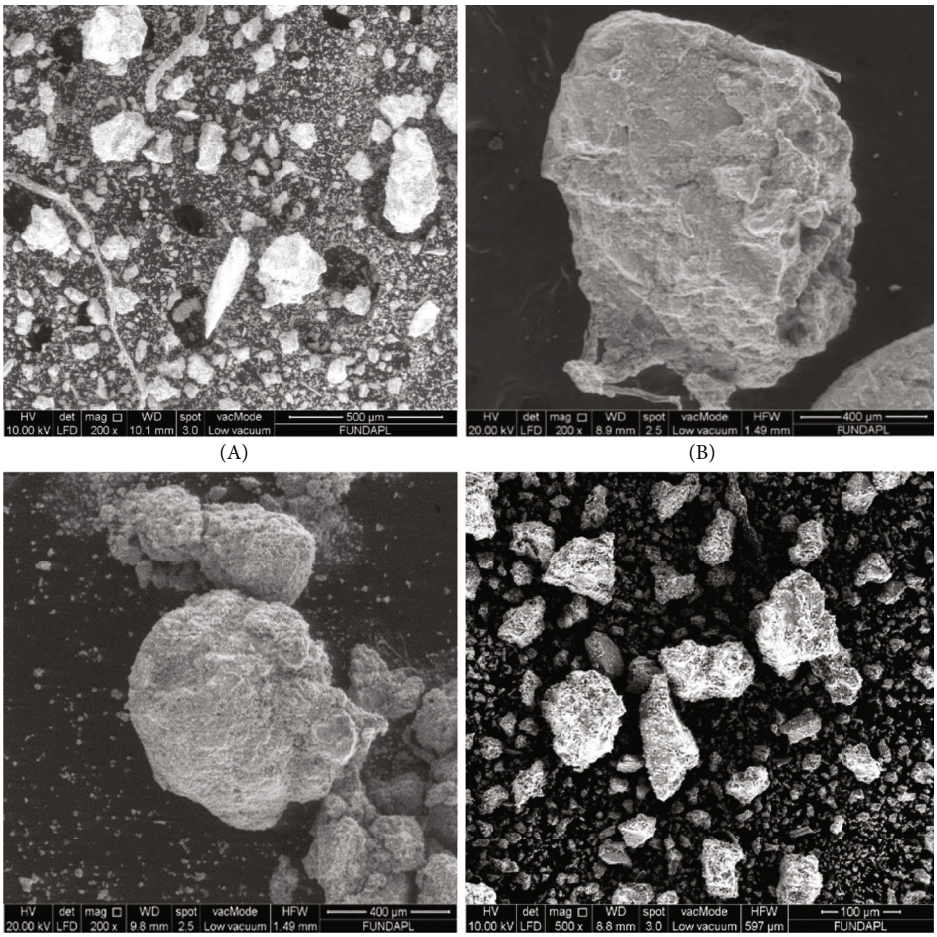


(a) SEM images

Figure 5: Continued.

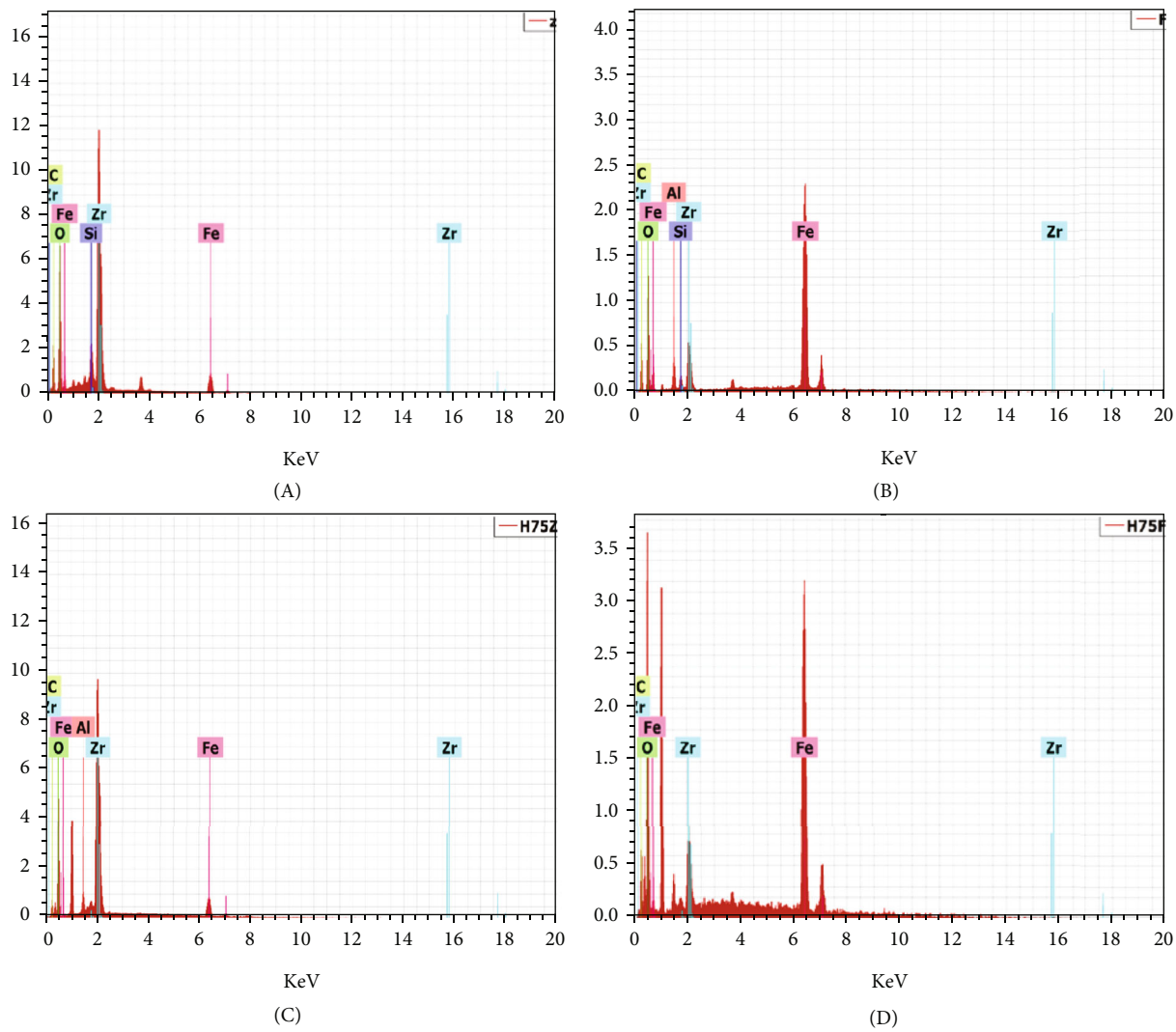


Figure 5: (a) SEM images and (b) EDX results of catalyst samples in grain form. Samples: (I) 25GFe75Zr, (II) 75GFe25Zr, (III) 25HFe75Zr, (IV) 75HFe25Zr.

Table 4: pH of point of zero charge (PZC) of catalysts used in the degradation of 4-nitrophenol.

| Sample | PZC | |
|---|---|---|
| | Powder | Grain 0.4 mm < $d$ < 1 mm |
| 25GFe75Zr | 7.13 | 9.17 |
| 75GFe25Zr | 7.18 | 11.12 |
| 50GFe50Zr | 7.01 | 9.40 |
| Goethite | 6.1 | 9.07 |
| 25HFe75Zr | 4.11 | 6.07 |
| 75HFe25Zr | 8.14 | 11.20 |
| 50HFe50Zr | 8.19 | 8.67 |
| HFO | 10.42 | 8.31 |

>90 min. These degradation rates can be explained by the effect of the external diffusion associated to the concentration gradient at the beginning of the reaction.

Table 5: Mechanical properties of the catalysts used in the degradation of 4-nitrophenol.

| Sample | Friability, % | Settlement, mL |
|---|---|---|
| HFO | 0.1 | 5 |
| 75HFe25Zr | 0.1 | 14.29 |
| 25HFe75Zr | 0.2 | 11.11 |
| Goethite | 0.2 | 14.28 |
| 75GFe25Zr | 0.1 | 15 |
| 25GFe75Zr | 0.3 | 16.66 |
| Standards | <1% | <20 |

Catalytic tests were also carried out with different catalyst amounts using an initial 4-NP concentration of 11 mg/L at pH 7 and 27°C, see Figure 6(b). Results showed that the best catalyst mass was 0.2 g to obtain a conversion rate of 81%. On the other hand, the effect of 4-NP concentration

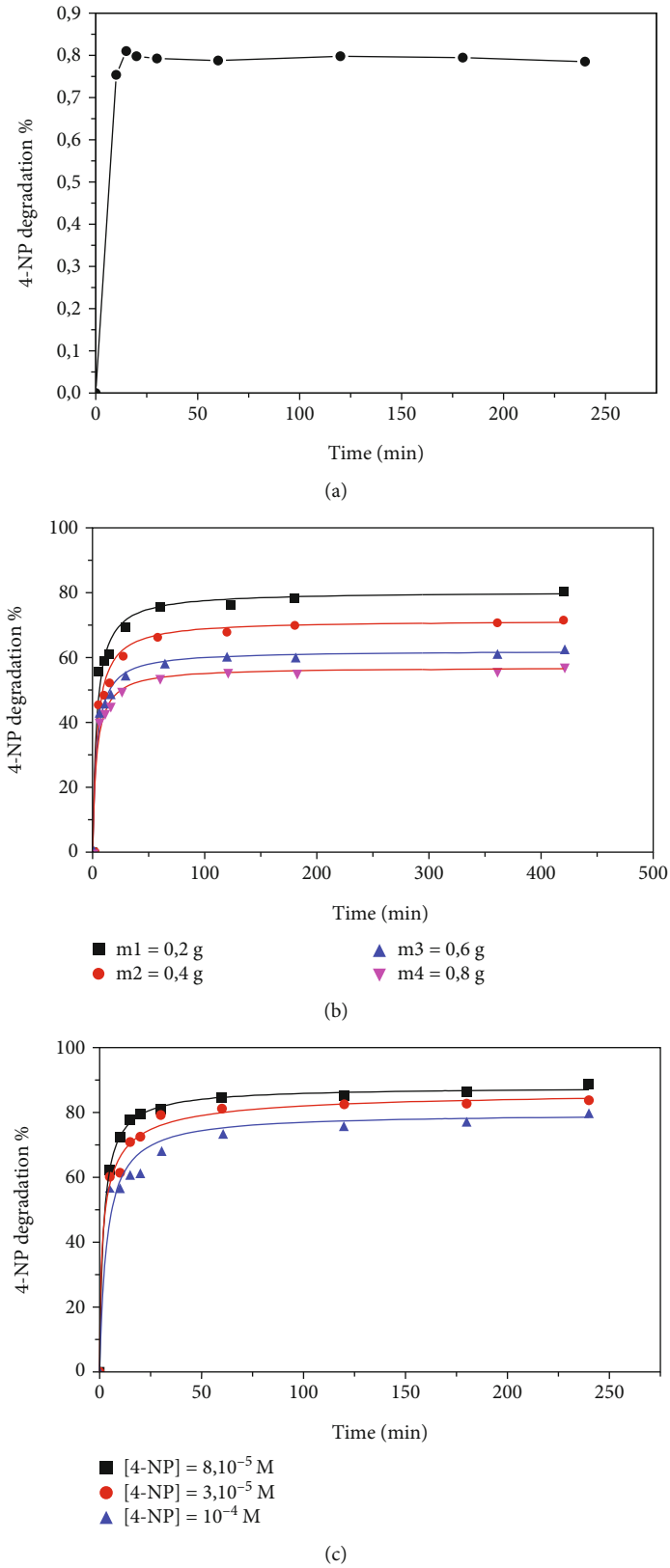


Figure 6: Effect of contact time, catalyst mass, and 4-nitrophenol concentration on the degradation yield via catalytic oxidation. Experimental conditions: (a) 0.2 g of catalyst, 11 mg/L of 4-nitrophenol concentration, pH 7, and 27°C, (b) 11 mg/L of 4-nitrophenol concentration, pH 7, and 27°C, (c) 0.2 g of catalyst, pH 7, and 27°C.

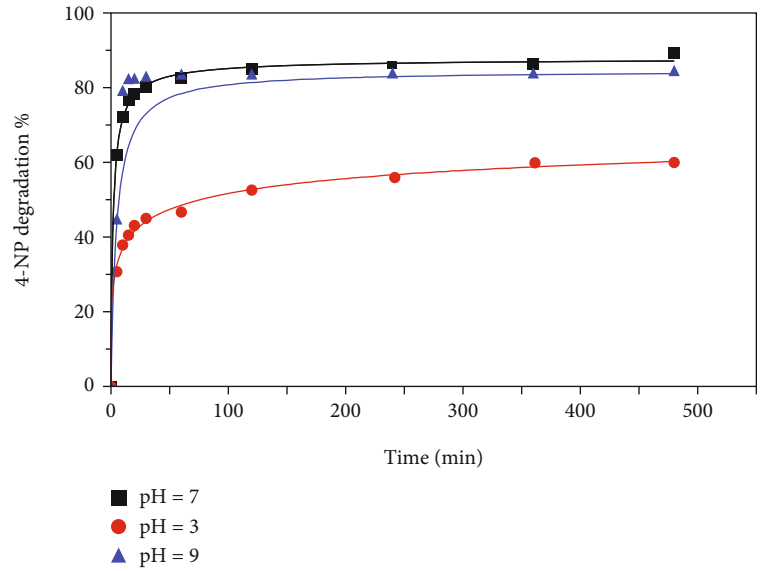


(a) 0.4 mm < $d$ < 1 mm

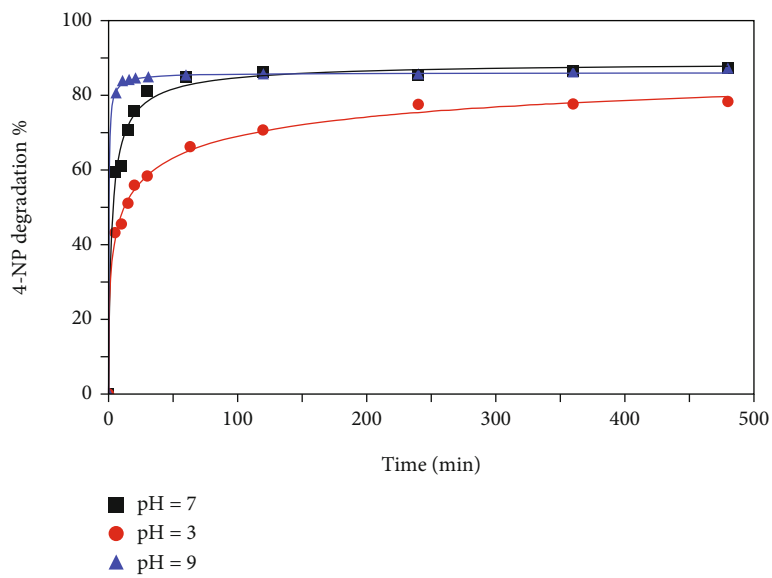


(b) 1 mm < $d$ < 2 mm

Figure 7: Continued.

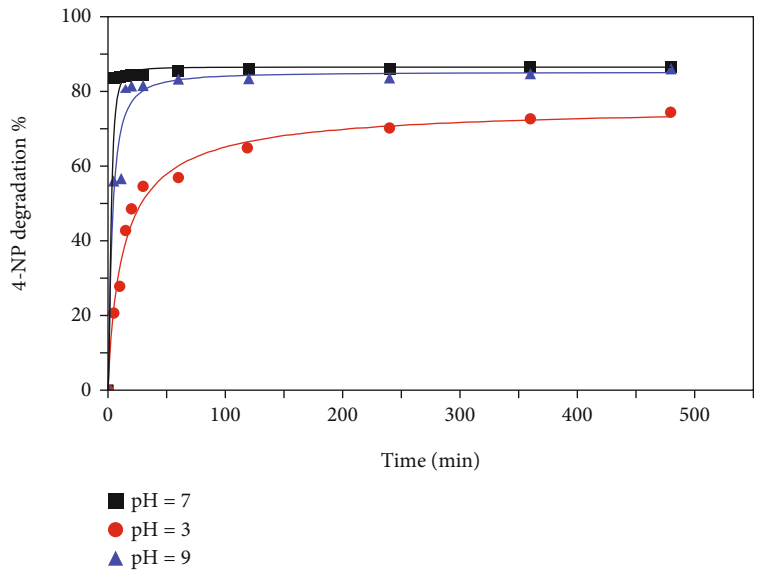


(c) 2 mm < $d$ < 2.5 mm

Figure 7: Effect of solution pH on the 4-nitrophenol degradation by catalytic oxidation using catalyst grains with different diameters. Experimental conditions: 0.2 g of catalyst, 11 mg/L of 4-nitrophenol concentration, and 27°C.

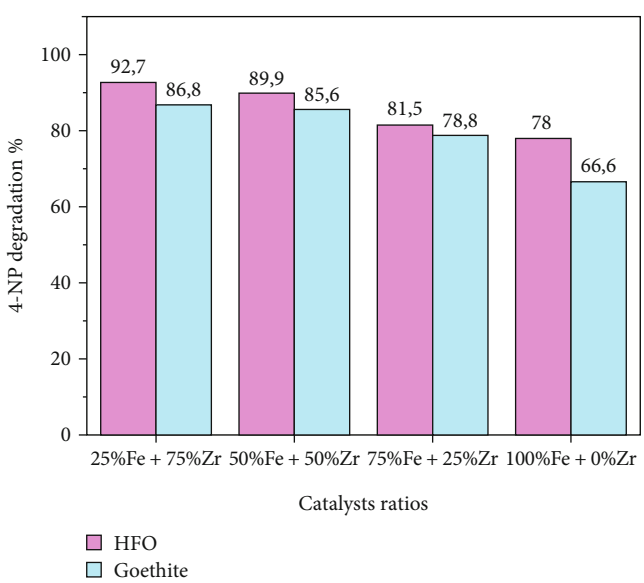


Figure 8: 4-Nitrophenol degradation efficacy of tested catalysts at pH 7, 27°C, and 4 h.

on the degradation efficiency was tested, and results are reported in Figure 6(c) for concentrations of $8{\cdot}10^{-5}$–$1{\cdot}10^{-4}$ M. An increment in the pollutant concentration implied a reduction of the degradation yield. In particular, the 4-NP degradation decreased from 89% at $8{\cdot}10^{-5}$ M to 84% at $3{\cdot}10^{-5}$ M, and 80% at $1{\cdot}10^{-4}$ M. According to recent studies [13, 34], high degradation yields at trace pollutant concentrations could be mainly due to the role of pollutant-catalyst surface attraction forces and the significant number of free active sites. On the other hand, the number of occupied active sites played a relevant role for degradation process at high pollutant concentrations because their saturation reduced the catalytic activity.

The effect of pH on the 4-NP degradation rates is illustrated in Figure 7. The reduction of solution pH decreased the degradation yield of 4-NP from 89% (pH 7) to 58% (pH 3) depending on the grain size. Note that pH reduction contributed to increase the attractive interactions between the pollutant molecule and the charged catalyst surface. At basic pH, these electrostatic interactions were limited due to there was a repulsion between the phenates (the molecular form of 4-NP at basic pH) and the catalyst. Figure 7 also showed that the 4-NP degradation by the catalytic oxidation process was higher than 80% at $pH \geq 7$ irrespective of the catalyst grain diameter.

Figure 8 shows a comparative of the 4-NP degradation for tested catalysts using an operating time of 4 h at pH 7. The best degradation performance was obtained with the catalysts based on HFO with a ratio of 75% Zr+25%Fe, which showed a conversion rate of 93%. Surface area of this catalyst was higher than 200 $m^2$/g. Overall, it can be expected that the textural parameters of heterogeneous catalysis played a relevant role for 4-NP degradation, thus contributing to increase its conversion rates.

Finally, assuming an ideal performance of tested catalyst, the following mechanism (Figure 9) has been proposed for the oxidation of 4-NP [24]:

$$H_2O_2 + \text{Catalyst (25HFe75Zr)} \longrightarrow 2OH^*, \quad (5)$$

$$2OH^* + 4-\text{NPhOH} \longrightarrow PhO^* + H_2O + NO_2, \quad (6)$$

$$H_2O_2 + PhO^* \longrightarrow \text{intermediate products} \longrightarrow CO_2 + H_2O. \quad (7)$$

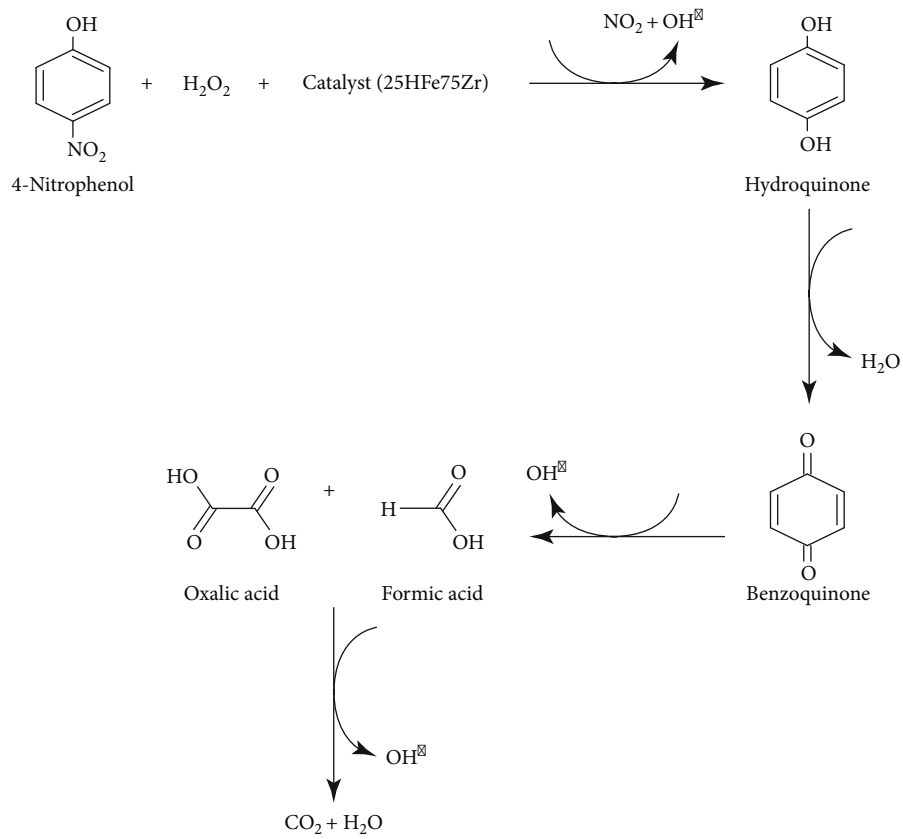


Figure 9: Illustration of degradation mechanism of 4-nitrophenol using the best catalyst obtained in this study.

Note that an adsorption interaction could occur during the oxidation according to the following equation:

$$4 - \text{NPhOH} + \text{catalyst (grains)} \longrightarrow \text{adsorption}. \quad (8)$$

Finally, it is convenient to indicate that HPLC analysis of samples obtained at different times of experiments confirmed the degradation of this pollutant where intermediate products were not found with the implemented analytical method. Therefore, further studies are required to determine if some intermediate products could be generated during this degradation process. These studies will imply the application of other analytical techniques, and their results will complement the analysis of catalyst performance in this application.

## 4. Conclusions

This study reports the synthesis and characterization of catalysts obtained from iron oxyhydroxide type supported on zirconium and their application in 4-NP degradation. This catalyst showed a BET surface area up to 267.66 $m^2/g$ with the predominance of mesoporous. Textural characteristics of this type of materials contributed to enhance their efficiency for 4-NP degradation. Overall, the degradation performance of these catalysts were depended on their composition. Results showed that a 4-NP degradation efficiency up to 93% were obtained with the best catalyst (particle size of 0.4–1 mm) at pH 7, 27°C, and 4 h. This result showed that the hybrid HFO/Zr was an attractive catalytic precursor. Catalytic tests showed that the grains synthesized on the basis of HFO supported on zirconium were active in the neutral medium for 4-NP degradation. HFO-based catalysts are promising materials for the oxidation of organic compounds in water treatment.

## Data Availability

Data of this paper are available on request to the corresponding author.

## Conflicts of Interest

The authors declared no potential conflicts of interest with respect to the research, authorship, and/or publication of this article.

## References

[1] Y. Y. Merve, S. B. Esra, and K. M. Çiğdem, "A polymer – zeolite composite for mixed metal removal from aqueous solution," *Water Science & Technology*, vol. 83, no. 5, pp. 1152–1166, 2021.

[2] H. Gaffour and M. Mokhtari, "Photocatalytic degradation of 4-nitrophenol using $TiO_2$ + $Fe_2O_3$ and $TiO_2/Fe_2O_3$-supported bentonite as heterogeneous catalysts," *Journal of Research Chemical Intermediates*, vol. 42, no. 6, pp. 6025–6038, 2016.

[3] S. Peretz and O. Cinteza, "Removal of some nitrophenol contaminants using alginate gel beads," *Colloids and Surfaces A: Physicochemical and Engineering Aspects*, vol. 319, no. 1-3, pp. 165–172, 2008.

[4] S. S. Sable, K. J. Shah, P. C. Chiang, and S. L. Lo, "Catalytic oxidative degradation of phenol using iron oxide promoted sulfonated-ZrO2 by advanced oxidation processes (AOPs)," *Journal of the Taiwan Institute of Chemical Engineers*, vol. 91, pp. 434–440, 2018.

[5] D. Rajkumar and K. Palanivelu, "Electrochemical degradation of cresols for wastewater treatment," *Industrial Engineering Chemistry Research*, vol. 42, no. 9, pp. 1833–1839, 2003.

[6] M. Saeed and M. Ilyas, "Oxidative removal of phenol from water catalyzed by nickel hydroxide," *Applied Catalysis B: Envirommental*, vol. 129, pp. 247–254, 2013.

[7] K. P. Mishra and P. R. Gogate, "Intensification of sonophotocatalytic degradation of p-nitrophenol at pilot scale capacity," *Ultrasonic Sonochemistry*, vol. 18, no. 3, pp. 739–744, 2011.

[8] X. Yang, J. Li, T. Wen, X. Ren, Y. Huang, and X. Wang, "Adsorption of naphthalene and its derivatives on magnetic graphene composites and the mechanism investigation," *Journal of Colloids and Surfaces A: Physicochemical and Engineering Aspects*, vol. 422, pp. 118–125, 2013.

[9] S. J. Kulkarni, R. W. Tapre, S. V. Patil, and M. B. Sawarkar, "Adsorption of phenol from wastewater in fluidized bed using coconut shell activated carbon," *Journal of Procedia Engineering*, vol. 15, pp. 300–307, 2013.

[10] S. A. Hosseini, M. Davodian, and A. R. Abbasian, "Remediation of phenol and phenolic derivatives by catalytic wet peroxide oxidation over Co-Ni layered double nanohydroxides," *Journal of the Taiwan Institute of Chemical Engineers*, vol. 75, pp. 97–104, 2017.

[11] W. Xu, J. Chen, Y. Qiu, W. Peng, N. Shi, and J. Zhou, "Highly efficient microwave catalytic oxidation degradation of 4-nitrophenol over magnetically separable $NiCO_2O_4$-$Bi_2O_2CO_3$ composite without adding oxidant," *Separation and Purification Technology*, vol. 213, pp. 426–436, 2018.

[12] M. S. A. Ángela, G. G. Gloria, and R. S. G. Nancy, "Degradation of phenol using mill scale as a Fenton-type catalyst," *Water and Environment Journal*, vol. 34, pp. 183–191, 2020.

[13] A. M. Mostafa and E. A. Mwafy, "Synthesis of ZnO/CdO thin film for catalytic degradation of 4-nitrophenol," *Journal of Molecular Structure.*, vol. 1221, p. 128872, 2020.

[14] Y. Wang, L. He, G. Lv, and X. Sun, "Experimental and theoretical insights into the RCS-involved electro-catalytic transformation of 4-nitrophenol," *Chemosphere*, vol. 262, p. 128015, 2021.

[15] M. B. Gawande, Y. Monga, R. Zboril, and R. K. Sharma, "Silica-decorated magnetic nanocomposites for catalytic applications," *Coordination Chemistry Reviews*, vol. 288, pp. 118–143, 2015.

[16] W. J. Liu, F. X. Zeng, H. Jiang, X. Zhang, and W. W. Li, "Composite Fe2O3 and ZrO2/Al2O3 photocatalyst: preparation, characterization, and studies on the photocatalytic activity and chemical stability," *Chemical. Engineering journal*, vol. 180, pp. 9–18, 2012.

[17] S. N. Basahel, T. T. Ali, M. Mokhtar, and K. Narasimharao, "Influence of crystal structure of nanosized $ZrO_2$ on photocatalytic degradation of methyl orange," *Nanoscale Research Letters*, vol. 10, no. 1, p. 73, 2015.

[18] D. Chen, S. Chen, Y. Jiang et al., "Heterogeneous Fenton-like catalysis of Fe-MOF derived magnetic carbon nanocomposites for degradation of 4-nitrophenol," *Royal Society of Chemistry Advances*, vol. 7, no. 77, pp. 49024–49030, 2017.

[19] N. Ayas, Y. B. Asci, and M. Yurdakul, "Using of Fe/ZrO2 catalyst to remove direct orange 26 from water by Fenton oxidation at wide pH values," *Fresenius Environmental Bulletin*, vol. 25, no. 8, pp. 3272–3279, 2016.

[20] S. S. Sable, S. C. Panchangam, and S. L. Lo, "Abatement of clofibric acid by Fenton-like process using iron oxide supported sulfonated-$ZrO_2$: efficient heterogeneous catalysts," *Journal of Water Process Engineering*, vol. 26, pp. 92–99, 2018.

[21] N. Lahbabi, M. Hajjaji, Z. Rais, and S. Kacim, "Oxidation of phenol on an iron-based catalyst supported on a Moroccan clay," *Africa Science*, vol. 5, no. 3, pp. 14–24, 2009.

[22] A. Espinosa de los Monteros, G. Lafaye, A. Cervantes, G. D. Angel, J. Barbier Jr., and G. Torres, "Catalytic wet air oxidation of phenol over metal catalyst (Ru,Pt) supported on TiO2–CeO2 oxides," *Catalysis Today*, vol. 258, pp. 564–569, 2015.

[23] M. Idrissi, Y. Miyah, M. Chaouch et al., "CWPO of phenol using manganese-based catalysts," *Journal of Materials Environmental Science*, vol. 5, pp. 2309–2313, 2014.

[24] I. Othman, M. Abu Haija, and F. Banat, "Catalytic properties of phosphate-coated $CuFe_2O_4$ nanoparticles for phenol degradation," *Journal of Nanomaterials*, vol. 2019, 8 pages, 2019.

[25] H. Mahmoodi, M. Fattahi, and M. Motevassel, "Graphene oxide–chitosan hydrogel for adsorptive removal of diclofenac from aqueous solution: preparation, characterization, kinetic and thermodynamic modelling," *Royal Society of Chemistry Advances*, vol. 11, no. 57, pp. 36289–36304, 2021.

[26] S. Dolatabadi, M. Fattahi, and M. Nabati, "Solid state dispersion and hydrothermal synthesis, characterization and evaluations of $TiO_2$/ZnO nanostructures for degradation of rhodamine B," *Desalination Water Treatment*, vol. 231, pp. 425–435, 2021.

[27] A. Garmroudi, M. Kheirollahi, S. A. Mousavi, M. Fattahi, and E. H. Mahvelati, "Effects of Graphene Oxide/$TiO_2$ Nanocomposite, Graphene Oxide Nanosheets and Cedr Extraction Solution on IFT Reduction and Ultimate Oil Recovery from a Carbonate Rock," in *Petroleum*, In Press, 2020.

[28] H. Asadzadeh Patehkhor, M. Fattahi, and M. Khosravi-Nikou, "Synthesis and characterization of ternary chitosan- $TiO_2$-ZnO over graphene for photocatalytic degradation of tetracycline from pharmaceutical wastewater," *Scientific Reports*, vol. 11, no. 1, pp. 1–17, 2021.

[29] X. Jiang, C. Peng, D. Fu et al., "Removal of arsenate by ferrihydrite via surface complexation and surface precipitation," *Applied Surface Science*, vol. 353, pp. 1087–1094, 2015.

[30] H. Wu, D. Xiaowen, D. Dayi, G. Yufeng, Z. Liguo, and H. Guangping, "Decolourization of the azo dye orange G in aqueous solution via a heterogeneous Fenton-like reaction catalysed by goethite," *Environmental Technology*, vol. 33, no. 14, pp. 1545–1552, 2012.

[31] B. Cheknane, O. Bouras, M. Baudu, J. P. Basly, and A. Cherguielaine, "Granular inorgano-organo pillared clays (GIOCs): Preparation by wet granulation, characterization and application to the removal of a Basic dye (BY28) from aqueous solutions," *Chemical Engineering Journal*, vol. 158, no. 3, pp. 528–534, 2010.

[32] V. Lenoble, O. Bouras, V. Deluchat, B. Serpaud, and J. C. Bollinger, "Arsenic adsorption onto pillared clays and iron oxides," *Journal of Colloid Interface Science*, vol. 255, no. 1, pp. 52–58, 2002.

[33] A. S. Pham, N. Shun, and E. Kohki, "Preparation of zirconium carbonate as water-tolerant solid base catalyst for glucose isomerization and one-pot synthesis of levulinic acid with solid acid catalyst," *Reaction Kinetics Mechanism Catalysis*, vol. 111, no. 1, pp. 183–197, 2014.

[34] H. Chen, Z. Sun, Z. Yang et al., "Degradation of 3,4-dichlorobenzotrifluoride by the Fenton-like process using zirconia-coated magnetite magnetic nanoparticles as an effective heterogeneous catalyst," *Environmental Science and Pollution Research*, vol. 24, no. 22, pp. 18575–18584, 2017.

Hindawi
Adsorption Science & Technology
Volume 2022, Article ID 4482263, 14 pages
https://doi.org/10.1155/2022/4482263

*Research Article*

# Physicochemical Modeling of the Adsorption of Pharmaceuticals on MIL-100-Fe and MIL-101-Fe MOFs

**Fátima Gisela Quintero-Álvarez,[1] Cintia Karina Rojas-Mayorga,[2] Didilia Ileana Mendoza-Castillo,[1,3] Ismael Alejandro Aguayo-Villarreal,[2] and Adrián Bonilla-Petriciolet[1]**

[1]*Instituto Tecnológico de Aguascalientes, 20256 Aguascalientes, Mexico*
[2]*Universidad de Colima, 28400 Colima, Mexico*
[3]*CONACYT, 03940 Ciudad de México, Mexico*

Correspondence should be addressed to Adrián Bonilla-Petriciolet; petriciolet@hotmail.com

Received 21 December 2021; Revised 15 January 2022; Accepted 17 February 2022; Published 8 March 2022

Academic Editor: Hesham Hamad



The adsorption of naproxen (NAP), diclofenac (DFC), and acetaminophen (APAP) molecules from aqueous solutions using MIL-100-Fe and MIL-101-Fe metal organic frameworks (MOFs) has been analyzed and modeled. Adsorption isotherms of these pharmaceuticals were experimentally quantified at 30 and 40°C and pH 7. Textural parameters and surface chemistry of these MOFs were analyzed, and results were utilized to explain the pharmaceutical adsorption mechanism. Density Functional Theory (DFT) calculations were performed to understand the reactivity of pharmaceutical molecules, and a statistical physics model was employed to calculate the main physicochemical parameters related to the adsorption mechanism. Results showed that the adsorption of these pharmaceuticals on MOFs was multimolecular and exothermic. Both MOFs displayed the highest adsorption capacities, up to 2.19 and 1.71 mmol/g, for NAP and DFC molecules, respectively. MIL-101-Fe showed better pharmaceutical adsorption properties than MIL-100-Fe due to its highest content of Fe-O clusters and mesopore volume. Adsorption mechanism of these organic molecules could involve hydrogen bond, van der Waals forces, and electrostatic interactions with MOF surfaces. In particular, MIL-101-Fe MOF is a promising material to prepare composites with competitive adsorption capacities for facing the water pollution caused by pharmaceutical compounds.

## 1. Introduction

In recent years, the literature has documented an increment of the water pollution caused by emerging compounds [1]. They are unregulated pollutants by the environmental legislation that include an extensive variety of chemicals such as pharmaceuticals, personal hygiene products, and surfactants [1]. In particular, the release of pharmaceutical molecules in the environment is a relevant issue since they can affect significantly the human health causing, for example, carcinogenesis, teratogenesis, and mutagenicity even at very low concentrations (i.e., from $\mu$g/L to ng/L) [2–5]. Diclofenac (DFC), naproxen (NAP), and acetaminophen (APAP) are nonsteroidal anti-inflammatory drugs that stand out due to their worldwide prescription for human healthcare [6, 7]. NAP is employed for the treatment of osteoarthritis, rheumatoid arthritis, and migraine and to reduce inflammation and fever [7, 8]. DFC is a widely used pharmaceutical to minimize pain and inflammation caused by ankylosing spondylitis, rheumatoid arthritis, and osteoporosis [9]. This drug is commonly identified as a water pollutant in environmental samples [7]. APAP is also an anti-inflammatory, antipyretic, and analgesic drug [10]. Overall, these pharmaceutical molecules can reach wastewater via the human excreta and by their inappropriate disposal after the drug expiration. Different studies have concluded that these

organic molecules can persist in the environment for a long time due to their resistance to biodegradability and stability to heat and light [11, 12].

The control and reduction of concentrations of pharmaceutical pollutants in the environment, and especially in water resources, can be performed via adsorption [13, 14] or using other treatment methods like photodegradation [15, 16]. Particularly, the removal of pharmaceutical molecules via adsorption processes can offer additional economical and technical advantages, and consequently, it is necessary to study the application of novel adsorbents to consolidate its application at industrial level. In this direction, the metal organic frameworks (MOFs) are interesting adsorbents with promising potential for wastewater treatment including the pharmaceutical depollution due to their surface area, controllable pore size (in micro and mesoporous domains), structural versatility, and composition [17–19]. There is a wide spectrum of metals and organic ligands that can be used for the preparation of MOFs, thus offering the possibility to obtain materials with different physicochemical characteristics and adsorption properties. Research on MOFs has indicated that their adsorption capacity to remove organic molecules is determined by their textural parameters (surface area and pore size) and surface functionalities. These physicochemical properties influence the $\pi$-$\pi$ interactions between the aromatic parts of the linker on the MOF structure and the organic molecules besides the electrostatic adsorbent–adsorbate interactions [20, 21]. Particularly, MIL-100-Fe MOF has been suggested as a promising material for liquid-phase adsorption due to its hydrothermal stability, surface area, and pore volume [22]. It has been utilized successfully as an adsorbent of organic pollutants and heavy metals from liquid phase [23, 24]. In this direction, MIL-101-Fe is another interesting MOF that has been proved as an adsorbent of various toxic chemicals due to the affinity of saturated or unsaturated metal sites [24]. Several studies on the water pollutant adsorption via MOFs have focused mainly on the assessment and improvement of the adsorption capacities of these materials including the preparation of composites. However, the discussion of the adsorbent-adsorbate interactions and physicochemical parameters related to the adsorption mechanism is usually excluded in these studies. Note that the structure of adsorbate molecules (e.g., molecular size, functional groups, polarity, and solubility) could also have a significant impact on the MOF adsorption performance [25, 26]. Therefore, the analysis and interpretation of the adsorption mechanism of pharmaceuticals on MOFs and the impact of their molecular properties are necessary to improve the application of these materials and to tailor their properties with the aim of enhancing the adsorption capacities in water depollution.

Under this perspective, this study reports the modeling and analysis of the physicochemical parameters of the adsorption of pharmaceutical molecules on MIL-100-Fe and MIL-101-Fe MOFs. These materials were synthesized and employed to adsorb DFC, NAP, and APAP as target pharmaceutical molecules from aqueous solutions. These MOFs were characterized and their adsorption properties were determined experimentally at 30–40°C and pH 7. The physicochemical parameters associated to the adsorption mechanism of these pharmaceuticals were calculated via the statistical physics-based modeling. Therefore, this study contributes with new experimental data and theoretical insights on the application of MOFs for the adsorption of pharmaceuticals molecules from aqueous solutions.

## 2. Methodology

*2.1. Synthesis and Characterization of MOFs.* MIL-100-Fe and MIL-101-Fe MOFs were prepared and employed to analyze the adsorption of different pharmaceutical molecules from aqueous solutions. MIL-100-Fe was synthetized with 1.76 g of $Fe(NO_3)_3{\cdot}9H_2O$ and 0.57 g of $H_3BTC$ (trimesic acid). The organic linker and metal source were dissolved in 20 mL of deionized water and stirred well for 1 h. The final solution was submitted to a thermal treatment at 160°C for 12 h using a Teflon-lined stainless-steel autoclave. The solid product obtained from the reaction was separated via centrifugation, washed several times with deionized water and ethanol, and finally dried at 80°C for 24 h. The preparation of MIL-101-Fe was performed with 0.675 g of $FeCl_3{\cdot}6H_2O$ and 0.206 g of $H_2BDC$ (terephthalic acid), which were dissolved in 30 mL of DMF. The thermochemical conversion of this solution was done at 110°C for 20 h with the Teflon-lined stainless-steel autoclave. The final solid product was also separated via centrifugation, washed with ethanol, and dried at 80°C and 24 h. Nanosized MOF particles were used in all the pharmaceutical adsorption studies reported in this paper.

Samples of these MOFs were characterized to determine their main surface and textural properties. Surface functional groups were identified by Fourier-transform infrared (FTIR) spectroscopy with a Thermo Nicolet Is10 FTIR spectrometer (Thermo Scientific). Spectra were recorded with KBr-based sample pellets in the 4000-400 $cm^{-1}$ range with a resolution of 4 $cm^{-1}$. Crystallinity analysis was done via the X-ray diffraction patterns using a Malvern-Panalytical X-ray diffractometer. Samples were analyzed at room temperature with copper radiation ($\lambda = 1.5406$ Å) in the angle of $5 \leq 2\theta^{\circ} \leq 60$ at 45 kV and 40 mA. The textural parameters were obtained from $N_2$ adsorption-desorption isotherms at -196°C using a Micromeritics ASAP 2020 equipment. These isotherms were analyzed with suitable models to estimate the main textural parameters of these MOFs. Morphology and surface elemental composition of these adsorbents were obtained by scanning electron microscopy (SEM) analysis using a TM3000 (Hitachi) microscope with an energy dispersion system (EDS) (Nano XFlash Bruker).

*2.2. Pharmaceutical Adsorption Studies.* NAP (≥98%), DFC (≥98%), and APAP (≥99%) were supplied by Sigma-Aldrich and utilized to prepare the adsorbate solutions with deionized water. The main characteristics and molecular structures of these pharmaceuticals are shown in Table 1. Adsorption isotherms of these pharmaceuticals using MIL-100-Fe and MIL-101-Fe MOFs were experimentally quantified at 30–40°C and pH 7. These isotherms were determined with a MOF ratio ($W/V$) of 10 g/L at batch adsorption

Table 1: Main characteristics of the naproxen, diclofenac, and acetaminophen molecules used as adsorbates in this study.

| | Pharmaceutical molecule | | |
|---|---|---|---|
| | Acetaminophen | Diclofenac | Naproxen |
| Chemical structure | 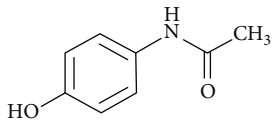 | 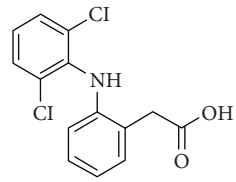 | 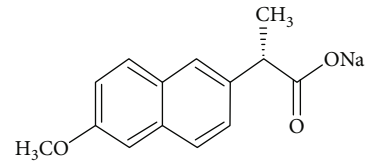 |
| | $C_8H_9NO_2$ | $C_{14}H_{11}Cl_2NO_2$ | $C_{14}H_{14}O_3$ |
| Molecular weight (g/mol) | 151.63 | 296.15 | 230.26 |
| Molecular dimension (Å) | 8.56 × 8.56 × 1.76 | 7.91 × 9.58 × 5.38 | 10.27 × 6.07 × 4.59 |

conditions under agitation of 120 rpm where the adsorption equilibrium was reached in 24 h. For these experiments, the initial concentrations ($C_0$) of NAP, DFC, and APAP solutions ranged from 0.157 to 5.292 mmol/L. The pharmaceutical adsorption capacities of tested MOFs ($q$, mmol/g) were calculated by a mass balance

$$q = \left(\frac{C_0 - C_e}{W}\right) V, \tag{1}$$

where $C_e$ (mmol/L) is the equilibrium concentration of tested pharmaceuticals in the aqueous solution. Concentrations of all pharmaceuticals in the aqueous solutions were quantified by high-performance liquid chromatography (HPLC) (Ultimate 3000TM Thermo Scientific™) at 220 nm with a Thermo Scientific™ Hypersil GOLD™ Aq C18, 3 $\mu$m, 4.6 mm × 250 mm reverse-phase HPLC column. A mixture of 0.1% formic acid in water and acetonitrile was the mobile phase with a flow rate of 1 mL/min. The reagents and water used for the mobile phase were HPLC grade. Thermo Scientific™ Chromeleon™ software was utilized to collect and process the pharmaceutical quantification data.

*2.3. Thermodynamics and Modeling of the Adsorption of Pharmaceutical Molecules.* The thermodynamics of the pharmaceutical adsorption was analyzed calculating the adsorption enthalpy ($\Delta H^\circ$, J/mol) with the van't Hoff approach employing the next equation [27].

$$\ln K_c = \frac{-\Delta H^\circ}{RT} + \frac{\Delta S^\circ}{R}, \tag{2}$$

where $R$ is the universal ideal gas constant (8.3144 J/mol·K), $T$ is the adsorption temperature (K), $\Delta S^\circ$ is the adsorption entropy (J/mol·K), and $K_c$ is the adsorption equilibrium constant that was calculated following the procedure reported by Tran et al. [28].

Results of MOF characterization and the analysis of adsorbate molecular structure were utilized to define a statistical-physics-based model to calculate the physicochemical parameters of the adsorption mechanism of pharmaceutical molecules [29–32]. Therefore, this model was utilized to fit the adsorption data and to determine these parameters. It is convenient to note that the adsorption of tested pharmaceutical molecules on these MOFs could imply two surface functionalities: oxygenated functional groups (e.g., -COOH and –OH) and Fe-O clusters. But the complex molecular structure of MOFs limits the possibility of identifying, with reliability, the specific contribution of these functionalities during the pharmaceutical adsorption. Based on these facts, the statistical physic model assumed that one functional group (i.e., oxygenated functionality with or without Fe) was involved in the adsorption of NAP, DFC, and APAP where an adsorbate monolayer was also formed. This model was defined as [33]

$$q_e = \frac{n_{\text{phar}} N_{\text{ads}}}{1 + (C_h/C_e)^{n_{\text{phar}}}}, \tag{3}$$

where $n_{\text{phar}}$ represents the number of pharmaceutical molecules adsorbed for each MOF functional group, $N_{\text{ads}}$ is the amount of MOF functional groups (mmol/g) involved in the pharmaceutical adsorption, and $C_h$ is the half saturation adsorbate concentration (mmol/L), respectively. The pharmaceutical adsorption capacity at the saturation condition ($q_{\text{sat}}$, mmol/g) of these MOF can be obtained from

$$q_{\text{sat}} = n_{\text{phar}} N_{\text{ads}}. \tag{4}$$

The adsorption energies ($\Delta E_{\text{ads}}$, J/mol) related to the molecular interactions between MOF surface and pharmaceutical molecules were calculated using

$$\Delta E_{\text{ads}} = RT \ln\left(\frac{S_{\text{phar}}}{C_h}\right), \tag{5}$$

where $S_{\text{phar}}$ is the pharmaceutical solubility (mmol/L) in aqueous solution.

Calculated statistical physics parameters were used to interpret the pharmaceutical adsorption mechanism. They were obtained from the isotherm data correlation via a nonlinear regression where the next objective function ($F_{\text{obj}}$) was minimized

$$F_{\text{obj}} = \sum_{i=1}^{n_{\text{dat}}} \left(q_i^{\text{exp}} - q_i^{\text{mod}}\right)^2, \tag{6}$$

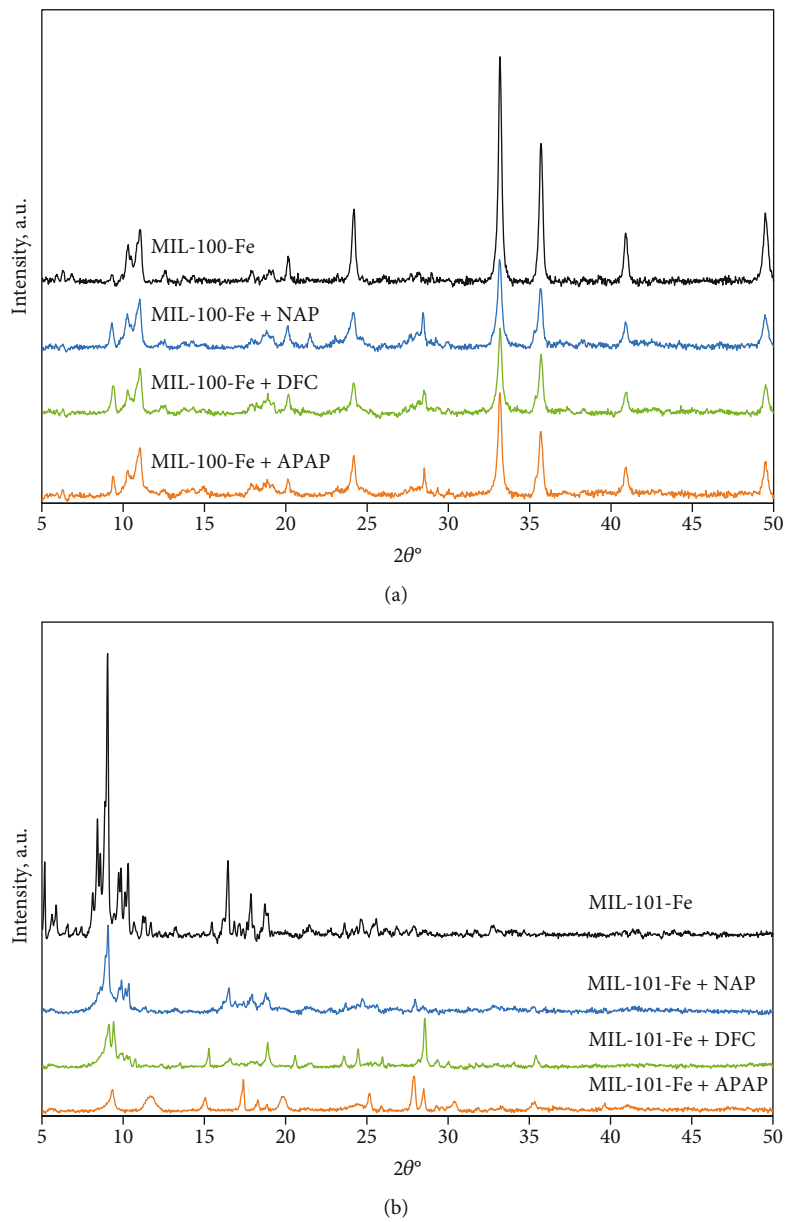


Figure 1: X-ray diffraction patterns of (a) MIL-100-Fe and (b) MIL-101-Fe before and after the adsorption of naproxen (NAP), diclofenac (DFC), and acetaminophen (APAP) molecules.

where exp and mod refer to the experimental and calculated pharmaceutical adsorption capacities, respectively, and $n_{\text{dat}}$ is the number of experimental data used in the correlation.

Finally, Density Functional Theory (DFT) calculations were performed with GAUSSIAN09 software to understand the electrostatic and reactive properties of APAP, DFC, and NAP molecules. The molecule optimization was carried out with a functional hybrid B3LYP with 6-311++G$(d, p)$ basis set. The charge distribution of these pharmaceutical molecules was identified with the molecular electrostatic potential (MEP), which was defined as

$$V(r) = \sum_A \frac{Z_A}{|R_A - r|} - \int \frac{\rho\left(r'\right) dr'}{|r' - r|}, \tag{7}$$

where $|r' - r|$ is the distance to point $r$, $\rho(r')dr'$ is the density of the electronic charge (measured as a volume for each element), $|R_A - r|$ is the distance from point $r$, $R_A$ is the position in space of nucleus $A$, and $Z_A$ is the atomic number of nucleus $A$, respectively [34]. Note that in any charge distribution, the electrons and atomic nuclei in molecules generate an electrostatic potential in the space. Therefore, this descriptor provides the electron density response when a unit of positive charge approaches.

## 3. Results and Discussion

*3.1. MOF Characterization.* The results of X-ray diffraction of the synthesized MIL-100-Fe and MIL-101-Fe MOFs are reported in Figure 1. X-ray diffractogram of MIL-100-Fe

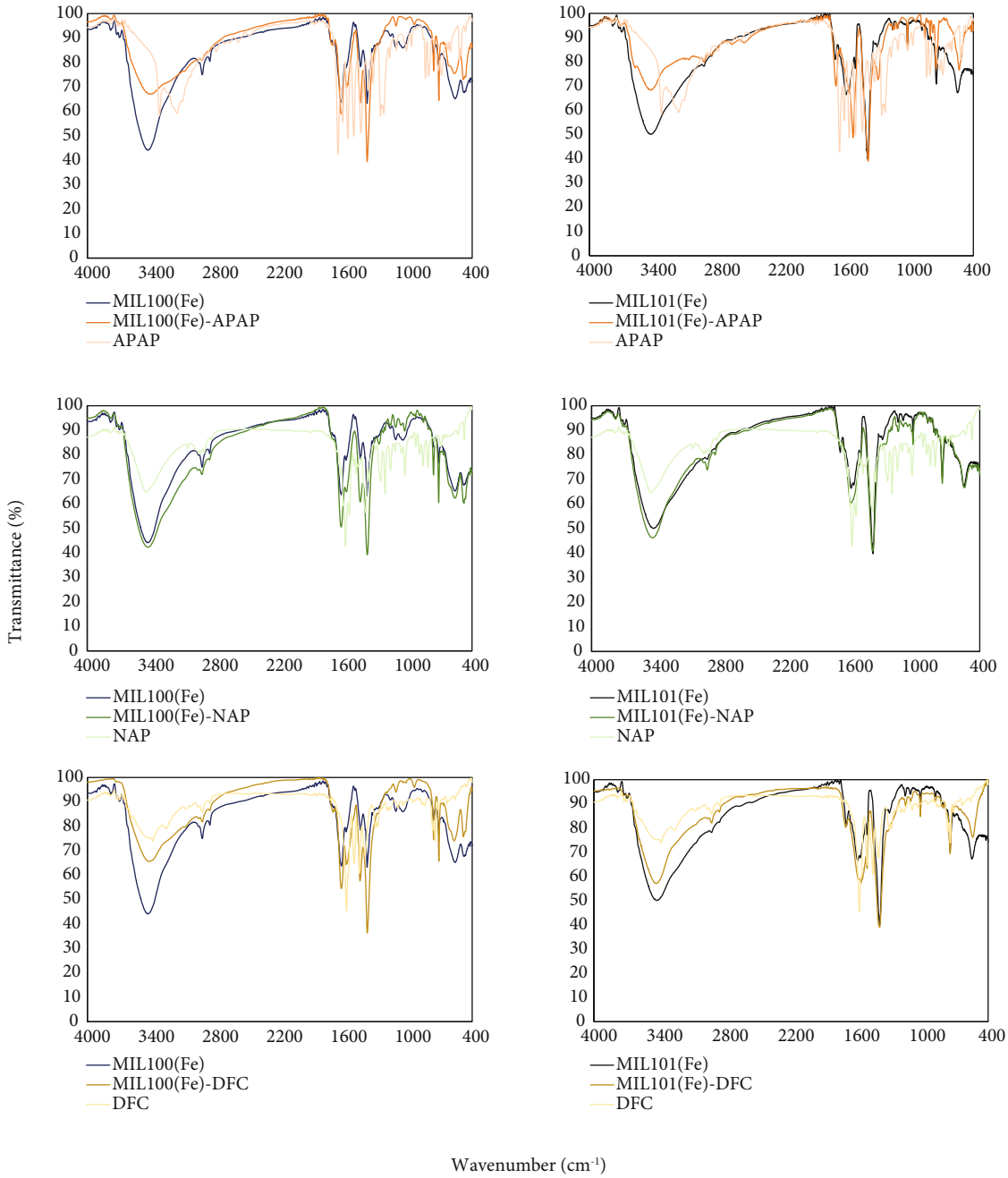


Figure 2: FTIR spectra of (a) MIL-100-Fe and (b) MIL-101-Fe before and after the adsorption of naproxen (NAP), diclofenac (DFC), and acetaminophen (APAP) molecules.

showed the characteristic diffraction peak at ~11.1° 2$\theta$, thus denoting the formation of a pure phase [35, 36]. This result was consistent with those reported by Chen et al. [35], Forghani et al. [36], Pil-Joong et al. [37], Zhang et al. [38], Fan et al. [39], Mahmoodi et al. [40], Nehra et al. [41], Shah et al. [42], Li et al. [43], Chaturvedi et al. [44], Chen et al. [45], and Chávez et al. [46]. After the adsorption of the different pharmaceutical molecules, the MOF crystalline structure was stable but the intensity of the diffraction peaks decreased. These changes in the MOF crystallinity were attributed to incorporation of each adsorbed pharmaceutical on the adsorbent surface [47, 48]. X-ray diffraction pattern of the MIL-101-Fe showed diffraction peaks at ~5.1, 9.2, 16.7, and 19.5° 2$\theta$, which confirmed the formation of the crystalline structure characteristic of this MOF [4, 49–53]. After the adsorption of pharmaceuticals, the X-ray diffraction patterns displayed some changes. Specifically, the disappearance of some diffraction peaks was observed and a change in the MOF crystallinity was also identified. This result could be related to the instability of MOF structure in the aqueous media generated by the incorporation of adsorbed pharmaceuticals on its surface [4, 47].

FTIR spectra of both MOFs are reported in Figure 2. They showed a broad absorption band at 3600–3000 $cm^{-1}$

Table 2: Elemental analysis and textural parameters of MIL-100-Fe and MIL-101-Fe MOFs.

| MOF | Structure | Composition | | | $S_{BET}$ ($m^2/g$) | Pore volume ($cm^3/g$) | | |
|---|---|---|---|---|---|---|---|---|
| | | Element | Wt% | At% | | Total | Micropore | Mesopore |
| MIL-100-Fe | 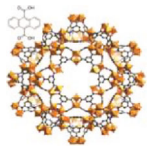 | C | 52.89 | 61.75 | 768.18 | 0.58 | 0.31 | 0.27 |
| | | O | 42.25 | 37.03 | | | | |
| | | Fe | 4.86 | 1.22 | | | | |
| MIL-101-Fe | 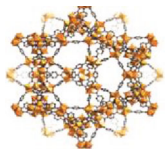 | C | 50.04 | 67.98 | 450.14 | 1.02 | 0.19 | 0.83 |
| | | O | 23.39 | 23.85 | | | | |
| | | Fe | 24.21 | 7.08 | | | | |
| | | Cl | 2.37 | 1.09 | | | | |

that was attributed to the stretching vibration of the O-H group [35, 36, 40, 41, 43–45, 52, 54, 55]. Iron-based MOFs showed an absorption band at ~1640 $cm^{-1}$ related to the C=O stretching vibration due to carboxyl groups [24, 36, 40, 41, 44, 46, 53, 56]. The spectrum of MIL-100-Fe also displayed the absorption bands of the symmetric (~1425 $cm^{-1}$) and asymmetric (~1378 $cm^{-1}$) vibration of the O-C-O group [36, 41, 45], CH bending vibrations (~1112 $cm^{-1}$) of the carboxylate groups in benzene rings [36, 39, 44], and CH vibrations (~760 and 708 $cm^{-1}$) of these aromatic structures [46]. FTIR spectrum of MIL-101-Fe showed the absorption bands of asymmetric (~1590 $cm^{-1}$) and symmetric (1390 $cm^{-1}$) stretching vibration of the carboxyl groups (O-C=O) present in terephthalic acid, thus indicating the presence of the organic linker (i.e., dicarboxylate) in this sample [49, 51–53]. The absorption band of C-H bending vibration (~746 $cm^{-1}$) was also identified and corresponded to the aromatic ring of dicarboxylic benzene [49, 52, 53]. Finally, the spectra of these iron-based MOFs also contained the Fe-O stretching vibration at ~550 $cm^{-1}$, which also agreed with the results of other studies that have reported the synthesis of these MOFs [35, 39, 40, 43, 44, 52, 53].

After the NAP, DFC, and APAP adsorption, FTIR spectra of these MOFs showed a decrement in the intensity of the absorption band associated with the -OH group; see Figure 2. This result suggested the formation of hydrogen bonds between pharmaceutical molecules and MOF surface [57]. Similarly, a change in the absorption band of Fe-O stretching vibration (~550 $cm^{-1}$) was also observed, which could be an indication that the metal clusters played an important role in the adsorption of these pharmaceuticals [58]. There was also a shift in the absorption band (~1590 $cm^{-1}$) of the stretching vibration of carboxyl groups (O-C=O) of MIL-101-Fe. According to Tomul et al. [59] and Yaah et al. [60], this change in FTIR spectrum could be also associated with the incorporation of pharmaceutical molecules in the MOF surface. To complement the surface chemistry analysis of adsorbent samples, FTIR spectra of the single pharmaceuticals were also included and compared in Figure 2. Results showed that the specific and characteristic absorption bands of pharmaceutical molecules were also identified in the spectra of MOF samples obtained after the adsorption experiments. Therefore, these findings were an indirect evidence of the adsorption of these molecules on the external surface of these MOFs thus agreeing the results reported in other studies [59, 60].

Table 2 and Figures 3 and 4 show the results obtained from the elemental analysis, SEM images, and textural parameters of tested MOFs. In general, these adsorbents were mainly composed of carbon and oxygen. The presence of iron was confirmed in both MIL-100-Fe (4.9 wt%) and MIL-101-Fe (24.2%) thus providing additional evidence of the successful synthesis of these organometallic structures. Note that chlorine was also identified in the MIL-101-Fe sample because $FeCl_3{\cdot}6H_2O$ was employed as precursor in its synthesis. SEM micrographs of these MOFS indicated that the size of MIL-100-Fe crystals varied from 0.05 to 0.5 $\mu$m, while the MIL-101-Fe particles showed an average diameter of 0.5–1 $\mu$m; see Figure 3. These results were consistent with other studies [36, 43, 53, 56, 61]. It was also observed that these MOFs presented an octahedral structure; however, the octahedral form of MIL-101-Fe MOF was imperfect [50–52, 62, 63]. $N_2$ adsorption-desorption isotherms of these MOFs are reported in Figure 4. These $N_2$ isotherms can be categorized between types I and IV of IUPAC classification, which are typical of micro- and mesoporous materials [23, 37, 41, 43, 52, 53]. The specific surface area, total pore, micropore, and mesopore volumes of these adsorbents are given in Table 2. BET surface area of MIL-100-Fe was 768.18 $m^2/g$ with a total pore volume of 0.58 $cm^3/g$. This surface area was similar to that reported by Nehra et al. [41] ($S_{BET}$ = 790.5 $m^2/g$) and Bezverkhyy et al. [64] ($S_{BET}$ = 750 $m^2/g$). However, the total pore volume differed from that obtained by these authors (i.e., 0.34 and 0.41 $cm^3/g$). BET surface area and pore volume of MIL-101-Fe were ~450 $m^2/g$ and 1.02 $cm^3/g$, respectively. Similar textural parameters for this MOF have been reported by Li et al. [49] and Jiang and Li [65]. Herein, it should be noted that the MOF textural parameters depend on the synthesis route because these materials can tune their size by changing the fraction of organic connectivity and the inorganic part, which in turn is associated to the preparation conditions of each organometallic compound.

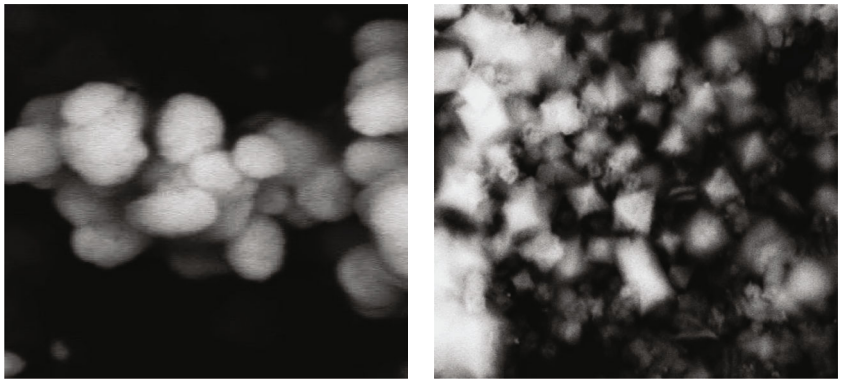

(a) (b)

Figure 3: SEM micrographs SEM (1000x) of (a) MIL-100-Fe and (b) MIL-101-Fe.

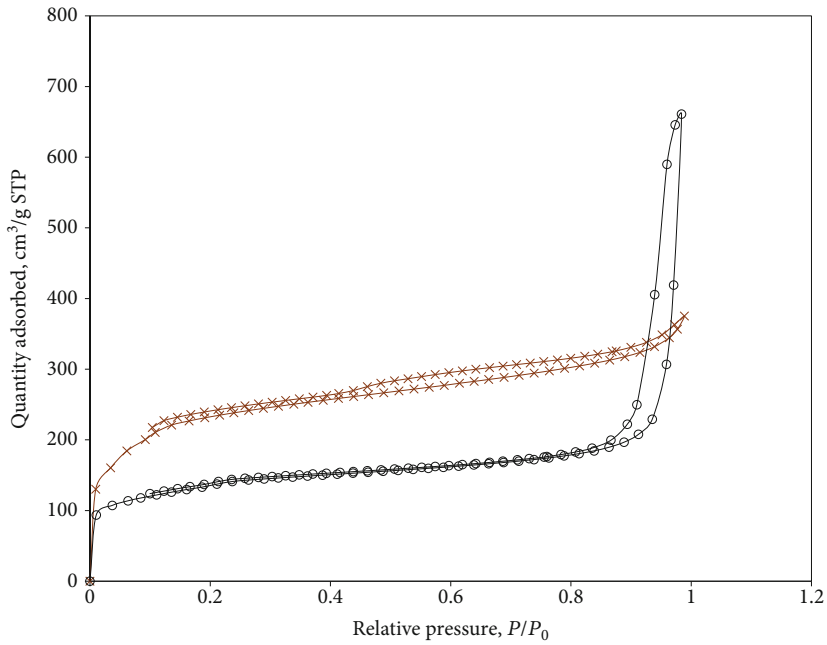


Figure 4: $N_2$ adsorption-desorption isotherms (at -196°C) of (x) MIL-100-Fe and (○) MIL-101-Fe.

*3.2. Adsorption of NAP, DFC, and APAP on MIL-100-Fe and MIL-101-Fe MOFs.* Adsorption isotherms of NAP, DFC, and APAP obtained with MIL-100-Fe and MIL-101-Fe MOFs are reported in Figure 5. All pharmaceutical isotherms were 2L type according to the Giles classification for liquid phase adsorption [66], which indicated that the adsorption of these compounds was proportional to the adsorbate concentration until reaching the saturation of the available adsorption sites (i.e., oxygenated functionalities and Fe-O clusters of these MOFs). NAP adsorption capacities of MIL-100-Fe and MIL-101-Fe ranged from 0.186 to 1.267 and 0.205 to 2.190 mmol/g at 30°C and from 0.149 to 1.206 and 0.185 to 1.889 mmol/g at 40°C, respectively. For the case of APAP, the adsorption capacities of these MOFs were 0.012–0.151 and 0.080–0.450 mmol/g at 30°C and 0.009–0.134 and 0.073–0.382 mmol/g at 40°C, respectively. DFC adsorption capacities of MIL-100-Fe varied from 0.182 to 1.708 mmol/g at 30°C and from 0.132 to 1.616 mmol/g at 40°C, while MIL-101-Fe showed DFC adsorption capacities from 0.398 to 1.469 and 0.127 to 1.072 mmol/g at 30 and 40°C, respectively. Table 3 reports and compares the adsorption capacities of MIL-100-Fe, MIL-101-Fe, and other MOFs used in the removal of different pharmaceutical from aqueous solutions [2, 4, 8, 18, 67–69]. Several adsorption capacities reported in the literature were lower than those obtained for NAP, DFC, and APAP with MIL-100-Fe and MIL-101-Fe MOFs. Therefore, these materials could be considered as an alternative separation medium for the adsorption of these three pharmaceuticals in water depollution.

In general, MIL-101-Fe showed a better performance than MIL-100-Fe for the adsorption of NAP and APAP, while the highest DFC adsorption capacities were obtained with MIL-100-Fe. The pharmaceutical adsorption capacities of MIL-100-Fe and MIL-101-Fe followed the next trends: APAP < <NAP < DFC and APAP < <DFC < NAP,

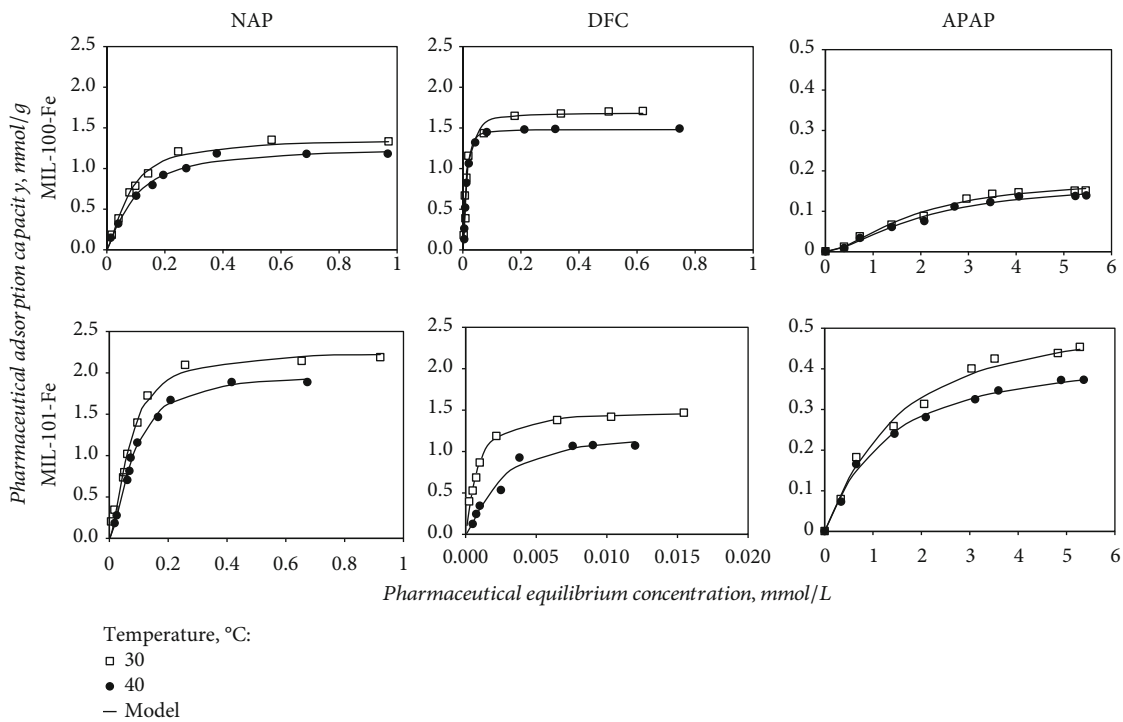


Figure 5: Isotherms of the adsorption of the adsorption of acetaminophen, diclofenac, and naproxen on MIL-100-Fe and MIL-101-Fe from aqueous solution at pH 7.

Table 3: Adsorption capacities for different pharmaceuticals using MOFs as adsorbents.

| MOF | Adsorbate | Experimental conditions pH | Temperature (°C) | Adsorption capacity (mmol/g) | Reference |
|---|---|---|---|---|---|
| MIL-100-Fe | Naproxen | 4.5 | 25 | 0.499 | Hasan et al. [2] |
| UiO-66 | | 5.4 | 25 | 0.638 | |
| NH2-UiO-66 | Diclofenac | | | 0.358 | Hasan et al. [18] |
| 18%$SO_3H$-UiO-66 | | | | 0.881 | |
| | Sulfamethoxazole | 4.9 | 25 | 0.343 | Ahmed [8] |
| ZIF-8 | Ibuprofen | 5 | 25 | 0.673 | Bhadra et al. [69] |
| | Diclofenac | | | 0.354 | |
| MIL-101-Cr | Naproxen | 7 | 25 | 0.429 | Sarker et al. [68] |
| | Ketoprofen | | | 0.259 | |
| MIL-101-Cr (Gno) | Naproxen | 7 | 25 | 0.538 | |
| | Ketoprofen | | | 0.361 | |
| $Fe_3O_4$@MIL-100-Fe | Diclofenac | 6.2 | 25 | 1.351 | Li et al. [67] |
| MIL-100-Fe | Tetracycline | 7 | 25 | 0.851 | Dong et al. [4] |
| | Acetaminophen | 7 | 30 | 0.143 | This study |
| MIL-100-Fe | Diclofenac | | | 1.542 | |
| | Naproxen | | | 1.354 | |
| | Acetaminophen | 7 | 30 | 0.423 | |
| MIL-101-Fe | Diclofenac | | | 1.760 | |
| | Naproxen | | | 1.730 | |

respectively. It was clear that these adsorption capacities depended on both MOF and pharmaceutical properties. As stated, BET surface area of MIL-100-Fe was higher than that of MIL-101-Fe. For both MOFs, it was expected that the pharmaceutical adsorption was performed mainly on the external adsorbent surface due to the size of these organic molecules. However, the volume of mesopores of MIL-100-Fe was lower than that of MIL-100-Fe; see

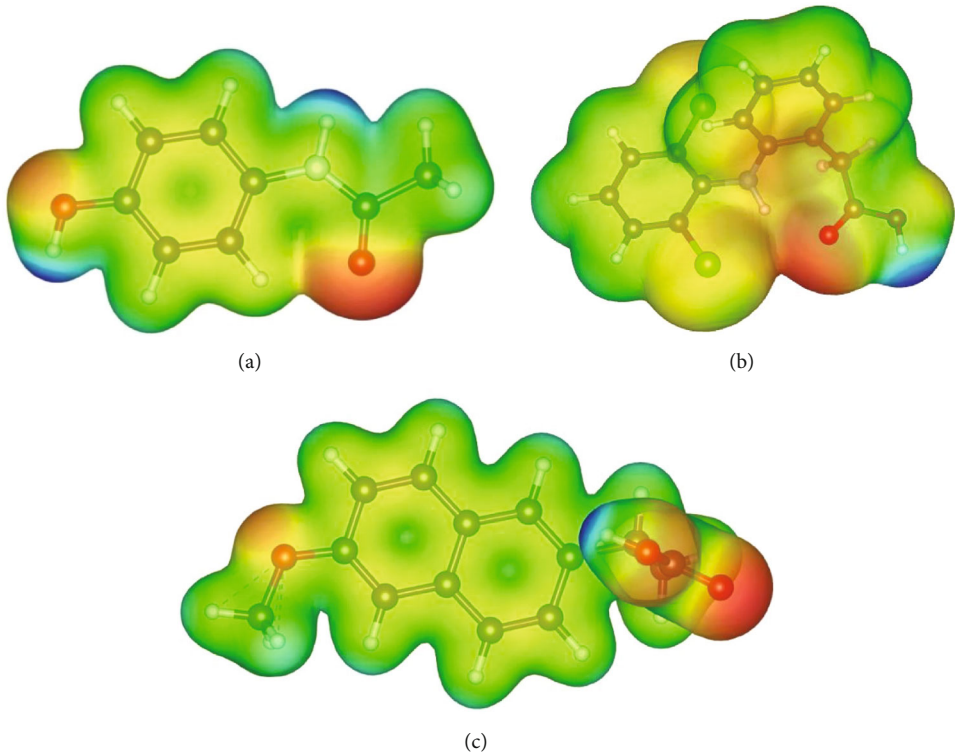


Figure 6: Molecular electrostatic potential of (a) acetaminophen, (b) diclofenac, and (c) naproxen molecules.

Table 2. These results suggested that the adsorption of these pharmaceutical molecules was favored by large pores in MOF structure. Also, the contribution of Fe-O clusters on these MOFs played a relevant role in the adsorption of APAP and NAP pharmaceuticals where the adsorbent with the highest Fe content (i.e., MIL-101-Fe) also showed the highest removal.

The solution temperature affected the pharmaceutical adsorption with these MOFs; see Figure 5. All the maximum adsorption capacities ranged from 0.14 to 2.19 mmol/g and decreased in 7.9–27% when the solution temperature increased from 30 to 40°C. Pharmaceutical adsorption on both MOFs was affected by the solution temperature according to the next trend: NAP < APAP < DFC. In particular, the removal performance of MIL-101-Fe was more sensitive to the solution temperature where its pharmaceutical adsorption capacities reduced from 13.7% for NAP to 27% for DFC. This exothermic adsorption was partially associated to the solubility of these pharmaceuticals in water and the energy exchange that occurred during the separation process [70]. Specifically, the solubility of these pharmaceutical molecules increased with the solution temperature thus affecting the intermolecular attractive forces between the MOF structure and these adsorbates [4, 70]. Calculated enthalpies for the exothermic adsorption of tested pharmaceuticals on these MOFs ranged from 19.1 to 65.1 kJ/mol. These enthalpy values could correspond to an adsorption caused by hydrogen bonds, van der Waals forces, and electrostatic interactions [71–73].

With respect to the pharmaceutical molecular properties, the literature indicates that the molecular weight and hydrophobicity of these organic compounds could impact their adsorption on MOFs [6, 8]. Figure 6 shows the MEPs of NAP, APAP, and DFC molecules that were calculated with DFT. These electrostatic potentials are illustrated via a color mapping where the scale indicates from the most reactive to the least reactive zone of the molecule (i.e., red > orange > yellow > green > blue). APAP molecule had negative charges located on the oxygen atoms, which were identified in the hydroxyl group in the para position and the oxygen of the acetate. This pharmaceutical molecule had two positive charges located on the hydrogen atoms of the secondary amine and on the hydrogen atom located in the -OH group in the para position. The remaining of this molecule showed a behavior mainly oriented towards the repulsion, which was identified by its green color [74, 75]. DFC molecule showed a high chemical reactivity where the area of interest of this adsorbate corresponded to the -COOH group. The molecular area of least reactivity (blue color) was identified in the hydroxyl group of the carboxyl (mainly in the H atom), and the most reactive area (red color) was found on the oxygen atom attached to the carbon from the carboxyl group. The rest of this molecule showed an intermediate reactivity (i.e., yellow zones) [76, 77]. Finally, the highest reactivity zone of NAP molecule was the oxygen of the methoxyl and -COOH groups, while the less reactivity zone was identified in the hydrogen of the -COOH group. The rest of this pharmaceutical molecule had a low reactivity [78, 79]. DFT calculations also supported that the more reactive zones of these pharmaceuticals molecules could interact mainly with Fe-O clusters on MOF structure during the adsorption.

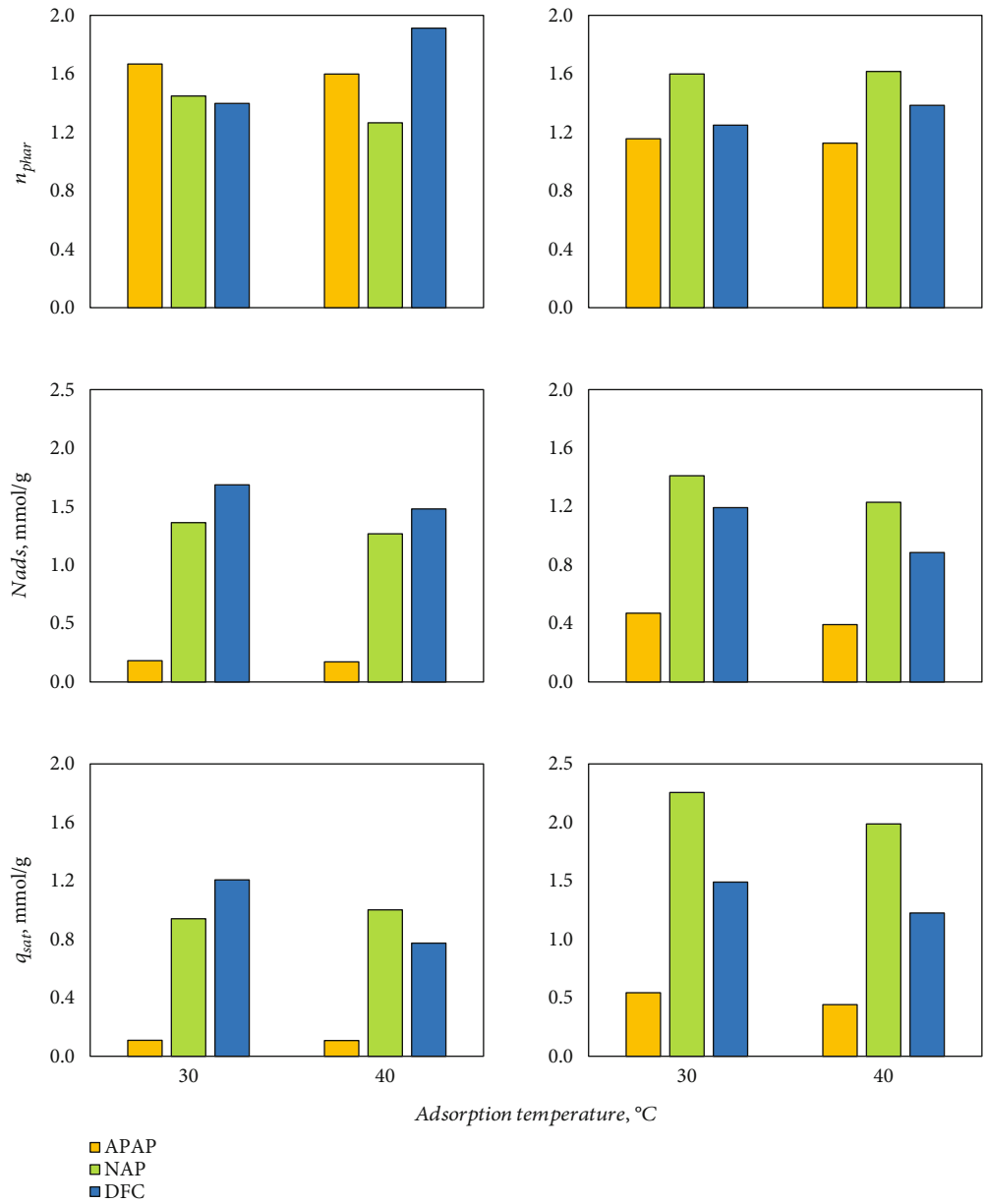


Figure 7: Calculated physicochemical parameters of the adsorption of acetaminophen, diclofenac, and naproxen on MIL-100-Fe and MIL-101-Fe from aqueous solution at pH 7.

Calculated physicochemical parameters for the adsorption of these pharmaceuticals on MIL-100-Fe and MIL-101-Fe MOFs are reported in Figure 7. This statistical physics model showed $R^2 \geq 0.97$ for all pharmaceutical isotherms. Modeling results indicated that the number of pharmaceutical molecules adsorbed per functional groups of MIL-100-Fe and MIL-101-Fe ranged from 1.3 to 1.9 and 1.1 to 1.6, respectively. A multimolecular adsorption of these pharmaceuticals occurred in both MOFs especially for MIL-101-Fe. As stated, MIL-101-Fe showed the highest Fe content and it could be expected that its Fe-O clusters could interact simultaneously with more than one pharmaceutical molecule during the adsorption. $N_{ads}$ ranged from 0.1 to 1.2 mmol/g for MIL-100-Fe and from 0.4 to 1.4 mmol/g for MIL-101-Fe, respectively. The increment of adsorption temperature reduced the number of functional groups involved in the pharmaceutical adsorption due to some adsorbate–functional group interactions were broken caused by the thermal agitation effect [33]. The saturation adsorption capacities were 0.17–1.69 mmol/g for MIL-100-Fe and 0.44–2.26 mmol/g for MIL-101-Fe. The lowest adsorption capacities at saturation were obtained for APAP with both MOFs. In particular, MIL-100-Fe showed the highest saturation adsorption capacities for DFC, while MIL-101-Fe had the highest saturation adsorption capacities for NAP. Calculated adsorption interaction energies were 10.6–22.6 kJ/mol for MIL-100-Fe and 11.4–28.6 kJ/mol for MIL-101-Fe. These pharmaceutical-MOF interaction energies were consistent with the calculated adsorption entropies thus confirming that hydrogen bonds,

van der Waals forces, and electrostatic interactions could be present in the adsorption mechanism of these organic molecules.

## 4. Conclusions

The adsorption of three relevant pharmaceuticals on MIL-100-Fe and MIL-101-Fe MOFs from aqueous solutions has been experimentally studied and modeled to understand their adsorption mechanism. Results showed that the pharmaceutical adsorption capacities of these MOFs were mainly related to the presence of Fe-O clusters where their mesopore structure contributed for the removal of these organic pollutants. Adsorption properties of MIL-101-Fe outperformed those obtained for MIL-100-Fe. Overall, both MOFs showed the lowest adsorption capacities for acetaminophen molecules. The adsorption of naproxen, diclofenac, and acetaminophen on these MOFs was a multimolecular and exothermic process where more than one pharmaceutical molecule can interact with one functional group from the adsorbent surface. The pharmaceutical adsorption properties of MIL-101-Fe MOF were more sensitive to increments of solution temperature and decreased up to 27% for diclofenac molecules. MOF characterization, DFT, and statistical physics calculations indicated that hydrogen bonds, van der Waals and electrostatic forces could be the main interactions involved in the pharmaceutical adsorption on tested MOFs. MIL-101-Fe is an interesting material with better pharmaceutical adsorption capacities than other MOFs reported in literature, and it can be utilized to prepare composites and other materials for water depollution. Therefore, the experimental and theoretical results reported in this study can contribute to enhance and consolidate the application of MOFs as adsorbents of emerging compounds for water treatment and purification.

## Data Availability

Data of this paper are available on request to the corresponding author.

## Conflicts of Interest

The authors declared no potential conflicts of interest with respect to the research, authorship, and/or publication of this article.

## Acknowledgments

The authors acknowledge the financial support provided by CONACYT (Grant No. A1-S-10035) for the present study.

## References

[1] C. Peña-Guzmán, S. Ulloa-Sánchez, K. Mora et al., "Emerging pollutants in the urban water cycle in Latin America: a review of the current literature," *Journal of Environmental Management*, vol. 237, pp. 408–423, 2019.

[2] Z. Hasan, J. Jeon, and S. H. Jhung, "Adsorptive removal of naproxen and clofibric acid from water using metal- organic frameworks," *Journal of Hazardous Materials*, vol. 209-210, pp. 151–157, 2012.

[3] L. Zhu, L. Meng, J. Shi, J. Li, X. Zhang, and M. Feng, "Metal-organic frameworks/carbon-based materials for environmental remediation: a state-of-the-art mini-review," *Journal of Environmental Management*, vol. 232, pp. 964–977, 2019.

[4] Y. Dong, T. Hu, M. Pudukudy et al., "Influence of microwave-assisted synthesis on the structural and textural properties of mesoporous MIL-101(Fe) and $NH_2$-MIL-101(Fe) for enhanced tetracycline adsorption," *Materials Chemistry and Physics*, vol. 251, article 123060, 2020.

[5] Z. Hasan, N. A. Khan, and S. H. Jhung, "Adsorptive purification of organic contaminants of emerging concern from water with metal-organic frameworks," *Contaminants of Emerging Concern in Water and Wastewater*, pp. 47–92, 2020.

[6] C. Jung, L. K. Boateng, J. R. V. Flora et al., "Competitive adsorption of selected non-steroidal anti-inflammatory drugs on activated biochars: experimental and molecular modeling study," *Chemical Engineering Journal*, vol. 264, pp. 1–9, 2015.

[7] M. Parolini, "Toxicity of the non-steroidal anti-inflammatory drugs (NSAIDs) acetylsalicylic acid, paracetamol, diclofenac, ibuprofen and naproxen towards freshwater invertebrates: a review," *Science of the Total Environment*, vol. 740, article 140043, 2020.

[8] M. J. Ahmed, "Adsorption of non-steroidal anti-inflammatory drugs from aqueous solution using activated carbons: review," *Journal of Environmental Management*, vol. 190, pp. 274–282, 2017.

[9] A. Gómez-Avilés, L. Sellaoui, M. Badawi, A. Bonilla-Petriciolet, J. Bedia, and C. Belver, "Simultaneous adsorption of acetaminophen, diclofenac and tetracycline by organo-sepiolite: experiments and statistical physics modelling," *Chemical Engineering Journal*, vol. 404, article 126601, 2021.

[10] D. A. G. Sumalinog, S. C. Capareda, and M. D. G. de Luna, "Evaluation of the effectiveness and mechanisms of acetaminophen and methylene blue dye adsorption on activated biochar derived from municipal solid wastes," *Journal of Environmental Management*, vol. 210, pp. 255–262, 2018.

[11] L. A. Al-Khateeb, W. Hakami, and M. A. Salam, "Removal of non-steroidal anti-inflammatory drugs from water using high surface area nanographene: kinetic and thermodynamic studies," *Journal of Molecular Liquids*, vol. 241, pp. 733–741, 2017.

[12] K. Vargas-Berrones, L. Bernal-Jácome, L. D. de León-Martínez, and R. Flores-Ramírez, "Emerging pollutants (EPs) in Latin America: a critical review of under-studied EPs, case of study -nonylphenol-," *Science of the Total Environment*, vol. 726, article 138493, 2020.

[13] C. R. Gadipelly, K. V. Marathe, and V. K. Rathod, "Effective adsorption of ciprofloxacin hydrochloride from aqueous solutions using metal-organic framework," *Separation Science and Technology*, vol. 53, no. 17, pp. 2826–2832, 2018.

[14] H. T. M. Thanh, T. T. T. Phuong, P. T. L. Hang et al., "Comparative study of Pb(II) adsorption onto MIL-101 and Fe-MIL-101 from aqueous solutions," *Journal of Environmental Chemical Engineering*, vol. 6, no. 4, pp. 4093–4102, 2018.

[15] G. Sharma, V. K. Gupta, S. Agarwal et al., "Fabrication and characterization of trimetallic nano-photocatalyst for remediation of ampicillin antibiotic," *Journal of Molecular Liquids*, vol. 260, pp. 342–350, 2018.

[16] A. Kumar, S. K. Sharma, G. Sharma et al., "Silicate glass [email protected]$_2$O/$Cu_2V_2O_7$ p-n heterojunction for enhanced

visible light photo-degradation of sulfamethoxazole: high charge separation and interfacial transfer," *Journal of Hazardous Materials*, vol. 402, article 123790, 2021.

[17] M. G. Orcajo, J. A. Botas, G. Calleja, and M. Sánchez-Sánchez, "Materiales MOF para el almacenamiento de hidrógeno," *Real Sociedad Española de Química*, vol. 108, no. 1, pp. 13–20, 2012.

[18] Z. Hasan, N. A. Khan, and S. H. Jhung, "Adsorptive removal of diclofenac sodium from water with Zr-based metal-organic frameworks," *Chemical Engineering Journal*, vol. 284, pp. 1406–1413, 2016.

[19] S. Dhaka, R. Kumar, A. Deep, M. B. Kurade, S. W. Ji, and B. H. Jeon, "Metal-organic frameworks (MOFs) for the removal of emerging contaminants from aquatic environments," *Coordination Chemistry Reviews*, vol. 380, pp. 330–352, 2019.

[20] A. Samokhvalov, "Adsorption on mesoporous metal–organic frameworks in solution: aromatic and heterocyclic compounds," *European Journal*, vol. 21, no. 47, pp. 16726–16742, 2015.

[21] D. Sompornpailin, C. Ratanatawanate, C. Sattayanon, S. Namuangruk, and P. Punyapalakul, "Selective adsorption mechanisms of pharmaceuticals on benzene-1,4-dicarboxylic acid-based MOFs: effects of a flexible framework, adsorptive interactions and the DFT study," *Science of the Total Environment*, vol. 720, article 137449, 2020.

[22] K. Ah-Reum, Y. Tae-Ung, K. Eun-Jung et al., "Facile loading of Cu(I) in MIL-100(Fe) through redox-active Fe(II) sites and remarkable propylene/propane separation performance," *Chemical Engineering Journal*, vol. 331, pp. 777–784, 2018.

[23] F. Tan, M. Liu, K. Li et al., "Facile synthesis of size-controlled MIL-100(Fe) with excellent adsorption capacity for methylene blue," *Chemical Engineering Journal*, vol. 281, pp. 360–367, 2015.

[24] R. Zhou, J. Yu, and R. Chi, "Selective removal of phosphate from aqueous solution by MIL-101(Fe)/bagasse composite prepared through bagasse size control," *Environmental Research*, vol. 188, article 109817, 2020.

[25] Y. Pi, X. Li, Q. Xia et al., "Adsorptive and photocatalytic removal of persistent organic pollutants (POPs) in water by metal-organic frameworks (MOFs)," *Chemical Engineering Journal*, vol. 337, pp. 351–371, 2018.

[26] Z. Abbasi, L. Cseri, X. Zhang, B. P. Ladewig, and H. Wang, "Metal–organic frameworks (MOFs) and MOF-derived porous carbon materials for sustainable adsorptive wastewater treatment," in *Sustainable Nanoscale Engineering*, pp. 163–194, Elsevier, 2020.

[27] H. V. Tran, L. T. Hoang, and C. D. Huynh, "An investigation on kinetic and thermodynamic parameters of methylene blue adsorption onto graphene-based nanocomposite," *Chemical Physics*, vol. 535, article 110793, 2020.

[28] H. N. Tran, S. J. You, A. Hosseini-Bandegharaei, and H. P. Chao, "Mistakes and inconsistencies regarding adsorption of contaminants from aqueous solutions: a critical review," *Water Research*, vol. 120, pp. 88–116, 2017.

[29] X. Pang, L. Sellaoui, D. Franco et al., "Adsorption of crystal violet on biomasses from pecan nutshell, para chestnut husk, araucaria bark and palm cactus: experimental study and theoretical modeling via monolayer and double layer statistical physics models," *Chemical Engineering Journal*, vol. 378, article 122101, 2019.

[30] Z. Li, L. Sellaoui, D. Franco et al., "Adsorption of hazardous dyes on functionalized multiwalled carbon nanotubes in single and binary systems: experimental study and physicochemical interpretation of the adsorption mechanism," *Chemical Engineering Journal*, vol. 389, article 124467, 2020.

[31] G. L. Dotto, M. L. G. Vieria, J. O. Goncalves, and P. L. A. de Almeida, "Remoção dos corantes azul brilhante, amarelo crepúsculo e amarelo tartrazina de soluções aquosas utilizando carvão ativado, terra ativada, terra diatomácea, quitina e quitosana: estudos de equilíbrio e termodinâmica," *Quimica Nova*, vol. 34, no. 7, pp. 1193–1199, 2011.

[32] B. S. Marques, T. S. Frantz, T. R. S. A. Cadaval Jr, L. A. de Almeida Pinto, and G. L. Dotto, "Adsorption of a textile dye onto piaçava fibers: kinetic, equilibrium, thermodynamics, and application in simulated effluents," *Pollution Research*, vol. 26, no. 28, pp. 28584–28592, 2019.

[33] O. Amrhar, L. El Gana, and M. Mobarak, "Calculation of adsorption isotherms by statistical physics models: a review," *Environmental Chemistry Letters*, vol. 19, no. 6, pp. 4519–4547, 2021.

[34] V. J. Landin-Sandoval, D. I. Mendoza-Castillo, M. K. Seliem et al., "Physicochemical analysis of multilayer adsorption mechanism of anionic dyes on lignocellulosic biomasses via statistical physics and density functional theory," *Journal of Molecular Liquids*, vol. 322, article 114511, 2021.

[35] S. Chen, K. Wen, X. Zhang, R. Zhang, and R. Han, "Adsorption of neutral red onto MIL-100(Fe) from solution: characterization, equilibrium, kinetics, thermodynamics and process design," *Desalination and Water Treatment*, vol. 177, pp. 197–208, 2020.

[36] M. Forghani, A. Azizi, M. J. Livani, and L. A. Kafshgari, "Adsorption of lead(II) and chromium(VI) from aqueous environment onto metal- organic framework MIL-100(Fe): synthesis, kinetics, equilibrium and thermodynamics," *Journal of Solid State Chemistry*, vol. 291, article 121636, 2020.

[37] K. Pil-Joong, Y. Young-Woo, P. Hosik et al., "Separation of $SF_6$ from $SF_6/N_2$ mixture using metal-organic framework MIL-100(Fe) granule," *Chemical Engineering Journal*, vol. 262, pp. 683–690, 2015.

[38] F. Zhang, Y. Jin, J. Shi, Y. Zhong, W. Zhu, and M. S. El-Shall, "Polyoxometalates confined in the mesoporous cages of metal-organic framework MIL-100(Fe): efficient heterogeneous catalysts for esterification and acetalization reactions," *Chemical Engineering Journal*, vol. 269, pp. 236–244, 2015.

[39] J. Fan, D. Chen, N. Li et al., "Adsorption and biodegradation of dye in wastewater with $Fe_3O_4$@MIL-100 (Fe) core-shell bionanocomposites," *Chemosphere*, vol. 191, pp. 315–323, 2018.

[40] N. M. Mahmoodi, J. Abdi, M. Oveisi, A. M. Asli, and M. Vossoughi, "Metal-organic framework (MIL-100 (Fe)): synthesis, detailed photocatalytic dye degradation ability in colored textile wastewater and recycling," *Materials Research Bulletin*, vol. 100, pp. 357–366, 2018.

[41] M. Nehra, N. Dilbaghi, N. K. Singhal, A. A. Hassan, K. H. Kim, and S. Kumar, "Metal organic frameworks MIL-100(Fe) as an efficient adsorptive material for phosphate management," *Environmental Research*, vol. 169, pp. 229–236, 2019.

[42] W. A. Shah, L. Noureen, M. A. Nadeem, and P. Kögerler, "Encapsulation of keggin-type manganese-polyoxomolybdates in MIL-100 (Fe) for efficient reduction of p-nitrophenol," *Journal of Solid State Chemistry*, vol. 268, pp. 75–82, 2018.

[43] H. Li, F. Liu, X. Ma et al., "Catalytic performance of strontium oxide supported by MIL-100(Fe) derivate as transesterification

catalyst for biodiesel production," *Energy Conversion and Management*, vol. 180, pp. 401–410, 2019.

[44] G. Chaturvedi, A. Kaur, A. Umar, M. A. Khan, H. Algarni, and S. K. Kansal, "Removal of fluoroquinolone drug, levofloxacin, from aqueous phase over iron based MOFs, MIL-100(Fe)," *Journal of Solid State Chemistry*, vol. 281, article 121029, 2020.

[45] T. Chen, T. Da, and Y. Ma, "Reasonable calculation of the thermodynamic parameters from adsorption equilibrium constant," *Journal of Molecular Liquids*, vol. 322, article 114980, 2021.

[46] A. M. Chávez, A. Rey, J. López, P. M. Álvarez, and F. J. Beltrán, "Critical aspects of the stability and catalytic activity of MIL-100(Fe) in different advanced oxidation processes," *Separation and Purification Technology*, vol. 255, article 117660, 2021.

[47] L. Zhao, M. R. Azhar, X. Li et al., "Adsorption of cerium (III) by HKUST-1 metal-organic framework from aqueous solution," *Journal of Colloid and Interface Science*, vol. 542, pp. 421–428, 2019.

[48] B. Anand, S. A. Younis, J. E. Szulejko, K. H. Kim, and W. Zhang, "The potential utility of HKUST-1 for adsorptive removal of benzene vapor from gaseous streams using a denuder versus a packed-bed adsorption system," *Journal of Cleaner Production*, vol. 275, article 122359, 2020.

[49] Z. Li, X. Liu, W. Jin, Q. Hu, and Y. Zhao, "Adsorption behavior of arsenicals on MIL-101(Fe): the role of arsenic chemical structures," *Journal of Colloid and Interface Science*, vol. 554, pp. 692–704, 2019.

[50] X. Q. Tang, Y. D. Zhang, Z. W. Jiang, D. M. Wang, C. Z. Huang, and Y. F. Li, "$Fe_3O_4$ and metal-organic framework MIL-101(Fe) composites catalyze luminol chemiluminescence for sensitively sensing hydrogen peroxide and glucose," *Talanta*, vol. 179, pp. 43–50, 2018.

[51] H. Fakhri, M. Farzadkia, R. Boukherroub, V. Srivastava, and M. Sillanpää, "Design and preparation of core-shell structured magnetic graphene [email protected](Fe): photocatalysis under shell to remove diazinon and atrazine pesticides," *Solar Energy*, vol. 208, pp. 990–1000, 2020.

[52] A. Jarrah and S. Farhadi, "Encapsulation of $K_6P_2W_{18}O_{62}$ into magnetic nanoporous $Fe_3O_4$/MIL-101 (Fe) for highly enhanced removal of organic dyes," *Journal of Solid State Chemistry*, vol. 285, article 121264, 2020.

[53] Z. Zhang, Y. Chen, Z. Wang et al., "Effective and structure-controlled adsorption of tetracycline hydrochloride from aqueous solution by using Fe-based metal-organic frameworks," *Applied Surface Science*, vol. 542, article 148662, 2021.

[54] G. I. Dzhardimalieva, R. K. Baimuratova, E. I. Knerelman et al., "Synthesis of copper(II) trimesinate coordination polymer and its use as a sorbent for organic dyes and a precursor for nanostructured material," *Polymers*, vol. 12, no. 5, p. 1024, 2020.

[55] M. Mohammadnejad and M. Fakhrefatemi, "Synthesis of magnetic HKUST-1 metal-organic framework for efficient removal of mefenamic acid from water," *Journal of Molecular Structure*, vol. 1224, article 129041, 2021.

[56] H. Y. Jang, J. K. Kang, J. A. Park, S. C. Lee, and S. B. Kim, "Metal-organic framework MIL-100(Fe) for dye removal in aqueous solutions: prediction by artificial neural network and response surface methodology modeling," *Environmental Pollution*, vol. 267, article 115583, 2020.

[57] D. T. Nguyen, H. N. Tran, R. S. Juang et al., "Adsorption process and mechanism of acetaminophen onto commercial activated carbon," *Journal of Environmental Chemical Engineering*, vol. 8, no. 6, article 104408, 2020.

[58] H. E. Reynel-Avila, D. I. Mendoza-Castillo, A. Bonilla-Petriciolet, and J. Silvestre-Albero, "Assessment of naproxen adsorption on bone char in aqueous solutions using batch and fixed-bed processes," *Journal of Molecular Liquids*, vol. 209, pp. 187–195, 2015.

[59] F. Tomul, Y. Arslan, B. Kabak, D. Trak, and H. N. Tran, "Adsorption process of naproxen onto peanut shell-derived biosorbent: important role of n–$\pi$ interaction and van der Waals force," *Journal of Chemical Technology & Biotechnology*, vol. 96, no. 4, pp. 869–880, 2021.

[60] K. V. B. Yaah, M. Zbair, B. de Oliveira, and S. Ojala, "Hydrochar-derived adsorbent for the removal of diclofenac from aqueous solution," *Nanotechnology for Environmental Engineering*, vol. 6, no. 1, pp. 2–12, 2021.

[61] P. B. So, H. T. Chen, and C. H. Lin, "*De novo* synthesis and particle size control of iron metal organic framework for diclofenac drug delivery," *Microporous and Mesoporous Materials*, vol. 309, article 110495, 2020.

[62] P. D. Du, H. T. M. Thanh, T. C. To et al., "Metal-organic framework MIL-101: synthesis and photocatalytic degradation of remazol black B dye," *Journal of Nanomaterials*, vol. 2019, Article ID 6061275, 15 pages, 2019.

[63] A. Hamedi, M. B. Zarandi, and M. R. Nateghi, "Highly efficient removal of dye pollutants by MIL-101(Fe) metal-organic framework loaded magnetic particles mediated by poly L-Dopa," *Journal of Environmental Chemical Engineering*, vol. 7, no. 1, article 102882, 2019.

[64] I. Bezverkhyy, G. Weber, and J. P. Bellat, "Degradation of fluoride-free MIL-100(Fe) and MIL-53(Fe) in water: effect of temperature and pH," *Microporous and Mesoporous Materials*, vol. 219, pp. 117–124, 2016.

[65] Z. Jiang and Y. Li, "Facile synthesis of magnetic hybrid $Fe_3O_4$/MIL-101 via heterogeneous coprecipitation assembly for efficient adsorption of anionic dyes," *Journal of the Taiwan Institute of Chemical Engineers*, vol. 59, pp. 373–379, 2016.

[66] C. H. Giles, T. H. MacEwan, S. N. Nakhwa, and D. Smith, "Studies in adsorption. Part XI. A system of classification of solution adsorption isotherms, and its use in diagnosis of adsorption mechanisms and in measurement of specific surface areas of solids," *Journal of the Chemical Society*, vol. 111, pp. 3973–3993, 1960.

[67] S. Li, J. Cui, X. Wu, X. Zhang, and X. Hou, "Rapid in situ microwave synthesis of $Fe_3O_4$@MIL-100(Fe) for aqueous diclofenac sodium removal through integrated adsorption and photodegradation," *Journal of Hazardous Materials*, vol. 373, pp. 408–416, 2019.

[68] M. Sarker, J. Y. Song, and S. H. Jhung, "Adsorptive removal of anti-inflammatory drugs from water using graphene oxide/metal-organic framework composites," *Chemical Engineering Journal*, vol. 335, pp. 74–81, 2018.

[69] B. N. Bhadra, A. Vinu, C. Serre, and S. H. Jhung, "MOF-derived carbonaceous materials enriched with nitrogen: preparation and applications in adsorption and catalysis," *Materials Today*, vol. 25, pp. 88–111, 2019.

[70] E. M. Cuerda-Correa, J. R. Domínguez-Vargas, F. J. Olivares-Marín, and J. B. de Heredia, "On the use of carbon blacks as potential low-cost adsorbents for the removal of non-steroidal anti-inflammatory drugs from river water," *Journal of Hazardous Materials*, vol. 177, no. 1-3, pp. 1046–1053, 2010.

[71] S. Jodeh, F. Abdelwahab, N. Jaradat, I. Warad, and W. Jodeh, "Adsorption of diclofenac from aqueous solution using Cyclamen persicum tubers based activated carbon (CTAC)," *Journal of the Association of Arab Universities for Basic and Applied Sciences*, vol. 20, no. 1, pp. 32–38, 2016.

[72] S. Raghav and D. Kumar, "Adsorption equilibrium, kinetics, and thermodynamic studies of fluoride adsorbed by tetrametallic oxide adsorbent," *Journal of Chemical & Engineering*, vol. 63, no. 5, pp. 1682–1697, 2018.

[73] S. Lombardo and W. Thielemans, "Thermodynamics of adsorption on nanocellulose surfaces," *Cellulose*, vol. 26, no. 1, pp. 249–279, 2019.

[74] K. A. Ford, "Role of electrostatic potential in the in silico prediction of molecular bioactivation and mutagenesis," *Molecular Pharmaceutics*, vol. 10, no. 4, pp. 1171–1182, 2013.

[75] N. Bouhmaida, F. Bonhomme, B. Guillot, C. Jelsch, and N. E. Ghermani, "Charge density and electrostatic potential analyses in paracetamol," *Acta Crystallographica Section B Structural Science*, vol. 65, no. 3, pp. 363–374, 2009.

[76] I. M. Kenawi, "DFT analysis of diclofenac activity and cation type influence on the theoretical parameters of some diclofenac complexes," *Journal of Molecular Structure: THEOCHEM*, vol. 761, no. 1-3, pp. 151–157, 2006.

[77] R. N. Devi, A. D. Stephen, P. Justin, K. Saravanan, P. Macchi, and C. Jelsch, "Topological and electrostatic properties of diclofenac molecule as a non- steroidal anti-inflammatory drug: an experimental and theoretical study," *Journal of Molecular Structure*, vol. 1196, pp. 42–53, 2019.

[78] A. Jubert, M. L. Legarto, N. E. Massa, L. L. Tévez, and N. B. Okulik, "Vibrational and theoretical studies of non-steroidal anti-inflammatory drugs Ibuprofen [2-(4-isobutylphenyl)propionic acid]; naproxen [6-methoxy-$\alpha$- methyl-2-naphthalene acetic acid] and tolmetin acids [1-methyl-5-(4-methylbenzoyl)-1H-pyrrole-2-acetic acid]," *Journal of Molecular Structure*, vol. 783, no. 1-3, pp. 34–51, 2006.

[79] A. E. Ahmed, L. M. Al-Harbi, G. O. Moustafa, M. A. El-Gazzar, R. F. Abdel-Rahman, and A. E. Salim, "Synthesis, comparative docking, and pharmacological activity of naproxen amino acid derivatives as possible anti-inflammatory and analgesic agents," *Drug Design, Development and Therapy*, vol. 13, pp. 1773–1790, 2019.

Hindawi
Adsorption Science & Technology
Volume 2022, Article ID 2441212, 14 pages
https://doi.org/10.1155/2022/2441212

*Research Article*

# On the Behavior of Newly Synthesized Functionalized Imidazolium-Based Ionic Liquids for Highly Efficient Extraction and Separation of Pirimicarb from Orchard Real Wastewater

**Sana Zulfiqar**,[1] **Uzaira Rafique**,[1] **M. Javed Akhtar**,[2] **and Hesham Hamad**[3]

[1]*Department of Environmental Sciences, Fatima Jinnah Women University, Rawalpindi, Pakistan*
[2]*Pakistan Institute of Nuclear Science and Technology, Nilore, Pakistan*
[3]*Fabrication Technology Research Department, Advanced Technology and New Materials Research Institute (ATNMRI), City of Scientific Research and Technological Applications (SRTA-City), Alexandria 21934, Egypt*

Correspondence should be addressed to Sana Zulfiqar; sanazulfiqar@fjwu.edu.pk and Hesham Hamad; hhamad@chem.uw.edu.pl

Received 8 December 2021; Revised 12 January 2022; Accepted 13 January 2022; Published 17 February 2022

Academic Editor: Tony Hadibarata



The presence of pirimicarb compounds as pollutants in orchard wastewater has sparked rising worries about their detrimental impacts on the ecosystem and human health, and their removal is critical for Pakistan's aquatic environment. It not only contaminates fruit, but it also leaches into the soil and contaminates groundwater. However, there is little data on the effective removal of pirimicarb from orchard wastewater. The main purpose of this study is to create a novel family of functionalized imidazolium-based ionic liquids (ILs) using a simple chemical process, which will be utilized for the first time to extract pirimicarb from orchard wastewater in an efficient, cost-effective, and environmentally acceptable manner. FTIR, SEM, XRD, TGA, BET, and $^1$H NMR spectroscopy were used to characterize the functionalized samples. The impact of the IL substituent on the separation capacity was studied. In addition, the extraction and separation of pirimicarb from orchard wastewater were investigated under a variety of conditions (time, concentration, and temperature) in order to better understand the adsorption behaviors of distinct ILs in an aqueous solution. The adsorption equilibrium was reached in 30 minutes, and the maximum removal of pirimicarb was achieved utilizing the synthesized $[C_2im][C_3H_6NH_2]Br^-$, according to the data. The pseudo-first-order model and the Langmuir model both suit well with the adsorption mechanism of pirimicarb with very good adsorptive capacities. Thermodynamic analyses indicated spontaneous, endothermic, and entropy-driven adsorption processes. The synthesized imidazolium-based ILs have good regeneration capability and recycling at least for six adsorption-desorption runs and have also been used to successfully detect pirimicarb orchard wastewater samples. The superior safety of the proposed method nominates it as a promising future strategy for pollution prevention. Consequently, this work has proven that the pirimicarb adsorption to various imidazolium-based ILs was dependent on the structures of the produced imidazolium-based ILs, which specifies its potential for practical applications in water pollutant removal and environmental remediation.

## 1. Introduction

The use of pesticides is critical for the management of pests and insect-borne diseases, which leads to an increased food supply. Although pesticides are beneficial to agriculture, their rising use has had a negative impact on humans and the environment as a whole. Because of its low persistence and great efficacy, the carbamate pesticide family has been widely used in the pest control of vegetable crops. The US Environmental Protection Agency (EPA) considers carbamate herbicide to be one of the most harmful contaminants in the environment [1, 2]. Because it is highly soluble in aqueous mediums and circulates into surface and groundwater through soil leaks, this family is poisonous and poses a threat to all living species [3].

In particular, pirimicarb (2-dimethylamino-5,6-dimethylpyrimidin-4-yldimethylcarbamate) is an important substituted N, N-dimethylcarbamate insecticide, and it has

been widely employed against aphids in fruit and vegetable [1, 4]. Pirimicarb has been classified as moderately hazardous (Class II) by the World Health Organization (WHO) because it has low toxicity, is potentially carcinogenic and mutagenic in mammals, and poses a threat to living organisms due to its inhibition of the enzyme acetylcholinesterase [3, 5, 6]. Pirimicarb is sprayed into the ground and surface water without being treated before being discharged into the streams. To protect human health, hydrolytic resources, and the aquatic environment, it is critical to investigate simple, inexpensive, and effective strategies for removing pirimicarb from water.

These strategies can be replaced by new alternate technologies for the removal of organic pollutants from wastewater such as biological treatment [7], electrochemical treatment [8], photocatalytic degradation [9], membrane separation process [10], and adsorption [11]. Among them, adsorption is a very efficient, greener, and cost-effective process for wastewater treatment [12]. Various adsorbents, zeolites, nanoparticles, carbon nanotubes, and metal-organic frameworks have been prepared and synthesized to detoxify/decontaminate wastewater by removing persistent organic pollutants (POPs) [13].

Ionic liquids (ILs) have been used as a solvent medium in different chemical reactions for environmental remediation, but very few scientists considered them for the adsorption process so far. The use of ILs as adsorbents possesses various advantages, i.e., ILs with any aromatic functional group are used for the removal of polyaromatic hydrocarbons (PAHs) from the environment while ILs that have amine as a functional group efficiently are used for toxic gases adsorptions, e.g., $CO_2$, $NO_2$, and $SO_2$.

ILs have also recently received a lot of attention for their green chemistry and clean processes and as functional inorganic materials for a variety of applications in various fields [14]. It has structural and chemical characteristics that distinguish it from other functional materials, including low vapor pressure, nonvolatility, nonflammability, noncorrosive, variable viscosities, adjustable miscibility, reusability, higher conductivity, and very high chemical and thermal stability [15, 16]. Because of their high stability, they could be long-term and high-efficiency materials in an environmental application.

At temperatures below 100°C, the strong coulumbic attraction between strong inorganic anions and asymmetric organic cations can be expressively changed to improve the physicochemical properties of ILs such as solvent selection, hydrophobicity, melting point, and viscosity [17, 18]. The modified ILs can perform exceptionally well in terms of separation. For example, cellulose acetate imidazolium-based ILs were utilized to extract pirimicarb from real wastewater, with a 74% removal efficiency under ideal conditions [19]. Similarly, researchers used ionic liquids for the removal of contaminants from water. According to the results, ILs were proved as a good alternative material option used for contaminants analysis in water as compared to solid-phase extraction materials due to their universality in liquid media and in an atmospheric environment [20].

The present study is conducted using eco-friendly, low-cost reactants to synthesize greener electrolytes "ionic liquids" in order to perform its real-world application. To the best of our knowledge, there is no comparative study for the carbamate removal from orchard wastewater using different types of imidazolium-based ILs ([im][$C_3H_6NH_2$]Br-, [im][$C_3H_6NH_2$]$BF_4$]-, [$C_2$im][$C_3H_6NH_2$]Br-, and [$C_2$im][$C_3H_6NH_2$]$BF_4$-) (Table 1). The goal of this research is to develop a new series of functionalized imidazolium-based ILs for the adsorption of pirimicarb from orchard wastewater. The morphology, crystallization, chemical structure, and textural characteristics of the various types of imidazolium-based ILs that were produced were studied. The effects of IL type, contact time, carbamate concentration, and temperature on removal efficiency were studied. Then, using adsorption kinetics, isotherms, and thermodynamic models, the adsorption performance was assessed. Possible carbamate adsorption mechanisms onto ILs and the regeneration and recycling studies of the adsorption process were discussed in detail. This research presents functionalized ILs as novel adsorbent materials, for adsorbing and removing carbamate from orchards in a complex environmental medium and projecting their use in large-scale wastewater treatment processes.

## 2. Materials and Methods

*2.1. Materials.* All chemicals and reagents used were of Sigma Aldrich Company and were of analytical grade.

*2.2. Synthesis of Functionalized Imidazolium-Based Ionic Liquids.* The chemical structure and its molecular models of the synthesized ILs are shown in Table 1. As shown in Figure 1, the synthesized functional imidazolium-based ILs were prepared by the following procedures.

*2.2.1. Synthesis of [im][$C_3H_6NH_2$]$Br^-$.* In a typical experiment, 5 mmol imidazole was added to 2-bromopropyl amine in 20 mL toluene and heated to 50°C under continuous reflux for 24 hours to form an oily colorless macrodroplet, which was then iced for 3 hours before being washed repeatedly with ethyl acetate to remove the unreacted materials. S-1 was assigned to the synthesized IL ([im][$C_3H_6NH_2$]$Br^-$).

*2.2.2. Synthesis of [im][$C_3H_6NH_2$]$BF_4$]$^-$.* IL based on the $BF_4^-$ anion was synthesized using sodium tetrafluoroborate and an ion exchange reaction mechanism. Using toluene (20 mL) as a solvent, a known amount of (S-1) was added to 5 mmol sodium tetrafluoroborate. For anionic exchange of bromide ion with tetrafluoroborate ion, the mixture was refluxed under heating for 24 hours. After 2-3 hours of condensation and washing, the crude liquid (ethyl acetate) was transformed into pale yellow droplets. S-2 was assigned to the product ([im][$C_3H_6NH_2$]$BF_4$]$^-$).

*2.2.3. Synthesis of ([$C_2$im][$C_3H_6NH_2$]$Br^-$).* An equimolar (5 mmol) ratio of 2-ethyl imidazole and 2-bromopropyl amine hydrobromide was dissolved in 20 mL toluene under constant stirring and reflux at 50°C. A condensed oily layer

Table 1: The chemical structures of the studied imidazolium-based ILs.

| Code | Ionic liquid | Chemical structure | Model | Yield (%) |
|---|---|---|---|---|
| S-1 | $[im][C_3H_6NH_2]Br^-$) | 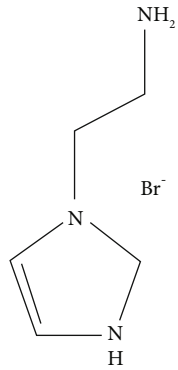 | 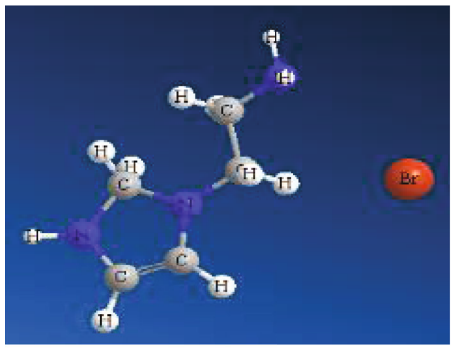 | 46.2 |
| S-2 | $[im][C_3H_6NH_2]BF_4]^-$ | 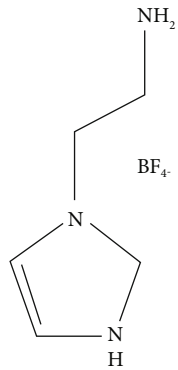 | 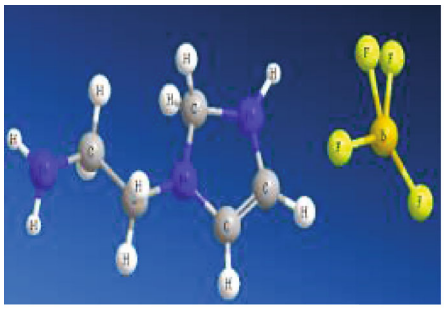 | 52.3 |
| S-3 | $[C_2im][C_3H_6NH_2]Br^-$ | 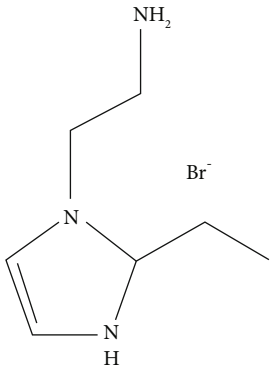 | 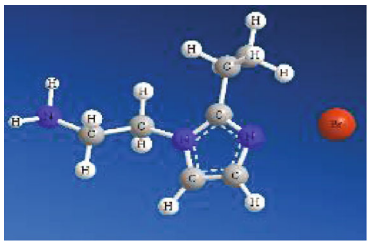 | 50.1 |
| S-4 | $[C_2im][C_3H_6NH_2]BF_4^-$ | 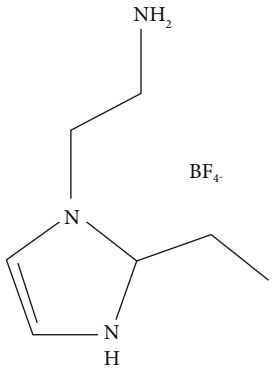 | 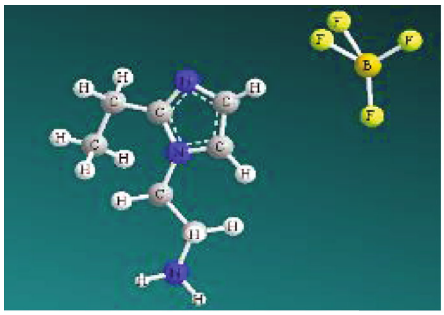 | 49.7 |

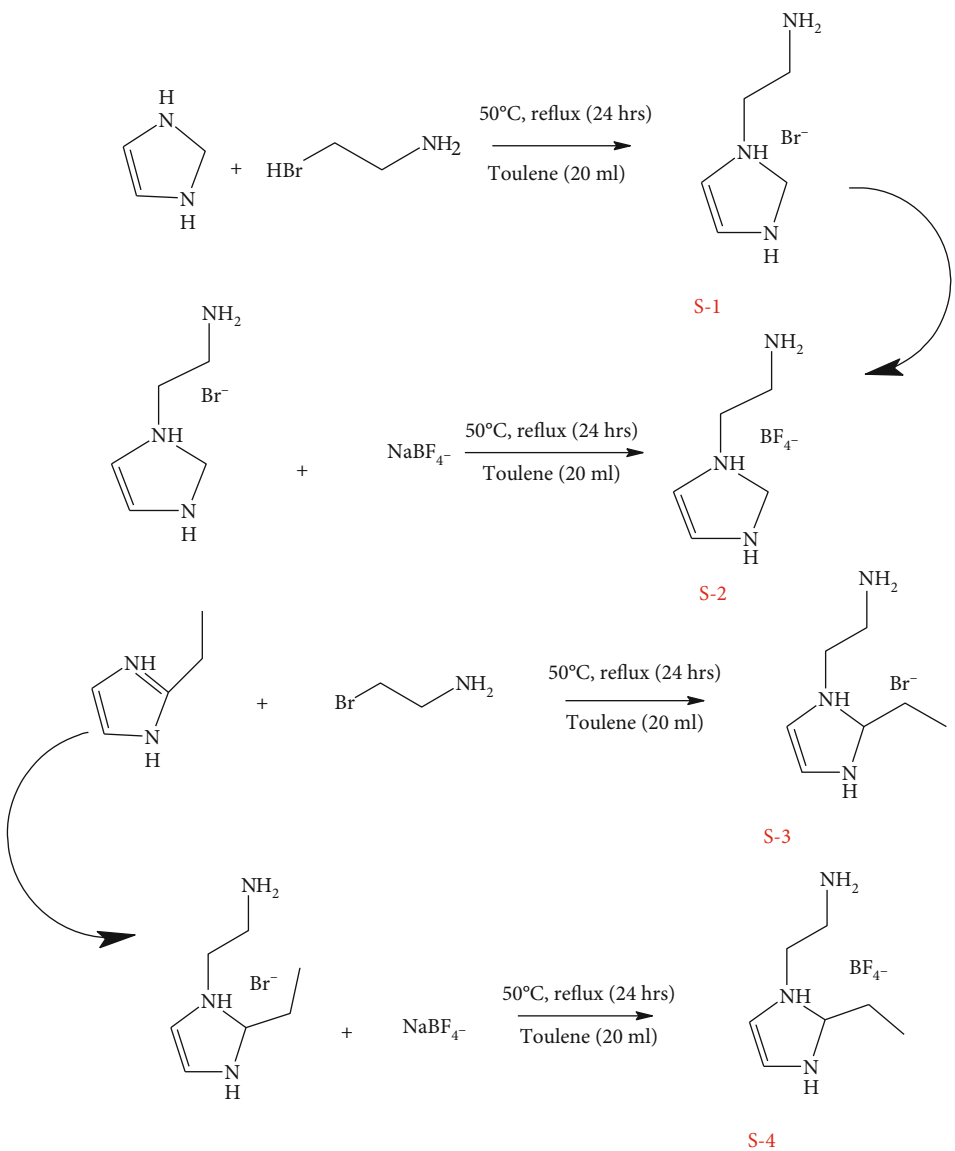


Figure 1: Schematic diagram of synthetic route of imidazolium-based ionic liquids.

washed with ethyl acetate was turned into new IL named as ($[im][C_3H_6NH_2]Br^-$) with code given as S-3.

*2.2.4. Synthesis of $[C_2im][C_3H_6NH_2]BF_4^-$.* Following the above-mentioned protocol for S-3, ($[C_2im][C_3H_6NH_2]BF_4^-$) was synthesized using an ion exchange reaction mechanism ($Br^-$ to $BF_4^-$). The sample was coded as S-4.

*2.2.5. Characterization of Adsorbents and Adsorption Studies.* The detailed characterization and adsorption experiments are stated in supporting information (Supp.1, and Supp.2), respectively.

## 3. Results and Discussion

The new imidazolium-based ILs were used to test the extraction of pirimicarb. Table S-1 lists the characteristics of pirimicarb. The pirimicarb was derived from real wastewater collected from orchard gardens in the District of Jhelum, Pakistan, which had recently been sprayed with the pesticide (see Supporting Information Fig.S-1). The designation of new ionic liquids with an aromatic and double-bond moiety could open up a new frontier in the separation studies of carbamate compounds due to the aromatic characteristics of pirimicarb. Figure 1 depicts the ILs studied and their synthesis. These ILs have high redox stability, are simple to synthesize, and have a low viscosity.

*3.1. Characteristics of the Prepared Imidazolium-Based ILs.* FTIR was used to identify changes in the functional groups of the various ILs that had been prepared. In pure ILs, the skeleton stretching vibration of the imidazolium ring can be assigned by two peaks at 1580 and 1470 $cm^{-1}$, which provide clear evidence for the successfully prepared products (S-1 to S-4) [21]. The total incorporation of ILs with alkyl groups and the formation of new functional groups

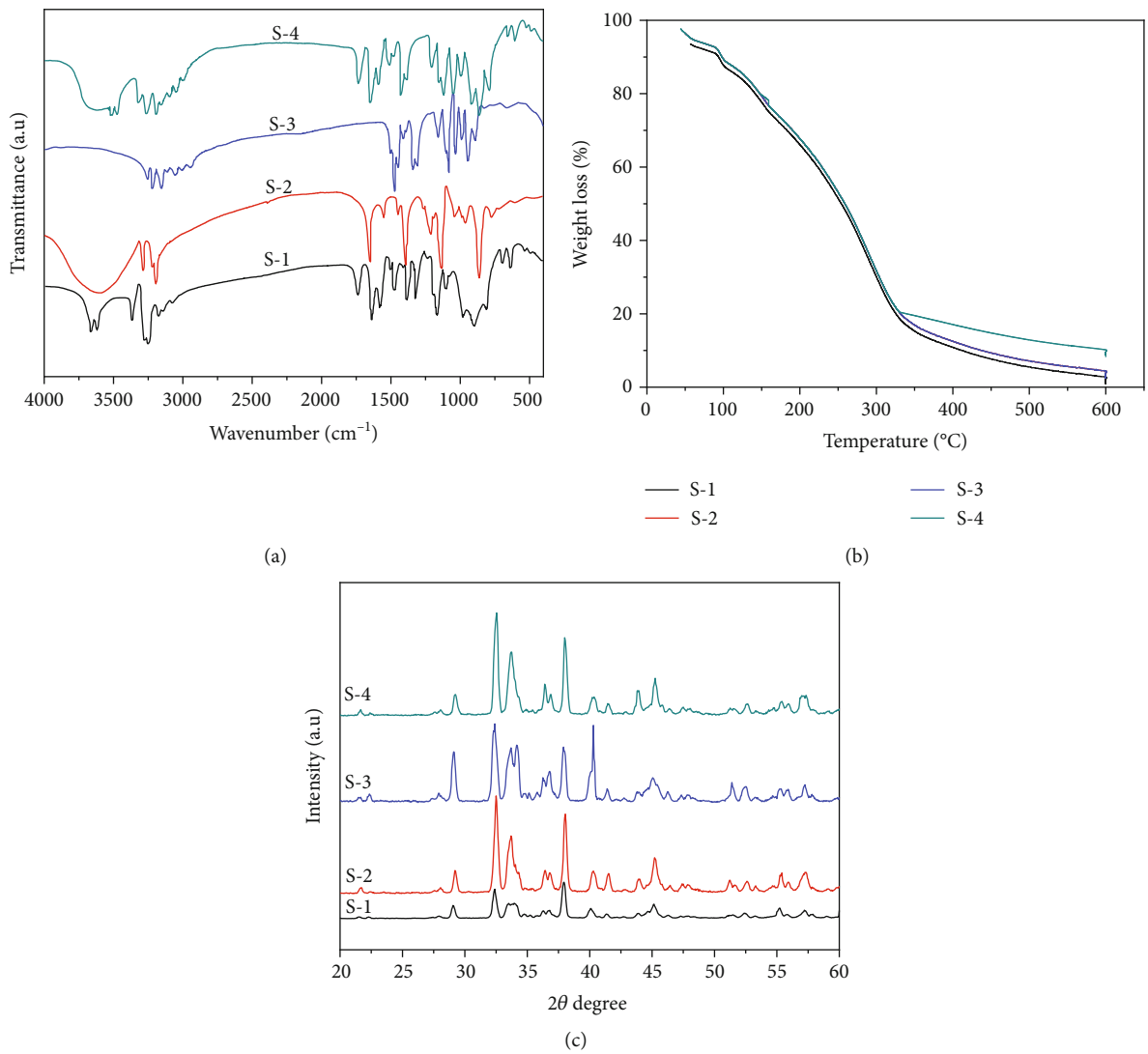


Figure 2: (a) FTIR, (b) TGA, and (c) XRD of the prepared imidazolium-based ILs.

composites with completely different properties can be stated as the disappearance or less intense of former pure ILs stretching vibration bands.

The change in intensity of sample S-1 between 2800 and 3000 cm$^{-1}$ indicated the presence of several alkyl groups [22]. The conjugated strong peaks at 1580 and 1633 cm$^{-1}$ were caused by the imidazolium ring's symmetric C=N and symmetric -C=C- bonds, respectively, indicating the presence of imidazolium cations [15]. The peaks at 3650 cm$^{-1}$ represent N-H stretching, whereas the stretching vibration of the -OH bond is due to the hydrobromide anion, which appears at 3300 cm$^{-1}$ and helps form hydrogen bonds with pirimicarb [23]. The symmetric aromatic C-H group in imidazolium cations of ILs was revealed by the peak at 3150 cm$^{-1}$ [24]. Furthermore, the imidazole cation's C-H stretching and bending were measured at 3100-3150 cm$^{-1}$ and 1450 cm$^{-1}$, respectively [25]. Furthermore, the FTIR spectra in Figure 2(a) revealed that the peaks at 1640 cm$^{-1}$ are due to -C=C stretching vibration [26]. C=N and C-N between the nitrogen of the imidazolium ring and the first carbon, respectively, are responsible for the peaks at 1417 and 1145 cm$^{-}$1, which are attributed to the functional group between the imidazolium ring and alkyl groups [27]. In comparison to bromide-containing IL counterparts, the FTIR spectra of samples S-2 and S-4, which are substituted by $BF_4^-$, show similar peaks but less shifted vibrational bands. The stretching vibration of anion $BF_4^-$ causes a new peak in the spectra of samples S-2 and S-4 at 1130 cm$^{-1}$ and 1050 cm$^{-1}$, respectively [28, 29]. The B-F peak (1050-1070 cm$^{-1}$) due to the long cationic group accompanying $BF_4^-$ is supported by the literature [28]. At 850 cm$^{-1}$, C-N (bop) can also be seen.

Thermogravimetric analysis (TGA) was used to collect data on the thermal degradation of the total % mass loss of imidazolium-based ILs that had been prepared. The results are plotted in Figure 2(b), indicating that the thermal stability of the four synthesized ionic liquids is ranked S-4, S-3, S-2, and S-1. At 100°C, the desorption of adsorbed water onto the surface of the samples resulted in a small weight loss. Small initial weight loss is due to remaining organic solvents

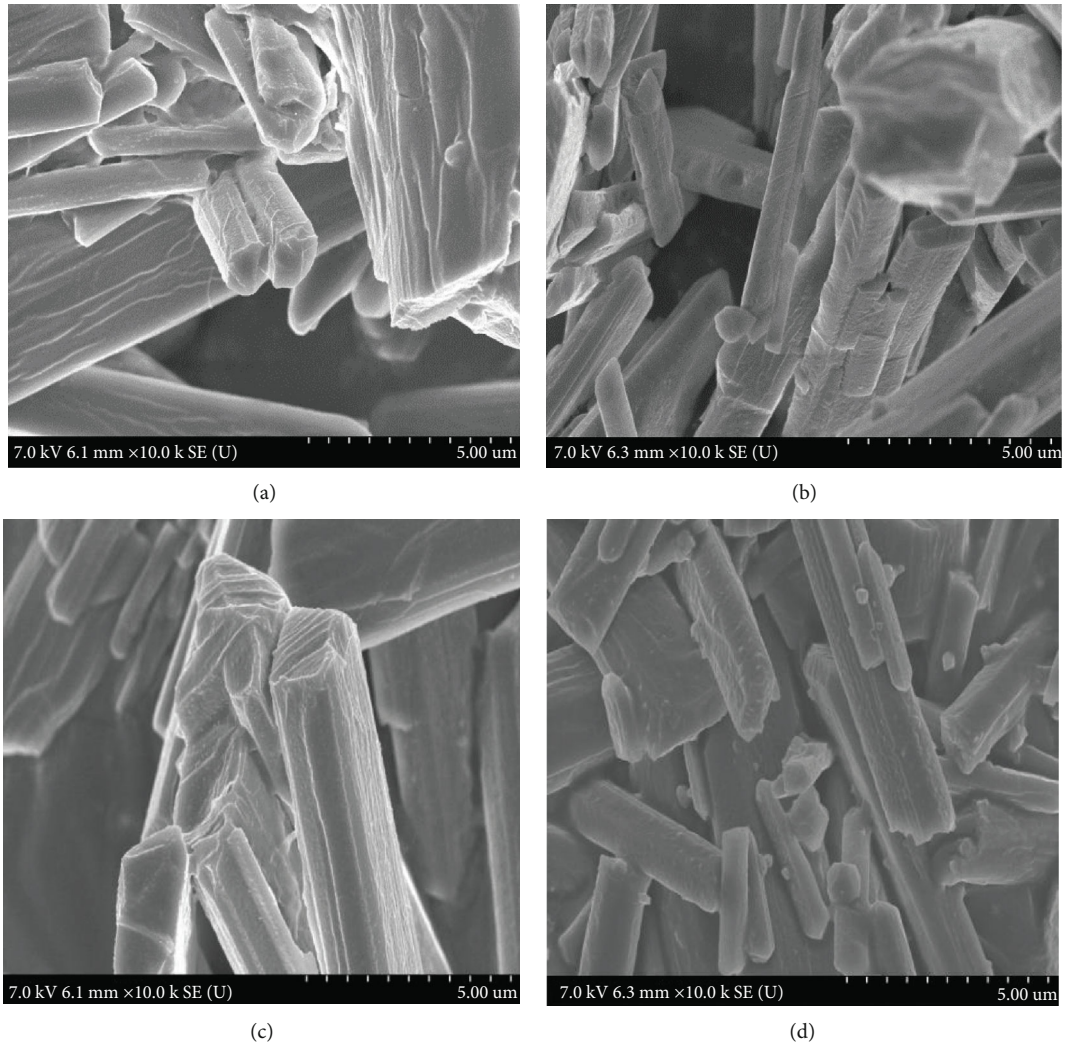


Figure 3: SEM of imidazolium-based ionic liquids: (a) S-1, (b) S-2, (c) S-3, and (d) S-4.

Table 2: BET isotherm of synthesized imidazolium-based ILs.

| Properties | S-1 | S-2 | S-3 | S-4 |
|---|---|---|---|---|
| BET surface area ($m^2/g$) | 289 | 296 | 300 | 292 |
| Micropore volume ($cm^3/g$) | 0.04 | 0.07 | 0.09 | 0.03 |
| Micropore area ($m^2/g$) | 57 | 59 | 61 | 52 |

and physically adsorbed water due to the hydrophilic nature of imidazolium-based ILs at temperatures between 100 and 200°C [30]. Then there was the 80 percent weight loss for all samples at temperatures ranging from room temperature to 323°C, which was attributed to the breakdown of the organic moieties. It can be seen from the curves that the samples are thermally stable above 300°C, which is useful information for the thermal stability of different ILs. Above 323°C, it can thus be concluded that the sample S-4 has the highest thermal stability which indicates that the stability increases with the increase in alkyl chain length of cations while the samples containing $BF_4^-$ are effectively thermally stable than samples containing -$Br^-$.

X-ray diffraction analysis was used to determine the crystallinity and purity of the synthesized ILs (Figure 2(c)). The sharp peaks and high intensity of reflections revealed that all samples had well-crystalline structures (S-1 to S-4). The reflections observed in the diffraction patterns of samples S-2 and S-4 were narrower and more intense than those observed in the diffraction patterns of samples S-1 and S-3, indicating that the $BF_4^-$ treatment crystallized better than the $Br^-$ treatment. Furthermore, the broadening of diffraction peaks in samples indicated very small crystallite sizes in the 22-24 nm range. The samples were all pure phases in every case. There are small shifts and differences in the intensity of the XRD diffraction patterns, indicating that the crystal structure of imidazolium-based ILs has changed as a result of the reaction.

According to the Scherrer equation, it can be noted that the crystal size of synthesized ILs decreased from 24.10 nm for sample S-1 to 22.65 nm for sample S-2, but it remained almost the same (22.30 nm) for sample S-3 and 22.70 nm for sample S-4.

Figure 3 shows the SEM images and surface morphology of the functionalized imidazolium-based ILs. All of the data

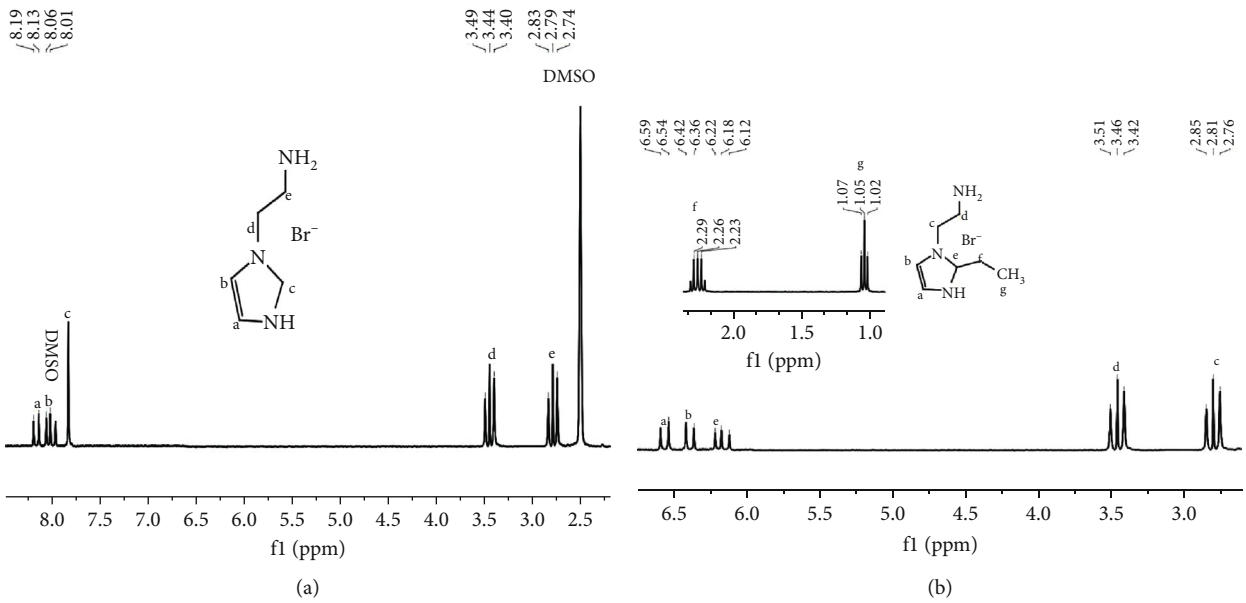


Figure 4: $^1$H NMR of (a) S-1 and (b) S-3 based on imidazolium-based ILs.

was collected at a magnification of 10 K, and a micrograph with a size of 5 m was chosen. The well-ordered arrays of agglomerated flat rod-like sheets, which were typical morphology of periodic imidazolium-based ILs, are clearly visible. When comparing sample S-3 to other samples, the highest uniformity was found, indicating the presence of various imidazolium-based ILs. When the carbon chain was increased from C1 to C2 (S-3, S-4), imidazolium-based ILs became more assembled, predicting cleared rod-like structures, as shown in Figure 3. These characteristics gain support from the cited literature [31] as well.

The specific surface area, micropore volume, and micropore area of as prepared imidazolium-based ILs are listed in Table 2, to obtain additional information regarding the textural properties of the prepared ILs. The surface area of the reported imidazolium-based ILs was much smaller in all cases than the ones found in this study [14]. The use of the solvent in the preparation resulted in a large surface area and porosity, also supported by cited research [32]. For all samples, there are no obvious changes in surface area or pore volume.

Ionic liquids based on cationic composition (imidazole, 2-ethyl imidazole) were subjected to $^1$H NMR analysis for structure elucidation. $^1$H NMR spectra of samples S-1 and S-3 were taken at 400 MHz using dimethyl sulfoxide (DMSO) as solvent as shown in Figure 4.

The strength of the C(2)-H bond can be seen in the $^1$H NMR chemical shift values ($\delta$, ppm) of imidazolium-based ILs such as sample S-1, which are 2.79 (2H, t, $CH_2$), 3.44 (2H, t, $CH_2$), 7.9 (2H, d, $CH_2$), 8.13 (1H, d, CH), and 8.19 (1H, d, CH), indicating different stereochemistry of protons [33]. The doublet (d) peak at 7.9 ppm shows the influence of NH groups on protons from both sides, as can be seen from the results. Protons present on neighboring positions at carbon "d" and "e," respectively, can be attributed to two triplet (t) peaks at 2.79 and 3.44 ppm. The splitting of peaks into a triplet is caused by neighboring protons of the imidazole ring.

Two doublet peaks at carbon position "a" and "b" (8.13 and 8.19 ppm) are designated to protons present inside the imidazole ring. It can be due to the change in the proton environment due to chemical shifts at carbon "a" and carbon "b" [34].

Similarly, in sample S-3, the chemical shifts are noted at $\delta$/ppm: 1.05 (3H, t, $CH_3$), 2.23-2.29 (2H, 2.26, qd, $CH_2$), 2.76-2.85 (2H, t, $CH_2$), 3.42-3.51 (2H, t, $CH_2$), 6.18 (1H, t, CH), 6.36-6.42 (1H, d, CH), and 6.54-6.59 (1H, d, CH). The quadrant at $\delta$ 2.2.3-2.29 ppm is due to the influence of $CH_3$ and CH present in the surroundings of carbon position "f."

*3.2. Adsorption of Pirimicarb by the Functionalized Imidazolium-Based ILs.* The efficiency of the prepared materials as a potential adsorbent was investigated after the successful synthesis of various types of imidazolium-based ILs. The synergy between two effects, (i) the counter anions (i.e., $Cl^-$ and $BF_4^-$) and (ii) the various cation substituents as a hydrocarbon chain attached with imidazolium-based ILs, initially affected the adsorption of pirimicarb onto the various types of imidazolium samples. This discovery revealed that the effect of $BF_4^-$ on adsorption characteristics is more noticeable than the effect of $Br^-$ and that the longer chain length has a significant impact on the adsorption process. It is possible that the lower effect of $Br^-$-based imidazolium adsorbent is due to $Br^-$'s complete dissociation in water, whereas hydrophobic $BF_4^-$ anions are very stable in solution and nearly immiscible [35]. However, as the chain of hydrocarbons lengthens, the effect of BF4- diminishes (sample S-4). The adsorption follows the sequence S-3 (75%) > S-2 (74%) > S-4 (58%) > S-1 (18%).

According to the literature, the weaker the intramolecular hydrogen bonding between the C(2)-H and the anions, the longer the N-alkyl side chains [36]. As a result, longer alkyl chain ILs have a greater ability to separate pirimicarb. This behavior can be seen in S-1, which has a shorter side

chain than S-3, resulting in less interaction to form hydrogen bonds with pirimicarb and due to the close proximity of the cation and $Br^-$ [3, 14]. Due to the large volume used by the benzyl group (in pirimicarb) matched to the allyl substituent, S-1's ability to extract pirimicarb from liquid outperformed S-3's, and as a result of the steric hindrance caused by the larger benzyl group, the chloride ion was unable to form an H-bond with phenol [37].

Following that, it is worth noting that the distance between the chloride ion and the cation is optimal for forming a hydrogen bond with phenol [3, 14]. The branched structure has higher hydrophilicity than the linear structure [38].

The change in separation capability has two justifications. For starters, it has to do with the ILs' ability to form hydrogen bonds with pirimicarb. The main mechanism in samples S-1 and S-3 is the bromide ion ($Br^-$) of the ILs, which acts as an electron donor to the pirimicarb groups containing N and/or O. The $Br^-$ ion has a higher chance of making contact with pirimicarb, resulting in a higher degree of hydrogen bonding in the system. Secondly, their $^1$H NMR spectrum demonstrates the role of aromatic moieties and unsaturated substitutes in the stronger interaction of ILs with the aromatic ring of pirimicarb. This is due to unsaturated substitutions on the cationic imidazolium ring, which can attract aromatic compounds more efficiently than their alkyl counterparts [18]. The intensity of the C(2)-H can be endorsed from the $^1$H NMR chemical shift ($\delta$, ppm) of the ILs. The higher the C(2)-H chemical shift, the stronger its interaction with the anion, thus decreasing the possibility of the anion to form H-bonding with pirimicarb [34]. Another point to consider is how the larger ethyl propyl group hampered the ability of the $BF_4^-$ ions to form a H-bond with pirimicarb in samples S-2 and S-4 (S4 is lower as a result of the hindrance). As a result, it is important to remember that there is an ideal distance between chloride ions and cations for forming a hydrogen bond with pirimicarb [3, 14, 38]. When the hydrophobicity of pirimicarb is lower, it offers dispersion, or/and hydrogen bond interactions appear to play a significant role in the separation capability of the studied ILs, this change is more pronounced.

The effect of contact time was investigated thoroughly from 5 to 200 minutes in the case of a dosage of 10 mg in order to establish the equilibrium required for mass transfer between two immiscible phases. It can be observed that from 5 to 30 min, the rejection capability was greatly improved (Figure 5). This pattern may have emerged as a result of the initial accumulation of pirimicarb on the active sites of ILs surface, with the majority of binding sites being used within 30 minutes. Further separation experiments are carried out above 30 min to confirm that the required equilibrium was reached, but there is no significant boost due to the lack of vacant adsorption sites [39]. The extraction capability of pirimicarb reached equilibrium after 30 min, and thus, the duration of 30 min was active as the optimum time for extraction of pirimicarb from the orchard waste water. Literature studies show that 30 min is a good time to attain equilibrium in order to remove pesticides using functionalized ILs [40].

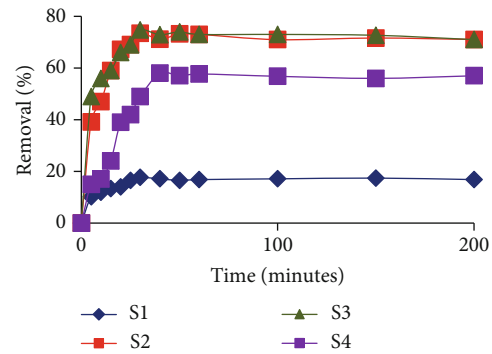


Figure 5: Removal of pirimicarb by synthesized ILs as a function of time.

The graphics plotted in Figure 6 can be used to analyze the effect of the initial pirimicarb concentration. According to logic, the separation efficiency decreases as the initial pirimicarb concentration rises, which could be due to pirimicarb equilibrium and saturation in ILs, as previously reported in the literature [6]. Experiments were carried out with varying lower concentrations of pirimicarb (3, 5, and 7 mg/L) in real wastewater from river streams, each sampled from a different area. Figure 6 shows that as the concentration of adsorbate increases from 3 to 5 mg/L, separation efficiency increases, followed by a decrease in adsorption rate at 7 mg/L. When interacting with pirimicarb at lower concentrations, the ratio of available binding sites on the surface of the adsorbent is larger [2]. It could be due to the saturation of active sites on the adsorbent surface. The S-3 is effective at removing pirimicarb at concentrations of 5 mg/L or less after 30 minutes.

*3.3. Adsorption Isotherms, Kinetics, and Thermodynamic Studies.* The adsorption rate is a critical factor in practical water treatment. The mass transfer and adsorption mechanisms were studied using kinetic models of pseudo-first-order, pseudo-second-order, and intraparticle diffusion (expressed in Table S-2). The deliberate correlations for the pseudo-first-kinetic and second-kinetic models, as listed in Table S-3, are close to unity, according to the obtained results. As a result, the pseudo-first-kinetic model is able to accurately predict pirimicarb adsorption kinetics on the surface of imidazolium-based ILs. Further, the chemisorption is not the rate-limiting for the process of adsorption which is maybe due to the degree and shape of porous available for adsorption, also supported by literature [41].

The intraparticle diffusion model [42] was applied to describe the competitive adsorption. The initial rate of intraparticle diffusion is obtained by linearization of the curve $q_t = a + k_{\text{int}}\ (t^{0.5})$. The plot of $q_t$ against $t^{0.5}$ may present multilinearity [43]. As presented in Table S-2, the linear plots are owing to the macropore distributions that are the available sites for adsorption. The results indicate that three steps occur in the adsorption processes for imidazolium-based ILs. The first linear step ($R^2 - 1$) is dedicated to the external surface adsorption or instantaneous adsorption stage. The second portion is attributed to the gradual adsorption stage where the intraparticle diffusion is rate-

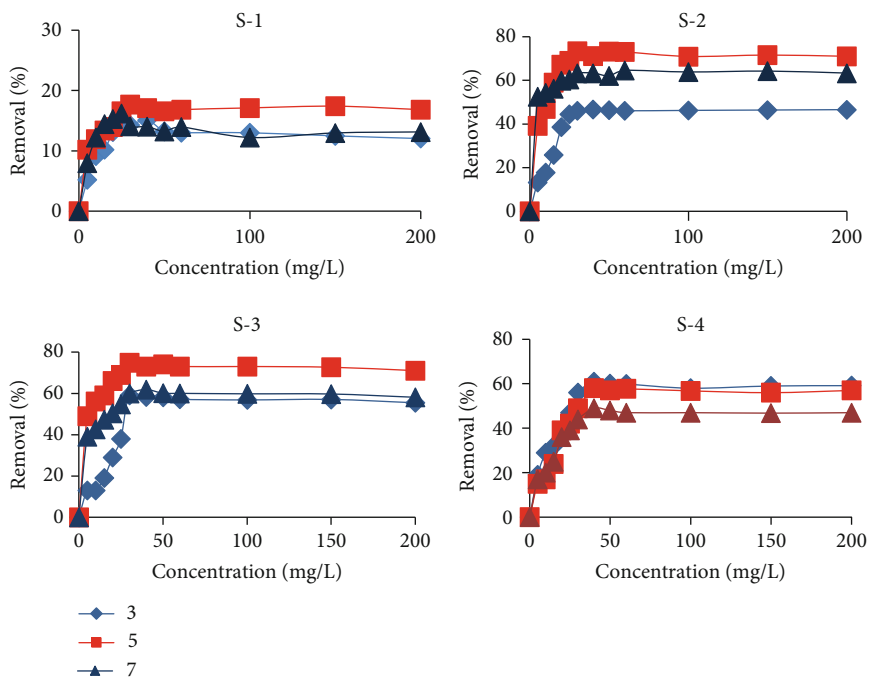


Figure 6: Removal of pirimicarb by the synthesized ILs as a function of concentration.

Table 3: Kinetic parameters of pirimicarb adsorption onto prepared imidazolium-based ILs.

| | Kinetics | | | | | | | | | |
|---|---|---|---|---|---|---|---|---|---|---|
| | Pseudo-first-order | | | Pseudo-second-order | | | Intraparticle diffusion | | | |
| | $K_1$ | $C_o$ | $R^2$ | $q_e$ | $K_2$ | $R^2$ | $K_{Int}$ | $R^2 - 1$ | $R^2 - 2$ | $R^2 - 3$ |
| S-1 | 0.04 | 2.66 | 0.99 | 0.37 | 3.05 | 0.99 | 0.08 | 0.98 | 0.84 | 0.89 |
| S-2 | 0.04 | 1.00 | 0.92 | 0.40 | 0.38 | 0.65 | 0.26 | 0.92 | 1 | 0.45 |
| S-3 | 0.04 | 1.06 | 0.81 | 0.28 | 0.64 | 0.7 | 0.13 | 0.91 | 0.93 | 0.72 |
| S-4 | 0.06 | 1.20 | 0.99 | 0.59 | 0.21 | 0.8 | 0.25 | 0.99 | 0.89 | 0.04 |

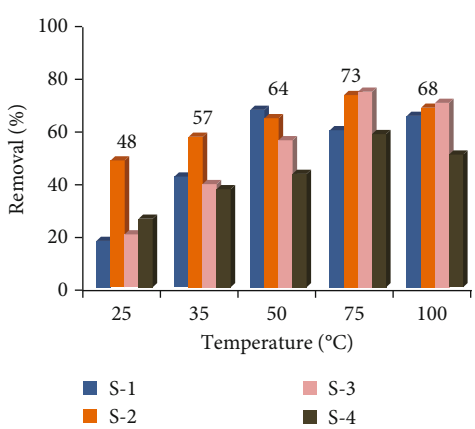


Figure 7: Removal of pirimicarb by synthesized ILs as a function of temperature.

controlled ($R^2 - 2$) while the third portion is the final equilibrium stage ($R^2 - 3$).

It could be discovered by comparing the $R^2$ values (Table 3), suggesting the sorption processes followed by the intraparticle diffusion model. It shows that the adsorption process takes place through the following steps: (i) transport of pirimicarb in the bulk solution; (ii) film diffusion of these solute at the boundary layer or diffusion of pirimicarb from bulk solution to the external surface of ILs; (iii) the transfer of pirimicarb into the active sites and/or pores (intraparticle diffusion) at the ILs; and (v) diffusion through small pores of ILs.

Finally, based on the kinetic modeling results, it was demonstrated that the adsorption of the polluted pirimicarb onto the prepared imidazolium is governed by physisorption and intraparticle diffusion mechanisms.

The adsorption isotherm is a useful tool for determining adsorption efficiency, which is based on information about the reaction's feasibility as well as the surface properties of the synthesized ILs. At different initial concentrations, Langmuir, Freundlich, and Temkin were used. Table S-2 shows the linear plotting of these adsorption isotherms. Table S-3 shows that using the Langmuir model to simulate adsorption onto imidazolium-based ILs yields a better fit for the experimental adsorption equilibrium, which is indicative of pirimicarb adsorption onto imidazolium-based ILs as monolayer coverage and constant adsorption energy.

Table 4: Thermodynamic studies of pirimicarb removal using synthesized ILs.

| Sample | Temp. (K) | $K_d$ | $\Delta G$ (kJ mol$^{-1}$) | $E_a$ (kJ mol$^{-1}$) | $\Delta H$ = slope × $R$/1000 | $\Delta S$ = (intercept × $R$)/1000 |
|---|---|---|---|---|---|---|
| | 298 | 41.07 | -9.21 | 8.11 | | |
| | 308 | 26.11 | -8.35 | 9.54 | | |
| S-1 | 323 | 16.75 | -7.57 | 11.20 | 26.39 | 0.06 |
| | 348 | 9.631 | -6.46 | 13.47 | | |
| | 373 | 4.635 | -4.76 | 16.92 | | |
| | 298 | 84.88 | -11.00 | -4.91 | | |
| | 308 | 83.27 | -11.32 | -5.03 | | |
| S-2 | 323 | 65.99 | -11.25 | -4.65 | 17.43 | 0.02 |
| | 348 | 37.40 | -10.33 | -3.32 | | |
| | 373 | 22.62 | -9.67 | -2.05 | | |
| | 298 | 78.52 | -10.81 | -1.60 | | |
| | 308 | 76.76 | -11.12 | -1.59 | | |
| S-3 | 323 | 75.05 | -11.60 | -1.61 | 20.58 | 0.03 |
| | 348 | 30.84 | -9.78 | 0.83 | | |
| | 373 | 16.70 | -8.73 | 2.80 | | |
| | 298 | 78.00 | -10.79 | 4.08 | | |
| | 308 | 49.04 | -9.97 | 5.40 | | |
| S-4 | 323 | 32.91 | -9.38 | 6.74 | 25.50 | 0.05 |
| | 348 | 18.20 | -8.27 | 8.84 | | |
| | 373 | 9.54 | -7.00 | 11.62 | | |

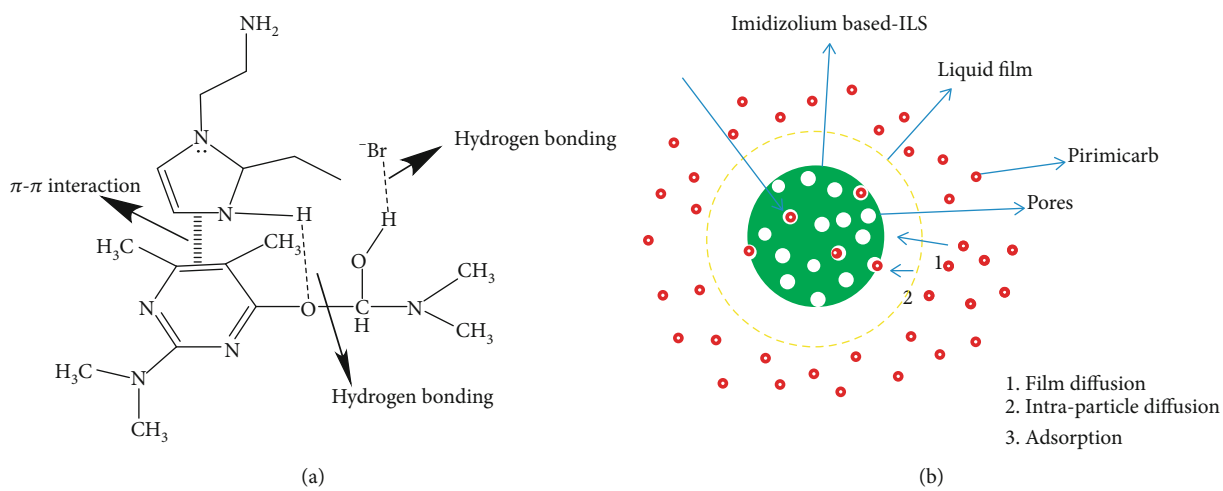


Figure 8: (a) Mechanism of removal of pirimicarb with ([$C_2$im] [$C_3H_6NH_2$]Br$^-$) by $\pi-\pi$ interaction and H-bonding, and (b) schematic diagram of physical mechanism with steps for adsorption of pirimicarb onto imidazolium-based ILs.

Furthermore, pirimicarb and the prepared imidazolium-based IL-bending sites have a strong electrostatic attraction [44]. The Temkin adsorption isotherm was developed to determine the heat of adsorption liberation. The adsorption system based on the heat and pirimicarb sorption processes was analyzed using a uniform distribution of binding energies up to a maximum binding energy, as shown in Table S-3.

The effect of temperature on the removal efficiency of pirimicarb was studied thoroughly at the temperature range 25-100°C at the constant dose of 10 mg/L, initial concentration, and contact time of 60 min, and the experimental data are plotted in Figure 7. The temperature was varied from 25°C onward by the varying intervals of 10, 15, 20, and 30, respectively. It is clear that increasing the reaction, temperature increases the pirimicarb removal efficiency. It can be justified from a thermodynamic standpoint because the adsorption process is endothermic in nature and controlled by the enthalpy term [45]. At 75°C, which is assumed to be the solution's equilibrium temperature, the maximum adsorption of 73 percent of pirimicarb was obtained. This could be because as the temperature rises, the randomness of pirimicarb decreases, resulting in increased adsorption. With each increase in temperature after that temperature, the adsorption decreases.

Table 5: Recyclability of functionalized ILs up to six adsorption cycles.

| Adsorbents | 1st cycle | 2nd cycle | 3rd cycle | 4th cycle | 5th cycle | 6th cycle |
|---|---|---|---|---|---|---|
| S-2 | 74 | 74 | 72.5 | 71.75 | 71 | 70 |
| S-3 | 75 | 74 | 73 | 73 | 72.5 | 72 |

Thermodynamics plays a significant role in understanding the conversion of energy into mass and vice versa. Thermodynamic studies provide vital information on internal energy variations, as well as the spontaneity and heat change of the adsorption process [45, 46]. The estimation of parameters standard free energy change ($\Delta G^\circ$), the standard enthalpy change ($\Delta H^\circ$), and the standard entropy change ($\Delta S^\circ$) is presented in Supp.3. Pirimicarb separation was better at 75°C, confirming the robustness of the adsorbate-adsorbent interaction at high temperatures. The weak compactness of the system, which is the core aspect of boosting the randomness at the solid-solution interface, is due to the $\pi$-anionic and cationic between pirimicarb and ILs. As a result, the extraction of pirimicarb is enhanced at high temperatures, as evidenced by $\Delta G^\circ$ values obtained at various temperature ranges. Negative $\Delta G^\circ$ values indicated the likelihood of extraction and the spontaneous nature of the separation process at a given temperature. The decreasing value of $\Delta G^\circ$ as temperature rises indicates an increase in the degree of pirimicarb extraction feasibility. Physical adsorption enthalpy ($\Delta H^\circ$) varies from -20 to 40 kJ mol$^{-1}$, whereas chemical adsorption enthalpy ($\Delta H^\circ$) varies from -80 to 400 kJ mol$^{-1}$. A negative charge on H in this study indicates that the extraction process is physisorption and endothermic in nature. During the separation process, the increased randomness leads to an increase in the degree of freedom at the IL-pirimicarb solution interface.

The positive $\Delta S^\circ$ could be reorganized from the point where sodium dehydration causes a large entropy boost in their transfer from water to the ILs [47]. Furthermore, all of the $\Delta H^\circ$ values in Table 4 are less than 40 kJ mol$^{-1}$, indicating that the pirimicarb extraction by imidazolium-based ILs is consistent with the physical adsorption process [48]. Furthermore, in this system, all of the $\Delta S^\circ$ values were positive, indicating that randomness was boosted on the solid-liquid interface during the extraction process. The possible cause was that the water molecules on the surface of ILs were replaced by pirimicarb, which has a larger molecule volume [37], increasing the system's entropy value. As a result, increasing the temperature to 75°C helps the synthesized ILs extract pirimicarb.

*3.4. Extraction Mechanism.* The pseudo-first-order model and intraparticle diffusion model fit the experimental data well. The imidazolium-based ILs enable the separation of pirimicarb from an aqueous solution, according to the pseudo-first-order model. The capability of imidazolium-based ILs to extract pirimicarb is governed by two significant interactions. In the structure of pirimicarb, the first is the formation of H-bonds, in which the bromide ions act as an electron donor to N. The Br-'s high electronegativity promotes H-bonding, which is important in the separation process. The second driving force for the separation of pirimicarb by imidazolium-based ILs is the $\pi - \pi$ conjugation between the modified imidazolium ring and the benzene ring of pirimicarb [11].

The role of aromatic moieties in the strengthening interaction of ILs with the ring of pirimicarb can be seen in their $^1$H NMR spectrum, which is surprising. This is because aromatic compounds attracted to cationic imidazolium rings modified with saturated substituents such as alkyl more efficiently than unmodified counterparts [49]. The $\pi - \pi$ interaction of pirimicarb's aromatic benzene ring with aromatic moieties of S-3, as well as the H-bonding of $Br^-$ with the carboxylic group of pirimicarb, is illustrated in Figure 8(a).

In addition, the solid-liquid extraction of pirimicarb-imidazolium-based ILs followed the intraparticle diffusion model. The transfer of pirimicarb ions in this mechanism is usually classified as external diffusion (film diffusion), internal diffusion (intraparticle diffusion), or both (film and intraparticle diffusion). Three sequential steps occur during the extraction of pirimicarb onto imidazolium-based ILs, as shown in Figure 8(b).

*3.5. Recycling Performance of the Adsorbent.* From an economic point of view, the ability to regenerate the IL for reuse is one of the important factors for industrial applications because regeneration will reduce reagent costs in removing pollutants.

In previous researches, toluene was used as an extracting solvent for pollutants which is very toxic so the desorption study was conducted after having many trials with chloroform or ethanol [50]. Our results showed a very encouraging potential of ILs for removal of pirimicarb even after six repeated cycles using ethanol.

After complete removal of pirimicarb from orchard wastewater using functionalized ILs, the regeneration capability of sorbents was investigated for repeated adsorption efficiency under the same conditions as those used for virgin adsorbents. After six (6) adsorption/desorption cycles (as shown in Table 5), the performance of the regenerated S-3 showed retention of >70% efficiencies, indicating that S-3 is an excellent reusable adsorbent [51]. Moreover, it was worth mentioning that as the desorption experiment before regeneration was performed using ethanol as extracting solvent [52], functionalized ILs are sustainable to use. The results are quite similar as reported in published literature.

## 4. Conclusions

For the first time, pirimicarb can be extracted from orchard wastewater using various imidazolium-based ionic liquids (S-1 to S-4). FTIR, SEM, XRD, TGA, BET, and $^1$H NMR spectroscopy confirmed that the fabricated imidazolium ILs were successfully synthesized. According to an XRD analysis, imidazolium-based ILs are crystalline, with an average particle size of >100 nm. The results of SEM were used to investigate the well-organized, needle-shaped surface

morphology of ILs with a high surface area to volume ratio. ILs that have been synthesized have the ability to extract and separate. In general, the fabricated ILs were more efficient at removing pirimicarb in the following order: S-3 > S-2 > S-4 > S-1. The ILs have good regeneration capability even after six (6) cycles, described by the pseudo-first-order and Langmuir models. The adsorption process is also controlled by the intraparticle diffusion. According to the thermodynamic parameters, pirimicarb extraction is spontaneous and endothermic. Our findings are very promising for the practical application of the synthesized ILs for the removal of pirimicarb from real orchard wastewater and grant a new perspective on the utilization of this approach in water treatment.

## Data Availability

The generated and analyzed data during the current study is supplied in this manuscript and is readily available from the corresponding authors upon reasonable request.

## Conflicts of Interest

The authors declare that there is no conflict of interest regarding the publication of this article.

## Authors' Contributions

Sana Zulfiqar is responsible for conceptualization, methodology, investigation, validation, formal analysis, visualization, data curation, resources, and supervision. Uzaira Rafique is responsible for methodology, investigation, visualization, and resources. M. Javed Akhtar is responsible for methodology, investigation, visualization, and resources. Hesham Hamad is responsible for conceptualization, methodology, investigation, validation, formal analysis, visualization, data curation, writing, editing, reviewing, supervision, and project administration.

## Acknowledgments

The authors are deeply grateful to Fatima Jinnah Women University and Pakistan Institute of Nuclear Science and Technology in Pakistan and the City of Scientific Research and Technological Applications (SRTA-City) and the Alexandria University in Egypt. H. Hamad also acknowledges the Faculty of Science, Warsaw University, for the computer services.

## Supplementary Materials

Supplementary 1. Characterization of ILs. Supplementary 2. Adsorption experiments. Supplementary 3. Estimation of thermodynamic parameters. Figure S1: study of area, Punjab, Jhelum District, Pakistan. Table S1: chemical structure and physicochemical properties of pirimicarb. Table S2: kinetic and equilibrium isotherm models utilized to describe pirimicarb adsorption process onto prepared ionic liquids. Table S3: isotherm parameters of pirimicarb adsorption onto prepared imidazolium-based ILs. *(Supplementary Materials)*

## References

[1] J. Fenoll, I. Garrido, P. Hellín, P. Flores, N. Vela, and S. Navarro, "Photocatalytic oxidation of pirimicarb in aqueous slurries containing binary and ternary oxides of zinc and titanium," *J Photochem Photobiol A Chem*, vol. 298, pp. 24–32, 2015.

[2] C.-C. Chen, H.-J. Fan, J. Shaya et al., "Accelerated ZnMoO4-photocatalytic degradation of pirimicarb under UV light mediated by peroxymonosulfate," *Applied Organometallic Chemistry*, vol. 33, p. 5113, 2019.

[3] Q. J. Luo, Y. X. Li, M. Q. Zhang, P. Qiu, and Y. H. Deng, "A highly sensitive, dual-signal assay based on rhodamine B covered silver nanoparticles for carbamate pesticides," *Chin Chem Lett*, vol. 28, no. 2, pp. 345–349, 2017.

[4] Y. Wang, B. Yang, P. Zhang et al., "Heterogeneous reactions of pirimiphos-methyl and pirimicarb with $NO_3$ radicals," *Journal of Physical Chemistry A*, vol. 116, pp. 10802–10809, 2012.

[5] G. S. Natale, J. Vera Candioti, C. Ruiz de Arcaute, S. Soloneski, M. L. Larramendy, and A. E. Ronco, "Lethal and sublethal effects of the pirimicarb-based formulation Aficida® on _Boana pulchella_ (Dum eril and Bibron, 1841) tadpoles (Anura, Hylidae)," *Ecotoxicology and Environmental Safety*, vol. 147, pp. 471–479, 2018.

[6] J. A. Turner, *the Pesticide Manual, 15th ed.*, C. D. Tomlin, Ed., British Crop Protection Council: Surrey, 2009.

[7] T. Shalaby, H. Hamad, E. Ibrahim, O. Mahmoud, and A. Al-Oufy, "Electrospun nanofibers hybrid composites membranes for highly efficient antibacterial activity," *Ecotoxicology and Environmental Safety*, vol. 162, pp. 354–364, 2018.

[8] D. G. Bassyouni, H. A. Hamad, E.-S. Z. El-Ashtoukhy, N. K. Amin, and M. M. Abd El-Latif, "Comparative performance of anodic oxidation and electrocoagulation as clean processes for electrocatalytic degradation of diazo dye Acid Brown 14 in aqueous medium," *Journal of Hazardous Materials*, vol. 335, pp. 178–187, 2017.

[9] W. A. Sadik, A. M. El-Demerdash, A. W. Nashed, A. A. Mostafa, and H. A. Hamad, "Highly efficient photocatalytic performance of $Cu_2$[email protected]$_2$ nanocomposite: influence of various inorganic oxidants and inorganic anions," *Journal of Materials Research and Technology*, vol. 8, no. 6, pp. 5405–5414, 2019.

[10] Z. Jia, S. Hao, and Z. Liu, "Synthesis of $BaSO_4$ nanoparticles with a membrane reactor: parameter effects on membrane fouling," *Journal of Membrane Science*, vol. 543, pp. 277–281, 2017.

[11] A. A. Hamad, M. S. Hassouna, T. I. Shalaby, M. F. Elkady, M. A. A. Elkawi, and H. A. Hamad, "Electrospun cellulose acetate nanofiber incorporated with hydroxyapatite for removal of heavy metals," *International Journal of Biological Macromolecules*, vol. 151, pp. 1299–1313, 2020.

[12] N. Nasrollahi, S. Aber, V. Vatanpour, and N. M. Mahmoodi, "Development of hydrophilic microporous PES ultrafiltration membrane containing CuO nanoparticles with improved antifouling and separation performance," *Materials Chemistry and Physics*, vol. 222, pp. 338–350, 2019.

[13] N. M. Mahmoodi, M. Oveisi, A. Taghizadeh, and M. Taghizadeh, "Novel magnetic amine functionalized carbon nanotube/metal-organic framework nanocomposites: from green ultrasound-assisted synthesis to detailed selective pollutant removal modelling from binary systems," *Journal of Hazardous Materials*, vol. 368, pp. 746–759, 2019.

[14] P. Wilczewska, A. Bielicka-Giełdońa, A. F. Borzyszkowsk, T. Klimczuk, and E. M. Siedlecka, "Photocatalytic activity of solvothermal prepared BiOClBr with imidazolium ionic liquids as a halogen sources in cytostatic drugs removal," *Journal of Photochemistry and Photobiology A: Chemistry*, vol. 382, article ???, 2019.

[15] M. Zhao, L. Wei, Y. Zheng, M. Liu, J. Wang, and Y. Qiu, "Structural effect of imidazolium-type ionic liquid adsorption to montmorillonite," *Science of the Total Environment*, vol. 666, pp. 858–864, 2019.

[16] R. Zarrougui, R. Mdimagh, and N. Raouafi, "Highly efficient extraction and selective separation of uranium (VI) from transition metals using new class of undiluted ionic liquids based on H-phosphonate anions," *Journal of Hazardous Materials*, vol. 342, pp. 464–476, 2018.

[17] R. A. El-Nagar, M. Nessim, A. Abd El-Wahab, R. Ibrahim, and S. Faramawy, "Investigating the efficiency of newly prepared imidazolium ionic liquids for carbon dioxide removal from natural gas," *Journal of Molecular Liquids*, vol. 237, pp. 484–489, 2017.

[18] N. Sidek, N. S. A. Manan, and S. Mohamad, "Efficient removal of phenolic compounds from model oil using benzyl imidazolium-based ionic liquids," *Journal of Molecular Liquids*, vol. 240, pp. 794–802, 2017.

[19] S. Zulfiqar, U. Rafique, and M. J. Akhtar, "Removal of pirimicarb from agricultural waste water using cellulose acetate–modified ionic liquid membrane," *Environmental Science and Pollution Research*, vol. 26, no. 16, pp. 15795–15802, 2019.

[20] J. Maszkowska, E. Synak, A. Fabiańska et al., "Preliminary study on suitability of ionic liquids as potential passive-sampling media of polyaromatic-hydrocarbon (PAH) analyses in water," *Analytical and Bioanalytical Chemistry*, vol. 407, no. 12, pp. 3531–3536, 2015.

[21] B. Ekka, R. S. Dhaka, R. K. Patel, and P. Dash, "Fluoride removal in waters using ionic liquid-functionalized alumina as a novel adsorbent," *Journal of Cleaner Production*, vol. 151, pp. 303–318, 2017.

[22] A. Hamadi, N. Yeddou-Mezenner, A. Lounis, R. M. Ali, and H. Hamad, "Upgrading of agro-industrial green biomass residues from chocolate industry for adsorption process: diffusion and mechanistic insights," *Journal of Food Science and Technology*, vol. 58, no. 3, pp. 1081–1092, 2021.

[23] W. Guo, Y. Hou, W. Wu, S. Ren, S. Tian, and K. N. Marsh, "Separation of phenol from model oils with quaternary ammonium saltsvia forming deep eutectic solvents," *Green Chemistry*, vol. 15, no. 1, pp. 226–229, 2013.

[24] R. Cooper, A. M. Zolot, J. A. Boatz, D. P. Sporleder, and J. A. Stearns, "IR and UV spectroscopy of vapor-phase jet-cooled ionic liquid $EMIM^+$ $Tf_2N^-$: ion pair structure and photodissociation dynamics," *Journal of Physical Chemistry A*, vol. 117, pp. 12419–12428, 2013.

[25] M. Matandabuzo and P. A. Ajibade, "Synthesis and surface functionalization of multi-walled carbon nanotubes with imidazolium and pyridinium-based ionic liquids: thermal stability, dispersibility and hydrophobicity characteristics," *Journal of Molecular Liquids*, vol. 268, pp. 284–293, 2018.

[26] Y. Lin, F. Wang, Z. Zhang, J. Yang, and Y. Wei, "Polymer-supported ionic liquids: synthesis, characterization and application in fuel desulfurization," *Fuel*, vol. 116, pp. 273–280, 2014.

[27] A. Chowdhury and S. T. Thynell, "Confined rapid thermolysis/FTIR/ToF studies of imidazolium-based ionic liquids," *Thermochimica Acta*, vol. 443, pp. 159–172, 2006.

[28] T. Erdmenger, J. Vitz, F. Wiesbrock, and U. S. Schubert, "Influence of different branched alkyl side chains on the properties of imidazolium-based ionic liquids," *Journal of Materials Chemistry A*, vol. 18, no. 43, pp. 5267–5273, 2008.

[29] N. M. Mahmoodi and J. Abdi, "Nanoporous metal-organic framework (MOF-199): synthesis, characterization and photocatalytic degradation of Basic Blue41," *Microchemical Journal*, vol. 144, pp. 436–442, 2019.

[30] H. Hamad, E. Bailón-García, S. Morales-Torres, F. Carrasco-Marín, A. F. Pérez-Cadenas, and F. J. Maldonado-Hódar, "Functionalized cellulose for the controlled synthesis of novel carbon–Ti nanocomposites: physicochemical and photocatalytic properties," *Nanomaterials*, vol. 10, p. 729, 2020.

[31] A. P. Abbott, T. J. Bell, S. Handa, and B. Stoddart, "O-Acetylation of cellulose and monosaccharides using a zinc based ionic liquid," *Green Chemistry*, vol. 7, no. 10, pp. 705–707, 2005.

[32] D. Yuan, D. He, S. Xu et al., "Imidazolium-based ionic liquids as novel organic SDA to synthesize high-silica Y zeolite," *Microporous and Mesoporous Materials*, vol. 204, pp. 1–7, 2015.

[33] K. Noack, P. S. Schulz, N. Paape, J. Kiefer, P. Wasserscheid, and A. Leipertz, "The role of the C2 position in interionic interactions of imidazolium based ionic liquids: a vibrational and NMR spectroscopic study," *Physical Chemistry Chemical Physics*, vol. 12, no. 42, pp. 14153–14161, 2010.

[34] J. Dai, D. Majhi, B. B. Kharkov, and S. V. Dvinskikh, "NMR spectroscopic study of orientational order in imidazolium-based ionic liquid crystals," *Crystals*, vol. 9, p. 495, 2019.

[35] R. Hayes, G. G. Warr, and R. Atkin, "Structure and nanostructure in ionic liquids," *Chemical Reviews*, vol. 115, no. 13, pp. 6357–6426, 2015.

[36] Y. Li, L. Wei, W. Zhang, Z. Dong, and Y. Qiu, "Counteranion-dependent sorption of imidazolium- and benzimidazolium-based ionic liquids by soot," *Chemosphere*, vol. 202, pp. 264–271, 2018.

[37] P. A. Hunt, C. R. Ashworth, and R. P. Matthews, "Hydrogen bonding in ionic liquids," *Chemical Society Reviews*, vol. 44, pp. 1257–1288, 2015.

[38] J. Zhang, S. S. Liu, J. Zhang, L. T. Qin, and H. P. Deng, "Two novel indices for quantitatively characterizing the toxicity interaction between ionic liquid and carbamate pesticides," *Journal of Hazardous Materials*, vol. 239-240, pp. 102–109, 2012.

[39] E. M. El-Sayed, H. A. Hamad, and R. M. Ali, "Journey from ceramic waste to highly efficient toxic dye adsorption from aqueous solutions via one-pot synthesis of $CaSO_4$ rod-shape with silica," *Journal of Materials Research and Technology*, vol. 9, pp. 16051–16063, 2020.

[40] L. He, W. Cui, Y. Wang et al., "Polymeric ionic liquid based on magnetic materials fabricated through layer- by-layer assembly as adsorbents for extraction of pesticides," *Journal of Chromatography A*, vol. 1522, pp. 9–15, 2017.

[41] H. Shokry, M. Elkady, and H. Hamad, "Nano activated carbon from industrial mine coal as adsorbents for removal of dye from simulated textile wastewater: operational parameters and mechanism study," *Journal of Materials Research and Technology*, vol. 8, pp. 4477–4488, 2019.

[42] F. C. Wu, R. L. Tseng, and R. S. Juang, "Initial behavior of intraparticle diffusion model used in the description of adsorption kinetics," *Chemical Engineering Journal*, vol. 153, no. 1-3, pp. 1–8, 2009.

[43] M. F. F. Sze and G. McKay, "An adsorption diffusion model for removal of para-chlorophenol by activated carbon derived from bituminous coal," *Environmental Pollution*, vol. 158, no. 5, pp. 1669–1674, 2010.

[44] M. Elkady, H. Shokry, and H. Hamad, "Effect of superparamagnetic nanoparticles on the physicochemical properties of nano hydroxyapatite for groundwater treatment: adsorption mechanism of Fe(ii) and Mn(ii)," *RSC Advances*, vol. 6, no. 85, pp. 82244–82259, 2016.

[45] S. Zulfiqar, U. Rafique, M. J. Akhtar, A. Hussain, and S. Mansab, "Thermodynamic and kinetics study of phosphonium-based cellulose acetate supported ionic liquid membrane: wastewater treatment," *Desalination and Water Treatment*, vol. 133, pp. 20–27, 2018.

[46] M. Doğan, H. Abak, and M. Alkan, "Adsorption of methylene blue onto hazelnut shell: kinetics, mechanism and activation parameters," *Journal of Hazardous Materials*, vol. 164, no. 1, pp. 172–181, 2009.

[47] Z. Wu, H. Zhong, X. Yuan et al., "Adsorptive removal of methylene blue by rhamnolipid-functionalized graphene oxide from wastewater," *Water Research*, vol. 67, pp. 330–344, 2014.

[48] M. Cobas, M. A. Sanromán, and M. Pazos, "Box–Behnken methodology for Cr (VI) and leather dyes removal by an eco-friendly biosorbent: F. vesiculosus," *Bioresource Technology*, vol. 160, pp. 166–174, 2014.

[49] A. Dimitrijević, L. Ignjatović, A. Tot et al., "Simultaneous extraction of pesticides of different polarity applying aqueous biphasic systems based on ionic liquids," *Journal of Molecular Liquids*, vol. 243, pp. 646–653, 2017.

[50] Q. Wu, G. Zhao, C. Feng, C. Wang, and Z. Wang, "Preparation of a graphene-based magnetic nanocomposite for the extraction of carbamate pesticides from environmental water samples," *Journal of Chromatography A*, vol. 1218, no. 44, pp. 7936–7942, 2011.

[51] C. W. G. Baojiao and S. H. I. Xuejun, "Preparation of functional grafted particles PSSS/$SiO_2$ and their adsorption character towards heterocyclic pesticides containing nitrogen atom," *Environmental Chemistry*, vol. 3, 2013.

[52] R. Rojas, E. Vanderlinden, J. Morillo, J. Usero, and H. El Bakouri, "Characterization of sorption processes for the development of low-cost pesticide decontamination techniques," *Science of the Total Environment*, vol. 488-489, pp. 124–135, 2014.

Hindawi
Adsorption Science & Technology
Volume 2022, Article ID 9417542, 14 pages
https://doi.org/10.1155/2022/9417542

*Research Article*

# The Synthesis of Magnetic Nitrogen-Doped Graphene Oxide Nanocomposite for the Removal of Reactive Orange 12 Dye

**Norah Salem Alsaiari**,[1] **Abdelfattah Amari**,[2,3] **Khadijah Mohammedsaleh Katubi**,[1] **Fatimah Mohammed Alzahrani**,[1] **Faouzi Ben Rebah**,[4] **and Mohamed A. Tahoon**[5,6]

[1]*Department of Chemistry, College of Science, Princess Nourah bint Abdulrahman University, P.O. Box 84428, Riyadh 11671, Saudi Arabia*
[2]*Department of Chemical Engineering, College of Engineering, King Khalid University, Abha 61411, Saudi Arabia*
[3]*Department of Chemical Engineering, Research Laboratory of Energy and Environment, National School of Engineers, Gabes University, Gabes 6072, Tunisia*
[4]*Higher Institute of Biotechnology of Sfax (ISBS), Sfax University, P.O. Box 263, Sfax 3000, Tunisia*
[5]*Department of Chemistry, College of Science, King Khalid University, P.O. Box 9004, Abha 61413, Saudi Arabia*
[6]*Chemistry Department, Faculty of Science, Mansoura University, Mansoura 35516, Egypt*

Correspondence should be addressed to Fatimah Mohammed Alzahrani; fmalzahrani@pnu.edu.sa

Received 19 November 2021; Revised 7 December 2021; Accepted 28 December 2021; Published 18 January 2022

Academic Editor: Hesham Hamad



Herein, we report the nanofabrication of magnetic calcium ferrite ($CaFe_2O_4$) with nitrogen-doped graphene oxide (N-GO) via facile ultrasonication method to produce $CaFe_2O_4$/N-GO nanocomposite for the potential removal of reactive orange 12 (RO12) dye from aqueous solution. The successful construction of the nanocomposite was confirmed using different characterization techniques including scanning electron microscopy (SEM), transmission electron microscopy (TEM), Fourier transform-infrared spectroscopy (FT-IR), and X-ray diffraction (XRD). The magnetic properties were studied using vibrating sample magnetometer (VSM) indicating ferromagnetic behavior of the synthesized materials that facilitate their separation using an external magnetic field after adsorption treatment. The addition of N-GO to $CaFe_2O_4$ nanoparticles enhanced the BET surface area from 24 to 52.93 $m^2/g$ as resulted from the $N_2$ adsorption-desorption isotherm. The adsorption of the synthesized nanomaterials is controlled by several parameters (initial concentration of dye, contact time, adsorbent dosage, and pH), and the RO12 dye removal on the surface of $CaFe_2O_4$ nanoparticles and $CaFe_2O_4$/N-GO nanocomposite was reached through the chemisorption process as indicated from the kinetic study. The adsorption isotherm study indicated that the adsorption process of RO12 dye was best described through the Langmuir isotherm approving the monolayer adsorption. According to the Langmuir model, the maximum adsorption capacity for RO12 was 250 and 333.33 mg/g for $CaFe_2O_4$ nanoparticles and $CaFe_2O_4$/N-GO nanocomposite, respectively. The adsorption capacity offered by $CaFe_2O_4$/N-GO nanocomposite was higher than reported in the literature for adsorbent materials. Additionally, the regeneration study indicated that $CaFe_2O_4$/N-GO nanocomposite is reusable and cost-effective adsorbent. Therefore, the nanofabricated $CaFe_2O_4$/N-GO hybrid material is a promising adsorbent for water treatment.

## 1. Introduction

Water is essential for human, plant, and animal life alike. From an environmental point of view, the water pollution causes concerns worldwide [1]. The environmental pollution causes about 25.0% of human diseases as stated by the World Health Organization (WHO) [2]. Dye wastewater is responsible for one of the major environmental pollution problems and represents about 20.0% of the industrial wastewater pollution as stated by the World Bank (WB) [2]. Dyes cause harmful effects on the environment and humans due to its carcinogenic, toxic, and mutagenic nature

[3]. Various synthetic dyes are used heavily in different industries (textile, pharmaceutical, leather, food, printing, and paper industries) and discharged along with different wastewaters into the natural ecosystem causing the human organs' toxicity [4]. The most serious problem of these dyes is their nonbiodegradable nature due to its complex chemical structure [5] that causes its accumulation inside human body. Serious problems associated to dyes pushed the scientists to find solutions for the treatment of dye wastewater. Various methods including biological treatment, anodic oxidation, oxidation, electrocoagulation, photocatalysis, flocculation/coagulation, adsorption, and membrane filtration were examined and used for the treatment of real textile and dyeing effluents [6–16]. Among the available technologies, adsorption is the most used method due to cost-effectiveness, high efficiency, and easy operation [17]. The adsorption is a procedure based on the transfer of pollutant from aqueous solution to the adsorbent. However, the using of conventional adsorbents faces many problems (insufficient hydrophilic surface, insufficient functional groups, material losses during regeneration, etc.). These problems of conventional adsorbents can be overcome by using nanomaterials with exceptional properties such as the ease synthesis, high surface area, simple functionalization, and low cost [18–20]. Dye removal was achieved using several types of materials included carbonaceous materials such as graphene oxide (GO), carbon-nanotube (CNT), and activated carbon [21–23] due to its large surface area. Among all carbonaceous materials, GO is the widely used carbon-based nanomaterials for the removal of dyes due to its fluorescence quenching properties, easy surface modification, and good water solubility. Additionally, GO has several oxygen-containing groups such as CO, OH, and COOH that represent about 60.0% of its surface and act as claws for capturing different pollutants. Moreover, hydrophilic oxygenated surface area and hydrophobic pristine graphene that are present in GO increase its surface heterogeneity and enhance its ability to bind different pollutants via hydrophobic interactions, Van der Waals interactions, electrostatic interactions, $\pi$-$\pi$ stacking, and H-bonding [24]. Carbon nanomaterials doping with a heteroatom like N, S, and O could increase its adsorption efficiency besides its surface area [25]. For instance, the adsorption capacity of reduced graphene oxide was folded 1.4 times toward the removal of 2-methylanthraquinone and anthracene when doped with N-atom as reported by Song et al. [26]. However, the advantages of GO as adsorbents, their separation from the reaction medium is a drawback that obstacles their application in water treatment applications. Interestingly, the presence of magnetic material in the adsorbents can facilitate their separation using an external magnetic field [27, 28]. This magnetic separation could reduce the overall cost of the treatment process and allowed the adsorbent reusability for several times. Adsorption of dyes and heavy metal using magnetically separable metal ferrite nanoparticles has been reported in many studies [29–32]. The reported magnetic nanoparticles used for the pollutants removal included $CaFe_2O_4$, $CoFe_2O_4$, $MgFe_2O_4$, $MnFe_2O_4$, and $ZnFe_2O_4$. Compared to other ferrites, $CaFe_2O_4$ is considered the most biocompatible due to its eco-friendly and nontoxicity nature [33]. In this context, various investigations showed the successful synthesis of magnetically separable crystalline $CaFe_2O_4$ nanoparticles and its potential use as an adsorbent for dyes such as reactive orange 12 (RO12) dye [34–39]. Therefore, GO can be combined with other nanomaterials such as $CaFe_2O_4$ nanoparticles to form nanohybrid material, to remove contaminants from water efficiently.

The purpose of the current research is to investigate the behavior of calcium ferrite/nitrogen-doped graphene oxide ($CaFe_2O_4$/N-GO) nanocomposite in the adsorption of RO12 dye. The produced $CaFe_2O_4$/N-GO nanocomposite using the facile ultrasonication synthesis benefits from the advantages of each nanocomposite part and allowed the enhancement of the nanomaterial adsorption efficiency. The synthesized nanocomposite was well-characterized using familiar techniques and examined for the removal of reactive orange 12 dye (RO12) from water. The effect of different parameters on the removal of dye was explored such as the initial concentration of dye, contact time, adsorbent dosage, and pH. Also, the experimental data were fitted using different models of isotherms and kinetics to well-understand the removal process.

## 2. Materials and Methods

*2.1. Chemicals.* All used chemicals including ferric nitrate nonahydrate ($Fe(NO_3)_3{\cdot}9H_2O$), calcium nitrate tetrahydrate ($Ca(NO_3)_2{\cdot}4H_2O$), citric acid, aqueous ammonia (33%), graphite powder, sodium hydroxide, hydrochloric acid, and RO12 dye were of analytical grade and used without any modification. All solutions were prepared using distilled water.

*2.2. Synthesis of $CaFe_2O_4$ Nanoparticles.* The $CaFe_2O_4$ nanoparticles were synthesized via the sol-gel method [40] as described briefly in the next steps. First, 20 mL of distilled $H_2O$ was used to dissolve calcium nitrate tetrahydrate ($Ca(NO_3)_2{\cdot}4H_2O$) and ferric nitrate nonahydrate ($Fe(NO_3)_3{\cdot}9H_2O$) with a molar ratio of 1 : 2. Then, to the above mixture, we added citric acid solution under continuous stirring at 65.0°C. After that, ammonium aqueous solution was added to the previous mixture until the pH value reached 7.0 at which the sol was formed. The stirring of sol was continued for 8 hours until the formation of gel. The gel was dried for 12.0 hours at 100.0°C. The formed gel was crushed and calcinated for 3.0 hours at 300.0°C. The formed $CaFe_2O_4$ nanoparticles became ready to be used in the next step.

*2.3. Synthesis of Nitrogen-Doped Graphene Oxide.* A facile ultrasonication method was used for the synthesis of nitrogen-doped graphene oxide (N-GO) as described in the following steps. Aqueous ammonium solution (25% (*v*/*v*), 20 mL) was used to dissolve 0.5 g of graphene oxide under sonication of solution for 1.0 hour at 25.0°C. The formed black precipitate was separated by centrifugation then washed several times with distilled $H_2O$ and dried overnight

at 60.0°C in oven. The obtained N-GO became ready to be used in the next step.

*2.4. Synthesis of ($CaFe_2O_4$/N-GO) Nanocomposite.* $CaFe_2O_4$/N-GO nanocomposite was synthesized via the sonication method. 15.0 mL of ethyl alcohol was used to dissolve $CaFe_2O_4$ nanoparticles and N-GO with w/w ratio of 1 : 2 under sonication for half hours. Then, the sonication was continued for an additional 1.0 hour. The formed precipitate was separated by centrifugation and washed several times with distilled $H_2O$. Finally, the synthesized $CaFe_2O_4$/N-GO nanocomposite was dried overnight at 60.0°C in an oven. Figure 1 illustrated the synthetic route of $CaFe_2O_4$/N-GO nanocomposite.

*2.5. Material Characterization.* The synthesized materials were characterized using various methods. Fourier-transform infrared spectroscopy (FT-IR-6100 Jasco, Tokyo, Japan) was used to carry out FT-IR spectra in the range of 400-4000 $cm^{-1}$ at room temperature and collected at a resolution of 4 $cm^{-1}$. X-ray diffractometer (XRD, X' Pert Pro, PAN analytical, Almelo, The Netherlands) was employed to determine XRD using CuKa radiation ($\lambda = 1.5406$ Å) operating at 45 kV. The diffraction intensities were recorded over the $2\theta$ ranging from 5° to 90° with the constant scanning rate of 1°$min^{-1}$. A vibrating sample magnetometer (Lake Shore 7410, Lake Shore (Cryotronics Inc., Westerville, OH, USA)) was used to measure the magnetization of the nanocomposite. The morphology and size materials were determined using a scanning electronmicroscope (SEM, Quanta FEG 250, Eindhoven, The Netherlands) and a transmission electron microscope (TEM, JEOL JEM-2100 Plus, Hillsboro, USA), respectively, operated at 200 KV.

*2.6. Adsorption of RO12 Dye.* The $CaFe_2O_4$/N-GO nanocomposite was investigated for the adsorption of RO12 dye. The effect of different parameters included contact time, initial dye concentration, adsorbent dosage, and pH value on the adsorption of RO12 dye was determined. The effect of the contact time was studied by varying the time from 10.0 to 120.0 minutes at an adsorbent dosage of 1.0 g/L, initial dye concentration 80.0 mg/L, and solution pH of 2.0. The adsorbent dosage effect was studied in the range of 0.125–1.50 g/L at an initial concentration of 80.0 mg/L, contact time of 80.0 minutes, and pH equal to 2.0. The initial dye concentration effect and pH effect were studied in the range of 20.0 to 150.0 mg/L and 2.0 to 7.0, respectively, at the same previous conditions. All previous adsorption experiments were repeated three times to determine the error. After each experiment, the adsorbent was collected from the reaction medium using an external magnet, and the solution was analyzed for the presence of dye using a UV-vis spectrophotometer at $\lambda_{max} = 416$ nm.

The adsorption capacity (in mg/g) and removal efficiency (in %) can be calculated using eqs. (1) and (2), respectively.

$$\text{Adsorption capacity } (qe) = \left(\frac{(C_i - C_e)}{W}\right) xV. \quad (1)$$

The symbols $C_i$, $C_e$, $V$, and $W$ denote the initial concentration, equilibrium concentration, volume of solution (L), and mass of adsorbent (g), respectively.

$$\text{Removal efficiency } (\%) = \left(\frac{C_i - C_e}{C_i}\right) x100. \quad (2)$$

The adsorption kinetics were studied using pseudo 1st order, pseudo 2nd order, and intraparticle diffusion models that represent by eq. (3), eq. (4), and eq. (5), respectively.

$$\log (qe - q_t) = \log q_e - \left(\frac{K_1}{2.303}\right) t, \quad (3)$$

$$\frac{t}{q_t} = \left(\frac{1}{K_2 q_e^2}\right) + \left(\frac{1}{q_e}\right) t, \quad (4)$$

$$q_t = K_{id} t^{0.5} + C^{id}, \quad (5)$$

where the symbols $k_2$, $k_1$, $q_t$, $q_e$, $K^{id}$, and $C^{id}$ denote pseudo 2nd order rate constant, pseudo 1st order rate constant, adsorption capacity (mg/g) at $t$ time, adsorption capacity at equilibrium (mg/g), intraparticle diffusion rate constant, and intraparticle diffusion constant, respectively.

The Langmuir and Freundlich adsorption isotherms models were used to study the adsorption mechanism. The Freundlich and Langmuir models can be represented by eq. (6) and eq. (7), respectively.

$$\ln q_e = \ln K_F + \left(\frac{1}{n}\right) \ln C_e, \quad (6)$$

$$\frac{C_e}{q_e} = \left(\frac{1}{q_m b}\right) + \left(\frac{C_e}{q_m}\right), \quad (7)$$

where $q_m$ and $C_e$ denote maximum adsorption capacity (mg/g) and equilibrium concentration, respectively, while $n$ and $K_F$ denote the Freundlich constants. The reusability of $CaFe_2O_4$/N-GO nanocomposite for the removal of RO12 dye was investigated up to six successive cycles using 0.1 M of HCl as eluent at the optimum conditions. After each cycle, the adsorbent was collected using magnet and washed several times with HCl and $H_2O$ then dried in oven at 60.0°C for the next cycle.

## 3. Results and Discussion

*3.1. Characterization of $CaFe_2O_4$/N-GO Nanocomposite.* The synthesized $CaFe_2O_4$ nanoparticles and $CaFe_2O_4$/N-GO nanocomposites were characterized using familiar techniques as shown in the next section. For the determination of functional groups, FT-IR spectra were performed (Figure 2(a)). The FT-IR spectrum of $CaFe_2O_4$ nanoparticles showed a band at 712.2 $cm^{-1}$ representing the stretching band of Fe-O. Also, the Fe-O stretching band was represented by the wide bands that appeared at 604 and 640.7 $cm^{-1}$. Fe-OH bending was represented by the bands that appeared at 857.6 and 875.3 $cm^{-1}$. The band that appeared at 3441 $cm^{-1}$ represents the stretching vibrations of OH

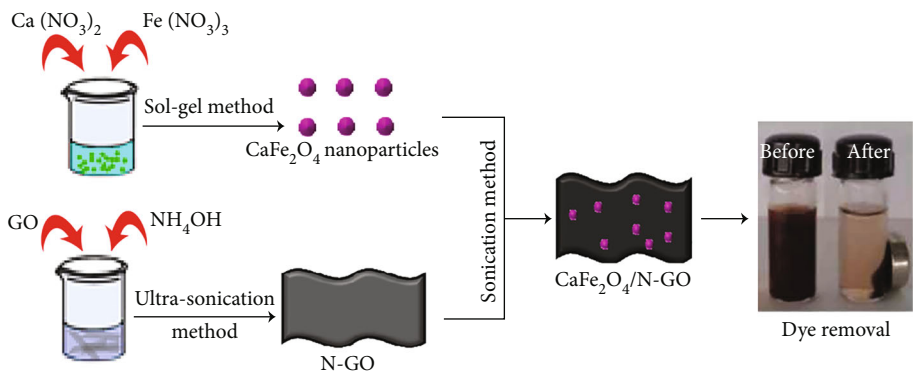


Figure 1: Schematic diagram for the synthesis $CaFe_2O_4$/N-GO nanocomposite.

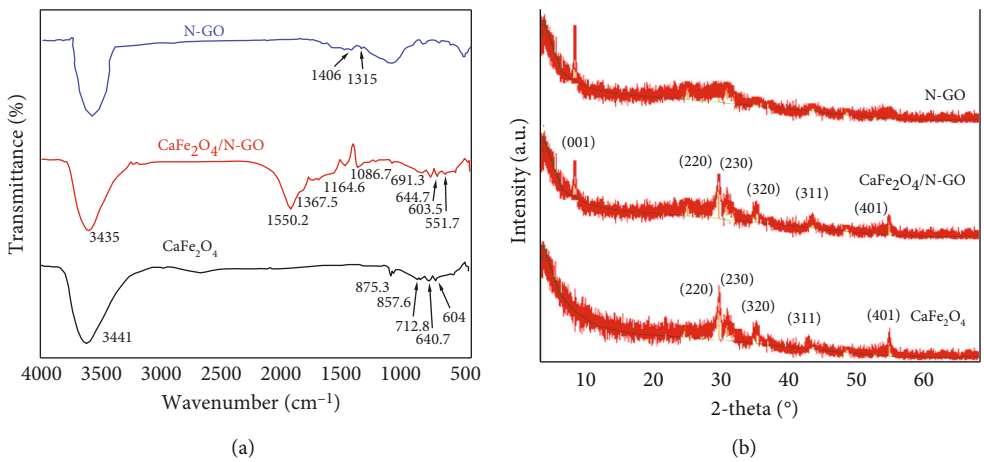


Figure 2: FT-IR (a) and XRD (b) of the synthesized $CaFe_2O_4$ nanoparticles, N-GO, and $CaFe_2O_4$/N-GO nanocomposite.

bond [34]. For the N-GO spectrum, the characteristic bands of GO are present such as the peaks at 1114 $cm^{-1}$ and 3410 $cm^{-1}$ that represent C-OH stretching vibration and O-H stretching vibrations, respectively [41, 42]. While the peak at 1315 $cm^{-1}$ represented the C=N stretching vibrations, the peak at 1406 $cm^{-1}$ represented the C-N stretching vibrations, and these two peaks are evidence for nitrogen doping [42, 43]. The FT-IR spectrum of the nanocomposite showed the appearance of new absorption bands due to the C-O, C-N, and C=N bonds that appeared at 1086.7, 1164.6, and 1367.5 $cm^{-1}$, respectively, and approved the doping of N atom in the GO sheets. Also, the addition of N-GO sheets caused the shift of the O-H stretching band. The disappearance of the band corresponding to Fe-OH could result from the breaking of the OH bond due to the interaction between the COOH group in the nanosheets and Fe-OH. Additionally, the interaction between the nanosheets and ferrite nanoparticles could be confirmed by the shift of the Fe-O band from 712.2 to 693 $cm^{-1}$. The existence of spinel ferrite in the $CaFe_2O_4$/N-GO nanocomposite was confirmed by the appearance of bands at 551.7 and 644.7 $cm^{-1}$ that represent the vibrations of the Fe-O bond. Also, the N-H bending vibration and O-H stretching vibration are represented by the bands that appeared at 1550.2 and 3435 $cm^{-1}$, respectively [44]. The FT-IR spectra of $CaFe_2O_4$ nanoparticles and $CaFe_2O_4$/N-GO nanocomposite indicated the well construction of the nanocomposite [34, 44].

For the determination of crystal structure and phase purity of $CaFe_2O_4$ nanoparticles and $CaFe_2O_4$/N-GO nanocomposite, the XRD was investigated (Figure 2(b)). According to Figure 2(b), XRD of $CaFe_2O_4$ nanoparticles showed the presence of (401), (311), (320), (230), and (220) planes represented by the peaks at 54.53, 43.66, 34.90, 30.17, and 29.57°, respectively, indicating the face-centered cubic lattice [45]. For XRD of N-GO, the strong diffraction peak at $2\theta = 10.2°$ can be attributed to the characteristic plane of GO. The XRD of the nanocomposite showed the appearance of the same peaks of $CaFe_2O_4$ nanoparticles with the appearance of an additional peak at 10.0°, which is resulted due to the addition of N-GO nanosheets. To study the particle morphology, TEM analysis was performed for the synthesized GO, N-GO, $CaFe_2O_4$ nanoparticles, and $CaFe_2O_4$/N-GO nanocomposite as shown in Figures 3(a), 3(b), 3(c) and 3(e), respectively. According to Figure 3(a), a layered structure was observed for pristine GO while the TEM image of doped GO nanosheets (Figure 3(b)) showed an increase in the wrinkling due to the doping of nanosheets by the heteroatom. The TEM image of $CaFe_2O_4$ nanoparticles (Figure 3(c)) indicated that the ferrite nanoparticles have size of 10.0 : 20.0 nm as confirmed from the size distribution

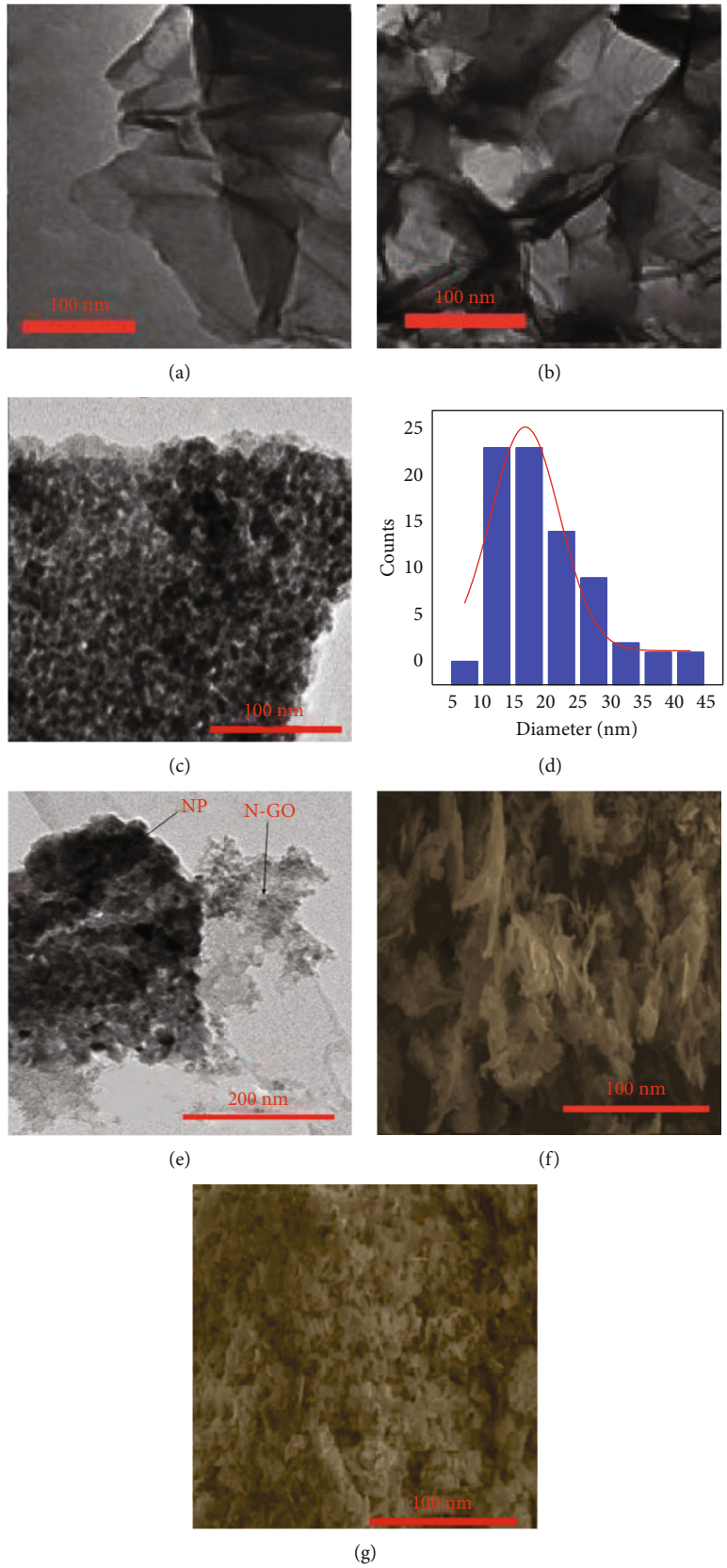


Figure 3: TEM images of GO (a), N-GO (b), $CaFe_2O_4$ nanoparticles (c), $CaFe_2O_4$ nanoparticles size histogram (d), $CaFe_2O_4$/N-GO nanocomposite (e), SEM images of $CaFe_2O_4$ nanoparticles (f), and $CaFe_2O_4$/N-GO nanocomposite (g).

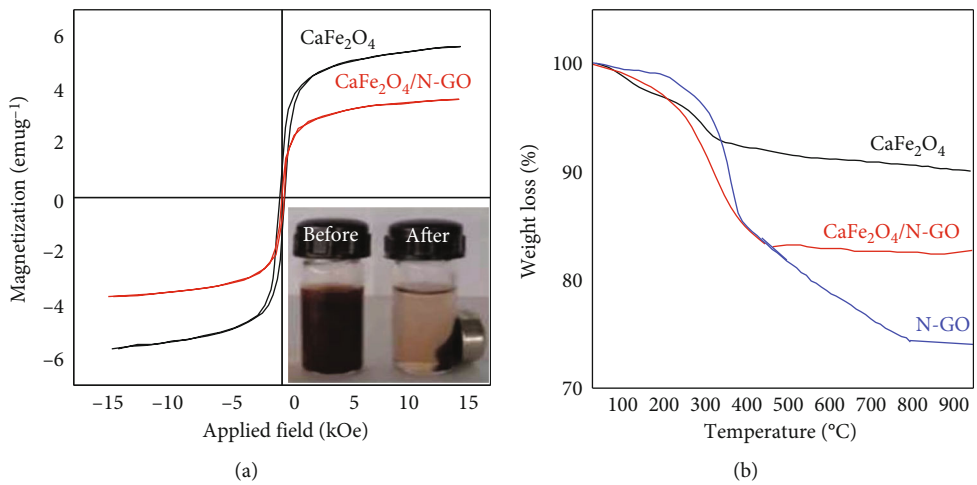


Figure 4: Magnetization curve of the synthesized $CaFe_2O_4$ nanoparticles and $CaFe_2O_4$/N-GO nanocomposite (inset: the magnetic separation of magnetic nanocomposite after dye removal) (a) and TGA curve of $CaFe_2O_4$ nanoparticles, N-GO, and $CaFe_2O_4$/N-GO nanocomposite (b).

histogram (Figure 3(d)) with an agglomeration resulted from their magnetic properties. The TEM image (Figure 3(e)) of the nanocomposite showed the distribution of ferrite nanoparticles over the nanosheets of doped GO.

To study the surface topography, the SEM analysis was performed for $CaFe_2O_4$ nanoparticles and $CaFe_2O_4$/N-GO nanocomposite as shown in Figures 3(f) and 3(g), respectively. According to Figure 3(f), the synthesized ferrite nanoparticles showed agglomeration behavior resulted from the magnetic properties of the nanoparticles and confirmed the results of TEM analysis. The SEM image of $CaFe_2O_4$/N-GO nanocomposite (Figure 3(g)) showed a great difference while compared to the SEM image of the nanoparticles illustrated by an increase in the surface roughness designating the distribution of calcium ferrite nanoparticles on the surface of doped nanosheets. Because the magnetic separation of any adsorbent after the treatment is an important advantage of the adsorption process, the magnetic properties of the synthesized $CaFe_2O_4$ nanoparticles and $CaFe_2O_4$/N-GO nanocomposite were investigated using VSM with applied field range from -15 KOe to 15 KOe as shown in Figure 4(a). According to Figure 4(a), the $CaFe_2O_4$ nanoparticles and $CaFe_2O_4$/N-GO nanocomposite showed ferromagnetic behavior, which is clear from the s-shaped hysteresis loops. The saturation magnetization ($M_S$) of the $CaFe_2O_4$ nanoparticles is 5.82 $emug^{-1}$ while this value was dropped to 3.05 $emug^{-1}$ after the addition of N-GO nanosheets. This drop was due to the nonmagnetic behavior of the doped nanosheets that cause quenching of magnetic moment and decrease the magnetic permeability of the material. The magnetic properties of the synthesized $CaFe_2O_4$/N-GO nanocomposite helped in the magnetic separation of the nanocomposite, after dye adsorption, using an external magnet as shown in Figure 4(a) (inset).

To study the thermal properties of the synthesized materials $CaFe_2O_4$ nanoparticles, N-GO, and $CaFe_2O_4$/N-GO nanocomposite, the thermogravimetric analysis (TGA) was used as shown in Figure 4(b). For $CaFe_2O_4$ nanoparticles, N-GO, and $CaFe_2O_4$/N-GO nanocomposite, the slight weight loss that occurred below 100°C was attributed to the evaporation of physically adsorbed water molecules. For N-GO, the weight loss at temperature between 120 and 220°C was attributed to the decomposition of different functional groups while at higher temperature; the weight loss was attributed to the decomposition of carbon skeleton. For $CaFe_2O_4$ nanoparticles, the TGA curve indicates their thermal stability with no notable weight loss with

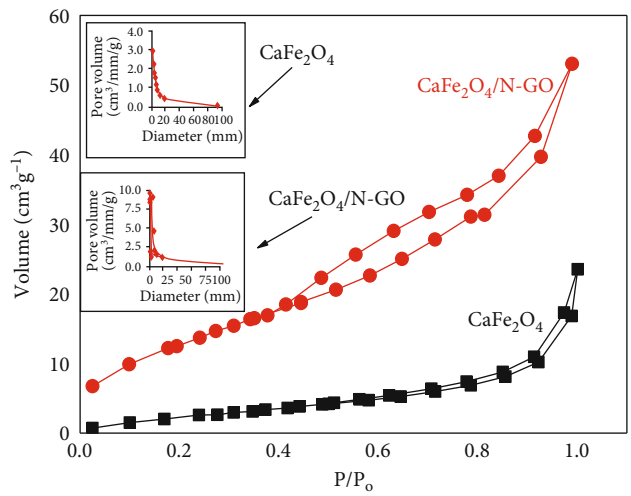


Figure 5: $N_2$ adsorption-desorption isotherm of the synthesized $CaFe_2O_4$ nanoparticles and $CaFe_2O_4$/N-GO nanocomposite.

Table 1: The determined surface area, pore diameter, and pore volume of $CaFe_2O_4$ nanoparticles and $CaFe_2O_4$/N-GO nano composite using BET study.

| Material | $S_{BET}$ ($m^2.g^{-1}$) | Pore diameter (nm) | Pore volume ($cm^3.g^{-1}$) |
|---|---|---|---|
| $CaFe_2O_4$/N-GO | 52.93 | 3.46 | 0.045 |
| $CaFe_2O_4$ | 24.0 | 3.25 | 0.034 |

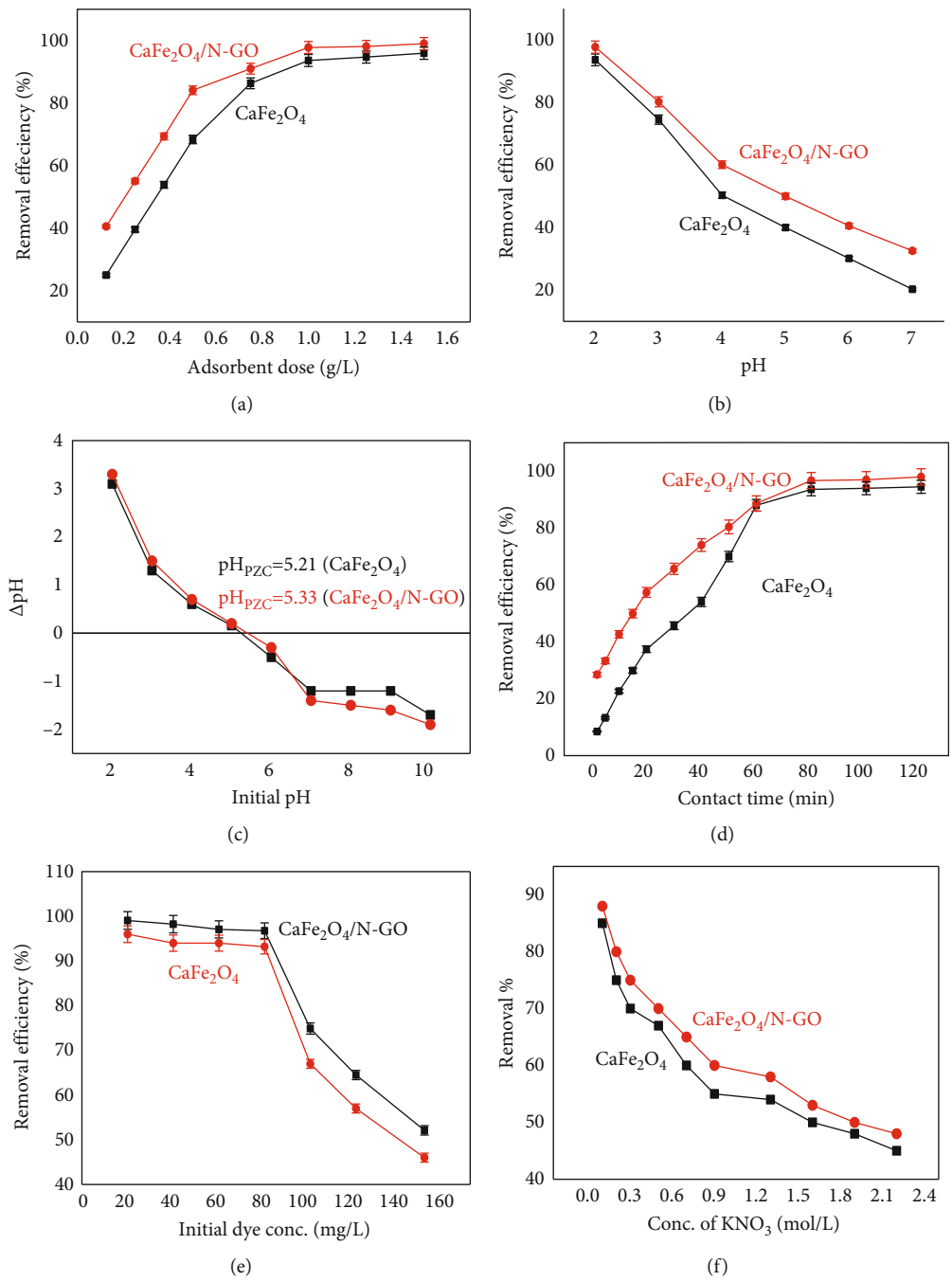


Figure 6: The effect of adsorbent dose (a), effect of pH (b), point of zero charge (c), effect of contact time (d), effect of initial dye concentration (e), and effect of ionic strength (f) for the removal of RO12 dye over $CaFe_2O_4$ nanoparticles and $CaFe_2O_4$/N-GO nanocomposite.

temperature. For the $CaFe_2O_4$/N-GO nanocomposite TGA curve, it is clear that the introduction of $CaFe_2O_4$ nanoparticles to the carbon skeleton of N-GO caused improvement to the thermal properties. This may be attributed to increased loadings of $CaFe_2O_4$ nanoparticles predictably decreasing the carbon content within the $CaFe_2O_4$/N-GO nanocomposite. The TGA data indicates the excellent thermal properties of the synthesized nanocomposite and confirms the well construction of the nanocomposite. Moreover, the $N_2$ adsorption-desorption isotherm was performed for $CaFe_2O_4$ nanoparticles and $CaFe_2O_4$/N-GO nanocomposite to determine their surface properties as shown in Figure 5. According to Figure 5, the synthesized materials have mesoporous structure as they have type IV isotherm of H3 type hysteresis loop. The $CaFe_2O_4$ nanoparticles showed BET surface area of 24.0 $m^2g^{-1}$. After the addition of N-GO nanosheets, this area was increased to 52.93 $m^2g^{-1}$. The addition of nanosheets caused the well distribution of magnetic nanoparticles and prevented their agglomeration by magnetic attraction. This well distribution of nanoparticles was the reason for

higher $CaFe_2O_4$/N-GO nanocomposite' BET surface area than $CaFe_2O_4$ nanoparticles. Also, the higher surface area of $CaFe_2O_4$/N-GO nanocomposite suggested the higher mesoporosity than $CaFe_2O_4$ nanoparticles. The determined surface area, pore volume, and pore diameter of synthesized materials using BET study were introduced in Table 1. $CaFe_2O_4$/N-GO nanocomposite showed a higher pore volume than $CaFe_2O_4$ nanoparticles that reflected the higher surface area of the nanocomposite. Also, the higher surface area of the nanocomposite was indicated from the micropore volume values. This large micropore volume and BET surface area play a significant role in the removal of pollutants from aqueous solution as described in the literature [9, 10, 46].

### 3.2. Dye Removal

*3.2.1. Optimization of the Adsorption Conditions.* The adsorption process is controlled by several parameters such as initial concentration of dye, contact time, adsorbent dosage, and pH, which are the basis of all laboratory experiments laboratories aiming to determine optimum conditions to get the highest efficiency of the adsorbent. Subsequently, the next section includes the study of the effect of different parameters on RO12 removal on the surface of the synthesized nanomaterials. To study the effect of the adsorbent dosage on RO12 removal, different dosages ranging from 0.125 to 1 g/L were investigated for the removal of RO12 dye as shown in Figure 6(a). According to Figure 5(a), the removal efficiency of RO12 dye was increased from 25.0% ± 0.5 to 93.26% ± 0.38 and from 40.56% ± 0.42 to 96.77% ± 0.63 for $CaFe_2O_4$ nanoparticles and $CaFe_2O_4$/N-GO nanocomposite, respectively, when the dosage increased from 0.125 to 1 g/L. This increase of removal efficiency associated with the increase of adsorbent dosage is attributed to the presence of more available adsorption sites by increasing the dosage. While at adsorbent dosage higher than 1 g/L, there was no significance increase of RO12 removal efficiency on the surface of $CaFe_2O_4$ nanoparticles or $CaFe_2O_4$/N-GO nanocomposite, which is attributed to the achievement of the saturation state and the agglomeration of the adsorbent particles and the blockage of adsorption sites [47]. The removal efficiency of dye on the surface of $CaFe_2O_4$/N-GO nanocomposite was higher than on the surface of $CaFe_2O_4$ nanoparticles due to the presence of N-GO nanosheets providing more active sites and N-atoms for the chelation of dye molecules.

The effect of pH on the removal of RO12 dye using $CaFe_2O_4$ nanoparticles and $CaFe_2O_4$/N-GO nanocomposite was studied by varying the initial pH within the range of 2.0 to 7.0 as shown in Figure 6(b). According to Figure 6(b), the pH increase caused a decrease in the removal efficiency of RO12 until reaching the lowest value at pH of 7.0, which is equal to 20.28% ± 0.36 and 32.56% ± 0.54 for $CaFe_2O_4$ nanoparticles and $CaFe_2O_4$/N-GO nanocomposite, respectively. The highest removal efficiency was achieved at a pH of 2.0, which is considered the optimum pH value for dye removal. This behavior could be interpreted as at low pH value, and the adsorbent surface was protonated to form positively charged functional groups that act as chelation sites to uptake the anionic RO12 dye via electrostatic interaction. While at higher pH values, the functional groups of adsorbent become negatively charged and repulsed with the anionic dye causing the decrease in the removal efficiency. Moreover, at high pH value, the presence of $OH^-$ groups could compete with the anionic dye for the active sites on the adsorbent surface which affect the removal efficiency negatively [48, 49]. As reported in the literature, pH affects the degree of ionization of the adsorptive molecules, the surface charge, and the dissociation degree of the functional groups of the adsorbent active site [50–52]. Therefore, the results of pH effect indicated that the pH is a key factor for dye adsorption. Moreover, the determination of point of zero charge ($pH_{PZC}$) for $CaFe_2O_4$ nanoparticles and $CaFe_2O_4$/N-GO nanocomposite is important to determine the pH effect on the adsorption process. Subsequently, the $pH_{PZC}$ was determined for $CaFe_2O_4$ nanoparticles and $CaFe_2O_4$/N-GO nanocomposite as shown in Figure 6(c). The $pH_{PZC}$ values were found to equal 5.21 and 5.33 for $CaFe_2O_4$ nanoparticles and $CaFe_2O_4$/N-GO nanocomposite, respectively. This means that below the $pH_{PZC}$, the adsorbent is positively charged while above the $pH_{PZC}$, and the adsorbent is negatively charged. The $pH_{PZC}$ determination interprets the high removal efficiency of RO12 dye at low pH values. At low pH value < $pH_{PZC}$, the adsorbent surface was positively charged and attracted the anionic dye via the electrostatic attractions. While at higher pH value > $pH_{PZC}$, the adsorbent surface was negatively charged and repulsed the anionic dye. So, the determination of $pH_{PZC}$ values enhances the results of pH effect on the adsorption process.

Table 2: The kinetics and isotherm parameters for the removal of RO12 dye on the surface of $CaFe_2O_4$ nanoparticles and $CaFe_2O_4$/N-GO nanocomposite.

| Item | Coefficient | Adsorbent | |
|---|---|---|---|
| | | $CaFe_2O_4$ | $CaFe_2O_4$/N-GO |
| Pseudo 1st order | $R^2$ | 0.916 | 0.949 |
| | $k_1$ (L/min) | 4.551 | 3.611 |
| | $q_e$ (mg/g) | 181.0 | 132.0 |
| Pseudo 2nd order | $R^2$ | 0.996 | 0.998 |
| | $K_2$ (g/mg.min) | 4.066 | 4.994 |
| | $q_e$ (mg/g) | 256.0 | 287.0 |
| Intraparticle diffusion | $R^2$ | 0.770 | 0.824 |
| | $C^{id}$ | 120.20 | 168.57 |
| | $K^{id}$ | 11.279 | 9.835 |
| Freundlich isotherm | $R^2$ | 0.952 | 0.951 |
| | $1/n$ | 0.4539 | 0.3934 |
| | $K_F$ (L.mg/g) | 33.0 | 61.0 |
| Langmuir isotherm | $R^2$ | 0.960 | 0.980 |
| | $B$ (L/mg) | 0.074 | 0.189 |
| | $q_{max}$ (mg/g) | 250.0 | 333.33 |

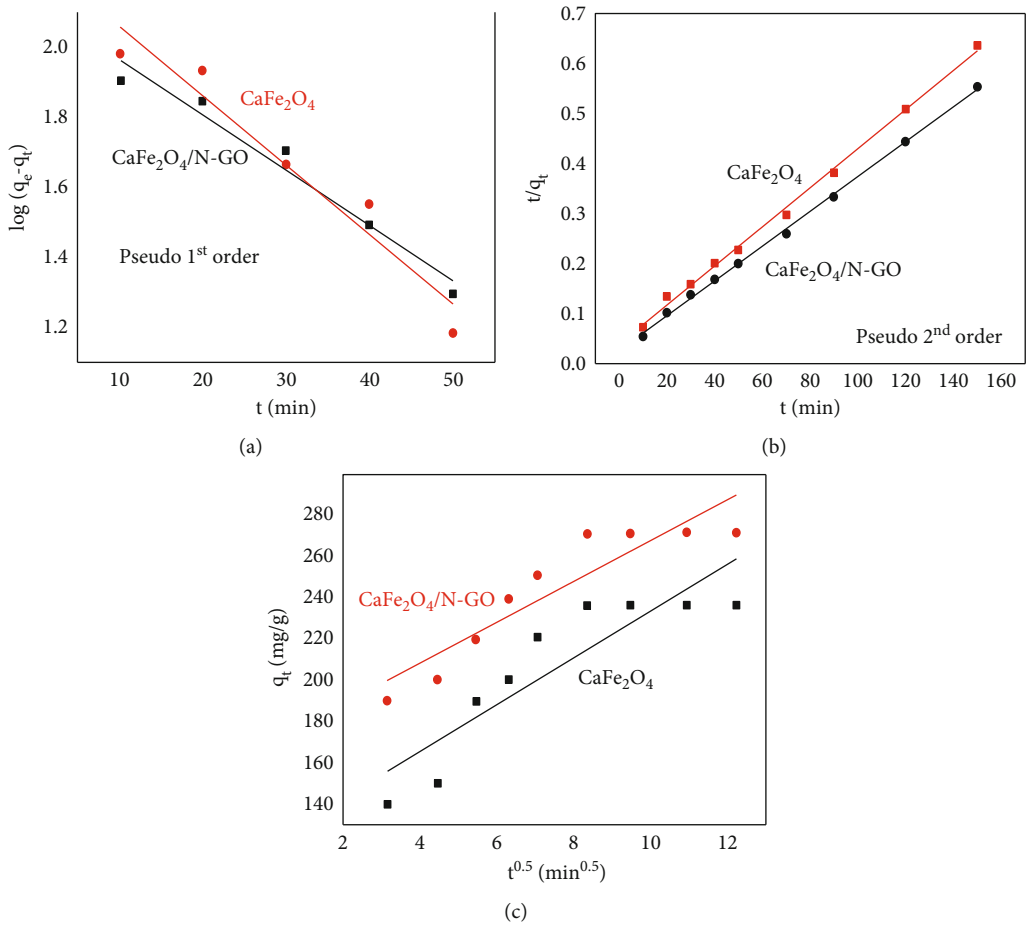


FIGURE 7: Fitting the experimental data to pseudo 1st order kinetics (a), pseudo 2nd order kinetics (b), and intraparticle diffusion model (c) for the adsorption of RO12 dye on the surface of $CaFe_2O_4$ nanoparticles and $CaFe_2O_4$/N-GO nanocomposite.

The effect of the contact time on dye removal by $CaFe_2O_4$ nanoparticles and $CaFe_2O_4$/N-GO nanocomposite was studied at different intervals ranging from 10.0 to 120 minutes as shown in Figure 6(d). According to Figure 6(c), the dye removal rate increased with an increase in contact time. At the beginning, a rapid removal was observed, which is attributed to the availability of protonated adsorbent sites to interact with anionic dye through the electrostatic interaction. Then, there was a decrease in the removal rate until reached the equilibrium that is attributed to the reduced surface area of the adsorbent due to the adsorbed dye, and also the adsorbed molecules are repulsed with each other [53]. The optimum contact time for the adsorption of RO12 dye on the surface of $CaFe_2O_4$ nanoparticles and $CaFe_2O_4$/N-GO nanocomposite was 80.0 minutes at which the equilibrium was reached as clearly shown in Figure 6(d). To study the effect of the initial dye concentration on the removal of RO12 using $CaFe_2O_4$ nanoparticles and $CaFe_2O_4$/N-GO nanocomposite, the initial concentration was varied from 20 to 150 mg/L as shown in Figure 6(e). According to Figure 6(e), the removal efficiency of dye was decreased by increasing the dye concentration gradually until 80 mg/L, at which there was a drop in the removal efficiency. This behavior was attributed to the increased amount of dye molecules against the fixed number of adsorption sites, causing the drop in the removal efficiency. However, at low dye concentration, several free adsorption sites are available to uptake the dye. To study the effect of ionic strength on the removal of RO12 dye on the surface of $CaFe_2O_4$ nanoparticles and $CaFe_2O_4$/N-GO nanocomposite, the removal efficiency was determined at different concentrations of $KNO_3$ salt as shown in Figure 6(f). According to Figure 6(f), the removal efficiency was decreased by increasing the ionic strength until reaching 45% and 48% for $CaFe_2O_4$ nanoparticles and $CaFe_2O_4$/N-GO nanocomposite, respectively, at ionic strength of 2.2 $mol.L^{-1}$. This behavior was expected in the presence of $KNO_3$ that supports the ion exchange mechanism of the adsorption process [51]. This means that the counterions around the adsorption sites weaken the attraction forces between adsorbent and adsorbate and cause a decrease in the removal efficiency [51].

*3.2.2. Adsorption Kinetics and Isotherm.* The adsorption process is perfectly imaged through the study of the adsorption rate [54, 55]. The adsorption rate is an important parameter that can be described using different kinetic models such as pseudo 1st order model and pseudo 2nd order model. Subsequently, the experimental data for the removal of RO12 dye

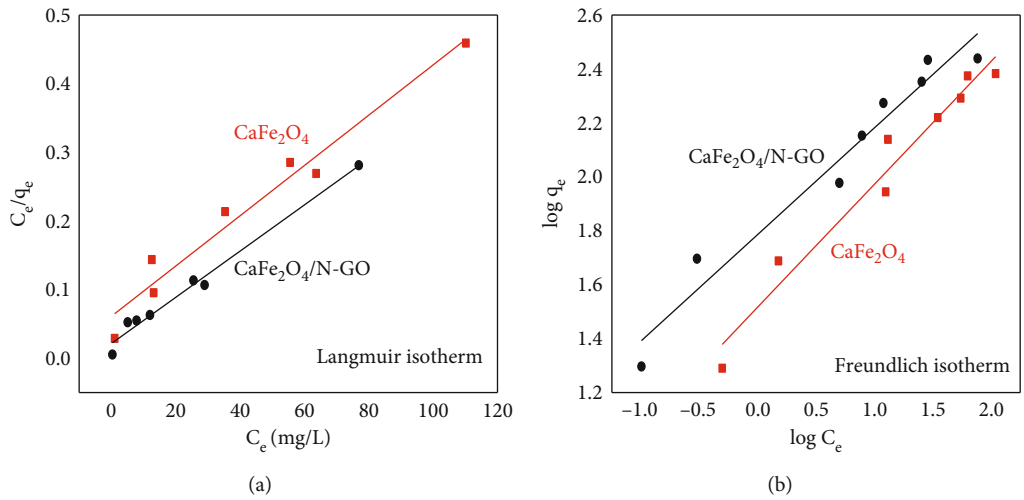


Figure 8: Fitting the experimental data to Langmuir isotherm model (a) and Freundlich isotherm model (b) for the adsorption of RO12 dye on the surface of $CaFe_2O_4$ nanoparticles and $CaFe_2O_4$/N-GO nanocomposite.

using $CaFe_2O_4$ nanoparticles and $CaFe_2O_4$/N-GO nanocomposite was fitted using the pseudo 1st order model and pseudo 2nd order model as shown in Figure 6. The kinetic parameters were calculated and presented in Table 2. From the results in Table 2, the $R^2$ values showed that pseudo 2nd order model is higher fitting the experimental data than pseudo 1st order model in case of $CaFe_2O_4$ nanoparticles and $CaFe_2O_4$/N-GO nanocomposite. Additionally, the experimental values of $q_e$ indicated the agreement with pseudo 2nd order. Also, Figure 7 indicates the excellent agreement with pseudo 2nd order model to the experimental adsorption data. This agreement of adsorption data with the pseudo 2nd order model indicates that the removal of RO12 dye achieved through the chemisorption between the dye and $CaFe_2O_4$ nanoparticles and $CaFe_2O_4$/N-GO nanocomposite [56, 57].

This kinetic behavior is similar to many previously reported studies for the removal of RO12 dye [37, 58]. To get an idea about the diffusion mechanism, the Webber's pore-diffusion model (intraparticle diffusion model) was used as shown in Figure 7(c). According to Figure 7(c), the plot of intraparticle diffusion model between $t^{0.5}$ and $q_t$ showed the existence of three different stages suggesting three different mechanisms of adsorption. The 1st stage represents the diffusion of RO12 dye on the surface of adsorbents ($CaFe_2O_4$ and $CaFe_2O_4$/N-GO) from the bulk solution, the 2nd stage represents the pore diffusion, and the 3rd stage represents the achievement of equilibrium state [18, 59].

More insights about the adsorption process can be obtained from the study of the adsorption isotherm as the isotherm can describe the distribution of toxic ions at an equilibrium state between the solid-liquid phases [60]. Also, the isotherm study can be used for the determination of adsorption capacity as well as understanding the affinities between adsorbent and adsorbate ions. Therefore, in this study, the adsorption behavior was described using the adsorption isotherm models including Langmuir model and Freundlich model. Langmuir model suggests that the

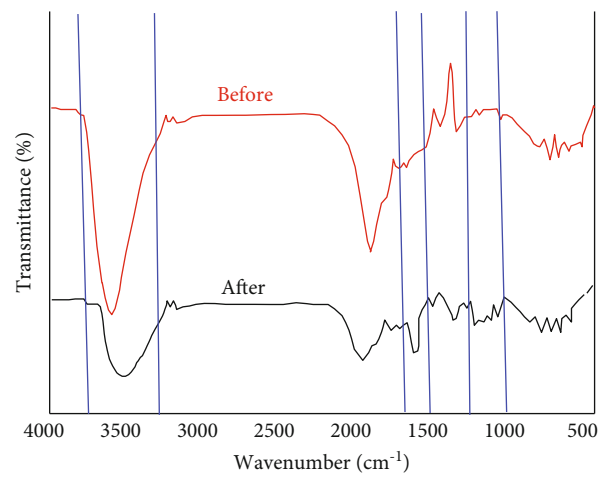


Figure 9: FT-IR spectra of $CaFe_2O_4$/N-GO nanocomposite before and after the adsorption of RO12 dye.

adsorbate molecules not interacted with each other and result a monolayer adsorption of the adsorbate on the homogeneous surface of adsorbent [61]. While the Langmuir model suggests multilayer adsorption process resulted from the adsorption of adsorbate molecules on the heterogeneous surface of adsorbent [62]. The linear plots of Langmuir and Freundlich isotherm models are shown in Figure 8, and the calculated parameters are presented in Table 2. According to the results in Table 1, $R^2$ values showed a higher agreement of the experimental data with Langmuir model than Freundlich model in the case of $CaFe_2O_4$ nanoparticles and $CaFe_2O_4$/N-GO nanocomposite. This indicated that the uptake of RO12 dye on the surface of $CaFe_2O_4$ nanoparticles and $CaFe_2O_4$/N-GO nanocomposite was reached as a monolayer attachment between the dye molecules and the uniformly dispersed active sites on the surface of adsorbents. The monolayer adsorption is indicated that the adsorption process is greatly dependent on the properties of the surface.

Table 3: Comparison between the removal of RO 12 over $CaFe_2O_4$/N-GO nanocomposite with previously reported adsorbents.

| Adsorbent | $q_m$ (mg/g) | Ref. |
|---|---|---|
| $CaFe_2O_4$/N-GO | 333.33 | This study |
| $CaFe_2O_4$ | 250 | This study |
| $CaFe_2O_4$ | 276.92 | [34] |
| Platinum nanoparticles loaded on activated carbon | 285.143 | [35] |
| Copper sulfide nanoparticles loaded on activated carbon | 96.9 | [36] |
| Mn nanoparticles loaded on activated carbon | 94.52 | [37] |
| Cadmium sulfide nanoparticle–loaded activated carbon | 150.0 | [38] |
| Tin sulfide nanoparticle loaded on activated carbon | 157.73 | [39] |

According to Langmuir fitting results, the maximum adsorption capacities ($q_m$) are 250 mg/g and 333.33 mg/g for $CaFe_2O_4$ nanoparticles and $CaFe_2O_4$/N-GO nanocomposite, respectively. The enhancement of the adsorption capacity of $CaFe_2O_4$/N-GO nanocomposite can be attributed to the increased active sites associated with the addition of N-GO sheets to the magnetic $CaFe_2O_4$ nanoparticles. As a result, N-GO sheets provide more quantities of functional groups to the adsorbent causing an increase in the capacity of the adsorbent. Moreover, the N-GO sheets provide 3-D porous skeleton that can uptake the adsorbate molecules inside and, hence, increase the adsorption capacity. Additionally, the doping of N atoms in GO provides the amine groups allowing the enhancement of the pollutants uptake via hydrogen bonding and electrostatic interaction. All these factors play a significant role in the enhanced adsorption process of RO12 dye on the surface of $CaFe_2O_4$/N-GO nanocomposite.

To get an insight about the removal mechanism of RO12 dye on the surface of $CaFe_2O_4$/N-GO nanocomposite, the FT-IR spectra of the nanocomposite were studied before and after the dye adsorption as shown in Figure 9. According to Figure 9, the FT-IR spectrum of $CaFe_2O_4$/N-GO nanocomposite showed many differences after the adsorption of RO12 dye. The band at 3435 $cm^{-1}$ that correspond to OH group stretching vibrations was shifted, and its intensity was decreased indicating the contribution of OH groups in the removal mechanism. Similarly, the bands of other functional groups were shifted as a result of their contribution in the dye removal. Also, the appearance of the new bands at 1550 $cm^{-1}$ and 1210 $cm^{-1}$ was attributed to the azo-bond (N=N) vibrations, and sulfonate group of the dye, respectively, indicated the successful adsorption of the dye on the surface of nanocomposite.

To highlight the effectiveness of the synthesized $CaFe_2O_4$/N-GO nanocomposite as an RO 12 adsorbent, the maximum adsorption capacity obtained here for RO 12 was compared with previously reported results (Table 3). According to previously reported results, $CaFe_2O_4$/N-GO nanocomposite revealed excellent adsorption capacity for RO12 compared to the reported adsorbents. Therefore, it could be concluded that the designed magnetic $CaFe_2O_4$/N-GO nanocomposite will be a promising hopeful hybrid nanomaterial useful as adsorbent for the elimination of dyes from wastewater.

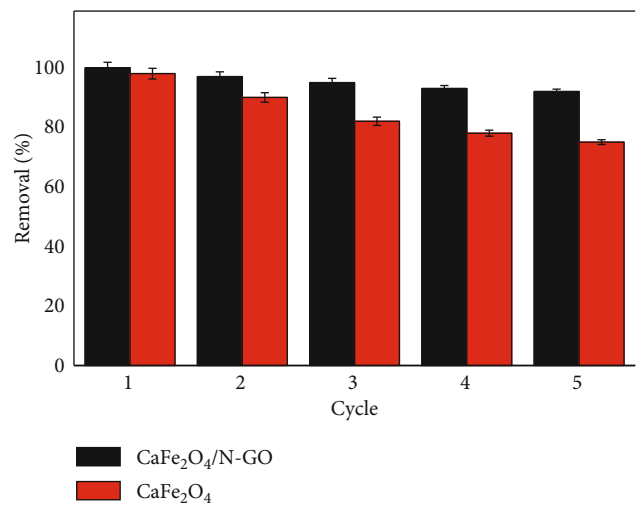


Figure 10: Reusability study of the synthesized $CaFe_2O_4$ nanoparticles and $CaFe_2O_4$/N-GO nanocomposite for the removal of RO12 dye up to five cycles.

*3.3. Reusability Study.* The important advantage of any adsorbent is its reusability which could reduce the process cost and enhance its application at large-scale [63–65]. The reusability of the synthesized $CaFe_2O_4$ nanoparticles and $CaFe_2O_4$/N-GO nanocomposites was determined by repeating the adsorption-desorption cycles up to 5 cycles. The adsorbents were allowed to adsorb the RO12 dye. Then, the adsorbents were collected using an external magnet, and the solution was examined for the presence of dye. The adsorbed dye molecules were desorbed by immersing the adsorbents in 0.1 M NaOH for half-hour. After that, the adsorbents were washed using 0.1 M HCl to be used in the next cycle. The reusability results for the removal of RO12 dye using $CaFe_2O_4$ nanoparticles and $CaFe_2O_4$/N-GO nanocomposite are shown in Figure 10. The removal efficiency of $CaFe_2O_4$ nanoparticles and $CaFe_2O_4$/N-GO nanocomposites remained above 80% ± 1 (after $3^{rd}$ cycle) and 90% ± 1 (after $5^{th}$ cycle), respectively.

Subsequently, both synthesized adsorbents are excellent choices for water treatment. But, the $CaFe_2O_4$/N-GO nanocomposite is better than $CaFe_2O_4$ nanoparticles and more efficient due to the higher adsorption capacity and higher reusability results. All results indicated that the $CaFe_2O_4$/N-GO nanocomposite is a promising nanosorbent for the

water treatment and must be examined for the removal of additional pollutants in the future.

## 4. Conclusion

The facile ultrasonication method was used for the successful synthesis of magnetic $CaFe_2O_4$/N-GO nanocomposite. The synthesized materials were characterized using different methods including FT-IR, XRD, SEM, TEM, magnetization curve, and $N_2$ adsorption-desorption isotherm. The synthesized magnetic $CaFe_2O_4$/N-GO nanocomposite was examined for the adsorption of RO12 dye and compared with $CaFe_2O_4$ nanoparticles. In order to optimize the adsorption process, the effects of different factors including the initial dye concentration, pH, contact time, and adsorbent dose on the adsorption process were studied. The adsorption kinetics that was studied indicated that the pseudo $2^{nd}$ order model was the best for the description of RO12 uptake on the surface of $CaFe_2O_4$/N-GO nanocomposite and $CaFe_2O_4$ nanoparticles. Langmuir and Freundlich isotherm models were used to study the adsorption isotherm, and the best fitting was achieved using Langmuir isotherm model. The addition of N-GO to $CaFe_2O_4$ nanoparticles during the nanofabrication of the nanocomposite enhanced the RO12 removal efficiency. The maximum adsorption capacity ($q_m$) of $CaFe_2O_4$/N-GO nanocomposite for RO12 dye was 333.33 mg/g which was greater than that of $CaFe_2O_4$ nanoparticles (250 mg/g). The higher adsorption capacity of $CaFe_2O_4$/N-GO nanocomposite was related to the addition of N-GO which increased the nanosorbent surface area and provided the nitrogen centers for capturing more toxic molecules. Interestingly, $CaFe_2O_4$/N-GO nanocomposite showed excellent adsorption capacity for RO12 compared to other adsorbents reported in the literature. Moreover, the reusability of the synthesized nanomaterials was studied up to 5 cycles with excellent results. Finally, it could be concluded that the nanofabricated $CaFe_2O_4$/N-GO will be a cost-effective and promising adsorbent for the elimination of RO12 from wastewater.

## Data Availability

The research data used to support the findings of this study are included within the article.

## Conflicts of Interest

The authors declare that they have no conflicts of interest.

## Acknowledgments

The authors extend their appreciation to the Deanship of Scientific Research at King Khalid University for funding this work through the research groups program under grant number RGP.2/157/42. Additionally, Princess Nourah bint Abdulrahman University Researchers Supporting Project number (PNURSP2022R19), Princess Nourah bint Abdulrahman University, Riyadh, Saudi Arabia.

## References

[1] S. M. Siddeeg, M. A. Tahoon, N. S. Alsaiari, M. Shabbir, and F. B. Rebah, "Application of functionalized nanomaterials as effective adsorbents for the removal of heavy metals from wastewater: a review," *Current Analytical Chemistry*, vol. 17, pp. 4–22, 2021.

[2] L. Zhou, C. Gao, and W. Xu, "Magnetic dendritic materials for highly efficient adsorption of dyes and drugs," *ACS Applied Materials & Interfaces*, vol. 2, no. 5, pp. 1483–1491, 2010.

[3] Q. Xu, D. Sun, Y. Qi, and L. Duan, "Efficient removal of anionic organic dyes from aqueous solution with cu-organic frameworks," *Chemical Engineering & Technology*, vol. 42, no. 5, pp. 1070–1077, 2019.

[4] N. K. Nga, P. T. T. Hong, T. Dai Lam, and T. Q. Huy, "A facile synthesis of nanostructured magnesium oxide particles for enhanced adsorption performance in reactive blue 19 removal," *Journal of Colloid and Interface Science*, vol. 398, pp. 210–216, 2013.

[5] M. Bhowmik, K. Deb, A. Debnath, and B. Saha, "Mixed phase Fe2O3/Mn3O4magnetic nanocomposite for enhanced adsorption of methyl orange dye: neural network modeling and response surface methodology optimization," *Applied Organometallic Chemistry*, vol. 32, no. 3, article e4186, 2018.

[6] S. Hwang, M. Choi, J. Lee et al., "Infiltrated thin film structure with hydrogel-mediated precursor ink for durable SOFCs," *Scientific Reports*, vol. 11, no. 1, p. 7109, 2021.

[7] K. Sathishkumar, M. S. AlSalhi, E. Sanganyado, S. Devanesan, A. Arulprakash, and A. Rajasekar, "Sequential electrochemical oxidation and bio-treatment of the azo dye Congo red and textile effluent," *Journal of Photochemistry and Photobiology B: Biology*, vol. 200, article 111655, 2019.

[8] P. Chanikya, P. V. Nidheesh, D. S. Babu, A. Gopinath, and M. S. Kumar, "Treatment of dyeing wastewater by combined sulfate radical based electrochemical advanced oxidation and electrocoagulation processes," *Separation and Purification Technology*, vol. 254, article 117570, 2021.

[9] S. Sugashini, T. Gomathi, R. A. Devi, P. N. Sudha, K. Rambabu, and F. Banat, "Nanochitosan/carboxymethyl cellulose/$TiO_2$ biocomposite for visible-light-induced photocatalytic degradation of crystal violet dye," *Environmental Research*, vol. 204, article 112047, 2022.

[10] C. Yu, Z. Wu, R. Liu et al., "Novel fluorinated $Bi_2MoO_6$ nanocrystals for efficient photocatalytic removal of water organic pollutants under different light source illumination," *Applied Catalysis B: Environmental*, vol. 209, pp. 1–11, 2017.

[11] M. L. Christensen, K. Keiding, P. H. Nielsen, and M. K. Jørgensen, "Dewatering in biological wastewater treatment: a review," *Water Research*, vol. 82, pp. 14–24, 2015.

[12] Y. K. Ong, F. Y. Li, S.-P. Sun, B.-W. Zhao, C.-Z. Liang, and T.-S. Chung, "Nanofiltration hollow fiber membranes for textile wastewater treatment: Lab- scale and pilot-scale studies," *Chemical Engineering Science*, vol. 114, pp. 51–57, 2014.

[13] G. R. Delpiano, D. Tocco, L. Medda, E. Magner, and A. Salis, "Adsorption of malachite green and alizarin red s dyes using fe-btc metal organic framework as adsorbent," *International Journal of Molecular Sciences*, vol. 22, no. 2, p. 788, 2021.

[14] B. Othmani, J. A. Gamelas, M. G. Rasteiro, and M. Khadhraoui, "Characterization of two cactus formulation-based flocculants and investigation on their flocculating ability for cationic and anionic dyes removal," *Polymers*, vol. 2020, p. 12, 1964.

[15] X. Luo, C. Liang, and Y. Hu, "Comparison of different enhanced coagulation methods for azo dye removal from wastewater," *Sustainability*, vol. 11, p. 4760, 2019.

[16] F. Sharif and E. P. Roberts, "Electrochemical oxidation of an organic dye adsorbed on tin oxide and antimony doped tin oxide graphene composites," *Catalysts*, vol. 10, p. 263, 2020.

[17] K. M. Katubi, F. M. Alzahrani, N. S. Alsaiari, A. Amari, F. B. Rebah, and M. A. Tahoon, "Partially reduced graphene oxide modified with polyacrylonitrile for the removal of Sm3+ from water," *Processes*, vol. 9, no. 5, p. 818, 2021.

[18] R. N. Queiroz, P. Prediger, and M. G. A. Vieira, "Adsorption of polycyclic aromatic hydrocarbons from wastewater using graphene- based nanomaterials synthesized by conventional chemistry and green synthesis: A critical review," *Journal of Hazardous Materials*, vol. 422, article 126904, 2022.

[19] A. Alonso, J. Moral-Vico, A. A. Markeb et al., "Critical review of existing nanomaterial adsorbents to capture carbon dioxide and methane," *Science of the Total Environment*, vol. 595, pp. 51–62, 2017.

[20] K. B. Tan, M. Vakili, B. A. Horri, P. E. Poh, A. Z. Abdullah, and B. Salamatinia, "Adsorption of dyes by nanomaterials: recent developments and adsorption mechanisms," *Separation and Purification Technology*, vol. 150, pp. 229–242, 2015.

[21] W. Zhu, X. Jiang, K. Jiang, F. Liu, F. You, and C. Yao, "Fabrication of reusable carboxymethyl cellulose/graphene oxide composite aerogel with large surface area for adsorption of methylene blue," *Nanomaterials*, vol. 11, no. 6, p. 1609, 2021.

[22] P. de Luca, A. Chiodo, A. Macario, C. Siciliano, and B. J. Nagy, "Semi-continuous adsorption processes with multi-walled carbon nanotubes for the treatment of water contaminated by an organic textile dye," *Applied Sciences*, vol. 11, no. 4, p. 1687, 2021.

[23] S. Alam, M. S. Khan, W. Bibi et al., "Preparation of activated carbon from the wood of Paulownia tomentosa as an efficient adsorbent for the removal of acid red 4 and methylene blue present in wastewater," *Water*, vol. 13, p. 1453, 2021.

[24] F. Duan, Y. Yang, Y. Li, H. Cao, Y. Wang, and Y. Zhang, "Heterogeneous Fenton-like degradation of 4-chlorophenol using iron/ordered mesoporous carbon catalyst," *Journal of Environmental Sciences*, vol. 26, no. 5, pp. 1171–1179, 2014.

[25] A. Amari, N. Elboughdiri, D. Ghernaout et al., "Multifunctional crosslinked chitosan/nitrogen-doped graphene quantum dot for wastewater treatment," *Ain Shams Engineering Journal*, vol. 12, no. 4, pp. 4007–4014, 2021.

[26] T. Song, W. Tian, K. Qiao et al., "Adsorption behaviors of polycyclic aromatic hydrocarbons and oxygen derivatives in wastewater on N-doped reduced graphene oxide," *Separation and Purification Technology*, vol. 254, article 117565, 2021.

[27] N. S. Alsaiari, F. M. Alzahrani, K. M. Katubi, A. Amari, F. B. Rebah, and M. A. Tahoon, "Polyethylenimine-modified magnetic chitosan for the uptake of arsenic from water," *Applied Sciences*, vol. 11, p. 5630, 2021.

[28] S. M. Siddeeg, A. Amari, M. A. Tahoon, N. S. Alsaiari, and F. B. Rebah, "Removal of meloxicam, piroxicam and $Cd^{+2}$ by $Fe_3O_4/SiO_2$/glycidyl methacrylate-S-SH nanocomposite loaded with laccase," *Alexandria Engineering Journal*, vol. 59, no. 2, pp. 905–914, 2020.

[29] F. M. Alzahrani, N. S. Alsaiari, K. M. Katubi, A. Amari, F. Ben Rebah, and M. A. Tahoon, "Synthesis of polymer-based magnetic nanocomposite for multi-pollutants removal from water," *Polymers*, vol. 13, no. 11, p. 1742, 2021.

[30] P. Koohi, A. Rahbar-kelishami, and H. Shayesteh, "Efficient removal of Congo red dye using Fe3O4/NiO nanocomposite: synthesis and characterization," *Environmental Technology & Innovation*, vol. 23, article 101559, 2021.

[31] P. Arabkhani, H. Javadian, A. Asfaram, F. Sadeghfar, and F. Sadegh, "Synthesis of magnetic tungsten disulfide/carbon nanotubes nanocomposite ($WS_2/Fe_3O_4$/CNTs- NC) for highly efficient ultrasound-assisted rapid removal of amaranth and brilliant blue FCF hazardous dyes," *Journal of Hazardous Materials*, vol. 420, article 126644, 2021.

[32] A. Didehban, M. Zabihi, M. Faghihi, F. Akbarbandari, and H. Akhtarivand, "Design and fabrication of core-shell magnetic and non-magnetic supported carbonaceous metal organic framework nanocomposites for adsorption of dye," *Journal of Physics and Chemistry of Solids*, vol. 152, article 109930, 2021.

[33] A. Syed, A. M. Elgorban, A. H. Bahkali, and M. Sillanpää, "Visible-light sensitization and recombination delay through coupling $CaFe_2O_4$ on $Bi_2O_3$ nanocomposite for high performance photocatalytic and antibacterial applications," *Surfaces and Interfaces*, vol. 26, article 101336, 2021.

[34] P. Das and A. Debnath, "Reactive orange 12 dye adsorption onto magnetically separable CaFe2O4 nanoparticles synthesized by simple chemical route: kinetic, isotherm and neural network modeling," *Water Practice & Technology*, vol. 16, no. 4, pp. 1141–1158, 2021.

[35] M. Ghaedi, J. Tashkhourian, A. A. Pebdani, B. Sadeghian, and F. N. Ana, "Equilibrium, kinetic and thermodynamic study of removal of reactive orange 12 on platinum nanoparticle loaded on activated carbon as novel adsorbent," *Korean Journal of Chemical Engineering*, vol. 28, no. 12, pp. 2255–2261, 2011.

[36] M. Ghaedi, A. M. Ghaedi, F. Abdi, M. Roosta, R. Sahraei, and A. Daneshfar, "Principal component analysis-artificial neural network and genetic algorithm optimization for removal of reactive orange 12 by copper sulfide nanoparticles-activated carbon," *Journal of Industrial and Engineering Chemistry*, vol. 20, no. 3, pp. 787–795, 2014.

[37] S. Hajati, M. Ghaedi, F. Karimi, B. Barazesh, R. Sahraei, and A. Daneshfar, "Competitive adsorption of direct yellow 12 and reactive orange 12 on ZnS: Mn nanoparticles loaded on activated carbon as novel adsorbent," *Journal of Industrial and Engineering Chemistry*, vol. 20, pp. 564–571, 2014.

[38] M. Ghaedi, A. A. Pebdani, B. Sadeghian, R. Sahraei, A. Daneshfar, and C. E. L. A. L. Duran, "Synthesis and characterization of cadmium sulfide nanoparticle–loaded activated carbon as a novel adsorbent for efficient removal of reactive orange 12," *Chemical Engineering Communications*, vol. 200, no. 8, pp. 1071–1088, 2013.

[39] M. Ghaedi and R. Hosseininia, "Adsorption removal of reactive orange 12 from agueous solution by gold nanoparticule loaded on activated carbon: kinetic and equilibrium study," *Iranian Chemical Society*, vol. 16, 2013.

[40] A. K. Das, R. Govindaraj, and A. Srinivasan, "Structural and magnetic properties of sol-gel derived $CaFe_2O_4$ nanoparticles," *Journal of Magnetism and Magnetic Materials*, vol. 451, pp. 526–531, 2018.

[41] M. A. Hosseini, S. Malekie, and N. Ebrahimi, "The analysis of linear dose-responses in gamma-irradiated graphene oxide: Can FTIR analysis be considered a novel approach to examining the linear dose- responses in carbon nanostructures?," *Radiation Physics and Chemistry*, vol. 176, article 109067, 2020.

[42] Y. Li, D. Pan, M. Zhang, J. Xie, and Z. Yan, "Ultrafine Co3O4embedded in nitrogen-doped graphene with synergistic effect and high stability for supercapacitors," *RSC Advances*, vol. 6, no. 54, pp. 48357–48364, 2016.

[43] C. Tan, J. Cao, A. M. Khattak et al., "High-performance tin oxide-nitrogen doped graphene aerogel hybrids as anode materials for lithium-ion batteries," *Journal of Power Sources*, vol. 270, pp. 28–33, 2014.

[44] M. Kaur, M. Kaur, D. Singh, A. C. Oliveira, V. K. Garg, and V. K. Sharma, "Synthesis of CaFe2O4-NGO nanocomposite for effective removal of heavy metal ion and photocatalytic degradation of organic pollutants," *Nanomaterials*, vol. 11, no. 6, p. 1471, 2021.

[45] H. Abd El-Wahab, A. Hassan, A. Naser, O. Fouad, A. El-Din, and O. Wahba, "Preparation and evaluation of nanosized mixed calcium iron oxide ($CaFe_2O_4$) as high heat resistant pigment in paints," *Pigment & Resin Technology*, vol. 44, no. 3, pp. 172–178, 2015.

[46] M. B. Tahir, M. Sagir, and K. Shahzad, "Removal of acetylsalicylate and methyl-theobromine from aqueous environment using nano-photocatalyst $WO_3$-$TiO_2$ @g-$C_3N_4$ composite," *Journal of Hazardous Materials*, vol. 363, pp. 205–213, 2019.

[47] S. Noreen, U. Khalid, S. M. Ibrahim et al., "ZnO, MgO and FeO adsorption efficiencies for direct sky blue dye: equilibrium, kinetics and thermodynamics studies," *Journal of Materials Research and Technology*, vol. 9, pp. 5881–5893, 2020.

[48] F. Ishtiaq, H. N. Bhatti, A. Khan, M. Iqbal, and A. Kausar, "Polypyrole, polyaniline and sodium alginate biocomposites and adsorption- desorption efficiency for imidacloprid insecticide," *International Journal of Biological Macromolecules*, vol. 147, pp. 217–232, 2020.

[49] R. Huang, Q. Liu, J. Huo, and B. Yang, "Adsorption of methyl orange onto protonated cross-linked chitosan," *Arabian Journal of Chemistry*, vol. 10, no. 1, pp. 24–32, 2017.

[50] Y. Liu, X. Liu, W. Dong, L. Zhang, Q. Kong, and W. Wang, "Efficient adsorption of sulfamethazine onto modified activated carbon: a plausible adsorption mechanism," *Scientific Reports*, vol. 7, no. 1, p. 12437, 2017.

[51] S. Afroze and T. K. Sen, "A review on heavy metal ions and dye adsorption from water by agricultural solid waste adsorbents," *Water, Air, & Soil Pollution*, vol. 229, no. 7, p. 225, 2018.

[52] L. Lonappan, T. Rouissi, S. K. Brar, M. Verma, and R. Y. Surampalli, "An insight into the adsorption of diclofenac on different biochars: mechanisms, surface chemistry, and thermodynamics," *Bioresource Technology*, vol. 249, pp. 386–394, 2018.

[53] T. J. M. Fraga, M. N. Carvalho, D. M. . S. M. Fraga, M. . C. L. da Silva, J. M. Ferreira, and M. A. da Motta Sobrinho, "Treated residue from aluminium lamination as adsorbent of toxic reactive dyes–a kinetic, equilibrium and thermodynamic study," *Environmental technology*, vol. 41, no. 6, pp. 669–681, 2020.

[54] A. Eltaweil, H. A. Mohamed, E. M. Abd El-Monaem, and G. El-Subruiti, "Mesoporous magnetic biochar composite for enhanced adsorption of malachite green dye: characterization, adsorption kinetics, thermodynamics and isotherms," *Advanced Powder Technology*, vol. 31, pp. 1253–1263, 2020.

[55] S. Kim, J. Lee, Y. Son, and M. Yoon, "Study of the dye adsorption kinetics ofMetal–OrganicFrameworks in aqueous media," *Bulletin of the Korean Chemical Society*, vol. 41, no. 8, pp. 843–850, 2020.

[56] Y. Yuan, W. Zhan, F. Jia, and S. Song, "Multi-edged molybdenite achieved by thermal modification for enhancing Pb(II) adsorption in aqueous solutions," *Chemosphere*, vol. 251, article 126369, 2020.

[57] P. Sirajudheen, P. Karthikeyan, S. Vigneshwaran, and S. Meenakshi, "Synthesis and characterization of La(III) supported carboxymethylcellulose- clay composite for toxic dyes removal: Evaluation of adsorption kinetics, isotherms and thermodynamics," *International Journal of Biological Macromolecules*, vol. 161, pp. 1117–1126, 2020.

[58] M. Ghaedi, F. Karimi, B. Barazesh, R. Sahraei, and A. Daneshfar, "Removal of reactive orange 12 from aqueous solutions by adsorption on tin sulfide nanoparticle loaded on activated carbon," *Journal of Industrial and Engineering Chemistry*, vol. 19, no. 3, pp. 756–763, 2013.

[59] Y. Dong, M. Gao, Z. Song, and W. Qiu, "Adsorption mechanism of As(III) on polytetrafluoroethylene particles of different size," *Environmental Pollution*, vol. 254, article 112950, 2019.

[60] A. S. Abdulhameed, A.-T. Mohammad, and A. H. Jawad, "Application of response surface methodology for enhanced synthesis of chitosan tripolyphosphate/$TiO_2$ nanocomposite and adsorption of reactive orange 16 dye," *Journal of Cleaner Production*, vol. 232, pp. 43–56, 2019.

[61] M. Naushad, T. Ahamad, G. Sharma et al., "Synthesis and characterization of a new starch/$SnO_2$ nanocomposite for efficient adsorption of toxic $Hg^{2+}$ metal ion," *Chemical Engineering Journal*, vol. 300, pp. 306–316, 2016.

[62] S. Rezania, M. A. Kamboh, S. S. Arian et al., "Nitrile-calixarene grafted magnetic graphene oxide for removal of arsenic from aqueous media: isotherm, kinetic and thermodynamic studies," *Chemosphere*, vol. 268, article 129348, 2021.

[63] Z. Ayazi, Z. M. Khoshhesab, F. F. Azhar, and Z. Mohajeri, "Modeling and optimization of adsorption removal of reactive orange 13 on the alginate–montmorillonite–polyaniline nanocomposite via response surface methodology," *Journal of the Chinese Chemical Society*, vol. 64, no. 6, pp. 627–639, 2017.

[64] N. S. Alsaiari, K. M. Katubi, F. M. Alzahrani et al., "Synthesis, characterization and application of polypyrrole functionalized nanocellulose for the removal of Cr(VI) from aqueous solution," *Polymers*, vol. 13, no. 21, p. 3691, 2021.

[65] N. S. Alsaiari, A. Amari, K. M. Katubi et al., "The biocatalytic degradation of organic dyes using laccase immobilized magnetic nanoparticles," *Applied Sciences*, vol. 11, no. 17, p. 8216, 2021.

Hindawi
Adsorption Science & Technology
Volume 2022, Article ID 9131597, 10 pages
https://doi.org/10.1155/2022/9131597

*Research Article*

# A Universal Synergistic Rule of Cd(II)-Sb(V) Coadsorption to Typical Soil Mineral and Organic Components

**Min Zhou,[1,2] Ruijia Yang,[1] Xiaoyu Tan,[1] Boqing Tie,[1] Ming Lei,[1] and Huihui Du[1]**

[1]*College of Resources and Environment, Hunan Agricultural University, Changsha 410128, China*
[2]*Yonker Environmental Protection Co., Ltd., Changsha 410128, China*

Correspondence should be addressed to Huihui Du; duhuihui@hunau.edu.cn

Received 4 November 2021; Revised 29 November 2021; Accepted 31 December 2021; Published 18 January 2022

Academic Editor: Hesham Hamad



Heavy metals and metalloids are common cooccurrence in contaminated soils, making their behaviors more complex than their individual presences. Adsorption to soil minerals and organic components determines the solubility and mobility of heavy metals. However, little information is available regarding coadsorbing metals (e.g., Cd) and metalloids (e.g., Sb) to soil components, and whether there is a universal coadsorption rule needs to be illuminated. This study investigated the coadsorption behaviors of Cd(II) and Sb(V) to goethite, kaolinite, and bacteria (*Bacillus cereus*) at both acidic (pH 4.5) and alkaline pH (pH 8.5). Equilibrium adsorption experiments, coupled with scanning electron microscopy- (SEM-) energy-dispersive X-ray spectrum (EDS) and X-ray photoelectron spectroscopy (XPS), were applied to determine the batch adsorption phenomena and possible mechanisms. Batch results showed that Cd(II) adsorption was greater at pH 8.5 whereas Sb(V) adsorption was greater at pH 4.5. The presence of Cd or Sb promoted each other's adsorption to goethite, kaolinite, and bacteria, but slight differences were that Sb(V) preferred to enhance Cd(II) adsorption at acidic pH, whereas Cd(II) was more able to increase Sb(V) adsorption at alkaline pH. SEM-EDS analyses further showed that the distribution of Cd and Sb was colocalized. The surface FeOH, AlOH, and COOH groups participated in the binding of Cd(II) and Sb(V), probably through the formation of inner-sphere complexes. Two possible ternary complexes, i.e., sorbent-$Cd^{2+}$-$Sb(OH)_6^-$ and sorbent-$Sb(OH)_6^-$-$Cd^{2+}$, were possibly formed. Both the charge effect and the formation of ternary complexes were responsible for the collaborative coadsorbing of Cd-Sb. The universal synergistic rule obtained suggests that current models for predicting Cd(II) or Sb(V) sequestration based on single systems may underestimate their solid-to-liquid distribution ratio in a coexistence situation. The results obtained have important implications for understanding the chemical behavior of Sb and Cd in contaminated soils.

## 1. Introduction

Soils contaminated with both elevated concentrations of heavy metals (e.g., Cd and Pb) and metalloids (e.g., As and Sb) are common in mining and smelting-impacted regions. For example, Sb/As-Cd combined pollution often occurs in soils surrounding mines due to the concomitant presence of Cd in Sb/As-containing ores [1–4]. The chemical properties of metals and metalloids are distinctly different; i.e., Sb and As commonly exist as oxyanion whereas Cd presents as cation, which makes a big difference in their reactivity, bioavailability, mobility, and fate in the environment. Moreover, the coexistence of metal cations and anions poses a higher risk to biologic organisms and ecological safety than their individual presences [5]. Unfortunately, studies focusing on the behaviors of coexisting metals-metalloids in soils are rare.

Adsorption-desorption is an important process determining the solubility and partitioning of metal pollutants between the solid and aqueous interfaces. The most important interfaces include phyllosilicates, metal (oxyhydr)oxides, organic matter, and microbes [6–11]. Metal cations and metalloids show quite different affinities towards soil components [12]. For metal cations, favorable adsorption is commonly observed on organic colloids such as humus, microbes, and extracellular secretions at environmentally relevant pH [13–18]. These organic constituents exhibit negative surface charge and abundant functional groups including carboxyl, phosphate, amino, phenolic hydroxyl, and

sulfhydryl [19–22], showing a strong ability to complex metal cations to form stable inner-sphere-type complexes. As for metalloids, they are inclined to bind to metal (oxyhydr)oxides [23–26] rather than the organic constituents. Strong inner-sphere surface complexes and structural incorporation were observed during As and Sb adsorption to Fe/Al/Mn (oxyhydr)oxides [27–34]. Several studies also demonstrated that pH is a dominant influencing factor; i.e., lower pH favors metalloid adsorption whereas higher pH favors metal cation adsorption.

There is an increasing number of studies investigating the coadsorption characteristics of metal-metalloid to soil metal (oxyhydr)oxides. For example, Jiang et al. [30] showed that the adsorption of Cd(II) on goethite was enhanced in the presence of As(V), which could be interpreted by the decreased electrostatic potential with adsorbed $AsO_4^{3-}$ and the formation of a Cd-As-goethite complex. In contrast, Cd(II) did not affect As(V) adsorption quantity but changed its coordination environments such as the As-Fe distance [30]. Carabante et al. [35] discovered that Zn(II) had no effect on As(V) adsorption to ferrihydrite at pH 4 but significantly enhanced adsorption at pH 8, possibly due to the formation of arsenate-zinc hydroxide carbonate complexes. For the Cd(II)-Sb(V) system, Liu et al. [36] observed a positive effect of Cd(II) on Sb(V) adsorption to Fe-Mn binary oxides, owing to the increased $\zeta$-potential and the formation of Cd(II)-Sb(V) precipitates. Similar metal-metalloid-mineral precipitates were also observed such as Cu(II)-As(V)-goethite [37] and Zn(II)-As(V)-goethite [38].

Although coadsorbing metal-metalloids to metal (oxyhydr)oxides have been well documented, information regarding clay mineral systems is rare. Clay minerals, a group of hydrous aluminum silicates, are also an important mineral host for heavy metals/metalloids in soils [6]. Clay minerals have completely different surface charge characteristics compared to metal (oxyhydr)oxides, which might show different impacts on coadsorbing metals-metalloids. In addition to minerals, soil organic constituents such as humus and microbes also play an important role in metal sequestration [39]. There is also an urgent need to investigate the behaviors of coadsorbing metal-metalloids in organo systems.

This investigation was aimed at elucidating whether there is a universal coadsorption rule of Cd-Sb to typical soil mineral and organic components and how this coadsorption behavior affects the mobility and fate of Cd and Sb in contaminated soils. We selected two kinds of minerals, i.e., kaolinite, a typical clay mineral, and goethite, a typical iron oxide, and one representative organic component, i.e., bacteria (*Bacillus cereus*), under both acidic and alkaline pH. Batch adsorption coupled with various spectroscopic tools was applied. The results of this study will provide a new perspective for realizing how Sb(V)-Cd(II) cointeracts with soil components, which helps predict their mobility and fate in contaminated soils and sediments.

## 2. Materials and Methods

*2.1. Materials.* Goethite was synthesized following the procedures described in Schwertmann et al. [40], by hydrolyzing a $Fe(NO_3)_3$ solution to pH 12, and aged at 60°C for 24 h. Kaolinite was purchased from the Clay Minerals Society. The <2 $\mu$m clay-sized fractions were separated via a sedimentation procedure reported in Rong et al. [41]. The *Bacillus cereus* is an autochthonous Gram-positive soil bacterium (GenBank accession number is MH34583). Bacterial cells were cultured in a Luria-Bertani nutrient medium at 28°C. The biomass was obtained by centrifugation, and the cells were suspended in the electrolyte (0.1 M $KNO_3$) to form a parent solution and stored at 4°C before use.

*2.2. Batch Experiments.* Adsorption experiments were conducted in a batch process at room temperature (25°C). Sb(V) and Cd(II) stock solutions were prepared from $KSb(OH)_6$ and $Cd(NO_3)_3$, respectively. Adsorption samples, containing 0.05 g/L sorbent (goethite/kaolinite/*Bacillus cereus*) and 0.2 mM adsorbate (Cd and/or Sb), were prepared in a 0.1 M $KNO_3$ electrolyte. Three different systems were considered: single Cd, single Sb, and binary Cd-Sb (1 : 1 molar ratio). The pH of the adsorption suspension was adjusted to either pH 4.5 or 8.5 using dilute NaOH or $HNO_3$, and the suspension was placed on an end-over-end shaker for 24 h. Adsorption suspensions were then centrifuged at 4500 g. The supernatants were filtered through a 0.45 $\mu$m syringe filter, acidified with 1% $HNO_3$, and analyzed using Inductively Coupled Plasma Optical Emission Spectroscopy (ICP-OES). The residual thick pastes left in the adsorption experiments were freeze-dried for SEM-EDS and XPS analyses. All batch experiments were conducted in triplicate.

*2.3. Characterization.* Scanning electron microscopy was recorded on a field emission scanning electron microscope (FE-SEM, Quanta 250, USA), equipped with a Flat QUAD probe (Bruker Quantax) for energy-dispersive spectroscopy (EDS) analysis. The $\zeta$-potentials of goethite, kaolinite, and *Bacillus cereus* cell were determined using a $\zeta$-potential analyzer (Zetaplus90, Brookhaven). X-ray photoelectron spectroscopy (XPS) was recorded using an X-ray photoelectron spectrometer (Thermo Fisher Scientific, USA) with a KRATOS Axis Ultra X-ray source (1486.7 eV). An energy range of 0–1100 eV was used with a step size of 1 eV for a wide-scan spectrum, and the high-resolution scans were recorded with a step size of 0.05 eV. The C 1s peak at 284.8 eV was used as an internal standard calibration peak for charge correction. The Shirley background and Gaussian/Lorentzian were set up to 20%.

## 3. Results and Discussion

*3.1. Synergistic Coadsorption of Cd(II)-Sb(V) to Goethite, Kaolinite, and Bacteria.* In goethite systems, Sb(V) adsorption was larger at pH 4.5 than at pH 8.5, with an equilibrium Sb(V) adsorption of 1.42 and 1.17 mmol/g, respectively (Table 1, batches 1 and 4). The uptake of Cd(II) was greater at pH 8.5 than at pH 4.5, with the final Cd adsorption of ~1.64 and 0.4 mmol/g, respectively (Table 1, batches 5 and 2). Our findings agree with previous observations [14, 34]. Goethite normally has a $pH_{pzc}$ (zero point of charge) around

Table 1: Summary of experimental conditions and final adsorption of Sb(V) and Cd(II) for the batch experiments.

| | Batch experiment | Initial concentration (mmol/L) | | pH | Adsorption (mmol/g) | |
|---|---|---|---|---|---|---|
| | | Sb(V) | Cd(II) | | Sb(V) | Cd(II) |
| Goethite | 1 | 0.2 | | 4.5 | 1.42 ± 0.04 | |
| | 2 | | 0.2 | | | 0.40 ± 0.01 |
| | 3 | 0.2 | 0.2 | | 1.60 ± 0.03 | 0.70 ± 0.07 |
| | 4 | 0.2 | | 8.5 | 1.17 ± 0.01 | |
| | 5 | | 0.2 | | | 1.64 ± 0.02 |
| | 6 | 0.2 | 0.2 | | 2.58 ± 0.14 | 1.99 ± 0.02 |
| Kaolinite | 7 | 0.2 | | 4.5 | 1.14 ± 0.03 | |
| | 8 | | 0.2 | | | 0.29 ± 0.01 |
| | 9 | 0.2 | 0.2 | | 1.50 ± 0.02 | 1.17 ± 0.01 |
| | 10 | 0.2 | | 8.5 | 0.64 ± 0.01 | |
| | 11 | | 0.2 | | | 1.23 ± 0.06 |
| | 12 | 0.2 | 0.2 | | 1.74 ± 0.01 | 1.99 ± 0.01 |
| Bacteria | 13 | 0.2 | | 4.5 | 0.28 ± 0.01 | |
| | 14 | | 0.2 | | | 1.03 ± 0.01 |
| | 15 | 0.2 | 0.2 | | 0.59 ± 0.03 | 1.63 ± 0.03 |
| | 16 | 0.2 | | 8.5 | 0.20 ± 0.01 | |
| | 17 | | 0.2 | | | 2.33 ± 0.01 |
| | 18 | 0.2 | 0.2 | | 1.05 ± 0.01 | 2.67 ± 0.07 |

7.5 [42]. At pH 4.5, goethite is positively charged ($\zeta$-potential = 17.33 mV, Table 2); an electrostatic attraction between Sb(V) oxyanions and goethite could facilitate adsorption, whereas a strong electrostatic repulsion between Cd(II) and the surface would inhibit adsorption. The opposite is true at pH 8.5. In binary systems, both Sb(V) and Cd adsorptions were greater than those in single systems. Specifically speaking, Sb(V) removal increased to 1.60 and 2.28 mmol/g, respectively, at pH 4.5 and 8.5 (Table 1, batches 3 and 6); Cd adsorption raised to 0.70 and 1.99 accordingly. It is therefore concluded that Cd-Sb coadsorption on goethite is a synergistic process. Notably, the increment in Sb(V) adsorption was much greater (~120%) at pH 8.5 than at pH 4.5 (~13%), whereas the enhancement in Cd(II) removal was greater (~75%) at pH 4.5 than at pH 8.5 (~21%).

In kaolinite systems, the removal of Sb(V) was greater at pH 4.5 than at pH 8.5 (Table 1, batches 7 and 10); the opposite was true for Cd(II) (Table 1, batches 8 and 11). This adsorption trend with pH is similar to that in goethite systems and agrees with previous observations in literature [43, 44]. Kaolinite is negatively charged at both pH 4.5 and 8.5 (Table 2); the increased negative charge with increasing pH may explain the different adsorption properties for Sb(V) and Cd(II). In binary systems, Sb(V) adsorption was increased to 1.50 and 1.75 mmol/g, respectively, at pH 4.5 and 8.5 (Table 1, batches 9 and 12), corresponding to an increment of ~32% and 173%, respectively. The uptake of Cd(II) was increased by ~315% and 62%, respectively, at pH 4.5 and 8.5. The presence of Cd(II) was more able to promote Sb(V) adsorption at alkaline pH, while Sb(V) was more capable of facilitating Cd(II) adsorption at acidic pH, which is consistent with the trend in goethite systems.

Table 2: The zeta potentials (mV) of goethite, kaolinite, and bacteria at different pH.

| | pH | Zeta potential (mV) |
|---|---|---|
| Goethite | 4.5 | 17.33 |
| | 8.5 | -23.73 |
| Kaolinite | 4.5 | -6.12 |
| | 8.5 | -25.01 |
| Bacteria | 4.5 | -16.68 |
| | 8.5 | -56.79 |

In bacteria systems, the uptake of Sb(V) was larger at pH 4.5 than at pH 8.5, with a final Sb(V) adsorption of 0.28 and 0.20 mmol/g, respectively (Table 1, batches 13 and 16). The much lower Sb(V) adsorption on bacteria than those on goethite and kaolinite is mainly because of the stronger repulsion between Sb(V) oxyanions and more negatively charged bacterial cells (see $\zeta$-potentials in Table 2). The adsorption of Cd(II) was much larger at pH 8.5 than at pH 4.5 (Table 1, batches 14 and 17). In binary systems, Sb(V) uptake was increased by ~111% and 425%, respectively, at pH 4.5 and 8.5, compared to those in single systems. The adsorption of Cd had increased by ~58% and 15%, respectively, at pH 4.5 and 8.5. Similar to goethite and

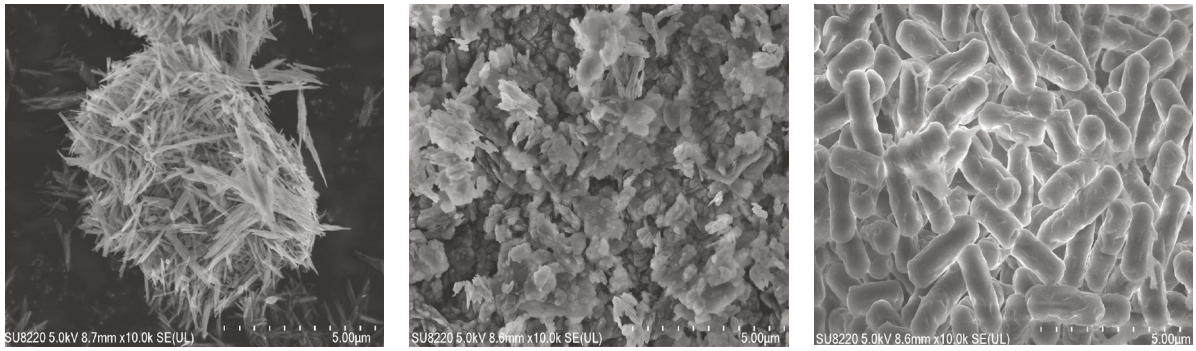


(a) (b) (c)

Figure 1: SEM images of (a) goethite, (b) kaolinite, and (c) *Bacillus cereus* cell.

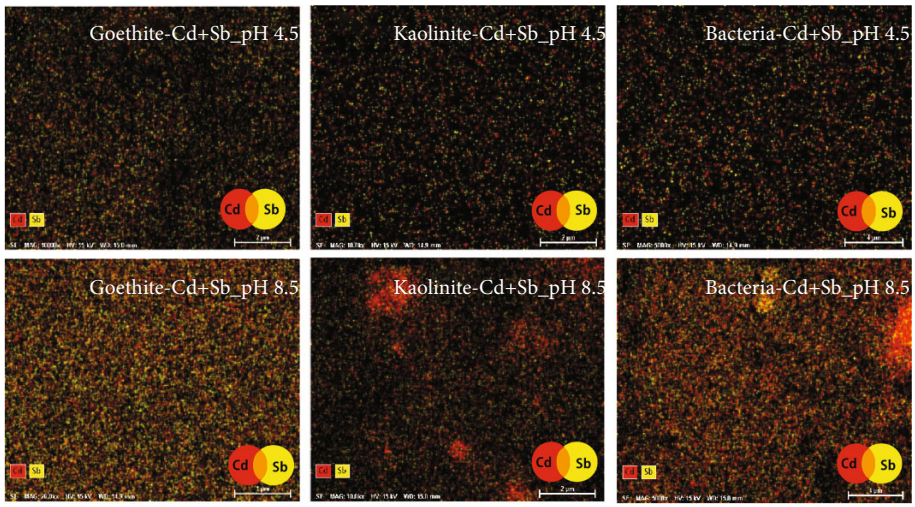


Figure 2: SEM-ED mapping of goethite, kaolinite, and *Bacillus cereus* cell after the sorption of Cd(II) and Sb(V) at pH 4.5 and 8.5.

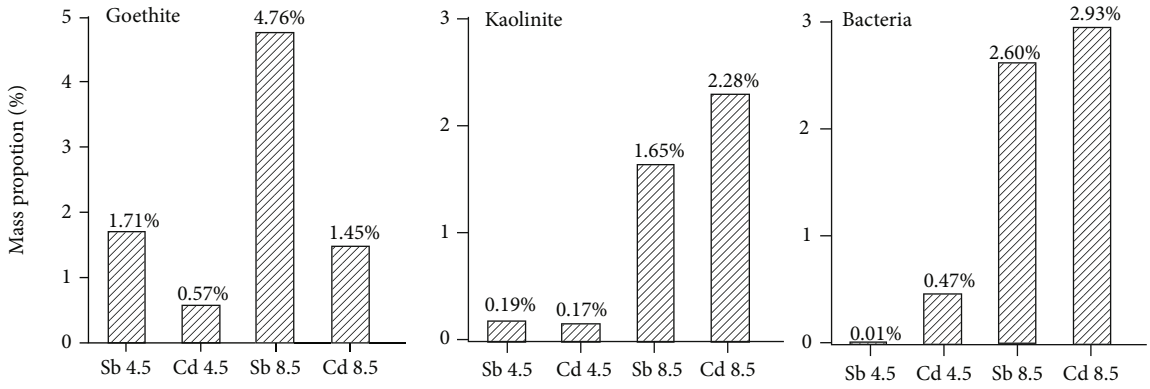


Figure 3: Mass percentage of Cd(II) and Sb(V) in goethite, kaolinite, and *Bacillus cereus* cell. Data are produced from Figure 2.

kaolinite systems, the promotion in Sb(V) adsorption was more pronounced at higher pH, whereas lower pH was more favorable to promote Cd(II) adsorption.

Overall, the batch results demonstrate a synergistic coadsorption behavior of Cd(II)-Sb(V) to typical soil clay minerals, iron (oxyhydr)oxides, and bacteria. The presence of Sb(V) significantly enhances Cd(II) adsorption at acidic pH, whereas Cd(II) prominently facilitates Sb(V) adsorption at alkaline pH.

*3.2. SEM-EDS Analyses.* Typical morphology pictures of goethite, kaolinite, and *Bacillus cereus* are shown in Figure 1. The synthesized goethite comprises <2 $\mu$m needle-type crystal. Kaolinite shows a layered hexagonal shape with a size

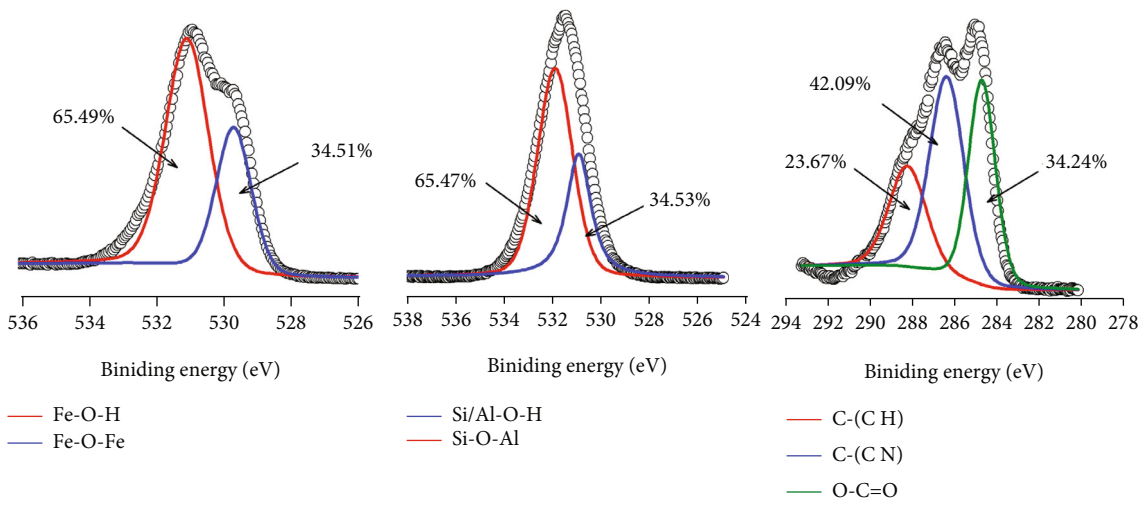


Figure 4: High-resolution O 1s XPS spectra of goethite and kaolinite and C 1s XPS spectrum of the *Bacillus cereus* cell.

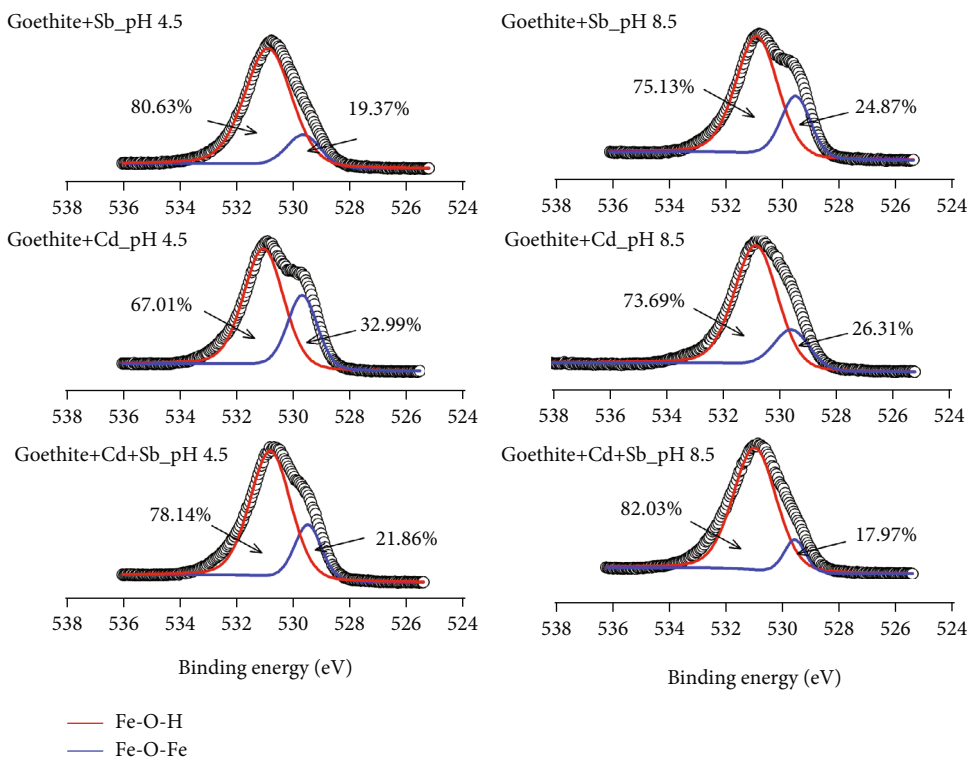


Figure 5: High-resolution O 1s XPS spectra of goethite after the sorption of Cd(II) and/or Sb(V).

mostly smaller than 2 $\mu$m. *Bacillus cereus* cells yield a rod shape with cell length and width of ~3.0 $\mu$m and 1 $\mu$m, respectively.

Two-color SEM-EDS elemental maps of the distribution of Sb (yellow) and Cd (red) in goethite, kaolinite, and *Bacillus cereus* are shown in Figure 2. There are few separated red or yellow areas (mostly orange, red+yellow), indicating that the distribution of Sb and Cd is positively correlated. This could be due to the formation of the ternary sorbent-Sb-Cd complexes at the same coordinated sites. The elemental mass percentage results (Figure 3) show clearly that kaolinite, goethite, and bacteria adsorb much more Cd/Sb at pH 8.5 than at pH 4.5 in the coexisting situation. This may indicate that Cd(II) and Sb(V) could be more easily coadsorbed by soil components in an alkaline environment.

*3.3. XPS Analyses.* To reveal the underlying mechanisms, goethite, kaolinite, and *Bacillus cereus* before and after the binding of Cd and/or Sb were characterized by XPS (Figures 4–7). XPS is a powerful tool for surface functional group analyses. For goethite, the O 1s spectrum can be subdivided into Fe–O–Fe (529.67 eV) and Fe–O–H (531.04 eV)

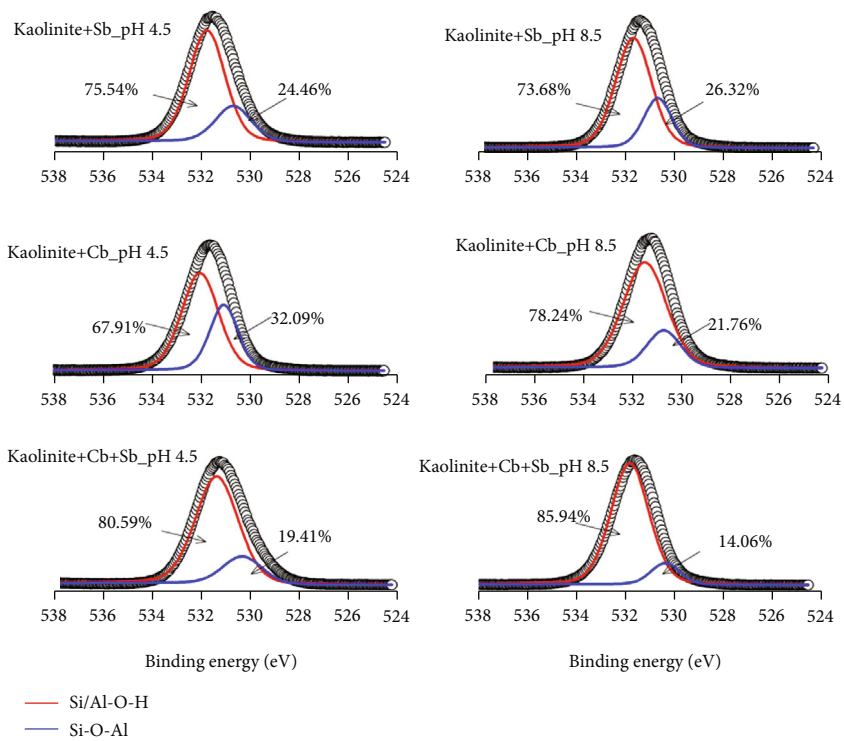


Figure 6: High-resolution O 1s XPS spectra of kaolinite after the sorption of Cd(II) and/or Sb(V).

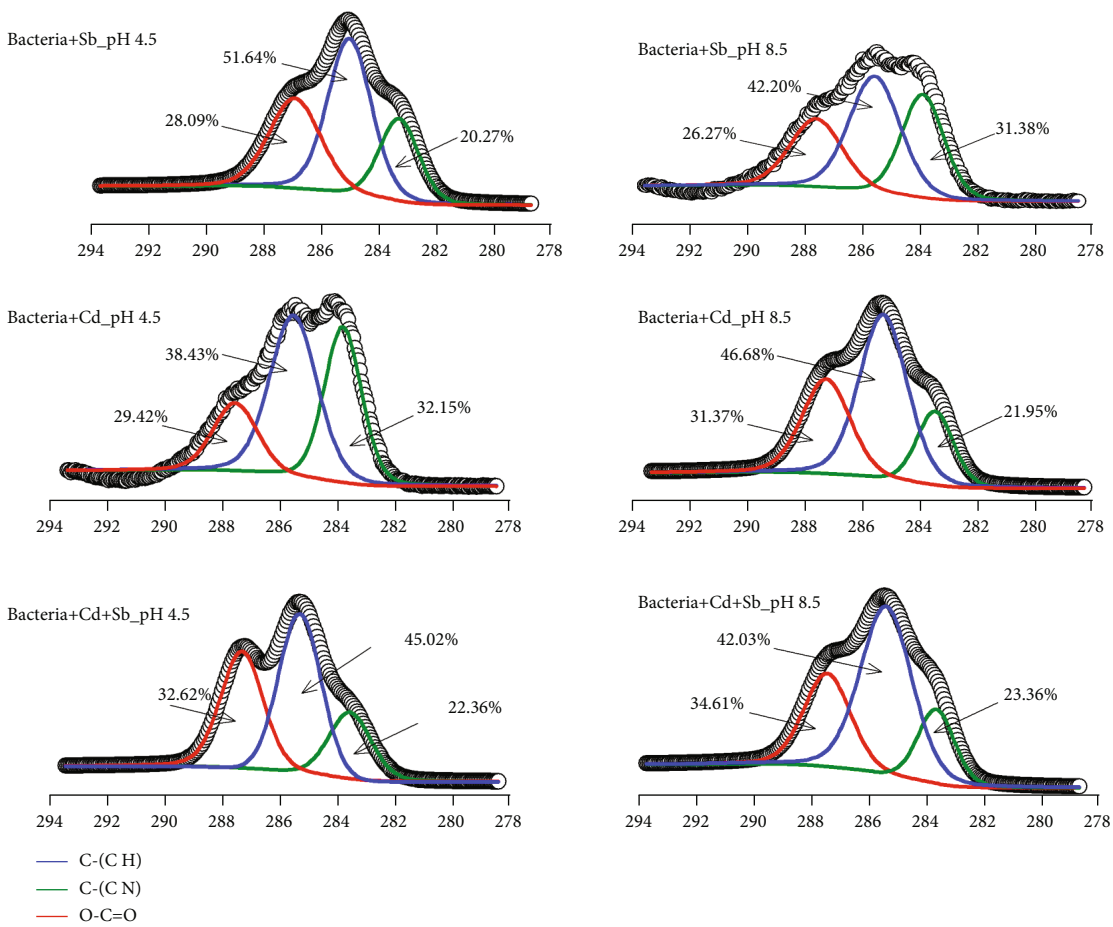


Figure 7: High-resolution C 1s XPS spectra of the *Bacillus cereus* cell after the sorption of Cd(II) and/or Sb(V).

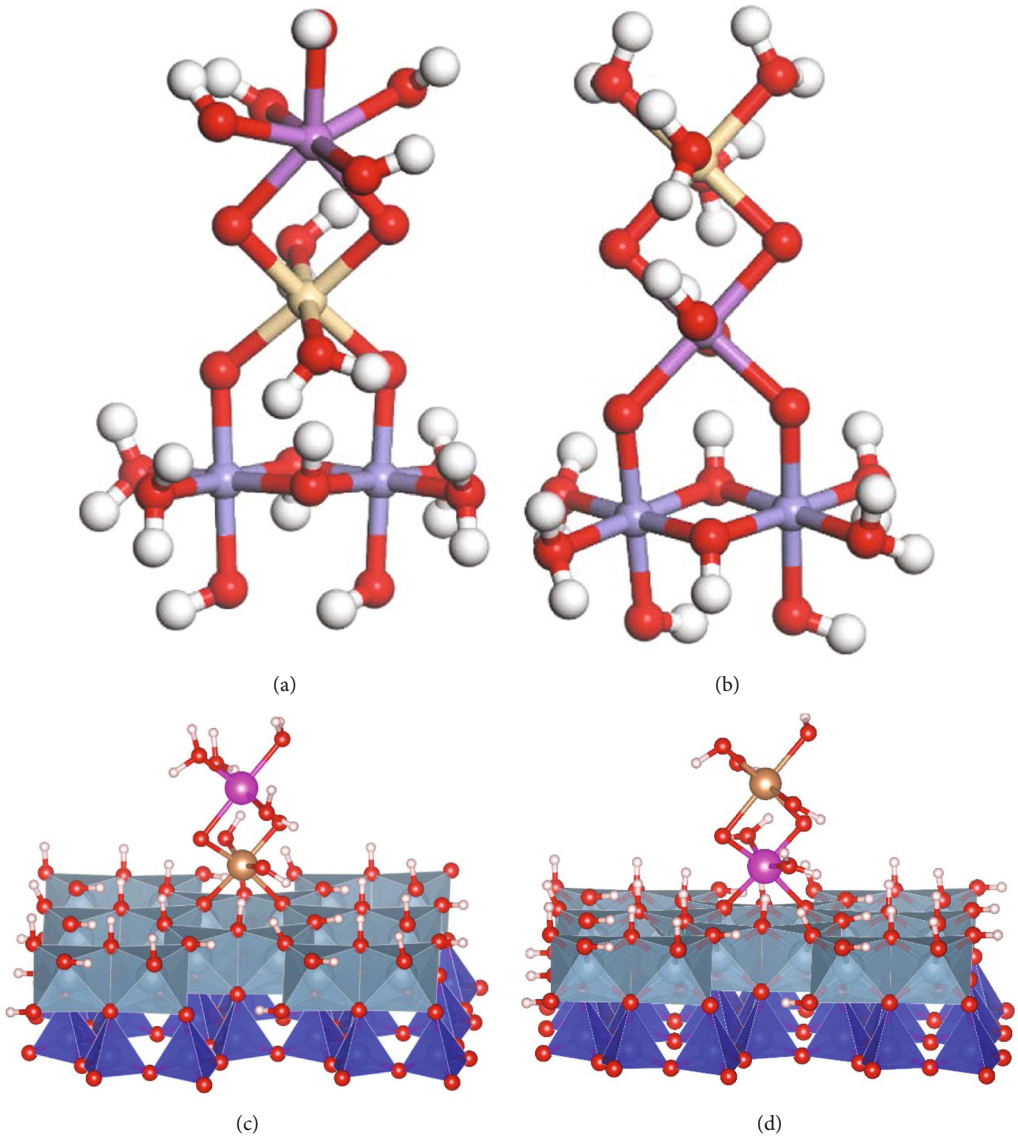


Figure 8: The structures of two possible ternary complexes on (a, b) goethite and (c, d) kaolinite.

[45]. The peak intensity of Fe-O-H is much higher (65.49%) than that of Fe–O–Fe (34.51%) (Figure 4), indicating the presence of abundant hydroxyl functional groups on the surface. For kaolinite, the O 1s spectrum can be subdivided into O atoms of silanol (≡SiOH) and aluminol (≡AlOH) on the basal/edge surface and O atoms bridging Si and Al (Si–O–Al) [44]. The Si/Al–O–H is located at ~531.91 eV while the Si–O–Al is located at ~530.94 eV, and the proportions are 65.47% and 34.53%, respectively (Figure 4). For bacteria, the peak of C 1s can be decomposed into three peaks which are assigned to the C–C/C–H (284.1 eV), C–O/N (286.5 eV), and O–C=O (288.2 eV), respectively [46].

When Sb(V) and/or Cd(II) adsorb on goethite, there is a significant increase in the Fe–O–H fraction (Figure 5). Specifically, the proportion of Fe–O–H is increased to 80.63%, 67.01%, and 78.14%, respectively, after Sb(V), Cd(II), and Sb(V)-Cd(II) adsorption at pH 4.5 and 75.13%, 73.69%, and 82.03%, respectively, at pH 8.5. These observations demonstrate that the ferric hydroxyl groups of goethite participate in the binding of Sb(V) and/or Cd(II), possibly through the formation of inner-sphere complexes, i.e., Fe–O–Cd/Sb [34, 47, 48]. These newly formed species would contribute to the increased peak intensity of the surface Fe–O–H. It is also interesting that the changes of Sb(V)-loaded spectra are more evident at pH 4.5, whereas the changes of Cd(II)-loaded spectra are more pronounced at pH 8.5. This again agrees with the batch results that Sb(V) adsorption increases with decreasing pH whereas Cd(II) sorption increases with elevated pH.

When Sb(V) and/or Cd(II) adsorb on kaolinite, the component of Si/Al–O–H is increased to 75.54%, 67.91%, and 80.59%, respectively, after Sb(V), Cd(II), and Sb(V)-Cd(II) adsorption at pH 4.5 (Figure 6). At pH 8.5, the component of Si/Al–O–H is enhanced to 73.68%, 78.24%, and 85.94%, respectively. Therefore, the Si/Al–O–H groups participate in the binding of Cd(II) and/or Sb(V) on kaolinite [49]. The gibbsite basal planes of kaolinite can have variable charges [50], which can complex Cd(II) and Sb(V) to form

various inner-sphere complexes. However, it cannot rule out the presence of outer-sphere complexes from XPS, and a previous study showed that Cd(II) can adsorb both as an outer-sphere complex at the negatively charged basal sites and as an inner-sphere complex at the edges of the clay [44, 51].

When Sb(V) and/or Cd(II) adsorb to bacteria, the component of the O–C=O fraction is increased to 28.09–32.62% at pH 4.5 and 26.42–34.61% at pH 8.5 (Figure 7). The O–C=O fraction is commonly assigned to the carbonyls, carboxylate, and/or aldehydes [52], which make up the peptidoglycan, phospholipid bilayer, lipopolysaccharides, and protein of the cell walls. The increase in this component suggests that carboxylic groups are responsible for the binding of Sb and/or Cd(II) on bacterial surfaces.

It is worth noting that for all sorbents (goethite, kaolinite, and bacteria), the changes of the Fe/Si/Al–O–H and O–C=O components are more evident in binary Sb-Cd systems than in single systems. On the one hand, this may be due to the higher adsorption of Cd-Sb in binary systems. On the other hand, the formation of a ternary sorbent-Cd-Sb or sorbent-Cd-Sb complexes may play a role.

*3.4. Possible Mechanisms and Implications.* Goethite, kaolinite, and *Bacillus cereus*, represented by the most ubiquitous soil components, play a crucial role in the sequestration of both metals and metalloids. Our results show that Cd(II)-Sb(V) coadsorption is a synergistic process that their sorption in binary systems is larger than that in single systems. Two possible explanations are as follows: (1) one is the charge effect. Because Cd(II) is positively charged whereas Sb(V) is negatively charged, therefore the adsorption of Cd(II) on the surface will facilitate the electrostatic attraction between Sb(V) and the surface and vice versa. (2) The second is the formation of the ternary complexes. As for the studied systems, two types of ternary complexes are possibly formed, one where the adsorbed Cd is near the surface (type A, sorbent-$Cd^{2+}$-$Sb(OH)_6^-$) and the other where the adsorbed Sb is near the surface (type B, sorbent-$Sb(OH)_6^-$-$Cd^{2+}$). For example, the structure of type A complexes on the goethite and kaolinite surface is shown in Figures 8(a) and 8(c), while that for type B is shown in Figures 8(b) and 8(d). The fact that Cd(II) and Sb(V) play a promoting role in each other's adsorption onto soil clay minerals and organic constituents is a nice addition to previous findings only concerning Fe (oxyhydr)oxide systems. Collectively, our results combined with previous findings demonstrate a universal synergistic effect regarding the coadsorbing Cd-Sb to soil components. In this scenario, current thermodynamic models for predicting Cd(II) or Sb(V) behaviors based on single-solute systems may underestimate their binding to soil solid phases in a coexistence situation. Our results also show that the promotion effects are dependent on pH; i.e., Sb(V) enhances Cd(II) adsorption more pronouncedly at acidic pH, whereas Cd(II) prominently facilities Sb(V) adsorption at alkaline pH. This reminds us that soil pH must be taken into consideration when evaluating the coadsorption behaviors of Cd-Sb. As soil components commonly interact with each other, it is therefore important to consider mineral-organo interaction when studying Cd-Sb coadsorbing behaviors in the future.

## 4. Conclusions

This study provides the first systematic evidence for coadsorbing Cd(II)-Sb(V) to typical mineral and organic components. The results show that Cd(II) and Sb(V) adsorption to goethite, kaolinite, and bacterial cells is greater in binary Cd-Sb systems than in their individual presences at both acidic and alkaline pH. Sb(V) is more able to enhance Cd(II) adsorption at acidic pH, whereas Cd(II) is more capable of increasing Sb(V) adsorption at alkaline pH. The distribution of Sb and Cd is colocalized. The ferric hydroxy groups (FeOH) of goethite, the aluminol (AlOH) of kaolinite, and the carboxyl groups of bacteria are responsible for the binding of Cd(II) and Sb(V), via the formation of inner-sphere-type complexes. Two possible ternary complexes are formed when coadsorption occurs, one where Cd is near the surface and the other where Sb is near the surface. All our observations have important implications for predicting Sb and Cd mobility and fate in contaminated soils.

## Data Availability

All data, models, and code generated or used during the study appear in the submitted article.

## Conflicts of Interest

The authors declare no conflicts of interest.

## Authors' Contributions

Min Zhou and Ruijia Yang contributed equally to this work.

## Acknowledgments

We acknowledge the National Natural Science Foundation of China (NSFC, No. 41907015) and the National Key Research and Development Program of China (2017YFD0801505) for the financial support.

## References

[1] Y. Liu, H. Luo, B. Tie et al., "The long-term effectiveness of ferromanganese biochar in soil Cd stabilization and reduction of Cd bioaccumulation in rice," *Biochar*, vol. 3, no. 4, pp. 499–509, 2021.

[2] J. Long, D. Tan, S. Deng, and M. Lei, "Pollution and ecological risk assessment of antimony and other heavy metals in soils from the world's largest antimony mine area, China," *Human and Ecological Risk Assessment*, vol. 24, no. 3, pp. 679–690, 2018.

[3] K. Loska, D. Wiechuła, and I. Korus, "Metal contamination of farming soils affected by industry," *Environment International*, vol. 30, no. 2, pp. 159–165, 2004.

[4] P. N. Williams, M. Lei, G. Sun et al., "Occurrence and partitioning of cadmium, arsenic and lead in mine impacted paddy rice: Hunan, China," *Environmental Science & Technology*, vol. 43, no. 3, pp. 637–642, 2009.

[5] M. Huang, S. Choi, D. Kim et al., "Risk assessment of low-level cadmium and arsenic on the kidney," *Journal of Toxicology and Environmental Health, Part A*, vol. 72, no. 21-22, pp. 1493–1498, 2009.

[6] H. B. Bradl, "Adsorption of heavy metal ions on soils and soils constituents," *Journal of Colloid and Interface Science*, vol. 277, no. 1, pp. 1–18, 2004.

[7] T. Cai, X. Liu, J. Zhang et al., "Silicate-modified oiltea camellia shell-derived biochar: A novel and cost- effective sorbent for cadmium removal," *Journal of Cleaner Production*, vol. 281, 2021.

[8] H. Du, Z. Xu, M. Hu et al., "Natural organic matter decreases uptake of W(VI), and reduces W(VI) to W(V), during adsorption to ferrihydrite," *Chemical Geology*, vol. 540, 2020.

[9] E. Kurek, J. Czaban, and J. M. Bollag, "Sorption of cadmium by microorganisms in competition with other soil constituents," *Applied and Environmental Microbiology*, vol. 43, no. 5, pp. 1011–1015, 1982.

[10] G. J. Lair, M. H. Gerzabek, and G. Haberhauer, "Sorption of heavy metals on organic and inorganic soil constituents," *Environmental Chemistry Letters*, vol. 5, no. 1, pp. 23–27, 2007.

[11] M. Ledin, C. Krantz-Rülcker, and B. Allard, "Microorganisms as metal sorbents: comparison with other soil constituents in multi-compartment systems," *Soil Biology and Biochemistry*, vol. 31, no. 12, pp. 1639–1648, 1999.

[12] H. Du, N. Nie, W. K. Rao, L. Lu, M. Lei, and B. Tie, "Ferrihydrite-organo composites are a suitable analog for predicting Cd(II)-As(V) coexistence behaviors at the soil solid-liquid interfaces," *Environmental Pollution*, vol. 290, 2021.

[13] H. Du, Q. Huang, M. Zhou et al., "Sorption of Cu(II) by Al hydroxide organo-mineral coprecipitates: microcalorimetry and NanoSIMS observations," *Chemical Geology*, vol. 499, pp. 165–171, 2018.

[14] H. Du, C. L. Peacock, W. Chen, and Q. Huang, "Binding of Cd by ferrihydrite organo-mineral composites: implications for Cd mobility and fate in natural and contaminated environments," *Chemosphere*, vol. 207, pp. 404–412, 2018.

[15] H. Du, C. Qu, M. Ma et al., "Insights into Pb(II) binding by Fe/Al hydroxide-microbe composite: XAFS spectroscopy and isothermal titration calorimetry study," *Chemical Geology*, vol. 510, pp. 84–90, 2019.

[16] L. Lu, F. Xu, W. Rao, N. Nie, and H. Du, "Binding of Cd(II) by amorphous aluminum hydroxide-organophosphorus coprecipitates: from macroscopic to microscopic investigation," *Adsorption Science & Technology*, vol. 2021, article 9943663, 8 pages, 2021.

[17] E. M. Moon and C. L. Peacock, "Adsorption of Cu(II) to ferrihydrite and ferrihydrite-bacteria composites: importance of the carboxyl group for Cu mobility in natural environments," *Geochimica et Cosmochimica Acta*, vol. 92, pp. 203–219, 2012.

[18] A. S. Templeton, A. M. Spormann, and G. E. Brown, "Speciation of Pb(II) sorbed by Burkholderia cepacia/goethite composites," *Environmental Science & Technology*, vol. 37, no. 10, pp. 2166–2172, 2003.

[19] I. Christl, A. Metzger, I. Heidmann, and R. Kretzschmar, "Effect of humic and fulvic acid concentrations and ionic strength on copper and lead binding," *Environmental Science & Technology*, vol. 39, no. 14, pp. 5319–5326, 2005.

[20] B. Mishra, M. Boyanov, B. A. Bunker, S. D. Kelly, K. M. Kemner, and J. B. Fein, "High- and low-affinity binding sites for Cd on the bacterial cell walls of Bacillus subtilis and Shewanella oneidensis," *Geochimica et Cosmochimica Acta*, vol. 74, no. 15, pp. 4219–4233, 2010.

[21] R. Sutton and G. Sposito, "Molecular structure in soil humic substances: the new view," *Environmental Science & Technology*, vol. 39, no. 23, pp. 9009–9015, 2005.

[22] Q. Yu and J. B. Fein, "Sulfhydryl binding sites within bacterial extracellular polymeric substances," *Environmental Science & Technology*, vol. 50, no. 11, pp. 5498–5505, 2016.

[23] M. Lei, J. Tao, R. Yang et al., "Binding of Sb (III) by Sb-tolerant Bacillus cereus cell and cell-goethite composite: implications for Sb mobility and fate in soils and sediments," *Journal of Soils and Sediments*, vol. 19, no. 6, pp. 2850–2858, 2019.

[24] L. Lu, W. Rao, Y. Song, M. Lei, B. Tie, and H. Du, "Natural dissolved organic matter (DOM) affects W(VI) adsorption onto Al (hydr)oxide: mechanisms and influencing factors," *Environmental Research*, vol. 205, 2022.

[25] C. Wu, J. Tu, C. Tian, J. Geng, Z. Lin, and Z. Dang, "Defective magnesium ferrite nano-platelets for the adsorption of As(V): the role of surface hydroxyl groups," *Environmental Pollution*, vol. 235, pp. 11–19, 2018.

[26] Q. Xue, Y. Ran, Y. Tan, C. L. Peacock, and H. Du, "Arsenite and arsenate binding to ferrihydrite organo-mineral coprecipitate: implications for arsenic mobility and fate in natural environments," *Chemosphere*, vol. 224, pp. 103–110, 2019.

[27] A. Adra, G. Morin, G. Ona-Nguema, and J. Brest, "Arsenate and arsenite adsorption onto Al-containing ferrihydrites. Implications for arsenic immobilization after neutralization of acid mine drainage," *Applied Geochemistry*, vol. 64, pp. 2–9, 2016.

[28] R. M. Bolanz, M. Wierzbicka-Wieczorek, M. Caplovicova et al., "Structural incorporation of $As^{5+}$ into hematite," *Environmental Science & Technology*, vol. 47, no. 16, pp. 9140–9147, 2013.

[29] X. Guo, Z. Wu, M. He et al., "Adsorption of antimony onto iron oxyhydroxides: adsorption behavior and surface structure," *Journal of Hazardous Materials*, vol. 276, pp. 339–345, 2014.

[30] W. Jiang, J. Lv, L. Luo et al., "Arsenate and cadmium co-adsorption and co-precipitation on goethite," *Journal of Hazardous Materials*, vol. 262, no. 22, pp. 55–63, 2013.

[31] T. D. Sowers, J. M. Harrington, M. L. Polizzotto, and O. W. Duckworth, "Sorption of arsenic to biogenic iron (oxyhydr)-oxides produced in circumneutral environments," *Geochimica et Cosmochimica Acta*, vol. 198, pp. 194–207, 2017.

[32] Q. Sun, P. X. Cui, C. Liu et al., "Antimony oxidation and sorption behavior on birnessites with different properties ($\delta$-$MnO_2$ and triclinic birnessite)," *Environmental Pollution*, vol. 246, pp. 990–998, 2019.

[33] D. Wu, S. P. Sun, M. He et al., "As(V) and Sb(V) co-adsorption onto ferrihydrite: synergistic effect of Sb(V) on As(V) under competitive conditions," *Environmental Science and Pollution Research*, vol. 25, no. 15, pp. 14585–14594, 2018.

[34] R. Yang, J. Tao, Q. Huang et al., "Co-adsorption of Cd(II) and Sb(III) by ferrihydrite: a combined XPS and ITC study," *Journal of Soils and Sediments*, vol. 19, no. 3, pp. 1319–1327, 2019.

[35] I. Carabante, M. Grahn, A. Holmgren, J. Kumpiene, and J. Hedlund, "Influence of Zn(II) on the adsorption of arsenate onto ferrihydrite," *Environmental Science & Technology*, vol. 46, no. 24, pp. 13152–13159, 2012.

[36] R. Liu, F. Liu, C. Hu, Z. He, H. Liu, and J. Qu, "Simultaneous removal of Cd(II) and Sb(V) by Fe-Mn binary oxide: positive

effects of Cd(II) on Sb(V) adsorption," *Journal of Hazardous Materials*, vol. 300, pp. 847–854, 2015.

[37] M. Gräfe, D. A. Beattie, E. Smith, W. M. Skinner, and B. Singh, "Copper and arsenate co-sorption at the mineral-water interfaces of goethite and jarosite," *Journal of Colloid and Interface Science*, vol. 322, no. 2, pp. 399–413, 2008.

[38] M. Gräfe and D. L. Sparks, "Kinetics of zinc and arsenate co-sorption at the goethite-water interface," *Geochimica et Cosmochimica Acta*, vol. 69, no. 19, pp. 4573–4595, 2005.

[39] J. H. Reuter and E. M. Perdue, "Importance of heavy metal-organic matter interactions in natural waters," *Geochimica et Cosmochimica Acta*, vol. 41, no. 2, pp. 325–334, 1977.

[40] U. Schwertmann, R. M. Cornell, U. Schwertmann, and R. M. Cornell, "Iron oxides in the laboratory: preparation and characterization," *Clay Minerals*, vol. 27, no. 3, pp. 393–393, 2000.

[41] X. Rong, Q. Huang, and W. Chen, "Microcalorimetric investigation on the metabolic activity of Bacillus thuringiensis as influenced by kaolinite, montmorillonite and goethite," *Applied Clay Science*, vol. 38, no. 1-2, pp. 97–103, 2007.

[42] R. S. Juang and W. L. Wu, "Adsorption of sulfate and copper(II) on goethite in relation to the changes of zeta potentials," *Journal of Colloid and Interface Science*, vol. 249, no. 1, pp. 22–29, 2002.

[43] S. Rakshit, D. Sarkar, and R. Datta, "Surface complexation of antimony on kaolinite," *Chemosphere*, vol. 119, pp. 349–354, 2015.

[44] I. F. Vasconcelos, E. A. Haack, P. A. Maurice, and B. A. Bunker, "EXAFS analysis of cadmium(II) adsorption to kaolinite," *Chemical Geology*, vol. 249, no. 3-4, pp. 237–249, 2008.

[45] L. Hao, T. Ouyang, L. Lai et al., "Temperature effects on arsenate adsorption onto goethite and its preliminary application to arsenate removal from simulative geothermal water," *RSC Advances*, vol. 4, no. 94, pp. 51984–51990, 2014.

[46] A. Naskar, A. K. Guha, M. Mukherjee, and L. Ray, "Adsorption of nickel onto Bacillus cereus M116: a mechanistic approach," *Separation Science and Technology*, vol. 51, no. 3, pp. 427–438, 2016.

[47] C. R. Collins, K. V. Ragnarsdottir, and D. M. Sherman, "Effect of inorganic and organic ligands on the mechanism of cadmium sorption to goethite," *Geochimica et Cosmochimica Acta*, vol. 63, no. 19-20, pp. 2989–3002, 1999.

[48] A. K. Leuz, H. Mönch, and C. A. Johnson, "Sorption of Sb(III) and Sb(V) to goethite: influence on Sb(III) oxidation and mobilization," *Environmental Science & Technology*, vol. 40, no. 23, pp. 7277–7282, 2006.

[49] A. G. Ilgen and T. P. Trainor, "Sb (III) and Sb (V) sorption onto Al-rich phases: hydrous Al oxide and the clay minerals kaolinite KGa-1b and oxidized and reduced nontronite NAu-1," *Environmental Science & Technology*, vol. 46, no. 2, pp. 843–851, 2012.

[50] F. Coppin, G. Berger, A. Bauer, S. Castet, and M. Loubet, "Sorption of lanthanides on smectite and kaolinite," *Chemical Geology*, vol. 182, no. 1, pp. 57–68, 2002.

[51] M. Gräfe, B. Singh, and M. Balasubramanian, "Surface speciation of Cd(II) and Pb(II) on kaolinite by XAFS spectroscopy," *Journal of Colloid and Interface Science*, vol. 315, no. 1, pp. 21–32, 2007.

[52] F. Ahimou, C. J. Boonaert, Y. Adriaensen et al., "XPS analysis of chemical functions at the surface of Bacillus subtilis," *Journal of Colloid and Interface Science*, vol. 309, no. 1, pp. 49–55, 2007.

Hindawi
Adsorption Science & Technology
Volume 2022, Article ID 5009124, 14 pages
https://doi.org/10.1155/2022/5009124

*Research Article*

# Selective Chelating Resin for Copper Removal and Recovery in Aqueous Acidic Solution Generated from Synthetic Copper-Citrate Complexes from Bioleaching of E-waste

**Kowit Suwannahong,[1] Jiyapa Sripirom,[2] Chadrudee Sirilamduan,[3] Vanlop Thathong,[4] Torpong Kreetachart,[5] Piyapat Panmuang,[6] Anat Deepatana,[7] Suphot Punbut,[8] and Surachai Wongcharee[9]**

[1]*Department of Environmental Health, Faculty of Public Health, Burapha University, Chonburi 20131, Thailand*
[2]*Department of Chemistry, Faculty of Science, Udon Thani Rajabhat University, Udon Thani 4100, Thailand*
[3]*Department of Business Management, Faculty of Management Science, Ubon Ratchathani University, Ubon Ratchathani 34150, Thailand*
[4]*Department of Environmental Science, Faculty of Science and Technology, Loei Rajabhat University, Loei 42000, Thailand*
[5]*Department of Environmental Engineering, School of Energy and Environment, University of Phayao, Phayao 56000, Thailand*
[6]*Field of Electrical Engineering, Faculty of Engineering, Mahasarakham University, Khamriang, Kantarawichai, Mahasarakham 44150, Thailand*
[7]*Department of Chemical Engineering, Faculty of Engineering, Burapha University, Chonburi 20131, Thailand*
[8]*Thailand Institute of Nuclear Technology, Vibhavadi-Rangsit Road, Chatuchak, Bangkok 10900, Thailand*
[9]*Field of Environmental Engineering, Faculty of Engineering, Mahasarakham University, Khamriang, Kantarawichai, Mahasarakham 44150, Thailand*

Correspondence should be addressed to Surachai Wongcharee; surachai.w@msu.ac.th

Received 2 December 2021; Revised 23 December 2021; Accepted 24 December 2021; Published 13 January 2022

Academic Editor: Hesham Hamad



This research focused on batch experiment using a new generation of chelating resins via an ion exchange process to describe the metabolic adsorption and desorption capacity onto iminodiacetic acid/Chelex 100, bis-pyridylmethyl amine/Dowex m4195, and aminomethyl phosphonic/Lewatit TP260 functional groups in bioleaching. The results showed that Dowex m4195 had the highest performance of adsorption capacity for copper removal in both H+-form and Na+-form. Results for Lewatit TP260 and Chelex 100 revealed lower adsorption performance than results for Dowex m4195. The investigation of desorption from chelating resins was carried out, and it was found that 2 M ammonium hydroxide concentration provided the best desorption capacity of about 64.86% for the H+-form Dowex m4195 followed by 52.55% with 2 M sulfuric acid. Lewatit with 2 M hydrochloric acid gave the best desorption performance in Na+-form while Chelex 100 using hydrochloric at 1 M and 2 M provided similar results in terms of the H+-form and Na+-form. As aspects of the selective chelating resins for copper (II) ions in aqueous acidic solution generated from synthetic copper-citrate complexes from bioleaching of e-waste were considered, H+-form Dowex m4195 was a good performer in adsorption using ammonium hydroxide for the desorption. However, chelating resins used were subsequently reused for more than five cycles with an acidic and basic solution. It can be concluded from these results that selective chelating resins could be used as an alternative for the treatment of copper (II) ions contained in e-waste or application to other divalent metals in wastewater for sustainable water and adsorbent reuse as circular economy.

## 1. Introduction

Copper (Cu) is a metal with significant usages forming an essential part of materials and products for human well-being. Sulfide ores and Cu oxides are the primary sources of Cu [1]. Cu is widely used in building and construction, power generation, industrial machinery and equipment, transport equipment, and general consumer items [2], especially electrical and electronic devices. Consequently, copper production has been increased from over 600 thousand tons in 2010 to over 850 million metric tons in 2021, an annual average growth rate of over 4 percent [3]. The major copper-producing countries are Chile, Peru, and China [3]. Development of new technologies using Cu has increased over the time and is associated with economic growth linked to electronic devices or components [4] as waste printed circuit boards (WPCBs) [5]. With the rapid advancement of electronic products, massive qualities of electronic waste (e-waste) have led to growing environmental concerns as there is no adequate management technology for more than 50 million metric tons of e-waste generated by the end of 2018 [6]. Therefore, the concept of reusing or recycling metals from e-waste plays an important role in allocating resources, and it is widely accepted that the recycling of Cu is an essential and beneficial supplement to primary metal production.

Currently, electronic waste is becoming valuable because it is known as waste electric and electronic equipment (WEEE) or e-waste and is a secondary source of Cu [7] and also contains a mixture of more than a thousand toxic substances [8]. Literature reported that 1 ton of e-waste contains up to 0.2 tons of Cu, of which Cu-rich waste was composed of 44.8% nonmetals by mass and 55.2% of metals (34% Cu, 11% Zn, 5.2% Al, 2.8% Fe, 1.3% Sn, 0.13% Mg, and 0.75% Pb) [9, 10]. Bachofen and Brandl [11] reported that metals contain 851.3 g/kg of Cu, 1.3 g/kg of Al, 0.6 g/kg of Mg, and 0.3 g/kg of Zn.

From 2017 to the present time, about 33% of e-waste (over 72 million metrics tons) will be generated worldwide. In Southeast Asia, the total of e-waste produced is around 16 metric tons giving rise to recent concerns for removal and recovery of Cu from e-waste [12] for sustainable development. Europe has also focused on Cu recycling from e-waste [4] using various recovery methods such as electrolysis, ion exchange electrochemical extraction [7], hydrometallurgy [13, 14], chemical precipitation, biotechnology [15, 16], solvent extraction, mechanical methods [17], or even adsorption [7, 18–21]. Therefore, its recovery and reusability from e-waste are important features of waste management/treatment, and appropriate technology must be developed for sustainable metal reuse.

Alternative technologies to extract a metal have been studied in the last few decades. Bioleaching is one such technology used in the extraction of metal from ores and e-waste, which is popular because it is environmentally friendly and economical [15, 22]. Numerous leaching solutions have been projected for leaching of valuable Cu from e-waste such as organic acids (tartaric acid, oxalic acid, and citric acid) [23], inorganic acid ($H_2SO_4$ with $H_2O_2$ and $H_2SO_4$ with $CuSO_4$ and NaCl) [24], microbes [25], and fungi [26]. Bioleaching processes are simple and effective and are like natural biological cycles based on the use of microorganisms. It has been successfully used to leach metal from ores, but a few studies have been applied in the leaching of metal from e-waste material. Currently, there are a few studies of using microorganisms from different e-wastes such as *Aspergillus niger* for leaching metals (Al, Cu, Pb, Ni, Sn, and Zn) [27] from e-waste, and there is a lack of recovery or reusability data from bioleaching solutions. Based on the sorption ability and selectivity, adsorption processes by ion exchange are more effective for the recovery of metal ions from bioleaching solutions, but again, the literature is limited and a detailed knowledge of adsorption mechanism is very important [17]. As reported by earlier studies, numerous materials have been used as adsorbents, and chelating ion exchange resins are extremely effective. A chelating resin sorbent basically comprises of two components, the chelate forming the functional group and a polymeric matrix that can be applied or used for the adsorption of metal ions in aqueous solutions, wastewater, and metal-organic complexes that originate from bioleaching processing [28–30].

In the bioleaching process, microorganisms such as *A. niger* excreted a metabolic acid during the leaching of metal. *A. niger* excreted 0.003 M oxalic acid and 0.18 M citric acid, *P. simplicissimum* produced 0.005 M oxalic acid, and heterotrophic fungi produced 0.02 nitric acid, 0.13-1.4 M citric acid, 0.00047-0.56 M malic, and 0.60-3.30 M lactic acids [31]. Metals are complexed with metabolic products such as metal-citrate, metal-oxalate, metal-malate, and metal-lactate. It can be seen that when leaching with fungi, citric acid is considered the most effective of the leaching metals [10, 32]. After the leaching process, the adsorption process is used as a key to reclamation of valuable metal ions from acidic solutions. The literature reveals that the adsorption mechanism of metal ions from metal complexes in acidic conditions is rare because most adsorbents can only be used on media with moderate pH values. Therefore, there is much research that has pointed out that most adsorbents have poor adsorption and selectivity for metals from strong acid media [33]. There is no in-depth understanding of metal-complex adsorption.

In recent years, researchers had studied the adsorption of Cu using a new novel chelating resin called Chelex 100 and found that the chelating iminodiacetic acid functional group is able to select Cu and divalent metal from wastewater produced from the manufacture of semiconductors and printed circuit boards (PCB contained Cu (II) ions, Ni (II) ions, and Cu-citrate complexes) [34–36]. In addition, the pH of the solution originating from bioleaching had been studied, and it was found that Chelex also had potential for Cu (II) ions and Zn (II) ions at pH 1-5 [37]. In addition, alternative choices of chelating resin such as the bispicolylamine functional group (Dowex m4195) have been effectively used for the adsorption of Cu from strong acid media with pH lower than 2 [33, 38, 39]. One other option of chelating resin is the methyl phosphonic acid functional group (Lewatit) which is selective for the removal and recovery of Cu from bioleaching solutions from sulfide and Cu oxide ores at acidic pH [40, 41]. It can be concluded that Chelex 100, Dowex

m4195, and Lewatit that is an ionic form of Na ion ($Na^+$) were achieved for Cu adsorption [42], while the ionic form of H ion ($H^+$) has not been investigated yet for the removal and recovery of Cu-organic complexes from bioleaching of e-waste that should be addressed.

There is an essential need for evaluation of data of Cu adsorption and recovery from Cu-organic complexes generated from bioleaching of e-waste using chelating resins. This work presents a selective chelating resin in both $Na^+$ and $H^+$ forms for Cu adsorption and recovery from Cu-organic complexes from bioleaching of e-waste. The potential of various commercial chelating resins with particular consideration of updated ion exchangers such as Chelex 100, Dowex m4195, and Lewatit TP260 for metabolic adsorption capacity onto iminodiacetic acid, bis-pyridylmethyl amine, and aminomethyl phosphonic functional groups and recovery of Cu-citrate complexes in a batch experimental system was investigated for sustainable water and adsorbent reuse.

## 2. Materials and Methods

*2.1. Chelating Resin Preparation.* To achieve its large-scale application in removing Cu (II) ions in aqueous acidic solutions generated from bioleaching of e-waste, modification of selective chelating resin had been studied with various types of functional groups, specifically, iminodiacetic acid, bispicolylamine, and aminomethyl phosphonic.

Three commercial macroporous chelating resins in Na+-form were used in this study: Chelex 100 (styrene-divinylbenzene matrix, iminodiacetic acid, Sigma-Aldrich Company), Dowex m4195 (polystyrene-divinylbenzene matrix, bispicolamine, Dow Chemical Company, supplied by Supelco), and Lewatit TP260 (polystyrene-divinylbenzene matrix, aminomethyl phosphonic, Sigma-Aldrich Company), which are shown in Table 1. Modified H+-form chelating resins were prepared and used as described in the literature [41, 43–47]. 100 g of the Na+-form of Chelex 100 was washed with 2 M of nitric acid ($HNO_3$, AR grade, Merck, Germany), 100 g of Dowex m4195 was washed with 1 M of sulfuric acid ($H_2SO_4$, AR grade, Ajax Finechem), and 100 g of Lewatit TP260 was washed with 1 M of hydrochloric acid (HCl, AR grade, Merck (Supelco)) at room temperature for 24 h with magnetic stirring at 60 rpm as described in the references. After that, the obtained wet H+-form chelating resins were subsequently decanted several times with deionized (DI) water to remove excess acid used at a neutral pH and dried in an oven at 60°C for 24 h. The dried H+-form chelating resins were kept at room temperature in a glass bottle for further batch sorption analysis.

*2.2. Synthetic Copper-Citrate Complex Preparation.* Aqueous acidic solutions from synthetic copper-citrate complexes (Cu-citrate complexes) generated from bioleaching of e-waste were prepared by dissolving about 690 mg/L of copper nitrate salts ($Cu(NO_3)_2{\cdot}3H_2O$, AR grade, Qrec, New Zealand) in 0.01 M of an aqueous solution of citric acid monohydrate ($C_6H_8O_7{\cdot}H_2O$, AR grade, Loba Chemie). 0.01 M citric acid concentration is typical of that produced by the microorganisms (*Bacillus megaterium*, *Pseudomonas putida*, *Acidithiobacillus* sp., and *Aspergillus niger*) used in bioleaching metal from e-waste [27]. Table 2 shows that the citric acid can metabolize and/or extract the maximum Cu (II) ions from e-waste using microorganisms (*Aspergillus Niger* or *A. Niger*) which are about 86% maximum of metal mobilization (metal solubilization in acidophilic microorganisms) from the initial Cu concentration (690 mg/L) [10, 31].

*2.3. Sorption Studies.* Batch sorption and/or adsorption were performed in batch experiments at an initial pH (2.30) of Cu-citrate complexes (mixed solution), using 250 mL Erlenmeyer flasks containing about 100 mL of synthetic Cu-citrate with 1 g of the unmodified and modified chelating resins (Chelex 100, Dowex m4195, and Lewatit TP260) added. The concentration and modified chelating resin mass were examined after evaluating literature data and characteristic discharge concentration and performing several screening experiments. The samples were then shaken at 120 rpm in a shaker (WiseShake SHO-2D model) at room temperature for 24 h in separate runs to ensure that equilibrium was reached without adjusting pH. At the end of the preset time, each modified chelating resin was removed by passing aliquots through a Whatman 0.45 $\mu$m GF/C filter for measuring the residual copper concentration. Eutech pH 700 was used to measure pH for all experiments.

Inductively Coupled Plasma Atomic Emission Spectroscopy (ICP-AES) model Optima 8000 (Perkin Elmer Inc. USA) was used to measure the initial and the final concentrations of copper in the solutions with the analytical wavelength of about 327.393 nm. The adsorption capacity per unit mass (mg copper/g resin) was determined at equilibrium from

$$q_e = \left(\frac{C_i - C_e}{m} \cdot V\right), \tag{1}$$

where $C_i$ is the initial concentration (mg/L) of Cu, $C_e$ is the equilibrium Cu concentration (mg/L), $m$ is the dry weight of the chelating resins (g), $V$ is the volume of the solution (L), and $q_e$ is mg of Cu (II) ion adsorbed per gram of chelating resin.

The percent sorption efficiency at equilibrium was determined following

$$S\,(\%) = \left(\frac{C_0 - C_i}{C_0}\right) \cdot 100, \tag{2}$$

where $S$ is the percent sorption efficiency (%) at the equilibrium of Cu (II) ions.

*2.4. Desorption Studies.* Desorption of loaded copper (II) ions onto unmodified and modified chelating resins was examined by rinsing with deionized water to remove any unadsorbed copper (II) ions. The adsorbents were then dried at room temperature for 24 h and kept in a desiccator. Afterward, adsorbents (1 g) were desorbed with 100 mL of the eluents including hydrochloric acid (HCl), sulfuric acid ($H_2SO_4$), and ammonium hydroxide ($NH_4OH$, AR grade, Qrec, New Zealand) of 0.5 M, 1 M, and 2 M solution,

Table 1: Characteristics and properties of Chelex 100, Dowex m4195, and Lewatit TP260 chelating resins.

| Properties | Chelating resin | | |
|---|---|---|---|
| | Chelex 100 | Dowex m4195 | Lewatit TP260 |
| Matrix | Styrene-divinylbenzene | Polystyrene-divinylbenzene | Polystyrene-divinylbenzene |
| Functional group | Iminodiacetic acid | Bispicolylamine | Aminomethyl phosphonic |
| Structure | Macroporous | Macroporous | Macroporous |
| Ionic form | $Na^+$ | $Na^+$ | $Na^+$ |
| Particle size ($\mu$m) | 150-300 | 300-850 | 400-1250 |
| pH range | 0-14 | 0-7 | 0-14 |
| Temperature (°C) | 75°C max temp. | 60°C max temp. | 85°C max temp. |

Table 2: Electronic scrap concentration and metal mobilization of e-waste leachates at different concentrations using *A. niger* for the biotechnology treatment of Cu (II) ions contained in solid waste [27, 31].

| Element | Electronic scarp concentration (g/L) | | | |
|---|---|---|---|---|
| | 1 (g/L) | 10 (g/L) | 50 (g/L) | 100 (g/L) |
| | Metal mobilization (%) | | | |
| $Cu^{2+}$ (copper (II) ions) | 85 (0.07 g/L) | 86 (0.69 g/L) | 70 (2.80 g/L) | 8 (0.60 g/L) |

respectively [48–50], and were mildly sonicated for 5 min under similar conditions to that of bath adsorption. The supernatants were filtered, and then, the desorbed copper concentration was analyzed using inductively coupled plasma atomic emission spectroscopy. The processes of the desorption batch experiment were repeated until negligible desorbed copper (II) ions were found in the supernatant. The percentage of desorption (%$D$) was calculated following

$$D\,(\%) = \left(\frac{q_{\text{desorbed}}}{q_{\text{adsorbed}}}\right) \cdot 100, \tag{3}$$

where $D$ is the percent desorption efficiency (%), $q_{\text{desorbed}}$ is mg of Cu (II) ions desorbed per gram of chelating resin at negligible desorbed Cu which was found in the supernatant, and $q_{\text{adsorbed}}$ is mg of Cu ion adsorbed per gram of chelating resin at equilibrium. The completion of all experiments was carried out in triplicate runs, and only mean values were presented.

## 3. Results and Discussion

*3.1. pH Behavior after the Adsorption Process in Acidic Solution.* In adsorption and desorption processes, pH behavior and/or value of solutions have effects on the coordination reactions and electrostatic interactions in physical and chemical mechanisms, due to iminodiacetic acid, bispicolylamine, and aminomethyl functional groups in unmodified and modified chelating resins affecting the pH value of its solution by changing the initial pH: Na+-form and H+-form chelating resins of Chelex 100, Dowex m4195, and Lewatit TP260. The influence of pH change after adsorption process characteristics is presented in Table 3. The initial pH of the synthetic Cu-citrate complex solution used in the experiment was about 2.30. As shown in Table 3, the H+-form chelating resins showed different changes after the sorption processes for Chelex 100 H+-form (pH 2.03), Dowex m4195 H+-form (pH 2.01), and Lewatit TP260 H+-form (pH 2.02) as compared to the initial pH. Hence, copper (II) ions preferred acidolysis at low pH, and lack of coprecipitation with H+-form chelating resin plays a supplementary role to an ion exchange mechanism in this case study. It was obviously seen that an affinity of H+-form chelating resin for copper (II) ions was sensitive to pH value attributable to competition of adsorption among the copper (II) ions and $H^+$ ions on the same active site (nitrogen atoms).

The Na+-form resins had contributed to the rise of pH value in the order of Dowex m4195 Na+-form (pH 2.35), Lewatit TP260 Na+-form (pH 2.43), and Chelex 100 Na+-form (pH 2.48), respectively. This indicated that when the resins in their Na+-form interacted with water, the hydrolysis of the resin resulted in the formation of a three-component ion exchange system of $H_3O^+/Na^+/M^{2+}$ as explained in the literature [32]. Divalent copper (II) ions will react with nitrogen atoms to form a very stable charge balance (strong ligand bonding).

It can be concluded that metal adsorption started when the pH reached a high enough range from which most acidic ion exchange sites started to exchange the $H_3O^+$ (hydronium ions) and reached their maximum uptake capacity. Likewise, pH promoted the ion exchange sites that contributed to the reaction and the functional group to shape the chelate rings with the metallic cations of copper divalent.

Comparison of three chelating resins in H+-form showed that the highest percentage of selective adsorption capacity of about 86% as represented in Table 3 occurred with a chelating resin ion exchange with the bispicolylamine or bis(2-pyridylmethyl) functional groups (uncharged tridentate ligand) containing two nitrogen atoms (donor atoms) of two chela (chaws) [51]. Nitrogen atoms can possess an electron pair to form charged complexes with divalent copper that shows very strong chelating properties at low pH (a weak base ion exchanger, Lewis acids) [52]. In terms of the Na+-form, it was also confirmed that Dowex

Table 3: Percentage copper (II) ions adsorbed onto Na+-form and H+-form chelating resins and changed pH of the acidic solutions.

| Chelating resin | Na+-form | | H+-form | |
|---|---|---|---|---|
| | Percent adsorption (*S*%) | Final pH | Percent adsorption (*S*%) | Final pH |
| Chelex 100 | 41.47 | 2.48 | 39.21 | 2.03 |
| Dowex m4195 | 56.97 | 2.35 | 86.20 | 2.01 |
| Lewatit TP260 | 52.91 | 2.43 | 46.84 | 2.02 |

m4195 demonstrated the highest percentage of selective adsorption capacity as compared to the other Na+-form chelating resins of Lewatit TP260 (52.91%) and Chelex 100 (41.47%), respectively. It is suggested that Dowex m4195 was appropriate for copper (II) ions in acidic solutions generated from bioleaching of e-waste; in other words, the cation species influence was greater than that of the anion species for these adsorbent chelating resins. However, isotherm and kinetic need a further study that will be impacted and vital in process design with a straightforward adsorption or desorption process.

Figure 1 presents the sorption process reaction formation of iminodiacetic acid, bispicolylamine, and aminomethyl groups in the acidic solutions, where nitrogen atoms will be protonated and may occur or combine.

*3.2. Metabolic Adsorption Capacity onto Iminodiacetic Acid (Chelex 100) Functional Group Chelating Resins.* Figure 2 demonstrates chelating resins of copper (II) ions adsorbed at different uptake levels using an initial copper concentration of about 690 mg/L with 0.01 M citric acid as the original model substrate for studying the adsorption capacity onto Chelex 100, Dowex m4195, and Lewatit TP260. Chelex 100 demonstrated a small adsorption capacity in both H+-form and Na+-form as compared with other chelating resins of Dowex m4915 and Lewatit TP260 for both H+-form and Na+-form. It could be indicated that iminodiacetic acid chelating resin (Chelex 100) had low capacity in acidic solution conditions (at the low pH) as compared to sulfate and tartrate complexes for bioleaching of e-waste that were predominant at low pH [36]. According to the literature, it was found that copper (II) ion adsorption capacity was not very well as compared with moderate pH for the iminodiacetic acid functional group [38]. In addition, it can be seen that iminodiacetate chelating resin in terms of H+-form and Na+-form has not shown much difference of about 5.45% for the adsorption capacity.

In contrast to literature reports, iminodiacetate resin was not able to adsorb copper (II) ions in 0.05 M citrate acid at pH < 2 [53]; however, it was successful at the lower concentration of citric acid at 0.005 M and 0.01 M. It might be pointed out that the functional group dissociates and since cation exchange reactions cannot be removed by neutral acids, the adsorption performance of iminodiacetate chelating resin with cations decreased due to the presence of acidic conditions. Furthermore, the pKa value of iminodiacetic acid was around 2, and at pH ≤ 2, the uptake of negatively charged anions was promoted whereas the surface charge of chelating resin and metal complexes was similar to low pH. It is unlikely to capture the metal complexes of two carboxylic groups that are protonated when the Chelex 100/chelating resin with its functional groups of iminodiacetic acid is behaving as a poorly/weakly basic anion exchanger as shown in Figure 3 [39, 54]. As a result of the weakly acidic nature of iminodiacetic acid, the exchanger strongly favored hydronium ions and the competitiveness of hydrogen ions with metal ions to active sites on the resin surface in the medium. In summary, the adsorption ability of the iminodiacetic acid functional group of Chelex 100 was weak in highly acidic solutions.

*3.3. Metabolic Adsorption Capacity onto Bis-pyridylmethyl Amine (Dowex m4195) Functional Group Chelating Resin.* Dowex m4195 showed a higher adsorption capacity compared to Lewatit TP260 and Chelex 100 chelating resins as presented in Figure 2. Dowex m4195 is a special adsorbent for metal recovery from strongly acidic media [55, 56]. It was found that the Cu-loaded Dowex m4195 chelating resin in H+-form gave the highest adsorption capacity of about 59.49 mg copper/g resin, which was virtually the same as in earlier reports [57], whereas Dowex m4195 was the best selective sorption agent for divalent metal of Ni (II) ions and Co (II) ions from acidic solution at low pH of about 1. In other words, Dowex m4195 was favored at a high citric acid concentration and low pH; therefore, sorption of Cu-loaded chelating resin was better than that of both iminodiacetic acid and aminomethyl phosphonic chelating resin functional groups of Chelex 100 and Lewatit TP260 for both H+-form and Na+-form, respectively. Literature reports [33, 53] found that Cu-loaded Dowex m4195 and iminodiacetic resin of Amberlite 748 and Lewatit TP270 had favorable properties in acidic solution that could be associated with the unique chemical characters of the bis-pyridylmethyl amine functional group or Dowex m4195, which is appropriate in the elimination of Cu (II) ions from very strong acid (pH lower than 2) solution. Dowex m4915 also forms complexes with divalent metal ions through their free electron pair-bearing nitrogen atom of the bis-pyridylmethyl amine functional group. In comparison to the H+-form and Na+-form of Dowex m4195, it was found that the H+-form was more effective than Na+-form. This might be because the H+-form helps to split complexes and take on the sorption of Cu loaded onto chelating resin [53]. Additionally, it can be explained that the bis-pyridylmethyl amine functional group ligand contains three nitrogen donor atoms (see Figure 4) of electron pairs and at low pH. It can be seen that three nitrogen donor atoms of chelating resin are protonated [58, 59] and formed a chelate ring with copper (II) ions as shown in Figure 1(b). It can be concluded that Dowex m4195 H+-form has superior adsorption

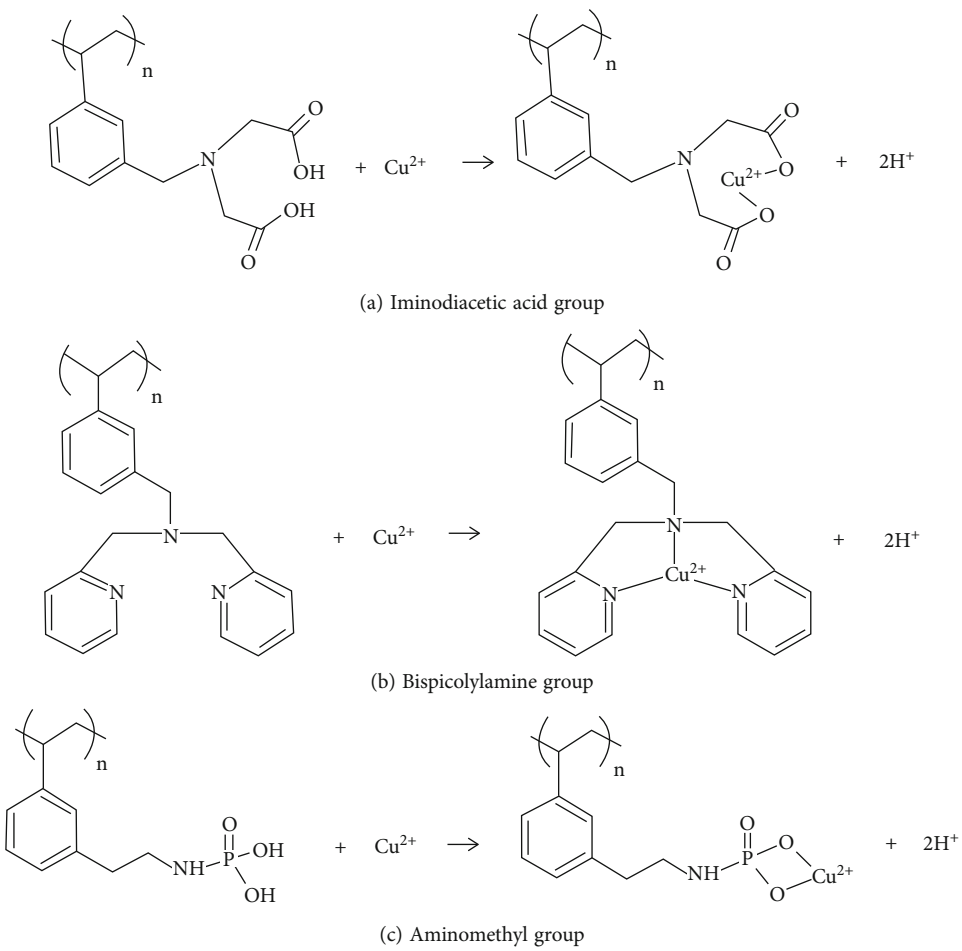


Figure 1: Possible sorption process reaction of copper (II) ion removal onto iminodiacetic acid (a), bispicolylamine (b), and aminomethyl (c) groups in the acidic solutions.

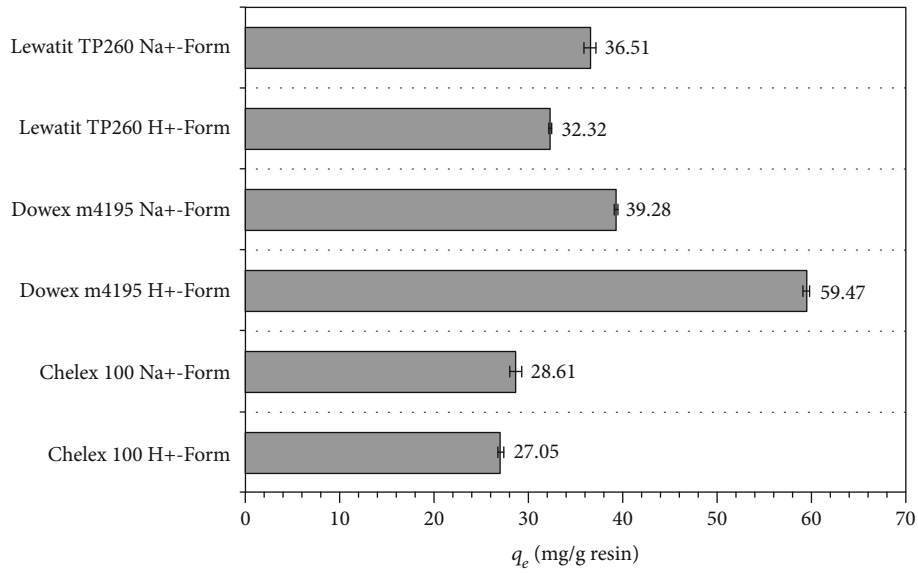


Figure 2: Adsorption capacity of copper (II) ions from Cu-citrate complexes prepared using 0.01 M citric acid by Lewatit TP260, Dowex m4195, and Chelex 100 chelating resins.

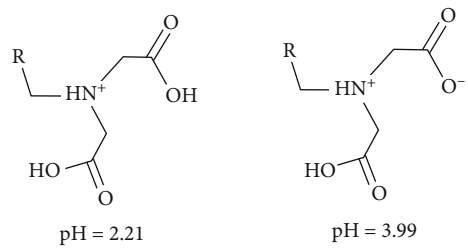


Figure 3: Structure of the iminodiacetic acid functional group at pH less than 2 and pH 3.99.

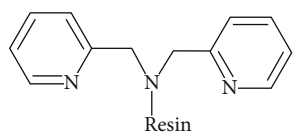


Figure 4: Structure of the bis-pyridylmethyl amine functional group.

performance than Lewatit TP260 and Chelex 100 chelating resins at the low pH for both forms. Figure 5 demonstrates the discussed before and after adsorption of Dowex m41954 for the visual confirmations of the results. Observation of the image confirms that H+-form shows complete adsorption onto the surface of the resin.

*3.4. Metabolic Adsorption Capacity onto Aminomethyl Phosphonic (Lewatit TP260) Functional Group Chelating Resin.* Lewatit TP260 has an aminomethyl phosphonic as a functional group in nature (Figure 6), and the results indicated an intermediate adsorption level as compared to Dowex m4195 and with similar results to Chelex 100. It can be seen that Na+-form of the chelating resin of Lewatit TP260 (36.51 mg/g) was superior to the H+-form of Chelex 100 (27.05 mg/g) based on the adsorption capacity for Cu. Due to the ability of Lewatit TP260 to function at low pH, the adsorption capacity also correlated with those suggested in the literature. It is owing to the effect of a competition binding among divalent copper metal ions and hydrogen ions over the surface of the chelating resins. It can be noticed that at low pH, an overabundance of hydrogen ions can achieve successfully with metal ions for binding sites, resulting in a lower level of metal adsorption on aminomethyl phosphonic/methylphosphonic chelating resin. Additionally, the pKa values of phosphonic acid were about 2 and 5; thus, at increasing pH, more negative sites become accessible for the adsorption, leading to an increase in uptake for the adsorption capacity. Therefore, the adsorption of metal complexes on methylphosphonic acid resin was beyond hindered by the strong affinity of the resin for hydrogen ions in accordance with the acidic solution conditions [32]. It can be concluded that the aminomethyl phosphonate functional group is affected by pH. Due to the fact that the aminomethyl phosphonate functional group is a tridentate ligand, it has two binding sites at a phosphonic acid group and one coordination site at the secondary nitrogen atom as shown in Figure 6 [41]. On the other hand, the adsorption capability of chelating ion exchangers was also influenced by the structure of functional groups, their position in relation to each other, and the characteristics of the matrix (skeleton). The possible schematic mechanism for ion exchange adsorption and desorption of copper (II) ions is shown in Figure 7. Based on adsorption capacity, Lewatit TP260 was not satisfactory for Cu (II) adsorption ability as compared to Dowex m4195. These results confirmed that Dowex m4195 had the capability to capture Cu (II) ions generated from synthetic copper-citrate complexes from bioleaching of e-waste at a low pH value.

*3.5. Copper Desorption.* Subsequent to the adsorption step, copper (II) ions loaded onto chelating resins were recovered/desorbed using 0.5 M, 1 M, and 2 M of HCl, $H_2SO_4$, and $NH_4OH$, respectively, in the liquid phase and batch mode experiments that were examined. Prior to each run of the desorption experiment, an adsorption step was performed as detailed in Section 2.4 for the three chelating resins used in both H+-form and Na+-form. Desorption efficiencies of copper (II) ions are shown in Table 4 (desorption capacity) and Figures 8–10 (desorption efficiency), and these can help to clarify the mechanism of adsorption processes and the reusability of the chelating resin used. If the copper (II) ions are adsorbed onto the chelating resins that can be desorbed easily by water/deionized water (useful for physical adsorption), arguably the attachment of the copper (II) ions onto the chelating resins involves relatively weak bonds (electric forces)/or van der Waals forces. However, this research comprised only preliminary experiments of desorption using water and found that copper (II) ions persisted on the surface of chelating reins used as a complex structure of ion exchanges. Therefore, strong acid and base were used to study the capability of copper (II) ion desorption that confirmed the attachment of copper (II) ions onto the chelating resin as an ion exchange mechanism process. As shown in Table 4, the desorption capacity increased with increasing eluent concentration substances in the order of 0.5 M, 1 M, and 2 M for HCl, $H_2SO_4$, and $NH_4OH$, respectively. Overall, H+-form chelating resins showed the best desorption as compared to Na+-form chelating resins whereas Chelex 100 had good selectivity with HCl 1 M (11.56 mg/g), Dowex m4195 has good selectivity with $NH_4OH$ (38.57 mg/g), and Lewatit TP260 has good selectivity with HCl 1 M (7.55 mg/g), $H_2SO_4$ 0.5 M (7.63), and $H_2SO_4$ 1 M (7.69 mg/g). However, Lewatit TP260 (HCl 2 M) was not shown to have a different desorption capacity with using $H_2SO_4$ 0.5 M and $H_2SO_4$ 1 M of the eluent; therefore, it depends on the user which is selective; desorbed substances are available in terms of cost, being environmentally friendly, and recovery or reusability.

Figure 8 illustrates the desorption efficiency of copper (II) ions loaded onto Chelex 100 chelating resin for both H+-form and Na+-form using 0.5, 1, and 2 M of HCl, $H_2SO_4$, and $NH_4OH$ desorbed substances.

It was revealed that HCl gave the highest desorption capacity of about 11.56 mg desorbed/g resin (42.74%) and was very similar to 1 M HCl (11.55 mg desorbed/g resin, 42.71%) of 0.07% difference. Therefore, it can be suggested that 1 M HCl is suited to the H+-form of Chelex 100 if the

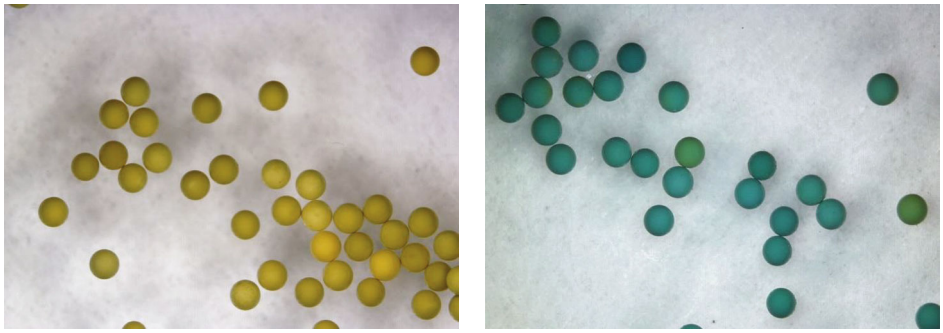

(a) (b)

Figure 5: Microscope image (a) before adsorption and (b) after adsorption of copper (II) ion removal onto Dowex m4195.

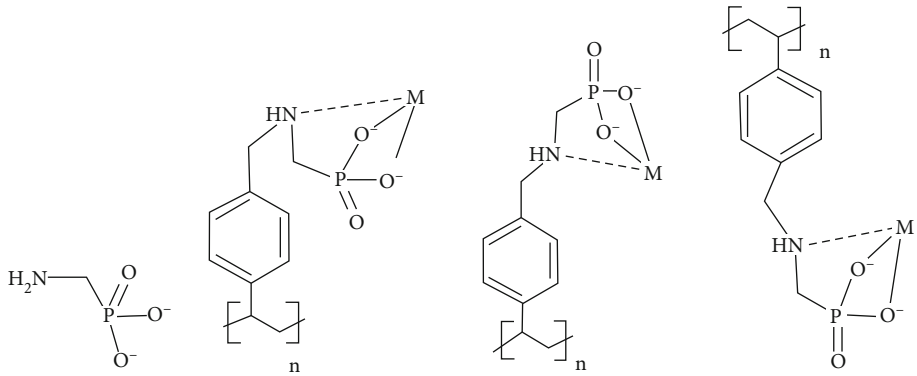


Figure 6: Aminomethyl phosphonic/methyl phosphonic functional group.

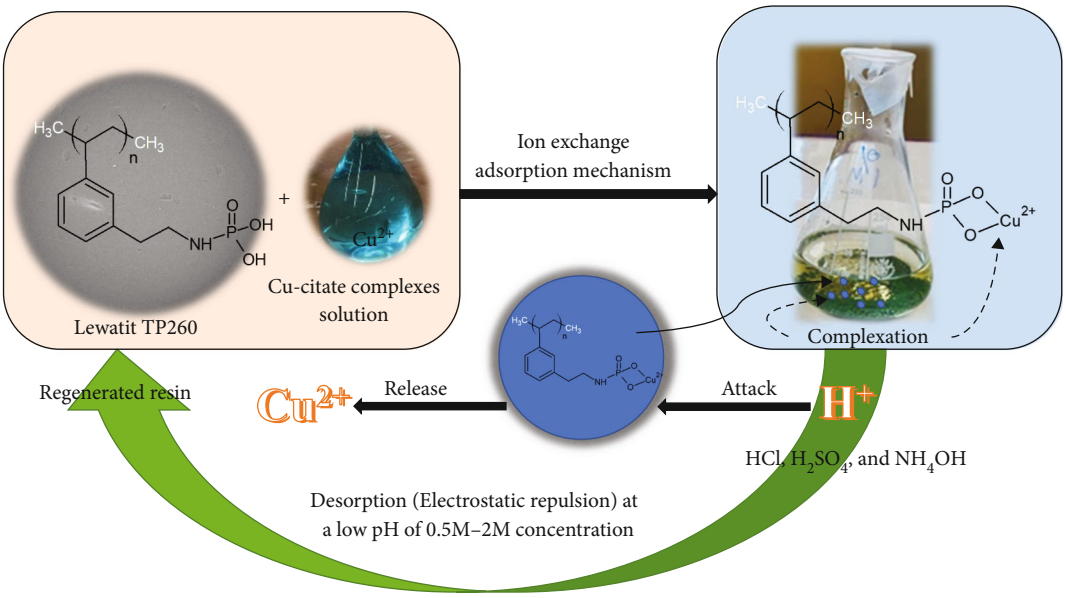


Figure 7: Possible schematic mechanism for adsorption and desorption of copper (II) ions using Lewatit TP260 chelating resin as an adsorbent.

user is concerned for cost and environment. With the Na+-form of Chelex 100, HCl showed the best percent desorption of about 43.52%. It can be seen that the percentage desorption significantly increased with increasing concentrations of the HCl. Sulfuric acid showed that at 2 M concentration, desorption capacity was indicated predominantly as demonstrated in Figure 8. In the case of $NH_4OH$, it can be concluded that desorption capacity was very low and similar

Table 4: Desorption capacity of copper (II) ions onto three chelating resins with various eluent concentrations.

| Eluent | $q_{e,\ desorption}$: H+-form(mg desorbed/g resin) | | | $q_{e,\ desorption}$: Na+-form (mg desorbed/g resin) | | |
|---|---|---|---|---|---|---|
| | Chelex 100 | Dowex m4195 | Lewatit TP260 | Chelex 100 | Dowex m4195 | Lewatit TP260 |
| HCl 0.5 M | 2.41 | 0.19 | 0.32 | 7.16 | 0.15 | 0.91 |
| HCl 1 M | 11.55 | 0.32 | 0.73 | 11.35 | 1.30 | 12.06 |
| HCl 2 M | 11.56 | 0.24 | 7.55 | 12.45 | 1.66 | 16.90 |
| $H_2SO_4$ 0.5 M | 0.22 | 3.33 | 7.63 | 2.87 | 1.38 | 7.19 |
| $H_2SO_4$ 1 M | 9.76 | 7.29 | 7.69 | 1.55 | 3.38 | 13.26 |
| $H_2SO_4$ 2 M | 10.50 | 31.25 | 1.41 | 11.30 | 10.39 | 15.26 |
| $NH_4OH$ 0.5 M | 0.02 | 4.42 | 0.02 | 0.03 | 1.46 | 0.03 |
| $NH_4OH$ 1 M | 0.03 | 8.79 | 0.03 | 0.04 | 6.12 | 0.03 |
| $NH_4OH$ 2 M | 0.03 | 38.57 | 0.03 | 0.04 | 9.71 | 0.03 |

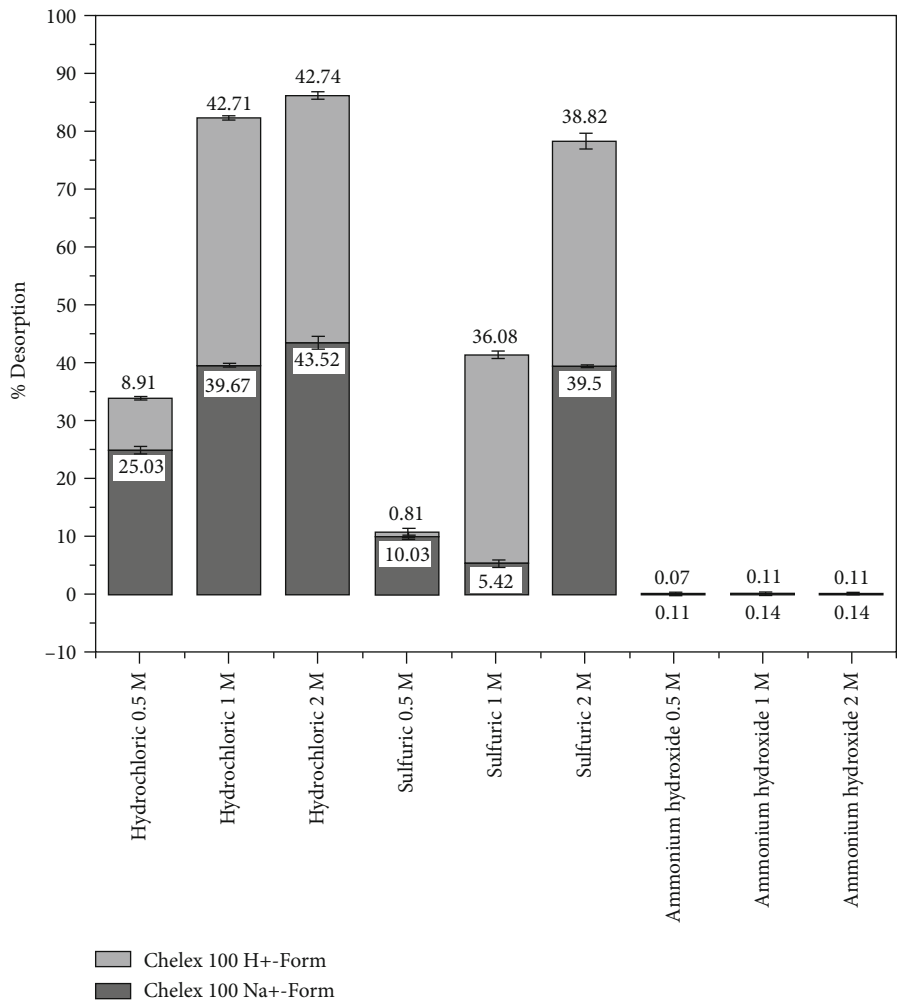


Figure 8: Desorption efficiency of copper (II) ions loaded onto Chelex 100 chelating resin at the differences of concentrations used of desorbed substances.

to that reported in the literature [57] due to it unsuccessfully eluting Cu, Ni, Co, Fe, and Zn from the functional group of iminodiacetic-Amberlite chelating resin, which has weak acidic functional groups. In other words, the functional group of iminodiacetic acid chelating resin was not selective towards $OH^-$ ions. In summary, HCl showed a high ability for the desorption of copper (II) ions loaded onto Chelex 100.

Figure 9 demonstrates the desorption efficiency of copper (II) ions loaded onto Dowex m4195 Chelex chelating resin for both H+-form and Na+-form using 0.5 M, 1 M, and 2 M HCl, $H_2SO_4$, and $NH_4OH$ eluents, respectively.

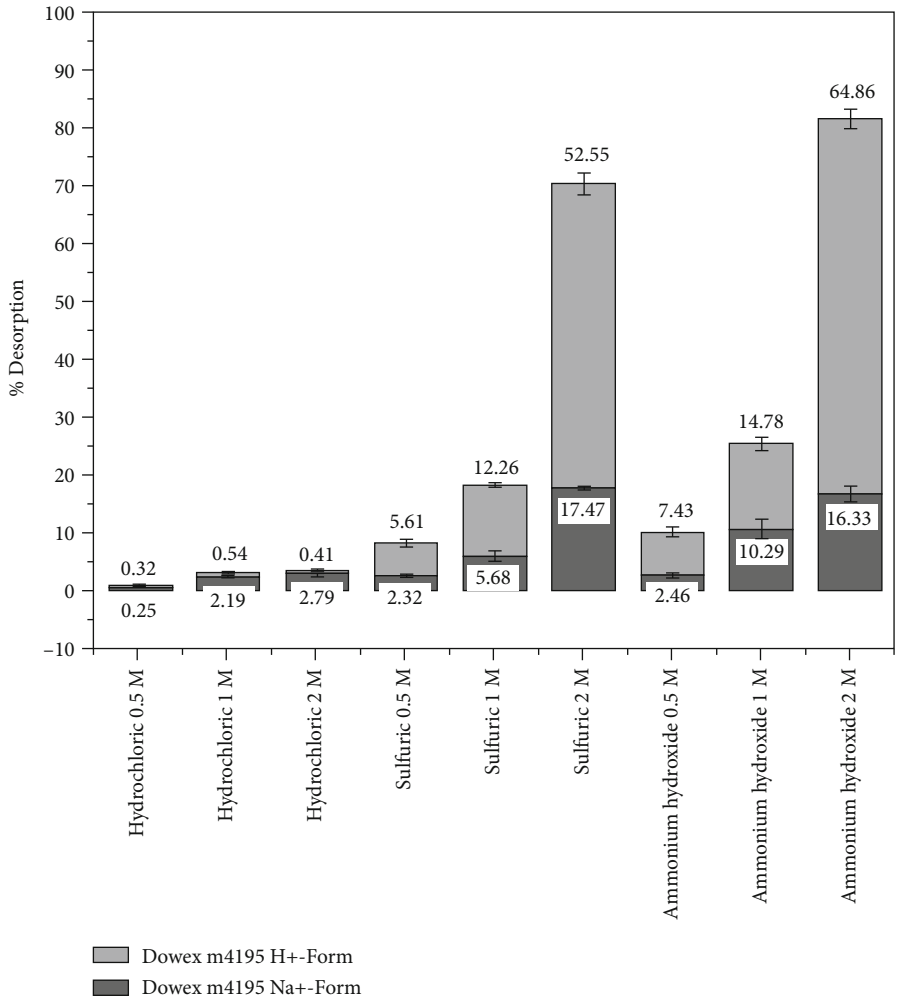


Figure 9: Desorption efficiency of copper (II) ions using Dowex m4195 chelating resin as an adsorbent with 0.5 M, 1 M, and 2 M concentrations of HCl, $H_2SO_4$, and $NH_4OH$ desorbing substances, respectively.

In the case of the H+-form Dowex m4195, 2 M $NH_4OH$ provided the highest desorption capacity (38.57 mg desorbed/g resin, 65.34%) followed by 2 M $H_2SO_4$ (31.25 mg desorbed/g resin, 52.55%) and 1 M $NH_4OH$ (8.79 mg desorbed/g resin, 14.84%). With Dowex m4195 Na+-form chelating resin, the elution by using 2 M $NH_4OH$ was 9.71 mg desorbed/g resin (24.59%) and 8.50 mg desorbed/g resin (21.52%) by using 2 M $H_2SO_4$ and 6.12 mg desorbed/g resin by using 1 M $NH_4OH$ (see Table 4 and Figure 9). Vice versa, all sample elution with HCl had the lowest desorption capacity for both the H+-form and Na+-form of Dowex m4195 chelating resin. These results were related to the previous report [38], which found that elution of copper (II) ions from Dowex m4195 with $H_2SO_4$ and with HCl was not very efficient at low concentration and at low to high concentration, respectively, but it had potential with 2 M $NH_4OH$ and 2 M $H_2SO_4$ eluent with a yield of copper (II) ion desorption.

Figure 10 reveals the desorption efficiency of copper (II) ions loaded onto Lewatit TP260 chelating resin for both H+-form and Na+-form using 0.5 M, 1 M, and 2 M of HCl, $H_2SO_4$, and $NH_4OH$ desorbing substances, respectively.

Desorption efficiency results of copper (II) ion elution from Lewatit TP260 chelating resin indicated that 2 M HCl concentration represented the highest desorption efficiency of about 59.07 percent (15.26 mg desorbed/g resin) for Na+-form chelating resin. For H+-form Lewatit chelating resin, using 0.5 M and 1 M $H_2SO_4$ concentrations for desorbing copper (II) ions loaded has similar desorption capacity of about 28.21% (7.63 mg desorbed/g resin) and 28.43% (7.69 mg desorbed/g resin), respectively. It can be concluded that high acid concentration provided higher copper desorption from the methyl phosphonic functional group [40].

There were two main aspects of the selective chelating resins for copper (II) ions in aqueous acidic solution generated from synthetic copper-citrate complexes from bioleaching of e-waste which were considered: the adsorption ability and the possible recovery of copper (II) ions by desorption from loaded chelating resins. In comparison with other chelating resins used, the H+-form of Dowex m4195 was a good performer in adsorption in acidic solution and in desorption by ammonium hydroxide 2 M concentration used for copper (II) ions generated from bioleaching of e-waste. Thus,

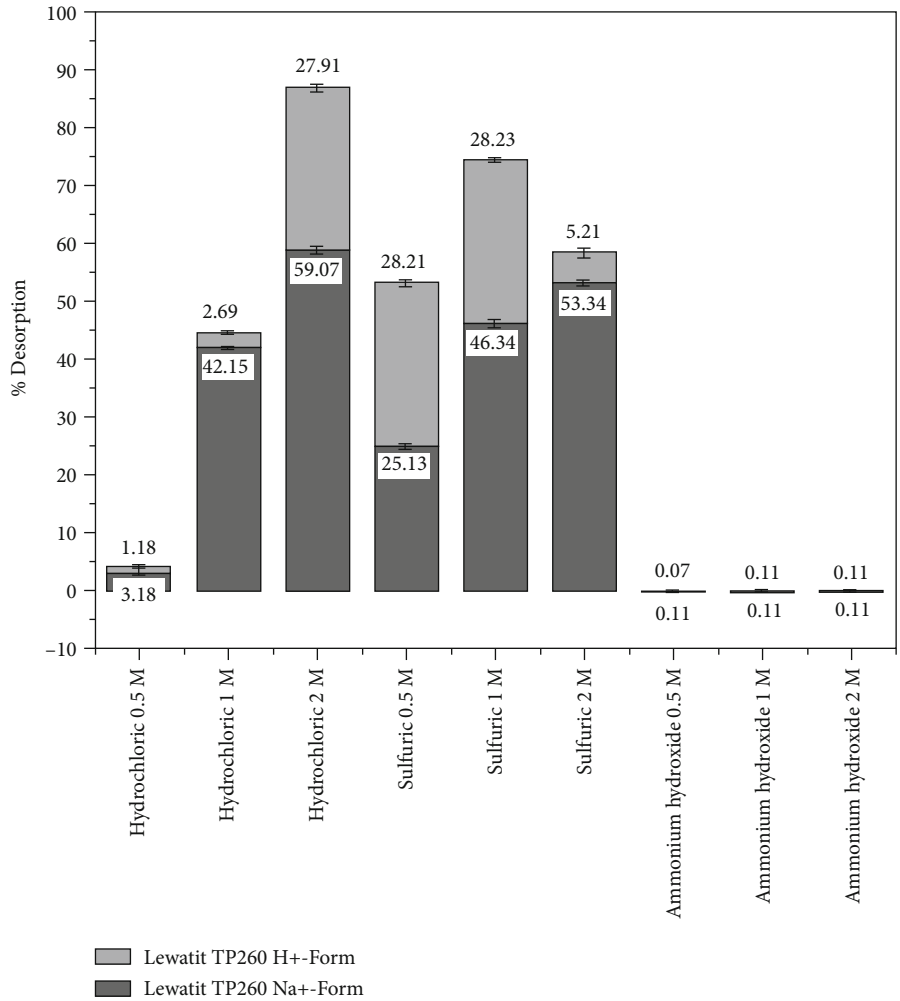


Figure 10: Desorption efficiency of copper (II) ions using Lewatit TP260 chelating resin as an adsorbent with 0.5 M, 1 M, and 2 M concentrations of HCl, $H_2SO_4$, and $NH_4OH$ desorbing substances, respectively.

Dowex m4195 H+-form was the best selective chelating resin for copper removal and was selected for future investigation, but that data is not shown here.

## 4. Conclusion

Copper (II) ion adsorption and recovery from e-waste are becoming an increasingly popular issue of scientific studies due to it being an essential metal for human life and the demand for urban planning and the development of crucial new technology to improve the quality of wastewater containing heavy metals. E-waste is a discarded product resulting from poor management that may have an environmental impact and cause loss of valuable metal especially copper. In this study, three chelating resins were used for adsorption and desorption of copper in an aqueous acidic solution generated from synthetic copper-citrate complexes from bioleaching of e-waste. In summing up these preparatory studies, it can conclude that bis-pyridylmethyl amine/Dowex m4195 was suited to the adsorption of copper in acidic solution at pH < 2 with a maximum adsorption capacity of about 86.20% (H+-form) and 56.97% (Na+-form) chelating resins. Absorption on Dowex m4195 H+-form was mainly dependent on a functional group of the resin and was affected by the pH of the solution. To select the most satisfactory recovery of Cu loaded onto chelating resin, desorption ability was investigated by the use of various concentrations of HCl, $H_2SO_4$, and $NH_4OH$. Desorption with 2 M $NH_4OH$ for the elution of Cu loaded onto Dowex m4195 (H+-form) had the highest percentage recovery of about more than 65%. Therefore, it is confirmed that the bis-picolylamine functional group chelating resin reduces the amount of e-waste and hazardous materials in the environment and decreases the scarcity of laterite ores for sustainable metal and water and adsorbent reuse.

## Data Availability

All the required data are available in the manuscript itself.

## Conflicts of Interest

The authors wish to confirm no conflict of interest regarding the publication of this manuscript.

## Acknowledgments

The authors would like to acknowledge that this research was financially supported by Faculty of Engineering, Mahasarakham University (Grant year 2021), for providing an opportunity to pursue this research work. The authors also thank the Thailand Institute of Nuclear Technology (TINT); Department of Chemical Engineering, Burapha University; Department of Environmental Health, Burapha University; Faculty of Science, Loei Rajabhat University; Department of Business Management, Ubon Ratchathani University; Department of Environmental Engineering, University of Phayao (Unit of Excellence from the University of Phayao (grant number FF65-UoE008); and Histocenter Company for the use of laboratory facilities.

## References

[1] J. Chen, Z. Xu, and Y. Chen, *Electronic Structure and Surfaces of Sulfide Minerals: Density Functional Theory and Applications*, Elsevier Science, 2020.

[2] S. Wstawski, M. Emmons-Burzyńska, M. Rzelewska-Piekut, A. Skrzypczak, and M. Regel-Rosocka, "Studies on copper(II) leaching from e-waste with hydrogen sulfate ionic liquids: effect of hydrogen peroxide," *Hydrometallurgy*, vol. 205, article 105730, 2021.

[3] Statista, "Copper industry worldwide: global copper reserves 2010-2020," 2021, https://www.statista.com/study/14271/copper-statista-dossier/.

[4] L. Ciacci, I. Vassura, and F. Passarini, "Urban mines of copper: size and potential for recycling in the EU," *Resources*, vol. 6, no. 1, p. 6, 2017.

[5] Y. Park, Y. Eom, K. Yoo, and M. K. Jha, "Leaching of Copper from Waste-Printed Circuit Boards (PCBs) in Sulfate Medium Using Cupric Ion and Oxygen," *Metals*, vol. 11, no. 9, p. 1369, 2021.

[6] B. Tansel, "From electronic consumer products to e-wastes: global outlook, waste quantities, recycling challenges," *Environment International*, vol. 98, pp. 35–45, 2017.

[7] Q. Song, Y. Liu, L. Zhang, and Z. Xu, "Selective electrochemical extraction of copper from multi-metal e-waste leaching solution and its enhanced recovery mechanism," *Journal of Hazardous Materials*, vol. 407, article 124799, 2021.

[8] M. Kaya, "Recovery of metals and nonmetals from electronic waste by physical and chemical recycling processes," *Waste Management*, vol. 57, pp. 64–90, 2016.

[9] R. Widmer, H. Oswald-Krapf, D. Sinha-Khetriwal, M. Schnellmann, and H. Böni, "Global perspectives on e-waste," *Environmental Impact Assessment Review*, vol. 25, no. 5, pp. 436–458, 2005.

[10] M. Saidan, B. Brown, and M. Valix, "Leaching of electronic waste using biometabolised acids," *Chinese Journal of Chemical Engineering*, vol. 20, no. 3, pp. 530–534, 2012.

[11] R. Bachofen and H. Brandl, "Microbial recovery of metals from solids," *FEMS Microbiology Reviews*, vol. 20, no. 3-4, pp. 605–617, 1997.

[12] S. Pandey and V. Divyasheesh, "E-waste challenge for developing countries," *International Journal of Innovative Research and Development*, vol. 5, no. 2, pp. 46–49, 2016.

[13] S. Fogarasi, F. Imre-Lucaci, A. Egedy, Á. Imre-Lucaci, and P. Ilea, "Eco-friendly copper recovery process from waste printed circuit boards using $Fe^{3+}/Fe^{2+}$ redox system," *Waste Management*, vol. 40, pp. 136–143, 2015.

[14] I. Birloaga, V. Coman, B. Kopacek, and F. Vegliò, "An advanced study on the hydrometallurgical processing of waste computer printed circuit boards to extract their valuable content of metals," *Waste Management*, vol. 34, no. 12, pp. 2581–2586, 2014.

[15] Y. Hong and M. Valix, "Bioleaching of electronic waste using acidophilic sulfur oxidising bacteria," *Journal of Cleaner Production*, vol. 65, pp. 465–472, 2014.

[16] N. Zhu, Y. Xiang, T. Zhang et al., "Bioleaching of metal concentrates of waste printed circuit boards by mixed culture of acidophilic bacteria," *Journal of Hazardous Materials*, vol. 192, no. 2, pp. 614–619, 2011.

[17] H. Duan, K. Hou, J. Li, and X. Zhu, "Examining the technology acceptance for dismantling of waste printed circuit boards in light of recycling and environmental concerns," *Journal of Environmental Management*, vol. 92, no. 3, pp. 392–399, 2011.

[18] K. Suwannahong, S. Wongcharee, T. Kreetachart, C. Sirilamduan, J. Rioyo, and A. Wongphat, "Evaluation of the Microsoft Excel Solver spreadsheet-based program for nonlinear expressions of adsorption isotherm models onto magnetic nanosorbent," *Applied Sciences*, vol. 11, no. 16, p. 7432, 2021.

[19] K. Suwannahong, S. Wongcharee, J. Rioyo, C. Sirilamduan, and T. Kreetachart, "Insight into molecular weight cut off characteristics and reduction of melanoidin using microporous and mesoporous adsorbent," *Engineering and Applied Science Research*, vol. 49, no. 1, pp. 47–57, 2022.

[20] S. Wongcharee and V. Aravinthan, "Application of mesoporous magnetic nanosorbent developed from macadamia nut shell residues for the removal of recalcitrant melanoidin and its fractions," *Separation Science and Technology*, vol. 55, no. 9, pp. 1636–1649, 2020.

[21] K. Suwannahong, S. Wongcharee, J. Kreanuarte, and T. Kreetachart, "Pre-treatment of acetic acid from food processing wastewater using response surface methodology via Fenton oxidation process for sustainable water reuse," *Journal of Sustainable Development of Energy, Water and Environment Systems*, vol. 9, no. 4 article 1080363, 2021.

[22] Y. Xiang, P. Wu, N. Zhu et al., "Bioleaching of copper from waste printed circuit boards by bacterial consortium enriched from acid mine drainage," *Journal of Hazardous Materials*, vol. 184, no. 1-3, pp. 812–818, 2010.

[23] M. Kolenčík, M. Urík, S. Čerňanský, M. Molnárová, and P. Matúš, "Leaching of zinc, cadmium, lead and copper from electronic scrap using organic acids and the Aspergillus niger strain," *Fresenius Environmental Bulletin*, vol. 22, no. 12a, pp. 3673–3679, 2013.

[24] A. Behnamfard, M. M. Salarirad, and F. Veglio, "Process development for recovery of copper and precious metals from waste printed circuit boards with emphasize on palladium and gold leaching and precipitation," *Waste Management*, vol. 33, no. 11, pp. 2354–2363, 2013.

[25] S. Dave, A. Sodha, and D. Tipre, "Microbial technology for metal recovery from e-waste printed circuit boards," *Journal of Bacteriology & Mycology: Open Access*, vol. 6, no. 4, pp. 241–247, 2018.

[26] M. Sethurajan and E. D. van Hullebusch, "Leaching and selective recovery of Cu from printed circuit boards," *Metals*, vol. 9, no. 10, p. 1034, 2019.

[27] H. Brandl and M. A. Faramarzi, "Microbe-metal-interactions for the biotechnological treatment of metal- containing solid waste," *China Particuology*, vol. 4, no. 2, pp. 93–97, 2006.

[28] S. Pandey, E. Fosso-Kankeu, J. Redelinghuys, J. Kim, and M. Kang, "Implication of biofilms in the sustainability of acid mine drainage and metal dispersion near coal tailings," *Science of the Total Environment*, vol. 788, article 147851, 2021.

[29] S. Pandey, E. Fosso-Kankeu, M. J. Spiro et al., "Equilibrium, kinetic, and thermodynamic studies of lead ion adsorption from mine wastewater onto $MoS_2$-clinoptilolite composite," *Materials Today Chemistry*, vol. 18, article 100376, 2020.

[30] S. Pandey, J. Y. Do, J. Kim, and M. Kang, "Fast and highly efficient removal of dye from aqueous solution using natural locust bean gum based hydrogels as adsorbent," *International Journal of Biological Macromolecules*, vol. 143, pp. 60–75, 2020.

[31] H. Brandl, R. Bosshard, and M. Wegmann, "Computer-munching microbes: metal leaching from electronic scrap by bacteria and fungi," *Hydrometallurgy*, vol. 59, no. 2-3, pp. 319–326, 2001.

[32] A. Deepatana, J. Tang, and M. Valix, "Comparative study of chelating ion exchange resins for metal recovery from bioleaching of nickel laterite ores," *Minerals Engineering*, vol. 19, no. 12, pp. 1280–1289, 2006.

[33] J. Gao, F. Liu, P. Ling et al., "High efficient removal of Cu(II) by a chelating resin from strong acidic solutions: Complex formation and DFT certification," *Chemical Engineering Journal*, vol. 222, pp. 240–247, 2013.

[34] K. Koyama, M. Tanaka, and J.-C. Lee, "Copper leaching behavior from waste printed circuit board in ammoniacal alkaline solution," *Materials Transactions*, vol. 47, no. 7, pp. 1788–1792, 2006.

[35] F. P. Silvas, M. M. Jiménez Correa, M. P. K. Caldas, V. T. de Moraes, D. C. R. Espinosa, and J. A. S. Tenório, "Printed circuit board recycling: physical processing and copper extraction by selective leaching," *Waste Management*, vol. 46, pp. 503–510, 2015.

[36] C. N. Haas and V. Tare, "Application of ion exchangers to recovery of metals from semiconductor wastes," *Reactive Polymers, Ion Exchangers, Sorbents*, vol. 2, no. 1-2, pp. 61–70, 1984.

[37] L.-C. Lin and R.-S. Juang, "Ion-exchange kinetics of Cu(II) and Zn(II) from aqueous solutions with two chelating resins," *Chemical Engineering Journal*, vol. 132, no. 1-3, pp. 205–213, 2007.

[38] M. Franz, "Phosphate fertilizer from sewage sludge ash (SSA)," *Waste Management*, vol. 28, no. 10, pp. 1809–1818, 2008.

[39] B. Esma, A. Omar, and D. M. Amine, "Comparative study on lanthanum (III) sorption onto Lewatit TP 207 and Lewatit TP 260," *Journal of Radioanalytical and Nuclear Chemistry*, vol. 299, no. 1, pp. 439–446, 2014.

[40] P. Georgiev, S. Groudev, I. Spasova, M. Nicolova, K. Mihaylova, and D. Karamfilov, "Desorption of copper from loaded ion-exchange resin Lewatit as a stage of processing of rich-in-copper bioleaching solutions," vol. 57, 2014.

[41] D. Kołodyńska, Z. Hubicki, and M. Geca, "Application of a new-generation complexing agent in removal of heavy metal ions from aqueous solutions," *Industrial & Engineering Chemistry Research*, vol. 47, no. 9, pp. 3192–3199, 2008.

[42] A. Wołowicz and M. Wawrzkiewicz, "Screening of ion exchange resins for hazardous Ni (II) removal from aqueous solutions: kinetic and equilibrium batch adsorption method," *Processes*, vol. 9, no. 2, p. 285, 2021.

[43] S. Kurkinen, S. Virolainen, and T. Sainio, "Recovery of rare earth elements from phosphogypsum waste in resin-in-leach process by eluting with biodegradable complexing agents," *Hydrometallurgy*, vol. 201, article 105569, 2021.

[44] M. R. Lutfor, S. Sidik, W. M. Z. Wan Yunus, M. Z. A. Rahman, A. Mansor, and M. J. Haron, "Synthesis and characterization of poly(hydroxamic acid) chelating resin from poly(methyl acrylate)-grafted sago starch," *Journal of Applied Polymer Science*, vol. 79, no. 7, pp. 1256–1264, 2001.

[45] N. D. Lane, S. Bhattacharya, P. Georgiev et al., "Deepx: a software accelerator for low-power deep learning inference on mobile devices," in *2016 15th ACM/IEEE International Conference on Information Processing in Sensor Networks (IPSN)*, pp. 1–12, Vienna, Austria, 2016.

[46] N. Ul Afsar, X. Ge, Z. Zhao et al., "Zwitterion membranes for selective cation separation via electrodialysis," *Separation and Purification Technology*, vol. 254, article 117619, 2021.

[47] R. P. Dhakal, K. N. Ghimire, and K. Inoue, "Adsorptive separation of heavy metals from an aquatic environment using orange waste," *Hydrometallurgy*, vol. 79, no. 3-4, pp. 182–190, 2005.

[48] C. Ji, D. Wu, J. Lu et al., "Temperature regulated adsorption and desorption of heavy metals to A-MIL-121: mechanisms and the role of exchangeable protons," *Water Research*, vol. 189, article 116599, 2021.

[49] S. Wongcharee, V. Aravinthan, and L. Erdei, "Mesoporous activated carbon-zeolite composite prepared from waste macadamia nut shell and synthetic faujasite," *Chinese Journal of Chemical Engineering*, vol. 27, no. 1, pp. 226–236, 2019.

[50] S. Wongcharee, V. Aravinthan, L. Erdei, and W. Sanongraj, "Mesoporous activated carbon prepared from macadamia nut shell waste by carbon dioxide activation: comparative characterisation and study of methylene blue removal from aqueous solution," *Asia-Pacific Journal of Chemical Engineering*, vol. 13, no. 2, article e2179, 2018.

[51] P. Myers, "How chelating resins behave," *Plating and Surface Finishing*, vol. 85, no. 10, pp. 22–29, 1998.

[52] A. Kilislioglu, *Ion Exchange Technologies*, BoD–Books on Demand, 2012.

[53] M. Chlupáčová, H. Parschová, and P. Kůs, "Sorption of heavy metals from aqueous solutions using different types of sorbents," in *Environmental Technology and Innovations: Proceedings of the 1st International Conference on Environmental Technology and Innovations (Ho Chi Minh City, Vietnam*, pp. 77–82, Ho Chi Minh City, Vietnam, November 2016.

[54] D. Kołodyńska, D. Fila, and Z. Hubicki, "Static and dynamic studies of lanthanum(III) ion adsorption/desorption from acidic solutions using chelating ion exchangers with different functionalities," *Environmental Research*, vol. 191, article 110171, 2020.

[55] M. D. Ogden, E. M. Moon, A. Wilson, and S. E. Pepper, "Application of chelating weak base resin Dowex M4195 to the recovery of uranium from mixed sulfate/chloride media," *Chemical Engineering Journal*, vol. 317, pp. 80–89, 2017.

[56] T. J. Robshaw, S. M. Griffiths, A. Canner et al., "Insights into the interaction of iodide and iodine with Cu(II)-loaded bispicolylamine chelating resin and applications for nuclear waste treatment," *Chemical Engineering Journal*, vol. 390, article 124647, 2020.

[57] F. Mendes and A. Martins, "Selective sorption of nickel and cobalt from sulphate solutions using chelating resins," *International Journal of Mineral Processing*, vol. 74, no. 1-4, pp. 359–371, 2004.

[58] S. S. F. Carvalho, A. C. C. Rodrigues, J. F. Lima, and N. M. F. Carvalho, "Photocatalytic degradation of dyes by mononuclear copper(II) complexes from bis-(2-pyridylmethyl)amine NNN-derivative ligands," *Inorganica Chimica Acta*, vol. 512, article 119924, 2020.

[59] C. V. Diniz, V. S. Ciminelli, and F. M. Doyle, "The use of the chelating resin Dowex M-4195 in the adsorption of selected heavy metal ions from manganese solutions," *Hydrometallurgy*, vol. 78, no. 3-4, pp. 147–155, 2005.

Hindawi
Adsorption Science & Technology
Volume 2021, Article ID 7694783, 13 pages
https://doi.org/10.1155/2021/7694783

*Research Article*

# Anionic Dye Removal by Polypyrrole-Modified Red Mud and Its Application to a Lab-Scale Column: Adsorption Performance and Phytotoxicity Assessment

**Feng Zhang,[1] Yue Yin,[1] Chunlei Qiao,[1] Ya-nan Luan,[1] Mengyan Guo,[1] Yihua Xiao,[1] and Changqing Liu[1,2]**

[1]*School of Environmental and Municipal Engineering, Qingdao University of Technology, Qingdao 266033, China*
[2]*Qingdao Research Center of Urban Water Environmental Pollution Control, Qingdao 266033, China*

Correspondence should be addressed to Changqing Liu; lcqlfyqut@126.com

Feng Zhang and Yue Yin contributed equally to this work.

Received 8 August 2021; Revised 27 September 2021; Accepted 4 October 2021; Published 1 November 2021

Academic Editor: Hesham Hamad



In this study, polypyrrole-modified red mud (PRM) was prepared for the efficient removal of anionic dyes (methyl orange and Congo red) from aqueous solutions. The phytotoxicity (bean sprouts) of the dye solution before and after dye removal was investigated. Adsorption kinetics confirmed that the adsorption of methyl orange (MO) and Congo red (CR) on PRM was controlled by chemical reactions between the functional groups of polypyrrole and dyes. From Langmuir isotherm fitting, we found the theoretical adsorption capacities of MO and CR on PRM were 194.1 and 314.9 mg/g, respectively. The adsorption progress of MO and CR on PRM was found to be spontaneous and endothermic. The column studies demonstrated that, under dynamic flow, the PRM can efficiently remove MO and CR from aqueous solution, with adsorption capacities of 31.08 and 55.04 mg/g, respectively. In the toxicity test, the phytotoxicity of the column effluents (after dye removal) was significantly lowered compared to the initial dye influents. After the removal of MO and CR, the average root length of bean sprouts was increased from 3.30 cm to 5.18 cm and from 3.01 cm to 7.00 cm, respectively. These findings highlighted the efficient removal of dyes by PRM from aqueous solution, demonstrating the possible application of PRM for the removal of dye from dye-contaminated wastewaters.

## 1. Introduction

Different types of contaminations in water bodies pose great threat to the environment and society [1, 2]. Among these contaminations, organic dyes are highly noteworthy because over 40,000 types of organic dyes are fabricated and widely used in a lot of industrial including textile, paper, and leather [3]. Due to inappropriate treatment process, large amount of dyes together with industrial wastewater are discharged into natural water bodies [4, 5]. The presence of dyes in the aqueous solutions poses a huge threat to the environmental livings because they have been confirmed to be carcinogenicity, genotoxicity, and neurotoxicity [6, 7]. Among these dyes, there are more than 7,000 different synthetic chemical molecules involved which are nonbiodegradable under environmental conditions [7, 8]. Hence, the sufficient removal of organic dyes before discharging into water bodies is of great significance to environmental safety.

Recently, different technologies have been investigated for the treatment of dye-contaminated wastewater including, coagulation, chemical oxidation, photocatalysis, and adsorption [9–12]. Among these technologies, adsorption progress has been confirmed to be a reliable and effective solution for dye removal from aqueous solutions [13, 14]. The removal of Congo red (CR) by using N,N-dimethyl dehydroabietylamine oxide-modified zeolites was investigated by Liu et al., and they found that the adsorption capacity of CR on modified zeolites was 69.9 mg/g [6]. Zhang et al. studied the dye adsorption capacity by g-C3N4/graphene oxide-wrapped sponge monoliths [15]. Most of these studies showed

Table 1: Characteristics and structures of methyl orange and Congo red.

| Generic name | Abbreviation | $\lambda_{max}$ (nm) | Molecular weight (g/mol) | Molecular formula |
|---|---|---|---|---|
| Methyl orange | MO | 497 | 327.33 | 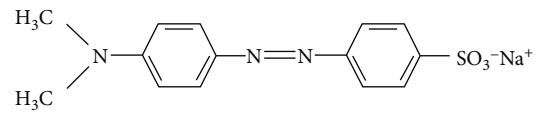 |
| Congo red | CR | 464 | 696.68 | 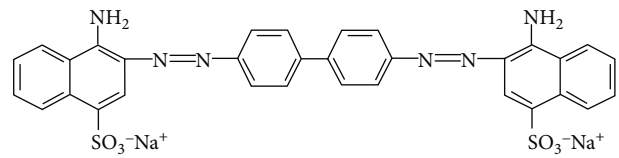 |

promising dye adsorption performance; however, few have calculated the potential cost of the fabricated adsorbents. With expensive raw materials used (such as precious metals), the cost of these adsorbents is not acceptable under real conditions. Hence, it is crucial for researchers to find affordable alternatives for the removal of dye from dye-contaminated wastewaters.

Red mud (RM), which is a by-product of aluminum industry, has been recognized as a hazardous waste due to its difficulty of disposal and large volumes [16]. The inappropriate placements of RM have caused several severe accidents in China and around the world. However, recent researches proposed that the red mud could be used as raw material of adsorbent due to its high content of iron and aluminum; this could transfer the "wastes" into "resources" and reduce the cost of raw materials. Successful fabrications of red mud-based adsorbents have been developed for the removal of fluoride [17], arsenic [18], antibiotics [19, 20], phosphate [21], and dyes [22].

In this manuscript, we report a detailed application of polypyrrole-modified red mud (PRM) as adsorbent for the removal of anionic dyes: methyl orange (MO) and CR. The morphology features of PRM were characterized by scanning electron microscopy (SEM), Fourier transform infrared spectroscopy (FT-IR), and energy-dispersive X-ray spectroscopy (EDS). The effects of initial pH, dye concentration, adsorbent dosage, adsorption time, and adsorption temperature were investigated through batch studies. A continuous-flow column study was designed and operated to investigate the adsorption performance of both dyes onto PRM under dynamic condition. Furthermore, the phytotoxicity of the column effluents was assessed. The objectives of this study are to (i) investigate the adsorption performance of MO and CR onto PRM in batch and column studies, (ii) elucidate the proper mechanisms by model fittings and adsorbent characteristics, and (iii) characterize the dye detoxication ability of PRM. The research provided a useful reference for future researches in dye adsorbent fabrications and application evaluations.

## 2. Materials and Methods

*2.1. Materials.* Methyl orange and Congo red are purchased from Ourchem Co., Ltd (Shanghai, China). The characteristics and structure of these two dyes are listed in Table 1. Other used chemicals are purchased from Sinopharm Chemical Reagent Co., Ltd, China, including ferric sulfate, HCl, NaOH, pyrrole, and methyl alcohol. All the used chemicals are of analytical grade and without further purification. Deionized water is used in all experiments. Red mud is collected from an alumina industry in Shandong province. Orion Star$^{TM}$ A211 (Thermo Fisher) is used in this study for pH adjustment.

*2.2. Preparation of PRM Adsorbents.* The PRM adsorbents are prepared using optimized procedures based on early studies [23, 24]. First, pyrrole solution is prepared using 0.6 mL pyrrole diluted into 100 mL with deionized water. Then, 2.5 red mud is added into 30 mL pyrrole solution and mixed in a rotator mixer for 1 h. After 1 hour of complete mixing, 1.25 g ferric sulfate is added into the solution. Finally, the red mud is rinsed with methyl alcohol and deionized water for several times until the supernatant reaches neutral and dried in an oven; the obtained PRM is collected in a desiccator for future use.

*2.3. Adsorption Experiments.* Batch and column studies are conducted to investigate the adsorption performance of both dyes onto PRM under static and dynamic conditions. 1000 mg/L of MO and CR stock solutions are prepared and stored in the refrigerator. The dye solutions of 10-100 mg/L are prepared by dilution of stock solutions. The pH of the dyes is adjusted by adding 0.1 M HCl or 0.1 M NaOH.

For static experiments, certain amount of PRM is added to 100 mL conical flasks with 50 mL of dye solutions. The flasks are sealed with parafilm and placed in a thermostatic orbital shaker with a shaking speed of 120 rpm (temperature is maintained constant). The concentrations of dyes are determined by a UV-Vis spectroscopy at 497 nm for MO and 464 nm for CR (DR2800, HACHI). All experiments are conducted in duplicates, and the data are average. The adsorption capacity $q_e$ of PRM and removal rate $R$ are calculated as follows:

$$q_e = \frac{(C_0 - C_e)}{a}, \quad (1)$$

$$R = \frac{(C_0 - C_e)}{C_0} \times 100\%, \quad (2)$$

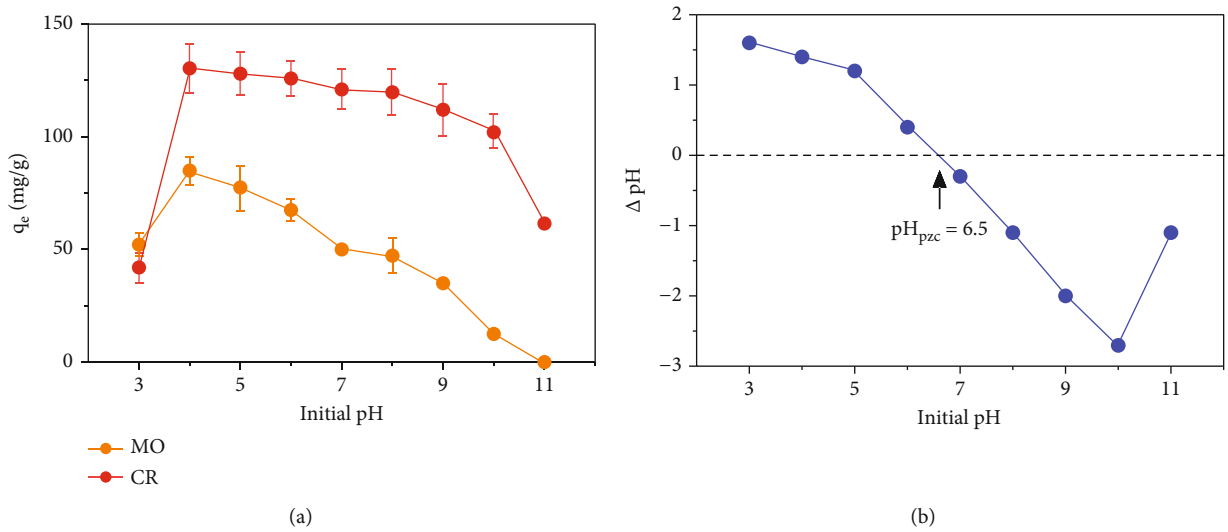


Figure 1: (a) Effect of initial pH on MO and CR adsorption; (b) $pH_{pzc}$ of the adsorbent (experiment conditions: initial concentration = 100 mg/L and dosage = 0.5 g/L).

where $C_0$ and $C_e$ are the dye concentration at initial stage and equilibrium stage (mg/L) and $a$ (g/L) is the dosage of PRM.

For dynamic experiments, a laboratory-scale column (bed volume ~ 5.5 mL) is used (Fig. S1). The concentration of feed solutions is maintained at 50 mg/L for both dyes, and the effluents are collected and determined. The phytotoxicity assessment of the effluents is conducted using the methods proposed by Patra et al. [25]. Specifically, bean sprout beads are selected as the indicator of phytotoxicity assessment. The dried beads are initially washed with 1% sodium hypochlorite and deionized water and then air-dried under room temperature. After that, the beads are planted on cotton soaked with solution (deionized water and dye solution with or without adsorption treatment) and allowed to germinate under dark conditions for 4 days. All experiments were conducted by triplicates, and the relative standard deviations were below 8%.

*2.4. Adsorption Models.* To better interpret the adsorption mechanism during the adsorption progress, several adsorption models are fitted in this research. Pseudo-first-order (Equation (3)), pseudo-second-order (Equation (4)), and intraparticle diffusion (Equation (5)) are three classical kinetic models to reveal the adsorption progress, and $h$ is the related initial adsorption rate. The equations are listed as follows:

$$\ln(q_e - q_t) = \ln q_e - K_1 t, \tag{3}$$

$$\frac{t}{q_t} = \frac{1}{K_2 q_e^2} + \frac{t}{q_e}, \tag{4}$$

$$q_t = K_d t^{1/2} + C, \tag{5}$$

$$h = q_e^2 K_2, \tag{6}$$

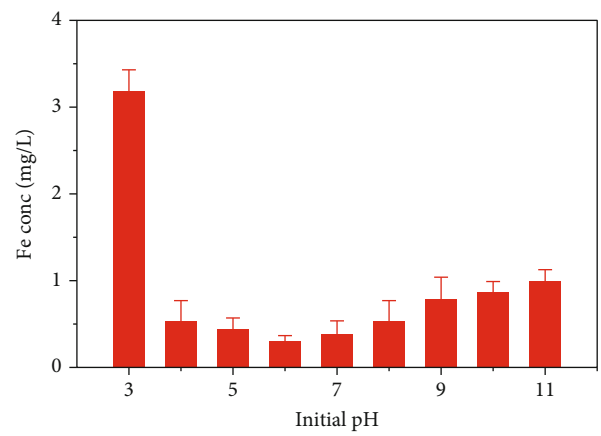


Figure 2: Effect of initial pH on dissolved Fe concentration (experiment condition: dosage = 1 g/L).

where $q_e$ and $q_t$ are the adsorption capacity of the PRM at equilibrium and at different times (mg/g). $t$ (min) is the adsorption time. $K_1$ ($min^{-1}$), $K_2$ (g/mg/min), and $K_d$ ($mg/g/min^{1/2}$) are the kinetic rate constants.

Adsorption isotherms for both dyes onto PRM are fitted using Langmuir model (Equation (7)), Freundlich model (Equation (8)), and Temkin mode (Equation (9)). The equations are listed as follows:

$$q_e = \frac{q_m K_L C_e}{1 + K_L C_e}, \tag{7}$$

$$q_e = K_F C_e^{1/n}, \tag{8}$$

$$q_e = K_T \ln(f C_e), \tag{9}$$

where $q_m$ (mg/g) is the theoretical maximum adsorption capacity of PRM; $K_L$ (L/mg), $K_F$ (mg/g), and $K_T$ (J/mol) are the constants of Langmuir, Freundlich, and Temkin

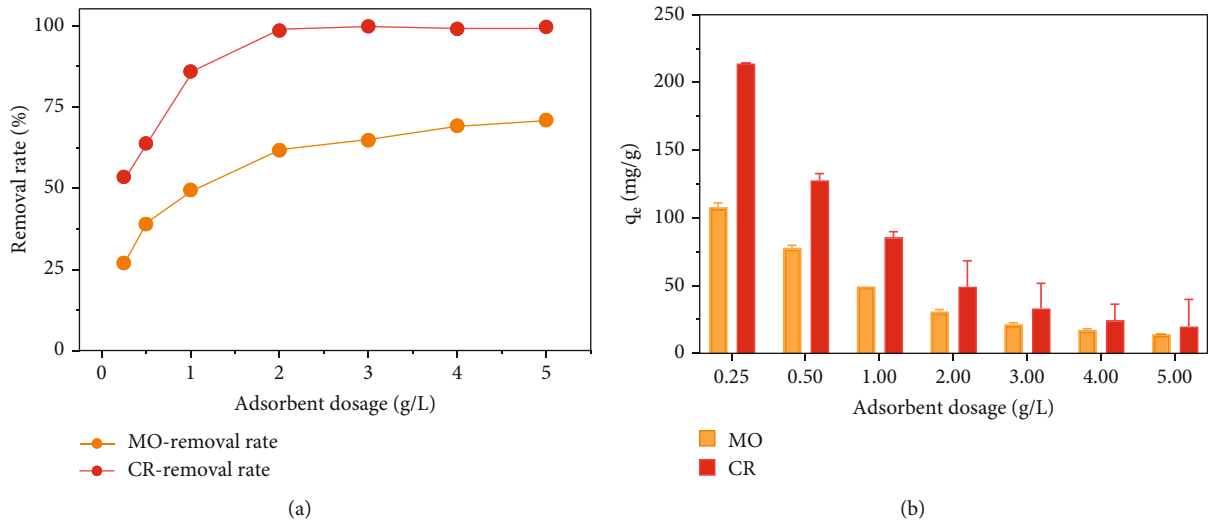


Figure 3: (a) Effect of adsorbent dosage on MO and CR removal; (b) dye adsorption capacity at different adsorbent dosages (experiment conditions: initial concentration = 100 mg/L, pH = 4).

isotherms. $n$ represents the adsorption intensity, and $f$ (L/mg) is the Temkin binding energy.

For further evaluation of the adsorption progress, dimensionless factor $R_L$ derived from Langmuir isotherm is calculated. This constant represents whether the progress is favorable or unfavorable. If $0 < R_L < 1$, the adsorption progress is favorable; otherwise, it will be unfavorable.

$$R_L = \frac{1}{1 + K_L C_0}. \tag{10}$$

Temperature is a vital parameter in adsorption progress; the effects of different operating temperatures (288.15 K, 298.15 K, and 308.15 K) are investigated in this research. The adsorption thermodynamic is revealed by the widely used Van't Hoff equation as follows [26]:

$$\Delta G^0 = -RT \ln \frac{q_e}{C_e}, \tag{11}$$

$$\Delta G^0 = \Delta H^0 - T\Delta S^0, \tag{12}$$

where $\Delta G^0$ is the free energy change (kJ/mol), $R$ is the ideal gas constant (kJ/mol/K), and $T$ is the solution temperature (K). $\Delta H^0$ (kJ/mol) and $\Delta S^0$ (kJ/mol/K) are referred to standard enthalpy and standard entropy.

In order to predict and evaluate the adsorption performance in column studies, the Thomas model is used in this research. The Thomas model assumes that the adsorption progress by mass transfer processes at the interphase species which can be expressed as follows [27, 28]:

$$C(t) = \frac{C_0}{1 + \exp\left(k_{th} q_{th} m/Q - k_{th} C_0 t\right)}, \tag{13}$$

where $k_{th}$ (mL/mg/min) and $q_{th}$ (mg/g) are the rate constant and theoretical maximum adsorption capacity of the Thomas model, $m$ (g) is the adsorbent dosage, and $Q$ (mL/min) is the flow velocity of influents.

*2.5. Adsorbent Characterization.* The surface morphology was determined by SEM (SU8010, Hitachi, Japan). The EDS was detected by ZEISS SEM (Gemini 300, Germany). FT-IR spectrophotometer (Thermo Fisher, USA) was used to analyze the functional groups of the adsorbents.

## 3. Results and Discussion

*3.1. Characterization of PRM.* SEM images and FT-IR spectrum of raw red mud and PRM are given in Fig. S2&3. The polypyrrole modification improved the roughness of the adsorbent surface, with increased granular-like morphology occurred on the surface of PRM. In FT-IR spectrum, the pyrrole monomer ring at antisymmetric and symmetric stretching vibrations was observed around 1540 and 1460 $cm^{-1}$ [29]. Moreover, the band at 880 and 680 $cm^{-1}$ was related to C-H and N-H bending vibrations. These results confirm the successful modification of polypyrrole onto the red mud. The SEM images and EDS of PRM after adsorption of MO and CR are shown in Fig. S4 and Fig. S5. The increase of S element in EDS confirmed the successful adsorption of MO and CR. After adsorption, the surface of PRM turned to a uniform and smooth surface without evident pores. Thus, in compliance with EDS results, it can be confirmed that both dyes are adsorbed onto the surface PRM.

*3.2. Effect of Initial pH and Dosage.* Before investigating the adsorption performance of MO and CR onto PRM, the effect of initial solution pH and adsorbent dosage should be thoroughly assessed due to their significant influence on adsorption progress [30]. The effect of initial solution pH on MO and CR adsorption is studied in the pH range from 3 to 11. In order to better understand the effect of initial solution pH on adsorbent itself, the point of zero charge ($pH_{pzc}$) of

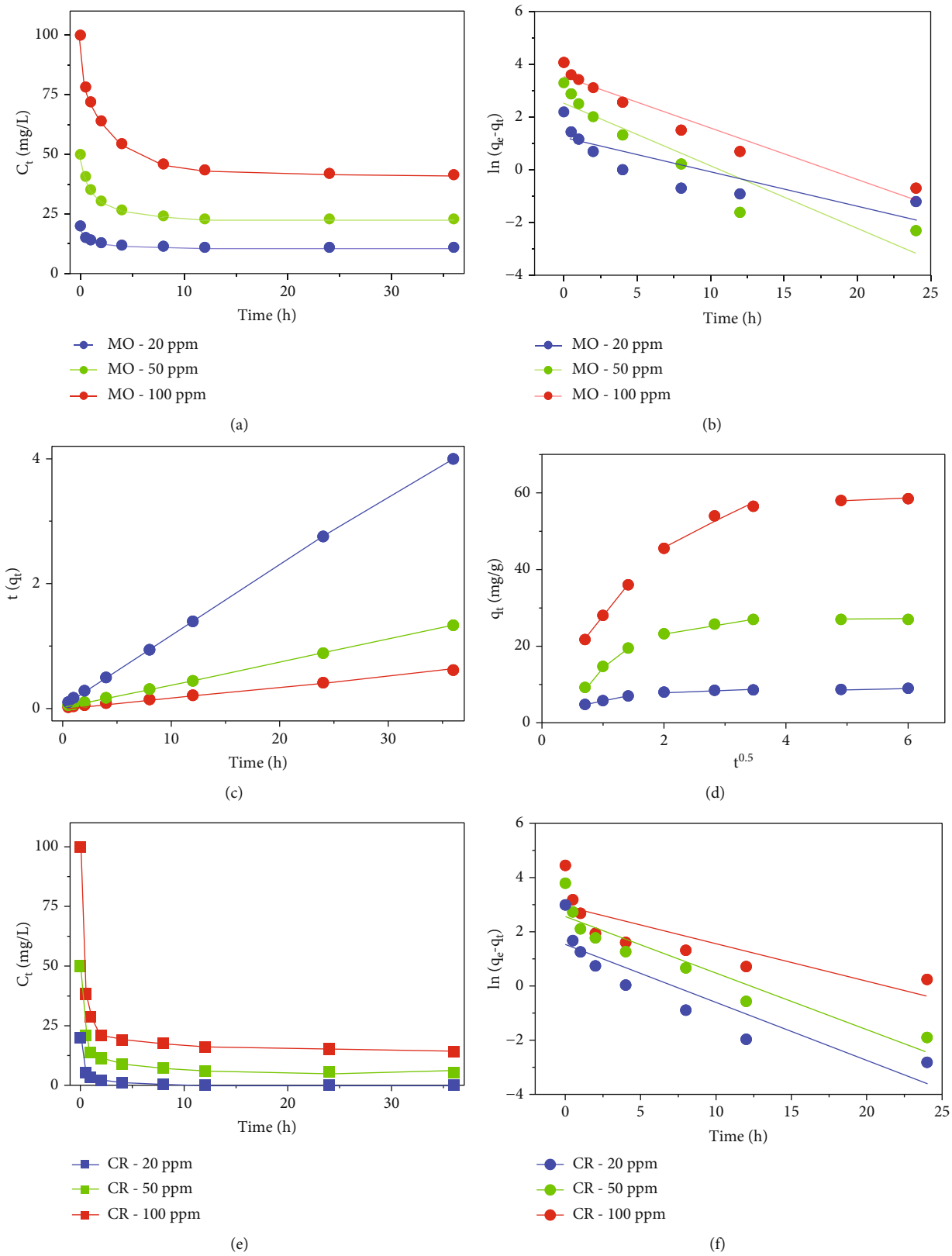


Figure 4: Continued.

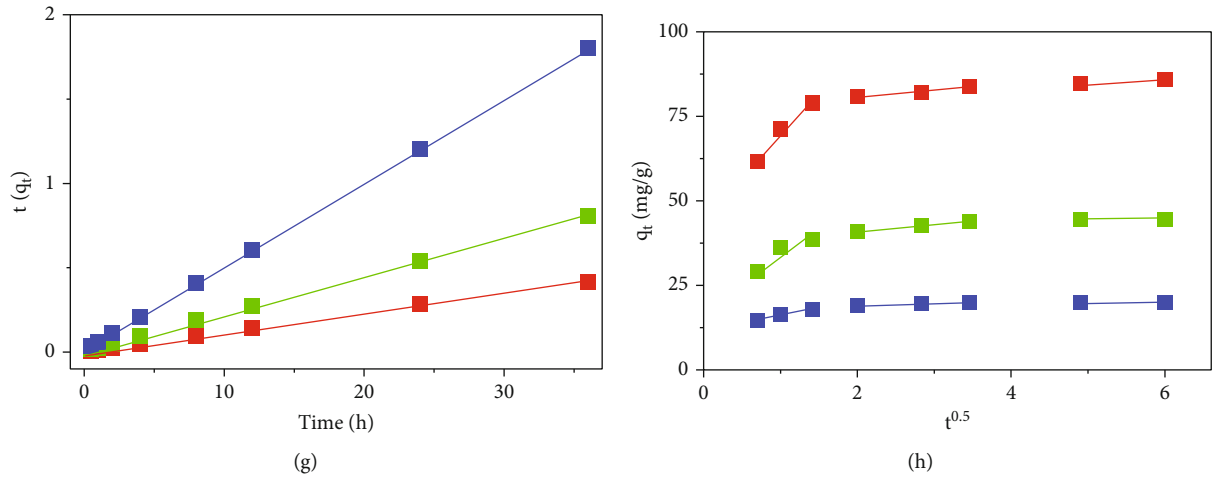


Figure 4: Effect of time on (a, d) MO and CR adsorption, (b, f) pseudo-first-order, (c, g) pseudo-second-order, and (d, h) intraparticle diffusion model fitting of MO and CR (experiment conditions: adsorbent dosage = 1 g/L, pH = 4).

Table 2: Kinetic parameters of pseudo-first-order and pseudo-second-order.

| | $C_0$ (mg/L) | $q_e$ (mg/g) | Pseudo-first-order constant | | | Pseudo-second-order constant | | | |
|---|---|---|---|---|---|---|---|---|---|
| | | | $q_e$ (mg/g) | $k_1$ (min$^{-1}$) | $R^2$ | $q_e$ (mg/g) | $k_2$ (g/mg/min) | $h$ (mg/g/min) | $R^2$ |
| MO | 20 | 9.10 | 2.39 | 0.0903 | 0.86 | 9.07 | 0.1916 | 15.76 | 0.99 |
| | 50 | 27.10 | 6.89 | 0.1518 | 0.73 | 27.78 | 0.0471 | 36.35 | 0.99 |
| | 100 | 58.50 | 26.95 | 0.1621 | 0.97 | 60.61 | 0.0150 | 55.10 | 0.99 |
| CR | 20 | 20.00 | 2.71 | 0.1632 | 0.93 | 20.12 | 0.2287 | 92.58 | 0.99 |
| | 50 | 44.60 | 8.57 | 0.1636 | 0.96 | 45.05 | 0.0694 | 140.85 | 0.99 |
| | 100 | 86.00 | 15.85 | 0.1638 | 0.90 | 86.21 | 0.0434 | 322.56 | 0.99 |

the PRM is also investigated. As shown in Figure 1(a), the adsorption capacities of MO and CR share the same trend, and both achieve highest adsorption capacity at pH = 4 and decrease with the increase of pH. These results are in accordance with previous researcher that highest adsorption capacity was achieved at pH of 2 [25]. At beginning, the adsorption seems to be deteriorated (pH = 3); this is due to the decomposition of the PRM under extremely acid conditions [31]. The effect of initial pH on the solution iron concentration is displayed in Figure 2. Under pH = 3, the Fe concentration exceeds 3 mg/L while it remained below 1 mg/L under other pH condition. This suggests that the extremely acid condition may lead to a potential decomposition of PRM; hence, future experiments are conducted above pH of 4. The $pH_{pzc}$ of PRM is around 6.5, which means that the surface of PRM is negatively charged at solution pH > 6.5 and has a positively charged surface when pH is lower than 6.5. As previously mentioned, both dyes are typical anionic species which means that the positively charged surface is beneficial to the adsorption progress due to the electrostatic attraction between positively charged surface and negatively charged dyes [32]. The molecular formula of MO and CR is given in Table 1; both contain sulphonic acid groups ($R\text{-}SO_3Na$) and turn into sulphonate groups ($R\text{-}SO_3^-$) at lower pH conditions. This is in accordance with the results in Figure 1(a) while lower pH results in higher adsorption capacity of both dyes. Therefore, the following experiments are conducted at an initial solution pH of 4 to achieve the highest adsorption capacity and prevent decomposition of PRM.

The proper adsorbent dosage is considered to be an important influencing factor in the adsorption progress, since it could change the equilibrium system between adsorbent and adsorbate [33]. The influence of adsorbent dosage is carried out with dosage ranging from 0.25 to 5 g/L, at initial solution pH of 4 and initial dye concentration of 100 mg/L for both MO and CR. As illustrated in Figure 3(a), the removal rates of MO and CR increase with dosage ranging from 0.25 to 3 g/L and reach equilibrium above 3 g/L. With the dosage amount increase from 0.25 g/L, the vacant active sites increased significantly which leads to a higher dye removal rate. Under dosage of 3 g/L, CR is removed 100% in the solutions and further increase in adsorbent dosage is unnecessary. However, after dosage of 3 g/L, the removal rate of MO reaches equilibrium of around 70% with no significant signs of continuously increase. This could be due to the interaction behavior between adsorbents when the dosage increases to a certain level, the active sites might be interfered. The adsorption capacity under different absorbent dosage is given in Figure 3(b). It is obvious that higher dosage leads to lower adsorption capacity; hence, in consideration of the removal rate and adsorption capacity, the dosage of 1 g/L is chosen in following experiments.

Table 3: Kinetics parameters of intraparticle diffusion model.

| | $C_0$ (mg/L) | Intra-particle diffusion $K_{d1}$ (mg/g/min$^{1/2}$) | $R^2$ | $K_{d2}$ (mg/g/min$^{1/2}$) | $R^2$ | $K_{d3}$ (mg/g/min$^{1/2}$) | $R^2$ |
|---|---|---|---|---|---|---|---|
| | 20 | 3.10 | 0.99 | 0.42 | 0.92 | 0.27 | 1.00 |
| MO | 50 | 14.29 | 0.98 | 2.58 | 0.99 | 0.54 | 1.00 |
| | 100 | 20.10 | 0.99 | 7.65 | 0.95 | 0.45 | 1.00 |
| | 20 | 4.51 | 0.97 | 0.62 | 0.98 | 0.05 | 1.00 |
| CR | 50 | 12.89 | 0.86 | 2.04 | 0.99 | 0.14 | 1.00 |
| | 100 | 24.06 | 0.97 | 2.00 | 0.98 | 1.16 | 1.00 |

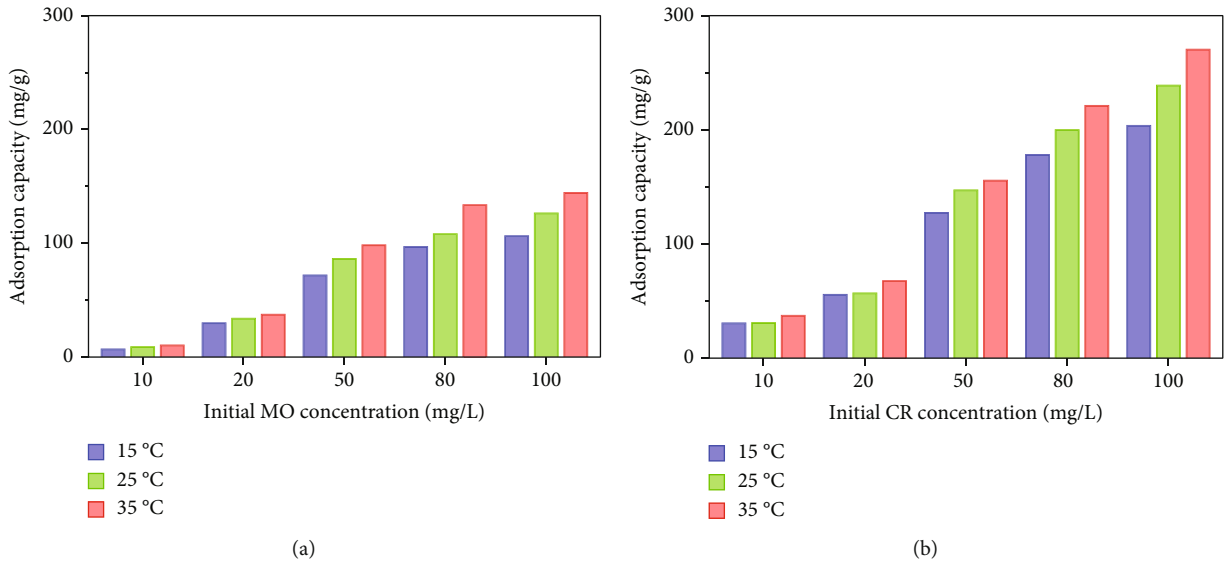


Figure 5: Effect of initial MO and CR concentration on PRM adsorption capacity (experiment conditions: adsorbent dosage = 0.5 g/L, pH = 4).

*3.3. Adsorption Kinetics.* The adsorption kinetics are of great significance to evaluating the adsorption efficiency and progress of MO and CR onto PRM during the adsorption [34]. Time-dependent adsorption experiments were carried out with different initial dye concentrations (20, 50, and 100 mg/L). As shown in Figures 4(a) and 4(d), the remaining concentrations of MO and CR are recorded at different time intervals in 36 h. Obviously, the adsorption reactions show rapid adsorption rates at initial stage and stabilized afterwards [35]. At initial concentration of 20, 50, and 100 mg/L, the equilibrium MO concentration decreased to 11.0, 23.0, and 41.5 mg/L. However, the adsorption of CR is more effective, with equilibrium concentrations plunge to 0.0, 5.5, and 14.0 mg/L. The possible mechanism is that MO and CR have different molecular weights (MW), with the MW of CR reaches 696.7 g/mol which is twice that of MO. Hence, the adsorption capacities for MO and CR are comparable in terms of adsorbed molecules (mM/g).

The fitting parameters of pseudo-first-order, pseudo-second-order, and intraparticle diffusion model are summarized in Tables 2 and 3. For pseudo-first-order model, the calculated $q_e$ value is significantly different from the experimental value, and the correlation coefficients ($R^2$) are not satisfying in both MO and CR data. By contrast, the calculated $q_e$ value in pseudo-second-order model is nearly close to the experimental value and each $R^2$ value is above 0.99 for different initial concentration of MO and CR (Figures 4(b) and 4(e)). Hence, it can be concluded that the dye adsorption progress is controlled by chemical reactions, and the rate $k_2$ and $h$ could be used to describe the removal rates of MO and CR [36]. The removal kinetics of MO are clearly slower than CR, and the $k_2$ value in pseudo-second-order of CR adsorption is higher than MO in every initial dye concentration. More importantly, the initial adsorption rate $h$ of CR adsorption is significantly higher (i.e., with at least three times higher). After 1 hour adsorption of 100 mg/L dyes by PRM, the CR concentration is lowered to 28.7 mg/L while the MO concentration remains at 72.0 mg/L. This confirms the rapid removal capacity of CR by PRM adsorbent.

The fitting of intraparticle diffusion model is shown in Table 3. The adsorption progress of dyes onto PRM can be divided into three stages; the first stage of fitted MO adsorption lines almost passes the origin while CR adsorption fitted lines could not pass, suggesting that the intraparticle diffusion plays a dominant role in MO adsorption onto PRM (likely the rate-limiting step) [8, 37]. For CR adsorption onto PRM, the adsorption progress could be jointly controlled by external mass transfer and intraparticle diffusion.

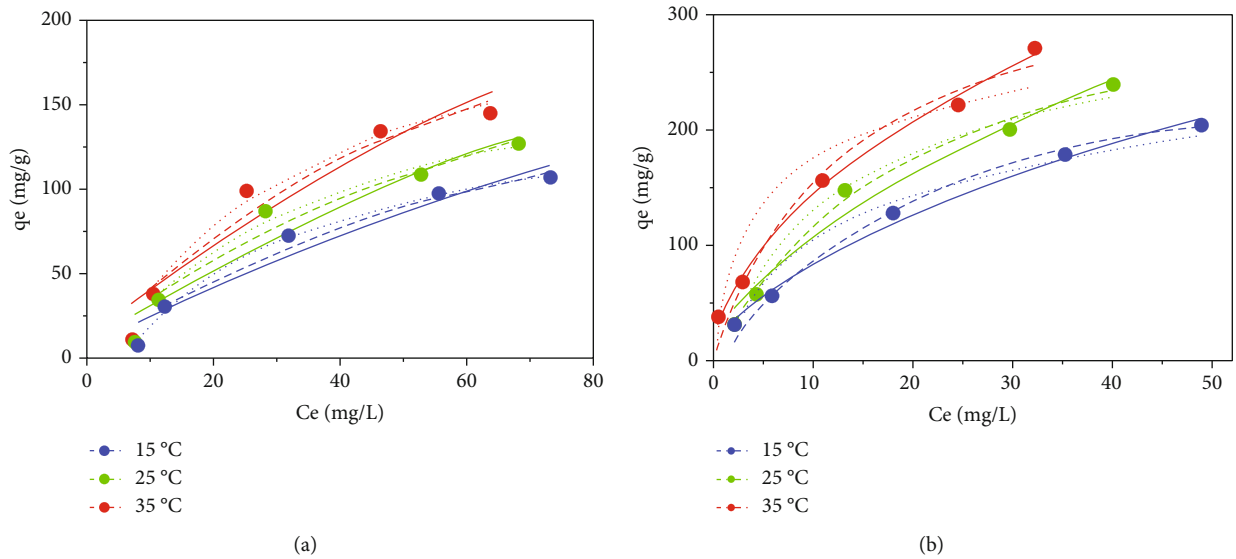


Figure 6: Isotherm fittings of (a) MO adsorption and (b) CR adsorption onto PRM (Langmuir isotherm: dash line, Freundlich isotherm: connecting line, and Temkin isotherm: dotted line) (experiment conditions: adsorbent dosage = 0.5 g/L, pH = 4).

Table 4: Kinetics parameters of Langmuir, Freundlich, and Temkin models.

| | $T$ (°C) | Langmuir constant | | | | Freundlich constant | | | Temkin constant | | |
|---|---|---|---|---|---|---|---|---|---|---|---|
| | | $q_{max}$ (mg/g) | $k_L$ (L/mg) | $R_L$ | $R^2$ | $K_F$ (mg/g) | $n$ | $R^2$ | $K_T$ (J/mol) | $f$ (L/mg) | $R^2$ |
| | 15 | 194.1 | 0.017 | 0.37 | 0.99 | 7.80 | 1.61 | 0.97 | 45.16 | 0.15 | 0.99 |
| MO | 25 | 223.9 | 0.019 | 0.34 | 0.98 | 9.44 | 1.60 | 0.96 | 52.15 | 0.17 | 0.99 |
| | 35 | 256.9 | 0.022 | 0.31 | 0.98 | 12.35 | 1.65 | 0.94 | 62.88 | 0.17 | 0.99 |
| | 15 | 314.9 | 0.038 | 0.21 | 0.99 | 24.31 | 1.81 | 0.99 | 56.77 | 0.63 | 0.97 |
| CR | 25 | 350.2 | 0.051 | 0.16 | 0.99 | 32.03 | 1.83 | 0.97 | 70.92 | 0.63 | 0.98 |
| | 35 | 389.5 | 0.062 | 0.14 | 0.99 | 40.50 | 1.84 | 0.94 | 79.13 | 0.64 | 0.94 |

*3.4. Adsorption Isotherms.* The adsorption isotherms of MO and CR onto PRM were conducted using different initial dye concentrations (Figure 5). As well investigated before, the adsorption capacity of CR exceeds the adsorption capacity of MO. With the increase of initial dye concentration, the adsorption capacity of CR rises dramatically while the adsorption capacity of MO reaches plateau related to the saturation of PRM. The adsorption isotherm data fitted by Langmuir, Freundlich, and Temkin isotherm models are tabulated in Figure 6 and Table 4.

Based on the fitted $R^2$ value of Langmuir and Freundlich models, it is found that the Langmuir isotherm could better describe the adsorption of MO and CR onto PRM, which further proves that the adsorption of MO and CR is monolayer progress [38]. As shown in Table 4, based on the Langmuir isotherm model data, the maximum adsorption capacities are found to be 194.1, 223.9, and 256.9 mg/g for MO adsorption at 15, 25, and 35°C and 314.9, 350.2, and 389.5 mg/g for CR adsorption at 15, 25, and 35°C, respectively. This suggests that the adsorption progress of both dyes is endothermic reaction, and the increase of the environment temperature accelerates the adsorption progress. The separation factor ($R_L$) of the Langmuir model could reflect the adsorption progress: $R_L < 1$ favorable, $R_L > 1$ unfavorable, and $R_L = 1$ linear. As shown in Table 5, the fitted $R_L$ values are in range of 0.31-0.85 for MO adsorption and 0.14-0.72 for CR adsorption. All values are within 1, indicating the adsorption of both dyes onto PRM is favorable, effective, and reversible [39, 40]. Moreover, the fitted $R^2$ values of the Temkin model in MO and CR adsorption are relatively high, suggesting that there is a strong electrostatic interaction between MO, CR, and PRM which contributes to the adsorptive removal of both dyes [37, 41]. A detailed comparison table with other reported dye adsorbents is given in Table 6 and suggested the great

Table 5: $R_L$ values under different initial dye concentrations and temperatures.

| | $T$ (°C) | Initial concentration (mg/L) | | | | |
|---|---|---|---|---|---|---|
| | | 10 | 20 | 50 | 80 | 100 |
| | 15 | 0.85 | 0.76 | 0.54 | 0.42 | 0.37 |
| MO | 25 | 0.84 | 0.72 | 0.51 | 0.40 | 0.34 |
| | 35 | 0.82 | 0.69 | 0.48 | 0.36 | 0.31 |
| | 15 | 0.72 | 0.57 | 0.34 | 0.25 | 0.21 |
| CR | 25 | 0.66 | 0.50 | 0.28 | 0.20 | 0.16 |
| | 35 | 0.62 | 0.45 | 0.24 | 0.17 | 0.14 |

Table 6: Detailed adsorption performance of different reported adsorbents.

| Adsorbent | Dye | pH | $q_{max}$ (mg/g) | Reference |
|---|---|---|---|---|
| PRM | MO | 4 | 194.1 | This work |
| PRM | CR | 4 | 314.9 | This work |
| CABI nanogoethite | CR | 3 | 181.1 | [42] |
| ZnO NRs-AC | CR | 7 | 142 | [43] |
| $\gamma$-Fe2O3 | CR | 5.9 | 208.33 | [44] |
| 3D hierarchical PbS/ZnO microspheres | MO | 7 | 159 | [45] |
| Sugar scum powder | MO | 7.2 | 15.24 | [46] |

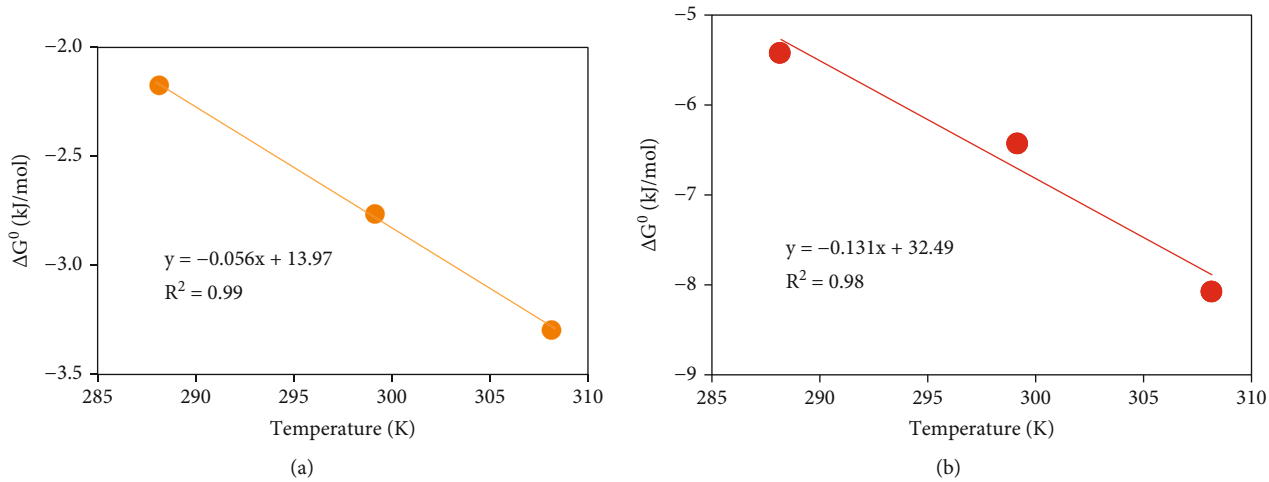


Figure 7: Thermodynamics of (a) MO and (b) CR onto PRM (experiment conditions: adsorbent dosage = 0.5 g/L, pH = 4).

Table 7: Fitting parameters of thermodynamic model.

| Adsorbate | $\Delta H^0$ (kJ/mol) | $\Delta S^0$ (J/(mol K)) | $\Delta G^0$ (kJ/mol) 288.15 K | 298.15 K | 308.15 K |
|---|---|---|---|---|---|
| MO | 13.97 | 55.98 | -2.17 | -2.76 | -3.30 |
| CR | 32.49 | 131.10 | -5.42 | -6.42 | -8.07 |

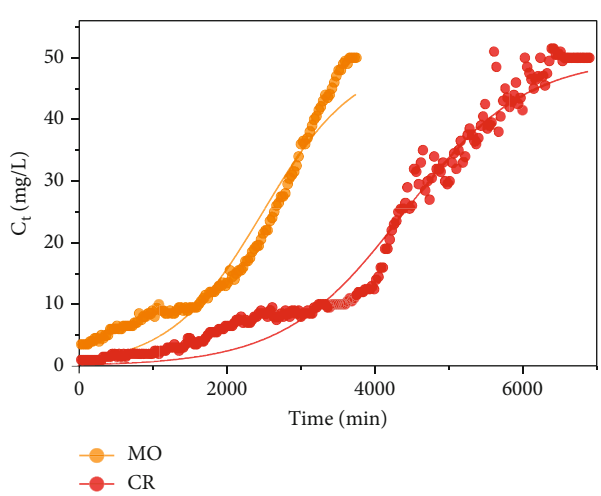


Figure 8: Effectivity of PRM in removing MO and CR in column study.

Table 8: Fitting parameters of Thomas model.

| Adsorbate | $q_e$ (mg/g) | Thomas model $k_{th}$ (L/mg/h) | $q_{th}$ (mg/g) | $R^2$ |
|---|---|---|---|---|
| MO | 28.83 | 1.48 | 31.08 | 0.94 |
| CR | 52.44 | 1.91 | 55.04 | 0.97 |

performance of PRM in removing MO and CR from aqueous solutions.

*3.5. Adsorption Thermodynamic.* As stated in Section 3.3, the environmental temperature has a pronouncedly favored effect on the adsorption of dyes, and the adsorption progress of dyes onto PRM is accelerated by increased temperature. Thus, the detailed thermodynamic of the adsorption progress is of significance to investigating the adsorption of dyes onto PRM (Figure 7 and Table 7). In all cases, the negative values of $\Delta G^0$ hint that the adsorption of both dyes onto PRM is spontaneous which supports its future applications

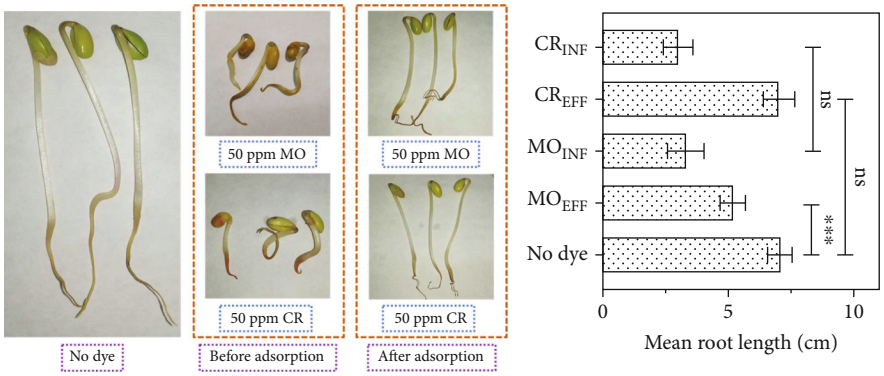


Figure 9: Toxicity assessment of PRM in removing MO and CR using bean sprout seeds ($t$-test, $n = 10$).

in dye adsorptive removal from aqueous solutions. The absolute value of $\Delta G^0$ increases with the increase of environment temperature, suggesting that the spontaneity degree increases at higher temperatures [47]. The positive values of $\Delta H^0$ (13.97 and 32.49 kJ/mol for MO and CR adsorption, respectively) confirm that the adsorption progress of both dyes onto PRM is endothermic [48]. The positive values of $\Delta S^0$ indicate that there is an increase in randomness at the solid/liquid interface [4]. The combination of positive value for $\Delta G^0$ and $\Delta H^0$ proves that the adsorption of MO and CR onto PRM is more spontaneous and favorable at higher environment temperatures.

*3.6. Column Study and Phytotoxicity Assessment.* The column study is conducted in this research to further investigate the adsorption performance of both dyes in real applications. Continues treatment of 50 mg/L of MO and CR in a continuous column system is given in Figure 8. The adsorption progress of both dyes follows the same trend although the adsorption saturation time is different. For MO adsorption, the adsorbent column is exhausted at 3500 min, while the adsorption saturation time for CR is more than 6000 min. Specifically, the concentrations of MO effluents increase slowly in the first 2000 min (~180 bed volumes) while a more rapid increase is observed afterwards. In contrast, no evident increase is observed before 4000 min for CR adsorption column (~360 bed volumes), indicating that the CR removal in column study is also better than MO removal which shares the same result from batch studies.

In order to have quantitative evaluations and thus have solid predictions on the adsorption performance in column studies and future applications, the Thomas model is used and its detailed parameters are summarized [28]. As shown in Table 8, the adsorption rate of the CR is higher than MO in column study which is in accordance with the fitted kinetic parameters in batch studies. In addition, the maximum adsorption capacity for MO and CR is 31.08 and 55.04 mg/g, respectively, and it is not surprising that the adsorption capacity in column studies is considerably lower than in batch studies (~20% of batch studies) [49]. Moreover, the calculated experimental adsorption capacity $q_e$ is close to the theoretical adsorption capacity $q_{th}$, suggesting the Thomas model can describe the column adsorption performance appropriately.

The effluents from the column study are used for further toxicity assessment (collected around 2000 min). The germination of bean sprouts is used as the indicator of PRM effectivity for eliminating anionic dyes in terms of aqueous toxicity. In this research, the deionized water is used as control group (no dye) and the influent (50 ppm for MO and CR) and effluent from the column study are used. After germinating the bean sprouts for 3 days under no light condition, the length of the roots is measured and summarized in Figure 9. As shown in Figure 9(a), the mean root length of the control group is 7.06 cm and the length is reduced to 3.30 and 3.01 cm, for MO influents ($MO_{INF}$) and CR influents ($CR_{INF}$), respectively. For the bean sprouts treated with MO effluents ($MO_{EFF}$) and CR effluents ($CR_{EFF}$), the mean root length is improved to 5.18 and 7.00 cm, respectively. This confirms the effectivity of PRM in reducing the toxicity of treated solutions. Moreover, the $t$-test suggests that the length difference between control and $CR_{EFF}$ is not significant but the difference between the control group and $MO_{EFF}$ is significant. Conclusively, it can be reported that the PRM can treat the CR dyes into nontoxic solutions like deionized water (in terms of phytotoxicity) and MO dye into relatively toxic solutions, under the experimental conditions as conducted in this research.

## 4. Conclusion

In this study, the adsorption performance of two anionic dyes by a red mud-based adsorbent was investigated. The removal of dyes (CR and MO) from aqueous solution by the red mud-based adsorbent was investigated by batch and column studies. The successful loading of the polypyrrole onto the surface of red mud helps to improve the adsorption capacity of the adsorbent: 194.1 mg/g for MO adsorption and 314.9 mg/g for CR adsorption at 15°C, respectively. The highest adsorption capacity was obtained at pH 4 and decreased with the increase of pH. Thermodynamic results suggested that the adsorption progress of MO and CR onto PRM was endothermic and spontaneous. Phytotoxicity assessment of the column study effluents confirmed the effectivity of PRM in eliminating the dye toxicity in terms of germination of bean sprouts. Therefore, the PRM adsorbent could be applied as a promising adsorbent for decolorization in aqueous solutions.

## Data Availability

The data that support the findings of this study are available on request from the corresponding author, Changqing Liu.

## Conflicts of Interest

The authors declare that there is no conflict of interest regarding the publication of this paper.

## Authors' Contributions

Conceptualization was done by Ya-nan Luan and Changqing Liu. Data curation was contributed by Feng Zhang, Yue Yin, and Chunlei Qiao. Funding acquisition was contributed by Changqing Liu. Investigation was conducted by Feng Zhang, Yue Yin, Ya-nan Luan, Mengyan Guo, and Yihua Xiao. Methodology was done by Yue Yin. Project administration was done by Changqing Liu. Software was contributed by Chunlei Qiao and Mengyan Guo. Writing—original draft was contributed by Feng Zhang and Yue Yin. Writing—review and editing was contributed by Yihua Xiao and Changqing Liu. Feng Zhang and Yue Yin contributed equally to this work.

## Acknowledgments

This study was funded by the Major Science and Technology Innovation Project of Shandong Province (Grant No. 2018YFJH0902) and the Taishan Scholar Foundation of Shandong Province (Grant No. tsqn201909126).

## Supplementary Materials

Fig. S1: laboratory column study schematic flow chart. Fig. S2: surface morphology of raw red mud (a) and PRM (b). Fig. S3: FT-IR spectrum of raw red mud and PRM. Fig. S4: surface morphology and EDS of PRM after adsorption of MO (a, b) and CR (c, d). Fig. S5: detailed surface morphology of PRM after adsorption of MO (a–d) and CR (e–h) at different magnifications. *(Supplementary Materials)*

## References

[1] I. Ali, O. M. L. Alharbi, Z. A. Alothman, and A. Alwarthan, "Facile and eco-friendly synthesis of functionalized iron nanoparticles for cyanazine removal in water," *Colloids and Surfaces. B, Biointerfaces*, vol. 171, pp. 606–613, 2018.

[2] I. Ali, O. M. L. Alharbi, Z. A. Alothman, and A. Y. Badjah, "Kinetics, thermodynamics, and modeling of amido black dye photodegradation in water using co/$TiO_2$ nanoparticles," *Photochemistry and Photobiology*, vol. 94, pp. 935–941, 2018.

[3] P. Kumar, R. Agnihotri, K. L. Wasewar, H. Uslu, and C. Yoo, "Status of adsorptive removal of dye from textile industry effluent," *Desalination and Water Treatment*, vol. 50, pp. 226–244, 2012.

[4] T. Kekes and C. Tzia, "Adsorption of indigo carmine on functional chitosan and $\beta$-cyclodextrin/chitosan beads: equilibrium, kinetics and mechanism studies," *Journal of Environmental Management*, vol. 262, p. 110372, 2020.

[5] A. Kausar, R. Shahzad, J. Iqbal, N. Muhammad, S. M. Ibrahim, and M. Iqbal, "Development of new organic-inorganic, hybrid bionanocomposite from cellulose and clay for enhanced removal of Drimarine Yellow HF-3GL dye," *International Journal of Biological Macromolecules*, vol. 149, pp. 1059–1071, 2020.

[6] S. Liu, Y. Ding, P. Li et al., "Adsorption of the anionic dye Congo red from aqueous solution onto natural zeolites modified with N, N-dimethyl dehydroabietylamine oxide," *Chemical Engineering Journal*, vol. 248, pp. 135–144, 2014.

[7] M. Abbas, M. Adil, S. Ehtisham-ul-Haque et al., "Vibrio fischeri bioluminescence inhibition assay for ecotoxicity assessment: a review," *Sci. Total Environ.*, vol. 626, pp. 1295–1309, 2018.

[8] H. Mahmoodian, O. Moradi, B. Shariatzadeha et al., "Enhanced removal of methyl orange from aqueous solutions by poly HEMA-chitosan-MWCNT nano-composite," *Journal of Molecular Liquids*, vol. 202, pp. 189–198, 2015.

[9] R. Li, B. Gao, K. Guo, Q. Yue, H. Zheng, and Y. Wang, "Effects of papermaking sludge-based polymer on coagulation behavior in the disperse and reactive dyes wastewater treatment," *Bioresource Technology*, vol. 240, pp. 59–67, 2017.

[10] O. Türgay, G. Ersöz, S. Atalay, J. Forss, and U. Welander, "The treatment of azo dyes found in textile industry wastewater by anaerobic biological method and chemical oxidation," *Separation and Purification Technology*, vol. 79, pp. 26–33, 2011.

[11] C. H. Nguyen, M. L. Tran, T. T. Van Tran, and R.-S. S. Juang, "Enhanced removal of various dyes from aqueous solutions by UV and simulated solar photocatalysis over TiO2/ZnO/rGO composites," *Separation and Purification Technology*, vol. 232, p. 115962, 2020.

[12] J. Stejskal, "Interaction of conducting polymers, polyaniline and polypyrrole, with organic dyes: polymer morphology control, dye adsorption and photocatalytic decomposition," *Chemical Papers*, vol. 74, no. 1, pp. 1–54, 2020.

[13] M. A. Khan, A. A. Alqadami, S. M. Wabaidur et al., "Oil industry waste based non-magnetic and magnetic hydrochar to sequester potentially toxic post-transition metal ions from water," *Journal of Hazardous Materials*, vol. 400, p. 123247, 2020.

[14] E. R. Kenawy, A. A. Ghfar, S. M. Wabaidur et al., "Cetyltrimethylammonium bromide intercalated and branched polyhydroxystyrene functionalized montmorillonite clay to sequester cationic dyes," *Journal of Environmental Management*, vol. 219, pp. 285–293, 2018.

[15] R. Zhang, M. Ma, Q. Zhang, F. Dong, and Y. Zhou, "Multifunctional g-C3N4/graphene oxide wrapped sponge monoliths as highly efficient adsorbent and photocatalyst," *Applied Catalysis B: Environmental*, vol. 235, pp. 17–25, 2018.

[16] C. Wu, L. Huang, S. G. Xue et al., "Arsenic sorption by red mud-modified biochar produced from rice straw," *Environmental Science and Pollution Research*, vol. 24, no. 22, pp. 18168–18178, 2017.

[17] N. B. A, K. M. Krishna, K. Kalpana, and K. Ravindhranath, "Removal of fluoride from water using $H_2O_2$-treated fine red mud doped in Zn-alginate beads as adsorbent," *Journal of Environmental Chemical Engineering*, vol. 6, no. 1, pp. 906–916, 2018.

[18] I. Akin, G. Arslan, A. Tor, M. Ersoz, and Y. Cengeloglu, "Arsenic(V) removal from underground water by magnetic nanoparticles synthesized from waste red mud," *Journal of Hazardous Materials*, vol. 235-236, pp. 62–68, 2012.

[19] Y. Wang, S. Gong, Y. Li, Z. Li, and J. Fu, "Adsorptive removal of tetracycline by sustainable ceramsite substrate from bentonite/red mud/pine sawdust," *Scientific Reports*, vol. 10, pp. 1–18, 2020.

[20] Y. Wang, Y. Yu, H. Li, and C. Shen, "Comparison study of phosphorus adsorption on different waste solids: Fly ash, red mud and ferric-alum water treatment residues," *Journal of Environmental Sciences (China)*, vol. 50, pp. 79–86, 2016.

[21] J. Ye, X. Cong, P. Zhang et al., "Phosphate adsorption onto granular-acid-activated-neutralized red mud: parameter optimization, kinetics, isotherms, and mechanism analysis," *Water, Air, and Soil Pollution*, vol. 226, no. 9, 2015.

[22] J. Li, L. Xu, P. Sun et al., "Novel application of red mud: facile hydrothermal-thermal conversion synthesis of hierarchical porous AlOOH and Al 2 O 3 microspheres as adsorbents for dye removal," *Chemical Engineering Journal*, vol. 321, pp. 622–634, 2017.

[23] X. Li, M. Ji, L. D. Nghiem et al., "A novel red mud adsorbent for phosphorus and diclofenac removal from wastewater," *Journal of Molecular Liquids*, vol. 303, p. 112286, 2020.

[24] C. Li, N. Chen, Y. Zhao, R. Li, and C. Feng, "Polypyrrole-grafted peanut shell biological carbon as a potential sorbent for fluoride removal: sorption capability and mechanism," *Chemosphere*, vol. 163, pp. 81–89, 2016.

[25] C. Patra, R. Gupta, D. Bedadeep, and S. Narayanasamy, "Surface treated acid-activated carbon for adsorption of anionic azo dyes from single and binary adsorptive systems: a detail insight," *Environmental Pollution*, vol. 266, p. 115102, 2020.

[26] A. Naga Babu, T. Raja Sree, D. Srinivasa Reddy, G. Suresh Kumar, and G. V. Krishna Mohan, "Experimental and statistical analysis of As (III) adsorption from contaminated water using activated red mud doped calcium-alginate beads," *Environ. Technol. (United Kingdom)*, vol. 42, pp. 1–34, 2021.

[27] J. Jang and D. S. Lee, "Effective phosphorus removal using chitosan/Ca-organically modified montmorillonite beads in batch and fixed-bed column studies," *Journal of Hazardous Materials*, vol. 375, pp. 9–18, 2019.

[28] A. F. Santos, A. L. Arim, D. V. Lopes, L. M. Gando-Ferreira, and M. J. Quina, "Recovery of phosphate from aqueous solutions using calcined eggshell as an eco-friendly adsorbent," *Journal of Environmental Management*, vol. 238, pp. 451–459, 2019.

[29] S. Hong, F. S. Cannon, P. Hou, T. Byrne, and C. Nieto-Delgado, "Adsorptive removal of sulfate from acid mine drainage by polypyrrole modified activated carbons: effects of polypyrrole deposition protocols and activated carbon source," *Chemosphere*, vol. 184, pp. 429–437, 2017.

[30] X. Yang, Y. Li, H. Gao, C. Wang, X. Zhang, and H. Zhou, "One-step fabrication of chitosan-Fe(OH)3 beads for efficient adsorption of anionic dyes," *International Journal of Biological Macromolecules*, vol. 117, pp. 30–41, 2018.

[31] M. Naushad, G. Sharma, and Z. A. Alothman, "Photodegradation of toxic dye using Gum Arabic-crosslinked-poly(acrylamide)/Ni(OH)2/FeOOH nanocomposites hydrogel," *Journal of Cleaner Production*, vol. 241, p. 118263, 2019.

[32] W. A. Khanday, M. J. Ahmed, P. U. Okoye, E. H. Hummadi, and B. H. Hameed, "Single-step pyrolysis of phosphoric acid-activated chitin for efficient adsorption of cephalexin antibiotic," *Bioresource Technology*, vol. 280, pp. 255–259, 2019.

[33] W. Qi, Y. Zhao, X. Zheng, M. Ji, and Z. Zhang, "Adsorption behavior and mechanism of Cr (VI) using Sakura waste from aqueous solution," *Applied Surface Science*, vol. 360, pp. 470–476, 2016.

[34] R. Liu, L. Chi, X. Wang et al., "Effective and selective adsorption of phosphate from aqueous solution via trivalent-metals-based amino-MIL-101 MOFs," *Chemical Engineering Journal*, vol. 357, pp. 159–168, 2019.

[35] G. Fu, Y. Zhao, S. Zhou, C. Chen, Y. Zhong, and Y. Xu, "Efficient removal of nitrogen and phosphorus in aqueous solutions using modified water treatment residuals–sodium alginate beads," *Environmental Science and Pollution Research*, 2021.

[36] W. Ding, X. Wan, H. Zheng, Y. Wu, and S. Muhammad, "Sulfite-assisted oxidation/adsorption coupled with a TiO2 supported CuO composite for rapid arsenic removal: performance and mechanistic studies," *Journal of Hazardous Materials*, vol. 413, p. 125449, 2021.

[37] I. Khatri, J. Amar, and J. Amar, "Prediction and optimization of adsorption properties for Cs + on [email protected] LDHs hollow spheres from aqueous solution: Kinetics, isotherms, and BBD model," *Journal of Hazardous Materials*, vol. 401, article 123374, 2021.

[38] Y. X. Zhang and Y. Jia, "Fluoride adsorption on manganese carbonate: ion-exchange based on the surface carbonate-like groups and hydroxyl groups," *Journal of Colloid and Interface Science*, vol. 510, pp. 407–417, 2018.

[39] J. Lin, Y. Wang, Y. Zhan, and Z. Zhang, "Magnetite-modified activated carbon based capping and mixing technology for sedimentary phosphorus release control," *Journal of Environmental Management*, vol. 248, p. 109287, 2019.

[40] V. M. Tangde, S. S. Prajapati, B. B. Mandal, and N. P. Kulkarni, "Study of kinetics and thermodynamics of removal of phosphate from aqueous solution using activated red mud," *Int. J. Environ. Res.*, vol. 11, no. 1, pp. 39–47, 2017.

[41] A. O. Babatunde and Y. Q. Zhao, "Equilibrium and kinetic analysis of phosphorus adsorption from aqueous solution using waste alum sludge," *Journal of Hazardous Materials*, vol. 184, no. 1-3, pp. 746–752, 2010.

[42] V. S. Munagapati and D.-S. Kim, "Equilibrium isotherms, kinetics, and thermodynamics studies for Congo red adsorption using calcium alginate beads impregnated with nano-goethite," *Ecotoxicology and Environmental Safety*, vol. 141, pp. 226–234, 2017.

[43] M. Ghaedi, M. N. Biyareh, S. N. Kokhdan et al., "Comparison of the efficiency of palladium and silver nanoparticles loaded on activated carbon and zinc oxide nanorods loaded on activated carbon as new adsorbents for removal of Congo red from aqueous solution: kinetic and isotherm study," *Materials Science and Engineering: C*, vol. 32, no. 4, pp. 725–734, 2012.

[44] A. Afkhami and R. Moosavi, "Adsorptive removal of Congo red, a carcinogenic textile dye, from aqueous solutions by maghemite nanoparticles," *Journal of Hazardous Materials*, vol. 174, no. 1-3, pp. 398–403, 2010.

[45] S. Liu, W. Wang, Y. Cheng et al., "Methyl orange adsorption from aqueous solutions on 3D hierarchical PbS/ZnO microspheres," *Journal of Colloid and Interface Science*, vol. 574, pp. 410–420, 2020.

[46] N. Elhadiri, M. Benchanaa, and R. Chikri, "Adsorption thermodynamic and kinetic studies of methyl orange onto sugar scum powder as a low-cost inorganic adsorbent," *Journal of Chemistry*, vol. 2020, 10 pages, 2020.

[47] Y. Y. Hu, C. Pan, X. Zheng et al., "Prediction and optimization of adsorption properties for Cs + on [email protected] LDHs hollow spheres from aqueous solution: Kinetics, isotherms, and BBD model," *Journal of Hazardous Materials*, vol. 401, article 123374, 2021.

[48] C. Li, Q. Yang, S. Lu, and Y. Liu, "Adsorption and mechanism study for phosphonate antiscalant HEDP removal from reverse osmosis concentrates by magnetic La/Zn/$Fe_3O_4$@PAC composite," *Colloids and Surfaces A: Physicochemical and Engineering Aspects*, vol. 613, p. 126056, 2021.

[49] O. Callery, M. G. G. Healy, F. Rognard, L. Barthelemy, and R. B. B. Brennan, "Evaluating the long-term performance of low-cost adsorbents using small-scale adsorption column experiments," *Water Research*, vol. 101, pp. 429–440, 2016.

Hindawi
Adsorption Science & Technology
Volume 2021, Article ID 2013259, 8 pages
https://doi.org/10.1155/2021/2013259

*Research Article*

# Removal of $Pb^{2+}$ Ions by ZSM-5/AC Composite in a Fixed-Bed Bench Scale System

**R. Lakshmipathy,[1] G. L. Balaji,[2] and Iván Leandro Rodríguez Rico[3]**

[1]*Department of Chemistry, KCG College of Technology, Karapakkam, 600097, Chennai, Tamilnadu, India*
[2]*School of Advanced Sciences and Languages, VIT Bhopal University, 466114, Bhopal, Madhya Pradesh, India*
[3]*Faculty of Chemical and Pharmacy, Department of Chemical Engineering, Central University "Marta Abreu" of Las Villas, Cuba*

Correspondence should be addressed to R. Lakshmipathy; lakshmipathy.che@kcgcollege.com
and Iván Leandro Rodríguez Rico; ivanl@uclv.edu.cu

Received 15 July 2021; Revised 28 September 2021; Accepted 11 October 2021; Published 21 October 2021

Academic Editor: Hesham Hamad



This investigation suggests the implementation of ZSM-5 activated carbon composite as a prolific adsorbent for the continuous elimination of $Pb^{2+}$ ions from water. Continuous adsorption experiments were performed by varying three parameters such as process flow rate (2-6 mL min$^{-1}$), bed height (2-6 cm), and initial concentration (250–750 mg L$^{-1}$). The highest loading capacity of the fixed-bed 213.3 mg L$^{-1}$ was achieved with optimal values of 2 mL min$^{-1}$ of flow rate, bed height of 6 cm, and initial concentration of 750 mg L$^{-1}$, respectively. The breakthrough curves and saturation points were found to appear quickly for increasing flow rates and initial concentration and vice versa for bed depth. The lower flow rates with higher bed depths have exhibited optimal performances of the fixed-bed column. The mechanism of adsorption of $Pb^{2+}$ ions was found to be ion exchange with $Na^{+}$ ions from ZMS-5 and pore adsorption onto activated carbon. The breakthrough curves were verified with three well-known mathematical models such as the Adams-Bohart, Thomas, and Yoon-Nelson models. The later models showed the best fit to the column data over the Adams-Bohart model that can be utilized to understand the binding of $Pb^{2+}$ ions onto the composite. Regeneration of ZSM-5/activated carbon was achieved successfully with 0.1 M HCl within 60 min of contact time. The outcomes conclude that ZSM-5 activated carbon composite is a prolific material for the continuous removal of water loaded with $Pb^{2+}$ ions.

## 1. Introduction

The burgeoning population and swift industrialization have led to the intense release of contaminant-loaded effluents into the natural ecosystem. Industries such as batteries, pigments, and glass widely use lead (Pb), and the effluents contain a considerable amount of $Pb^{2+}$ ions. Lead is a heavy metal that is nonbiodegradable and carcinogenic to human and aquatic life [1]. Therefore, it is highly essential to remove the $Pb^{2+}$ ions from industrial effluents to conserve the natural ecosystem.

Various physical and chemical treatment techniques such as ion exchange [2], membrane filtration [3], flocculation [4], coagulation [5], adsorption [6], solvent extraction [7], chemical precipitation [8], and electrochemical treatments [9] are developed for the remediation of wastewater laden with heavy metal ions. Ion exchangers were quite popular for the removal of heavy metal ions from wastewater, and resins are usually employed as prolific ion exchangers [2]. Membranes are another important class of technique that is efficient in the removal of heavy metal ions from wastewater [3]. However, the cost of the ion exchangers and membranes limits the applications [10]. Similarly, flocculation and coagulation have disadvantages such as disposal and use of toxic chemicals [11]. The chemical extractions are quite useful, but the cost of the solvents, disposal of precipitations, and energy requirements limit the applications [12].

Adsorption is one of the powerful and well-established techniques for wastewater treatment due to its simplicity and economic factors [13]. In recent decades, adsorbents from agricultural sources have been developed, and these adsorbents are economical and do not cause any disposal issues unlike chemical precipitations or coagulation and flocculation [14]. Adsorption does not require any energy requirements such as electrochemical treatments [15]. Furthermore, the aptness of adsorption to eliminate hazardous contaminants without generating any toxic byproducts and retaining the standards of water unaltered has also favored it [16]. Adsorbents such as activated carbon [17], zeolites [18], nanosorbents [19], and biopolymers [20] were found to be effective and efficient sorbents for the remediation of contaminated water. In an interesting study, Hanbali et al. [21] reported the use of magnetic multiwalled carbon nanotubes as potential adsorbents for the removal of $Pb^{2+}$ ions. The loading capacity was found to be 9.09 mg $g^{-1}$ at a pH of 8. Mohd et al. [22] reported the modified palm oil industry solid waste as a useful adsorbent for the removal of $Pb^{2+}$ ions. The maximum removal efficiency of fruit bunch of palm was reported to be 92.2 mg $g^{-1}$ at a pH of 1 with a contact time of 15 min. Iron oxide nanocomposites produced from biowaste were reported for the removal of $Pb^{2+}$ ions [23]. The T-$Fe_3O_4$ exhibited 95% removal efficiency with a contact time of 95 min at pH 4.5.

Zeolites are naturally available crystalline microporous solids that form a network of cavities and channels [24]. They are proven to be very good adsorbents, ion exchangers, and catalysts [25]. Aluminosilicate zeolites (ZSM-5) are microporous materials that are commonly used in the isomerization of hydrocarbons in the petro industry as catalysts [26]. Natural zeolites are prolifically utilized as adsorbents for the sequestration of $Pb^{2+}$ ions [27]. The NaX zeolite exhibited an adsorption capacity of 14.2 mg $g^{-1}$ at pH 6 with a contact time of 60 min. ZSM-5 zeolites are modified with several organic and inorganic compounds and elements to enhance the sorption capacity. Polyvinyl alcohol and carboxymethyl cellulose-incorporated zeolites are utilized for the effective adsorption of synthetic organic molecules from aqueous solution [28]. ZSM-5 modified with mixed metal oxides was found to be potential adsorbents for the removal of elemental mercury [29]. However, the literature reveals that very little study is available on the application of the natural and modified ZSM-5 zeolites for the sequestration of cations. The majority of studies report the elimination of cationic contaminants from aqueous solution by batch and fixed-bed method. The potential of ZSM-5 zeolites for the elimination of cations in the batch process is investigated but in continuous columns is yet to be explored. The synthesis of ZSM-5 activated carbon composite and its potential use for the remediation of $Pb^{2+}$ and $Cd^{2+}$ ions from contaminated water have been reported [30].

In continuation of the above, the present investigation describes the sequestration of $Pb^{2+}$ ions through the fixed-bed process by using ZSM-5 activated carbon composite as an ecofriendly sorbent. The impacts of various governing components were investigated, and various breakthrough models were adopted to analyze the experimental data.

## 2. Materials and Methods

*2.1. Reagents.* Tetraethyl orthosilicate and Sodium Aluminate were obtained from Sd fine chemicals. Tetra propyl ammonium hydroxide and lead nitrate were obtained from Merck chemicals. Distilled water was used for all the experiments. Hydrochloric acid, acetic acid, and Sodium Hydroxide were obtained from Sd fine chemicals. Activated carbon was obtained from local chemical suppliers, and all the reagents used were of AR grade.

*2.2. Preparation of ZSM-5/Activated Carbon Composite and Metal Stock Solution.* The ZSM-5 activated carbon composite was prepared by mixing 10 mL of tetraethyl orthosilicate (TEOS), 3 g of Sodium Aluminate ($NaAlO_2$), and 2 g activated carbon (AC). The mixture was stirred overnight followed by drying at 80°C for 12 h. After drying, a gel was obtained which was added to 15 mL of tetra propyl ammonium hydroxide, mixed by stirring, and dried overnight at 100°C. The dried gel was kept in a vial which was then placed in an autoclave containing 2 mL of water. Then, it was heated in an oven at 170°C for 72 h. The added water that generated steam assisted in the dry gel conversion. The resulting dried sample was calcined in a tubular furnace at 550°C for 3 h under $N_2$ flow (150 mL/min). The dried and calcined sample was named ZSM-5/AC which was found to be around 0.5 $\mu$m in size and used for further investigation. Lead (II) nitrate (1.6 g) was solubilized in one litre of demineralized water to prepare 1000 mg $L^{-1}$ of metal ion stock solution, and 0.01 M hydrochloric acid (HCl) and Sodium Hydroxide (NaOH) were used for the pH adjustments.

*2.3. Fixed-Bed Column Investigations.* A small-scale glass column with a height of 15 cm having an internal diameter of 10 mm was chosen for performing the fixed-bed column investigations (Figure 1). Firstly, the glass column was filled with ZSM-5/AC (1.112 g $cm^{-1}$), and the $Pb^{2+}$ ions were pumped into the top of the column with the help of a peristaltic pump with a desired rate of flow. The eluents were saved at various preset time intervals at the exit of the fixed-bed. An atomic absorption spectrophotometer (AA240, Varian) was utilized to estimate the residual concentrations of collected samples. To investigate the influence of rate of flow for the elimination of $Pb^{2+}$ ions by ZSM-5/AC, investigations were performed with varying flow rates from 2 to 6 mL $min^{-1}$ with a difference of 2 mL. The influence of bed depth was investigated by deferring the bed depth from 2 to 6 cm in height with a height interval of 2 cm, and the remaining influential parameters were kept constant. Further to the optimization of bed height and flow rate, the influence of adsorbate concentration was experimented with by deferring the initial concentration of $Pb^{2+}$ ions from 250 to 750 mg $L^{-1}$. The inlet of $Pb^{2+}$ ions was continued until the inlet and exit concentration was found to be unchanged suggesting the saturation of the column [31]. To ensure that the data analysis was accurate and reproducible, the fixed-bed investigations were performed thrice and the mean values were considered with a standard deviation of less than 4%.

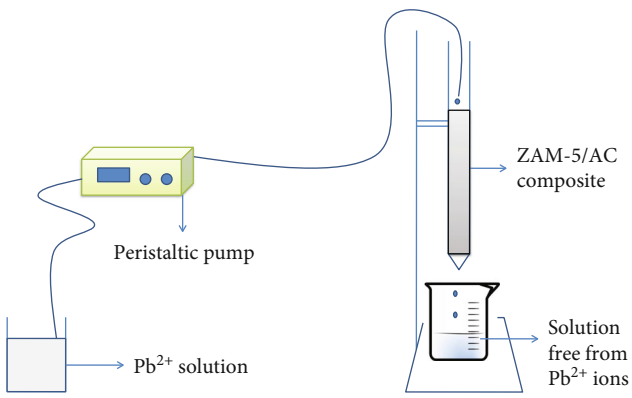


Figure 1: Schematic diagram fixed-bed column setup for the removal of $Pb^{2+}$ ions by ZSM-5/AC composite.

*2.4. Fixed-Bed Data Analysis.* The breakthrough curves are the output of experimental runs from packed bed column studies. In general, the behaviour and dynamic reply of adsorption in columns can be easily determined from the time and figure of the breakthrough curve that is considered to be an imperative characteristic [32]. The breakthrough position of the S form curve is examined when the eluent concentration ($C_t$) from the fixed-bed attains about 0.1% of influent concentration. The exhaustion of fixed-bed is attained when the position of concentration of eluent attains 95% or above. The volume of effluent ($V_{\text{eff}}$) can be understood with equation

$$V_{\text{eff}} = Qt_{\text{total}}, \tag{1}$$

where $Q$ is the volumetric rate of flow and $t_{\text{total}}$ is the complete flow time (min).

The amount of $Pb^{2+}$ taken up, $M_{\text{ad}}$ (mg), in the sorption bed can be determined by the following equation:

$$M_{\text{ad}} = \frac{Q}{1000}\int_{t=0}^{t=\text{total}} C_{\text{ad}}dt, \tag{2}$$

where $C_{\text{ad}}$ is the amount of $Pb^{2+}$ ions removed (mg $L^{-1}$).

The absolute quantity of $Pb^{2+}$ ions getting into the bed ($M_{\text{total}}$) can be estimated from equation

$$M_{\text{total}} = \frac{C_o Q t_{\text{total}}}{1000}, \tag{3}$$

where $C_0$ is the initial concentration of the $Pb^{2+}$ ions.

Finally, the total $Pb^{2+}$ ion removal percentage is known from equation

$$Y\,(\%) = \frac{M_{\text{ad}}}{M_{\text{total}}} \times 100, \tag{4}$$

where $Y$ is the yield percentage.

*2.5. Column Breakthrough Curve Modeling.* The simple mathematical models can well explain the prolific behaviour of lab-scale column processes to large-scale processes typically used in industries [33, 34]. The familiar and common mathematical models such as Adams-Bohart, Thomas, and Yoon-Nelson models were employed in understanding the breakthrough curves obtained for various influential parameters of the column.

One of the commonly considered models in the understanding of breakthrough curves is the Adams-Bohart model [35]. This model suggests that the fraction of loading magnitude is proportional to the rate of sorption and further suggests that the equilibrium is not instantaneous [36, 37]. The major advantage is that the initial part of the breakthrough curve is very well inferred, and the equation is conveyed as below:

$$\ln\frac{C_t}{C_o} = k_{AB}C_o t - k_{AB}N_o\frac{z}{U_o}, \tag{5}$$

where $C_o$ and $C_t$ are the entry and exit concentrations of $Pb^{2+}$ ions (mg $L^{-1}$), $k_{AB}$ is the kinetic constant (L $mg^{-1}$ $min^{-1}$), $N_o$ is the exhaustion amount (mg $L^{-1}$), $z$ is the depth of the bed (cm), and $U_o$ is the peripheral velocity (cm $min^{-1}$).

The Thomas model is the best-known theoretical model for explaining the efficiency of binding of lead ions onto an adsorbent in a packed bed column [38]. The plug flow process in a packed column is the assumption made by the Thomas model, and the model equation is as given below:

$$\ln\left(\frac{C_0}{C_t} - 1\right) = \frac{k_{\text{Th}}q_o m}{Q} - k_{\text{Th}}C_o t, \tag{6}$$

where $k_{\text{Th}}$ is considered constant of the Thomas model (mL $min^{-1}$ $g^{-1}$), $m$ is the mass of the adsorbent, and $q_o$ is the loading magnitude (mg $g^{-1}$).

One of the simplest methods and models for the adsorption of gas-phase molecules onto activated coal was proposed by Yoon and Nelson [39]. Yoon and Nelson considered that the decrease in the rate in the likelihood of sorption of $Pb^{2+}$ is comparable to the likelihood of sorbate sorption and the prospect of $Pb^{2+}$ ion breakthrough on ZSM-5/AC. The linearized equation of this model is expressed as

$$\ln\left(\frac{C_t}{C_o - C_t}\right) = k_{\text{YN}}t - \tau k_{\text{YN}}, \tag{7}$$

where $k_{\text{YN}}$ is the proportionality constant in $min^{-1}$ of the Yoon-Nelson model and $\tau$ is the 50% retaining time of the initial sorbate (min).

## 3. Results and Discussion

*3.1. Influence of Rate of Flow.* One of the crucial parameters in the removal of contaminants from wastewater especially during the continuous treatment process is flow rate. Therefore, in the present investigation, the rate of flow was varied between 2 and 6 mL $min^{-1}$ at fixed column length (2 cm) and opening concentration (250 mg $L^{-1}$) for the sequestration of

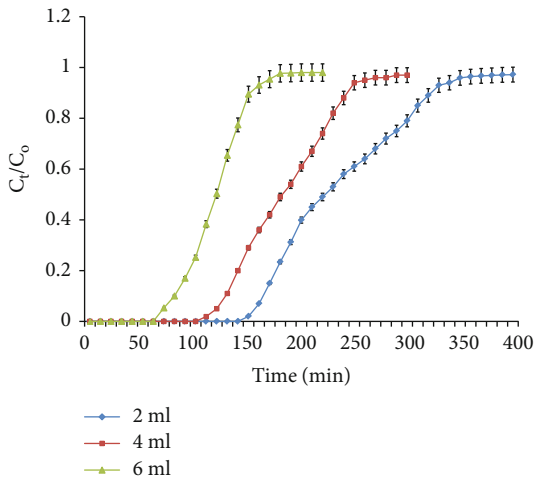


Figure 2: Effect of flow rate on breakthrough curves obtained for the removal of $Pb^{2+}$ by ZSM-5/AC (fixed column length 2 cm, initial metal concentration 250 mg $L^{-1}$, pH 6, 303°C, and error bars represent the standard deviation at $n = 3$).

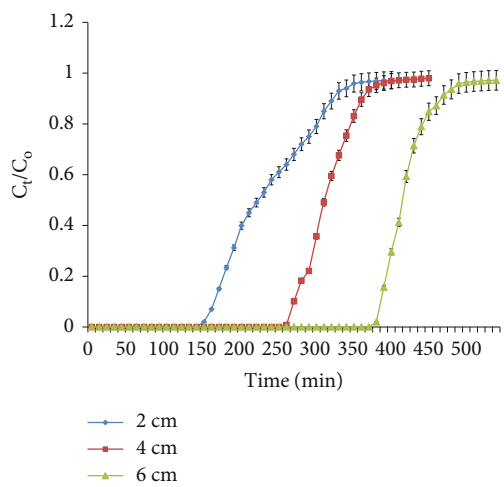


Figure 3: Effect of bed height on breakthrough curves obtained for the removal of $Pb^{2+}$ by ZSM-5/AC (flow rate 2 mL $min^{-1}$, initial metal concentration 250 mg $L^{-1}$, pH 6, 303°C, and error bars represent the standard deviation at $n = 3$).

$Pb^{2+}$ ions by ZSM-5/AC from aqueous solution. The breakthrough curves obtained for different rates of flow are represented in Figure 2. It is observed that with the burgeoning flow rate, the breakthrough and saturation time tend to decrease. This is well elucidated on the reality that, at a minimal rate of flow, the time of residence of $Pb^{2+}$ ions to interact with the surface of the ZSM-5/AC is high. At higher flow rates, the time for adsorption onto the surface or pore diffusion decreases. It is also seen that the breakthrough curves became steep with an increase in flow rates suggesting the faster saturation of column and lesser time spent by the metal ion. Hence, the efficiency and breakthrough time decrease with burgeoning flow rates. Similar observations have been reported for the continuous sorption of $Pb^{2+}$ ions in the column by WR powder [16].

Table 1: Fixed-bed column parameters for the adsorption of $Pb^{2+}$ ions by ZSM-5/AC.

| $C_o$ (mg $L^{-1}$) | $Q$ (mL $min^{-1}$) | $Z$ (cm) | $M_{ad}$ (mg) | $M_{total}$ (mg) | $Y$ (%) | EBCT (min) |
|---|---|---|---|---|---|---|
| 250 | 2 | 2 | 136.6 | 200 | 68.6 | 2.3 |
| 250 | 4 | 2 | 190.6 | 300 | 63.5 | 1.7 |
| 250 | 6 | 2 | 186.6 | 330 | 56.5 | 1.2 |
| 250 | 2 | 2 | 136.6 | 200 | 68.6 | 2.3 |
| 250 | 2 | 4 | 161.0 | 225 | 71.5 | 4.5 |
| 250 | 2 | 6 | 213.3 | 270 | 79.0 | 6.5 |
| 500 | 2 | 6 | 154.7 | 225 | 68.7 | 6.5 |
| 750 | 2 | 6 | 93.5 | 175 | 53.2 | 6.5 |

*3.2. Influence of Height of Bed.* The influence of the height of the bed for the removal of $Pb^{2+}$ ions by ZSM-5/AC was explored by changing the bed height between 2 and 6 cm, and the breakthrough shapes attained are represented in Figure 3. With the burgeoning bed heights, the time of saturation and breakthrough extends, and further, removal efficiency also increased with increasing bed heights. The time of breakthrough extends from 150 to 400 min with augmenting the height of the bed from 2 to 6 cm. The empty bed column time (EBCT) also extended from 2.3 to 6.5 min (Table 1). This is attributed to the fact that the $Pb^{2+}$ ions have more chance to interact with the ZSM-5/AC and more surface active sites are available for interaction. Hence, the removal efficiency and adsorption capacity increase at higher bed heights. Similar observations have been reported for the removal of $Pb^{2+}$ ions by dead calcareous skeletons [40].

*3.3. Influence of Initial Concentration.* The influence of $Pb^{2+}$ ions on the breakthrough shapes was experimented by considering the concentrations from 250 to 750 mg $L^{-1}$ and the respective breakthrough; shapes are illustrated in Figure 4. As observed from the figure, various crucial components decreased with burgeoning $Pb^{2+}$ ion concentrations such as removal efficiency, breakthrough, and exhaustion time. The total amount of influent passing into the fixed-bed also reduced with burgeoning entry concentration (Table 1). The observations suggest that the time taken for the attainment of 50% breakthrough tendency reduced with burgeoning initial metal ion concentration. This can be expounded on the basis that a minimal concentration gradient resulted in moderate adsorption of $Pb^{2+}$ ions due to the reduced diffusion coefficient and reduced mass transfer coefficients [20]. Hence, lower concentrations will benefit the increased diffusion coefficient and increased mass transfer coefficients resulting in greater adsorption efficiency. Similar observations have been reported for the removal of $Pb^{2+}$ ions by natural clinoptilolite [41].

*3.4. Modeling of Breakthrough Curves.* The design of fixed-bed columns and its prediction can be carried out from breakthrough curves of studied parameters. The scale-up of lab-scale process to industrial process can be performed by various mathematical models that have been put forward.

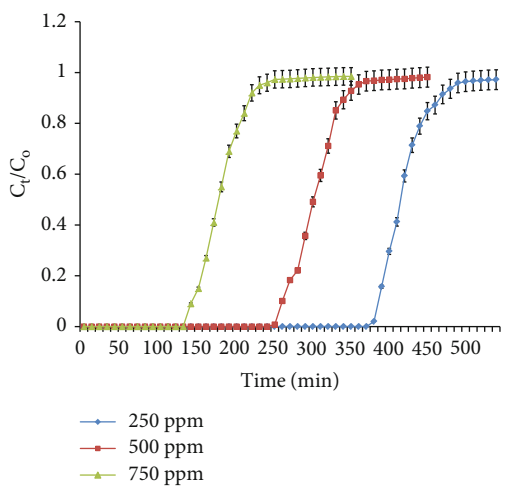


Figure 4: Effect of initial metal ion concentration on breakthrough curves obtained for the removal of $Pb^{2+}$ by ZSM-5/AC (bed height 6 cm, flow rate 2 mL $min^{-1}$, pH 6, 303°C, and error bars represent the standard deviation at $n = 3$).

In the present investigations, the vital actions of the fixed-bed column were studied and analyzed with the Adams-Bohart, Thomas, and Yoon-Nelson models.

*3.4.1. Adams-Bohart Model.* For parameter assessment, the range of $t$ values was considered from 0 to 0.5 $C_0/C_t$ of the breakthrough shapes. The slope $k_{AB}$ and intercept $N_o$ were tabulated from the graph of ln $(C_t/C_o)$ vs. $t$ (figure not shown), and the respective values and correlation coefficients are outlined in Table 2. As outlined in Table 2, the $k_{AB}$ values increased with growing bed depth and tend to drop with the growing rate of flow and preliminary $Pb^{2+}$ ion concentration. The results suggested that the external mass transfer dominated the overall kinetics of the process [42]. The applicability of the Adams-Bohart model for understanding the beginning of breakthrough curves of the present process was elucidated by the moderately high correlation coefficients.

*3.4.2. Thomas Model.* The performance prediction of the breakthrough of columns can be very well described by the Thomas model. The constants and respective coefficients of correlation derived for the Thomas model from the linear regression equation are summarized in Table 3. The values of $K_{Th}$ are observed to reduce with an increase in bed height, but the opposite trend was observed with a burgeoning rate of flow and preliminary concentration. But $q_o$ depicted the opposite trend to that of $K_{Th}$. The correlation coefficients obtained are found to be very high suggesting the suitability of the model for the removal of $Pb^{2+}$ ions by ZSM-5/AC. These observations suggest that the Thomas model was applicable for the adsorption of $Pb^{2+}$ ions and the rate-limiting step was not just due to internal and external mass transfer [31].

*3.4.3. Yoon-Nelson Model.* The correlation coefficients and values of $k_{YN}$ and $\tau$ acquired using the linear regression analysis for breakthrough curves are outlined in Table 4. The coefficients of correlation were between 0.955 and 0.993, suggesting the applicability of the Yoon-Nelson model in addition to the Thomas model. The $K_{YN}$ values were found to decrease with a surge in preliminary concentration but increase with the growing rate of flow and bed depth. The component $\tau$ which is considered a time for 50% retention was observed to surge with surging bed height due to relaxed exhaustion of the column at elevated peaks of packed beds. On the other end, the $\tau$ values profoundly reduce with the burgeoning flow rate and preliminary entry concentration [26]. This is due to the quick attainment of exhaustion of fixed-bed columns [41]. This observation suggests that both Yoon-Nelson and Thomas models describe well for the elimination of $Pb^{2+}$ ions by ZSM-5/AC from an aqueous solution.

Table 2: Adams-Bohart model parameters for the removal of $Pb^{2+}$ ions at various conditions.

| Parameter | | $K_{AB}$ (L/mg min) | $N_o$ (mg/L) | $R^2$ |
|---|---|---|---|---|
| Rate of flow | 2 mL/min | $2.2 \times 10^{-4}$ | 18342 | 0.947 |
| | 4 mL/min | $1.2 \times 10^{-4}$ | 21767 | 0.934 |
| | 6 mL/min | $1.1 \times 10^{-4}$ | 23608 | 0.915 |
| Bed depth | 2 cm | $2.2 \times 10^{-4}$ | 18342 | 0.947 |
| | 4 cm | $3.4 \times 10^{-4}$ | 17510 | 0.916 |
| | 6 cm | $4.2 \times 10^{-4}$ | 16072 | 0.933 |
| Preliminary concentration | 250 mg $L^{-1}$ | $4.2 \times 10^{-4}$ | 16072 | 0.933 |
| | 500 mg $L^{-1}$ | $3.1 \times 10^{-4}$ | 18567 | 0.921 |
| | 750 mg $L^{-1}$ | $2.6 \times 10^{-4}$ | 21487 | 0.919 |

Table 3: Thomas model parameters for the removal of $Pb^{2+}$ ions by ZSM-5/AC from aqueous solution.

| Parameter | | $K_{Th}$ (mL/min mg) | $q_o$ (mg/g) | $R^2$ |
|---|---|---|---|---|
| Rate of flow | 2 mL/min | $1.7 \times 10^{-3}$ | 141.3 | 0.992 |
| | 4 mL/min | $2.1 \times 10^{-3}$ | 187.0 | 0.984 |
| | 6 mL/min | $2.2 \times 10^{-3}$ | 185.4 | 0.990 |
| Bed depth | 2 cm | $1.7 \times 10^{-3}$ | 141.3 | 0.992 |
| | 4 cm | $1.6 \times 10^{-3}$ | 169.7 | 0.991 |
| | 6 cm | $1.5 \times 10^{-3}$ | 231.1 | 0.972 |
| Preliminary concentration | 250 mg $L^{-1}$ | $1.5 \times 10^{-3}$ | 231.1 | 0.972 |
| | 500 mg $L^{-1}$ | $1.7 \times 10^{-3}$ | 145.7 | 0.989 |
| | 750 mg $L^{-1}$ | $2.6 \times 10^{-4}$ | 100.3 | 0.957 |

*3.5. Regeneration of ZSM-5/AC.* Desorption of $Pb^{2+}$ ions and revival of ZSM-5/AC studies were carried out to investigate the reusability capacity of ZSM-5/AC. Desorption studies were performed with two desorbing agents such as 0.1 M $CH_3COOH$ and 0.1 M HCl. Initially, the fixed-bed column

Table 4: Yoon-Nelson model parameters for the removal of $Pb^{2+}$ ions by ZSM-5/AC.

| Parameter | | $K_{YN}$ ($min^{-1}$) | $\tau$ (min) | $R^2$ |
|---|---|---|---|---|
| Rate of flow | 2 mL/min | 0.954 | 222.3 | 0.993 |
| | 4 mL/min | 0.977 | 182.6 | 0.965 |
| | 6 mL/min | 0.987 | 110.3 | 0.989 |
| Bed depth | 2 cm | 0.954 | 222.3 | 0.993 |
| | 4 cm | 0.979 | 304.9 | 0.984 |
| | 6 cm | 0.986 | 413.7 | 0.971 |
| Preliminary concentration | 250 mg $L^{-1}$ | 0.986 | 413.7 | 0.971 |
| | 500 mg $L^{-1}$ | 0.963 | 283.9 | 0.976 |
| | 750 mg $L^{-1}$ | 0.953 | 171.3 | 0.955 |

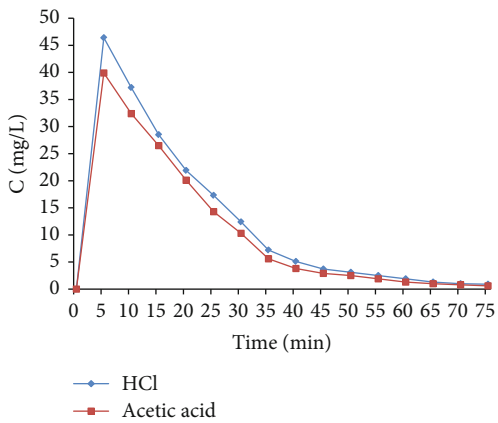


Figure 5: Desorption curves of lead ions with respect to time from ZSM-5/AC.

was packed with $Pb^{2+}$ ion-loaded ZSM-5/AC for 6 cm, and the desorbing agent was allowed to flow from the top of the column with a flow rate of 2 mL/min. The pH of the desorbing agents was pH 1.2 and 3.0, respectively, for 0.1 M HCl and 0.1 M $CH_3COOH$. The eluent was collected at the exit of the column at prefixed time intervals, and the amount of $Pb^{2+}$ ions desorbed was calculated using an atomic absorption spectrometer. Desorption of $Pb^{2+}$ ions versus time plot is represented in Figure 5. It can be observed that initially the amount of $Pb^{2+}$ ions in the eluent was found to be high and gradually decreased with an increase in time. The high amount of $Pb^{2+}$ ion concentration released at the initial time period is due to ion exchange with the $H^+$ ions of desorbing agents. The decrease in concentration with respect to time is due to exhaustion of $Pb^{2+}$ ions and regeneration of ZSM-5/AC. The maximum desorption efficiency of ZSM-5/AC was found to be 83% and 92%, respectively, for 0.1 M $CH_3COOH$ and 0.1 M HCl solutions. The higher efficiency observed for HCl over $CH_3COOH$ was due to the strength of the acids. Stronger acids exhibit higher desorption efficiency due to the quick release of $H^+$ ions compared to weak acids such as $CH_3COOH$. The high revival efficiency exhibited by ZSM-5/AC was due to the exchange of $Pb^{2+}$ ions with hydronium ions. The ion exchange capability of zeolites helped in the effective regeneration of the composite materials. These results suggest that ZSM-5/AC could be efficiently considered in repeated cycles for the elimination of $Pb^{2+}$ ions from an aqueous solution.

Table 5: Comparison of loading capacity of various adsorbents towards $Pb^{2+}$ ions reported in literature.

| Adsorbent | Loading capacity (mg $g^{-1}$) | Reference |
|---|---|---|
| Ferrihydrite coated brick | 6.74 | [42] |
| Titanosilicate ETS-10 | 30.2 | [43] |
| Brick kiln waste | 81.5 | [44] |
| Nanomagnetite-loaded polyhydrogel | 14.4 | [45] |
| Nanostructured $\gamma$-alumina | 49.6 | [46] |
| Modified sugarcane bagasse | 73.7 | [47] |
| Watermelon rind | 55.0 | [16] |
| ZSM-5/AC | 213.3 | This study |

*3.6. Adsorption Potential.* The supreme adsorption potential of ZSM-5/AC towards $Pb^{2+}$ ions was calculated to be 213.3 mg $g^{-1}$ which was considered to be very significant in comparison to many other reported adsorbents in the literature (Table 5). The higher loading potential was due to the combined effect exhibited by porous ZSM-5 and activated carbon materials. The adsorption of $Pb^{2+}$ ions onto ZSM-5/AC could be due to pore adsorption as well as binding onto acidic sites present on the surface of the activated carbon.

## 4. Conclusion

This study utilized the ZSM-5/AC composite as an adsorbent for the removal of $Pb^{2+}$ ions from an aqueous solution and explored its potential in a fixed-bed column. It was observed that low flow rate, higher bed height, and lower initial inlet concentration yielded maximum removal efficiency for $Pb^{2+}$ ion removal by ZSM-5/AC. The breakthrough curves were predicted with linear regression models such as the Adams-Bohart, Thomas, and Yoon-Nelson models. Based on the coefficients of correlation and relative constants, all three models were found to fit and well describe the breakthrough curves. Desorption and regeneration studies suggested that ZSM-5/AC could be repeatedly used for several cycles. These results conclude that ZSM-5/AC is a prolific composite material for the sequestration of $Pb^{2+}$ ions from water streams.

## Data Availability

All the required data are available in the manuscript itself.

## Conflicts of Interest

The authors declare that they have no conflicts of interest.

## Acknowledgments

Dr. Ivan Rico thanks the Department of Chemical Engineering, Central University "Marta Abreu" of Las Villas, Cuba, for providing the necessary facilities to carry out the investigations.

## References

[1] M. Basu, A. K. Guha, and L. Ray, "Adsorption of lead on cucumber peel," *Journal of Cleaner Production*, vol. 151, pp. 603–615, 2017.

[2] A. Bożęcka, M. Orlof-Naturalna, and S. Sanak-Rydlewska, "Removal of lead, cadmium and copper ions from aqueous solutions by using ion exchange resin C 160," *Gospodarka Surowcami Mineralnymi.*, vol. 32, no. 4, pp. 129–140, 2016.

[3] A. Peigneux, J. D. Puentes-Pardo, A. B. Rodríguez-Navarro, M. T. Hincke, and C. Jimenez-Lopez, "Development and characterization of magnetic eggshell membranes for lead removal from wastewater," *Ecotoxicology and Environmental Safety*, vol. 192, no. 2020, article 110307, 2020.

[4] J. Beltrán Heredia and J. Sánchez Martín, "Removing heavy metals from polluted surface water with a tannin-based flocculant agent," *Journal of Hazardous Materials*, vol. 165, no. 1-3, pp. 1215–1218, 2009.

[5] Q. Chang and G. Wang, "Study on the macromolecular coagulant PEX which traps heavy metals," *Chemical Engineering Science*, vol. 62, no. 17, pp. 4636–4643, 2007.

[6] M. K. Uddin, "A review on the adsorption of heavy metals by clay minerals, with special focus on the past decade," *Chemical Engineering Journal*, vol. 308, pp. 438–462, 2017.

[7] A. Mellah and D. Benachour, "Solvent extraction of heavy metals contained in phosphoric acid solutions by 7-(4-ethyl-1-methyloctyl)-8-hydroxyquinoline in kerosene diluent," *Hydrometallurgy*, vol. 81, no. 2, pp. 100–103, 2006.

[8] Q. Chen, Y. Yao, X. Li, J. Lu, Z. Zhou, and Z. Huang, "Comparison of heavy metal removals from aqueous solutions by chemical precipitation and characteristics of precipitates," *Journal of Water Process Engineering*, vol. 26, pp. 289–300, 2018.

[9] T. Tran, K. Chiu, C. Lin, and H. Leu, "Electrochemical treatment of wastewater: selectivity of the heavy metals removal process," *International Journal of Hydrogen Energy*, vol. 42, no. 45, pp. 27741–27748, 2017.

[10] H. Qin, T. Hu, Y. Zhai, N. Lu, and J. Aliyeva, "The improved methods of heavy metals removal by biosorbents: a review," *Environmental Pollution*, vol. 258, article 113777, 2020.

[11] C. F. Carolin, P. S. Kumar, A. Saravanan, G. J. Joshiba, and M. Naushad, "Efficient techniques for the removal of toxic heavy metals from aquatic environment: a review," *Journal of Environmental Chemical Engineering*, vol. 5, no. 3, pp. 2782–2799, 2017.

[12] L. Joseph, B. Jun, J. R. V. Flora, C. M. Park, and Y. Yoon, "Removal of heavy metals from water sources in the developing world using low- cost materials: a review," *Chemosphere*, vol. 229, pp. 142–159, 2019.

[13] R. Arora, "Adsorption of Heavy Metals-A Review," *Materials Today: Proceedings*, vol. 18, pp. 4745–4750, 2019.

[14] E. Da'na, "Adsorption of heavy metals on functionalized-mesoporous silica: a review," *Microporous and Mesoporous Materials*, vol. 247, pp. 145–157, 2017.

[15] N. K. Soliman and A. F. Moustafa, "Industrial solid waste for heavy metals adsorption features and challenges; a review," *Journal of Materials Research and Technology*, vol. 9, no. 5, pp. 10235–10253, 2020.

[16] R. Lakshmipathy and N. C. Sarada, "A fixed bed column study for the removal of $Pb^{2+}$ ions by watermelon rind," *Environmental Science: Water Research & Technology*, vol. 1, no. 2, pp. 244–250, 2015.

[17] M. Ozacar and I. A. Sengil, "Adsorption of acid dyes from aqueous solutions by calcined alunite and granular activated carbon," *Adsorption*, vol. 8, no. 4, pp. 301–308, 2002.

[18] H. Adel Niaei and M. Rostamizadeh, "Adsorption of metformin from an aqueous solution by Fe-ZSM-5 nano-adsorbent: isotherm, kinetic and thermodynamic studies," *The Journal of Chemical Thermodynamics*, vol. 142, article 106003, 2020.

[19] T. Sheela, Y. A. Nayaka, R. Viswanatha, S. Basavanna, and T. G. Venkatesha, "Kinetics and thermodynamics studies on the adsorption of Zn(II), Cd(II) and Hg(II) from aqueous solution using zinc oxide nanoparticles," *Powder Technology*, vol. 217, pp. 163–170, 2012.

[20] N. Salman Tabrizi and M. Yavari, "Fixed bed study of nitrate removal from water by protonated cross-linked chitosan supported by biomass-derived carbon particles," *Journal of Environmental Science and Health, Part-A*, vol. 55, no. 7, pp. 777–787, 2020.

[21] G. Hanbali, S. Jodeh, O. Hamed et al., "Magnetic multiwall carbon nanotube decorated with novel functionalities: synthesis and application as adsorbents for lead removal from aqueous medium," *PRO*, vol. 8, no. 8, p. 986, 2020.

[22] M. A. Elias, T. Hadibarata, and P. Sathishkumar, "Modified oil palm industry solid waste as a potential adsorbent for lead removal," *Environmental Chemistry and Ecotoxicology*, vol. 3, no. 2021, pp. 1–7, 2021.

[23] L. P. Lingamdinne, K. R. Vemula, Y. Y. Chang, J. K. Yang, R. R. Karri, and J. R. Koduru, "Process optimization and modeling of lead removal using iron oxide nanocomposites generated from bio-waste mass," *Chemosphere*, vol. 243, article 125257, 2020.

[24] C. Bläker, C. Pasel, M. Luckas, F. Dreisbach, and D. Bathen, "A study on the load-dependent enthalpy of adsorption and interactions in adsorption of C5 and C6 hydrocarbons on zeolites 13X and ZSM-5 and an activated carbon," *Microporous and Mesoporous Materials*, vol. 302, article 110205, 2020.

[25] A. Kostyniuk, D. Key, and M. Mdleleni, "1-hexene isomerization over bimetallic M-Mo-ZSM-5 (M: Fe, Co, Ni) zeolite catalysts: effects of transition metals addition on the catalytic performance," *Journal of the Energy Institute*, vol. 93, no. 2, pp. 552–564, 2020.

[26] A. López-Martín, A. Caballero, and G. Colón, "Structural and surface considerations on Mo/ZSM-5 systems for methane dehydroaromatization reaction," *Molecular Catalysis*, vol. 486, article 110787, 2020.

[27] P. K. Pandey, S. K. Sharma, and S. S. Sambi, "Removal of lead(II) from waste water on zeolite-NaX," *Journal of Environmental Chemical Engineering*, vol. 3, no. 4, pp. 2604–2610, 2015.

[28] R. Sabarish and G. Unnikrishnan, "Polyvinyl alcohol/carboxymethyl cellulose/ZSM-5 zeolite biocomposite membranes for dye adsorption applications," *Carbohydrate Polymers*, vol. 199, pp. 129–140, 2018.

[29] Z. Zhang, J. Wu, B. Li, H. Xu, and D. Liu, "Removal of elemental mercury from simulated flue gas by ZSM-5 modified with

Mn-Fe mixed oxides," *Chemical Engineering Journal*, vol. 375, article 121946, 2019.

[30] P. J. Isaac, S. Amaravadi, M. S. M. Kamil, K. K. Cheralathan, and R. Lakshmipathy, "Synthesis of zeolite/activated carbon composite material for the removal of lead (II) and cadmium (II) ions," *Environmental Progress Sustainable energy*, vol. 38, no. 6, article e13246, 2019.

[31] S. S. Baral, N. Das, T. S. Ramulu, S. K. Sahoo, S. N. Das, and G. R. Chaudhury, "Removal of Cr(VI) by thermally activated weed *Salvinia cucullata* in a fixed-bed column," *Journal of Hazardous Materials*, vol. 161, no. 2-3, pp. 1427–1435, 2009.

[32] A. A. Ahmad and B. H. Hameed, "Fixed-bed adsorption of reactive azo dye onto granular activated carbon prepared from waste," *Journal of Hazardous Materials*, vol. 175, no. 1-3, pp. 298–303, 2010.

[33] P. A. Kumar and S. Chakraborty, "Fixed-bed column study for hexavalent chromium removal and recovery by short- chain polyaniline synthesized on jute fiber," *Journal of Hazardous Materials*, vol. 162, no. 2-3, pp. 1086–1098, 2009.

[34] V. Vinodhini and N. Das, "Packed bed column studies on Cr (VI) removal from tannery wastewater by neem sawdust," *Desalination*, vol. 264, no. 1-2, pp. 9–14, 2010.

[35] G. Bohart and E. Q. Adams, "Some aspects of the behavior of charcoal with respect to chlorine.1," *Journal of American Chemical Society*, vol. 42, no. 3, pp. 523–544, 1920.

[36] B. J. Clark, W. W. Eckenfelder, and J. M. Morriss, *Industrial Water Pollution Control*, McGraw Hill, USA, 1989.

[37] M. Lehmann, A. I. Zouboulis, and K. A. Matis, "Modelling the sorption of metals from aqueous solutions on goethite fixed-beds," *Environmental Pollution*, vol. 113, no. 2, pp. 121–128, 2001.

[38] H. C. Thomas, "Heterogeneous ion exchange in a flowing system," *Journal of American Chemical Society*, vol. 66, no. 10, pp. 1664–1666, 1944.

[39] Y. H. Yoon and J. H. Nelson, "Application of gas adsorption kinetics I. A theorical model for respirator cartridge service life," *American Industrial Hygiene Association Journal*, vol. 45, no. 8, pp. 509–516, 1984.

[40] A. P. Lim and A. Z. Aris, "Continuous fixed-bed column study and adsorption modeling: removal of cadmium (II) and lead (II) ions in aqueous solution by dead calcareous skeletons," *Biochemical Engineering Journal*, vol. 87, pp. 50–61, 2014.

[41] M. A. Stylianou, M. P. Hadjiconstantinou, V. J. Inglezakis, K. G. Moustakas, and M. D. Loizidou, "Use of natural clinoptilolite for the removal of lead, copper and zinc in fixed bed column," *Journal of Hazardous Materials*, vol. 143, no. 1–2, pp. 575–581, 2007.

[42] O. Allahdin, J. Mabingui, M. Wartel, and A. Boughriet, "Removal of $Pb^{2+}$ ions from aqueous solutions by fixed-BED column using a modified brick: (micro)structural, electrokinetic and mechanistic aspects," *Applied Clay Science*, vol. 148, pp. 56–67, 2017.

[43] L. Lv, K. Wang, and X. S. Zhao, "Effect of operating conditions on the removal of $Pb^{2+}$ by microporous titanosilicate ETS-10 in a fixed-bed column," *Journal of Colloid and Interface Science*, vol. 305, no. 2, pp. 218–225, 2007.

[44] S. S. Metwally, E. A. el-Sherief, and H. S. Mekhamer, "Fixedbed column for the removal of cesium, strontium, and lead ions from aqueous solutions using brick kiln waste," *Separation Science and Technology*, vol. 55, no. 4, pp. 635–647, 2020.

[45] N. Sharma and A. Tiwari, "Assessment of $Pb^{2+}$ions removal efficiency of nanomagnetite-loaded poly (acrylamide-co-acrylic acid) hydrogel in fixed-bed microcolumn from aqueous solution," *Desalination and Water Treatment*, vol. 57, no. 8, pp. 3642–3653, 2016.

[46] Z. Saadi, R. Saadi, and R. Fazaeli, "Fixed-bed adsorption dynamics of Pb (II) adsorption from aqueous solution using nanostructured $\gamma$-alumina," *Journal of Nanostructure in Chemistry*, vol. 3, no. 1, p. 48, 2013.

[47] W. L. Xiong, J. Zhang, J. X. Yu, and R.-a. Chi, "Competitive adsorption behavior and mechanism for $Pb^{2+}$ selective removal from aqueous solution on phosphoric acid modified sugarcane bagasse fixed-bed column," *Process Safety and Environmental Protection*, vol. 124, pp. 75–83, 2019.